Cranfield University

School of Industrial and Manufacturing Science

Advanced Materials Department

PhD Thesis

Academic years 1996-2000

Alexandros A. Skordos

Modelling and monitoring of resin transfer moulding

Supervisor: Dr Ivana K. Partridge

September 2000

ABSTRACT

Modelling and monitoring tools appropriate for the resin transfer moulding composites manufacturing route were developed in this study. A simulation of the curing stage of the process based on a finite elements solution of the non-linear heat conduction equation was implemented. The simulation involved appropriate submodels for the incorporation of thermal properties and cure kinetics. A novel non-parametric procedure which utilises interpolation applied directly to experimental kinetics data proved adequate for the simulation of chemical and structural phenomena occurring during the cure. The application of the heat transfer model was successful, the magnitude of thermal gradients was shown to be significant and the character of degree of cure gradients temporary. An inversion of the heat transfer simulation based on genetic algorithms enabled an optimisation of the cure process parameters to be performed. The heat transfer simulation was combined with thermal monitoring results in order to achieve an extension of the local temperature measurements to the whole component. This combined scheme reproduced successfully the temperature and degree of cure distributions. The same approach was implemented with similar outcomes using artificial cure monitoring results.

Impedance cure monitoring was used in order to follow in real time the reaction progress. An interpretation was found for the manifestation of vitrification in the impedance signals. A new equivalent circuit representing accurately the behaviour of the resin system investigated was developed. A methodology which correlates the progress of cure with the imaginary impedance spectrum evolution was established.

Dielectric flow monitoring techniques appropriate for the filling stage of resin transfer moulding were devised. Lineal sensors enabled monitoring of the progress of filling to be made in both conductive and non-conductive reinforcements.

Στα λυγισμένα ράφια της αβάσταχτης μαρτυρίας
Με πλάνες και αλήθειες δέθηκα
Σαν να περίμενα το δαίμονά μου
Να βάλει κάποια τάξη

ACKNOWLEDGEMENTS

I am very grateful to my supervisor Dr I. K. Partridge for her support, guidance and continuous effort to improve this work, Prof. C. B. Bucknall for his help in crucial moments, and Dr P. I. Karkanas, Dr G. M. Maistros and Prof. H. Block for the several stimulating discussions on various aspects of this work.

I would like to thank Dr D. J.-P. Turmel for introducing me to the technique of resin transfer moulding and Mr J. Hurley for the technical assistance that made part of the experimental work possible.

I would especially like to thank Kiki and Antonis Skordos for their constant encouragement and financial backing and Theophilos Skordos for the moral support and the continuous provision of up-to-date computer hardware.

The funding for this work was provided by the EU, via a Marie Curie Fellowship, and by the DTI, via an IMI initiative project.

CONTENTS

LIST OF FIGURES

LIST OF TABLES

NOTATION

A) Symbols (by order of appearance)

α	fractional conversion or degree of cure
K_o	reaction rate constant
K_1	reaction rate constant
m	exponent of the cure kinetics model
n	exponent of the cure kinetics model
$n1$	exponent of the cure kinetics model
$n2$	exponent of the cure kinetics model
α_{max}	maximum fractional conversion at a specific temperature
T	temperature
T_{go}	the glass transition temperature of the unreacted material
$T_{g\infty}$	the glass transition temperature when the reaction is complete
$K_{overall}$	rate constant of the overall reaction
K_{diffl}	rate constant of the diffusion process
K_{chem}	rate constant of the chemically controlled reaction
$\vec{q}_{fluid}$	fluid flux
$\overline{S}$	permeability of a porous medium
p	pressure
$\vec{u}$	resin velocity
ρ	density
$\overline{K}$	permeability of a porous medium
μ	resin viscosity
γ_s	surface tension
θ	contact angle
D_t	coefficient characteristic of the fibre bundle
c_p	specific heat capacity
S_i	heat generation per unit volume per unit time

$\vec{q}_{cd}$	heat conduction through a surface per unit area per unit time
$\vec{q}_r$	heat radiation through a surface per unit area per unit time
$[K]$	thermal conductivity tensor
ρ_r	resin density
ρ_f	fibre density
c_{pr}	resin specific heat capacity
c_{pf}	fibre specific heat capacity
H_{tot}	total heat of reaction
v_f	fibre volume fraction
T_r	resin temperature
T_f	fibre temperature
K_r	resin thermal conductivity
K_f	fibre thermal conductivity
h_v	heat transfer exchange coefficient
K_D	dispersion contribution to the thermal conductivity
w_f	fibre weight fraction
V	speed of a fibre layer during consolidation
A	cross sectional area
p_o	external pressure
p_i	pressure on the resin front in the bleeder
h_b	thickness of permeated bleeder area
$\overline{K}_b$	bleeder permeability
W	width of the channel between fibre layers
x_l	half of the length of the channel between fibre layers
p_h	pressure at the centre of the channel between fibre layers
σ	pressure applied to the fibre network
$\overline{p}_r$	pressure applied to the resin

v_o	initial fibre volume fraction
u_x	velocity component in the x-axis
u_y	velocity component in the y-axis
u_z	velocity component in the z-axis
$\overline{K}_{xx}$	thermal conductivity in the x-axis
$\overline{K}_{yy}$	thermal conductivity in the y-axis
$\overline{K}_{zz}$	thermal conductivity in the z-axis
$\vec{k}$	body forces
v_r	resin volume fraction
u_r	velocity in the radial direction
$\dot{m}_b$	mass backflow
α_v	volumetric expansion coefficient
U	pultrusion speed
γ	volumetric shrinkage
k_b	compressibility
τ_v	shear stress
f_c	friction coefficient
$\vec{t}$	surface stress
ψ	pultrusion angle
ϕ	filament winding angle
σ_θ	hoop stress
σ_r	radial stress
σ_f	stress on the fibre
u_f	fibre velocity relative to resin
u_r	resin velocity relative to the fibre
$\Delta\varepsilon$	strain change
E_f	fibre modulus

Δw	fibre displacement induced by consolidation
σ_{fr}	radial stresses on the fibre
$\sigma_{\theta r}$	hoop stresses on the fibre
ε_r	radial strain
ε_θ	hoop strain
S_{ij}	fibre network compliance
σ_r^k	total radial stresses after winding the k layer
σ_θ^k	total hoop stresses after winding the k layer
σ_r^∞	steady state radial stress
σ_θ^∞	steady state hoop stress
σ_r^t	transient radial stress
σ_θ^r	transient hoop
w^k	fibre displacement after winding the k layer
w^∞	steady state fibre displacement
w^t	transient fibre displacement
E_r	radial modulus
$\nu_{r\theta}$	Poissons' ratio
M'	real modulus corresponding to the wave mode used
M''	imaginary modulus corresponding to the wave mode used
ω	frequency
c	ultrasound velocity
α_u	attenuation of the ultrasonic wave
A_r	absorbance of radiation
J_o	incident radiation intensity
J	transmitted radiation intensity
κ	molar extinction coefficient
C	concentration
d	thickness

d_p	penetration depth of the evanescence field
λ	wave length
θ_i	incidence angle
η_1	refractive index of the transmitting medium
η_2	refractive index of the reflecting medium
ε^*	complex dielectric constant
ε_∞	permittivity at very high frequencies
ε_r	permittivity at very low frequencies
τ	macroscopic relaxation time
τ_m	molecular relaxation time
$\tilde{\sigma}$	conductivity
q	charge
u_{mi}	mobility
r_i	ion radius
ε''	dielectric loss
ε''_d	dipolar contribution to the dielectric loss
ε_o	free space permittivity
ε'_x	measured component of the dielectric constant
ε''_x	measured component of the dielectric constant
$tan\,\delta$	dissipation factor
t_b	blocking layer thickness
C_{sd}	capacitance corresponding to permanent dipoles
R_{sd}	resistance corresponding to permanent dipoles
C_{id}	capacitance corresponding to induced dipoles
R_i	migrating charges resistor
C_e	electrode polarisation capacitor
Z	complex impedance

Z'	real impedance
Z''	imaginary impedance
C_o	free space capacitance
τ_∞	average relaxation time at the completion of the cure
τ_o	relaxation time at the beginning of the cure
α_{max}	maximum degree of cure at the curing temperature des 109
$\tilde{\rho}$	resistivity
$\tilde{\rho}_o$	resistivity of the unreacted resin
$\tilde{\rho}_{max}$	resistivity of the fully reacted resin.
$\dot{Q}$	heat generation
Ω	domain of a heat transfer problem
$\tilde{T}(\hat{r},t)$	predefined temperature
$\tilde{q}(\hat{r},t)$	predefined heat flux
$\hat{n}$	surface vector
S	boundary of a heat transfer problem
h	heat transfer coefficient
T_∞	temperature of the fluid at a convective boundary
S_1	boundary of the predefined temperature condition
S_2	boundary of the predefined heat flux condition
S_3	boundary of the convection boundary condition
T_o	initial temperature
$\tilde{S}_{ij}$	Interfacial boundary
Ra	Rayleigh number
α_v	volumetric thermal expansion
g	gravitational acceleration
R_L	residual error
R_B	residual error
$\bar{T}$	temperature approximation

W	weighting function
$\overline{W}$	weighting function
N_i	interpolation function
$\overline{\Omega}_e$	closed domain corresponding to an element
Ω_e	open domain corresponding to an element
δ_{ij}	Kronecker's function
G	number of nodes
a_i	coefficient of the approximation function
Δt	time step
$\tilde{\theta}$	theta parameter for the time discretisation
$[L]$	matrix of the finite element formulation
$[F]$	matrix of the finite element formulation
$[M]$	matrix of the finite element formulation
K_{xy}	shear conductivity
$S(t)$	DSC signal
$B(t)$	DSC baseline
t_f	final time
α_{vr}	volumetric thermal expansion coefficient of the resin
α_{vf}	volumetric thermal expansion coefficient of the fibre
ρ_i	density at the end of the i^{th} time step
T_s	MDSC sample temperature
b	slope of the MDSC underlying linear segment
A_T	amplitude of modulation
C_s	sample heat capacity
C_r	reference heat capacity
f	reaction or transition heat flux
$A_{\Delta T}$	amplitude of the temperature difference in MDSC

c_{pG}	specific heat capacity of the glass fibre
c_{pC}	specific heat capacity of the carbon fibre
I_0	modified Bessel function
ber	real part of the modified Bessel function
bei	imaginary part of the modified Bessel function
K_l	longitudinal conductivity
K_t	transverse conductivity
K_{fl}	fibre longitudinal conductivity
K_{fr}	fibre radial conductivity
Z_{CPE}	impedance of the constant phase element
A_e	coefficient electrode polarisation CPE
$D\log f$	Difference between the imaginary impedance maximum and minimum frequencies
f_{max}	frequency of the imaginary impedance maximum
f_{min}	frequency of the imaginary impedance minimum
ω_{max}	angular frequency of the imaginary impedance maximum
ω_{min}	angular frequency of the imaginary impedance minimum
z_s	impedance per unit length of the substrate
z_f	impedance per unit length of the adhesive
z_g	impedance per unit length of the film
z_a	impedance per unit length of the entrapped air
z	impedance per unit length
Z_{sensor}	impedance of the sensor
l_w	length of the covered by resin part
z_w	impedance per unit length of the wetted part
z_d	impedance per unit length of the dry part
Y_{sensor}	admittance of the sensor
Y_{dry}	admittance of the dry sensor

Y_{cov}	admittance of the partially covered by resin sensor
Z''_{min}	minimum value of the imaginary impedance during the cure
Z''_{max}	maximum value of the imaginary impedance during the cure
z_c	impedance per unit length of the insulating layer of the sensing wire
t_c	curing completion time
$Par1$	parameter of the inverse solution
$Par2$	parameter of the inverse solution
$Par3$	parameter of the inverse solution
$Par4$	parameter of the inverse solution
$Par5$	parameter of the inverse solution

B) Abbreviations (by order of appearance)

RTM	Resin Transfer Moulding
RIFT	Resin Infusion under Flexible Tooling
SCRIMP	Seeman Composites Resin Infusion Process
SRIM	Structural Injection Reaction Moulding
DGEBF	DiGlycidylEther of Bisphenol A
MDA	MethyleneDiAniline
DGEBA	DiGlycidylEther of Bisphenol A
VARI	Vacuum Assisted Resin Infusion
DGEPA	DiGlycidylEther of Para-Aminophenole
DSC	Differential Scanning Calorimetry
MDSC	Modulated Differential Scanning Calorimetry
CPE	Constant Phase Element

Chapter One

1 Introduction

1.1 Motivation and goals

Advanced composite materials comprising polymeric matrices and continuous reinforcements were introduced in the early 1960s. They offered a very attractive combination of material properties, in terms of structural design, namely high stiffness and strength with low specific weight. The demand for high performance and/or reduced weight led the military aircraft industry to take up composites as materials offering new design possibilities. As a result, the advanced composites research and development focused on material performance improvements.

In recent years, drastic cutbacks in defence spending increased the criticality of cost in the military aircraft industry. Simultaneously the world demand for commercial and civil aircraft increased as a result of the general economic growth and globalisation and opportunities for advanced composites use in the commercial automotive sector begun to be recognised. These events have changed the focus of composites research and development from increased performance at lower weight to increased product quality at a lower cost.

In this context the need for predictive modelling and for in-situ real time monitoring of the manufacturing process has arisen and been met by the development of a family of appropriate techniques. The modelling of composites manufacturing has been

investigated extensively (see chapter 2) and monitoring methods, such as dielectric and fibre optic cure monitoring, begun to be tested in an industrial environment (see chapter 3). At the same time composite manufacturing techniques, such as liquid composite moulding (LCM), having a greater potential for automation and control, begun to be considered advantageous in comparison with the conventional labour intensive production route of laying up-autoclaving.

Currently, resin transfer moulding (RTM) is the most widely used liquid composite moulding method. The state-of-the-art in RTM modelling and monitoring can be summarised as follows:

- Flow phenomena occurring during resin transfer moulding have been studied and modelled extensively. In contrast, the curing stage of the process has not received analogous attention (see chapter 2).
- Cure monitoring techniques have been adapted for use in RTM. The inherent drawbacks of local measurement character and inadequate correlation between monitoring signals and progress of curing under non-isothermal conditions have not been resolved (see chapter 3).
- Flow monitoring techniques have begun to be developed, but an industrially realisable method has yet to be established (see chapter 3).

The present study aims to address these matters. A heat transfer simulation appropriate for RTM curing, with minimal assumptions as far as the material thermal properties, the cure kinetics and the problem dimensionality are concerned, will be developed and applied. Impedance cure monitoring will be investigated and methods which connect monitoring signals with the progress of the curing reaction and with structural phenomena, will be devised. Flow monitoring techniques using dielectric sensors will be developed and tested. The problem of monitoring signal locality will be addressed and a monitoring-modelling scheme, which enables the extension of local cure and thermal monitoring results to the whole curing component to be made, will be formed and validated.

The focus of the work is on the RTM process, however, some of the tools can be applied to a range of composite manufacturing processes. The cure kinetics and the thermal properties models are of a generic nature and can be equally utilised within models of any other manufacturing route. Similarly, the work on cure monitoring concerns

thermosetting systems in general and as such can find use in any relevant application. The flow monitoring devices are appropriate for any liquid moulding process. The heat transfer simulation as well as the combined monitoring-modelling scheme can be adapted for use in any other batch composite production method.

1.2 Road map

The main body of this study is divided into four parts.

- The first part, which consists of chapters 2 and 3, reviews the ***state of the art of composites manufacturing modelling and monitoring***. Chapter 2 summarises modelling efforts on heat transfer and flow phenomena occurring during liquid moulding, autoclaving, pultrusion and filament winding. Chapter 3 describes the up to date application of acoustic, spectroscopic and dielectric techniques to cure monitoring and reviews the relatively new field of flow monitoring.
- The second part (chapters 4-7) describes the ***development and application of a finite element heat transfer model appropriate for resin transfer moulding curing***. In chapter 4 the background of the modelling method is discussed, its implementation in a computer code is outlined and validation of the computer code is performed. Chapter 5 describes and evaluates a novel cure kinetics modelling method, which has been used as a kinetics submodel in the general heat transfer model. Chapter 6 presents the thermal properties submodels used in the model. In chapter 7 experimental results of the temperature distribution during RTM curing of composites and its evolution during the cure are presented and compared with simulation results in order to validate the heat transfer model. The simulation is used to study the temperature, the degree-of-cure and the thermal gradient distributions during the cure of carbon/epoxy and glass/epoxy composites.
- The third part (chapters 8 and 9) concerns experimental and development work performed in the area of ***process monitoring***. In chapter 8 results from the application of impedance monitoring to resin cure and advancements concerning the identification of vitrification and the measurement of the progress of reaction using this technique are presented. In chapter 9 the development and application of flow monitoring devices based on dielectric sensing are described.

- The fourth part (chapter 10) concerns the application of ***inverse heat transfer modelling to composite curing***. In this chapter an inversion procedure based on genetic algorithms is described and results from its application to both process design and process control are presented.

In chapter 11 an overall discussion of the main results and outcomes of the study is presented and in chapters 12 and 13 the main conclusions together with some suggestions for further investigation arising from this research are summarised.

Chapter Two

2 Cure and flow modelling in the processing of thermosetting composites

2.1 Introduction

The main phenomena governing composites production are flow through porous media, conduction heat transfer and exothermic curing reaction.

Flow through porous media occurs during impregnation in *liquid moulding* and *pultrusion* and during consolidation in *autoclaving* and *filament winding* and it governs:

- the duration of the impregnation or consolidation stage;
- the formation of voids and
- the creation of macroscopic dry spots.

Heat conduction and the exothermic reaction take place during the curing stage of all processes, usually after flow completion or in some cases alongside with flow and they control:

- the duration of the curing stage;
- the uniformity of final degree of cure;
- the existence of thermal gradients during the cure which subsequently governs the built up of residual stresses and
- the extent of exothermic phenomena which can give rise to degradation.

Accordingly flow and heat transfer-cure models become important in the context of cost-effective manufacturing and quality control. Their role within the manufacturing process is dual:

I. As purely predictive tools during the design of the process. In that case process parameters can be adjusted and optimised using simulation instead of experiments.

II. Within a scheme which combines process monitoring and modelling in order to achieve control of the process parameters.

In this chapter the main modelling principles for impregnation/consolidation and heat transfer/cure modelling are reviewed, and implementation issues relevant to each of the four main composite manufacturing routes (liquid moulding, autoclaving, pultrusion and filament winding) are presented. The modelling of the cure reaction is carried out with general methodologies which are not specific to the manufacturing route, therefore is reviewed independently at the beginning of the chapter. In contrast, flow and heat transfer modelling, although based on similar basic principles, are adapted to each manufacturing route. Thus, the resulting different modelling methodologies are presented independently for each process.

2.2 Modelling of the curing reaction

The drive for cost-effectiveness in composite manufacturing has given a new impetus to the development of process models. An adequate model of cure kinetics is a primary component of thermosetting composites manufacturing simulations. In the case of heat transfer, cure kinetics provide information on the exothermic heat of reaction. That information is used directly in the formation of an appropriate heat balance. In general in models, including flow and consolidation, cure kinetics are used indirectly in the calculation of material properties (e.g. viscosity, heat capacity, density) which present a dependence on the state of the material as manifested by the progress of the reaction. Two main approaches used for cure kinetics can be distinguished: (i) phenomenological; and (ii) mechanistic modelling.

(i) Phenomenological or ***empirical*** models tend to ignore the chemical detail of the reacting system and to utilise approximate relationships, which usually resemble chemical kinetics expressions but have limited validity in rigorous chemistry terms.

The simplest empirical model used is the nth order rate equation:

$$\frac{d\alpha}{dt} = K_o(1-\alpha)^n \qquad \text{(Eq. 2.1)}$$

where α is the fractional conversion or degree of cure and K_o is the rate constant which is an Arrhenius function of temperature. Recent examples of the use of this type of model include resin kinetics behaviour during pultrusion (1-4) and kinetics of cure of maleic polyester resins (5). The nth order kinetics model predicts a maximum of the reaction rate at the beginning of the curing and cannot account for any autocatalytic effects.

In cases where autocatalytic behaviour has been observed the following expression has been utilised:

$$\frac{d\alpha}{dt} = K_o\alpha^m(1-\alpha)^n \qquad \text{(Eq. 2.2)}$$

Here the maximum reaction rate is shifted to intermediate conversions and the bell shape reaction rate versus time curve of an autocatalytic reaction at constant temperature can be reproduced. Such models have been applied to the cure of unsaturated polyester (6) and vinyl ester (7) resins.

Both the nth order and the autocatalytic model assume the existence of a single rate constant throughout the cure. Since these expressions are empirical and the events occurring during the cure complicate the reaction behaviour, the use of a single rate constant can lead to limited accuracy of models (8). Kamal's model involving two rate constants has been applied successfully to the modelling of a variety of resins (9, 10) and has been used as a cure kinetics submodel of heat transfer models for autoclave (11) and resin transfer moulding (12):

$$\frac{d\alpha}{dt} = (K_o + K_1\alpha^m)(1-\alpha)^n \qquad \text{(Eq. 2.3)}$$

An extension of Kamal's model that allows increased accuracy at the later stages of dynamic cure has been developed by Karkanas et al (13, 14):

$$\frac{d\alpha}{dt} = K_o(1-\alpha)^{n1} + K_1\alpha^m(1-\alpha)^{n2} \qquad \text{(Eq. 2.4)}$$

and applied successfully to the curing of Hexcel RTM6 resin.

(ii) Mechanistic modelling takes into account the balance of chemical species involved in the reaction to form mathematical relations connecting the reaction rate path to cure time and temperature.

A reaction scheme representing the curing mechanism is selected according to theoretical and experimental evidence and the reaction rate equations system is formed. The aim is to either simplify this scheme sufficiently to derive a closed form expression representing the cure kinetics (15) or to produce a more complicated system comprising just one differential equation and algebraic equations which are impossible to transform into closed form expressions (16, 17). An alternative approach is to integrate the entire system of differential rate equations directly, avoiding the adoption of simplifying assumptions (18).

Mechanistic models offer some advantages, in that they can be adapted easily for changes in the resin formulation and have a higher possibility of being valid outside the experimental envelope. However, the need to apply a multiple parameter estimation procedure for a non-analytical expression of resin kinetics makes mechanistic models unattractive. When the versatility of the model is compromised in order to obtain a simple kinetics expression, as is the case when mechanistic models are applied to composites manufacturing simulations (19, 20), it becomes equivalent to a phenomenological model. Furthermore, the most significant advantage of non-simplified mechanistic models, which is the ability to simulate systems in which the temperature history plays a role (i.e. the rate of reaction is not a unique function of fractional conversion and temperature), has not been demonstrated to be important for the currently utilized industrial composite resin systems within the temperature ranges and heating rates applied. In these cases phenomenological expressions and simplified mechanistic expressions have simulated the experimental data with satisfactory accuracy.

An additional characteristic of practical interest is the incorporation of diffusion limitation considerations in the kinetics modelling. The cure is a serial combination of species diffusion and molecular collisions. In the early stages of the reaction the diffusion is fast and the reaction is chemically controlled, but as the cure progresses and a rigid three-dimensional network is formed, mobility of the chemical species drops and diffusion

starts to influence the reaction kinetics. Near and above the glass transition diffusion becomes very slow and governs the curing reaction. Therefore, in order to achieve greater accuracy at high conversions, some modifications have been introduced in both phenomenological and mechanistic kinetic models. Two main approaches can be distinguished:

The first method is based on a modification of the actual kinetic expression in a way that results in lower reaction rates as the material approaches vitrification. That is achieved by including a term that does not allow fractional conversion to exceed the degree of cure associated with vitrification at the specific temperature. The resulting kinetic model is of the form:

$$\frac{d\alpha}{dt} = K_o(\alpha_{max} - \alpha)^n g(\alpha) \qquad \text{(Eq. 2.5)}$$

where α_{max} denotes the maximum fractional conversion at the specific temperature and $g(\alpha)$ is defined by the kinetic model type (21).

An expression that operates in a similar way results from normalisation of conversion in the autocatalytic model (7):

$$\frac{d\alpha}{dt} = K_o\left(1 - \frac{\alpha}{\alpha_{max}}\right)^n \left(\frac{\alpha}{\alpha_{max}}\right)^m \qquad \text{(Eq. 2.6)}$$

Such models require the incorporation of a relation connecting the maximum degree of cure to the temperature. An example of such a relation is Di Benedetto's model, which has been used for that purpose by Gonzalez et al (21):

$$\alpha_{max}(T) = \frac{T_{go}T_{g\infty}}{(T_{go} - T_{g\infty})T} - \frac{T_{g\infty}}{(T_{go} - T_{g\infty})} \qquad \text{(Eq. 2.7)}$$

Here T_{go} denotes the glass transition temperature of the unreacted material and $T_{g\infty}$ the glass transition temperature when the reaction is complete.

A second approach allowing for incorporation of diffusion in cure kinetics is based on the fact that the overall reaction is a serial combination of chemical reaction and diffusion. Thus, rate constants contained in the models can be modified as follows (15):

$$\frac{1}{K_{overall}} = \frac{1}{K_{diff}} + \frac{1}{K_{chem}} \qquad \text{(Eq. 2.8)}$$

where $K_{overall}$, K_{diff}, K_{chem} are the rate constants of the overall reaction, the diffusion process and the chemically controlled reaction respectively.

This approach is supplemented by a model relating the diffusion rate constant to the instantaneous temperature and state of the curing material, as expressed by either the degree of cure or the glass transition temperature.

Finally, cure kinetics applied to composites manufacturing simulations must be appropriate to allow other phenomena related to the presence of the fibre reinforcement. The reinforcement can influence the reaction either physically, by imposing mobility limitations (22), or chemically by interactions of the chemical species resulting from the surface treatment of the fibre with the resin (23).

Case studies carried out on specific reinforced thermosets have shown that the reaction mechanism is not altered by the presence of the reinforcement, although a difference in reaction rate at low temperatures has been observed (22, 24). In cases where this difference is significant, the kinetic model should be altered in order to include the interactions between resin and fibre.

2.3 Modelling of liquid moulding

The term liquid moulding represents a family of composites production techniques which have as their main features the use of dry reinforcement with an initial shape similar to that of the final product, and the injection of liquid resin into it.

Currently the most significant liquid moulding technique is resin transfer moulding (RTM). RTM is a three step process: (i) initially the dry reinforcement is placed into a rigid cavity; then (ii) impregnation by liquid resin takes place, either by vacuum or simultaneous application of pressure and vacuum; and eventually (iii) curing of the fully impregnated green composite is performed by heating up the tool if required (Fig. 2.1).

Other liquid moulding techniques include:

- Resin infusion under flexible tooling (RIFT), SCRIMP (Seeman composites resin infusion moulding process) and vacuum infusion where one side of the tooling is flexible, and the impregnation takes place while the reinforcement is loose. Directly after impregnation further consolidation occurs by the application of vacuum;
- Compression-RTM where one side of the tooling can move vertically and operates similarly to the flexible bag in the infusion techniques;

- Structural reaction injection moulding (SRIM) where highly reactive resins are mixed just before injection which takes place under high pressure in a very short time.

Modelling of RTM, and liquid moulding in general, has been focused on the impregnation stage and numerous recent studies exist on this subject. Other aspects of the process like the draping of the dry reinforcement and the reaction and heat transfer connected phenomena have not been studied to the same extent.

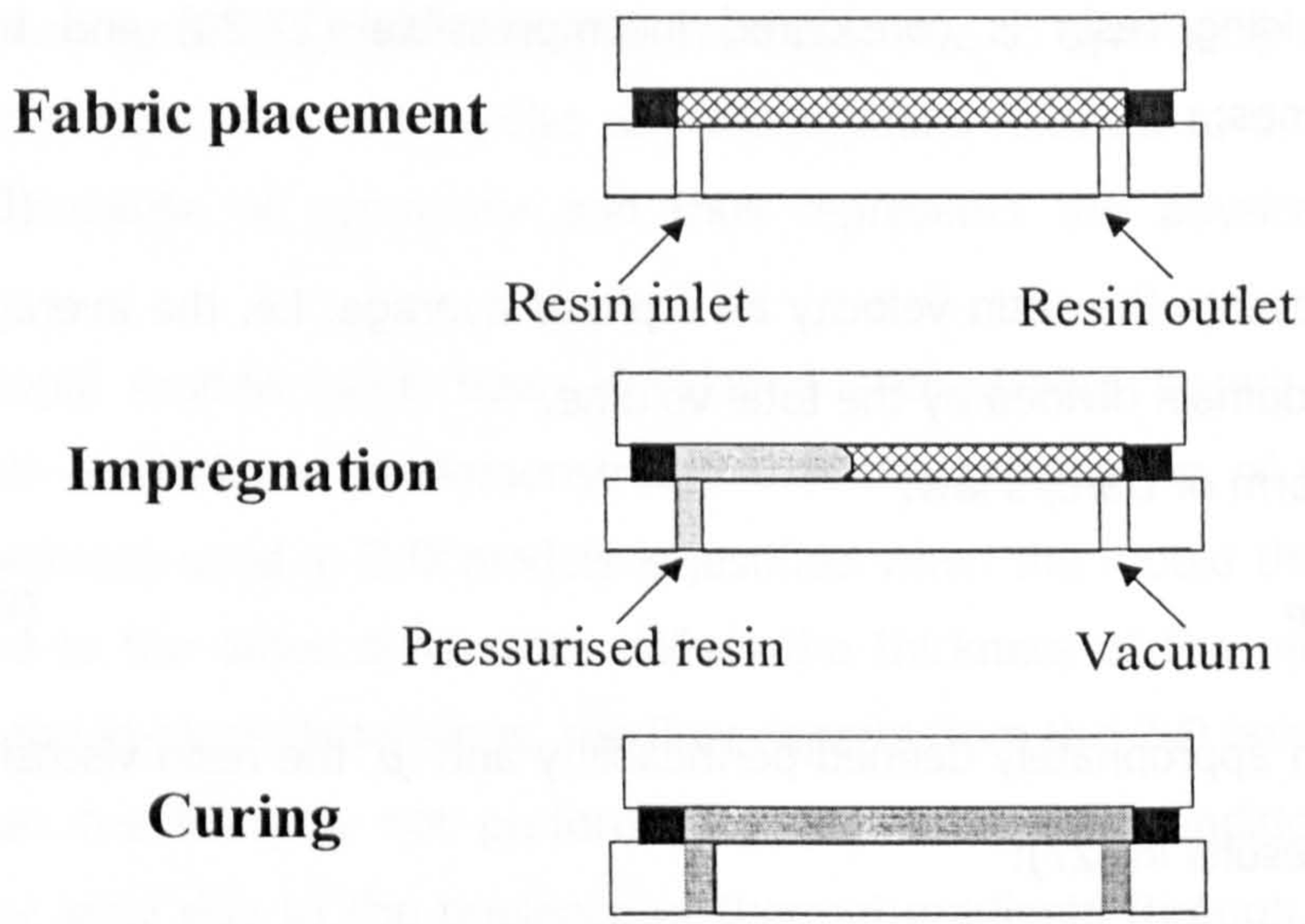

Fig.2.1 *Schematic representation of resin transfer moulding*

2.3.1 Modelling of resin flow through the dry reinforcement

Modelling studies of the impregnation stage of liquid moulding are based on application of Darcy's law, which describes fluid flow in porous media. Its general form is (25):

$$\vec{q}_{fluid} = -\overline{\overline{S}}\vec{\nabla}p \qquad \text{(Eq. 2.9)}$$

where $\vec{q}_{fluid}$ is the flux of fluid, S the permeability of the porous medium and p the pressure.

Darcy's law is the generalisation of a proportionality relation between pressure gradient and fluid flux that has been observed in one-dimensional ground-water flow when inertia effects are negligible compared to viscous flow. For some cases of simplified model porous media, Darcy's law has been derived from first principles, but in the case of

complicated systems like composite reinforcements its validity is subject to experimental verification.

Darcy's law has been applied in different forms in combination with the continuity equation under various, usually numerical, solution schemes. The continuity or mass balance equation has the form (26):

$$\frac{\partial \rho}{\partial t} + \nabla \cdot (\rho \vec{u}) = 0 \qquad \text{(Eq. 2.10)}$$

In liquid moulding resin is considered incompressible (27-30) and the continuity equation becomes:

$$\nabla \cdot (\vec{u}) = 0 \qquad \text{(Eq. 2.11)}$$

where $\vec{u}$ represents the resin velocity as a phase average, i.e. the average of velocity over the resin domain divided by the total volume.

A convenient form of Darcy's law:

$$\vec{u} = -\frac{\overline{K}}{\mu} \vec{\nabla} p \qquad \text{(Eq. 2.12)}$$

where $\overline{K}$ is an appropriately defined permeability and μ the resin viscosity, combined with Eq. 2.11 results in (27):

$$\nabla \cdot \left(\frac{\overline{K}}{\mu} \vec{\nabla} p \right) = 0 \qquad \text{(Eq. 2.13)}$$

Note that various notions of permeability such as the ones presented in Eq. 2.9 and Eq. 2.12, and different meanings of resin velocity as actual or apparent, have been incorporated in the formulation of the problem by different authors. In all cases the resulting formulae are equivalent, the definition of permeability is altered accordingly in order to include density, resin volume fraction or viscosity.

Boundary conditions which complement Eq. 2.13 in order to form the boundary value problem are:

- zero relative pressure (27, 31) at the flow front;
- prescribed pressure (27, 32) or prescribed flow rate (31, 33) at the inlet gate;
- zero flow rate across the mould walls (27, 31-33);

The solution procedure usually implemented is quasi-static. Finite elements are employed in order to obtain an approximate solution for the boundary value problem described by Eq. 2.13 and the corresponding boundary conditions in steady state. Then,

using Eq. 2.12, the position of the flow front is updated and the solution of the boundary value problem is repeated in the new domain (27, 32).

In basic studies the preform is seen as a two-dimensional surface, as the flow through the thickness is considered negligible, and the problem is solved in 2-D (30, 34). Simplified 1-D models aiming at deriving analytical solutions have been developed (35) also, in order to provide an easy to analyse input to optimisation studies. In the case of axisymmetric mould geometries 2-D modelling has been implemented, but the angular direction has been ignored rather than the thickness, due to symmetry (33). This 2-D (axial and radial) model does not involve any assumptions relevant to the flow through the thickness, because of symmetry and thus represents the physical phenomena realistically.

Three dimensional models have been developed successfully, based on the same principles. Their application has demonstrated that the assumption of negligible flow through the thickness used in 2-D models is justified when the mould thickness is very small compared to the other dimensions. When the thickness of the modelled part is comparable to the in-plane dimensions, the flow departs from the 2-D behaviour (32). In any case, when the filling is not performed under isothermal conditions, significant differences may arise due to the presence of thermal gradients through the thickness. Refined 3-D finite element models which involve more than 10^5 nodes are impossible to execute in real time or reasonably close to it (27). Some alternative modelling strategies have been developed in order to overcome this problem. Hybrid models which combine 2-D and 3-D elements in the same simulation have been used in complicated geometries, where part of the modelled domain can be simulated adequately by a 2-D surface and part of it requires the consideration of the third dimension (31). Thus the 3-D part of the domain is modelled accurately while no additional computer time is spent on the 2-D domain.

Impregnation models, operating as described previously, constitute idealisations of the real process and tend to ignore some significant phenomena like the edge effect or race tracking and the existence of voids in the impregnated reinforcement. Some modelling approaches have been developed in order to include these effects in process models.

Race tracking occurs when due to poor conformance between the dry fabric and the mould walls, a gap is produced at the boundaries. This phenomenon if uncontrolled can

lead to resin arrival at the mould outlet before full impregnation and cause the production of large dry areas in the component.

Two approaches have been implemented for the incorporation of the edge effect in models. One approach uses the concept of equivalent permeability, according to which the race tracking area is treated as a porous medium with a permeability value that represents the average flow capacity in that area (36). Values for the effective permeability can be obtained using analytical solutions for the flow in channels (37). Thus the whole flow is modelled as a Darcian flow and the permeability is altered near the boundary in order to represent the edge effect. The second approach models the gap domain using forms of the Navier-Stokes equation for flow in the channel which then couple to the Darcy's law based model (38).

In all RTM simulations mentioned, it is assumed that the pore volume of the portion of the preform behind the resin flow front is fully saturated with resin. This assumption allows the implementation of the quasi-static approach used to model the pressure field. It has been shown experimentally that situations may arise where micro-pores are created in a preform due to either different flow rates around and within fibre tows or imperfections of the reinforcements (39).

In order to take into account these effects the flow through the reinforcement is considered as a multiscale phenomenon. Macroscopically the flow advances in the whole reinforcement, whereas in the micro-scale it is considered to occur within two different types of tows-(i) parallel to the flow and (ii) transverse to the flow, as illustrated in Fig.2.2. Formation of voids occurs when the macro and microflow rates differ.

The macroflow can be expressed by Darcy's law using an effective value of permeability (39, 40). The microflow within tows is governed by two mechanisms: (i) pressure driven flow due to the higher pressure of the surrounding fluid and (ii) capillary flow (wicking). In the former case the macroflow progresses ahead of the microflow whereas in the latter case, which occurs at very low impregnation rates (39), capillary forces cause the opposite effect (40).

In order to model this combination of effects the problem is treated as a flow through a porous medium with a very low permeability characteristic of the tow and the boundary condition of zero relative pressure at the flow front is replaced by the relation (41, 42):

$$P = 4\gamma_s D_t \cos\theta \qquad \text{(Eq. 2.14)}$$

where γ_s denotes the surface tension, θ the contact angle and D_t a coefficient characteristic of the fibre bundle geometry.

The models for macro- and micro-flow are coupled and solved simultaneously in order to simulate the void formation.

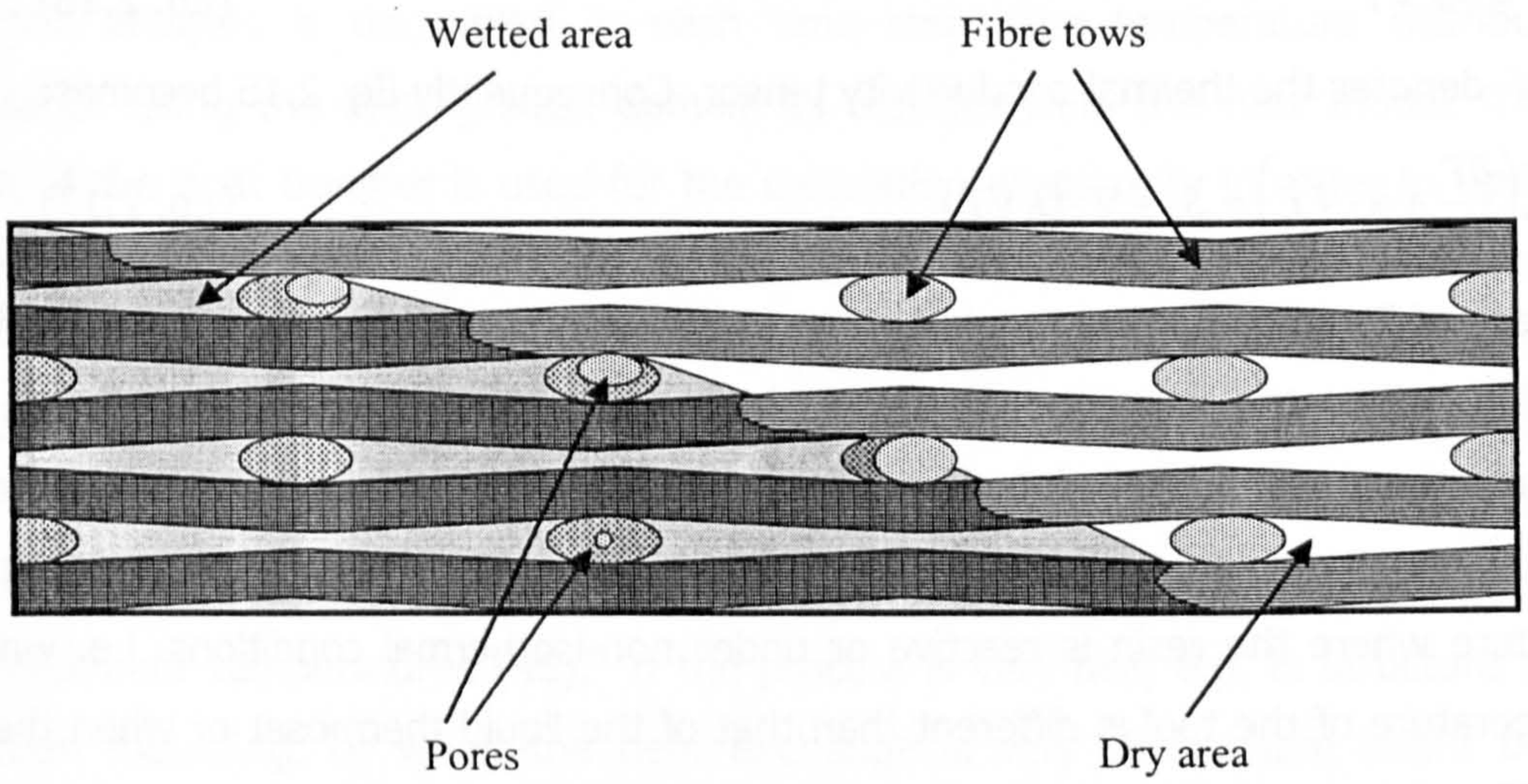

Fig.2.2 *Interaction of micro and macro-flows in RTM*

2.3.2 Modelling of heat transfer and curing

Heat transfer modelling is performed by the application of an energy balance in an appropriate form. The general form of energy balance as it arises from the first law of thermodynamics for an incompressible medium is (43):

$$\rho c_p \frac{dT}{dt} = \rho c_p \left(\frac{\partial T}{\partial t} + \vec{u} \cdot \nabla T \right) = S_i - \nabla \cdot \left(\vec{q}_{cd} + \vec{q}_r \right) \qquad \text{(Eq. 2.15)}$$

The left side of Eq. 2.15 represents the time derivative of specific enthalpy (ρ is the density, c_p the specific heat capacity, T the temperature and $\vec{u}$ the velocity). The right side is the sum of the powers per unit volume generated within the material (S_i is the heat generated per unit volume per unit time) and crossing a surface element ($\vec{q}_{cd}$ is the heat conduction through a surface per unit area per unit time and $\vec{q}_r$ is the heat radiation through a surface per unit area per unit time). As shown in Eq. 2.15 the time derivative of temperature can be analysed further in the variation of temperature with

time at a fixed position, represented by $\frac{\partial T}{\partial t}$, and the variation of temperature with time of a material element followed during its motion, represented by $\vec{u} \cdot \nabla T$.

The conduction heat flux can be expressed by Fourier's law (43), as follows:

$$\vec{q}_{cd} = -K\nabla T \qquad \text{(Eq. 2.16)}$$

where K denotes the thermal conductivity tensor. Consequently Eq. 2.15 becomes:

$$\rho c_p\left(\frac{\partial T}{\partial t} + \vec{u} \cdot \nabla T\right) = S_i + \nabla \cdot (K\nabla T) \qquad \text{(Eq. 2.17)}$$

In the case of liquid composite moulding, heat transfer occurs during both impregnation and curing. When the impregnation takes place at a constant temperature which is lower than the onset of reaction, the filling can be considered isothermal and heat transfer phenomena can be ignored. In contrast, when the filling takes place at a temperature where the resin is reactive or under non-isothermal conditions, i.e. when the temperature of the tool is different than that of the liquid thermoset or when there are significant temperature variations across the tool, heat transfer should be coupled with the flow models. During the curing stage a heat transfer model coupled with a cure model operates independently, since forced convection does not take place.

The implementation of heat transfer models varies according to the stage of the process (filling or curing) they simulate. In filling stage simulations which do not consider the reaction, assuming that although the filling stage is non-isothermal the reaction is very slow, the form of the heat balance used is (44):

$$\rho c_p \frac{\partial T}{\partial t} + \rho_r c_{pr} \vec{u} \cdot \nabla T = K\nabla^2 T \qquad \text{(Eq. 2.18)}$$

where ρ_r is the resin density and c_{pr} the resin specific heat capacity.

In cases where the reaction plays a role in impregnation, Eq. 2.17 becomes (34):

$$\rho c_p \frac{\partial T}{\partial t} + \rho_r c_{pr} \vec{u} \cdot \nabla T = K\nabla^2 T + (1 - v_f)\rho_r H_{tot} \frac{d\alpha}{dt} \qquad \text{(Eq. 2.19)}$$

where H_{tot} is the total heat of reaction.

Here the conductivity tensor has been considered isotropic and independent of temperature. Typical boundary conditions complementing such models are:

- temperature at the inlet is equal to resin temperature prior to injection (34, 44);
- temperature on the mould wall is equal to a prescribed value (34) or;

- temperature on the flow front is equal to the preform temperature (44);
- heat gained due to the flow progress is equal to the heat flux on the flow front boundary (34).

In order to solve this model coupled with a Darcy flow model, finite elements are used, and the analysis is decoupled in each time step. The temperature distribution is calculated using the impregnated domain as resulted from the flow model. Then the result of the heat transfer is used for the calculation of viscosity in order to update the finite elements representation of Eq. 2.13 for the next time step of the flow model (44). These representations of the heat transfer problem assume a local thermal equilibrium which enables the local averaging of temperature, in order to treat the filling composite as a uniform material. In microscopic terms that means that the heat exchange through the resin-reinforcement interface rapidly erases any difference between the resin and reinforcement temperatures (45). If the process is very fast, e.g. in structure reaction injection moulding, or when the heat exchange is very slow; there might be some differences between the temperatures of the two phases. In that case a separate energy balance should be formed for each of them. The resulting equations include some unexpected terms and some difficult to determine coefficients (46). In practice, the only term used in models is the one representing the heat exchange. The corresponding formulation is (34):

- For the liquid phase

$$\rho_r c_{pr} \frac{\partial T_r}{\partial t} + \frac{1}{(1-v_f)} \rho_r c_{pr} \vec{u} \cdot \nabla T_r = \nabla \cdot K_r \nabla T_r + \rho_r H_{tot} \frac{d\alpha}{dt} + h_v (T_f - T_r) \qquad \text{(Eq. 2.20)}$$

- For the solid phase

$$v_f \rho_f c_{pf} \frac{\partial T_f}{\partial t} = v_f \nabla \cdot K_f \nabla T_f + (1-v_f) h_v (T_r - T_f) \qquad \text{(Eq. 2.21)}$$

where T_r, T_f are the resin and fibre temperatures, K_r, K_f the resin and fibre thermal conductivities and h_v the heat transfer exchange coefficient.

Another phenomenon that may affect heat transfer during impregnation is dispersion. It occurs when microscopic velocities are different from their average values. This results in significant mechanical mixing which contributes to the transfer of heat by convection

and can override diffusion. Thus, a term which acts similarly to conductivity should be included in the energy balance (46, 47) which is modified as follows:

$$\rho c_p \frac{\partial T}{\partial t} + \rho_r c_{pr} \vec{u} \cdot \nabla T = \nabla \cdot (K + K_D) \nabla T + (1 - v_f) \rho_r H_{tot} \frac{d\alpha}{dt} \qquad \text{(Eq. 2.22)}$$

where $K_D \nabla T$ is the dispersion contribution to the heat flux.

The heat transfer modelling of the curing stage of liquid moulding is based on the same principles as the modelling of impregnation. The energy balance is simplified in that case, since no convective terms are included and there is no need to allow for two phase modelling or to account for dispersion effects. The appropriate expression of the energy balance becomes (48):

$$\rho c_p \frac{\partial T}{\partial t} = \nabla \cdot [K] \nabla T + (1 - v_f) \rho_r H_{tot} \frac{d\alpha}{dt} \qquad \text{(Eq. 2.23)}$$

The curing stage of liquid moulding has received much less attention than the impregnation stage up to now. Only one dimensional models aiming at modelling the whole curing cycle in the RTM have been developed using 1-D finite differences representations of Eq. 2.23.

Some of the kinetic modelling methods described in paragraph 2.2 have been used to incorporate resin cure kinetics in the models. For the incorporation of thermal properties in heat transfer models for both impregnation and curing, all the previously mentioned studies use constant values throughout the filling and cure cycle, which is an extreme simplification considering the changes, like gelation and vitrification, that the resin undergoes. Some models incorporate relations in order to obtain the composite material properties from its constituents values (34):

$$\rho = \frac{\rho_r \rho_f}{w_f \rho_r + (1 - w_f) \rho_f} \qquad \text{(Eq. 2.24)}$$

$$c_p = w_f c_{pf} + (1 - w_f) c_{pr} \qquad \text{(Eq. 2.25)}$$

$$K = \frac{K_r K_f}{w_f K_r + (1 - w_f) K_f} \qquad \text{(Eq. 2.26)}$$

where w_f is the fibre weight fraction.

2.4 Modelling of laying up /autoclaving

The combination of laying-up and autoclaving is the most widely used technique for the production of high performance thermosetting matrix-continuous fibres composites. This processing route comprises two steps (i) manual or semiautomatic laying up of pre-impregnated fibre sheets (pre-pregs) and arrangement of the pre-preg stack within a set-up of tooling and (ii) consolidation and curing of the green composite by simultaneous application of pressure and heat in the autoclave. A typical configuration of the cure assembly which is loaded in the autoclave is shown in Fig. 2.3.

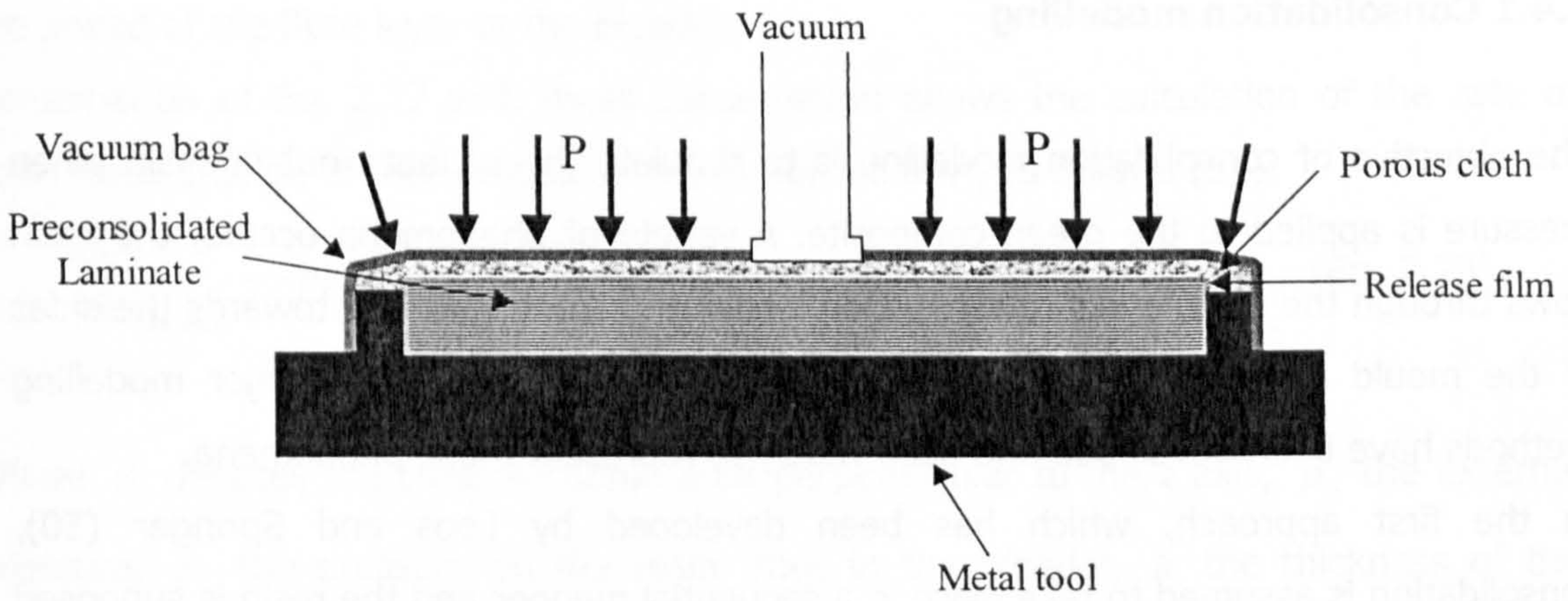

Fig.2.3 *Cure assembly for autoclaving*

The prepregs are placed in the metal tool. A film of release material separates the preconsolidated laminate from the rest of the cure assembly in order to ensure easy detachment of the cured part. A porous material (bleeder) is placed on top of the prepregs in order to absorb any excess resin during consolidation. Finally a vacuum bag encloses the whole assembly.

The process usually takes place as follows (49):

1. Vacuum is applied and temperature starts to increase. In that stage the viscosity of the resin starts to decrease while some of the voids are removed.
2. Pressure is applied when a prescribed temperature is reached. Temperature is stabilised at that level. The viscosity has reached its minimum value and consolidation occurs.

3. Temperature increases and application of vacuum stops. Consolidation has been completed and the curing reaction is initiated.
4. Temperature is stabilised. The curing is completed during this isothermal segment. At some point when the reaction has progressed and gelation has occurred the pressure is taken off.
5. The assembly is cooled down to ambient temperature.

The main phenomena governing the process and the quality of the final product are (i) resin flow during initial heating up and consolidation and (ii) transfer of heat during consolidation and curing.

2.4.1 Consolidation modelling

The objective of consolidation modelling is to simulate the squeeze out of resin when pressure is applied to the green composite. A variety of phenomena occurs, the resin flows through the fibre layers towards the bleeder and along the fibre towards the sides of the mould assembly, and the fibre layers are compressed. Two major modelling methods have been developed and used widely to represent those phenomena.

In the first approach, which has been developed by Loos and Springer (50), consolidation is assumed to take place in a sequential manner and the resin is supposed to carry all the applied load. Consolidation occurs by resin flow normal to the tool plate and resin flow parallel to the tool as illustrated in Fig.2.4.

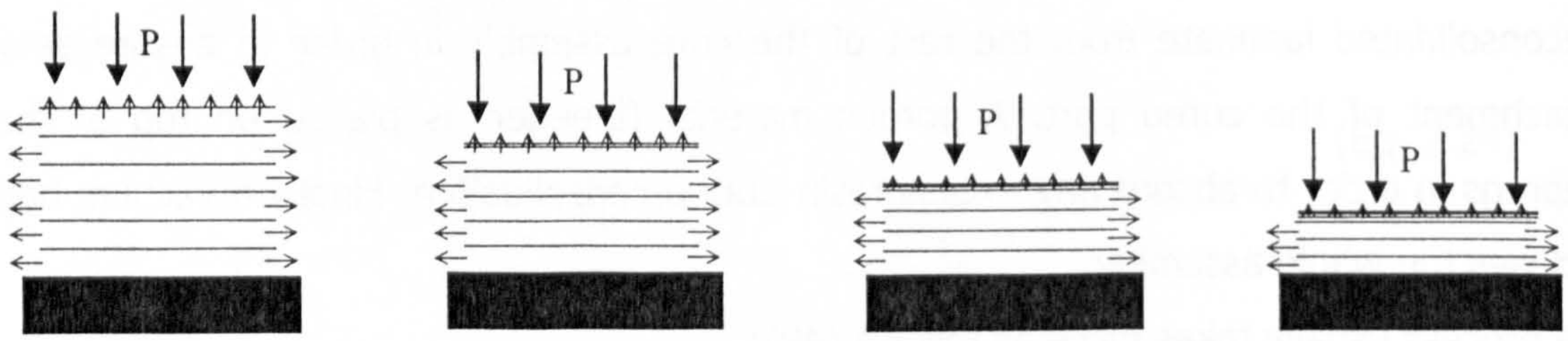

Fig.2.4 *Mechanisms of normal and parallel to the plate flows during consolidation*

Flow normal to the tool occurs as follows. As the pressure is applied, the top ply moves towards the second ply and resin is squeezed out from the space between these two plies, through the fibre tows of the first ply. When equilibrium between these two plies has been established, they move together towards the third ply. This procedure is

repeated for all the subsequent plies until the excess resin of the space between the last ply and the tool has been squeezed out. In contrast, flow parallel to the tooling plate does not occur sequentially. As long as there is excess resin between a pair of plies, resin is squeezed out continuously along the direction parallel to the fibre. The parallel to the tool flow normal to the fibre direction is negligible.

According to these (50), the flow normal to the tool plate is expressed by the one dimensional form of Darcy's law (Eq. 2.12):

$$u_z - V = -\frac{\overline{K}}{\mu}\cdot\frac{\partial p}{\partial z} \qquad \text{(Eq. 2.27)}$$

where u_z is the phase average of the normal to the plate velocity component and V is the speed of the fibre layer or the bleeder.

Combination of Eq. 2.27 with mass conservation allows the calculation of the rate of resin mass change of the composite due to normal flow, as follows (51):

$$\left.\frac{dM}{dt}\right|_{normal} = -\rho_r A\overline{K}\frac{p_o - p_i}{\int_0^h \mu dz + \frac{\overline{K}\mu h_b}{\overline{K}_b}} \qquad \text{(Eq. 2.28)}$$

where A denotes the cross sectional area perpendicular to the z axis, p_o the external pressure, p_i the pressure on the resin front in the bleeder, h the thickness of the compacted fibre layers, h_b the thickness of permeated area of the bleeder and $\overline{K}_b$ the permeability of the bleeder.

The flow parallel to the tool is simulated using a combination of the momentum balance for channel flow and mass conservation. The rate of resin mass change in the n-th prepreg is (50):

$$\left.\frac{dM}{dt}\right|_{parallel}^{n} = -2B\frac{d_n^3}{\mu}\rho_r W\frac{p_h - p_i}{x_l} \qquad \text{(Eq. 2.29)}$$

where B is an experimental constant, W the width of the channel between the fibre layers, x_l half of the length of the channel, p_h the pressure at the centre of the channel.

The pressure distribution at a point at distance x from the centre of the channel is given by the relation (50):

$$p = \frac{p_h - p_i}{x_l} x + p_i \qquad \text{(Eq. 2.30)}$$

The total resin flow is estimated by superimposing the results of the two flow mechanisms as follows:

$$\frac{dM}{dt} = \left.\frac{dM}{dt}\right|_{normal} + \sum_{n=1}^{N-n_s} \left.\frac{dM}{dt}\right|_{parallel}^{n} \qquad \text{(Eq. 2.31)}$$

while the composite thickness is:

$$L = \frac{M}{2x_l W \rho} \qquad \text{(Eq. 2.32)}$$

where N is the total number of plies and n_s the number of compacted plies.

A second model proposed by Gutowski et al (52, 53) and Dave (54) considers consolidation as the combination of two phenomena: (i) resin flow through porous media and (ii) fibre elastic deformation. The uncured composite is seen as a porous elastic material that is filled with a viscous liquid. The pressure applied to the laminate must be carried by both the resin and the fibre. Initially the fibre layers are not in contact, consequently pressure is carried by the resin only. As the resin flows out, the composite is compacted and the fibre network starts to support some of the pressure. If the resin is free to flow then the whole load is transferred to the fibre. However, in practice the resin flow is limited by a number of factors, and therefore both the resin and the fibre should be considered in the modelling.

Consider an element of the uncured composite as shown in Fig. 2.5. The velocity components are phase averages, i.e. average of the liquid velocity over the whole (resin and fibre) volume. The variable ξ expresses the sum of the initial z coordinate and the displacement.

Application of momentum balance results in the relation:

$$p_o = \sigma + \bar{p}_r \qquad \text{(Eq. 2.33)}$$

where σ is the pressure applied to the fibre network and $\bar{p}_r$ the pressure applied to the resin.

Continuity in the fibre can be expressed as:

$$v_o = v_f \frac{\partial \xi}{\partial z} \qquad \text{(Eq. 2.34)}$$

where v_o is the initial fibre volume fraction.

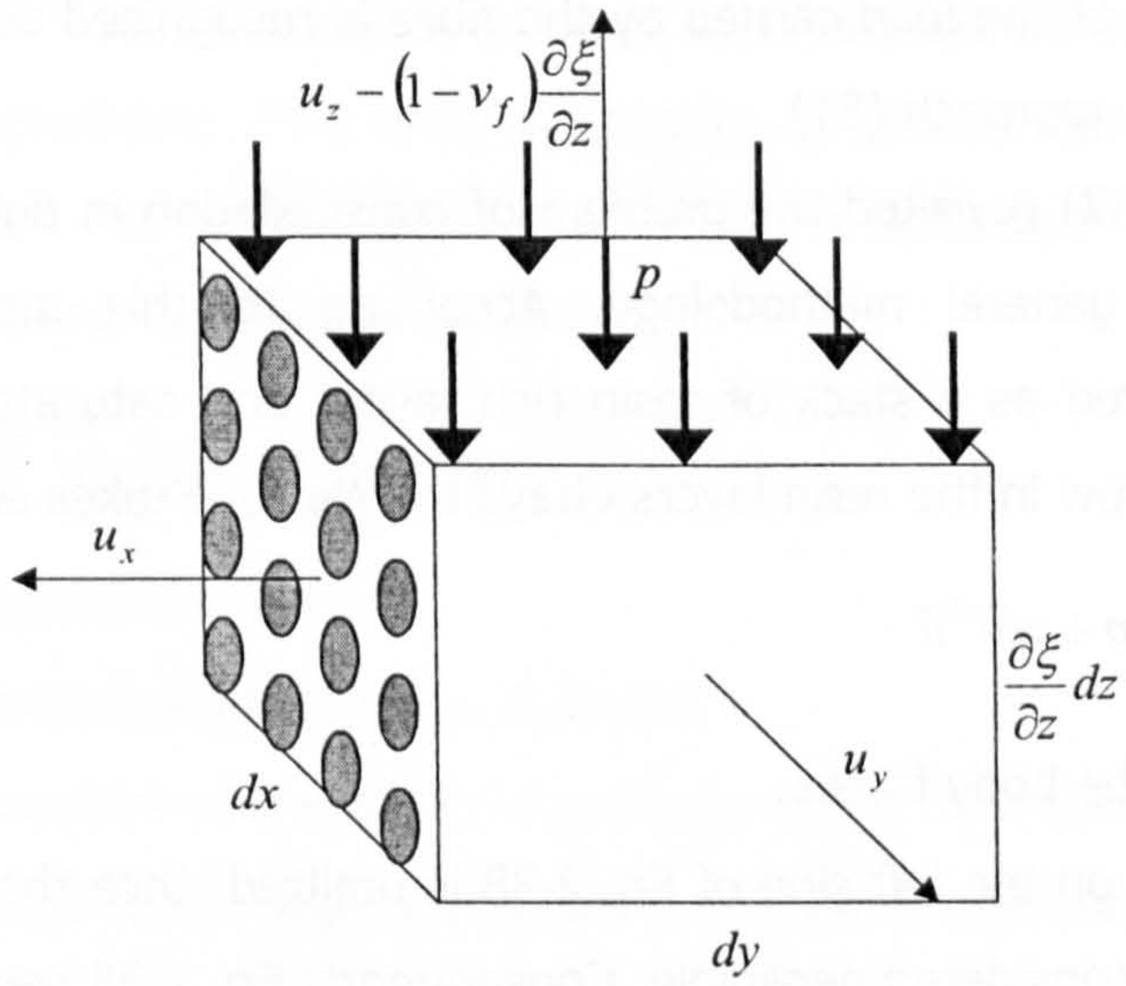

Fig.2.5 *Deforming element during consolidation*

Continuity of the resin (Eq. 2.10) results in:

$$\frac{\partial}{\partial x}\left(u_x \frac{\partial \xi}{\partial z}\right)+\frac{\partial}{\partial x}\left(u_y \frac{\partial \xi}{\partial z}\right)+\frac{\partial u_z}{\partial x}+\frac{\partial}{\partial t}\left[(1-v_f)\frac{\partial \xi}{\partial z}\right]=0 \qquad \text{(Eq. 2.35)}$$

The flow through the fibre network can be expressed by Darcy's law in tensorial form:

$$\begin{bmatrix} u_x \\ u_y \\ u_z \end{bmatrix} = -\frac{1}{\mu}\begin{bmatrix} \overline{K}_{xx} & 0 & 0 \\ 0 & \overline{K}_{yy} & 0 \\ 0 & 0 & \overline{K}_{zz} \end{bmatrix}\begin{bmatrix} \partial \overline{p}_r/\partial x \\ \partial \overline{p}_r/\partial y \\ \partial \overline{p}_r/\partial z \end{bmatrix} \qquad \text{(Eq. 2.36)}$$

Assuming that the permeabilities depend only on the fibre volume fraction, Eqs. 2.34, 2.35 and 2.36 result in (52):

$$\frac{\overline{K}_{xx}}{v_f}\frac{\partial^2 \overline{p}_r}{\partial x^2}+\frac{\overline{K}_{yy}}{v_f}\frac{\partial^2 \overline{p}_r}{\partial z^2}+\frac{1}{v_o}\frac{\partial}{\partial z}\left(v_f \overline{K}_{zz}\frac{\partial \overline{p}_r}{\partial z}\right)=\mu\frac{\partial}{\partial t}\left(\frac{1-v_f}{v_f}\right) \qquad \text{(Eq. 2.37)}$$

Eq. 2.37 can be integrated in order to provide the pressure field, the thickness and the fibre volume fraction distribution evolution during consolidation provided that there are submodels expressing the permeability and the stiffness of the fibre network as a function of the fibre volume fraction. The Kozeny-Carman equation has served as a submodel for permeability (52) and a variety of empirical relations for the stiffness has been used in different implementations of the model (52, 53, 55).

The second modelling approach is considered as more rigorous (56) since the contribution of the fibre network to the force balance has been validated experimentally (53). The importance of the load carried by the fibre is recognised also in studies which are based on the first approach (51).

Recently Blest et al (57) revisited the problem of consolidation in autoclave following a more rigorous and general methodology. According to this model, the uncured composite is considered as a stack of resin rich layers and saturated porous medium layers. Naturally the flow in the resin layers obeys the Navier-Stokes equation (26):

$$\rho_r \frac{d\vec{u}}{dt} = \rho_r \vec{k} - \nabla p + \mu \nabla^2 \vec{u} \qquad \text{(Eq. 2.38)}$$

where $\vec{k}$ represents the body forces.

The accelerative term on the left side of Eq. 2.38 is omitted since the flow is very slow, and the body force is considered negligible. Consequently Eq. 2.38 becomes:

$$\nabla p = \mu \nabla^2 \vec{u} \qquad \text{(Eq. 2.39)}$$

The flow in the fibre layers is expressed by Darcy's law (Eq. 2.12). Both domains are provided with the continuity equation (Eq. 2.11). This system of equations together with the boundary conditions of

- no slip at the top and bottom of the composite;
- no flow at the top and the bottom of the composite;
- velocity continuity at the layers interfaces;
- pressure continuity at the interfaces.

can be integrated numerically in order to provide the pressure and velocity field evolution during consolidation.

2.4.2 Modelling of heat transfer and curing

Heat transfer phenomena occurring mainly during autoclave cure have been the subject of extensive study. The principles of modelling are the same as in liquid moulding, i. e. an energy balance either of the form of Eq. 2.19 when consolidation is taken into account or of the form of Eq. 2.23 when the model excludes forced convection. Since consolidation is a slow process there is no requirement to form different energy balances for the resin and the reinforcement or to consider dispersion.

In the study by Loos and Springer (50) which has laid the foundations for composite manufacturing modelling, the heat transfer during the cure is treated as an one dimensional problem. The thickness of the part is considered as the only direction with significant thermal gradients. The shell geometries produced using autoclaving justify this assumption which has been adopted in most of the subsequent studies (19, 55, 58-61). The one-dimensional energy balance is:

$$\rho c_p \frac{\partial T}{\partial t} = \frac{\partial}{\partial z}\left(K \frac{\partial T}{\partial z}\right) + \left(1 - v_f\right)\rho_r H_{tot} \frac{d\alpha}{dt} \qquad \text{(Eq. 2.40)}$$

where z is the thickness direction.

Boundary conditions complementing Eq. 2.23 are:

- prescribed temperature at the external surfaces of the cure assembly (19, 50, 58);
- complete insulation at the boundary which is in contact with the bleeder-vacuum bag stack (59);
- convective heat transfer at the external surface of the cure assembly (61).

Extension of these models to two dimensions has been performed in order to provide suitable two-dimensional input for residual stress build up models (62), to include in the analysis the whole cure assembly (63), and to account for two-dimensional convection due to consolidation (57). The governing equation is the two dimensional form of the energy balance (Eq. 2.19 or 2.23) complemented by appropriate boundary conditions. A three-dimensional model has been developed in order to enable the use of non-dimensional parameters in process design (64). Usually the above equations are solved using finite differences. In some cases finite elements have been employed also (56).

The kinetic modelling methods described in paragraph 2.2 have been used in order to incorporate resin cure kinetics in the models. In some cases the parameters of the kinetics are estimated directly for the pre-preg involved in the process (50, 62) thus avoiding the distinction between different densities in the heat balance.

A variety of expressions has been utilised for the estimation of thermal properties, which arise from the rule of mixtures for the density and specific heat capacity, and from geometrical considerations for thermal conductivity:

$$\rho = \left(1 - v_f\right)\rho_r + v_f \rho_f \text{ (55, 58-60)} \qquad \text{(Eq. 2.41)}$$

$$c_p = \frac{\rho_r}{\rho}\left(1 - v_f\right)c_{pr} + \frac{\rho_f v_f}{\rho}\rho_{pf} \text{ (11, 55, 58, 60)} \qquad \text{(Eq. 2.42)}$$

$$K = \frac{K_r K_f}{w_f K_r + (1 - w_f) K_f} \quad (55, 59) \qquad \text{(Eq. 2.43)}$$

$$K = \frac{K_r (1 - B_1 B_2 v_f)}{(1 - B_1 v_f)}$$

$$B_1 = \frac{K_f - K_r}{K_f - B_2 K_r} \quad (58) \qquad \text{(Eq. 2.44)}$$

$$B_2 = \frac{1}{4 - 3(1 - v_f)}$$

$$K = K_r \left[1 - 2\sqrt{\frac{v_f}{\pi}} + \frac{\pi}{B} - \frac{4}{\sqrt{1 - \frac{B^2 v_f}{\pi}}} Ar\tan \frac{\sqrt{1 - \frac{B^2 v_f}{\pi}}}{1 + B\sqrt{\frac{v_f}{\pi}}} \right] (19, 60) \qquad \text{(Eq. 2.45)}$$

$$B = 2\left(\frac{K_r}{K_f} - 1\right)$$

2.5 Modelling of pultrusion

Pultrusion is a potentially continuous process used for producing constant cross-section parts. It comprises pulling of continuous reinforcement through impregnation, shaping and curing operations, as illustrated in Fig.2.6.

Any form of continuous reinforcement can be used. There are two variants of the impregnation stage of the process, (i) bath impregnation where the reinforcement is drawn through a liquid thermosetting material bath and subsequently through a preforming die and (ii) die impregnation where the infiltration and preforming occur simultaneously in a die. After impregnation, the wet reinforcement is pulled through a heated die and curing takes place.

The stages of the pultrusion of the greatest interest in terms of process duration and final product quality are the preforming and the curing in the heated die. Consequently modelling has been focused on flow, pressure rise, reaction and heat transfer phenomena which occur during these two stages.

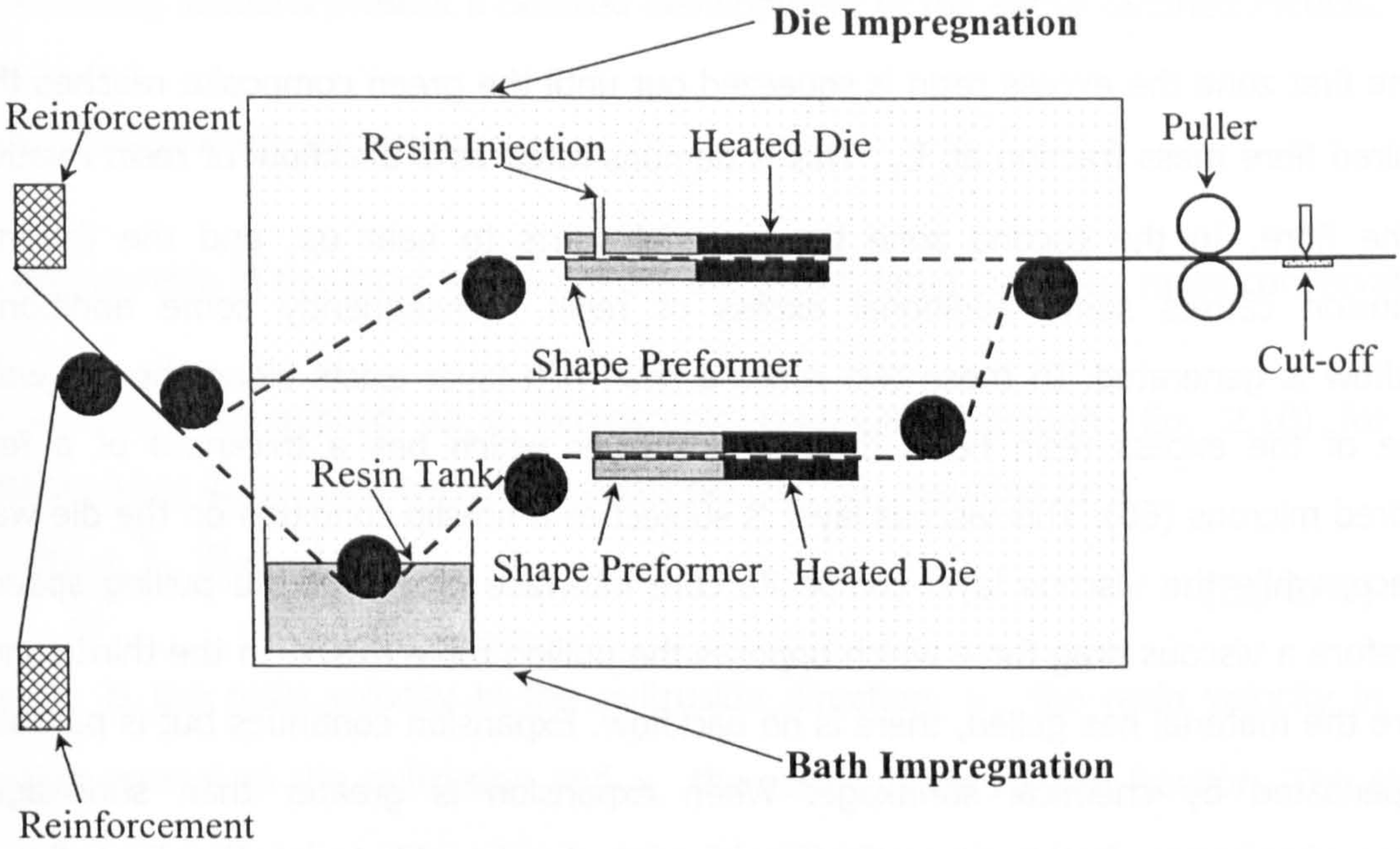

Fig.2.6 *Schematic representation of die and bath impregnation pultrusion*

2.5.1 Pressure rise and pulling force

The sequence of states of a pultruded composite is shown in Fig.2.7. Three zones can be distinguished (65):

- Decreasing cross-sectional area zone: $0 \le z \le L_t$
- Constant cross-section liquid resin zone: $L_t \le z \le L_g$
- Constant cross-section gelled resin zone: $L_g \le z \le L_f$

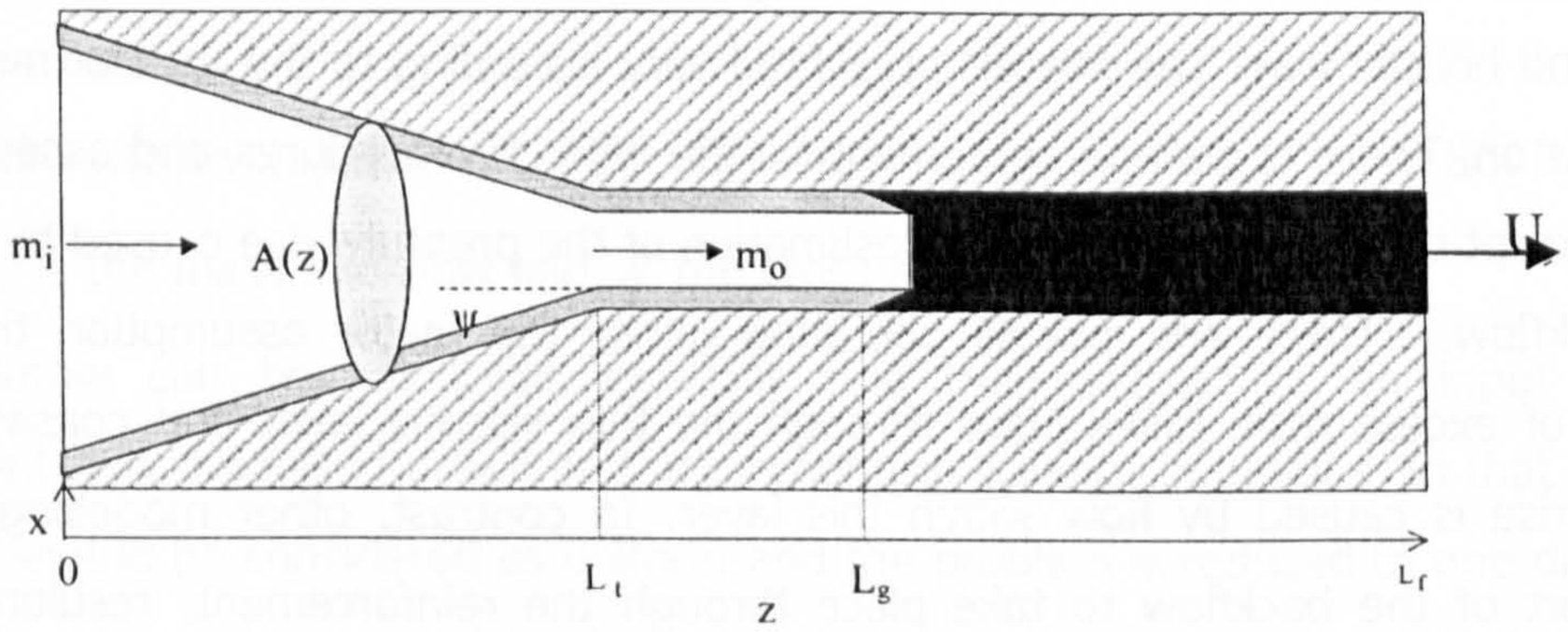

Fig. 2.7 *Forming and curing in a pultrusion die*

In the first zone the excess resin is squeezed out until the green composite reaches the required fibre mass fraction at L_t. This is demonstrated as a backflow of resin relative to the fibre. In the second zone the material starts to heat up, and the thermal expansion causes some additional excess of resin. Consequently some additional backflow is generated. In these two zones a resin rich layer exists along the die wall. Some of the excess resin flows through this layer which has a thickness of a few hundred microns (66). This viscous layer is subject to a no-slip condition on the die wall surface, while the viscous layer-composite core interface moves at the pulling speed. Therefore a viscous drag force which opposes the pulling force exists. In the third zone, where the material has gelled, there is no backflow. Expansion continues but is partially compensated by chemical shrinkage. When expansion is greater than shrinkage, compression occurs. In this zone a frictional force is developed between the die wall and the gelled matrix resulting in another term opposing the pulling. The existence of this force is not limited only to the gelled resin zone, since the no-slip condition decelerates the resin in the wall proximity, which consequently gels at an earlier point.

The modelling steps required for the entire simulation of the pulling through a pultrusion die are:

- Excess resin calculation in the taper and the straight area of the die;
- Estimation of the pressure distribution in the area where backflow occurs;
- Estimation of the pressure distribution in the area where compression takes place;
- Computation of the viscous drag;
- Computation of the friction force.

This procedure is partially followed in the literature but it has not been implemented in a generic and holistic way. The models presented vary according to the type of modelling they focus on. There is general agreement on the type of procedures and assumptions utilised except the method used for the estimation of the pressure rise caused by excess resin backflow. There are models operating under the major assumption that the backflow of excess resin takes place through the thin viscous layer and consequently pressure rise is caused by flow within this layer. In contrast, other modelling works regard part of the backflow to take place through the reinforcement, resulting in a pressure rise due to flow through a porous medium.

The following sections present a detailed development of the above outlined models.

2.5.1.1 Excess resin calculation

The excess resin in the taper section of the die is calculated using the mass conservation law.

The law can be applied as a microscopic continuity equation (Eq. 2.10) for an incompressible liquid for a two dimensional die (67, 68) resulting in:

$$\frac{\partial(v_r u_z)}{\partial z}+\frac{\partial(v_r u_x)}{\partial x}=0 \qquad \text{(Eq. 2.46)}$$

Here u_z is the resin velocity in the pultrusion direction, u_x the resin velocity in the direction normal to the pultrusion and v_r the resin matrix volume fraction. The same law can be applied in cylindrical co-ordinates (3) when the pultrusion die geometry necessitates such a formulation:

$$\frac{\partial(v_r u_r)}{\partial r}+\frac{v_r u_r}{r}+\frac{\partial(v_r u_z)}{\partial z}=0 \qquad \text{(Eq. 2.47)}$$

Here r is the radial co-ordinate and u_r is the resin velocity in the radial direction.

The continuity equation is connected with the boundary condition of zero velocity normal to the die wall, applied at the die wall. It is not solved independently, but is incorporated in a system of equations which contains the momentum balance equations and the corresponding boundary conditions.

In an alternative approach implemented in some modelling studies (66, 69) the continuity equation is applied as a macroscopic mass conservation law. The excess resin backflow, which is caused by the decreasing cross-section area of the taper section, can be expressed as:

$$\dot{m}_b(z)=\rho(z)Uv_r(z)A(z)-\rho(L_t)Uv_r(L_t)A(L_t) \qquad \text{(Eq. 2.48)}$$

where $\dot{m}_b$ is the mass backflow and A the cross-sectional area.

The backflow can be calculated explicitly and then utilised as an input for the subsequent flow modelling based on the momentum balance equations. In that case the backflow should be considered as uniform and the problem is reduced to one dimension (69). If the dimension normal to the pultrusion direction is considered (66), then the

mass flow corresponds to the integral of the local resin mass flow contributions over the cross-section area:

$$\dot{m}(z) = \oiint_A \rho v_r u_z dA \qquad \text{(Eq. 2.49)}$$

The excess resin and the corresponding backflow in the straight sector of the die can be calculated in a similar way, taking into account the fact that the backflow in not a result of decreasing cross-sectional area but is caused only by the resin density changes along the pultrusion direction:

$$\dot{m}_b(z) = \rho(z) U v_r(z) A - \rho(L_f) U v_r(L_f) A \qquad \text{(Eq. 2.50)}$$

The resin density is a function of temperature and degree of cure. If the effect of chemical conversion on the thermal expansion coefficient is ignored, the change in density is given by the expression (69):

$$\frac{\Delta\rho}{\rho} = -\alpha_v \Delta T \qquad \text{(Eq. 2.51)}$$

where α_v is the volumetric expansion coefficient.

A similar procedure could be implemented with the use of a continuity equation, allowing for varying resin density:

$$\frac{\partial(\rho v_r u_z)}{\partial z} + \frac{\partial(\rho v_r u_x)}{\partial x} = 0 \qquad \text{(Eq. 2.52)}$$

Such a method has not been used up to now in the published models, which incorporate the continuity equation in the partial differential equations system. In these cases the density is considered constant and the excess resin in the straight part as well as the corresponding pressure rise are not taken into account (70).

2.5.1.2 Pressure arising from backflow

As mentioned previously calculations of the pressure rise due to excess resin have been based on the assumption either that the backflow takes place through the viscous layer or that the backflow takes place through the reinforcement.

In the first case Navier-Stokes is the governing equation (Eq. 2.38). In the works using this approach (3, 66), the excess resin has been calculated explicitly by the macroscopic mass conservation law and resin local speed has been calculated across the radial

direction ignoring the axial component in the Navier-Stokes equation. The die has been considered to be in a steady state and the viscosity constant. Consequently the following equation is obtained:

$$\frac{\mu}{r}\frac{\partial}{\partial r}\left(r\frac{\partial u_z}{\partial r}\right)=\frac{\partial p}{\partial z} \qquad \text{(Eq. 2.53)}$$

For a cylindrical taper a semi-analytical solution has been obtained but the results were unclear (71). Therefore the assumption of backflow through the viscous layer has been abandoned in further studies by the same authors.

The alternative approach uses Darcy's law as momentum balance equation. In simplified models (65, 69) the one dimensional equation is used:

$$u_z=-\frac{1}{\mu}\overline{K}_{zz}\cdot\frac{dp}{dz}+v_rU \qquad \text{(Eq. 2.54)}.$$

where u_z is a phase average speed.

The backflow can be related to the resin speed by the expression:

$$\dot{m}_b=A\rho\left(v_rU-u_z\right) \qquad \text{(Eq. 2.55)}$$

Consequently:

$$\dot{m}_b=\frac{A\rho\overline{K}_{zz}}{\mu}\frac{dp}{dz} \qquad \text{(Eq. 2.56)}$$

From the geometry of the problem (Fig.2.7) the resin volume fraction is:

$$v_r(z)=1-\frac{1-(v_r(L))A(L)}{A(z)} \qquad \text{(Eq. 2.57)}$$

Combination of Eq. 2.56 and the Cozeny-Carman equation for permeability estimation with the macroscopic backflow calculation Eq. 2.48 leads to an analytical expression of the pressure rise derivative (69):

$$\frac{dp}{dz}=U\mu\frac{16k}{D_f^2}\frac{(1-v_r(z))^2}{v_r^3(z)}\left[v_r(z)-\left(1+\frac{\Delta\rho}{\rho}\right)\left(\frac{1-v_r(z)}{1-v_r(L)}+v_r(z)-1\right)\right] \qquad \text{(Eq. 2.58)}$$

Substitution of Eqs. 2.51 and 2.57 in Eq. 2.58 and a numerical integration lead to an estimation of the pressure rise in the taper region.

The same procedure can be used for the straight part of the die, where Eq. 2.58 is simplified since the resin volume fraction can be considered as constant.

Some more generic methods based on the same principles but implementing multidimensional numerical models have been developed. Work by Sharma et al (67, 71 and 72), Raper et al (68) and Voorakaranam et al (73) is based on the use of two-dimensional Darcy's law combined with the continuity equation in the form of Eq. 2.46:

$$\frac{\partial\left(v_r U-\frac{\overline{K}_{zz}}{\mu}\frac{\partial p}{\partial z}\right)}{\partial z}+\frac{\partial\left(-\frac{\overline{K}_{xx}}{\mu}\frac{\partial p}{\partial x}\right)}{\partial x}=0 \qquad \text{(Eq. 2.59)}$$

In most cases a Cozeny-Carman relation has been used for permeability estimation, but a comparative study of different permeability models application (68) showed that isotropic models like the Cozeny-Carman equation do not lead to adequate agreement between model values and experimental results. In contrast anisotropic models give much better performance. The effect of die geometry (71) and other process parameters like pull speed, fibre volume fraction and resin viscosity (67) on the pressure rise have been investigated using such a model.

2.5.1.3 Compression of the solidified resin and pressure rise

The specific volume change in part of the die where the resin has gelled is the combined result of two phenomena:- (i) the thermal expansion or contraction of the resin due to temperature variations along the pultrusion direction and (ii) the curing shrinkage. This can be expressed as:

$$\frac{dv}{Vdz}=\alpha_v\frac{dT}{dz}-\gamma\frac{d\alpha}{dz} \qquad \text{(Eq. 2.60)}$$

where γ is the volumetric shrinkage.

This relation leads to the following expression (69):

$$\frac{dp}{dz}=\frac{1}{k_b}\left[\alpha_v\frac{dT}{dz}-\gamma\frac{d\alpha}{dz}\right] \qquad \text{(Eq. 2.61)}$$

where k_b is the compressibility of the resin.

2.5.1.4 Viscous drag and friction

The presence of the viscous layer at the die wall, subject to no-slip condition at the die wall and pull-speed at the viscous layer-green composite interface, causes a shear stress and consequently generates a pressure rise in the pultrusion direction.

The shear stress is:

$$\tau_v(z) = \mu(z)\frac{\partial u_z}{\partial x} \qquad \text{(Eq. 2.62)}$$

If the velocity profile along the x-axis in the viscous layer is considered as linear (65, 69, 74), the shear stress at any point is given by the relation:

$$\tau_v(z) = \mu(z)\frac{U}{\delta(z)} \qquad \text{(Eq. 2.63)}$$

where $\delta(z)$ is the viscous layer thickness.

If this assumption is not used, the velocity profile in the viscous layer has to be obtained as a result of the Navier-Stokes equation. Giordano and Nicolais (70) followed this method and obtained the following expression:

$$u_z = U\left[2\frac{x-h(z)}{\delta(z)} - 3\left(\frac{x-h(z)}{\delta(z)}\right)^2 + 1\right] \qquad \text{(Eq. 2.64)}$$

where x is the distance from the centre of the die and $h(z)$ the distance between the die wall and the centre of the die.

Consequently the shear stress profile is:

$$\tau_v(z,x) = U\mu\left[2\frac{1}{\delta(z)} - 6\frac{x-h(z)}{\delta(z)}\right] \qquad \text{(Eq. 2.65)}$$

Its value at the die wall is:

$$\tau_v(z,h(z)) = -\mu(z,\delta)U\frac{4}{\delta} \qquad \text{(Eq. 2.66)}$$

Where gelation of the viscous layer has taken place, a friction force is developed between the die wall and the gelled resin. The interfacial shear stress corresponding to this effect is:

$$\tau_f(z,h(z)) = f_c p(z,h(z)) \qquad \text{(Eq. 2.67)}$$

where f_c is the friction coefficient.

2.5.1.5 Pulling force

In order to estimate the necessary pulling force, the combined effects of all the previously mentioned phenomena have to be considered. The procedure followed in all the models is the equation of the pulling force with the opposing forces. Although a force balance is applied in order to obtain such a relation, it is not clear how this balance is formed. There are cases where only the viscous drag and the friction forces are considered as opposing to the pulling (65, 70, 74), while other studies include the taper wall force in the calculation (69). Experimental studies have demonstrated that the effect of backflow is dominant at high pulling speed (1 m/min) while viscous drag and friction dominate when the process is slow (0.1 m/min) (75).

In all these force balances the dynamic character of the pultrusion process is ignored. Although the process is in a steady state a change in speed along the pultrusion direction occurs. Therefore a correct balance should include momentum terms as expressed by the general momentum balance equation (26):

$$\iiint_V \frac{\partial \rho \vec{u}}{\partial t} dV + \iint_S \rho \vec{u}(\vec{u} \cdot \vec{n}) dS - \iiint_V \vec{k} \rho dV - \iint_S \vec{t} dS = 0 \qquad \text{(Eq. 2.68)}$$

where $\vec{k}$ is the mass body force and $\vec{t}$ the stress on the surface. The first two integrals express the change in momentum with time, the third corresponds to the effect of a body force like gravity and the last to the effect of forces on the surface. However, the low speed of the process lessens the error caused by the adoption of a force balance in the place of a momentum balance.

Application of Eq. 2.68 for steady state and no body force action in the control volume defined by the composite in Fig.2.7 leads to:

$$F_p = \rho U^2 A(L_f) - \rho U^2 \left(\frac{A(L_f)}{A(0)} \right)^2 A(0)$$

$$- p_o A(0) + \int_{L_g}^{L_f} f_c p(z, h(z)) dS + \int_{L_1}^{L_g} 4 \frac{U}{\delta(z)} \mu(z, h(z)) dS \qquad \text{(Eq. 2.69)}$$

$$+ \int_0^{L_1} 4 \frac{U}{\delta(z)} \mu(z, h(z)) \cos\psi dS + \int_0^{L_1} p(z, h(z)) \sin\psi dS$$

The first two terms correspond to the momentum difference between the inlet and the outlet of the die, the third term expresses the force applied at the inlet, the fourth term

the friction force between the die wall and the gelled material, the fifth and the sixth term the viscous drag and the last term the force exerted by the taper wall.

2.5.2 Heat transfer and curing

Modelling of cure in a pultrusion die involves the incorporation of an energy balance, of thermal properties and kinetic models in a general model, which gives the temperature and the degree of cure distribution within the curing component. Phenomena governing the process of heat transfer in a pultrusion die are:

- heat conduction in the composite;
- heat generation by the exothermic curing reaction;
- heat transfer due to macroscopic movement of the bulk composite.

The material is considered as incompressible, the viscous friction is ignored and radiation heat transfer is considered negligible. According to Eq. 2.19, heat transfer can be described by the relation:

$$\rho c_p \frac{dT}{dt} = \vec{\nabla} \cdot (K \nabla T) + \rho_r v_r H_{tot} \frac{d\alpha}{dt} \qquad \text{(Eq. 2.70)}$$

The substantial time derivative of temperature can be expressed as (76):

$$\frac{dT}{dt} = \frac{\partial T}{\partial t} + \vec{u} \cdot \vec{\nabla} T \qquad \text{(Eq. 2.71)}$$

The partial time derivative in Eq. 2.71 vanishes when the process is in a steady state. Therefore Eq. 2.70 becomes:

$$\rho c_p \vec{u} \cdot \vec{\nabla} T = \vec{\nabla} \cdot (K \nabla T) + \rho_r v_r H_{tot} \frac{d\alpha}{dt} \qquad \text{(Eq. 2.72)}$$

The first term corresponds to heat convection due to macroscopic movement, the second term to heat conduction and the third expresses the exothermic heat produced by the reaction.

The various models developed can be classified according to the geometry and dimensionality of the problem they consider.

The simplest class of models, appropriate for cylindrical geometry, assumes negligible heat conduction in the angular and axial directions and a flat velocity profile (65, 74, 77, 78) resulting in the following problem:

$$\rho c_p U \frac{\partial T}{\partial z} = \frac{1}{r}\frac{\partial}{\partial r}\left(rK\frac{\partial T}{\partial r}\right) + \frac{d\alpha}{dt} v_r \rho_r H_{tot} \qquad \text{(Eq. 2.73)}$$

If the assumption of negligible axial conduction is omitted (3), the conduction heat flux partial derivative in respect to the axial direction should be added in the right hand side of Eq. 2.73.

Three-dimensional models have been developed in cartesian coordinates (1, 2, 79). The form of the energy equation used is:

$$\rho c_p \frac{\partial T}{\partial t} + \rho c_p U \frac{\partial T}{\partial z} = \frac{\partial}{\partial z}\left(K_{zz}\frac{\partial T}{\partial z}\right) + \frac{\partial}{\partial y}\left(K_{yy}\frac{\partial T}{\partial y}\right) + \frac{\partial}{\partial x}\left(K_{xx}\frac{\partial T}{\partial x}\right) + \rho_r v_r H_{tot}\frac{d\alpha}{dt} \qquad \text{(Eq. 2.74)}$$

Typical boundary conditions utilised are natural convection at the surface of the tooling, zero initial degree of cure and constant temperature and degree of cure at die exit. Limiting cases of such models, where the domain is considered as two dimensional, have been presented (4, 73, 80).

Similarly to Eq. 2.71 the degree of cure time derivative can be expressed as:

$$\frac{d\alpha}{dt} = \frac{\partial \alpha}{\partial t} + \vec{u}\cdot\vec{\nabla}\alpha \qquad \text{(Eq. 2.75)}$$

which for models corresponding to Eq. 2.73 and Eq. 2.74 becomes:

$$\frac{d\alpha}{dt} = U\frac{\partial \alpha}{\partial z} \qquad \text{(Eq. 2.76)}$$

This expression can be incorporated directly to the general heat transfer model.

The model solution is carried out using a finite elements or finite differences representation of the boundary value problems presented in Eq. 2.73 and Eq. 2.74. An initial guess of the temperature distribution, usually a uniform value, is given, then the model calculates the degree of cure and thermal properties values, which are fed back to the model. A new temperature distribution is calculated and the same procedure is iterated until the residual error satisfies a predefined convergence criterion. Typical iteration number required for convergence is 4 to 8 (80).

2.6 Modelling of filament winding

Filament winding is a process appropriate for the manufacturing of axisymmetric composite components. Continuous reinforcement, usually wetted (with the exception of the production of RTM pre-forms), is wrapped on a rotating mandrel. The process can include a wetting stage where the dry reinforcement is drawn through resin (wet filament winding), or can utilise pre-impregnated reinforcement as raw material (pre-preg winding), as shown in Fig.2.8.

The curing takes place on the mandrel, which is usually removed and placed in an oven. In some cases the curing and winding operations are performed simultaneously on the mandrel. This can be achieved by either placing the whole tooling assembly in an oven, or using electric or radiation heating.

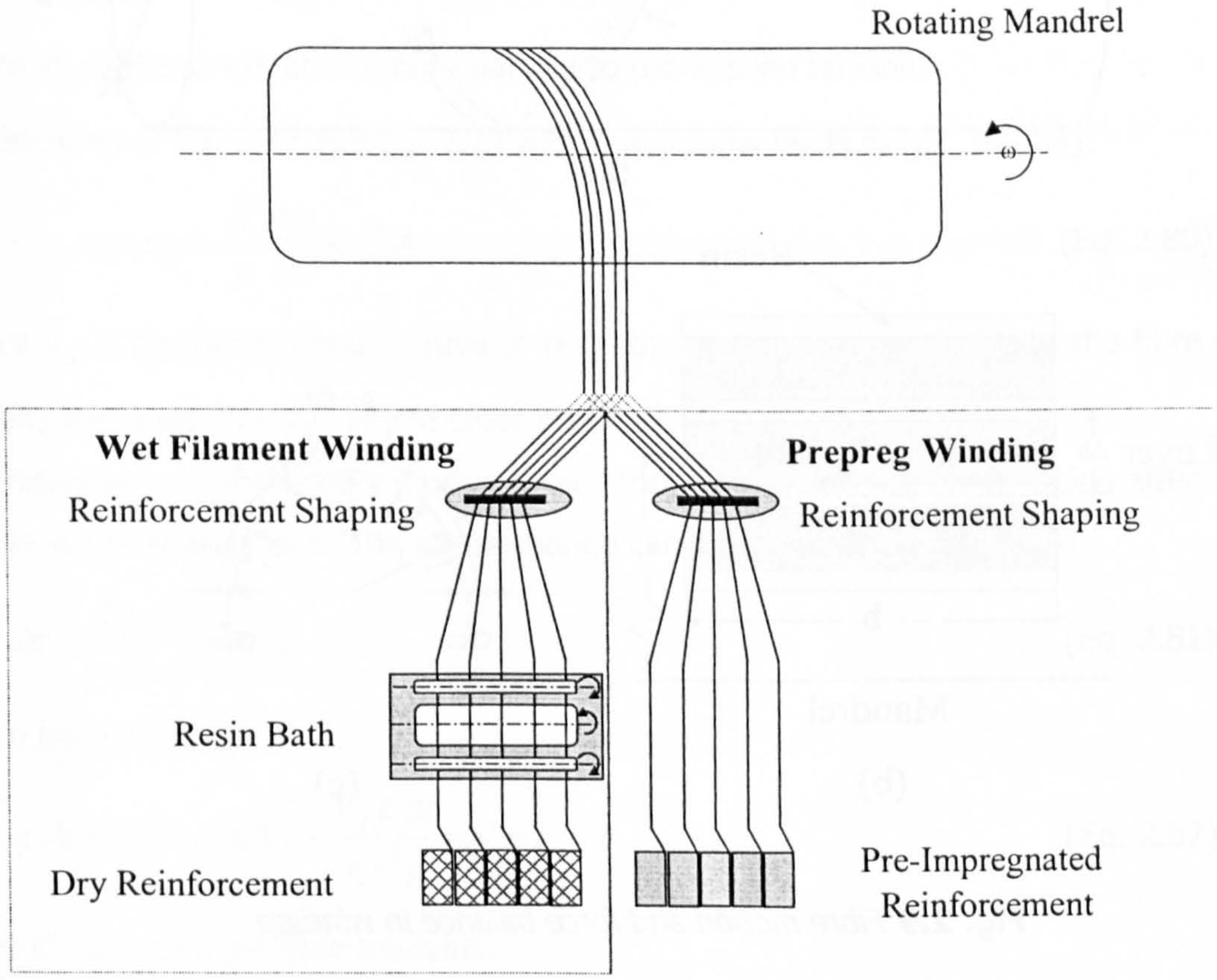

Fig. 2.8 *Schematic representation of wet and prepreg filament winding*

2.6.1 Modelling of fibre motion and consolidation during winding

The problem of analysis and simulation of resin flow and fibre motion occurring as the fibre tows are being wound on the mandrel has been addressed in the literature. During winding a tensile force F is applied to the fibre (Fig.2.9.a). This force causes compaction of the already wound composite and results in consolidation, which takes place by a combination of squeezing resin out and reinforcement deformation.

In general the composite is considered as a sequence of wet reinforcement layers and resin rich layers (Fig.2.9.b).

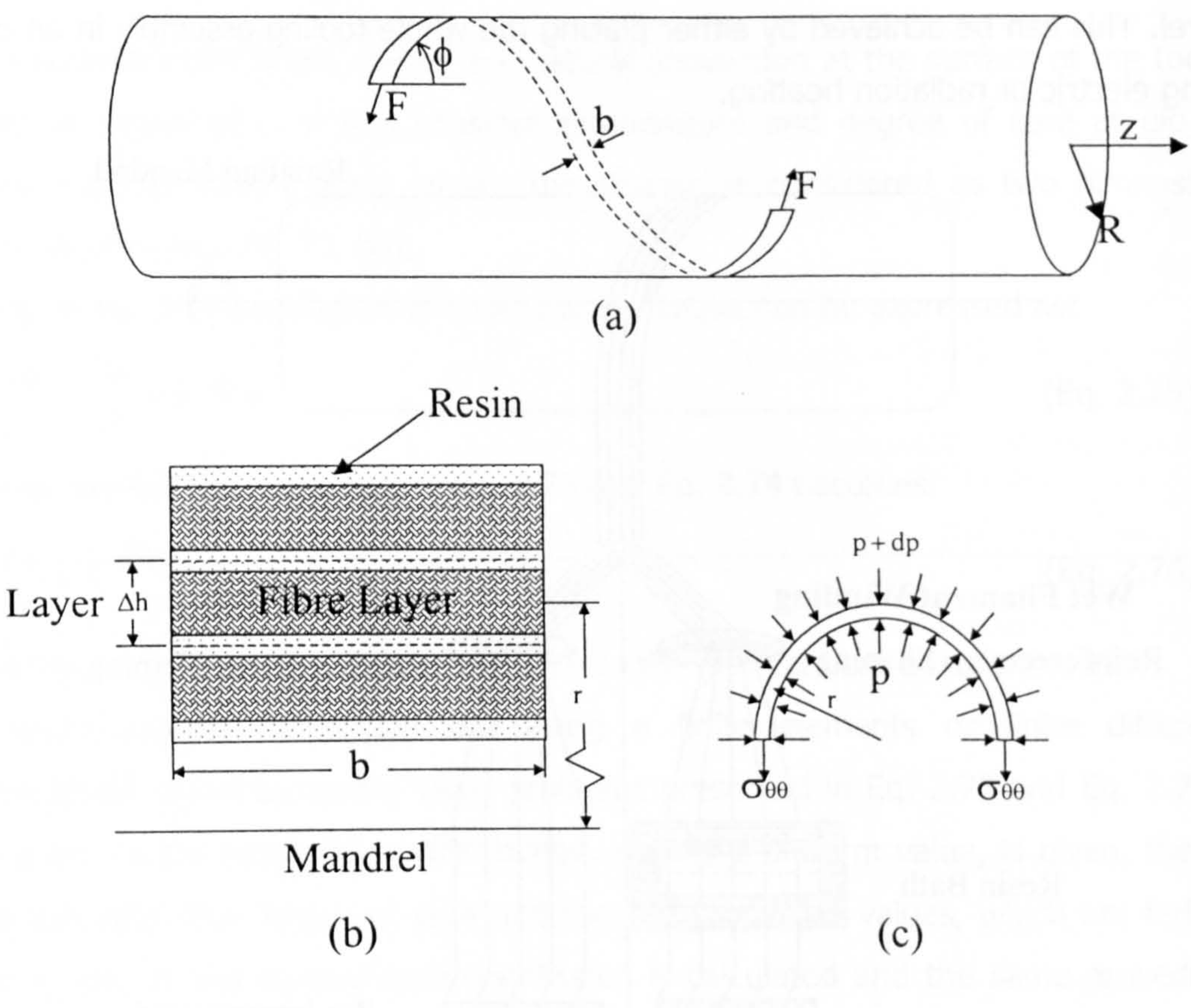

Fig. 2.9 *Fibre motion and force balance in winding*

In all the models a force balance is applied to a single layer wound on the mandrel (Fig.2.9.c). If an internal layer of the composite is considered (81, 82) the balance results in:

$$\frac{dp}{dr} = -\frac{\sigma_\theta}{r} \qquad \text{(Eq. 2.77)}$$

The same calculation for an external layer (81, 83) results in:

$$p = -\frac{\sigma_\theta \Delta h}{r} \qquad \text{(Eq. 2.78)}$$

In both cases the force balance has been applied in its equilibrium form, although the system is not equilibrated. A rigorous expression should be based on a momentum balance. However the fact that the process is very slow justifies the consideration of the inertia as negligible in all relevant published models.

The hoop stress is related to the radial stress and to the actual tension on the fibre band according to the relation (81):

$$\sigma_\theta = \sigma_f \sin^2\phi = \frac{F^*}{A_f}\sin^2\phi \qquad \text{(Eq. 2.79)}$$

where σ_f is the stress on the fibre parallel to the applied tension.

Combination of Eq. 2.77 and Eq. 2.79 with Darcy's law leads to (81, 82, 84):

$$-u_r = v_r u_f = \frac{\overline{K}}{\mu}\frac{\sigma_f}{r}\sin^2\phi \qquad \text{(Eq. 2.80)}$$

where u_f is the fibre speed relative to resin the and u_r is the relative to the fibre resin velocity averaged over the whole cross section.

The displacement of the fibre causes some strain change on the band, which affects the tensile stress applied to it. The strain change can be approximated (81) as:

$$\Delta\varepsilon = \frac{\overline{K}\Delta t}{v_r \mu}\frac{\sigma_f}{r^2}\sin^4\varphi \qquad \text{(Eq. 2.81)}$$

which leads to (81):

$$\sigma_f(t+\Delta t) = \sigma_f(t)\left(1 - \frac{E_f \overline{K}\Delta t}{v_r r^2 \mu}\sin^4\varphi\right) \qquad \text{(Eq. 2.82)}$$

Here E_f denotes the fibre modulus.

Integration of Eq. 2.80 over time leads to:

$$\Delta w = \frac{\overline{K}}{v_r \mu}\frac{\sigma_f}{r}\Delta t \sin^2\varphi \qquad \text{(Eq. 2.83)}$$

where Δw is the fibre displacement induced by consolidation within time interval Δt.

Eqs. 2.82 and 2.83 combined with zero displacement and predefined stress initial conditions, can be integrated in order to calculate radial displacement and fibre stress time evolution. This modelling work is based on the assumption that stress relaxation is governed by the resin flow through the fibre which is considered as a porous medium, hence Darcy's law has been used.

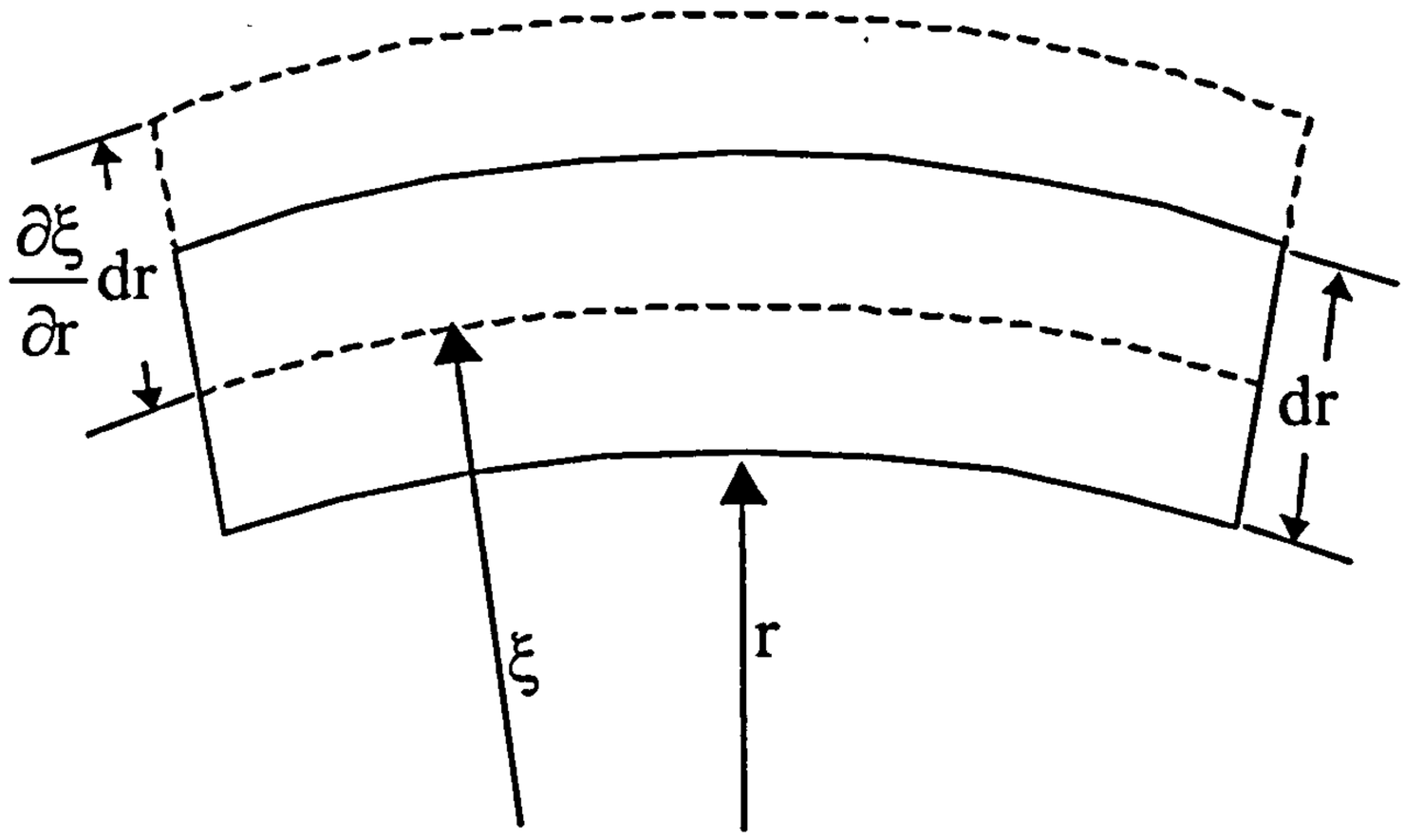

Fig. 2.10 *Behaviour of the element of composite layer during consolidation*

A different modelling procedure has been implemented by Cai and Gutowski (83). This approach takes into account the load carried by the fibre. The consolidation pressure is considered to be balanced by two components: (i) the compressive load carried by the fibre and (ii) the resin pressure.

The composite layer behaviour is illustrated in Fig.2.10. In the general case the layer moves form radial position r to ξ as a result of the consolidation pressure and the expansion of both the mandrel and the wound composite.

Mass conservation for the fibre and the resin leads to:

$$\frac{v_{fo}}{v_f} = \frac{\xi}{r}\frac{\partial \xi}{\partial r} \qquad \text{(Eq. 2.84)}$$

$$\frac{\partial}{\partial t}\left[\left(1-v_f\right)\xi\frac{\partial \xi}{\partial r}\right]+\frac{\partial \xi u_r}{\partial r}=0 \qquad \text{(Eq. 2.85)}$$

where v_{fo} is the fibre volume fraction at r. Combination of Eq. 2.85 with Darcy's law results in:

$$\frac{1}{v_f}\frac{\partial v_f}{\partial t}+\frac{1}{\xi}\frac{\partial}{\partial \xi}\left[\frac{\overline{K}}{\mu}\xi\frac{\partial p_r}{\partial \xi}\right]=0 \qquad \text{(Eq. 2.86)}$$

where p_r is the resin pressure

In the Cai-Gutowski model the permeability is approximated by the Cozeny-Karman model. The modelling is completed by incorporation of the phenomena related to the fibre. The general equilibrium condition for a cylindrical element is (85):

$$\frac{d\sigma_r}{dr}+\frac{\sigma_r-\sigma_\theta}{r}=0 \qquad \text{(Eq. 2.87)}$$

The stresses can be decomposed as follows:

$$\sigma_r=\sigma_{fr}-p_r \qquad \text{(Eq. 2.88)}$$

$$\sigma_\theta=\sigma_{f\theta}-p_r \qquad \text{(Eq. 2.89)}$$

where σ_{fr} and $\sigma_{\theta r}$ are the radial and hoop stresses on the fibre correspondingly.

Using a first order approximation to express the strain and implementing the incremental form of the stress-strain constitutive relations the following equations are obtained (83):

$$\varepsilon_r=\frac{\partial \xi}{\partial r}-1 \qquad \text{(Eq. 2.90)}$$

$$\varepsilon_\theta=\frac{\xi}{r}-1 \qquad \text{(Eq. 2.91)}$$

$$\Delta\varepsilon_\theta=S_{\theta\theta}\Delta\sigma_{f\theta}+S_{\theta r}\Delta\sigma_{fr}+\alpha_\theta\Delta T \qquad \text{(Eq. 2.92)}$$

$$\Delta\varepsilon_r=S_{rr}\Delta\sigma_{fr}+S_{\theta r}\Delta\sigma_{f\theta}+\alpha_r\Delta T \qquad \text{(Eq. 2.93)}$$

where the S_{ij} terms are the fibre network compliance, which can be expressed as a function of fibre volume fraction, the maximum packing volume fraction and the fibre stiffness (86).

Eqs. 2.84 and 2.86-2.93 with the boundary condition of zero resin pressure at the external surface can provide the solution for the stress, strain, fibre volume fraction and resin pressure distributions during winding (83). The solution of the model is repeated for each new layer wound on the mandrel.

A third modelling procedure for the winding stage, which considers the static and dynamic effects as separate, has been developed. When a new layer is wound

consolidation takes place and the stress equilibrates on a value, which corresponds to the elastic response of the composite ring. This can be expressed by the relations (87):

$$\sigma_r^{k+1} = \sigma_r^k + \sigma_r^\infty + \sigma_r^t(t) \qquad \text{(Eq. 2.94)}$$

$$\sigma_\theta^{k+1} = \sigma_\theta^k + \sigma_\theta^\infty + \sigma_\theta^t(t) \qquad \text{(Eq. 2.95)}$$

$$w^{k+1} = w^k + w^\infty + w^t(t) \qquad \text{(Eq. 2.96)}$$

where $\sigma_r^{k+1}, \sigma_\theta^{k+1}$ and σ_r^k, σ_θ^k are the total radial and hoop stresses after winding the $k+1$ and the k layer correspondingly, σ_r^∞ and σ_θ^∞ are the steady state stress components, $\sigma_r^t(t)$ and $\sigma_\theta^r(t)$ are the transient stress components which relax after consolidation and w^{k+1}, w^k, w^∞, $w^t(t)$ are the corresponding quantities for fibre displacement from the original position.

The steady state components can be calculated by elastic response analysis. An analytical solution of the problem has been produced by Hahn (88). In order to perform the analysis of the transient effects, a proportionality law is assumed in order to relate the transient strain radial time derivative with the total radial stress (87):

$$\frac{\partial \varepsilon_r^t}{\partial t} = C\sigma_r^{k+1} \qquad \text{(Eq. 2.97)}$$

The proportionality coefficient C depends on the fibre volume fraction as follows:

$$C = C_o e^{-a(v_f - v_{fo})} \qquad \text{(Eq. 2.98)}$$

where C_o and a are coefficients.

Eq. 2.97 is equivalent to Darcy's law (Eq. 2.80), and coefficient C behaves similarly to permeability, since it increases as the fibre volume fraction increases. Therefore the model could incorporate Darcy's law with similar results and a more sensible justification of its physical meaning.

Combination of Eq. 2.97 with an equilibrium condition (Eq. 2.87), the strain-displacement relations presented in Eq. 2.90 and Eq. 2.91 and the strain-stress relations obtained by application of Hooke's law for cylindrical coordinates (85) leads to the differential equation (87):

$$\frac{\partial \varepsilon_r^t}{\partial t} + \frac{CE_r}{1-\nu_{\theta r}\nu_{r\theta}}\varepsilon_r^t = C\left[\sigma_r^k + \sigma_r^\infty + \frac{E_r}{1-\nu_{\theta r}\nu_{r\theta}}\left(\frac{\partial w^t}{\partial r} + \nu_{r\theta}\frac{w^t}{r}\right)\right] \qquad \text{(Eq. 2.99)}$$

which can be solved, using a zero displacement on the mandrel and a zero radial stress on the outer surface boundary conditions. The application of Hooke's law limits the suitability of this model, since Hooke's law is an appropriate stress-strain relation only in the case of prepreg winding, where resin outward flow is slower then winding (83).

2.6.2 Heat transfer and cure modelling

Heat transfer modelling applied to the curing of filament wound composites is performed by solving an energy balance equation which combines heat conduction phenomena and heat generation arising from the curing reaction. The general differential equation expressing the phenomenon is Eq. 2.18. Features of the process affecting the form of the energy balance equation are:

- curing and winding are usually decoupled, therefore the term corresponding to convection due to macroscopic movement is ignored;
- the process is used for the production of axisymmetric components, for that reason cylindrical co-ordinates are appropriate;
- the heating during the cure is uniform along the circumference of the component and the angular terms of the energy balance are negligible.

Thus, Eq. 2.18 becomes (89):

$$\rho c_p \frac{\partial T}{\partial t} = \frac{1}{r}\frac{\partial}{\partial r}\left[r\left(K_{rr}\frac{\partial T}{\partial r} + K_{rz}\frac{\partial T}{\partial z}\right)\right] + \frac{\partial}{\partial z}\left[K_{zz}\frac{\partial T}{\partial z} + K_{rz}\frac{\partial T}{\partial r}\right] + \frac{d\alpha}{dt} v_r \rho_r H_{tot} \qquad \text{(Eq. 2.100)}$$

Variations of the energy equation have been implemented according to the assumptions utilised in different models. Lee and Springer (81) have considered the axial and the radial directions as the principal directions, which is reasonable when a symmetric laying pattern is modelled. Consequently their model neglects the non-diagonal terms of the conductivity tensor and Eq. 2.102 becomes:

$$\rho c_p \frac{\partial T}{\partial t} = \frac{1}{r}\frac{\partial}{\partial r}\left[r\left(K_{rr}\frac{\partial T}{\partial r}\right)\right] + \frac{\partial}{\partial z}\left(K_{zz}\frac{\partial T}{\partial z}\right) + \frac{d\alpha}{dt} v_r \rho_r H_{tot} \qquad \text{(Eq. 2.101)}$$

In other cases (90, 91) the temperature gradient along the axial direction is assumed to be negligible and the one dimensional energy balance is regarded as adequate to model the curing:

$$\rho c_p \frac{\partial T}{\partial t} = \frac{1}{r}\frac{\partial}{\partial r}\left[r\left(K_{rr}\frac{\partial T}{\partial r}\right)\right] + \frac{d\alpha}{dt} v_r \rho_r H_{tot} \qquad \text{(Eq. 2.102)}$$

Different variations of the energy balance equation have been used in cases where the required heating is not provided by an oven. If internal electric heating is utilised the heat source term includes, apart from the curing exothermic heat, the heat generated by resistance heating (92). If the case of infrared curing is modelled the appropriate radiation term is included in the energy balance (93).

Usually the model domain comprises the composite and the mandrel. The energy equation for the mandrel is identical to the one applied to the composite without the exothermic heat term.

Typical boundary conditions are:

- air convection on the external surface, controlling the heating of the composite;
- specified temperature on the external surface.

If the mandrel considered is hollow the same boundary conditions can be applied to the internal surface. In case the mandrel is solid, a zero heat flux boundary conditions at the centre should be incorporated in the model. When the solution scheme does not satisfy automatically the temperature and heat flux density continuity conditions, continuity conditions at the mandrel-composite interface should be used.

Solution is usually performed by application of finite element techniques. The problem is transient and non-linear, therefore a form of time discretisation and an iterative procedure for the calculation of the thermal properties and the rate of reaction are required.

2.7 Overview

Modelling of flow processes involved in composites manufacturing is performed using a momentum balance combined with mass continuity. The composite is usually assumed to have the behaviour of a porous medium, therefore Darcy's law is utilised as a momentum balance. Although there is a significant amount of research work completed

on the subject there are disagreements between different models. In some cases, despite the fact that the phenomena governing flow and consolidation have been proved to be complicated, simplified models are implemented.

Formulation of heat transfer simulations is more coherent. Models are based on combinations of energy balance with Fourier's law of heat conduction. Cure kinetics are incorporated in the energy balance where applicable. Most of the implementations contain gross simplifications, which are not always justified, as far as the dimensionality of the problem and the treatment of thermal properties are concerned.

Chapter Three

3 Cure and flow monitoring in the processing of thermosetting composites

3.1 Introduction

Cure monitoring is the observation of the reaction occurring in a thermosetting polymer resin. It is performed by measuring the evolution of some physical quantity connected directly or indirectly to the cure state. Any technique that measures a material property or a material-measuring system physical quantity related unequivocally to the cure state qualifies as a cure monitoring technique. In this context, methods such as calorimetry, infrared spectroscopy, rheometry, dilatometry, dielectric spectroscopy, thermo-mechanical analysis, Raman spectroscopy and fluorescence can be used in laboratory tests in order to characterise the thermoset and its curing behaviour.

When application of a cure monitoring technique aims to monitor the cure during processing it should meet some additional criteria. The technique should not interfere with the process, the sensing devices should be non-intrusive and the measurement should be feasible in real time i.e. measurement and interpretation should be performed within a period during which the cure state does not alter substantially. Currently, techniques that meet the above criteria to an acceptable extent and are viable can be classified as follows:

- Dielectric cure monitoring;

- Fibre optic spectroscopy;
- Acoustic cure monitoring;
- Thermal monitoring.

At present, their application is focused mainly on research and development but they are the most likely techniques to be implemented on the production line in the future.

Recent rise of interest in liquid moulding has generated an additional application area for monitoring. The criticality of the filling stage necessitates the development and implementation of flow monitoring methods. Although this area of study is relatively new, methods based on electric, dielectric and optical measurements have been developed already and applied to laboratory or pilot scale liquid moulding equipment.

3.2 Acoustic cure monitoring

Application of acoustic measurements as a cure monitoring tool is based on the sensitivity of wave propagation, in the sonic and ultrasonic frequency ranges, to the macroscopic polymer structure. The correlation between state of cure of thermosetting materials and features of the ultrasonic waves propagation was recognised as early as 1974. Thus, ultrasonic resonance, reflection and transit time were utilised as an off-line characterisation tool of cured thermosets and thermoset based composites (94, 95).

The implementation of the technique as an in-situ monitoring tool requires an experimental configuration, which includes a transmitter and a receptor of the ultrasonic wave, which propagates through the material. A wide range of transmission and reception set-ups has been used. Some typical configurations are given in Fig. 3.1.

The same probe can be used as a transmitter and a receptor (Fig. 3.1.c) (96) but in most cases two different probes perform these two tasks (97-99). The typical ultrasound monitoring set-up utilises piezoelectric transducers in contact with the mass (Fig. 3.1.a), which can be either the curing material or a part of the tool. In some cases rod shaped waveguides (Fig. 3.1.b) have been used in order to transfer the wave into the curing material (96, 100), aiming to avoid problems due to the contact of the sensor with the curing material and to achieve remote monitoring. The use of optical fibres as transmission and reception probes has been attempted (101) also. In this case, a laser pulse generates the ultrasound and the signal is received using optical fibre

interferometry. This configuration is an alternative solution for remote monitoring, but the resulting noise to signal ratio appears to be very high in comparison with more conventional ultrasonic measurements.

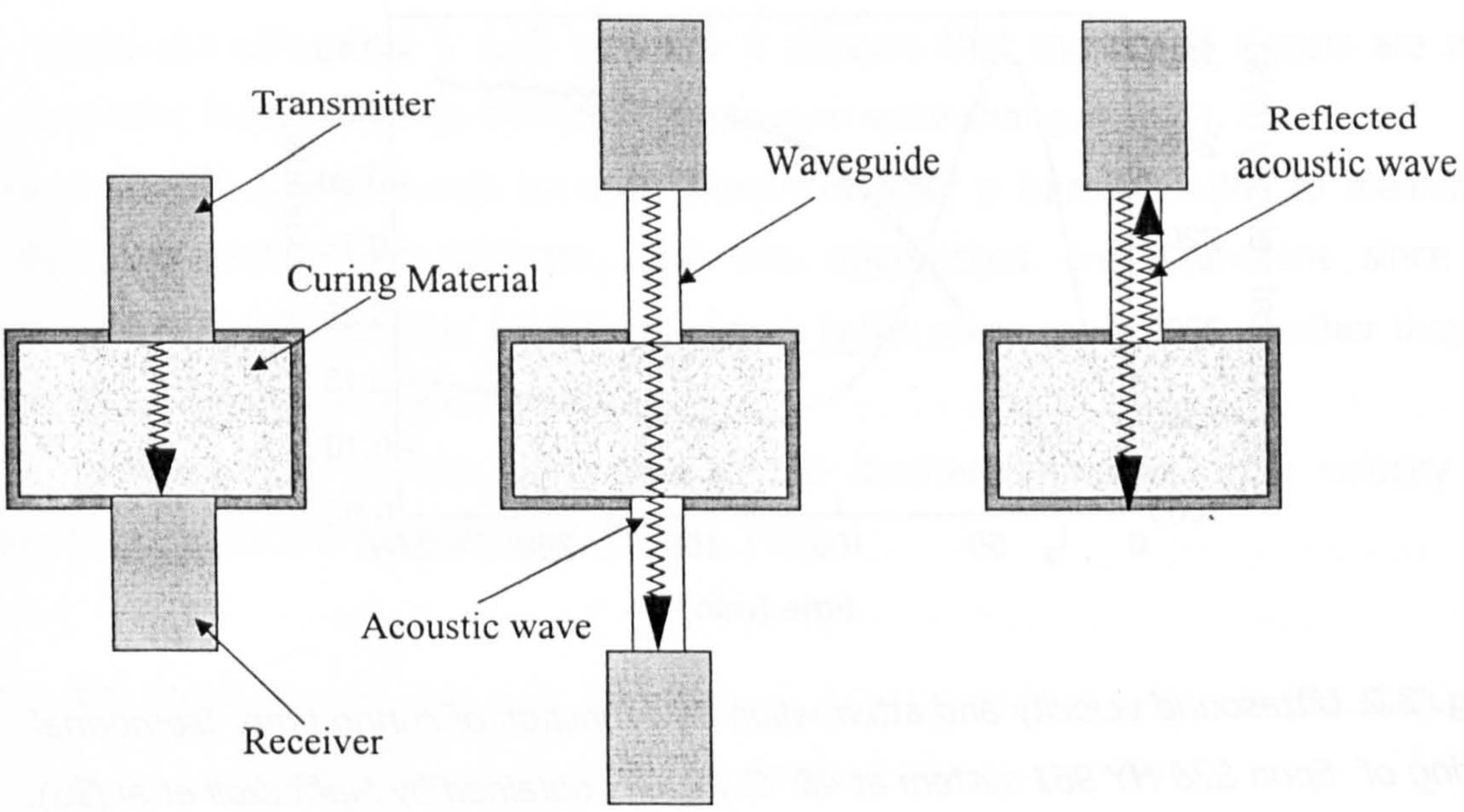

Fig. 3.1 *Acoustic cure monitoring experimental configurations*

Longitudinal waves are the most common form of acoustic signal used for cure monitoring (96, 97, 102, 103). Shear waves have negligible propagation through liquid resin, and thus are not usually appropriate for monitoring the initial stages of cure (96, 102); however, in some cases propagation of shear waves has been reported to be measurable even at the beginning of the cure (99). In the case of adhesives the curing has been followed using interfacial ultrasonic waves propagating along the adhesive film-bulk material interface (104).

The signal type recorded and processed in order to follow the cure is specific to the particular experimental configuration and to the application. The velocity of the ultrasound in the curing material or the time transit of the propagating pulse wave (97-99, 101-104), the attenuation or the absorption of the wave (98, 102, 103), the reflection coefficient at the probe-curing material interface (96) and the frequency of the

resonance peaks (105) have all been used by different researchers. Typical velocity and attenuation signals obtained during the cure of an epoxy resin are given in Fig. 3.2 .

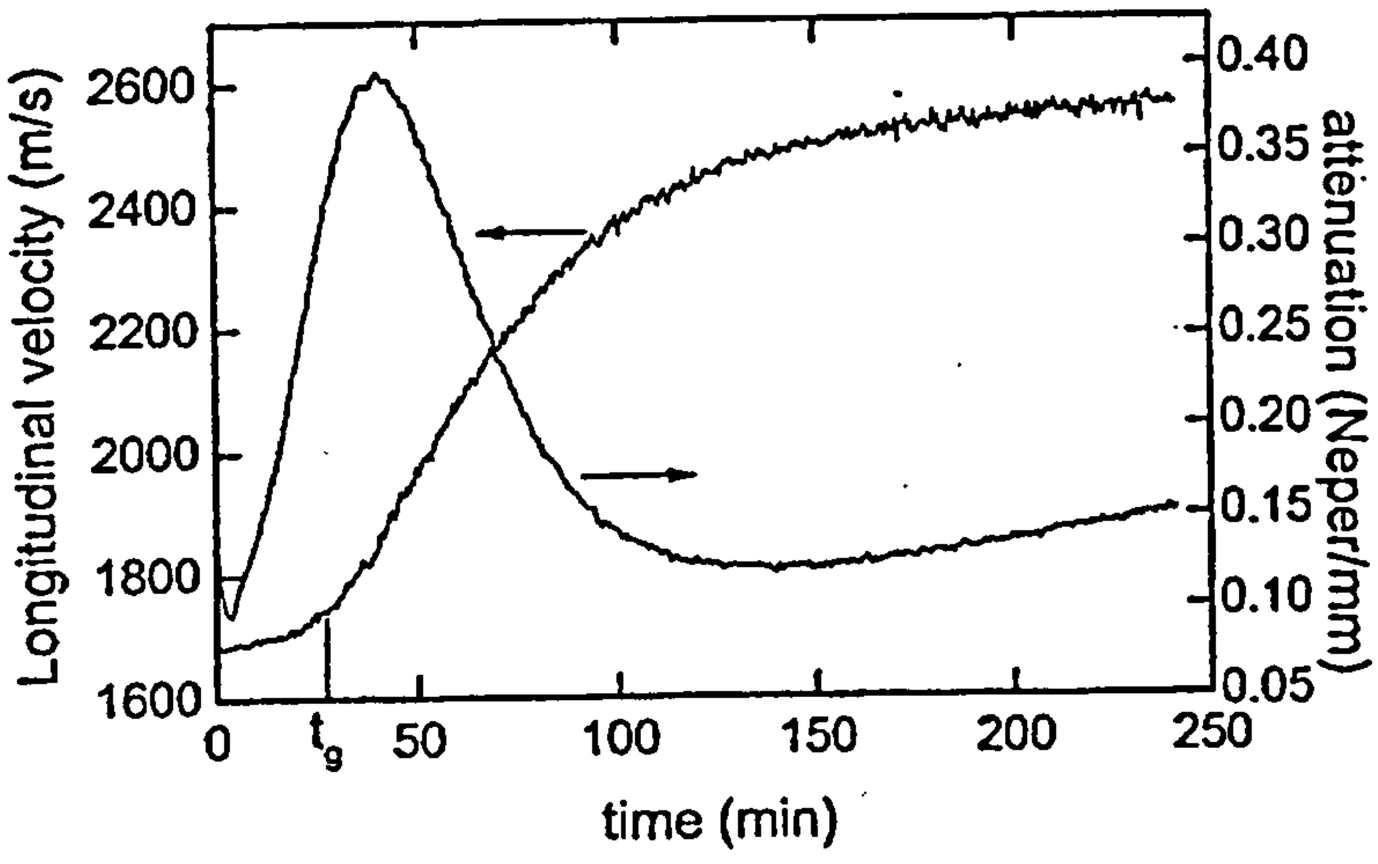

Fig. 3.2 *Ultrasound velocity and attenuation as a function of curing time. Isothermal curing of Epon 828-HY 961 system at 48 °C. Results obtained by Maffezzoli et al* (98).

The general behaviour of the ultrasonic signals during the cure can be summarised as follows:

- The ultrasound velocity increases as the curing reaction progresses in a step like fashion (98, 101, 102, 104). This increase is explained by the building up of the modulus during the cure.
- The attenuation presents a peak during the cure (98, 102, 103). Some authors connect this peak with the vitrification (98, 103) in analogy with dynamic mechanical analysis, but experimental data do not reinforce this view (98). Other researchers attribute the peak to the development of two competing phenomena during the cure (102); (i) the raise of the polymeric chain length which increases the absorption and (ii) the chain mobility drop which results in lower ultrasound absorption as the curing progresses.
- The reflection coefficient at the probe-curing material interface undergoes a step drop during the cure (96). This is attributed to the change of mechanical impedance of the curing material toward a value closer to the mechanical impedance of the solid probe.

- Temperature has a significant effect on the acoustic signals. Velocity changes with temperature through its dependence on modulus (97, 98, 104) i.e. it decreases as the temperature increases. The sensitivity of sound velocity to temperature changes is similar to that to the cure state changes. When the frequencies of the resonance peaks are utilised as a cure indicator it appears that the useful signals are more sensitive to temperature changes than to cure state changes (105).

The measured quantities can be used directly or after a transformation to meaningful material properties like stiffness. The two approaches are equivalent since the information provided by the monitoring signals is the same regardless whether they are translated to material properties or not.

The relations used for the calculation of the mechanical moduli from velocity and attenuation data are the following (98, 99, 102):

$$M' = \rho c^2 \frac{1-\frac{\alpha_u^2 c^2}{\omega^2}}{\left(1+\frac{\alpha_u^2 c^2}{\omega^2}\right)^2} \qquad \text{(Eq. 3.1)}$$

$$M'' = 2\rho c^2 \frac{\frac{\alpha_u c}{\omega}}{\left(1+\frac{\alpha_u^2 c^2}{\omega^2}\right)^2} \qquad \text{(Eq. 3.2)}$$

where M' and M'' denote the real and the imaginary modulus corresponding to the wave mode used, ρ is the density of the medium, ω the frequency, c velocity of the ultrasound and α_u the attenuation of the ultrasonic wave.

Similar calculations can be performed when the reflection coefficient is measured (96). In the case of resonant spectroscopy the calculation of the moduli has to be performed with due consideration of the geometry (105) and in complicated cases it should be the subject of an inverse solution of the equations of motion.

Comparative studies of the moduli determined using acoustic techniques and dynamic mechanical analysis demonstrated qualitatively similar behaviour during the cure (99). The resulting moduli, however, present significant differences in absolute values and the sensitivity of the dynamic mechanical modulus to the cure state appears to be much greater than that of the acoustic modulus. This difference can be attributed to the

difference in the frequency range of the techniques, which from the order of 0.01 to 100 Hz in dynamic mechanical analysis becomes closer to kHz and MHz in acoustic monitoring.

3.3 Optical techniques

The use of optical techniques for cure monitoring is based on the sensitivity of the spectroscopic response or optical properties to the chemical and structural states of the curing material. The following types of optical measurement have been applied successfully to the characterisation of the curing process:

- Infrared spectroscopy;
- Raman Spectroscopy;
- Fluorescence.

Other techniques based on measurement of an optical property e.g. refractive index or reflectance (106) have also been used, but their applicability is very limited in comparison with spectroscopic techniques.

Adaptation of these techniques to serve as in-situ cure monitoring tools assumes successful transmission of the optical signals to the manufacturing tool and back. This critical feature governs the ability to transform any technique from a laboratory scale characterisation tool to an in-situ real time monitoring tool appropriate for the manufacturing environment.

3.3.1 Infrared Spectroscopy

Infrared techniques exploit the fact that the vibrational response spectrum of a polymeric material is characteristic of the configurations of different functional groups contained in the polymer chain. Thus, observation of the spectra during the cure can provide direct chemical information on the curing system. Application of the technique has been performed in the mid-infrared (wavelength: 2.5-25 μm) and in the near infrared (wavelength: 0.7-2.5 μm) ranges.

Most of the fundamental studies on epoxy cure kinetics have been performed in the mid-infrared range where most of the bands of the epoxy resin spectrum are located.

However, the need to perform the measurement remotely in the manufacturing environment introduces some practical difficulties, since transmission of the mid-infrared radiation is possible only through chalcogenide glass fibres (107) or gold coated waveguides (108). In contrast, radiation in the near infrared range can be transmitted through common silica type optical fibres (109, 110), which are inexpensive and easy to use. Additionally, as found by Mijovic and Andjelic (111), peaks in the near-infrared range correlate with chemical behaviour of epoxy/amine systems in a more satisfactory way than the standard epoxy absorption which appears in the mid-infrared spectrum. For these reasons, application of infrared fibre optic cure monitoring to composite manufacturing is performed preferably in the near-infrared region of the spectrum.

In most cases the transmission (107-109, 112) or reflection-evanescence (113-115) response of the material to the radiation is measured. A variation of the technique utilises the radiation emitted from the material at elevated temperatures (116).

In transmission mode the experimental configuration involves the placement of two optical fibres in the curing material exactly opposite to each other. One of them transmits the excitation radiation and the other collects the radiation transmitted through the curing material. The absorbance or extinction of radiation can be calculated as follows (117):

$$A_r = log\left(\frac{J_o}{J}\right) \qquad \text{(Eq. 3.3)}$$

where J_o is the incident radiation and J the transmitted radiation.

The absorbance is proportional to the concentration of the absorbing species, according to Beer's law (118):

$$A_r = \kappa C d \qquad \text{(Eq. 3.4)}$$

where κ is the molar extinction coefficient, C the concentration and d the sample thickness. This relation is the basis of quantification of the method.

Evolution of typical absorbance spectra during the cure is illustrated in Fig.3.3. Different peaks can be assigned to different modes of vibration of functional groups. Some peaks are selected as reaction indicators and their change relative to an inert reference peak is calculated. Such normalisation is performed in order to allow for bulk changes of the spectrum caused by phenomena irrelevant to the chemistry of the system, such as dimensional changes. Results obtained using infrared transmission spectroscopy present

an excellent correlation with degree of cure changes and a low noise to signal ration (107-109, 112).

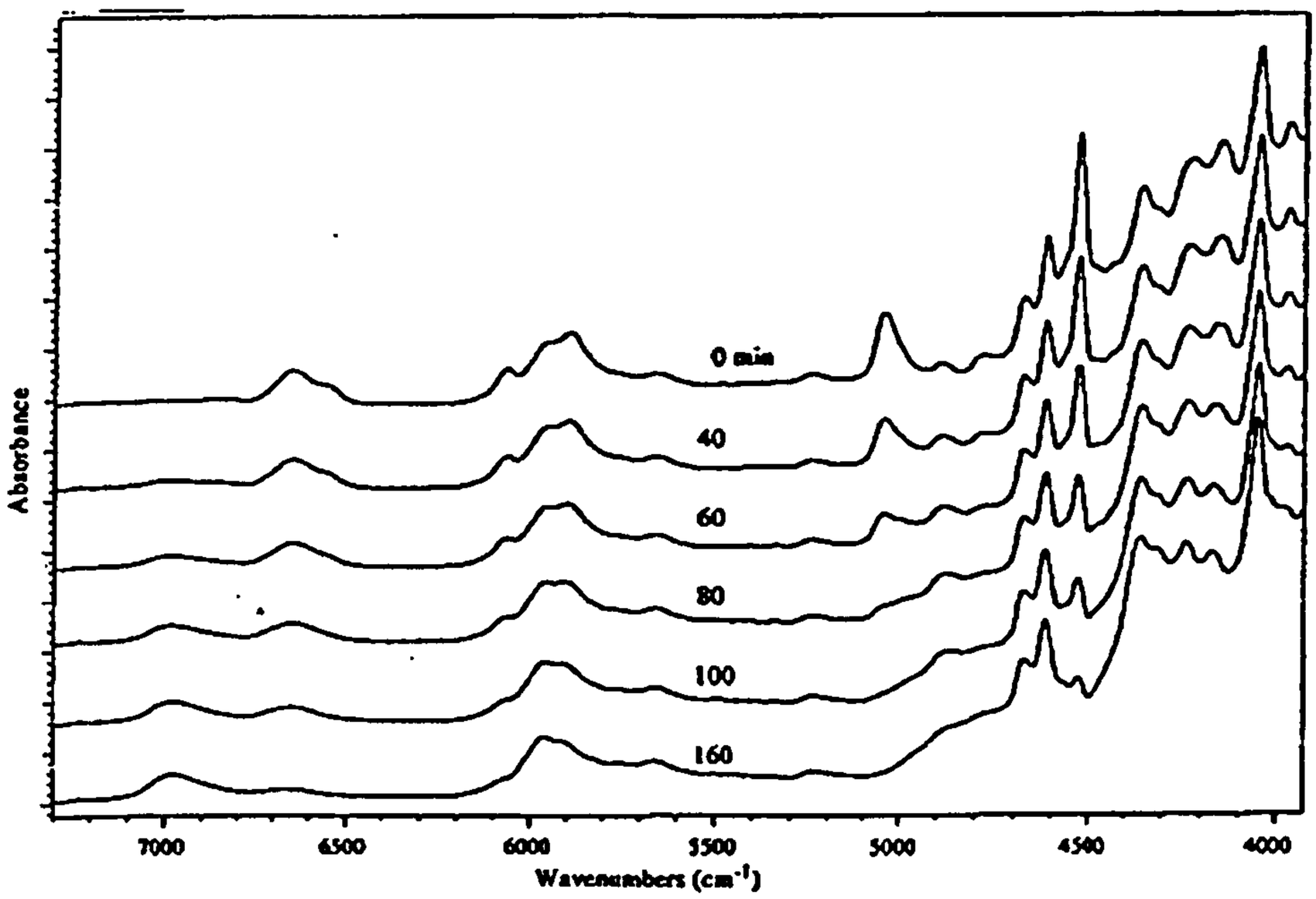

Fig. 3.3 *Absorbance spectra in the near-infrared range. Isothermal curing of a DGEBF-MDA system at 84 °C. Results obtained by Mijovic et al (109).*

In some studies the phenomenon of total internal reflection combined with the presence of an evanescent field has been used for infrared cure monitoring. If radiation passes from an optically more dense medium to one that is less dense, there is a critical angle of incidence above which there is no refraction and the radiation is reflected totally. The interference of the incident and reflected beams results in a slight penetration of the electromagnetic field into the second medium. The depth of penetration, i.e. the distance over which the field decays to $1/e$, of the exponentially decaying evanescent field is given by the relation (119):

$$d_p = \frac{\lambda}{2\pi\sqrt{\sin^2\theta_i - \left(\frac{\eta_2}{\eta_1}\right)^2}} \qquad \text{(Eq. 3.5)}$$

where λ is the wave length of the radiation, θ the incidence angle, η_1 the refractive index of the transmitting medium and η_2 the refractive index of the reflecting medium.

Since the radiation penetrates into the medium it interacts with it and absorption occurs. This phenomenon can be exploited to monitor the cure using the reflected infrared spectrum evolution during the cure. Measurements have been performed in both the mid-infrared (114) and the near infrared (113, 115) ranges. The measurement is feasible using an appropriate prism (113, 114) or optical fibres (115) as guiding media. The resulting spectra demonstrate behaviour similar to that observed using transmission techniques.

In cases where the curing temperature is high, the emission of infrared radiation can be sufficient to allow the performance of a spectroscopic measurement without the use of excitation. The probability of emission at one wavelength is proportional to the absorbance at that wavelength. Thus, the vibrational spectral information is equivalent to the information gathered using transmission spectroscopy. Some complications arise due to reabsorption and internal reflection, but, as has been shown by George et al (116), changes in emissivity can be related directly to changes in concentration of functional groups.

3.3.2 Raman Spectroscopy

Raman spectroscopy is based on the Raman scattering effect. This occurs when the radiation interacts with a molecule with an anisotropic polarizability tensor. Then internal vibrations or rotations result in scattering of the incident radiation at frequencies lower or higher than that of the incident radiation (120). Consequently, the excited sample emits some radiation at different frequencies which are characteristic of the molecule.
The technique has not found such wide use as the rest of the spectroscopic techniques, mainly due to noise problems caused by fluorescence, but the use of near-infrared laser excitation radiation allowed the improvement of the measurement quality (121). An in-situ configuration comprising two optical fibres, one transmitting the excitation and the other receiving the scattered radiation, has been tested in the curing of DGEBA epoxy resin and the results were found to be in good agreement with results obtained using infrared absorbance spectroscopy (122).

3.3.3 Fluorescence

A large family of optical techniques applied to cure monitoring make use of fluorescence phenomena. Fluorescence occurs when absorption of radiation excites the molecular or atomic system, which then decays back in a short time by emitting radiation at a frequency equal or lower than the frequency of the incident radiation (120).

Various studies have used fluorescence connected phenomena in different ways in order to monitor the cure. One approach relies on the fluorescence enhancement that occurs in certain fluorophores when the viscosity of the medium increases. These are functional groups that, when excited, can undergo non-radiative decay by twisting or torsion motions. Increase of viscosity inhibits this type of decay, giving rise to fluorescence as an alternative mode of energy emission. The probing functional group can be extrinsic (123, 124) or intrinsic (125). As reported by Levy et al (125) implementation of this approach in micro-autoclave curing, using optical fibres as optical signal waveguides, gives satisfactory results. The implementation of the technique and the interpretation of the results vary according to the probing chemicals. For example in the case studied by Wang et al (123) illustrated in Fig.3.4 there are two regions of the fluorescence spectrum, one viscosity dependent and one independent. The fluorescence band at 480 nm is connected with pyrene which is formed by a diffusion-controlled process and depends on viscosity, whereas the band at 377 nm is due to the emission from isolated pyrenyl groups and does not depend on viscosity. Thus, their relative intensity exhibits a direct dependence on viscosity.

A second technique monitors fluorescence resulting from the association of an excited molecule with another molecule in its ground state (excimer fluorescence). The formation of the excimer probe is diffusion-controlled, therefore the fluorescence intensity decreases with increasing viscosity of the carrying medium. Implementation of the technique using an internal reference substance allows monitoring of the initial and intermediate stages of the reaction, but photodegradation can cause problems at the final stages of the cure (123).

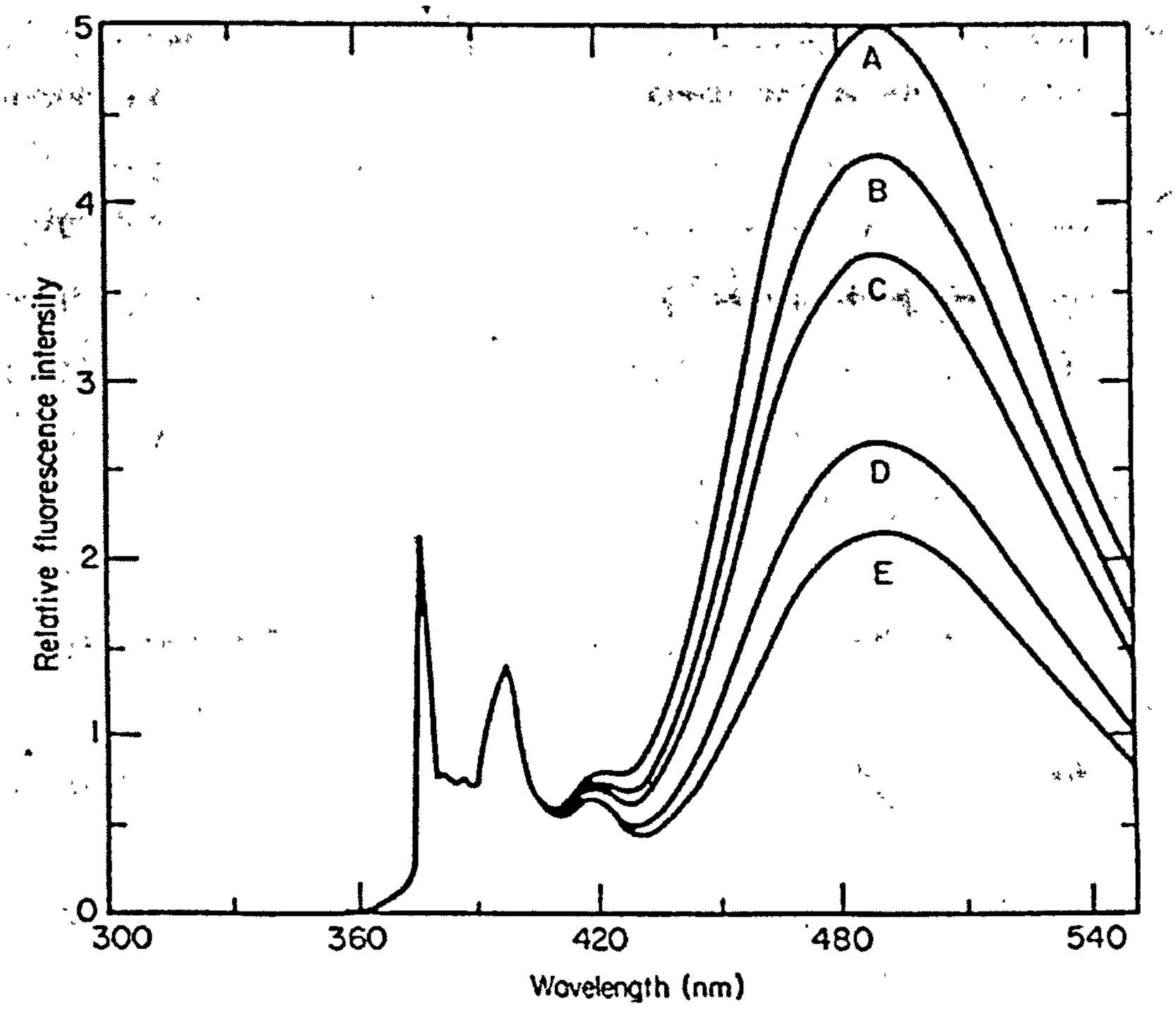

Fig. 3.4 *Evolution of fluorescence spectra with increasing viscosity from A to E. Results obtained by Wang et al* (123).

Another technique that monitors the diffusion coefficient changes during cure is based on the combination of fluorescence with photobleaching. Photobleaching occurs when a high energy radiation causes photochemical reactions such that the fluorescence ceases. Momentarily irradiation of the sample with a localised high energy beam causes a temporary gradient of the fluophores concentration. Thus, measurement of the fluorescence intensity rise after photobleaching on the same area monitors the diffusion of fluorophores from the surrounding material. Application of the technique by Wang et al demonstrated its ability to follow viscosity and monitor the vitrification of a DGEBA epoxy resin (126).

Implementation of fluorescence monitoring can be performed using reactive extrinsic fluorophores, which mimic the chemical behaviour of some of the reactants of the curing reaction. These substances exhibit fluorescence intensity changes and fluorescence spectrum peak shifts as they react. Although the reproducibility of these phenomena is

low, the use of an internal reference substance makes quantification of the technique possible (127). Application of this technique to the liquid moulding of thermoset composites has been reported by Parnas et al in a series of papers (128-130). Fluorescence arising due to the evanescent field around an optical fibre has been monitored and the wavelength of the fluorescence spectrum maximum has been shown to correlate well with the progress of the reaction.

3.4 Dielectric cure monitoring

Dielectric techniques are based on the dependence of the electric and dielectric measures (complex dielectric constant, conductivity and impedance) on structural properties of the curing system (degree of cure, glass transition temperature and viscosity).

The behaviour of a thermoset, when an AC electric field is applied to it, is governed by three phenomena: (i) dipole polarisation, (ii) migrating charges conduction and (iii) electrode polarisation.

3.4.1 Dipolar Relaxation

Dipoles are present in a material as permanent dipoles due to molecular asymmetry or are induced by the electric field. In the absence of an electric field the orientation of the permanent dipoles is random. The electric field disturbs the random arrangement of polar molecules and functional groups towards a configuration relatively more aligned to the electric field and induces some polarity in symmetrical molecules (131). Thus, macroscopic polarisation of the material, which affects the dielectric constant and consequently all the relevant electrical physical quantities, occurs. The part of the material response which is attributed to the induced dipoles is considered instantaneous and corresponds to optical polarisation. The permanent dipole contribution is time dependent and therefore also frequency dependent as well (132).

In the case of dipole orientation the real part of the complex dielectric constant (permittivity) expresses the capability of the material to store part of the energy emitted by the electric field. It has high values at low frequencies (relaxed permittivity) where

the dipoles can orientate and low values at high frequencies (unrelaxed permittivity) where the field alteration is too fast for the dipoles to follow. The imaginary part (loss) expresses the capability of the material to dissipate energy as a result of the interaction of the rotating dipoles with the surrounding environment. At very high frequencies, the movement performed by the dipoles is very limited. Consequently the corresponding dissipation is small and the loss is low. At very low frequencies, the dipoles can be aligned to the field but their movement is slow. Therefore the dissipation, which is dependent on time derivatives (e.g. viscous force is proportional to the velocity gradient), is also small, resulting in low loss values. At intermediate frequencies, where the rotation performed is large enough and the orientation process speed is high, the loss becomes significant.

According to the previous considerations, when a dipole orientation mechanism is operational in a material, the permittivity spectrum presents a step change, while the dielectric loss spectrum is a bell shaped curve. This general behaviour is illustrated in Fig. 3.5.

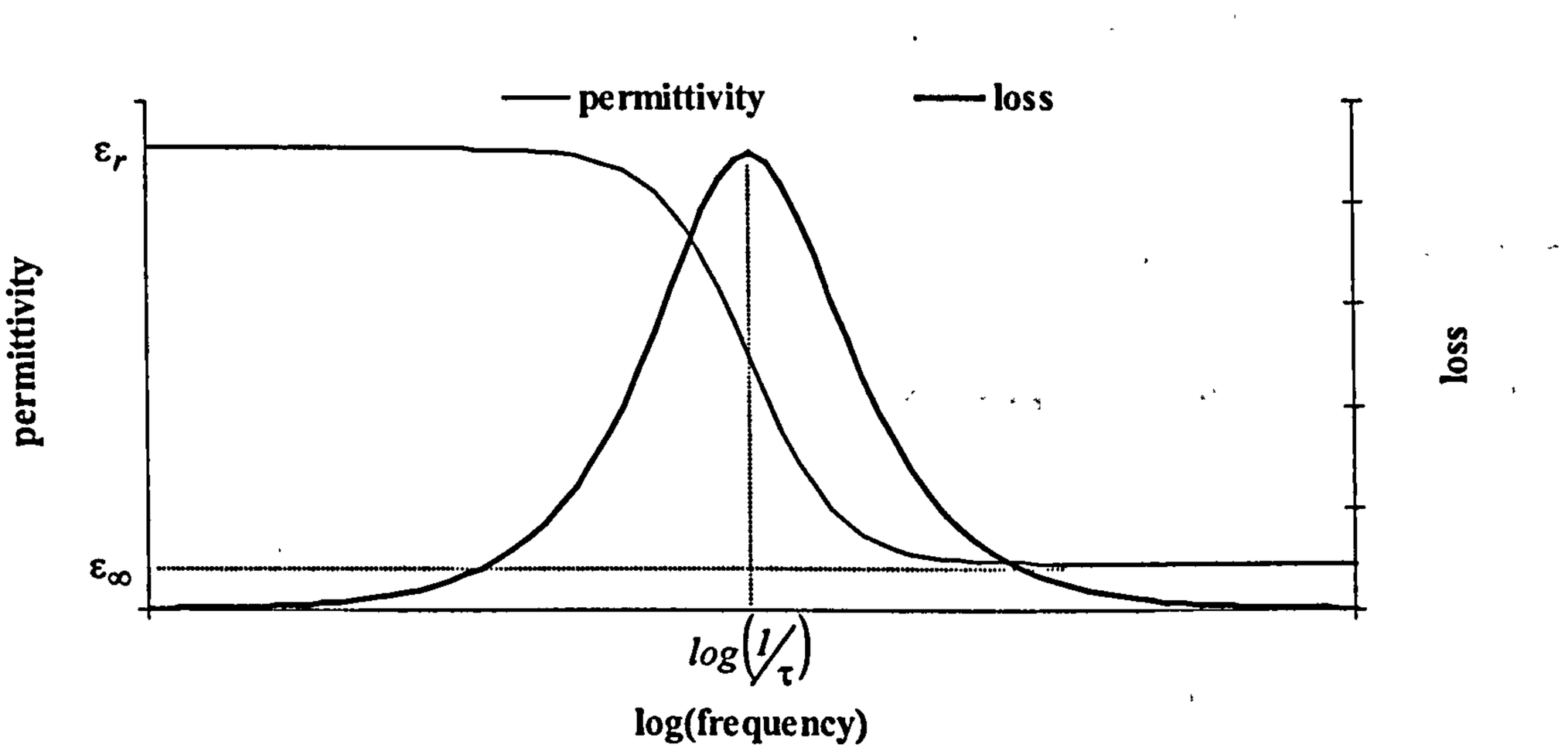

Fig. 3.5 *Spectra of dielectric permitivity and loss when dielectric relaxation occurs*

The phenomenon of dipole orientation is modelled assuming an exponential decay of dipole orientation with time (131), i.e. the polarisation is considered to be a first order process (133). Under a sinusoidal field the complex dielectric constant, where permittivity and loss are considered positive, becomes:

$$\frac{\varepsilon^* - \varepsilon_\infty}{\varepsilon_r - \varepsilon_\infty} = \frac{1}{1 + j\omega\tau} \qquad \text{(Eq. 3.6)}$$

where ε_∞ is the permittivity at very high frequencies, which corresponds to induced dipoles, ε_r is the permittivity at low frequencies, which corresponds to the maximum attainable orientation and τ is the macroscopic relaxation time of the orientation process i. e. the time to decay to $1/e$ of the initial polarisation after an abrupt change of the electric field. The macroscopic relaxation time is related to a molecular relaxation τ_m according to the expression (132):

$$\tau = \frac{\varepsilon_r + 2}{\varepsilon_\infty + 2}\tau_m \qquad \text{(Eq. 3.7)}$$

Experimental results obtained from measurements on polymeric materials have shown that the frequency response behaviour deviates from the one predicted by Eq. 3.6 (134). This is attributed to the existence of a distribution of relaxation times in a real polymer, which results in the modification of Eq. 3.6 to:

$$\frac{\varepsilon^* - \varepsilon_\infty}{\varepsilon_r - \varepsilon_\infty} = \int_{-\infty}^{+\infty} \frac{F(ln\tau)}{1 + j\omega\tau} d\, ln\tau \qquad \text{(Eq. 3.8)}$$

As the relaxation time distributions are very difficult to determine (134), empirical modifications have been introduced in the single relaxation time model.

3.4.2 Migrating charges conduction

Another mechanism that contributes to the energy dissipation when an alternating voltage is applied to a thermosetting polymer is the transport of charge carriers. Most of the thermosetting systems have some measurable DC conductive behaviour of this type. The DC conductivity is attributed solely to the presence of free ions, usually sodium and chloride originating from the production of raw materials, by some researchers (135, 136). Other studies have indicated that other charge carriers, like protons transferred along H-bonds and ions provided by some of the active constituents of the material (137-140), are present in thermosets.

The conductivity can be calculated as follows:

$$\tilde{\sigma} = \sum_i q_i N_i u_{mi} \qquad \text{(Eq. 3.9)}$$

where the index represents the charge carriers species, q the charge, N the number of charge carriers and u_m the mobility, which is the proportionality coefficient connecting the charge velocity to the applied electric field.

If the assumption of completely ionic conductivity holds, the mobility of charge carriers can be approximated by the mobility of a sphere embedded in a viscous liquid (135):

$$u_{mi} = \frac{q_i}{6\pi\mu r_i} \qquad \text{(Eq. 3.10)}$$

where η is the medium viscosity and r_i the radius of the ion. From Eq. 3.9 and Eq. 3.10, the resistivity is directly proportional to the viscosity of the medium. Such a correlation is valid in the early stages of the curing but fails when the material approaches gelation (139, 141).

In terms of dielectric constants the effect of the existence of a conductive mechanism is expressed by the following relation (135):

$$\varepsilon^* = \frac{\sigma}{\omega\varepsilon_o} + \varepsilon_d^* \qquad \text{(Eq. 3.11)}$$

where ε'' is the dielectric loss, ε_d'' the dipolar contribution to the dielectric loss and ε_o the permittivity of free space.

When the conductive term dominates the material response the following approximation is valid (142):

$$\varepsilon^* \omega \cong \frac{\tilde{\sigma}}{\varepsilon_o} \qquad \text{(Eq. 3.12)}$$

Eq. 3.12 allows the determination of the DC conductivity and simultaneously the verification of the conductivity dominance assumption to be made, when the measurement is performed in a multi-frequency mode.

3.4.3 Electrode polarisation

The influence of electrode polarisation on dielectric cure monitoring has been recognised from the early 70s (143). The existence of a conductive mechanism in combination with some diffusion limitation of the charge discharging on the electrodes results in the

formation of a thin layer next to the electrode, which has low conductivity and permittivity similar to that of the bulk material. The effect of this blocking layer on the measured complex dielectric constant can be approximated as (144):

$$\varepsilon_x^{'} = \varepsilon^{'} \frac{L}{2t_b} \frac{tan\delta^2 + \frac{L}{2t_b}}{tan\delta^2 + \left(\frac{L}{2t_b}\right)^2} \qquad \text{(Eq. 3.13)}$$

$$\varepsilon_x^{''} = \varepsilon^{''} \frac{L}{2t_b} \frac{\frac{L-2t_b}{2t_b}}{tan\delta^2 + \left(\frac{L}{2t_b}\right)^2} \qquad \text{(Eq. 3.14)}$$

where $\varepsilon_x^{'}$ and $\varepsilon_x^{''}$ denote the measured components of the dielectric constant, L the interelectrode distance, $tan\delta$ the dissipation factor and t_b the blocking layer thickness. It has been demonstrated by Adamec et al (145) that the polarisation presents a relaxation which can be distinguished from dipolar relaxation by the high values of dielectric permittivity (order of 100).

3.4.4 Impedance representation of dielectrics

A few research groups have chosen to present and process dielectric cure monitoring results in terms of the complex impedance. The essential meaning of the measurement is exactly the same as in the dielectric constants representation, since the phenomena taking place are the same, but in some cases the impedance representation appears to be a more direct way to describe them. The electric response of a thermosetting system can be represented by an equivalent circuit, as illustrated in Fig. 3.6 (146).

The presence of *dipolar relaxation* is accounted for by introducing a capacitance C_{sd}, in series with a resistance R_{sd}, corresponding to the permanent dipoles and connected in parallel with another capacitance C_{id}, corresponding to the induced dipoles. The *migrating charges* mechanism is represented by a resistor R_i connected in parallel with

the dipolar relaxation sub-circuit and the *electrode polarisation* by two capacitors C_e, one for each electrode, connected in series with the overall circuit.

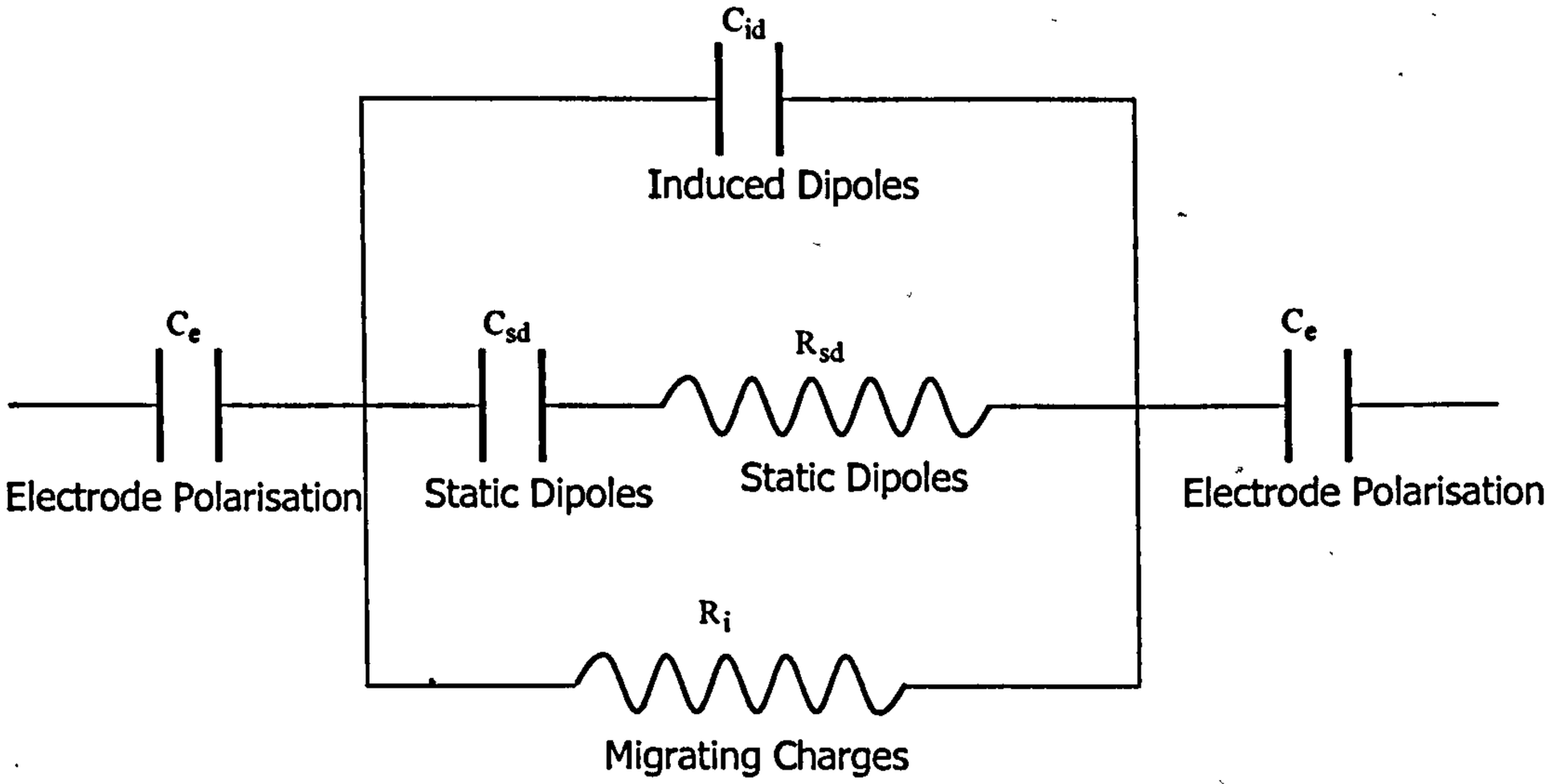

Fig. 3.6 *Equivalent circuit representation of the electrical response of thermosetting materials*

The complex impedance of the circuit is (146):

$$Z = Z' - jZ'' \qquad \text{(Eq. 3.15)}$$

Where

$$Z' = \frac{R_i\left|\omega^2 C_{sd}{}^2 R_{sd}(R_{sd}+R_i)+1\right|}{\omega^2(C_{sd}R_i + C_{sd}R_{sd} + C_{id}R_i)^2 + \left(\omega^2 C_{sd}R_{sd}R_iC_{id} - 1\right)^2} \qquad \text{(Eq. 3.16)}$$

$$Z'' = \frac{R_i\left|\omega^3 C_{sd}{}^2 R_{sd}{}^2 R_iC_{id} + \omega R_i(C_{id}+C_{sd})\right|}{\omega^2(C_{sd}R_i + C_{sd}R_{sd} + C_{id}R_i)^2 + \left(\omega^2 C_{sd}R_{sd}R_iC_{id} - 1\right)^2} + \frac{2}{C_e\omega} \qquad \text{(Eq. 3.17)}$$

The impedance spectrum of such a circuit is illustrated in Fig. 3.7. The response at low frequencies is dominated by the electrode polarisation effect, the conduction mechanism becomes dominant at intermediate frequencies and the dipolar relaxation at high frequencies.

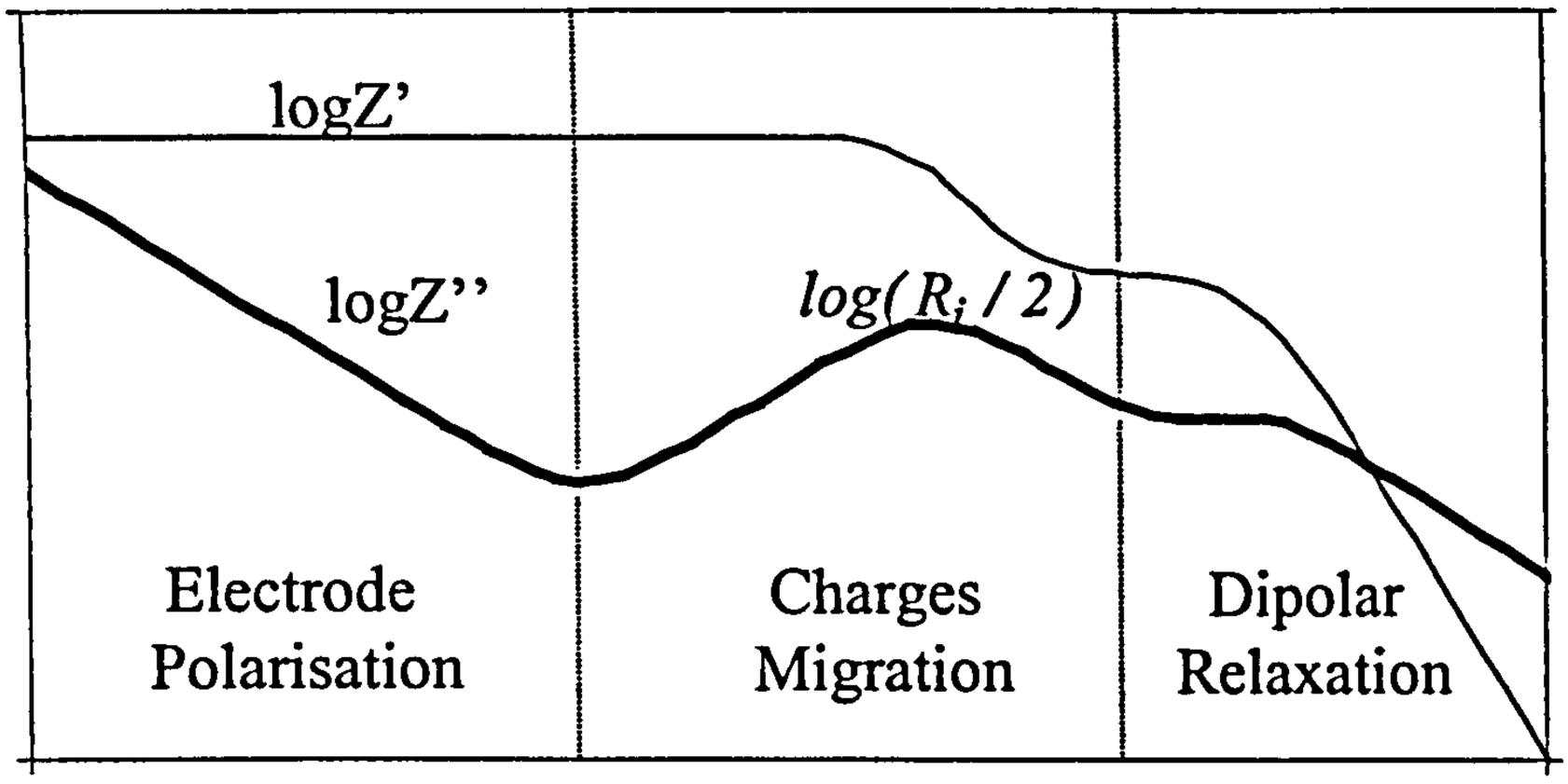

Fig. 3.7 *Impedance spectrum of the electrode polarisation-charge migration-dipolar relaxation circuit*

The equivalence between material response characterisation by the dielectric and the impedance representations is expressed by the relations (140):

$$C_{id} = \varepsilon_\infty C_o \qquad \text{(Eq. 3.18)}$$

$$C_{sd} = (\varepsilon_o - \varepsilon_\infty) C_o \qquad \text{(Eq. 3.19)}$$

$$R_{sd} = \frac{\tau}{C_{sd}} \qquad \text{(Eq. 3.20)}$$

$$R_i = \frac{\varepsilon_o}{C_o \tilde{\sigma}} \qquad \text{(Eq. 3.21)}$$

where

$$C_o = \frac{\varepsilon_o S}{L} \qquad \text{(Eq. 3.22)}$$

denotes the free space capacitance of the measuring system. S and L express its geometry and correspond to the area and the length in the case of a parallel plate capacitor.

3.4.5 Application to process cure monitoring

Numerous investigations have been carried out into the implementation of dielectric and impedance cure monitoring to the curing of thermosetting polymeric materials. Here, only that part of this literature which focuses on the application of the technique to composites manufacturing is reviewed.

In order to apply monitoring to practical manufacturing it is necessary to translate the dielectric/impedance results to information related to the chemical or the structural state of the curing material. Thus, relations connecting monitoring signals to the viscosity, the degree of cure or to the state of the material (i.e.glass, rubber or liquid) are required.

The relation between viscosity and conductivity is evident from the combination of Eq. 3.9 and Eq. 3.10. Thus, a linear relation between them should be expected. Experiments have confirmed that viscosity and conductivity follow the same trend but the conductivity levels off at a slower rate (147). This difference in behaviour is attributed to the small size of the charge carriers in comparison with polymer chain segments. The charge carriers require much less free volume in order to move, consequently their mobility continues to change behaviour after the chain mobility dependent viscosity has been stabilised.

The degree of cure has been connected to dielectric data using the relaxation times and the electrical resistivity. The following model connecting relaxation times to the degree of cure has been developed by Nass and Seferis (148):

$$\frac{1}{\tau} = \frac{1}{\tau_\infty} + \left[\frac{1}{\tau_o} - \frac{1}{\tau_\infty}\right](1-\alpha)^{\phi} \qquad \text{(Eq. 3.23)}$$

where τ_∞ is the average relaxation time at the completion of the cure, τ_o the relaxation time at the beginning of the cure, α the degree of cure and ϕ is a constant of the resin system.

For the correlation of resistivity with the degree of cure the same researchers have proposed a logarithmic relation, which subsequently has been used and modified by other researchers. The normalised resistivity correlates in a satisfactory fashion with fractional conversion, in the case of isothermal curing, according to the relation (138, 149, 150):

$$\alpha = \alpha_{max} \frac{\log \tilde{\rho} - \log \tilde{\rho}_o}{\log \tilde{\rho}_{max} - \log \tilde{\rho}_o} \qquad \text{(Eq. 3.24)}$$

where α_{max} is the maximum degree of cure at the curing temperature, $\tilde{\rho}$ the resistivity, $\tilde{\rho}_o$ the resistivity of the unreacted resin and $\tilde{\rho}_{max}$ the resistivity of the fully reacted resin.

An extension of that model involving an empirical parameter p, has been proposed by Maffezzoli et (151):

$$\alpha = \alpha_{max} \frac{\log \tilde{\rho} - \log \tilde{\rho}_o}{\log \tilde{\rho}_{max} - \log \tilde{\rho}_o} \left(\frac{\log \tilde{\rho}_{max}}{\log \tilde{\rho}} \right)^p \qquad \text{(Eq. 3.25)}$$

Similarly, normalised dielectric constants showed a good correlation with reaction kinetics data obtained using differential scanning calorimetry (152).

The vitrification can be identified by the dielectric loss peak corresponding to dipolar relaxation (135, 153, 154). Alternatively, when the impedance representation is used, vitrification is manifested as a step change in the imaginary impedance (150, 155). As shown in Fig. 3.8, the imaginary impedance presents two steps during the cure of a thermosetting material. The first step corresponds to the curing reaction and the second to vitrification.

The identification of the gel 'point' is a major point of disagreement as far as the applicability of dielectric cure monitoring is concerned (150). As mentioned previously, electric effects take place in the micro-scale, whereas gelation is a macroscopic phenomenon. Therefore, there is no direct fundamental justification of a connection between dielectric and impedance measures and gelation. However, experimental evidence has demonstrated a good empirical correlation between the narrow gelation regime and the inflection point of conductivity curves in many epoxy resins (150, 154). It should be noted that this experimental fact relates the point of maximum change in conductivity to the macroscopic change in the structure of the polymer from liquid to rubber.

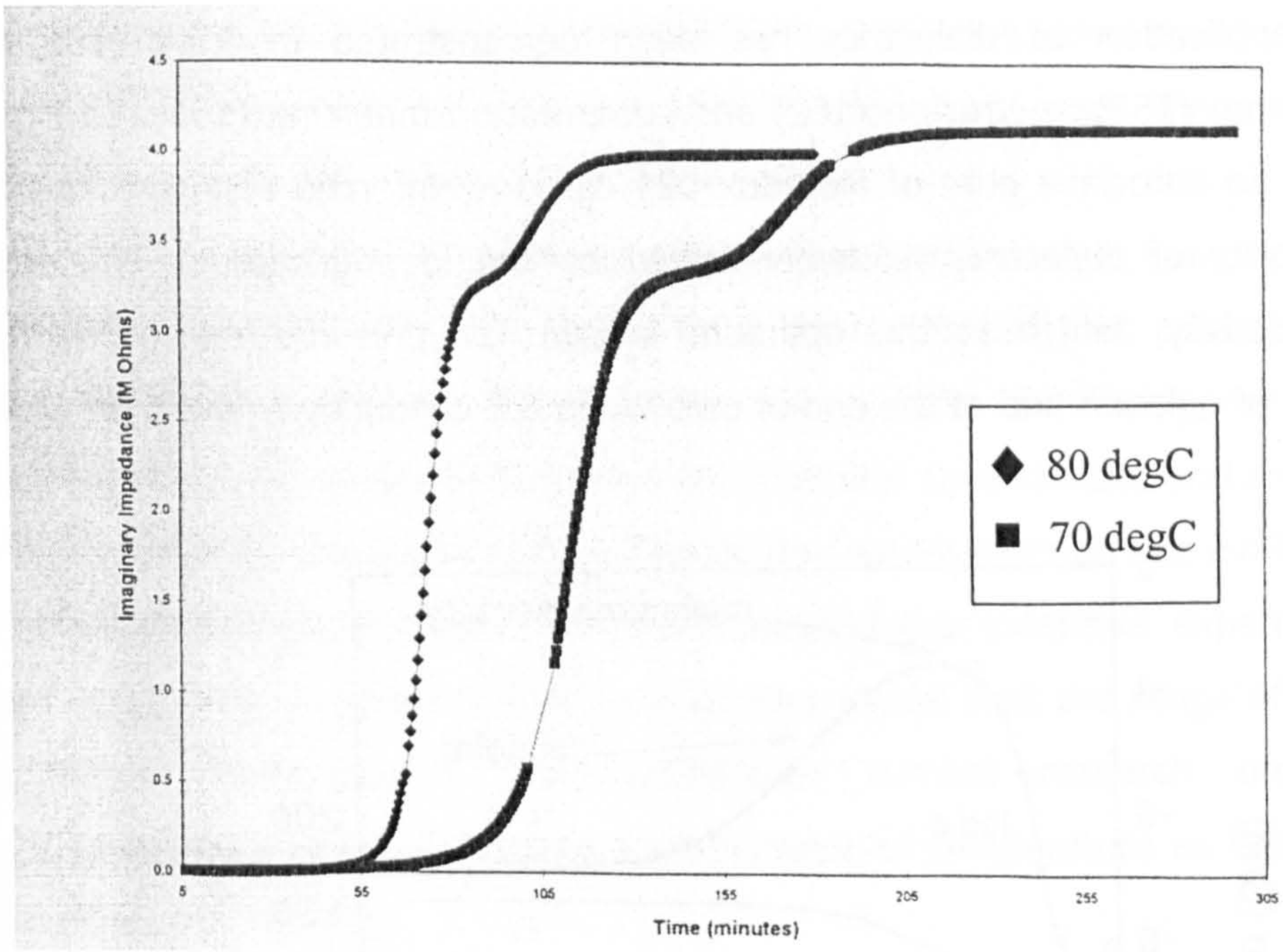

Fig. 3.8 *Imaginary impedance evolution during the cure. Isothermal curing of TGEPA/MDA. Results obtained by Mijovic et al (150).*

The implementation of dielectric/impedance cure monitoring requires the use of a sensing system, which can be inserted in the manufacturing tool. The majority of applications has been performed using interdigitated (comb) micro-electrodes (Fig. 3.9) (156-158). In some cases parallel plate configurations have been incorporated in the mould (159, 160).

Fig. 3.9 *Interdigitated dielectric sensor*

Successful application of dielectrics has been demonstrated in RTM (156, 161), autoclave curing (158), pultrusion (162) and compression moulding (163). In Fig. 3.10 results from an autoclave cure of Fibredux 924 carbon reinforced resin are illustrated. The applicability of dielectrics is demonstrated by the identification of the point of minimum viscosity, which is the optimum instant for pressure consolidation, the identification of gelation and of the end of cure when the conductivity levels off.

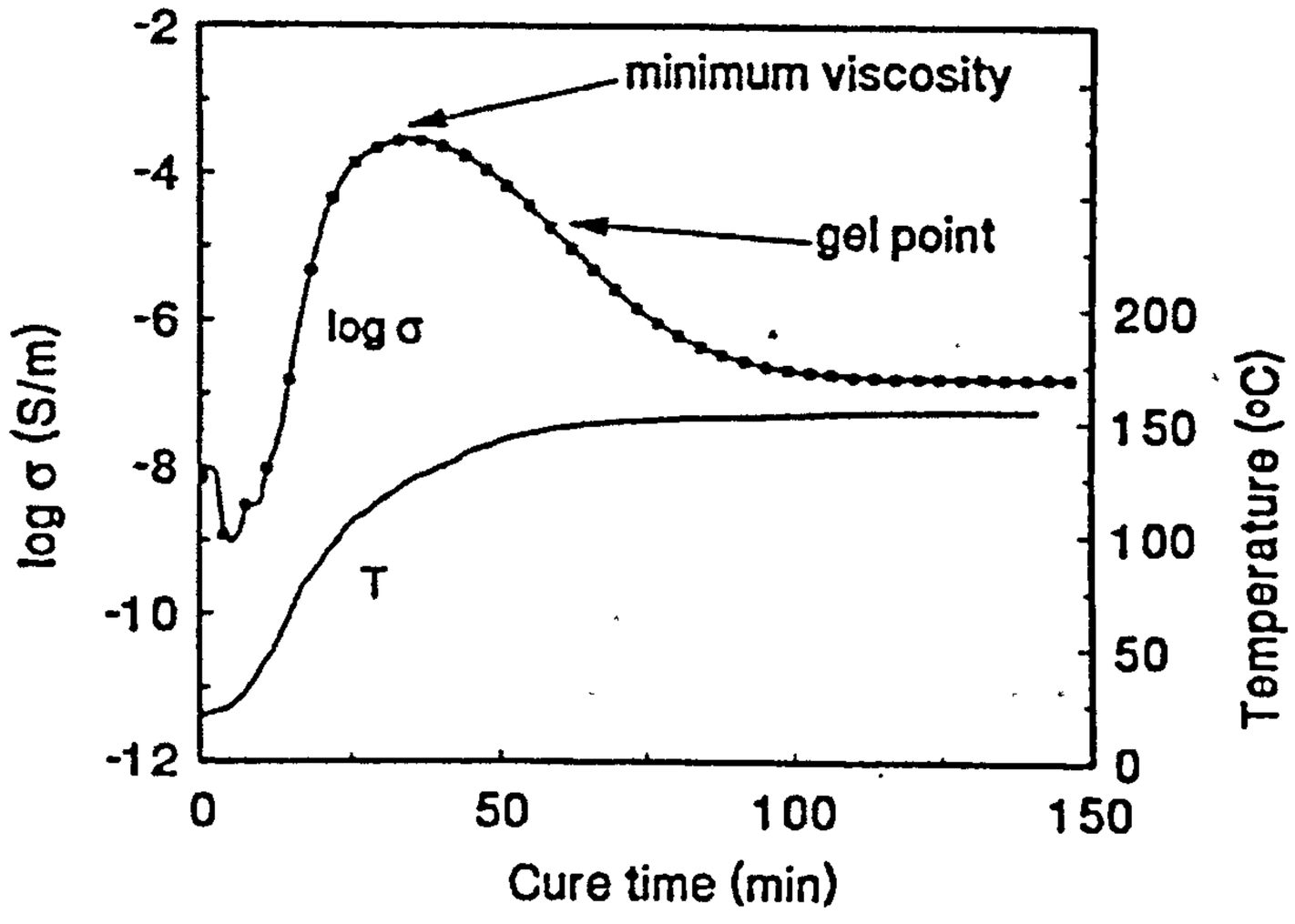

Fig. 3.10 *Temperature profile and conductivity changes during the cure of carbon reinforced Fibredux 924 resin. Results obtained by Maistros et al (157).*

3.5 Thermal monitoring

The role of temperature monitoring in the composites manufacturing research is up to now mainly auxiliary. Its uses can be classified as follows:

- As a tool for studying and gaining a better insight into the process (164)
- As a validation technique for the heat transfer models of composites curing (60, 165, 166)
- As the control signal for the implementation of expert system algorithms (167-169)

Thermal monitoring is the simplest monitoring technique to implement. Every mould control system makes use of thermocouples and in some cases the presence of an exotherm is considered empirically as an indication of the progress of the reaction. However, thermal monitoring has a lower level of sophistication in comparison with the rest of the cure monitoring techniques, since its results are not related with a cure progress dependent property. In order to derive cure monitoring results, thermal monitoring should be combined with accurate chemical cure kinetics and chemorheology models. Methods for appropriate modelling of the curing reaction are available (8), but batch to batch variations of the raw materials and the extensive experimental effort required to produce a representative cure kinetics model limit the range of uses of such an approach. Consequently the mainstream current research on composites manufacturing does not consider the measurement of temperature as being within the context of cure monitoring.

Monitoring based on heat flux signals measured using a variety of combinations of temperature sensors has been presented in the research literature. In this approach the thermal properties of the system are considered to be constant during the cure and all changes in the measured signals are attributed to the exothermic character of the curing reaction. This way the heat flux signal produced presented a dependence on the progress of the reaction, but significant signal processing and noise problems appeared to reduce the quality of the results (170, 171).

3.6 Flow monitoring in liquid moulding

Liquid moulding processes have received increased attention in recent years as a potentially cost-efficient and easily automated alternative to the conventional laying up – autoclaving process. A variety of liquid moulding processes using either rigid, (e.g. resin transfer moulding (RTM)) or flexible (e.g. vacuum assisted resin infusion (VARI)) tooling has been developed. The central characteristic of all these processes is that the filling/consolidation stage is separated from the curing stage and becomes the critical phase of the manufacturing process. Therefore, the resin filling and the phenomena connected to it have become a point of focus for the composites manufacturing

research. Models attempting to simulate the impregnation of liquid resin into a dry fabric have been developed.

Since the parameter dictating the impregnation phenomena is the permeability of the reinforcement, a number of studies have addressed the problem of measuring the permeability using visual observation of the filling. A general feature of these measurements is the use of transparent tooling, which allows the observation and recording of the flow front position. In most cases the in plane permeability is measured and the experimental mould has either a flat elongated shape which is filled uniaxially from one end (39, 172, 173) or a flat symmetrical shape which is filled radially from the centre (174-176). The former configuration is suitable for the determination of the one-directional permeability whereas the latter allows the simultaneous determination of the components of the two dimensional permeability tensor in anisotropic fabrics. Other studies have used similar transparent tooling configurations in order to investigate the filling behaviour in complicated shape moulds. The aim of these studies was mainly the evaluation of the performance of flow models in real components (28, 177).

Although this area of research utilises flow monitoring, this approach cannot be adapted for in-situ process monitoring, since the presence of transparent tooling would be impractical in most of the industrial cases.

In addition, it has been shown that using the current techniques the reproducibility and repeatability of permeability measurements is poor (178, 179). Therefore the performance of flow models, which use the permeability as core parameter, is limited.

Methods for in-situ flow monitoring, adaptable to the industrial environment, started to be investigated as an alternative to the modelling approach. These methods can be divided into two main categories; (i) discrete methods where the instant of resin arrival at a specific location is recorded and (ii) continuous methods where the response of the monitoring system, which is related to the resin flow front position, is measured continuously.

In discrete methods, a sensing system which reacts to the arrival of the resin is placed at specific locations in the mould. The first implementation of such a technique was performed by Kranbhuel and co-workers (156). Their system comprised a number of interdigitated dielectric sensors placed on the bottom tool face of an RTM mould. The resin arrival was noted as a discrete jump in the dielectric properties when the resin

came in contact with the sensor. Similar systems, based on the abrupt change of DC conductivity when a liquid polymer shorts out the area between the ends of two conductive wires, have been developed by other workers (180). A grid of electric wires arranged in two sets, orthogonal and at some distance to each other, which allows with appropriate multiplexing to decide whether or not a specific node of the grid has been covered by resin, has also been used to monitor the in-plane filling progress in RTM (181). Other set-ups based on the same principle have been implemented to monitor the flow progress along the thickness of the fabric (182). Another approach aiming to measure the three dimensional permeability of reinforcements is based on the use of thermistors instead of electrical contacts and makes use of the drop in temperature when the resin touches a thermal sensor (183).

The discrete character of all these measurement methods limits their applicability since, in order to acquire a global view of the flow patterns in a complicated component, a large number of point sensors would be required. This was the reason for investigations of continuous flow sensing techniques, resulting in the development of new methods.

Two techniques have been implemented and investigated up to now. Use of the DC conductivity changes measured between two wires running along the mould has proved adequate for the location of the flow front (184). Similarly, fibre optic technique based on fluorescence of a dye dissolved the resin has been used in order to determine the percentage of a fibre covered by the resin during the filling. This technique uses the evanescence field created at the interface between the fibre and the surrounding medium due to the interference of the incoming and reflected rays (185).

All these techniques are appropriate for the manufacturing of composites with non-conductive reinforcement and require the sensing set-up to be in direct contact with the composite. The presence of carbon fibres, which is the reinforcement used in most advanced composites, would disturb the electric field in dielectric sensing and the evanescence field in fibre optic sensing and would short the electric contacts in DC conductivity sensing.

3.7 Overview

Monitoring of cure has been a subject of extensive study during the last fifteen years. The main techniques developed are optical, dielectric and acoustic cure monitoring. Dielectric cure monitoring is at the moment the most widely used technique. It offers a combination of indirect chemical information and the ability to monitor the structural state of the material. Acoustic monitoring gives direct information on the mechanical properties of the material and can be implemented remotely, but the interpretation of its results requires further attention. Infrared spectroscopy and near infrared spectroscopy provide direct chemical information which is not affected by temperature, but their implementation in industrial environment is currently not cost-efficient. Thermal monitoring has not received enough attention, although it is inexpensive and is already incorporated in most manufacturing tools.

Flow monitoring is a relatively new subject of study. Discrete and continuous methods based on DC measurements and dielectric measurements have been developed and implemented successfully. As yet none of them can operate in composites comprising conductive reinforcements or in a remote manner.

Chapter Four

4 Heat transfer model

4.1 Introduction

In this chapter the central heat transfer model developed and used in this study is described. The model simulates heat transfer phenomena occurring during the curing of composite parts produced by resin transfer moulding. The background of the implementation of finite elements in heat transfer problems is given. The specific routines for mesh generation, matrices formation and solution in 1-D, 2-D and 3-D are described and the interdependencies of the core model with submodels for cure kinetics and material properties, which will be presented in subsequent chapters, are outlined.

4.2 Formulation of the model

4.2.1 The boundary value problem

The general differential equation expressing heat transfer during the cure in a resin transfer mould, as analysed in paragraph 2.3.2, is:

$$\rho c_p \frac{\partial T}{\partial t} = \nabla \cdot [K] \nabla T + (1 - v_f) \rho_r H_{tot} \frac{d\alpha}{dt} \qquad \text{(Eq. 4.1)}$$

By incorporating the heat generation in a source term $\dot{Q}$ Eq. 4.1 becomes

$$\rho c_p \frac{\partial T(\hat{r},t)}{\partial t} = \nabla \cdot [K] \nabla T(\hat{r},t) + \dot{Q}, \quad \hat{r} \in \Omega \qquad \text{(Eq. 4.2)}$$

where $\hat{r}$ denotes the spatial coordinates and Ω the domain of the problem.

This equation is accompanied by a set of boundary conditions. In the general case there are three kinds of possible boundary conditions (186, 187):

i. Prescribed temperature

$$T(\hat{r},t) = \tilde{T}(\hat{r},t), \quad \hat{r} \in S_1 \qquad \text{(Eq. 4.3)}$$

ii. Prescribed heat flux

$$\hat{n} \cdot [K] \nabla T(\hat{r},t) = \tilde{q}(\hat{r},t), \quad \hat{r} \in S_2 \qquad \text{(Eq. 4.4)}$$

iii. Convection

$$\hat{n} \cdot [K] \nabla T(\hat{r},t) = h(T(\hat{r},t) - T_\infty), \quad \hat{r} \in S_3 \qquad \text{(Eq. 4.5)}$$

where

$$S_1 \cup S_2 \cup S_3 = S \qquad \text{(Eq. 4.6)}$$

and $\hat{n}$ denotes the surface vector at the boundary S, h the heat transfer coefficient and T_∞ the temperature of the fluid at the convective boundary.

In transient problems an initial condition describing the initial temperature distribution is necessary:

$$T(\hat{r},0) = T_o(\hat{r}), \quad \hat{r} \in \Omega \qquad \text{(Eq. 4.7)}$$

When the heat transfer problem is multimaterial, i. e. thermal properties and especially thermal conductivity present a discontinuity at an interface, continuity requirements do not allow the representation over the whole domain of the problem by Eq. 4.2. Thus, the domain should be partitioned in subdomains representing the different materials. A separate boundary value problem, of the type expressed by Eqs. 4.2-4.7, is formed over each subdomain. An additional set of interfacial conditions which ensures temperature and heat flux continuity, should be defined as follows (186, 187):

$$T_i(\hat{r},t) = T_j(\hat{r},t), \quad \hat{r} \in \tilde{S}_{ij} \qquad \text{(Eq. 4.8)}$$

$$\hat{n} \cdot [K_i] \nabla T_i(\hat{r},t) = \hat{n} \cdot [K_j] \nabla T_j(\hat{r},t), \quad \hat{r} \in \tilde{S}_{ij} \qquad \text{(Eq. 4.9)}$$

where i and j denote two different domains and $\tilde{S}_{ij}$ their interface.

4.2.2 Heat transfer mechanisms in RTM curing

The curing of a composite part in a mould, where the material in terms of heat transfer is considered as homogeneous and convection transfer is assumed negligible, is fully described Eqs. 4.2-4.7. The homogeneity assumption holds because curing is a slow process and does not involve forced convection, thus even if the heat transfer coefficient between the matrix and the fibre is low, local equilibrium can be established and the temperature is uniform on the micro scale. Convection occurs due to macroscopic mass transfer. The mass transfer can result from pressure gradients (forced convection) or temperature gradients (natural convection). Forced convection is active during the filling of an RTM mould but it stops when the filling is completed and curing starts. In contrast, natural convection may be active during the cure. This mechanism occurs when the density variation due to thermal gradients creates a considerable buoyancy flow, which contributes considerably to the transfer of heat.

A dimensionless quantity, Rayleigh number, can be used in order to estimate whether such a mechanism contributes significantly to the transfer of heat in a fluid. For a uniform fluid Rayleigh number is defined by the relation (43):

$$Ra = \frac{\alpha_v \rho^2 c_p g \Delta T L^3}{\mu K} \qquad \text{(Eq. 4.10)}$$

where α_v is the volumetric thermal expansion, ρ the density, g the gravitational acceleration, c_p the specific heat capacity, μ the viscosity, K the thermal conductivity, L the length scale of the problem and ΔT the thermal gradient.

A similar number, the Rayleigh-Darcy number, can be defined for a porous medium saturated by fluid (188):

$$RaD = \frac{\beta \rho^2 c_p \overline{K} g \Delta T L}{\mu K} \qquad \text{(Eq. 4.11)}$$

where $\overline{K}$ denotes the permeability of the porous medium. This number has high values when natural convection is dominant and low values when conduction is dominant. It has been demonstrated that a value of 40 is the threshold for domination of the convective mechanism (188).

In order to test whether natural convection participates in heat transfer during the cure, the Rayleigh-Darcy number values have been calculated for a typical curing profile of an

RTM6 resin based composite. Since the order of magnitude of the Rayleigh-Darcy number suffices for the characterisation of the relative significance of natural convection, approximate values characteristic of a thermoset-glass fibre for the specific heat capacity, the thermal conductivity and the permeability have been utilised (Table 4.1). The case of glass reinforcement has been considered, since due to their low thermal conductivity in comparison with carbon, glass composites are more likely to allow convection domination. The permeability value is among the highest referred to in the literature for a realistic composite. The length scale of the problem is similar to the thickness of a typical resin transfer moulded part, where the maximum thermal gradient and the maximum natural convection are expected. The thermal gradient has been assumed equal to the highest thermal gradient values reported in the literature (164). The density and the thermal expansion coefficient have been assumed equal to the uncured RTM6 resin values (Table 4.1).

$\alpha_v\left(\frac{1}{^oC}\right)$	$c_p\left(\frac{J}{gr^oC}\right)$	$K\left(\frac{W}{cm^2{}^oC}\right)$	$\overline{K}\left(cm^2\right)$	$\rho\left(\frac{gr}{cm^3}\right)$	$L\,(cm)$	$\Delta T\,(^oC)$
(189)	(62)	(62)	(179)	(189)		(164)
$4.1\ 10^{-4}$	1.2	$0.2\ 10^{-2}$	$1.6\ 10^{-6}$	1.1	0.4	10

Table 4.1 *Properties values used for the calculation of the Rayleigh-Darcy number*

The values for the viscosity have been obtained using a model developed for RTM6 resin by Karkanas (17):

$$\mu = 10^{12}\, e^{-5.485+\frac{3562}{T+273}-\frac{\left(2.91+\frac{291.8}{T+273}\right)\left(-145+1.239T-T_g\right)}{-145+1.239T-T}} \qquad \text{(Eq. 4.12)}$$

where the temperature is given in °C, and the viscosity in Pas.

The glass transition temperature has been calculated as follows (17):

$$T_g = -11+\frac{94.4\alpha}{1-0.565\alpha} \qquad \text{(Eq. 4.13)}$$

and the fractional conversion determined by integrating an implementation of Kamal's

kinetic model (Eq. 2.3) for the specific resin system (17):

$$\frac{d\alpha}{dt} = \left(K_o + K_1\alpha^{1.202}\right)(1-\alpha)^{1.298} \qquad \text{(Eq. 4.14)}$$

In the integration time t is given in minutes.

The rate constants incorporate diffusion limitations to cure kinetics (Eq. 2.8) as follows:

$$K_o = \frac{K_{chemo}K_{dif}}{K_{chemo} + K_{dif}} \qquad \text{(Eq. 4.15)}$$

$$K_1 = \frac{K_{chem1}K_{dif}}{K_{chem1} + K_{dif}} \qquad \text{(Eq. 4.16)}$$

where

$$K_{dif} = 6.5\,10^{18} e^{-\frac{136}{0.0083(T+273)}} e^{-\frac{0.0019(T+273)-0.5367}{0.00048(T-T_g)+0.025}} \qquad \text{(Eq. 4.17)}$$

$$K_{chemo} = 4.5\,10^{6} e^{-\frac{74.69}{0.0083(T+273)}} \qquad \text{(Eq. 4.18)}$$

$$K_{chemo} = 1.6\,10^{6} e^{-\frac{59.18}{0.0083(T+273)}} \qquad \text{(Eq. 4.19)}$$

It should be noted that equivalent results would be obtained if the thermal properties and cure kinetics were calculated using some of the models described in the following chapters. The additional accuracy is not necessary since only the order of magnitude of the dimensionless Rayleigh-Darcy number is meaningful in this analysis. The results of the calculation of Rayleigh-Darcy number based on Eqs. 4.11-4.19 and the data given in Table 4.1 are illustrated in Figs. 4.1 and 4.2. The Rayleigh-Darcy number increases as the temperature increases during the heating ramp, then reaches a maximum at the beginning of the isothermal segment and decreases as the curing progresses. Its maximum value is approximately four orders of magnitude lower than the threshold of natural convection domination. This value has been calculated using the most conservative values of the properties involved. Consequently the natural convection can be ignored securely and heat transfer modelling of RTM curing can be based on the pure heat conduction equation as expressed by Eq. 4.2.

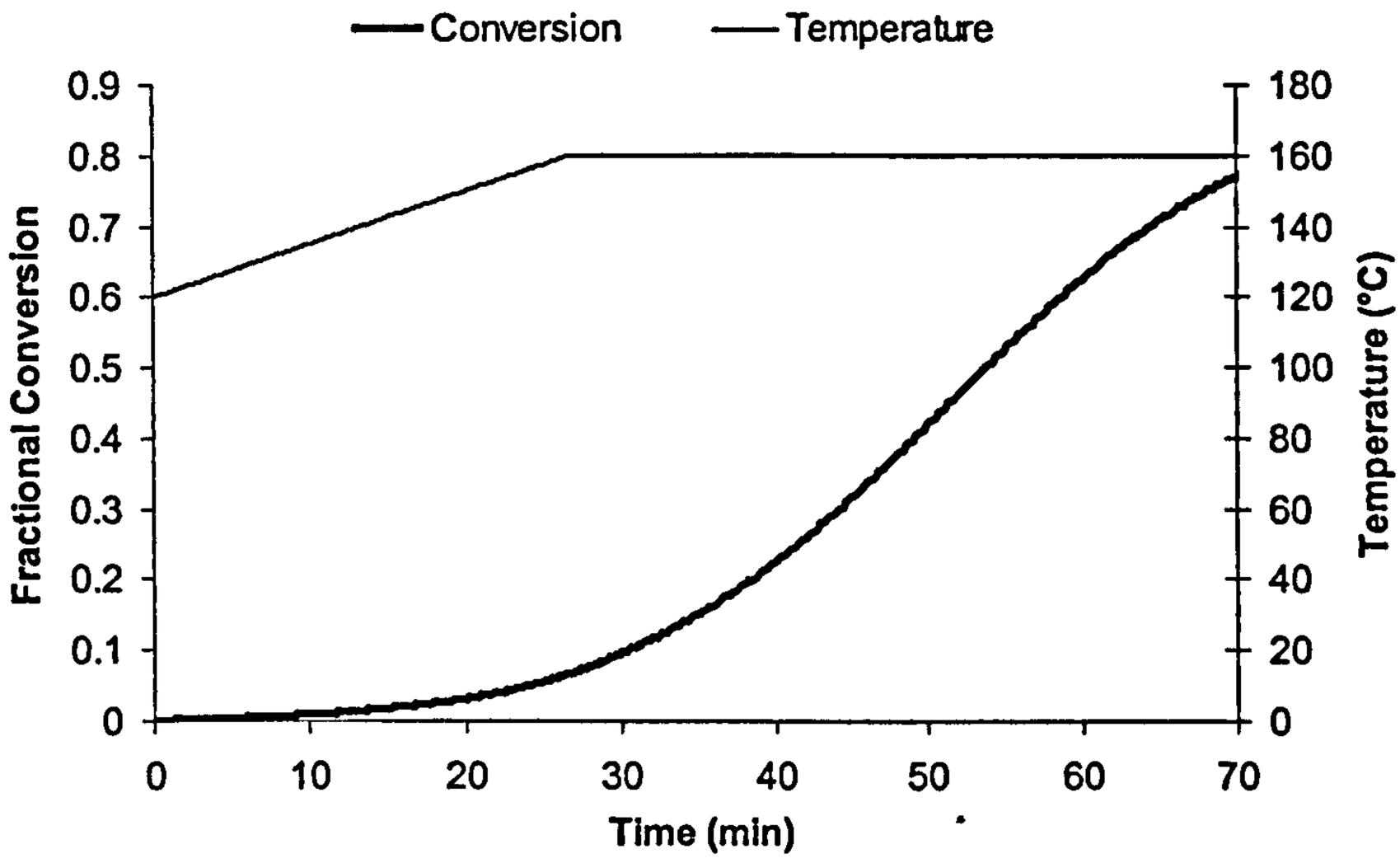

Fig.4.1 *Thermal profile and the corresponding fractional conversion evolution for a typical cure of an RTM6 based composite*

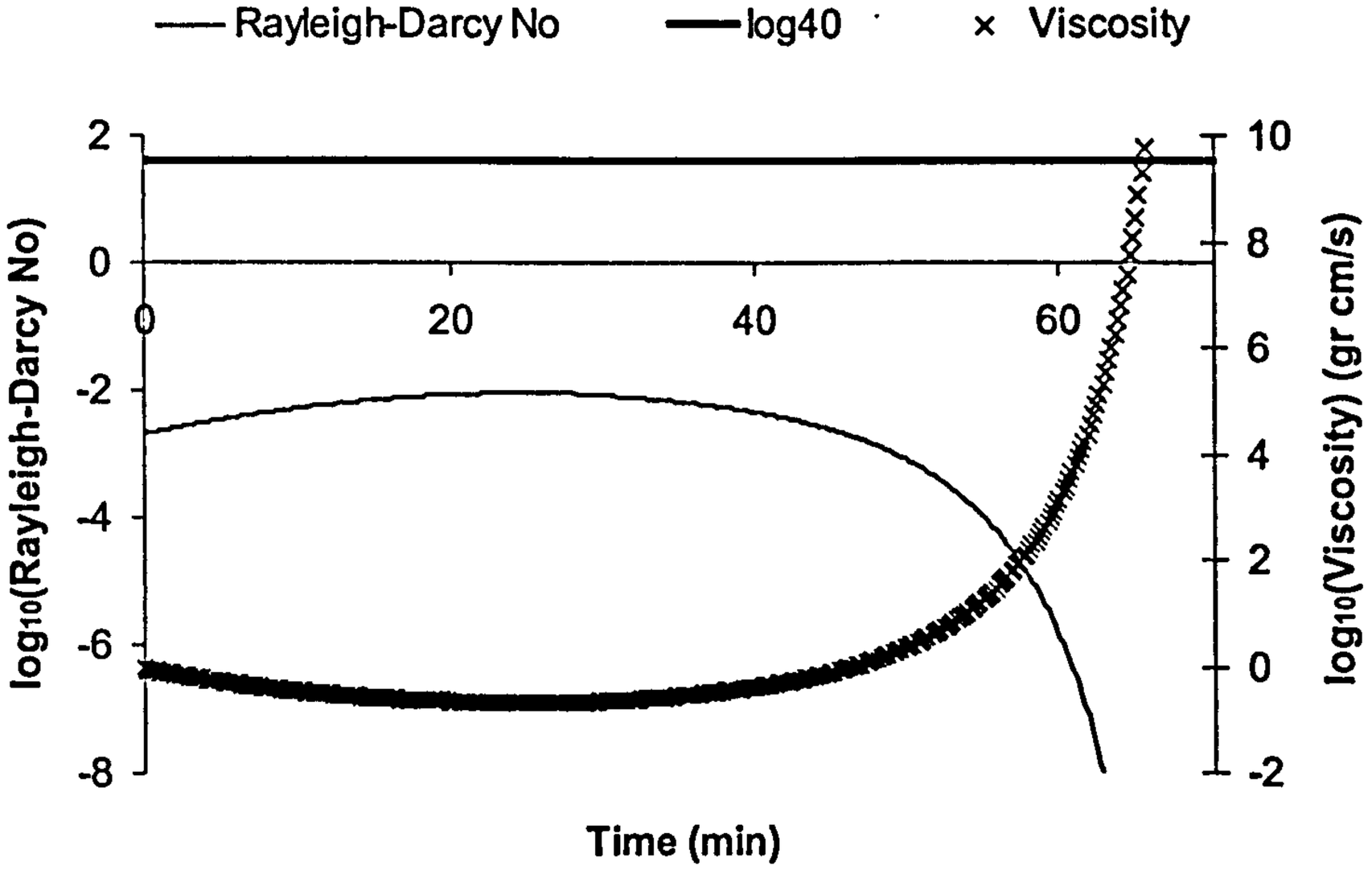

Fig.4.2 *Resin viscosity evolution and the corresponding Rayleigh-Darcy number for a typical cure of an RTM6 based composite*

4.2.3 Finite elements formulation of the problem

The finite elements formulation of a heat transfer problem can be obtained using two approaches:-(i) weighted residuals and (ii) variational principles, which result in equivalent approximations of the problem (190). Here the weighted residuals approach will be used for the description of the approximation formulation, since the variational approach requires the definition of a functional which has a complicated physical interpretation in heat transfer terms.

In the weighted residual a solution to the boundary value problem is sought in the form of an approximation $\overline{T}(\hat{r},t)$, which satisfies the prescribed temperature boundary condition (Eq. 4.3) and results in residual errors:

$$R_L(\hat{r},t) = \nabla \cdot [K] \nabla \overline{T}(\hat{r},t) + \dot{Q} - \rho c_p \frac{\partial \overline{T}(\hat{r},t)}{\partial t} \qquad \text{(Eq. 4.20)}$$

$$R_B(\hat{r},t) = \begin{cases} \hat{n} \cdot [K] \nabla \overline{T}(\hat{r},t) - \tilde{q}(\hat{r},t), & \hat{r} \in S_2 \\ \hat{n} \cdot [K] \nabla \overline{T}(\hat{r},t) - h\left(\overline{T}(\hat{r},t) - T_\infty\right), & \hat{r} \in S_3 \end{cases} \qquad \text{(Eq. 4.21)}$$

The objective of the approximation is to minimise the residual errors. The minimisation is performed by selecting appropriate weighting functions W and $\overline{W}$ and requiring their scalar products with the residual errors to vanish (187):

$$\int_\Omega W R_L(\hat{r},t) d\Omega + \int_{S_2 \cup S_3} \overline{W} R_B(\hat{r},t) dS = 0 \qquad \text{(Eq. 4.22)}$$

Consequently, by incorporation of Eqs. 4.20 and 4.21, Eq. 4.22 becomes:

$$\int_\Omega W \left[\nabla \cdot [K] \nabla \overline{T}(\hat{r},t) + \dot{Q} - \rho c_p \frac{\partial \overline{T}(\hat{r},t)}{\partial t} \right] d\Omega + \int_{S_2} \overline{W} \left[\hat{n} \cdot [K] \nabla \overline{T}(\hat{r},t) - \tilde{q}(\hat{r},t) \right] dS + \int_{S_3} \overline{W} \left[\hat{n} \cdot [K] \nabla \overline{T}(\hat{r},t) - h\left(\overline{T}(\hat{r},t) - T_\infty\right) \right] dS = 0 \qquad \text{(Eq. 4.23)}$$

This formulation requires the approximation function $\overline{T}(\hat{r},t)$ to have continuous first spatial derivatives (C^1 continuity) and the weighting functions $W, \overline{W}$ to have continuous integrals (C^{-1} continuity). The continuity requirements can be relaxed by integrating Eq. 4.23 by parts and applying the divergence theorem (186), which result in:

$$\int_{\Omega}\nabla W\cdot[K]\nabla\overline{T}d\Omega-\int_{\Omega}W\dot{Q}d\Omega+\int_{\Omega}\rho c_{p}W\frac{\partial\overline{T}}{\partial t}d\Omega+\int_{S_2}W\tilde{q}dS+\int_{S_3}Wh\left(\overline{T}-T_{\infty}\right)dS=0 \qquad \text{(Eq. 4.24)}$$

Here the set of weighting functions is limited to the functions which vanish at the prescribed temperature part of the boundary:

$$W(\hat{r},t)=0,\quad \hat{r}\in S_1$$
$$\overline{W}(\hat{r},t)=0,\quad \hat{r}\in S_1 \qquad \text{(Eq. 4.25)}$$

and

$$\overline{W}(\hat{r},t)=-W(\hat{r},t) \qquad \text{(Eq. 4.26)}$$

The problem of finding an approximation function $\overline{T}$ that satisfies Eq. 4.24 for any weighting function W is equivalent to the boundary value problem. Now $\overline{T}$ and W must show C^o continuity, i. e. it is not necessary for the approximation function to have continuous spatial derivatives. An additional advantage of the formulation expressed by Eq. 4.24 is that the thermal conductivity continuity requirement is relaxed also, since even if thermal conductivity is discontinuous Eq. 4.24 is integratable. Thus it is possible to treat a multimaterial problem as a single domain case. The interfacial boundary conditions (Eqs. 4.8 and 4.9) are satisfied automatically as the approximation function is continuous and the heat flux interfacial condition is eliminated by the use of the divergence theorem for the different domains (186).

The next step in the formulation of the problem is to express the approximation function in the form of a linear combination of a set of functions $N_1, N_2, .., N_m$ which always satisfies the prescribed temperature boundary condition (191):

$$\overline{T}=\widetilde{T}+\sum_{i=1}^{m}a_i(t)N_i(\hat{r}) \qquad \text{(Eq. 4.27)}$$

where

$$N_i(\hat{r})=0,\quad \hat{r}\in S_1 \qquad \text{(Eq. 4.28)}$$

A finite element model of the closed domain of the problem Ω is a region $\widetilde{\Omega}$ which is the union of E closed subregions $\overline{\Omega}_e$ of R^n

$$\widetilde{\Omega}=\bigcup_{e=1}^{E}\overline{\Omega}_e \qquad \text{(Eq. 4.29)}$$

where

$$\overline{\Omega}_e = \Omega_e \cup \partial\Omega_e \qquad \text{(Eq. 4.30)}$$

and the open elements Ω_e are pairwise disjoint:

$$\Omega_e \cap \Omega_f = \varnothing \quad e \neq f \qquad \text{(Eq. 4.31)}$$

A finite number G of points $r^1, r^2, ..., r^g$ called nodes can be identified in the finite element model. The basis of the set of approximate functions $N_1, N_2, .., N_m$ is defined so that one basis function corresponds to each node. The basis function of a node vanishes at all other nodes and within all the elements to which the node does not belong and becomes unity at the specific node. Thus

$$N_i(r^j) = \delta_{ij} \qquad \text{(Eq. 4.32)}$$

Here δ_{ij} denotes Kronecker's function, and

$$N_i(\hat{r}) = 0, \quad r^i \notin \overline{\Omega}_e \ \ and \ \ \hat{r} \in \Omega \qquad \text{(Eq. 4.33)}$$

The term corresponding to the prescribed temperature boundary condition in Eq. 4.27 can be similarly expressed as

$$\tilde{T} = \sum_{i=1}^{m'} \tilde{T}(r^i, t) N_i(\hat{r}) \qquad \text{(Eq. 4.34)}$$

where m' the number of nodes on the prescribed temperature boundary and

$$G = m + m' \qquad \text{(Eq. 4.35)}$$

Then Eq. 4.27 becomes

$$\overline{T} = \sum_{i=1}^{G} a_i(t) N_i(\hat{r}), \quad a_i(t) = \tilde{T}(r^i, t) \ if \ r^i \in S_1 \qquad \text{(Eq. 4.36)}$$

and the coefficients $a_i(t)$ represent nodal temperatures.

Substitution of Eq. 4.36 in Eq. 4.24 results in:

$$\begin{aligned} &\sum_{i=1}^{G}\left[a_i(t)\int_{\Omega}\nabla W\cdot[K]\nabla N_i d\Omega\right] - \int_{\Omega} W\dot{Q}d\Omega + \sum_{i=1}^{G}\left[\frac{\partial a_i(t)}{\partial t}\int_{\Omega}\rho c_p W N_i d\Omega\right] \\ &\sum_{i=1}^{G}\left[a_i(t)\int_{S_3} WhN_i dS\right] + \int_{S_2} W\tilde{q}dS - \int_{S_3} WhT_\infty dS = 0 \end{aligned} \qquad \text{(Eq. 4.37)}$$

Different varieties of the weighted residuals are produced using different weighting functions in Eq. 4.37. Here the Galerkin-Bubnov approach, which is most widely used in heat transfer problems (190), has been applied. In this approach the basis functions of

the approximation are utilised as the weighting functions. Consequently, Eq. 4.37 becomes

$$\sum_{i=1}^{G}\left[a_i(t)\int_{\Omega}\nabla N_j\cdot[K]\nabla N_i d\Omega\right]-\int_{\Omega}N_j\dot{Q}d\Omega+\sum_{i=1}^{G}\left[\frac{\partial a_i(t)}{\partial t}\int_{\Omega}\rho c_p N_j N_i d\Omega\right]$$
$$\sum_{i=1}^{G}\left[a_i(t)\int_{S_3}N_j h N_i dS\right]+\int_{S_2}N_j\tilde{q}dS-\int_{S_3}N_j hT_\infty dS=0 \qquad \text{(Eq. 4.38)}$$

where N_j can be any of the basis function corresponding to nodes which do not belong to the prescribed temperature boundary.

It can be observed that Eq. 4.38 involves the time derivative of nodal temperatures. Consequently an approximation in the time dimension is required also. Here the θ-method (192) has been used according to which the time derivative is approximated by

$$\frac{\partial a_i(t)}{\partial t}=\frac{a_i^{n+1}(t)-a_i^{n}(t)}{\Delta t} \qquad \text{(Eq. 4.39)}$$

where Δt is the time step and the upper index denotes the time step. The terms involving $a_i(t)$ are evaluated at an intermediate time as follows:

$$a_i(t)=\tilde{\theta}a_i^{n+1}+\left(1-\tilde{\theta}\right)a_i^{n} \qquad \text{(Eq. 4.40)}$$

Then Eq. 4.38 becomes

$$\left[\sum_{i=1}^{G}a_i^{n}\left(-\int_{\Omega}\rho c_p N_j N_i d\Omega\right)+\left(1-\tilde{\theta}\right)\Delta t\sum_{i=1}^{G}\left(\int_{\Omega}\nabla N_j\cdot[K]\nabla N_i d\Omega+\int_{S_3}N_j h N_i dS\right)\right]$$
$$+\left[\sum_{i=1}^{G}a_i^{n+1}\left(\int_{\Omega}\rho c_p N_j N_i d\Omega\right)+\tilde{\theta}\Delta t\sum_{i=1}^{G}\left(\int_{\Omega}\nabla N_j\cdot[K]\nabla N_i d\Omega+\int_{S_3}N_j h N_i dS\right)\right] \qquad \text{(Eq. 4.41)}$$
$$+\Delta t\left[\int_{S_2}N_j\tilde{q}dS-\int_{S_3}N_j hT_\infty dS-\int_{\Omega}N_j\dot{Q}d\Omega\right]=0$$

Eq. 4.41 can be formed for each basis function which does not belong to the prescribed temperature boundary. Thus a system of $G-m'$ equations involving $G-m'$ unknowns is assembled

$$\left([M]+\tilde{\theta}\Delta t[L]\right)\left[a^{n+1}\right]-\left([M]-\left(1-\tilde{\theta}\right)\Delta t[L]\right)\left[a^{n}\right]-\Delta t[F]=0 \qquad \text{(Eq. 4.42)}$$

where

$$M_{ji}=\int_{\Omega}\rho c_p N_j N_i d\Omega \qquad \text{(Eq. 4.43)}$$

$$L_{ji} = \int_{\Omega} \nabla N_j \cdot [K] \nabla N_i d\Omega + \int_{S_3} N_j h N_i dS \qquad \text{(Eq. 4.44)}$$

$$F_j = -\int_{S_2} N_j \tilde{q} dS + \int_{S_3} N_j h T_\infty dS + \int_{\Omega} N_j \dot{Q} d\Omega \qquad \text{(Eq. 4.45)}$$

This system when formed can be solved for each time step starting from the initial condition of the problem, in order to obtain the temperature distribution evolution.

4.3 Implementation of the heat transfer model

A set of computer codes has been developed in order to perform the calculations outlined in paragraph 4.2.3. Three algorithms were developed using Visual Basic 5, implementing the following tasks:

- Mesh generation.
- Formation of the approximation function basis and calculation of the integrals involved in Eqs. 4.43-4.45.
- Formation of the matrices involved in the linear system expressed by Eq. 4.42 and solution of the system for a sequence of time steps.

The first two tasks are auxiliary and implement the discretisation of the domain, whereas the last task implements the actual heat transfer model. The communication between the different codes is performed using data files, which act as interfaces. The implementation of the spatial discretisation imposes limitations in the geometry of the modelled domain and the geometry of the elements used, but effort has been made so that the heat transfer solver is compatible with any type of finite element discretisation. Thus the code implementation of the heat transfer model can be used with the geometrical discretisation produced by any other code or software as long as the required data can be stored in a file with a known format.

4.3.1 Mesh generation

The mesh generation routine builds a finite element mesh by creating a set of internal nodal point coordinates using as an input the coordinates of the boundary nodes. The mesh produced is structured, i. e. the connectivity between nodes and the total number of nodes are known in advance. The implementation differs according to the dimensionality of the problem.

In the one dimensional case the algorithm is very simple. The two boundary node coordinates and the desired number of nodes are input from a file and the intermediate nodal coordinates are calculated by partitioning the linear segment which is defined by the two boundary nodes. Then the resulting coordinates are written in a file.

In two dimensional problems the domain is considered as a four sided shape. The sides consist of a number of linear segments, each of them defined by two nodes. The number of nodes of opposite sides should be equal and the total number of nodes of the produced mesh is equal to the product of the number of nodes of two intersecting sides of the domain. The procedure starts by reading four different files that contain the nodal coordinates of each of the sides. The order the files are read is specific, and implies the sides which are opposite to each other. Then, four iterative procedures are executed, each of them starting form one of the corners of the mesh.

The general principle of these procedures is that using the nodal coordinates of three nodes at the corners of a quadrilateral element and the slopes of the boundary segments, the coordinates of the fourth node are calculated. The three known nodes define two sides of the element and the objective is to find the other two sides which intersect at the unknown node. In order to produce a mesh which gradually relaxes irregularities of a boundary as the distance from it increases, but at the same time follows the irregularities close to the boundary, the slopes of the unknown sides are evaluated as weighted averages of the slopes of the corresponding boundary segments. Then the lines which have these slopes and pass from the known nodes of the element can be found. Their intersection defines the fourth node.

An example of this procedure is illustrated in Fig.4.3. The unknown node is N_{ij}. The slopes of the linear segments $N_{i-1,j}N_{i,j}$ and $N_{i,j-1}N_{i,j}$ are calculated as follows:

$$Slope\left(N_{i-1,j}N_{i,j}\right)=\frac{I\ Slope\left(N_{i-1,n}N_{i,n}\right)+\left(n-I\right)Slope\left(N_{i-1,1}N_{i,1}\right)}{n} \quad \text{(Eq. 4.46)}$$

$$Slope\left(N_{i,j-1}N_{i,j}\right)=\frac{I\ Slope\left(N_{m,j-1}N_{m,j}\right)+\left(m-I\right)Slope\left(N_{1,j-1}N_{1,j}\right)}{m} \quad \text{(Eq. 4.47)}$$

where m is the number of nodes in the horizontal direction and n the number of nodes in the vertical direction.

Substitution of the nodal coordinates $\left(X_{i,j-1},Y_{i,j-1}\right)$, $\left(X_{i-1,j},Y_{i-1,j}\right)$ and the corresponding slopes $Slope\left(N_{i,j-1}N_{i,j}\right)$, $Slope\left(N_{i-1,j}N_{i,j}\right)$ in the general line equation, leads to the estimation of the linear segments $N_{i,j-1}N_{i,j}$ and $N_{i-1,j}N_{i,j}$ equations. Subsequently the system of the two equations is solved and the coordinates of $N_{i,j}$ are calculated.

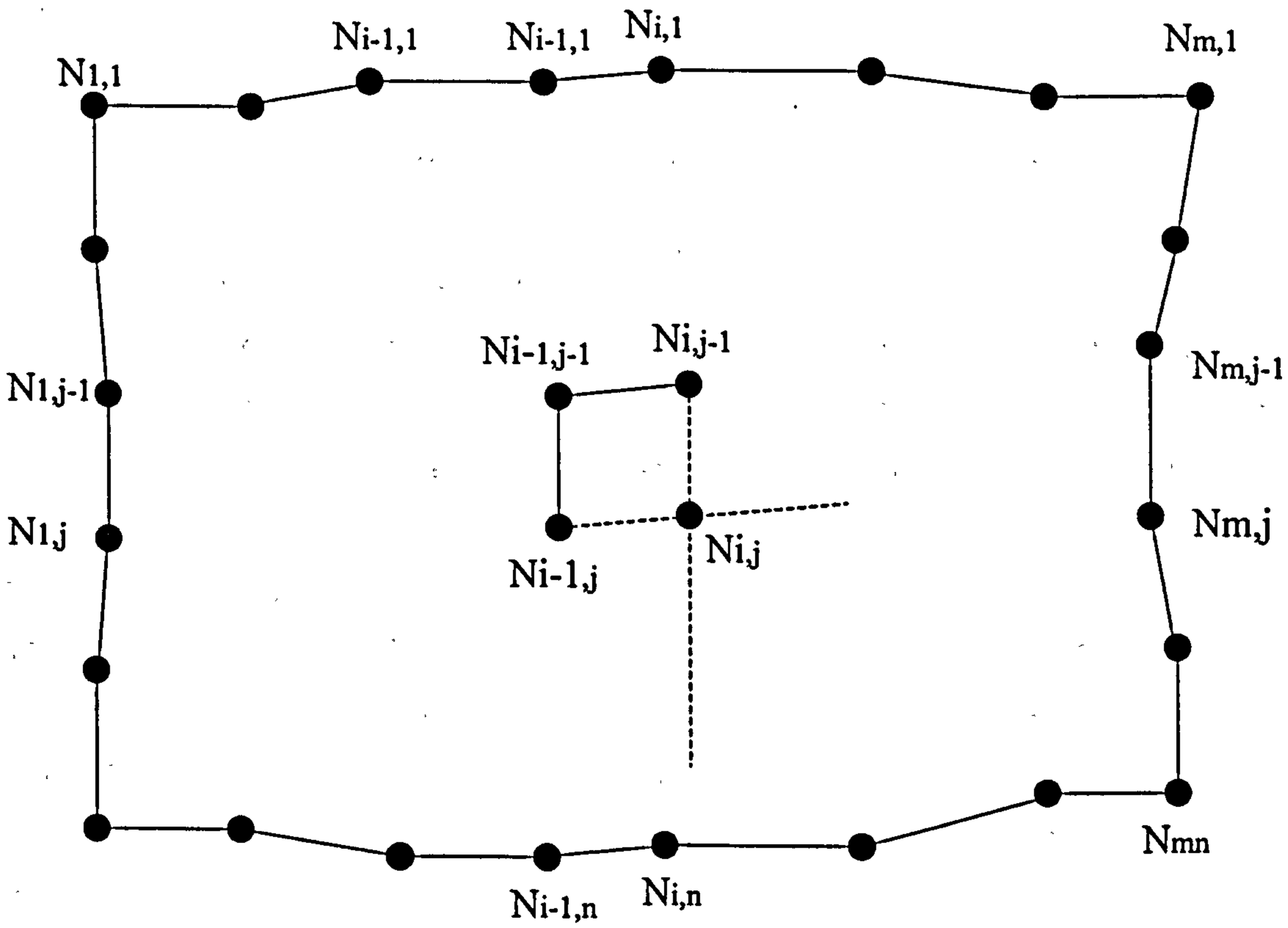

Fig.4.3 *Generation of a node from the mesh generation algorithm*

Thus, four sets of nodal coordinates are calculated starting from each corner. The four results are averaged and the final mesh is produced. An illustration of a mesh generation using this algorithm is given in Fig. 4.4.

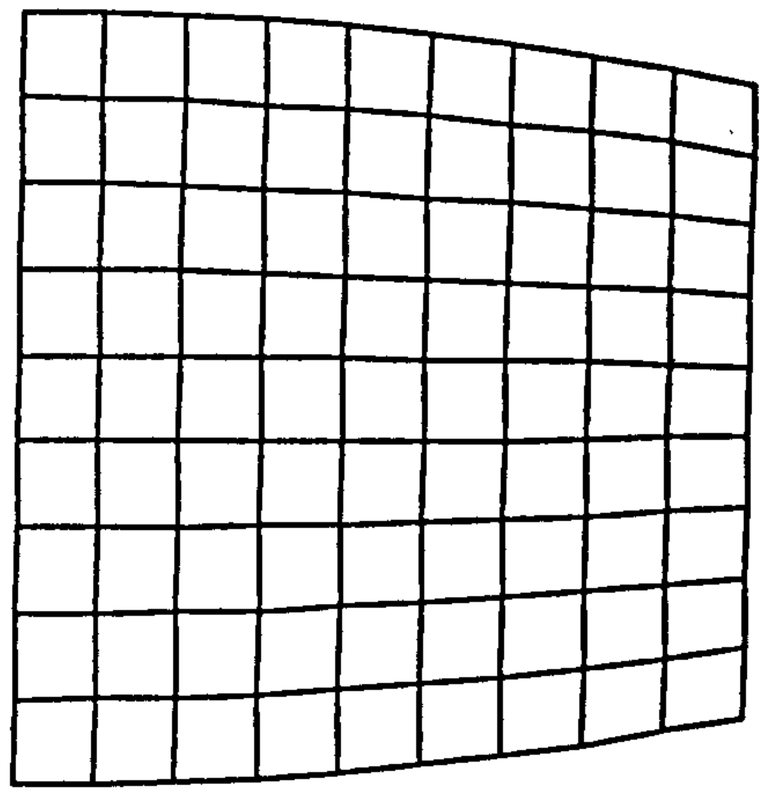

Fig.4.4 *Mesh resulted from the mesh generation algorithm*

The mesh generation algorithm for the three dimensional case is based on the same principle. The mesh is built in layers the first of which is produced using the procedure described previously. Each of the next layers is generated using the coordinates of the base layer and a set of parameters which map the boundary of the second layer to the boundary of the first layer. Thus, operations of magnification, horizontal and vertical displacement and rotation allow the projection of the two dimensional mesh corresponding to the first layer to the rest of the domain. Apart from the nodal coordinates files the mesh generation algorithms in all dimensions give as an output two additional files, defining the nodal points which correspond to each element and the connectivity of nodes.

The procedure applied is general and can be used for the discretisation of a wide variety of domains. However, the definition of the basis of approximation functions combined with the necessary continuity requirements forces us to limit the two dimensional

meshes to meshes comprising rectangular elements and the three dimensional meshes to meshes comprising brick (rectangular block) elements.

4.3.2 Integrals calculation

This procedure is used for the calculation of the members of the matrices involved in Eqs. 4.43-4.45. The thermal properties and the heat source term are considered constant within each element of the finite element model, thus the integrals involving the approximation functions basis are estimated independently. The code receives as input the nodal coordinates and the connectivity information from the mesh generation procedure described in the previous paragraph. Although the implementation differs according to the dimensionality of the heat transfer problem, the tasks involved are the same. Thus, a common description is given here and where necessary the specific features governed by the dimensionality of the problem are mentioned. An outline of the code developed is illustrated in Fig.4.5.

The first task is the input of the mesh generation algorithm output. Then the basis of the approximation functions set is found. The basis functions were selected to have the simplest form that can fulfil the requirements of Eqs. 4.32 and 4.33 for the linear elements in 1-D, the quadrilateral elements in 2-D and the hexahedral element in 3-D. Thus, two linear functions of the form:

$$N_{ei}(x) = A_{ei} + B_{ei}x \qquad \text{(Eq. 4.48)}$$

correspond to each 1-D element, four surfaces of the form:

$$N_{ei}(x,y) = A_{ei} + B_{ei}x + C_{ei}y + D_{ei}xy \qquad \text{(Eq. 4.49)}$$

correspond to each 2-D element and eight hypersurfaces which have the form:

$$N_{ei}(x,y,z) = A_{ei} + B_{ei}x + C_{ei}y + D_{ei}xy + E_{ei}z + F_{ei}xz + G_{ei}yz + H_{ei}xyz \qquad \text{(Eq. 4.50)}$$

correspond to each 3-D element. Here the indexes e and i denote the element and the node respectively. Note that these functions satisfy the interelemental continuity requirement for specific meshes which comprise rectangular elements in 2-D and rectangular block elements in 3-D. Condition 4.32 result in a 2 X 2 system in 1-D, in a 4 X 4 system in 2-D and in a 8 X 8 system in 3-D. These systems are solved using Gauss

elimination for each element and the coefficients involved in Eqs. 4.48, 4.49 or 4.50 are calculated.

The integrals required for the formation of the matrices of Eqs. 4.43-4.45 are:

$$\int_{\Omega_e} N_j d\Omega,\ \int_{\Omega_e} N_j N_i d\Omega,\ \int_{S_{e3}} N_j d\Omega,\ \int_{S_{e3}} N_j N_i d\Omega,\ \int_{S_{e2}} N_j d\Omega,$$

$$\int_{\Omega} \frac{\partial N_j}{\partial x}\frac{\partial N_j}{\partial x} d\Omega,\ \int_{\Omega} \frac{\partial N_j}{\partial y}\frac{\partial N_j}{\partial y} d\Omega,\ \int_{\Omega} \frac{\partial N_j}{\partial z}\frac{\partial N_j}{\partial z} d\Omega,$$

$$\int_{\Omega} \frac{\partial N_j}{\partial x}\frac{\partial N_j}{\partial y} d\Omega,\ \int_{\Omega} \frac{\partial N_j}{\partial y}\frac{\partial N_j}{\partial x} d\Omega,\ \int_{\Omega} \frac{\partial N_j}{\partial x}\frac{\partial N_j}{\partial z} d\Omega,$$

$$\int_{\Omega} \frac{\partial N_j}{\partial z}\frac{\partial N_j}{\partial x} d\Omega,\ \int_{\Omega} \frac{\partial N_j}{\partial y}\frac{\partial N_j}{\partial z} d\Omega,\ \int_{\Omega} \frac{\partial N_j}{\partial z}\frac{\partial N_j}{\partial y} d\Omega$$

The boundary integrals are calculated over the sides of the element which coincide with the boundary of the prescribed heat flux or the convection conditions respectively. Use of the partial derivatives that correspond to the dimensionality of the problem is necessary.

The integrals of the following elementary functions:

in 1-D:

$$1,\ x,\ x^2$$

in 2-D:

$$1,\ x,\ y,\ xy, x^2,\ y^2,\ xy^2,\ x^2y,\ x^2y^2$$

in 3-D:

$$1,\ x,\ y, z\ \ xy, xz,\ yz,\ x^2,\ y^2,\ z^2,\ xy^2,\ x^2y,\ x^2z,\ xz^2,\ y^2z,\ yz^2,$$

$$xyz, x^2y^2,\ x^2z^2,\ y^2z^2, x^2yz,\ xy^2z,\ xyz^2,\ x^2y^2z,\ x^2yz^2,\ xy^2z^2,\ x^2y^2z^2$$

over the domain corresponding to each element are analytically calculated. Subsequently the integrals of the basis functions which can be expressed as functions of the coefficients involved in Eqs. 4.48-4.50 and the integrals of the elementary functions are estimated.

The final step of the code is to output these results in a text file. All the necessary integrals for all pairs of connected nodes over each one of the elements which connects the specific pair of nodes are written in a file which is then available to the heat transfer model solver.

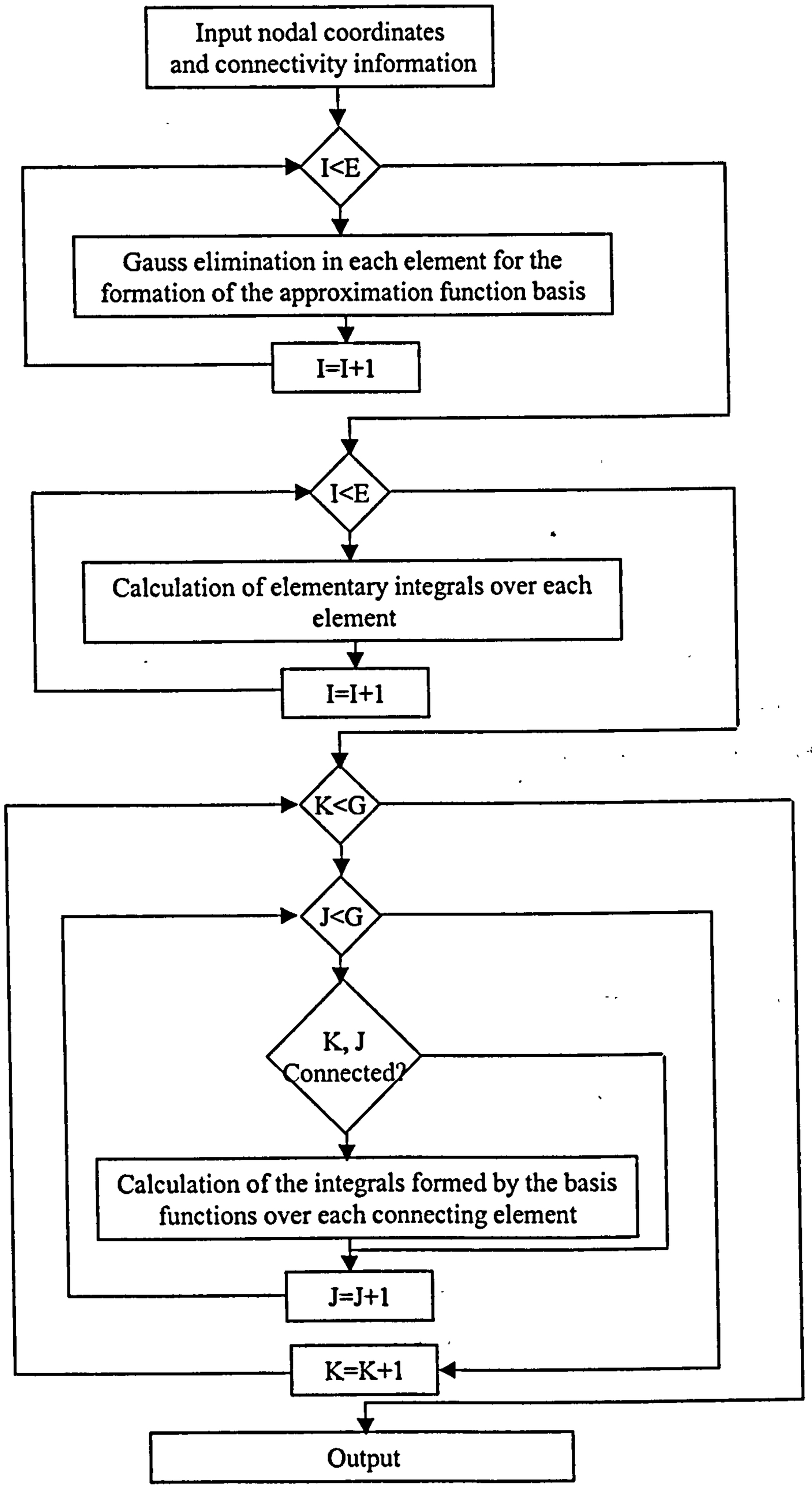

Fig.4.5 *Algorithm for the calculation of basis function integrals*

4.3.3 Heat transfer solver

This code implements the finite element solution of the heat transfer model as expressed by Eqs. 4.42-4.45. The first step in this procedure is the insertion of the discretisation information and the corresponding integrals of the basis functions as produced by the previous procedures. Subsequently, the nodes where each of the three types of conditions applies are defined. This is performed by the activation of a variable which becomes unity when the specific boundary condition applies at the node and zero otherwise. In the next step the initial condition (i. e. the temperature at each node and the progress of the reaction in each element at time zero are prescribed), the duration of the time step and the number of time steps Nt are defined.

Then the time solution of the heat transfer model starts in a loop which is repeated Nt times. This loop executes the following processes:

1. Calculation of the prescribed temperatures at the nodal points the prescribed temperature boundary condition applies to.
2. Calculation of the reaction rates for all elements. This is performed using the average temperature of the element calculated from the temperature values obtained by the solution of the model for the previous time step, or the initial condition for the first time step; and the degree of cure corresponding to the specific element for the previous time step. The temperature and fractional conversion are fed into the cure kinetics submodel, which is described in chapter 5. This submodel returns the reaction rate value to the main model. The reaction rate, the time step duration and the degree of cure of the previous time step are used for the calculation of the new fractional conversion value.
3. Calculation of the thermal properties (thermal conductivity, specific heat capacity and density) for all elements. The average temperature of the previous time step and the degree of cure are sent to the appropriate thermal properties submodels, which are described in chapter 6, and the submodels return the values of the thermal properties.
4. Formation of Eq. 4.42 for each node which is not subjected to the prescribed temperature boundary condition. This procedure, which is executed $G-m'$ times, tests whether the node is subject to prescribed heat flux or convection boundary

condition. Subsequently, it performs a loop over all nodes and if one node is connected with the node Eq. 4.42 is built for, uses the integral input from the previous procedure and the thermal properties and rate of reaction to calculate the coefficients M_{ji}, L_{ji} and F_j given by Eqs. 4.43-4.45.

5. Formation of Eq. 4.42 for the m' nodes of the prescribed temperature boundary so that it gives as a solution the prescribed temperature at the node.
6. Solution of the system of G equations using Gauss elimination in order to obtain the temperature at the nodal points.

After the completion of the time integration loop the results of the heat transfer model comprising the nodal temperature and the degree of cure of each element for all time steps are output in the form of a text file. This implementation of the heat transfer model solution, which is identical for problems of different dimensionality, is illustrated in Fig. 4.6.

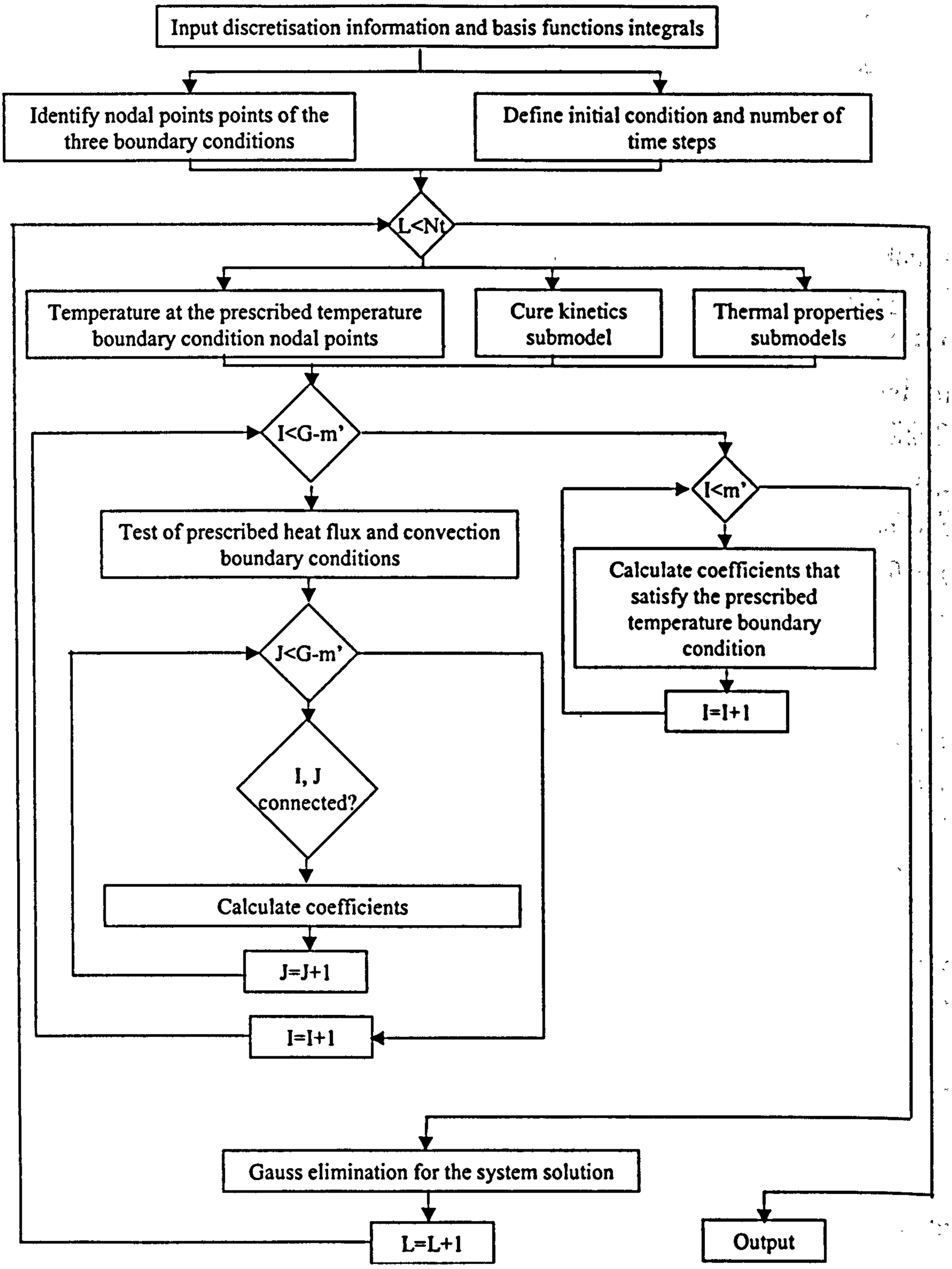

Fig.4.6 *Algorithm for the code implementation of the heat transfer model solver*

4.4 Validation of the codes

In order to validate the code implementation of the heat transfer model simulation, runs for cases which accept closed form solutions were performed and their results compared with the corresponding analytical solutions. This validation aims to verify the quality of the finite element procedure used and to ensure the correctness of the numerical procedure implementation.

Four test cases were selected. Three of them represent linear transient problems in 1-D, 2-D and 3-D, and the fourth represents a non-linear (includes heat generation) transient problem in 1-D. All the types of boundary conditions have been included in these problems. Thus, the basic blocks of code which implement: (i) meshing, integrals calculation and model solution in 1-D, 2-D and 3-D; (ii) prescribed temperature, prescribed temperature and convection boundary conditions; (iii) internal heating; (iv) incorporation of thermal properties; are tested. Note that this validation does not include the evaluation of the cure kinetics and thermal properties submodels. The evaluation of submodels will follow their description in subsequent chapters (5 and 6).

4.4.1 Test case 1: One dimensional transient problem

The transient heat conduction problem in a slab, subject to a heat flux boundary condition at one end and a convection boundary condition at the other end, with a uniform initial condition and constant thermal properties, accepts the general solution (43):

$$\frac{T-T_\infty}{T_o-T_\infty}=\sum_{i=0}^{\infty}\left(\frac{2\sin(k_i)}{k_i+\sin(k_i)\cos(k_i)}\right)\cos\left(\frac{k_i x}{L}\right)e^{-k_i^2\frac{Kt}{c_p\rho L^2}} \qquad \text{(Eq. 4.51)}$$

where T_o is the initial uniform temperature, L the thickness of the slab and the coefficients k_i are the solution of the relation:

$$k_i\tan(k_i)=\frac{hL}{K} \qquad \text{(Eq. 4.52)}$$

The temperature distribution evolution of the above system during 5 seconds, for thermal properties equal to unity, external temperature equal to zero and initial temperature 10 °C, has been evaluated using the exact solution and the finite element

model. The slab was considered insulated at $x=0$ and subject to a convection boundary condition at $x=1$. For the calculation of the analytical solution the first 500 terms of the series in Eq. 4.51 were taken into account. The finite element models consisted of 101 nodal points, and a number of different time discretisations was used. Results of the model for 2000 time steps are set against the exact solution in Fig. 4.7, where excelent agreement is observed. The average percentage error of the simulation was calculated for 25, 50, 125, 250, 500, 1000 and 2000 time steps and is illustrated in Fig. 4.8. It is observed that the algorithm results converge to the exact solution for more than 500 time steps.

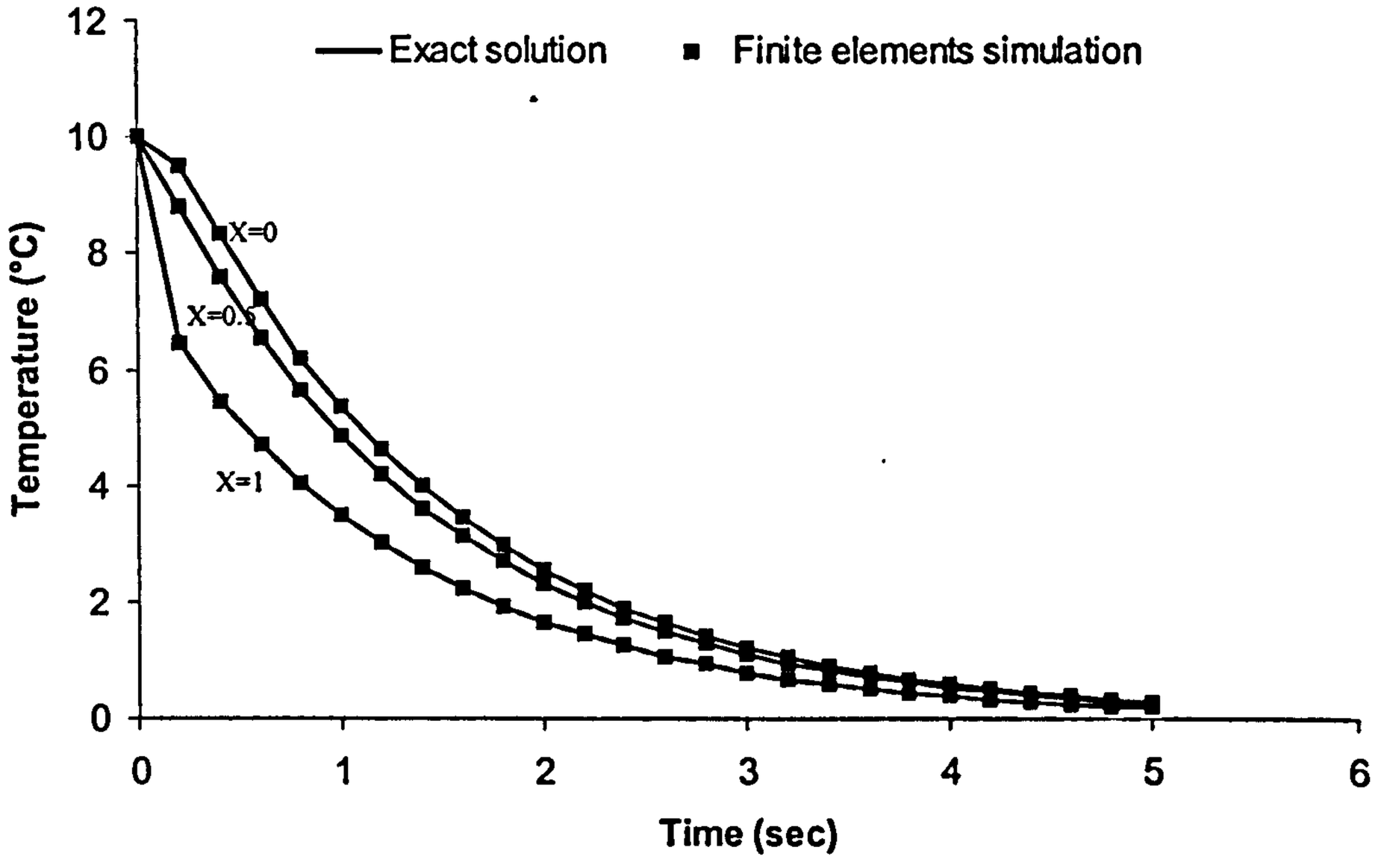

Fig.4.7 *Comparison of analytical solution and finite element model results for the cooling of an 1-D slab. 2000 time steps were used in the finite element model solution*

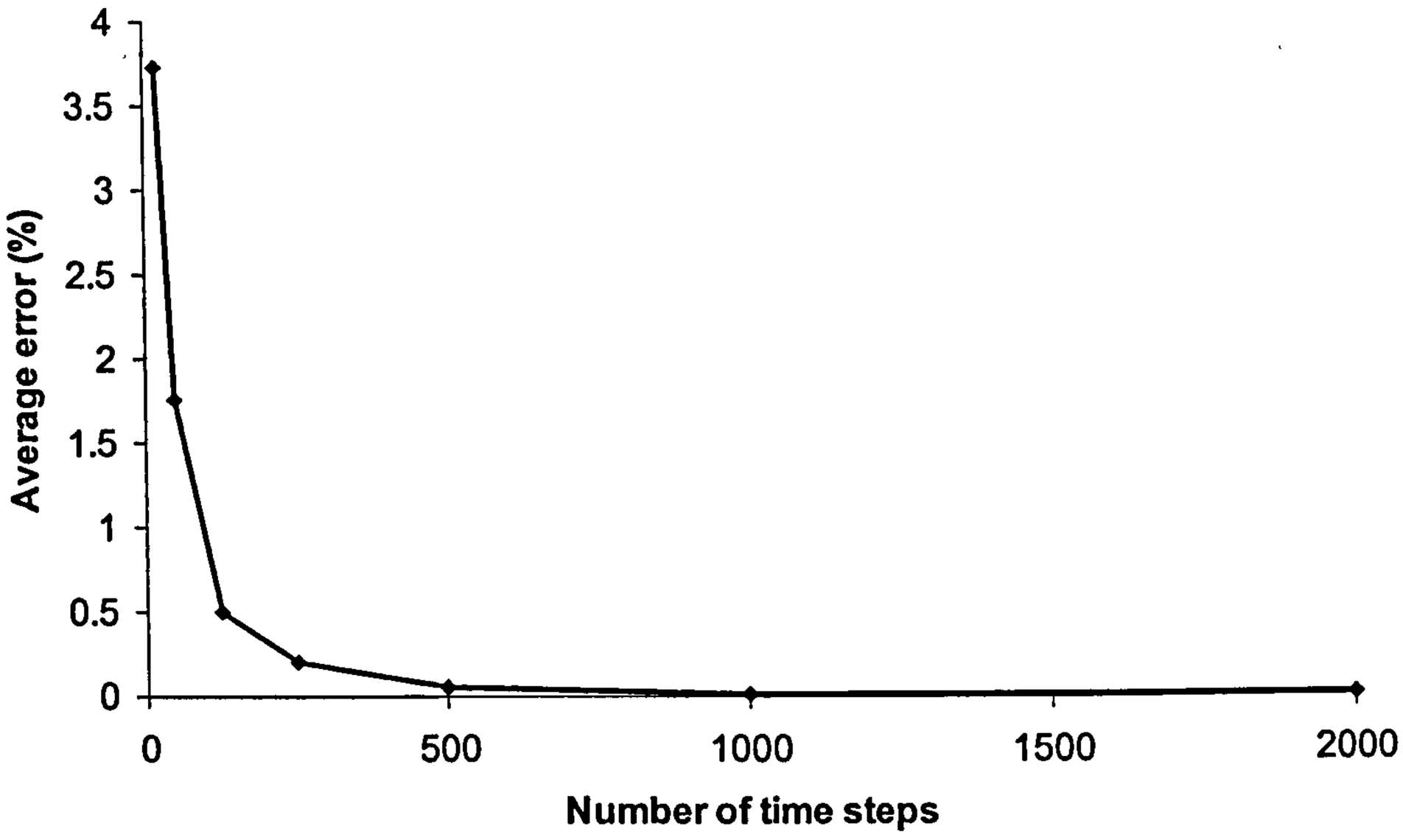

Fig.4.8 *Average error of the finite element simulation of the cooling of an 1-D slab versus the number of time steps*

4.4.2 Test case 2: One dimensional transient problem with a source term

The transient heat conduction problem in a slab of length unity, when all thermal properties are unity and the rate of heat generation is:

$$\dot{Q} = 10\sin(3\pi x) \qquad \text{(Eq. 4.53)}$$

subject to the boundary conditions:

$$T(0,t) = T(1,t) = 0 \qquad \text{(Eq. 4.54)}$$

and the initial condition

$$T(x,0) = \sin(\pi x) \qquad \text{(Eq. 4.55)}$$

has the solution:

$$T(x,t) = \sin(\pi x)e^{-\pi^2 t} + \frac{10}{9\pi^2}\sin(3\pi x)\left(1 - e^{-9\pi^2 t}\right) \qquad \text{(Eq. 4.56)}$$

A finite element model comprising 21 nodes has been built to represent this case. A comparison of simulation results and the analytical solution is given in Fig.4.9. The two sets of data points are very close. The average error in temperature calculation for

different time discretisations (10, 20, 40, 80 and 160 time steps) is illustrated in Fig. 4.10. The convergence of the algorithm is evident for more than 40 time steps.

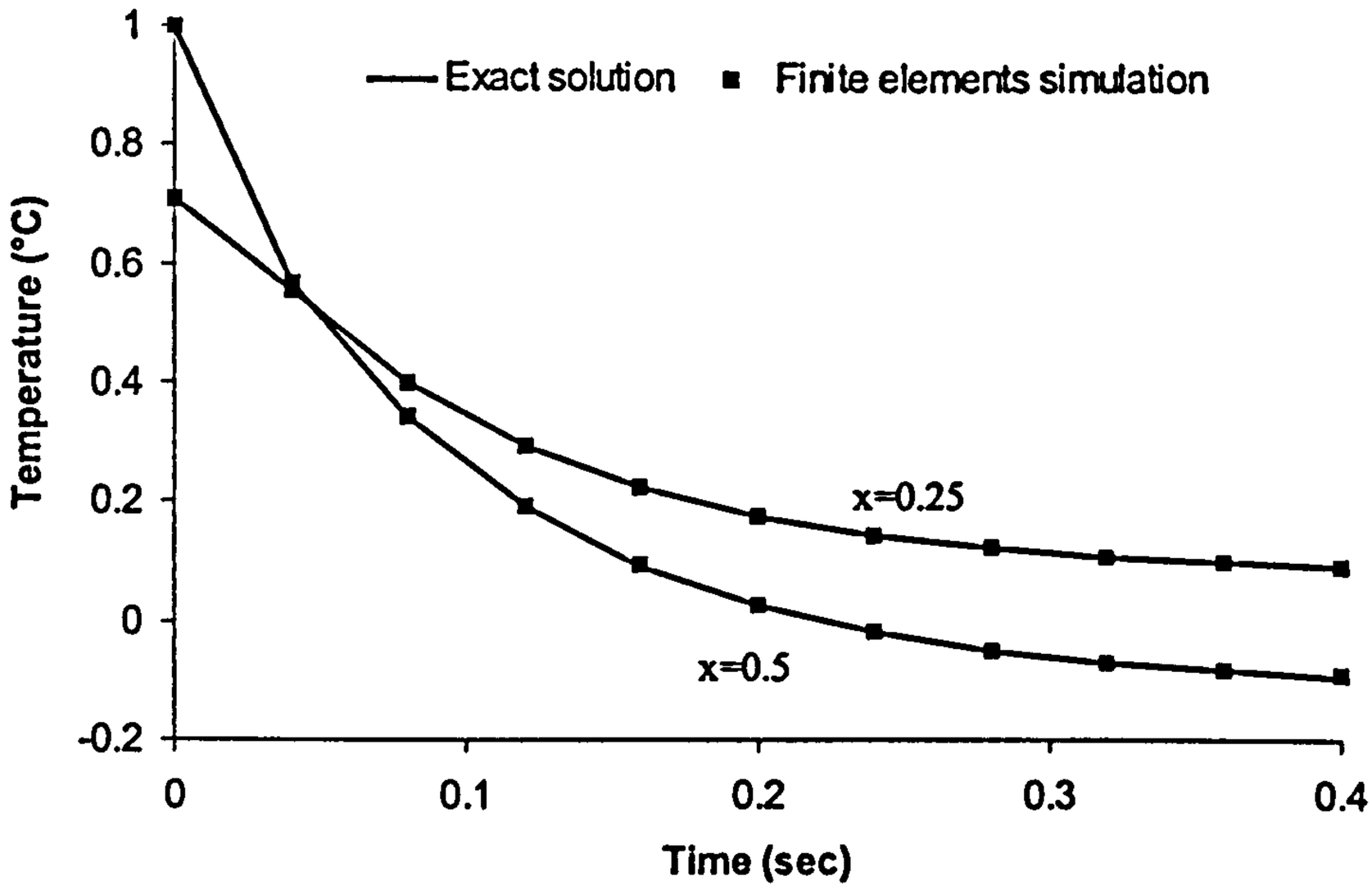

Fig.4.9 *Comparison of analytical solution and finite element model results for the cooling of an 1-D slab with internal heating. 160 time steps were used in the finite element model solution.*

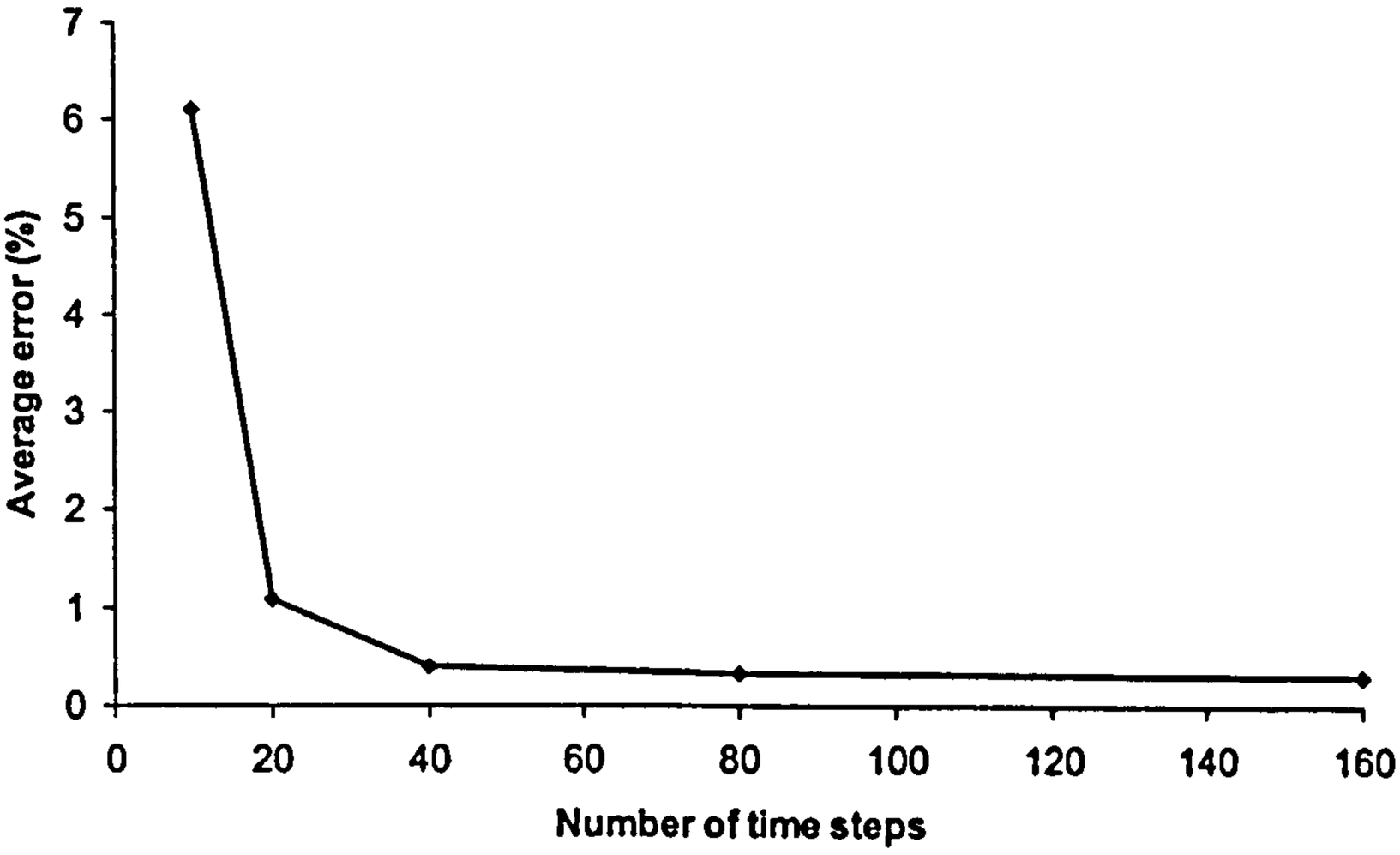

Fig.4.10 *Average error of the finite element simulation of the cooling of an 1-D slab with internal heating versus the number of time steps*

4.4.3 Test case 3: Two dimensional transient problem

The transient heat conduction problem in a rectangular domain subject to the boundary conditions:

$$T(0,y,t)=T(L_x,y,t)=T(x,0,t)=T(x,L_y,t)=0 \qquad \text{(Eq. 4.57)}$$

and the initial condition:

$$T(x,y,0)=30, \quad x\neq 0,L_x,\ y\neq 0,L_y \qquad \text{(Eq. 4.58)}$$

where L_x, L_y are the dimensions of the domain, has the analytical solution (193):

$$T=\sum_{i=1}^{\infty}\sum_{j=1}^{\infty}k_{ij}\sin\left(\frac{i\pi x}{L_x}\right)\sin\left(\frac{j\pi y}{L_y}\right)e^{-\left(\frac{K_{xx}i^2\pi^2}{L_x^2}+\frac{K_{yy}j^2\pi^2}{L_y^2}\right)t} \qquad \text{(Eq. 4.59)}$$

where the shear K_{xy} conductivity is zero and the product of specific heat capacity and density is unity. The coefficients k_{ij} are given by the relation:

$$k_{ij}=\frac{120}{ij\pi^2}\left[(-1)^i-1\right]\left[(-1)^j-1\right] \qquad \text{(Eq. 4.60)}$$

When the lengths of the domain and the thermal conductivities are unity the solution becomes:

$$T=\sum_{i=1}^{\infty}\sum_{j=1}^{\infty}k_{ij}\sin(i\pi x)\sin(j\pi y)e^{-(i^2\pi^2+j^2\pi^2)t} \qquad \text{(Eq. 4.61)}$$

The analytical solution has been calculated using the members of the series for which

$$ij<100000 \qquad \text{(Eq. 4.62)}$$

The finite element model comprised 256 equally spaced nodes. Results of the simulation are compared with the analytical solution in Fig. 4.11. It can be observed that the model follows the exact solution very closely. The average error of the model as a function of the number of time steps is illustrated in Fig. 4.12. The algorithm converges for more than 50 time steps. The relatively high error (approximately 1%) after convergence is attributed to the coarse mesh (16x16) that has been utilised. Refinement of the mesh can lead to the same level of accuracy observed in the one dimensional test cases.

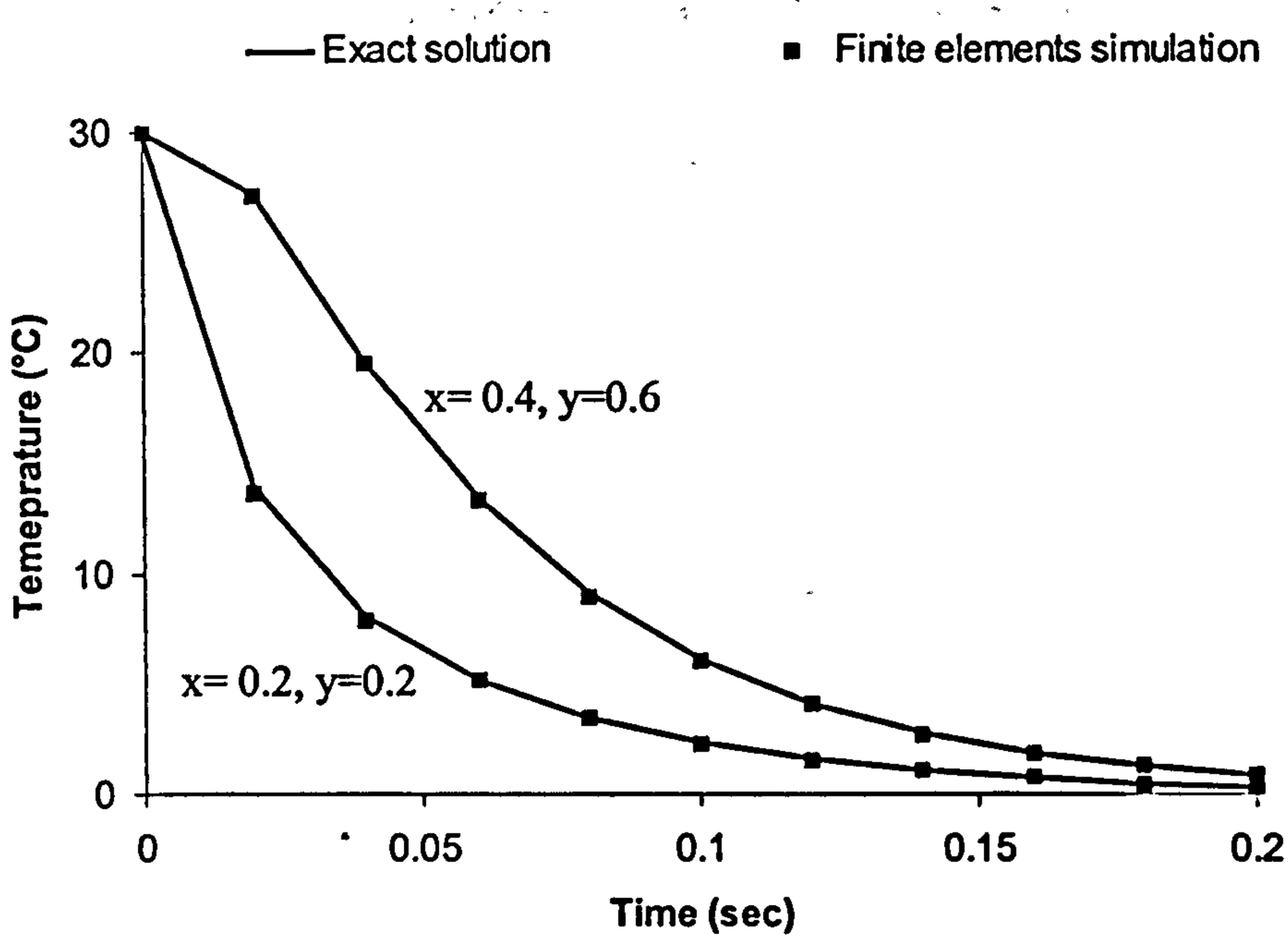

Fig.4.11 *Comparison of analytical solution and finite element model results for the cooling of a 2-D domain. 200 time steps were used in the finite element model solution.*

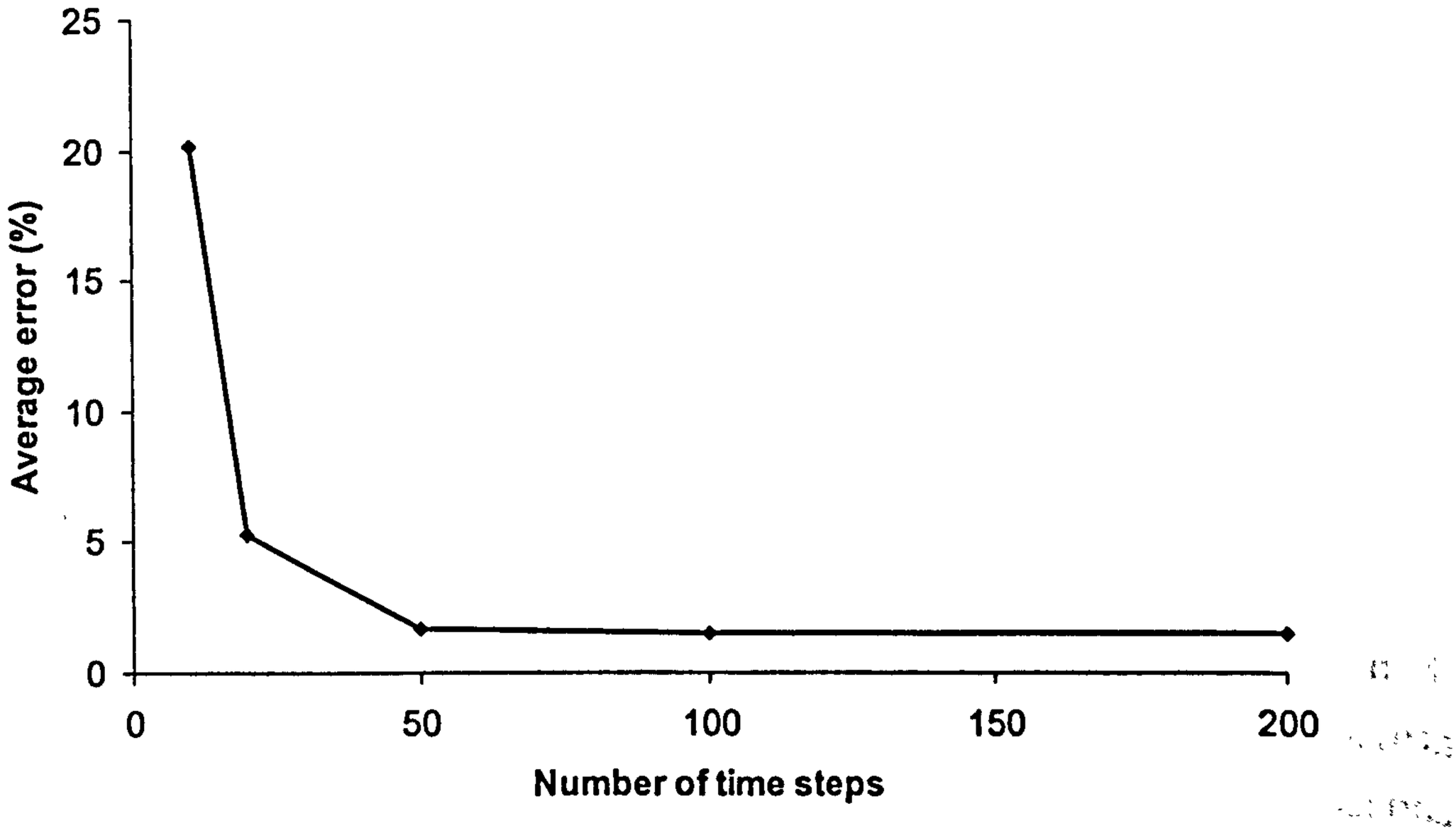

Fig.4.12 *Average error of the finite element simulation of the cooling of a 2-D domain versus the number of time steps*

4.4.4 Test case 4: Three dimensional problem

The transient heat conduction problem in a rectangular block domain subject to the boundary conditions:

$$T(0,y,z,t)=T(L_x,y,z,t)=T(x,0,z,t)=T(x,L_y,z,t) \\ =T(x,y,0,t)=T(x,y,L_z,t)=T_b \quad \text{(Eq. 4.63)}$$

and the initial condition:

$$T(x,y,z,0)=0, \quad x\neq 0,L_x,\ y\neq 0,L_y,\ z\neq 0,L_z \quad \text{(Eq. 4.64)}$$

where L_x, L_y, L_z are the dimensions of the domain, has the solution (194):

$$T=T_b-\frac{64}{\pi^3}T_b\sum_{l=0}^{\infty}\sum_{i=0}^{\infty}\sum_{j=0}^{\infty}\frac{(-1)^{l+i+j}}{(2l+1)(2i+1)(2j+1)}\cos\left(\frac{(2j+1)\pi\left(x-L_x/2\right)}{L_x}\right) \quad \text{(Eq. 4.65)}$$
$$\cos\left(\frac{(2i+1)\pi\left(y-L_x/2\right)}{L_y}\right)\cos\left(\frac{(2l+1)\pi\left(z-L_x/2\right)}{L_z}\right)e^{a_{lji}t}$$

where the material is isotropic and the product of specific heat capacity and density is unity. The coefficients a_{lji} are given by the relation:

$$a_{lji}=K\pi^2\left[\frac{(2j+1)^2}{L_x^2}+\frac{(2i+1)^2}{L_y^2}+\frac{(2l+1)^2}{L_z^2}\right] \quad \text{(Eq. 4.66)}$$

When the lengths of the domain and the thermal conductivities are equal to unity and the temperature at the boundary 10 °C, the solution becomes:

$$T=10-\frac{64}{\pi^3}10\sum_{l=0}^{\infty}\sum_{i=0}^{\infty}\sum_{j=0}^{\infty}\frac{(-1)^{l+i+j}}{(2l+1)(2i+1)(2j+1)}\cos[(2j+1)\pi(x-0.5)] \quad \text{(Eq. 4.67)}$$
$$\cos[(2l+1)\pi(y-0.5)]\cos[(2i+1)\pi(z-0.5)]e^{a_{lji}t}$$

and

$$a_{lji}=\pi^2\left[(2j+1)^2+(2i+1)^2+(2l+1)^2\right] \quad \text{(Eq. 4.68)}$$

The analytical solution has been calculated using the members of the series of Eq. 4.67 for which

$$ijl<1000000 \quad \text{(Eq. 4.69)}$$

Two finite element models comprising 1536 and 9161 nodes respectively were used. A comparison of the finite element models results with the analytical solution is illustrated in Fig. 4.13. Although 10 time steps were used, the temperature values calculated using the fine mesh are very close to the analytical solution (average error 0.7%). In the coarse mesh case the average error in temperature estimation is significantly higher (9.2%). Thus, geometrical refinement results in convergence of the algorithm.

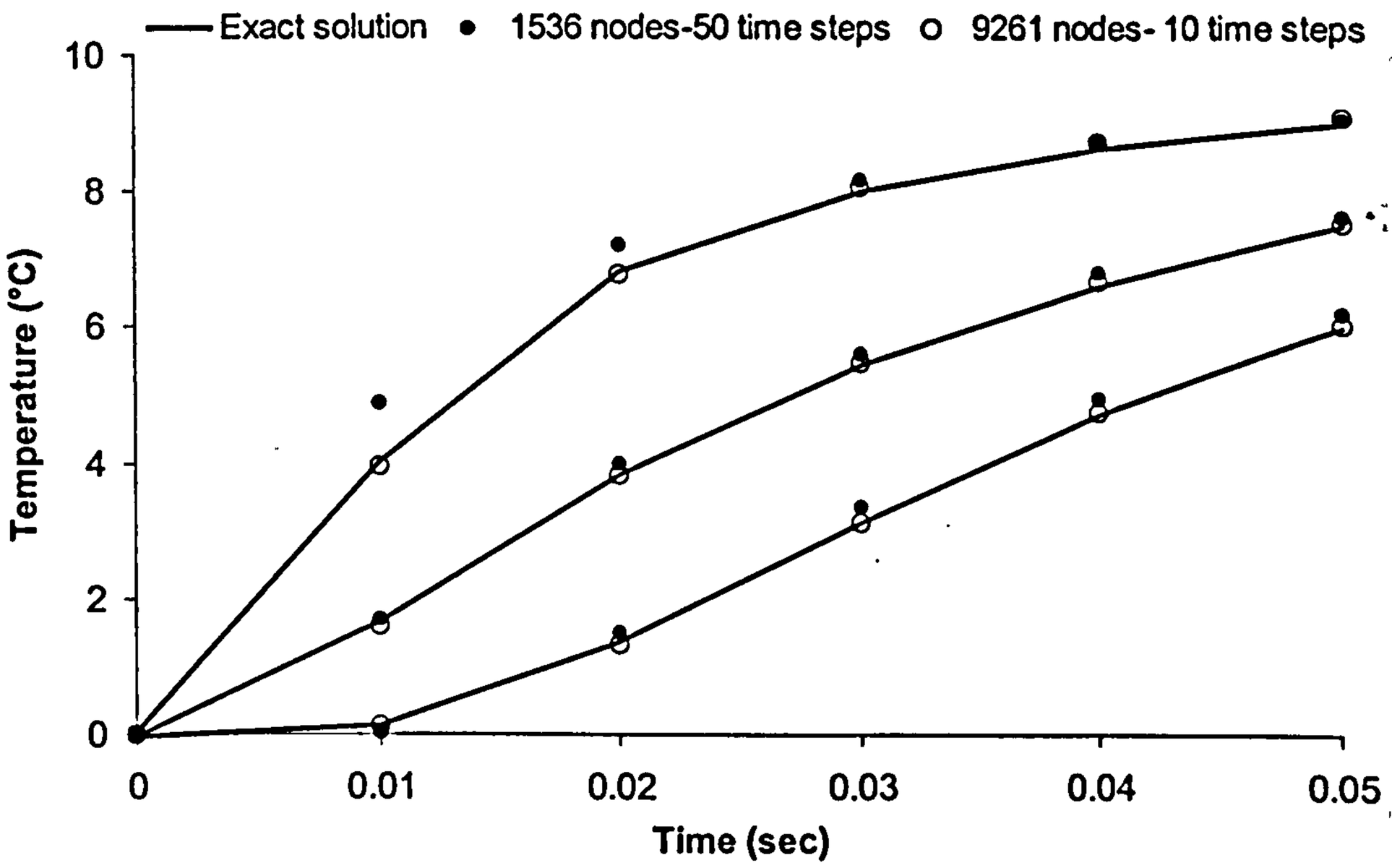

Fig.4.13 *Comparison of analytical solution and finite element model results for the heating of a 3-D cube*

4.5 Overview

It was demonstrated that heat conduction is the only significant heat transfer mechanism in composites curing. Accordingly a software code implementing finite element heat transfer modelling appropriate for curing simulations has been developed. The core of the model has been described here; the description of submodels used for the incorporation of cure kinetics and thermal properties will follow in the next two chapters. The heat transfer solver was tested against analytical solutions of heat transfer

problems involving all the types of boundary conditions in 1-D, 2-D and 3-D. These tests confirmed the validity of the code implementation and demonstrated its convergence to the exact solution with mesh and time stepping refinement.

Chapter Five

5 Cure kinetics submodel

5.1 Introduction

The scope of this chapter is the description of the cure kinetics modelling method, which is used as a subroutine of the heat transfer model. The results on which the model is based are reported, the background of the modelling method selection is given and the method and its implementation procedure are described. The validity of the model is tested against experimental data and an evaluation of the modelling procedure used is presented.

5.2 Differential scanning calorimetry

Data for the cure kinetics model were gathered using differential scanning calorimetry (DSC). DSC measures the rate of heat absorption or emission by a sample. There are two variations of the technique:

- *Power compensation* DSC, which measures the difference between the power required to impose a thermal program to the sample and the power required to impose the same thermal program to a reference. This experimental configuration uses two identical furnaces and two different heating and temperature control systems.

- *Heat flux* DSC, which measures indirectly the heat flow between the sample and the reference when they are subjected to the same thermal program. In this configuration one furnace, which contains both the sample and the reference is used.

The instrument used in this study was a heat flux DSC (TA Instruments 1920). A schematic representation of a heat flux DSC cell is given in Fig. 5.1.

It comprises an externally heated chamber, a constantan disc with two raised parts for the sample and the reference and two thermocouples fitted on the constantan disc under the sample and reference positions. The temperature difference between the sample and the reference is monitored using these thermocouples. The heat flow required to equilibrate the temperature is a linear function of this temperature difference over a wide range of experimental conditions (195). Consequently, using an appropriate calibration procedure, the difference in heat flux emitted or absorbed by the sample and the reference can be calculated.

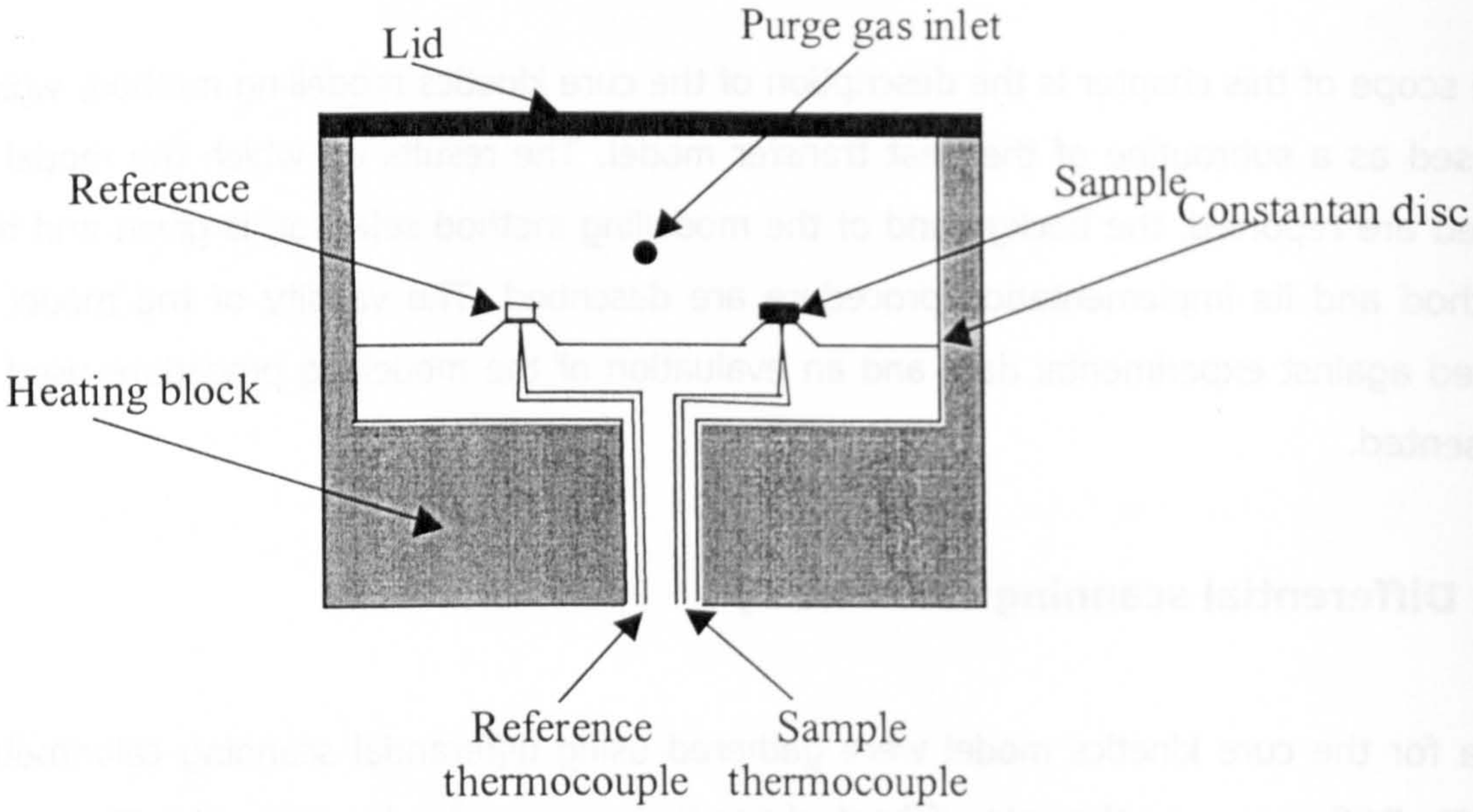

Fig.5.1 *Schematic representation of a heat flux DSC cell*

The operation of DSC and its use for characterisation of resin cure kinetics is based on three assumptions:

- the temperature gradient within the sample is negligible;
- the rate of the reaction is proportional to the heat flow and

- in the case of dynamic runs, the part of the response which is due to the heat capacity of the material can be subtracted using an appropriate baseline.

The validity of the first assumption can be ensured by using very small samples. The second assumption can be justified in cases where the same groups of the macromolecule are transformed throughout the whole reaction. Then, the exothermic heat per molecule reacted is given by the same energy balance, and proportionality holds:

$$\frac{d\alpha}{dt} = \frac{dH}{dt}\frac{1}{H_{tot}} \qquad \text{(Eq. 5.1)}$$

where H_{tot} denotes the total heat of reaction.

In the case of epoxy resin cure, although the reaction always involves the opening of the epoxy ring, different reaction mechanisms involving different functional groups can take place simultaneously (196). Thus the proportionality assumption cannot be expected to hold in all cases. However, DSC based kinetics models have been successfully applied to epoxy cure in numerous investigations. Furthermore the information required, when cure kinetics modelling aims to provide input in a heat transfer model, is the exothermic heat. A model based on DSC measurements gives this information accurately even if it does not correspond to the exact chemistry of the system. In this respect the meaning of fractional conversion can be modified from the proportion of reacted epoxy rings to a 'calorimetric' conversion. This 'calorimetric' conversion may or may not coincide with the chemical conversion. As long as there is a one to one correspondence between the two, the results of a model for kinetics will be identical in terms of curing process characterisation. Since in DSC measurement the state of the material is represented by a single conversion, this one to one correspondence is expected to hold in all resin systems for which reaction rate is a unique function of progress of reaction and temperature. For the specific resin system used (RTM6) in this study the validity of such an approach is reinforced by the successful application of empirical cure kinetics model based on DSC (17).

The third assumption refers to the contribution of the material heat capacity to the DSC signal in dynamic cure experiments. When the temperature changes, the sample absorbs or emits heat, at a rate defined by its heat capacity. When the heat capacity

changes during the experimental run, as it is the case in curing, a baseline which reflects its behaviour must be found and subtracted from the DSC signal before integration. Typically a dynamic DSC curve has a bell shape, which starts and ends at a plateau, corresponding to zero reaction rate at low temperatures and at very high conversion. The baseline should connect the two plateaus which are not necessarily level. The general practice is to use a linear or a sigmoidal baseline. However, there is no theoretical justification for the use of such a baseline, since the heat capacity is not expected to change in a linear or sigmoidal fashion during the cure.

5.3 Experimental details

Dynamic cure experiments of RTM6 resin were carried out at 0.25, 0.5, 1, 2, 4, 6, 8, 10 and 20 °C/min and isothermal experiments at 120, 130, 140, 150, 160, 170, 180, 190 and 200 °C. Samples were encapsulated in aluminium pans. An empty pan was placed on the reference side of the instrument. After equilibrating the DSC cell at 80 °C (the resin is essentially inert at that temperature) the thermal program was imposed, by following the required heating rate in the case of dynamic experiments or by jumping to the cure temperature using a heating rate of 20 °C/min in the case of isothermal experiments. In all experiments carried out in this study the weight of the sample ranged from 3 to 4 mg, in order to ensure that the thermal gradients were negligible. Three types of calibration of the instrument were carried out prior to the experiments:

- *Temperature calibration*: -performed by melting standard substances and measuring the difference of the melting points in respect to literature values. This information is used for temperature correction when the instrument translates raw thermocouple signals to temperature. In this study indium was used as the standard.
- *Cell calibration*: -performed by melting a standard of Indium and calculating the latent heat melting. The ratio of this value to the literature value constitutes the cell constant of the instrument and is used during the computation of heat flow from the raw thermocouple signals.
- *Empty cell calibration*: -accounts for cell assymmetry. It is carried out by imposing to the empty cell a thermal program identical to that of the actual experiment. The measured signal is subtracted from the subsequent experiment raw signal.

The raw experimental result has been obtained by averaging two curves of raw data obtained in each case. Although DSC experiments have demonstrated very high repeatability in preliminary testing, this procedure was adopted in order to ensure that no accidental variations would deteriorate results quality. In all runs the two curves were very close to each other, confirming the high repeatability of the method.

In this study a method proposed by Bandara (197) has been implemented for the baseline correction of dynamic runs. As mentioned in paragraph 5.2 the initial and final plateaus correspond to the initial and the final heat capacity of the curing material. The heat capacity is expected to change gradually from the initial to the final value. Its value at an intermediate point is considered to be a linear function of the progress of reaction which at zero conversion results in the initial heat capacity value and at maximum conversion results in the final heat capacity value.

For computational reasons the baseline is considered to be the sum of a fixed number (1000) of linear segments. For such short temperature intervals a linear function would interpolate satisfactorily the dependence of heat capacity on the temperature. Thus the baseline is described by the relations:

$$Slope_i = Slope_{in}(1-\alpha_i) + Slope_{fin}\alpha_i \qquad \text{(Eq. 5.2)}$$

$$Intercept_i = Intercept_{in}(1-\alpha_i) + Intercept_{fin}\alpha_i \qquad \text{(Eq. 5.3)}$$

where $Slope_i$, $Slope_{in}$ and $Slope_{fin}$ are the slopes of the ith, the initial and final segment respectively. Similarly $Intercept_i$, $Intercept_{in}$ and $Intercept_{fin}$ are the intercepts of the ith, the initial and final segment respectively.

The degree of cure is calculated according to the relation:

$$\alpha = \frac{\int_0^t (S(t) - B(t))dt}{\int_0^{t_f} (S(t) - B(t))dt} \qquad \text{(Eq. 5.4)}$$

here $S(t)$ denotes the DSC signal, $B(t)$ its baseline value and t_f the final time, while the denominator is the total heat of reaction.

Combining Eqs. 5.2, 5.3 and 5.4 results in:

$$B(t)=\left(1-\frac{\int_0^t (S(t)-B(t))dt}{\int_0^{t_f} (S(t)-B(t))dt}\right)B(0)+\left(\frac{\int_0^t (S(t)-B(t))dt}{\int_0^{t_f} (S(t)-B(t))dt}\right)B(t_f) \qquad \text{(Eq. 5.5)}$$

Since the baseline is required for the integration, but it also depends on the result of the integration, a recursive procedure is adopted.

A representation of the developed algorithm for baseline correction, integration and reaction rate calculation is given in Fig. 5.2.

The algorithm begins with the input of raw data which are subsequently interpolated in order to form 1000 experimental data points at regular intervals. Then the baseline calculation algorithm starts by selecting its initial and final segments. An iterative solution of Eq 5.2, 5.3 and 5.4 takes place, having as initial values zero conversion and baseline equal to that of the first segment. When a convergence criterion is met the algorithm exits and the reaction rate is computed numerically.

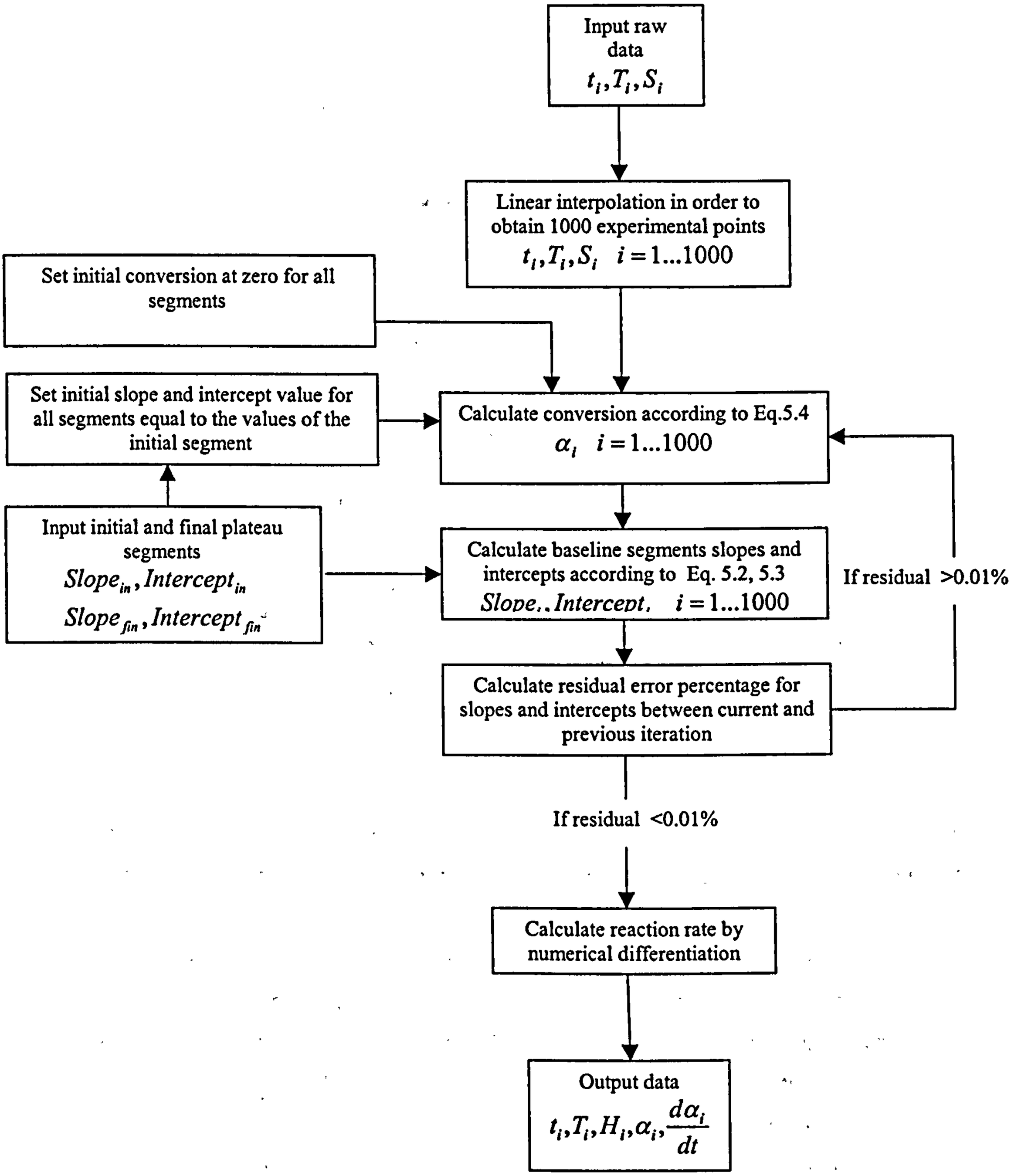

Fig.5.2 *Iterative algorithm for baseline subtraction and integration of DSC curves*

5.4 Experimental results

Results of dynamic experiments are summarised in Figs.5.3 and 5.4.

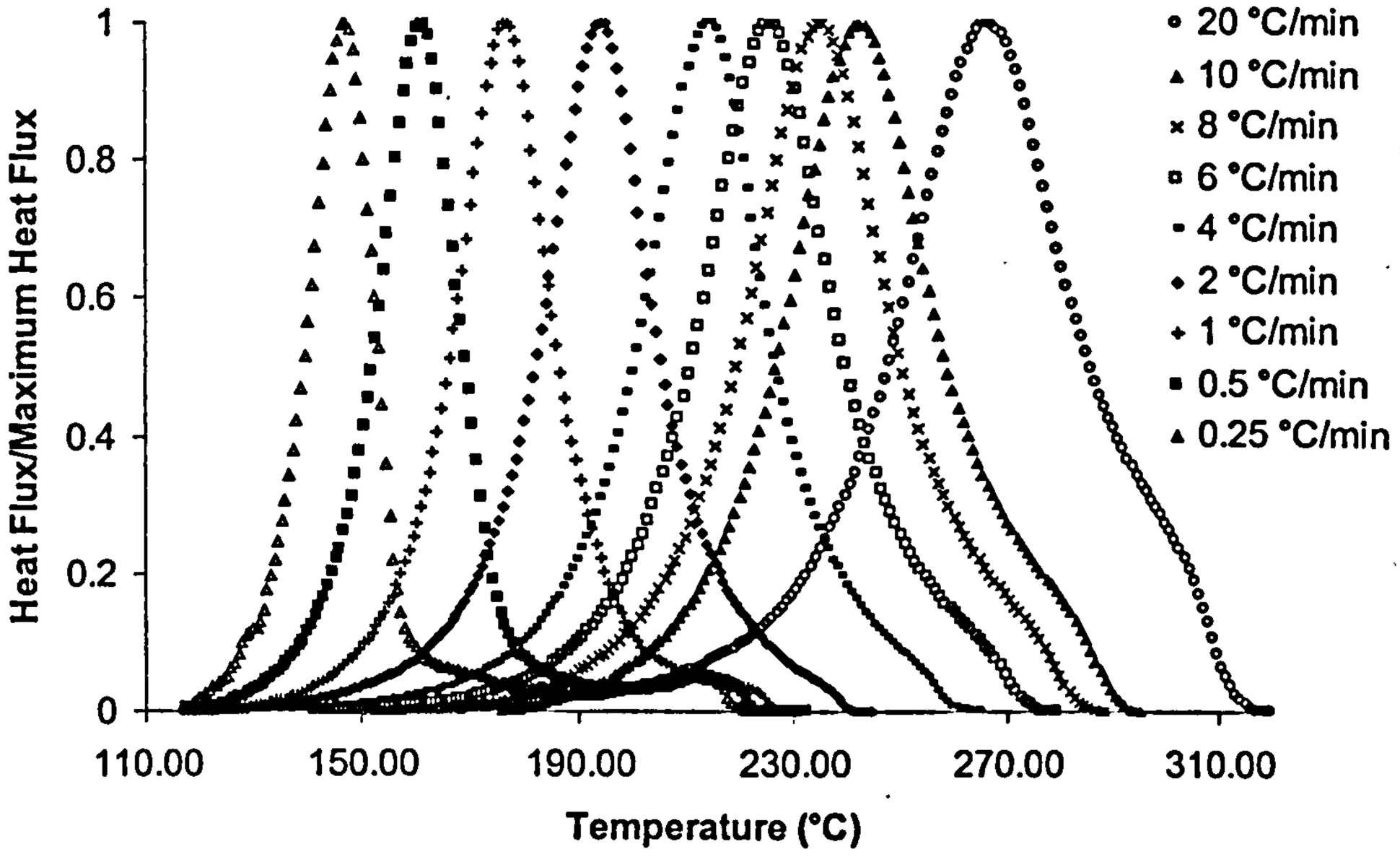

Fig.5.3 *Normalised heat flux versus temperature in the dynamic cure of RTM6*

The normalised heat flux curves have the bell shape characteristic of a dynamic cure. At low temperatures the reaction is very slow. As the temperature increases the reaction is activated until it reaches a peak value and then deceleration occurs towards a plateau value at near complete conversions. At very low heating rates (up to 1 °C/min) a second peak is observed towards the end of the cure. In the case of rate-conversion curves this is manifested as a second, very small semicircle, which is not visible in the non-normalised data of Fig.5.4. The second peak is attributed to devitrification (198) which occurs when the cure temperature exceeds the ultimate glass transition of the material. At higher heating rates the temperature change is too fast for the material to reach a conversion sufficient to cause vitrification before the ultimate glass transition has been exceeded. Consequently vitrification and devitrification do not occur at these rates.

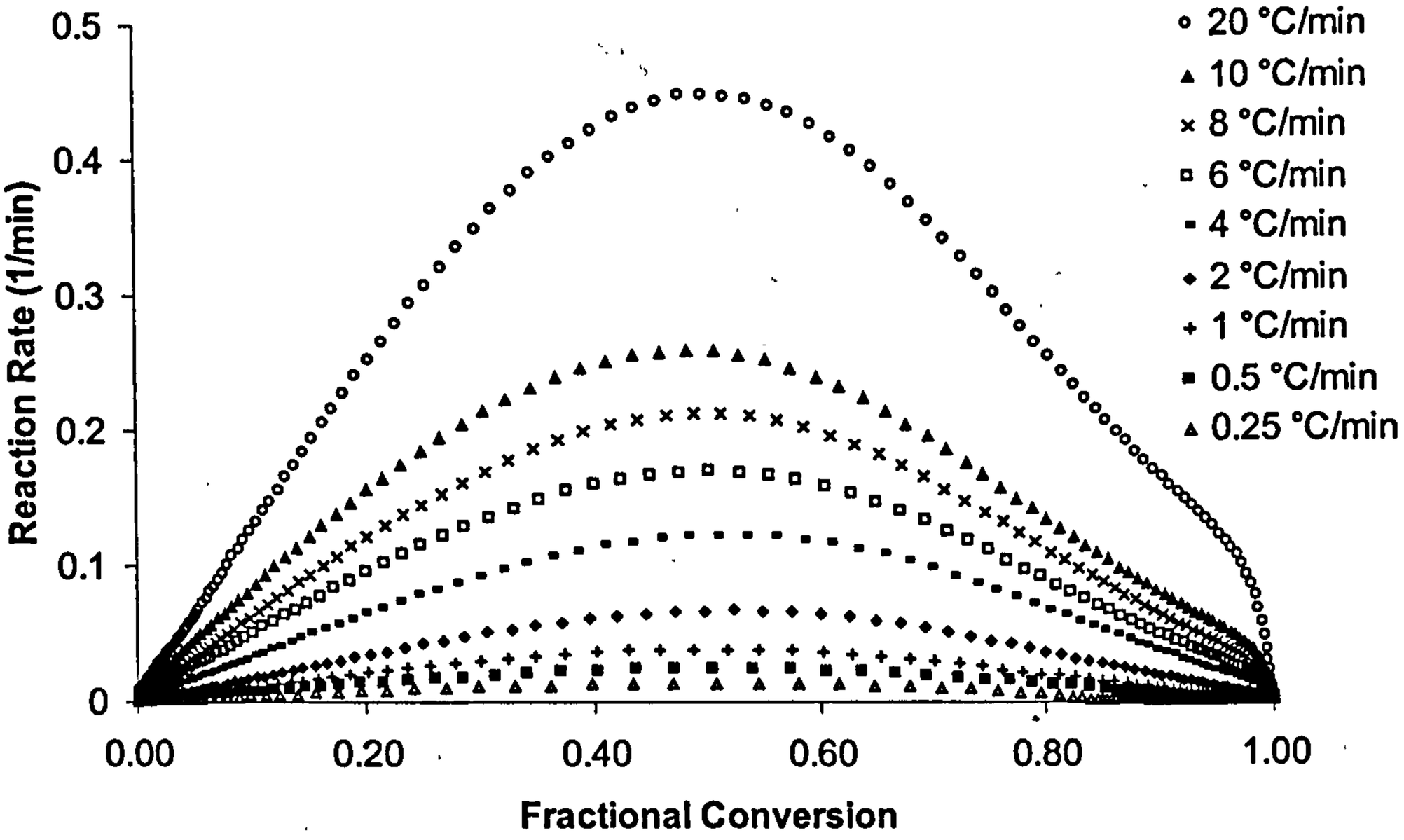

Fig.5.4 *Reaction rate versus fractional conversion in the dynamic cure of RTM6*

Rate(°C/min)	0.25	0.5	1	2	4	6	8	10	20	Average	Standard Deviation
Heat(J/g)	457	453	448	455	444	440	448	435	433	446	9

Table 5.1 *RTM6 epoxy resin heats of reaction at different heating rates*

The total heat of reaction obtained from these data is 446 ± 9 J/g (Table 5.1). It does not vary systematically as a function of the heating rate, except in the case of the two faster experiments at 10 and 20 °C/min, where the total heat of reaction appears slightly lower. This effect can be explained by the presence of some spikes in the thermogram towards the end of cure. At heating rates up to 8 °C/min the spikes occur well after the end of the reaction, whereas at higher heating rates they interfere with it, forcing the integration for the total heating rate estimation to stop slightly earlier than it should. Consequently the total heat of reaction is underestimated.

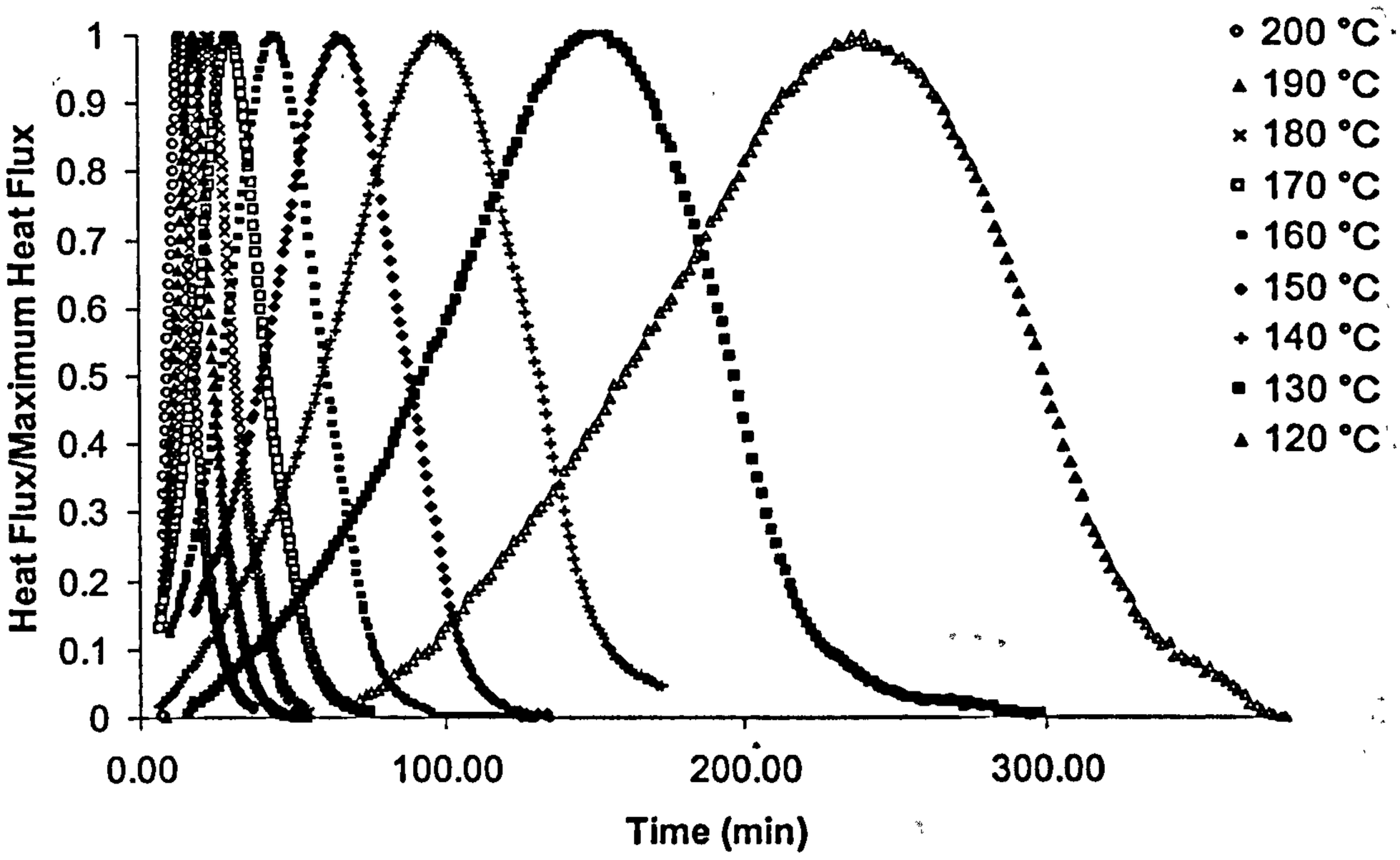

Fig.5.5 *Normalised heat flux versus time in the isothermal cure of RTM6*

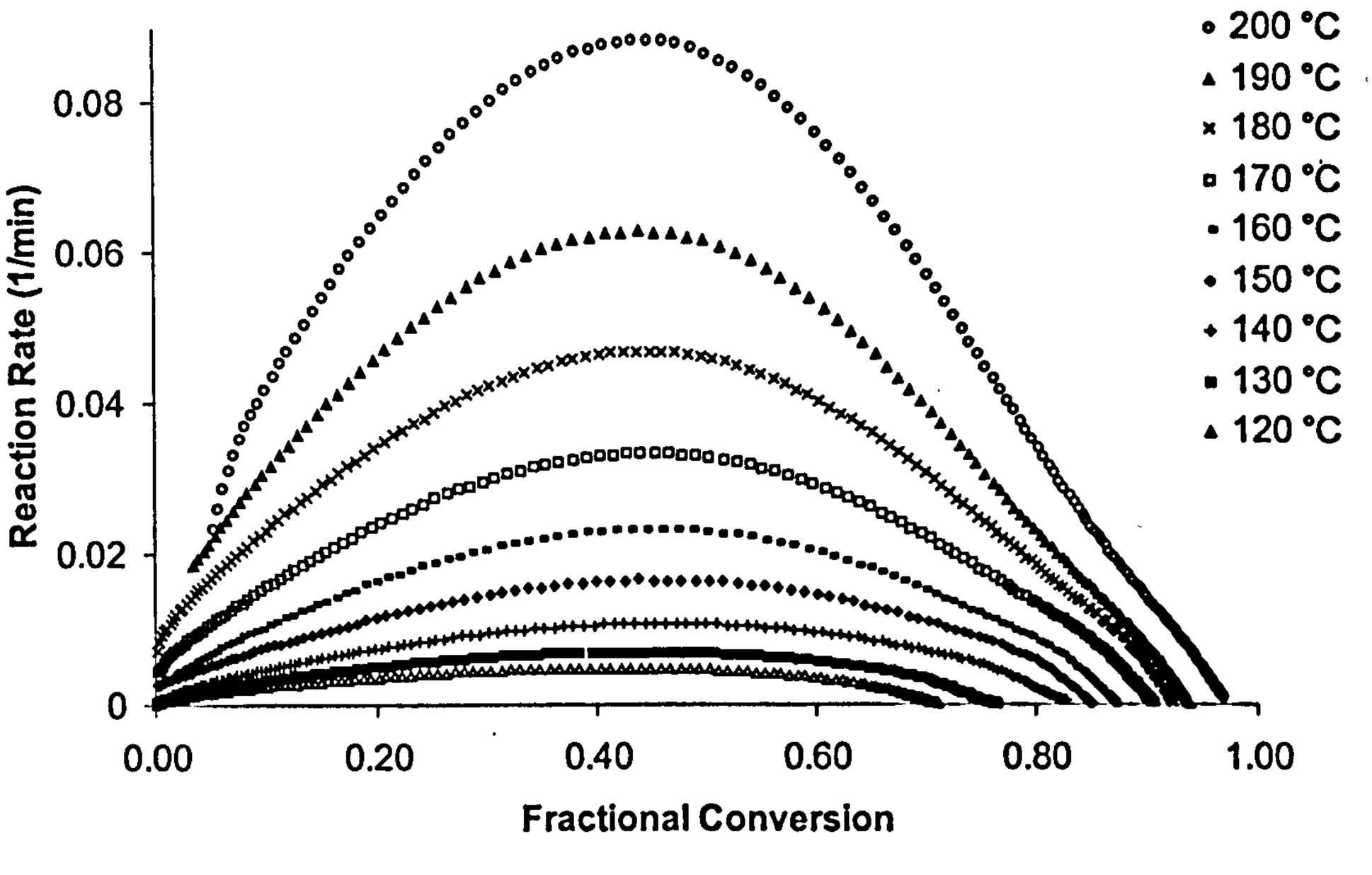

Fig.5.6 *Reaction rate versus fractional conversion in the isothermal cure of RTM6*

Results obtained under isothermal measurements conditions are illustrated in Fig.5.5 and Fig.5.6. The bell shape of the isothermal heat flow curves in Fig.5.5 is attributed to the existence of an autocatalytic mechanism in the reaction. The cure at all temperatures is completed with the vitrification of the resin after which the reaction becomes very slow. Consequently the final conversion reached is less than one and it increases as the cure temperature increases, as illustrated in Fig.5.6.

It can be observed in Fig.5.5 that the initial heat flow is non zero as a consequence of the commencement of the reaction during the heating ramp towards the isothermal temperature. This introduces an error which, as shown in Fig.5.3 (curve for 20 °C/min) is insignificant up to 180 °C. For cures at higher temperatures the effect of the heating ramp had to be incorporated in the integration for the degree of cure and reaction rate calculation, by starting the integration at a conversion which corresponds to a 20 °C/min dynamic cure up to the temperature of the experiment. Therefore the reaction versus degree of cure starts at finite conversions for cure at 190 and 200 °C (Fig.5.6).

5.5 Modelling method

The numerical procedure implemented here to model the cure kinetics is based on the essential assumption that the reaction rate at any moment during the curing is a unique function of the fractional conversion and of the temperature. As analysed in paragraphs 5.2 and 2.2 this assumption must hold in order to apply any kind of empirical or mechanistic cure kinetics model which results in an expression of the form,

$$\frac{d\alpha}{dt} = f(\alpha, T) \qquad \text{(Eq. 5.6)}$$

and in order to enable the DSC data to be used as a reaction monitoring technique.

The validity of such an assumption can be verified by analysing the effects of different thermal histories, corresponding to different fractional conversion trajectories, on the reaction rate, in cases where the conversions and temperatures are identical despite different thermal histories. This can be achieved by comparing reaction rates measured at the same points of the conversion temperature phase space, by isothermal and dynamic calorimetry. The superposition of data obtained by dynamic experiments onto the isothermal reaction rate-conversion curves is illustrated in Fig. 5.7.

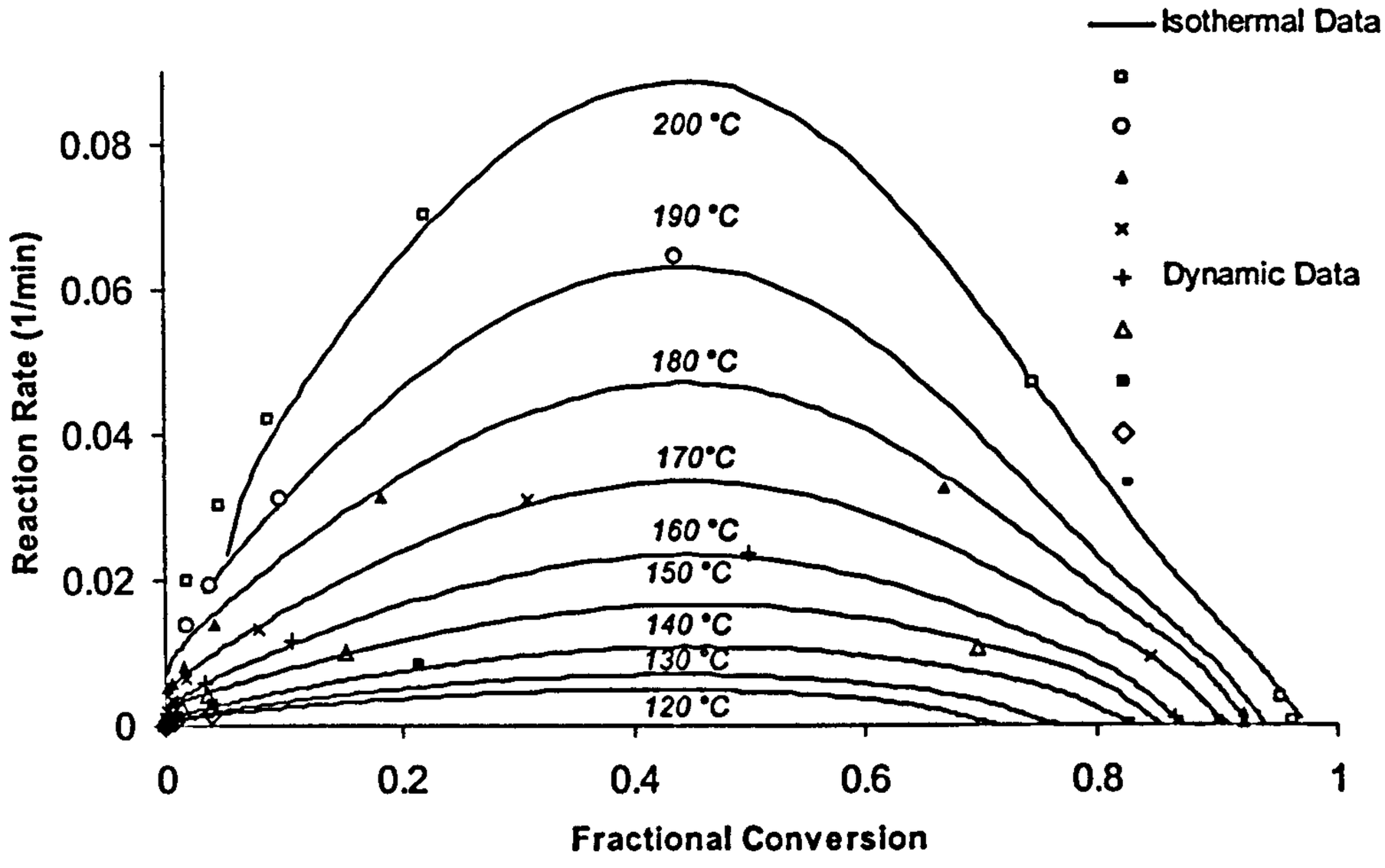

Fig.5.7 *Superposition of dynamic and isothermal DSC reaction rate-conversion data for RTM6*

It can be observed that the reaction rate values obtained dynamically are very close to the isothermal measurement curves. Regression analysis applied to the two sets of reaction rate values showed that they are related with a linear relationship, with slope of 1.02 and regression constant 0.997. Thus, thermal and reaction histories do not play a role in the cure kinetics of RTM6 epoxy resin. The basic assumption of reaction rate uniqueness within the conversion-temperature phase space is valid, and the reaction rate can be considered as a surface in the space defined by the reaction rate, the conversion and the temperature.

The method used can be described as non-parametric kinetics modelling, and constitutes direct application of interpolation on the experimental data. Before proceeding to the description of the model operation, it is useful to reconsider alternative approaches.

The applicability of empirical modelling based on an analytical expression of the type of Eq. 5.6 has been investigated by Karkanas (17). It has been found that for the RTM6 resin system the most appropriate model has the form:

$$\frac{d\alpha}{dt} = k_1(1-\alpha)^{n_1} + k_2(1-\alpha)^{n_2}\alpha^m \qquad \text{(Eq. 5.7)}$$

which is appropriate when the reaction is chemically controlled. As mentioned in paragraph 2.2, when diffusion becomes significant the rate constants should be replaced by apparent rate constants, which are a combination of the diffusion rate constant and of the above chemical reaction constants. This results in the derivation of a 7 to 11 parameter non-linear equation which has to fit the experimental data. Although the final model is well suited to the specific resin system, any alteration of the resin system will require the reiteration of the laborious model parameters estimation procedure. Therefore a non-parametric method based on direct interpolation of the experimental data, which requires only the collection of a new set of DSC curves for every new resin system, is considered as advantageous.

A non-parametric method applied to thermoanalytical kinetics has been developed by Serra et al. (199) and is based on the assumption that the kinetics are of the form:

$$\frac{d\alpha}{dt} = f(\alpha)g(T) \qquad \text{(Eq. 5.8)}$$

This has been tested as a possible modelling method for the specific resin used in this study. If such an expression is valid the following relation should hold:

$$\frac{\frac{d\alpha}{dt}(\alpha,T)}{\frac{d\alpha}{dt}(\alpha,T_o)} = \frac{g(T)}{g(T_o)} \qquad \text{(Eq. 5.9)}$$

which means that the reaction rate at a specific temperature and conversion divided by the reaction rate at a reference temperature at the same fractional conversion depends only on temperature. That implies that the curves of the ratio of reaction rate to the reaction rate at the same conversion at a reference temperature versus the temperature should coincide for any conversion. Figs. 5.8 and 5.9 show these curves using 180 °C and 140 °C as the reference temperatures.

It can be observed that the ratios do not follow a master curve. A similar deviation from a master curve is observed at other reference temperatures. Consequently, the simplification implied by Eq. 5.8 cannot be made for RTM6 and the kinetics data should be treated as a general surface spanned in the temperature-conversion phase space.

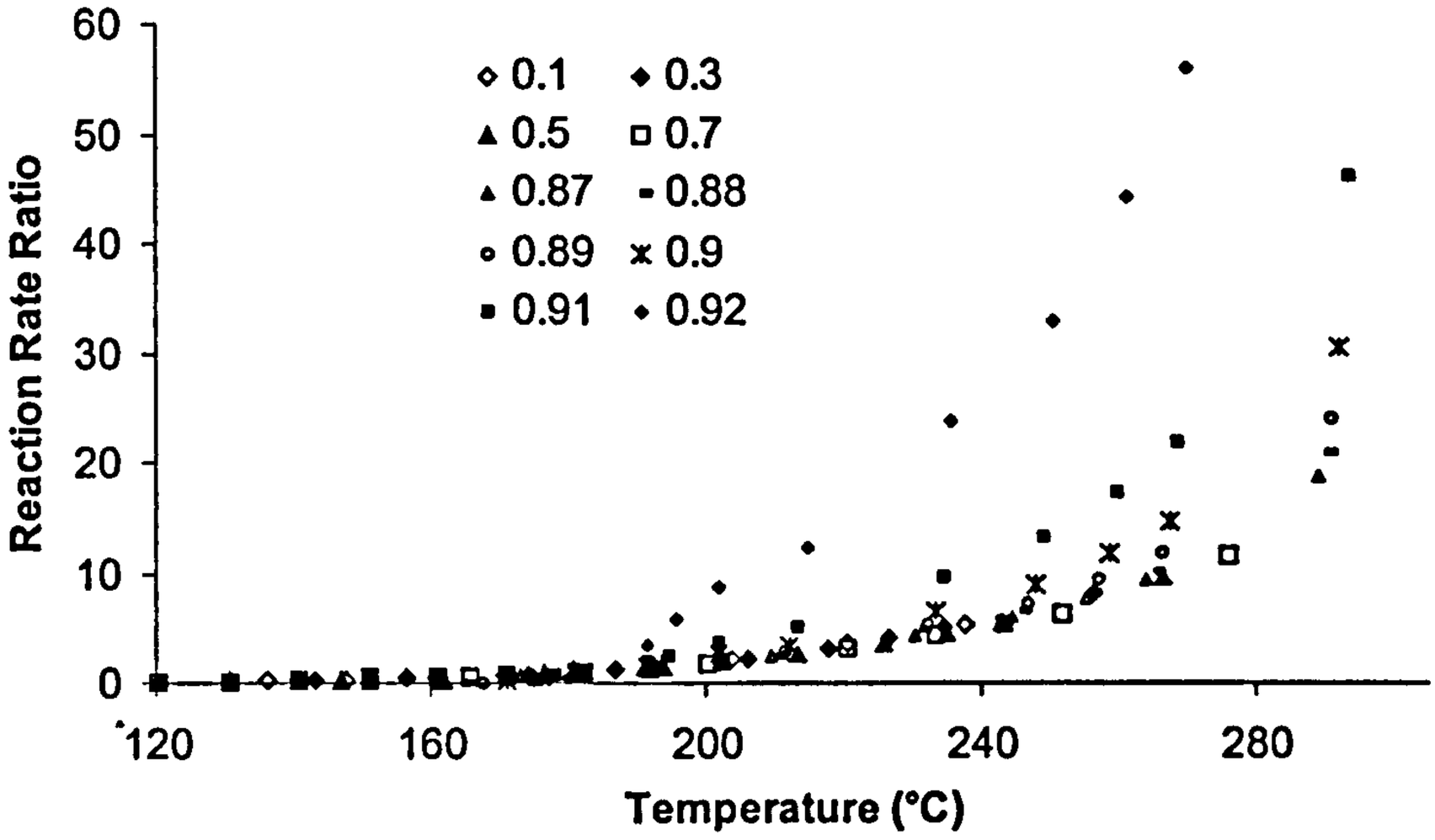

Fig.5.8 *Reaction rate ratio to reaction rate at 180 °C at different conversions for RTM6 epoxy resin*

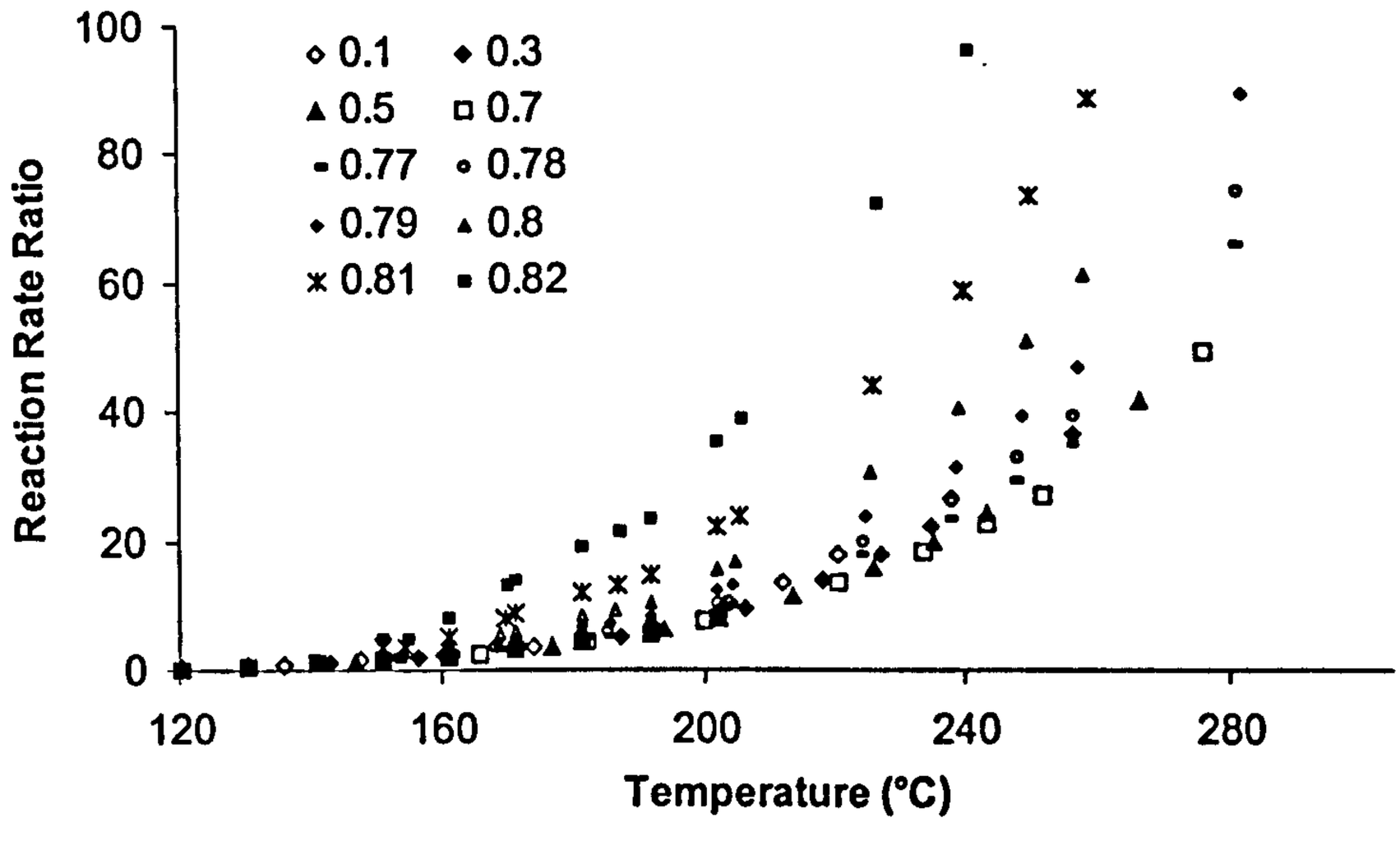

Fig.5.9 *Reaction rate ratio to reaction rate at 140 °C at different conversions for RTM6 epoxy resin*

In order to perform the two-dimensional interpolation of the experimental data a three stage algorithm was developed. Initially the experimental data curves and the point of temperature-conversion space for which the reaction rate is required are inserted. Then the reaction rate at the specific conversion for all curves is calculated using linear interpolation. Thus an 'isoconversional' curve of the reaction rate as a function of the temperature is built. The isoconversional curves of RTM6 for various fractional conversions are illustrated in Figs. 5.10 and 5.11. Finally, the isoconversional curve is interpolated, by a second degree polynomial, in the vicinity of the required output temperature and the reaction rate is calculated. A schematic representation of the algorithm developed for the above described task of modelling the cure kinetics is given in Fig. 5.12.

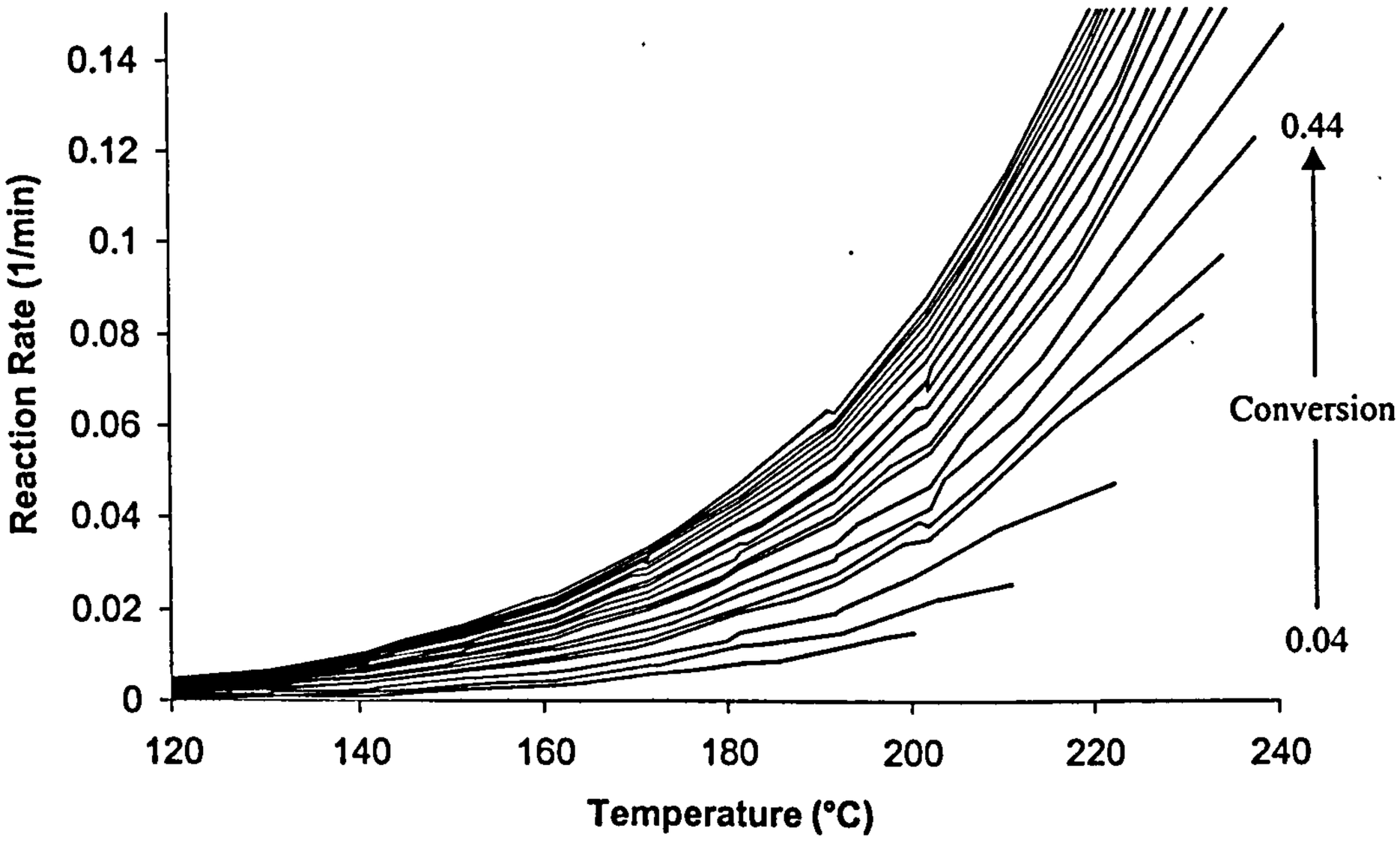

Fig.5.10 *Reaction rate versus temperature isoconversional curves of RTM6 for conversions from 0.02 to 0.44*

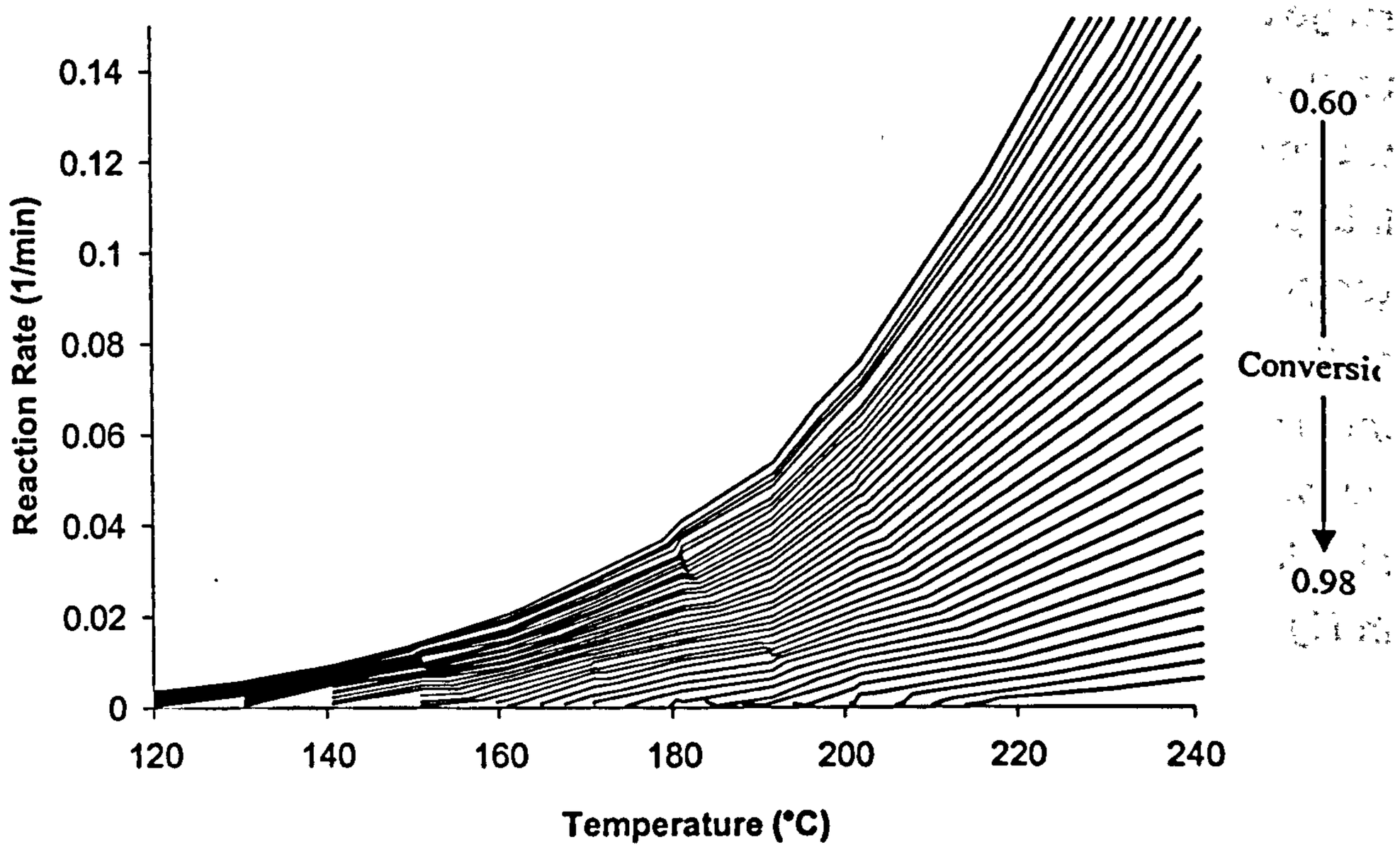

Fig.5.11 *Reaction rate versus temperature isoconversional curves of RTM6 for conversions from 0.60 to 0.98*

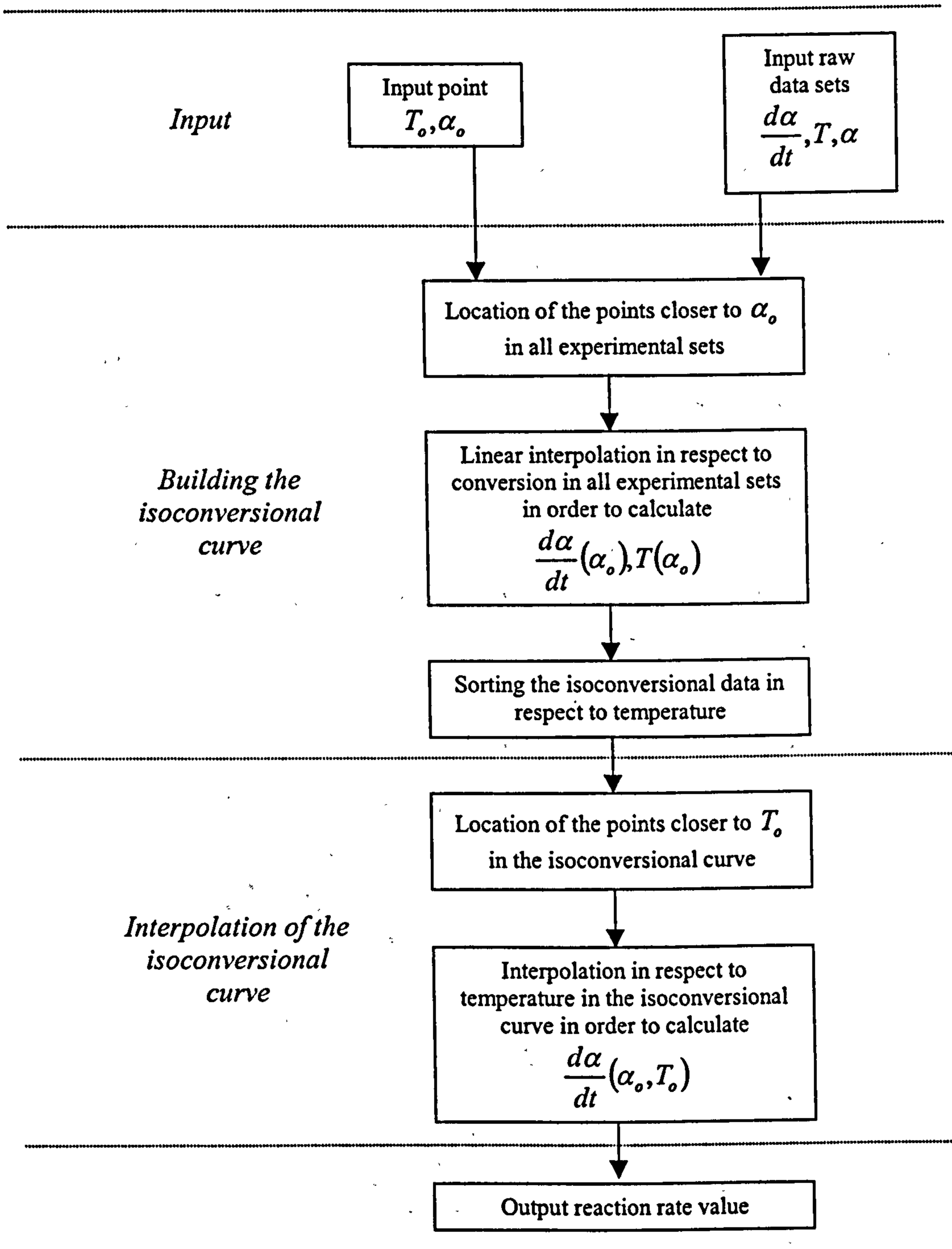

Fig.5.12 *Numerical kinetics modelling algorithm*

5.6 Model results, validation and applicability

Results of the numerical kinetics modelling algorithm are compared with experimental data obtained by isothermal and dynamic DSC measurements in Figs. 5.13 and 5.14. Prior to each test application of the model, the experimental curve corresponding to the thermal program simulated was removed from the data used in the interpolation routine. Thus the non-parametric kinetics algorithm operates in a predictive manner since no data exist for the simulated thermal program.

It can be observed that the agreement is excellent. The algorithm closely follows the chemically controlled part of the curing and successfully reproduces structural phenomena like the vitrification and devitrification (see for example the knee corresponding to the vitrification-devitrification sequence in dynamic runs at very slow heating rates and the final degree of cure under isothermal conditions). The latter is impossible to achieve in a one step process and without the incorporation of structural models with any other modelling technique.

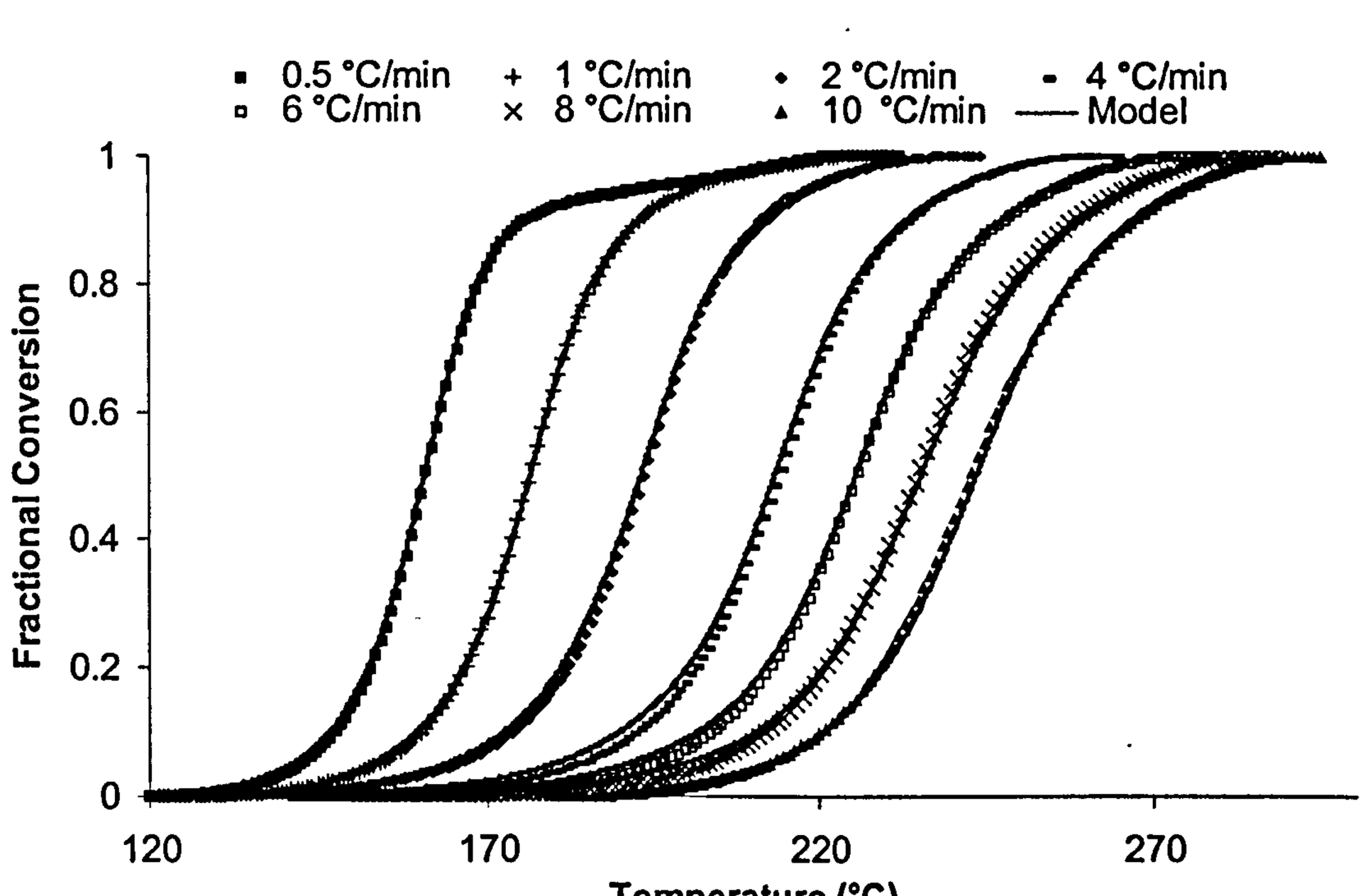

Fig.5.13 *Comparison of experiment and model dynamic degree of cure versus temperature curves*

A statistical analysis of the results has been carried out in order to quantify the fit. The temperature to reach a specific conversion in dynamic runs and the time to reach a specific conversion in isothermal runs have been determined using both experimental and simulation data. This procedure has been iterated from zero conversion up to the maximum conversion for each thermal programme, using a step of 0.01. The percentage error has been calculated as an average over the whole thermal programme in each case. The results given in tables 5.2 and 5.3 show that the error of the fit is insignificant (below 1%) in all cases.

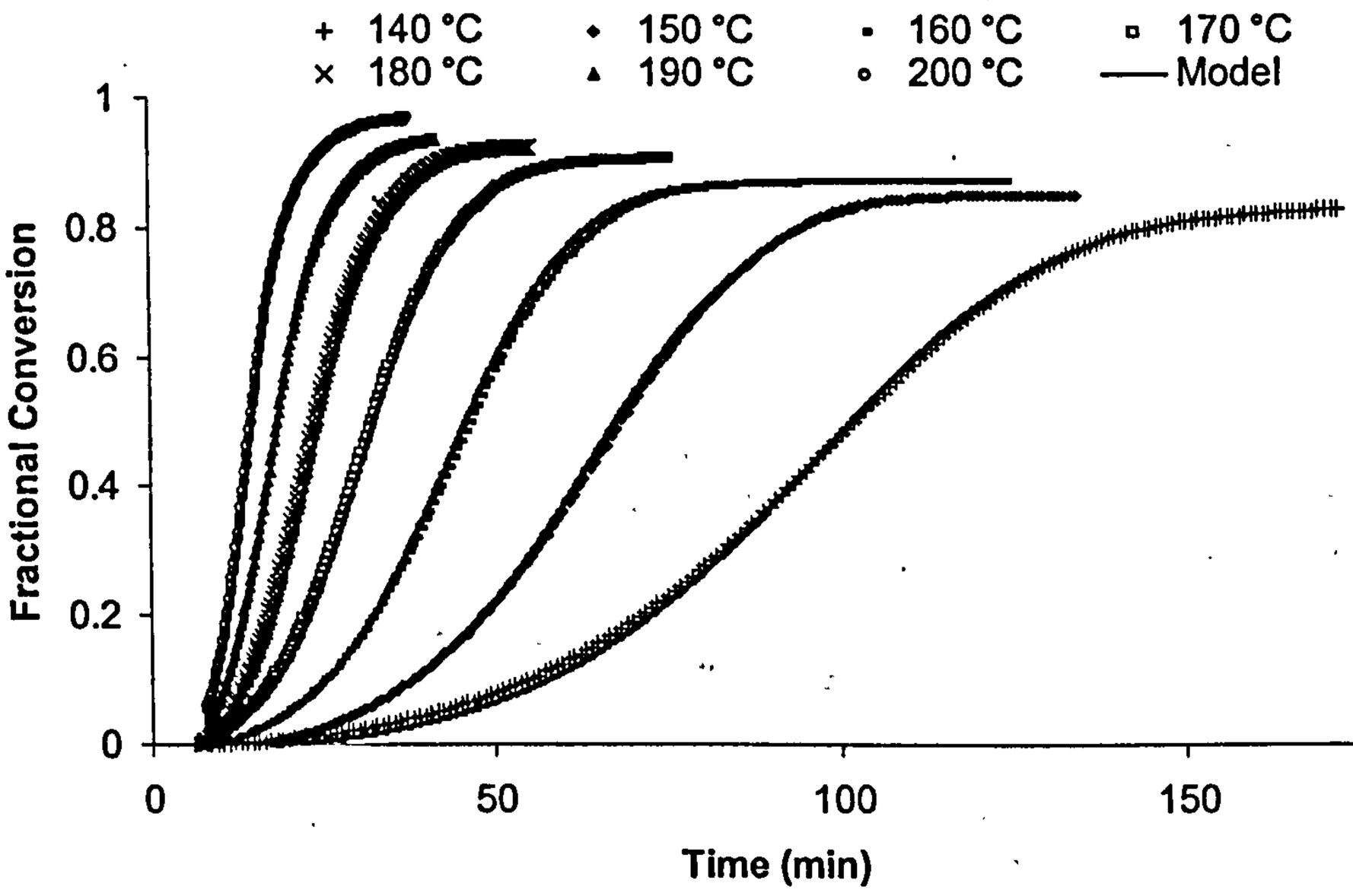

Fig.5.14 *Comparison of experiment and model isothermal degree of cure versus time curves*

Rate(°C/min)	0.5	1	2	4	6	8	10
$\sum_{1}^{n}\frac{\lvert T_{exp}-T_{sim}\rvert}{nT_{exp}}$ %	0.09	0.06	0.14	0.07	0.09	0.06	0.04

Table 5.2 *Percentage error in modelling dynamic cures*

Temperature(°C)	130	140	150	160	170	180	190	200
$\sum_{1}^{n}\frac{\lvert t_{exp}-t_{sim}\rvert}{nt_{exp}}$ %	0.77	0.70	0.32	0.32	0.69	0.74	0.37	0.23

Table 5.3 *Percentage error in modelling isothermal cures*

Since the model is based on direct interpolation of the experimental data the quality of the simulation depends on the density of experimental data available. Thus, an investigation of the influence of the number of experimental points on the quality of the model results has been carried out. A characteristic thermal programme, illustrated in Fig. 5.15, corresponding to a cure and postcure cycle has been used in order to compare the conversion-time curves obtained by using different number of experimental DSC sets.

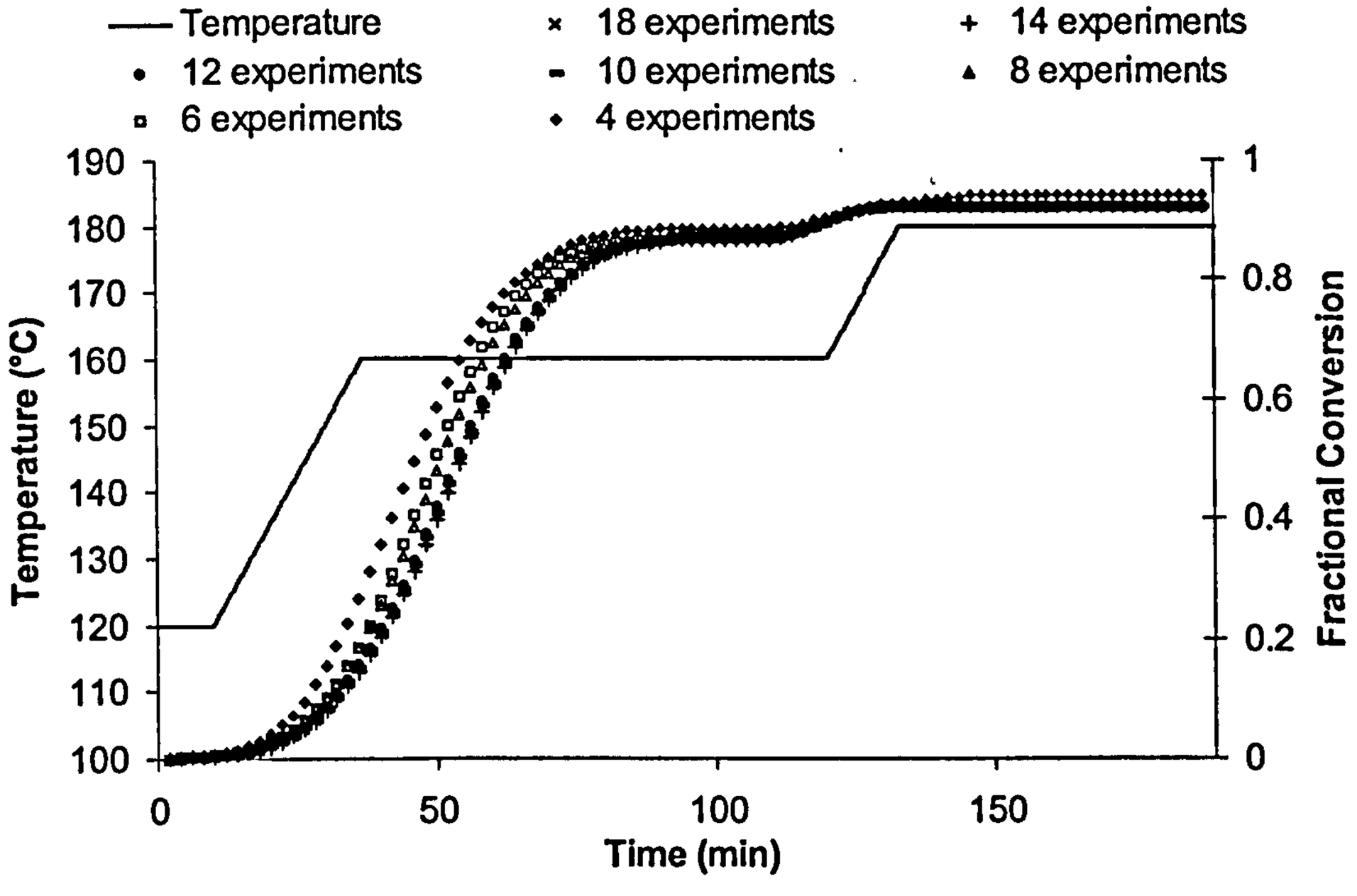

Fig.5.15 *Cure kinetics modelling variation as a function of the number of DSC experiments used. Conversion versus time curves for a cure-postcure thermal cycle applied to RTM6 resin.*

The experimental curves used in each of the cases illustrated in Fig. 5.15 are given in table 5.4.

	18	14	12	10	8	6	4
0.25 °C/min	✓	✓	✓	✓	✓	✓	
0.5 °C/min	✓	✓	✓				✓
1 °C/min	✓	✓		✓			
2 °C/min	✓		✓		✓	✓	
4 °C/min	✓	✓	✓	✓			
6 °C/min	✓	✓			✓		
8 °C/min	✓	✓	✓	✓		✓	
10 °C/min	✓		✓		✓		✓
20 °C/min	✓	✓		✓			
120 °C	✓	✓	✓	✓	✓	✓	
130 °C	✓	✓	✓				✓
140 °C	✓	✓		✓			
150 °C	✓		✓		✓	✓	
160 °C	✓	✓	✓	✓			
170 °C	✓	✓			✓		
180 °C	✓	✓	✓	✓		✓	
190 °C	✓		✓		✓		✓
200 °C	✓	✓		✓			

Table 5.4 *Experiments used in the different runs of the kinetics model in order to establish the dependence of results on the number of input data sets*

The curve based on data from 18 experiments is considered as the correct result since the modelling procedure applied to the same density of data resulted in insignificant errors. The curves based on 14, 12 and 10 DSC runs are very close to the actual conversion history. In the case of 8 experimental data sets the conversion curve start to deviate, especially in the steep part of the degree of cure curve, while modelling based on 6 and 4 DSC measurements sets also deviates in the plateau regions.

Average errors calculated as the average percentage deviation of conversion from the 18 experiment based case are given in Fig. 5.16.

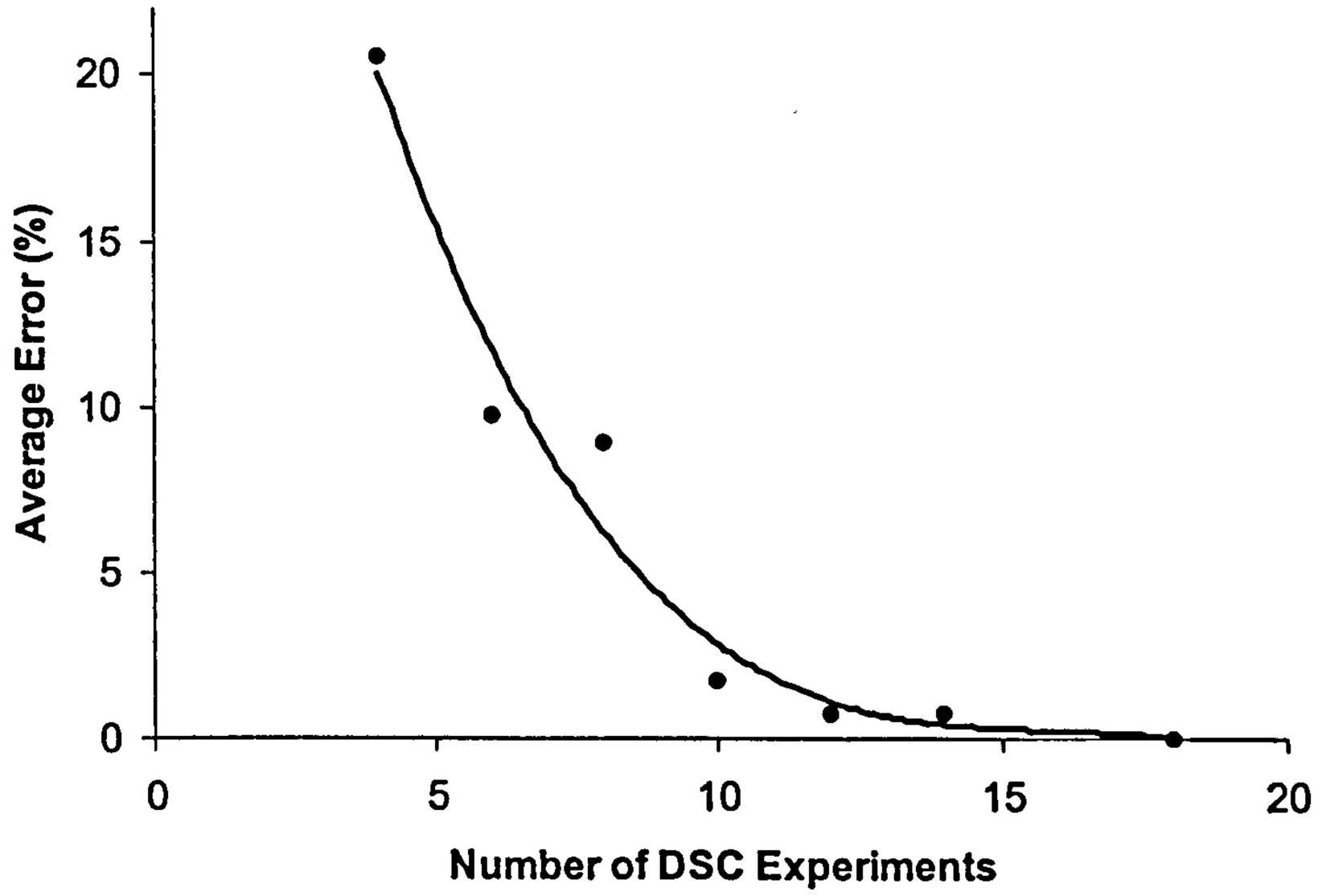

Fig.5.16 *Kinetics modelling error versus number of input DSC runs*

The error exhibits a high sensitivity to the number of experiments used, up to a point (12 experiments in this case). Any further increase in the number of experiments offers insignificant additional accuracy. Thus, when such a cure modelling approach is utilised the number of experiments should be in the plateau area of the sensitivity curve in order to ensure optimum accuracy.

Whenever the model has been used in this study, it was based on the maximum number (18) of experimental data sets, which is well in its converged regime.

5.7 Investigation of the effect of reinforcements

In order to ensure that the cure kinetics model described previously is appropriate for the simulation of kinetics in composites curing, the effect of the presence of the reinforcement had to be investigated. Thus, dynamic DSC experiments were performed in order to study the curing of RTM6 when reinforcements are present.

These experiments were carried out at an intermediate heating rate (4 °C/min). Glass and carbon fibres, taken from the reinforcements used in this study (E-glass and T300

carbon), were enclosed in the DSC pan with the resin (50-70 %wt). The conversion versus temperature curves obtained are given in Fig. 5.17.

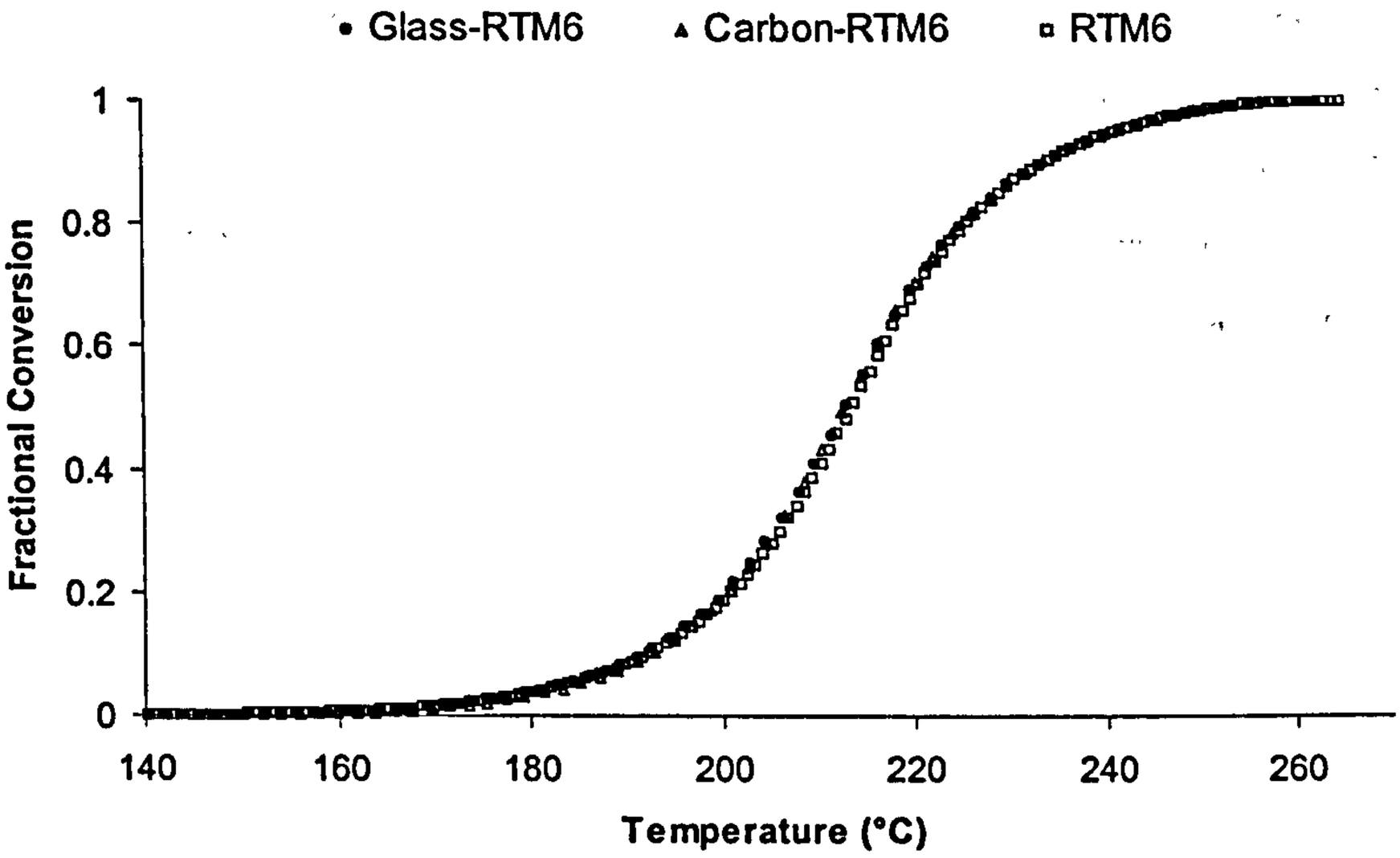

Fig.5.17 *Effect of reinforcements on the kinetics of RTM6: Conversion versus temperature curves for dynamic cure at 4°C/min*

The average percentage difference between the curves, calculated as described for the data in 5.2 and 5.3 is 0.054 % for the carbon reinforcement and 0.066 % for the glass reinforcement, which is considered negligible. Consequently the kinetics model developed for the unreinforced resin is valid when these two specific reinforcements are present in the composite.

5.8 Overview

DSC experiments were used for the development of a numerical procedure that simulates RTM6 cure kinetics by direct interpolation of the experimental data. It has been established that the cure kinetics of the specific resin system used do not depend on the temperature history. Thus exothermic heat flux measured by DSC corresponds to chemical conversion and reaction rate is a unique function of conversion and of temperature.

The application of the numerical model demonstrated an excellent agreement between experimental data and simulation results. The algorithm closely follows chemical and structural phenomena. The modelling error presents a dependence on the number of experiments the interpolation is applied to. There is a critical number of experiments above which numerical modelling converges to the correct output.

The effect of reinforcement on the cure kinetics has been investigated. DSC experiments proved that the specific reinforcements do not influence the cure kinetics.

Chapter Six

6 Thermal properties submodels

6.1 Introduction

This chapter presents the submodels which perform the incorporation of thermal properties in the heat transfer model described in chapter 4. Three submodels, which express the changes in density, heat capacity and thermal conductivity during the cure of the composite, have been developed. The experimental and theoretical bases of these submodels are given and their implementation in the form of subroutines is outlined.

6.2 Density submodel

The volumetric behaviour of thermosetting systems (fibre reinforced or unreinforced) is governed by two phenomena: -(i) thermal expansion or contraction and (ii) chemical shrinkage. The former is a result of temperature variations during the cure and is a reversible phenomenon, while the latter has irreversible character and is a consequence of the network formation during crosslinking. In epoxy cure, the resin expands during heating up, then shrinks as the reaction starts and eventually contracts during cooling down (200). The total volume change during cure is a result of the combination of the chemical shrinkage and of the volume change due to the accompanying difference in the thermal expansion coefficient of the uncured and of the fully cured material.

Taking into account the definitions of volumetric thermal expansion α_v as the fractional rate of volume change as a function of temperature, and of shrinkage γ as the fractional rate of volume change as a function of degree of cure, the instantaneous volume change can be expressed as follows:

$$\frac{dV}{dt} = V\alpha_v \frac{dT}{dt} - V\gamma \frac{d\alpha}{dt} \qquad \text{(Eq. 6.1)}$$

The density change as a function of time is:

$$\frac{d\rho}{dt} = -\frac{\rho}{V}\frac{dV}{dt} \qquad \text{(Eq. 6.2)}$$

Substitution of Eq. 6.1 in Eq. 6.2 yields:

$$\frac{d\rho_r}{dt} = -\rho_r\left(\alpha_{vr}\frac{dT}{dt} - \gamma\frac{d\alpha}{dt}\right) \qquad \text{(Eq. 6.3)}$$

where α_{vr} denotes the coefficient of thermal expansion of the resin.

In the case of a reinforcing fibre, chemical phenomena do not take place and Eq. 6.3 becomes:

$$\frac{d\rho_f}{dt} = -\rho_f\alpha_{vf}\frac{dT}{dt} \qquad \text{(Eq. 6.4)}$$

where α_{vf} denotes the coefficient of thermal expansion of the fibre.

Eqs. 6.3 and 6.4 can be integrated approximately in a stepwise fashion for each element of the heat transfer model. Their incremental forms are:

$$\rho_{ri} = \frac{\rho_{ri-1}}{1+\alpha_{vr}\Delta T - \gamma\Delta\alpha} \qquad \text{(Eq. 6.5)}$$

$$\rho_{fi} = \frac{\rho_{fi-1}}{1+\alpha_{vf}\Delta T} \qquad \text{(Eq. 6.6)}$$

Here, ρ_i is the density at the end of the ith time step, ρ_{i-1} the density at the end of the ith-1 time step, ΔT the temperature change during the time step and $\Delta\alpha$ the fractional conversion change during the time step.

In order to calculate the density of a composite, the rule of mixtures has to be considered. The form which uses the fibre weight fraction is preferred (Eq. 2.24), since in contrast to the fibre volume fraction, the weight fraction does not change during the cure. Thus

$$\rho_i = \frac{\rho_{ri}\rho_{fi}}{w_f\rho_{ri} + (1-w_f)\rho_{fi}} \qquad \text{(Eq. 6.7)}$$

The volumetric behaviour of RTM6 epoxy resin has been studied extensively by Holmberg (189). According to his study the coefficient of thermal expansion of RTM6 epoxy resin is:

$$\alpha_{vr} = \begin{cases} 4.08\,10^{-4}\ {}^{o}C^{-1} & ,T \geq T_g \\ 1.62\,10^{-4} + 0.4810^{-6}T\ {}^{o}C^{-1} & ,T < T_g \end{cases} \qquad \text{(Eq. 6.8)}$$

The density of uncured resin at ambient temperature is 1.117 g/cm^3 and the total chemical shrinkage 4.9 %. The glass transition temperature required in Eq. 6.8 can be calculated using Eq. 4.13. These values, together with Eq. 6.4, can be used for the calculation of the matrix density in each time step, starting from the density of the unreacted material.

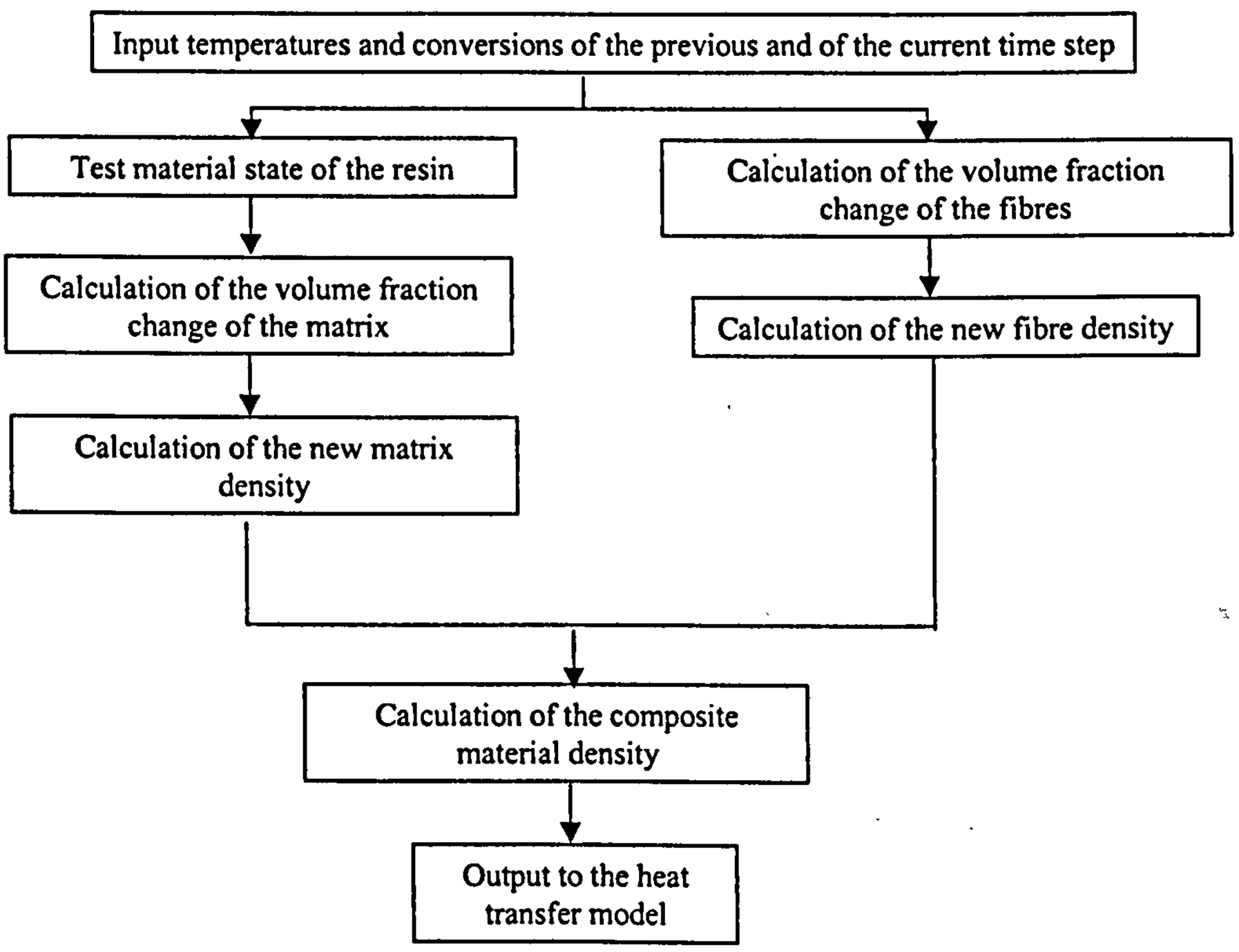

Fig.6.1 *Schematic representation of the density submodel algorithm*

The calculation of the fibre density can be performed in a similar manner. The density of E-glass fibre is 2.54 g/cm^3 and of carbon fibre (T300 type) 1.8 g/cm^3, at ambient temperature. The corresponding coefficients of volumetric thermal expansion are 15.1 × 10^{-6} °C^{-1} and 5.0 × 10^{-6} °C^{-1} (201, 202). After calculation of the density of the constituents, Eq. 6.7 can be used for the estimation of the composite density.

The density calculation procedure, as described previously, has been implemented in a computer subroutine. The algorithmic structure of this subroutine is illustrated in Fig. 6.1 and the results obtained for 50 % weight fraction glass and carbon composites are shown in Fig. 6.2.

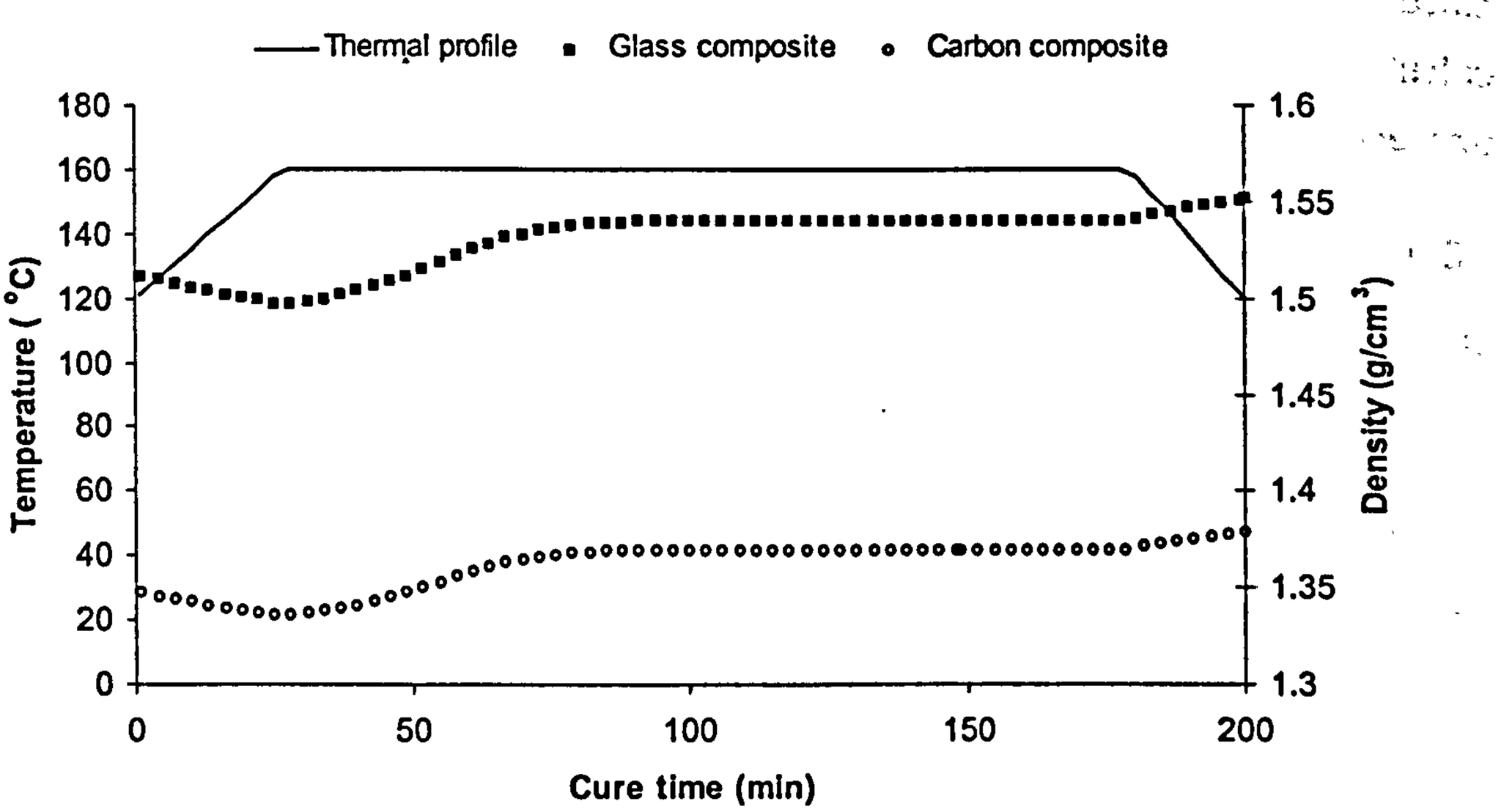

Fig.6.2 *Results of the density submodel for 50 wt% carbon fibre/RTM6 and glass fibre/RTM6 composites*

6.3 Heat capacity submodel

The submodel used for the incorporation of the specific heat capacity in the heat transfer operates similarly to the cure kinetics submodel presented in chapter 5. The technique employed is a direct interpolation on experimental data, which cover a region of the degree of cure and temperature phase space enclosing the processing window.

Modulated differential scanning calorimetry (MDSC) has been used to measure the heat capacity of RTM6 epoxy resin during the cure and that of the reinforcements used in this study. An algorithm has been developed and implemented.

6.3.1 Experimental method and results

MDSC is a recent variation of the differential scanning calorimetry technique (203, 204), which, by using complex thermal profiles, enables the separation of some of the phenomena taking place simultaneously during a calorimetric experiment to be made. The novelty of the technique is the superposition of a sinusoidal perturbation on the linear thermal programme used in standard DSC measurements. The resulting DSC signal can then be analysed using a combination of an averaging and a Fourier transform in order to deconvolute the response of the sample to the underlying linear segment from its response to the modulation. This way, phenomena which follow the time scale of the modulation (reversing phenomena) can be separated from phenomena which do not follow it (non-reversing phenomena).

The thermal programme imposed on the sample has the general form:

$$T_s = T_o + bt + A_T \sin(\omega t) \qquad \text{(Eq. 6.9)}$$

Here T_o and b are the intercept and slope of the underlying linear segment and A_T and ω the amplitude and the frequency of the modulation respectively.

The response of a differential heat flux calorimeter can be expressed as (205):

$$C_r \frac{d\Delta T}{dt} + K\Delta T = (C_s - C_r)\frac{dT_s}{dt} - f \qquad \text{(Eq. 6.10)}$$

where ΔT denotes the measured temperature difference of the reference side form the sample side, C_s the heat capacity of the sample, C_r the heat capacity of the reference, f the heat flux arising from any events like reaction or transition and K the proportionality coefficient connecting temperature difference and the heat flux.

In the case of an inert sample Eqs. 6.9 and 6.10 have the solution (205):

$$\Delta T = \frac{(C_s - C_r)b}{K} + (C_s - C_r)\frac{C_s A_T \omega}{K^2 + \omega^2 C_R^2}(K\cos\omega t + \omega C_r \sin\omega t) \qquad \text{(Eq. 6.11)}$$

or

$$\Delta T = \frac{(C_s - C_r)b}{K} + \frac{(C_s - C_r)A_T\omega}{\sqrt{K^2 + \omega^2 C_R^2}} cos(\omega t - \phi) \qquad \text{(Eq. 6.12)}$$

where

$$tan\phi = \frac{\omega C_r}{K} \qquad \text{(Eq. 6.13)}$$

In the case of an empty pan with heat capacity C on the reference position and an identical pan and the sample material with specific heat capacity c_p on the sample side Eq. 6.11 yields (206):

$$c_p = \frac{A_{\Delta T}}{mA_T}\sqrt{\left(\frac{K}{\omega}\right)^2 + C^2} \qquad \text{(Eq. 6.14)}$$

where m is the mass of the sample.

In an ideal calorimeter $C\omega << K$ (205) and

$$c_p = \frac{KA_{\Delta T}}{m\omega A_T} \qquad \text{(Eq. 6.15)}$$

Eq. 6.15 is the basis of the calculation of specific heat capacity using MDSC (207, 208).

The phase difference ϕ provides a criterion for the calorimeter performance. If the phase difference is very small the temperature difference and the measured heat flux are in phase with the time derivative of the sample temperature and Eq. 6.15 for the calculation of the specific heat capacity holds.

In the case of a material undergoing a reaction or a transition, the previous analysis cannot be applied without ensuring that the contribution of f in Eq. 6.10 is negligible.

For the heat capacity measurements performed in this study a different approach has been adopted using the fact that a validated cure kinetics model is already available. Assuming that the first term on the left side of Eq. 6.10 is negligible, i.e. the calorimeter behaves in an ideal way, the following relation can be derived:

$$f + K\Delta T = (C_s - C_r)\frac{dT_s}{dt} \qquad \text{(Eq. 6.16)}$$

The term $K\Delta T$ corresponds to the endothermic heat flux measured by the DSC. Consequently

$$f - \frac{dQ}{dt} = (C_s - C_r)\frac{dT_s}{dt} \qquad \text{(Eq. 6.17)}$$

Accordingly, the two sides of Eq. 6.17 are in phase and the sample heat capacity is:

$$c_p = \frac{A_M}{m\omega A_T} \qquad \text{(Eq. 6.18)}$$

where A_M is the amplitude of the calculated quantity $f - \frac{dQ}{dt}$.

This procedure for the calculation of the heat capacity, which is illustrated in Fig. 6.3 for the isothermal cure of RTM6 resin at 180 °C, has been applied to MDSC results obtained under isothermal conditions at 130, 140, 150, 160, 170, 180, 190 and 200 °C, using a TA Instruments 1920 MDSC. Two experiments were performed in each case. The temperature of the isothermal experiment has been reached by heating the sample at a rate of 20 °C/min. The period and the amplitude of modulation were 60 sec and 1 °C respectively. The cure kinetics model described in chapter 5 has been used for the calculation of the term f in Eq. 6.18.

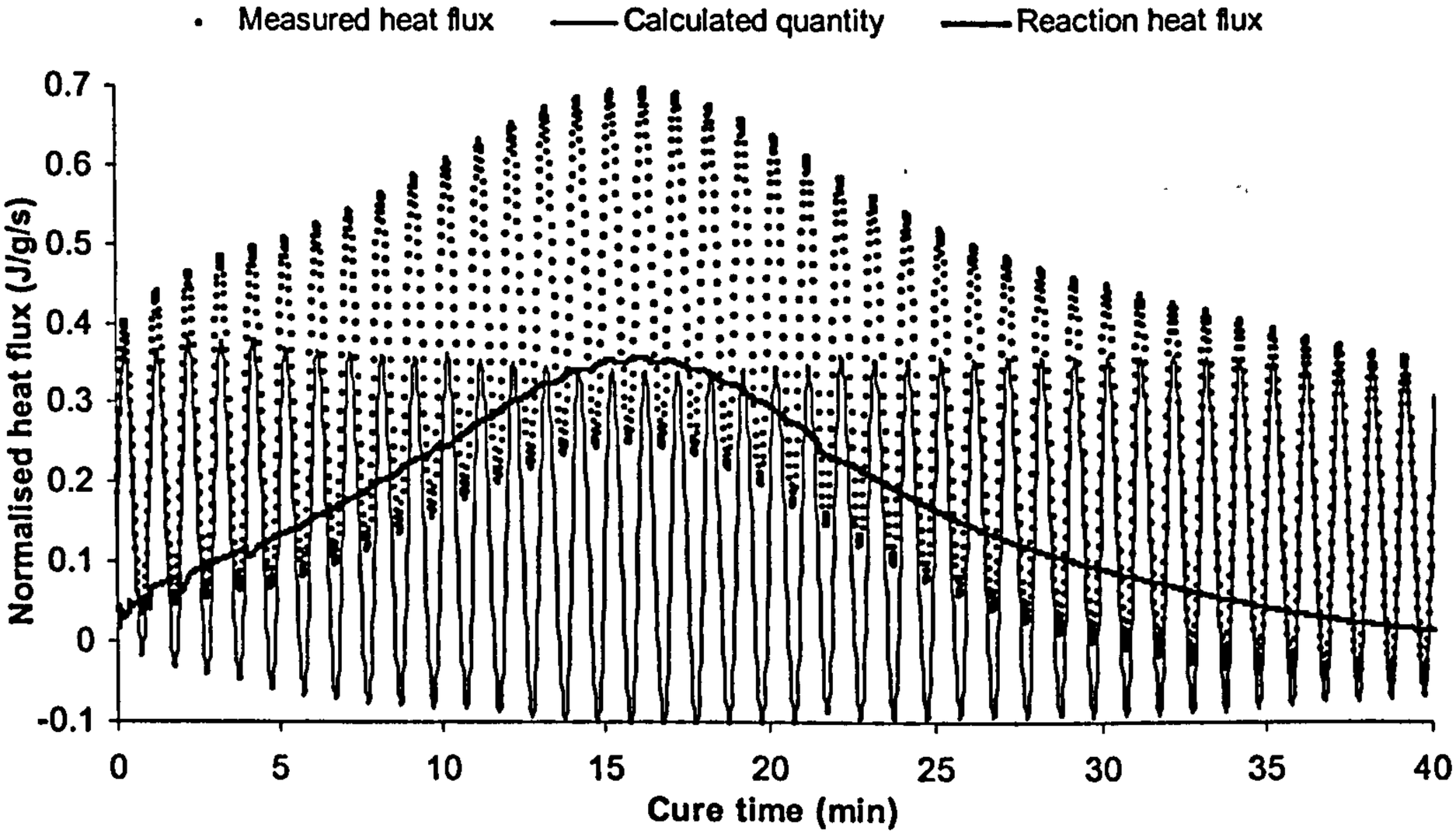

Fig.6.3 *Raw, kinetic and reversing heat flows as calculated using Eq. 6.18*

The specific heat capacity versus time curves resulting from these experiments and the from calculation procedure described previously, are illustrated in Fig. 6.4. It can be observed that the heat capacity undergoes a step transition during isothermal cure. This step corresponds to vitrification.

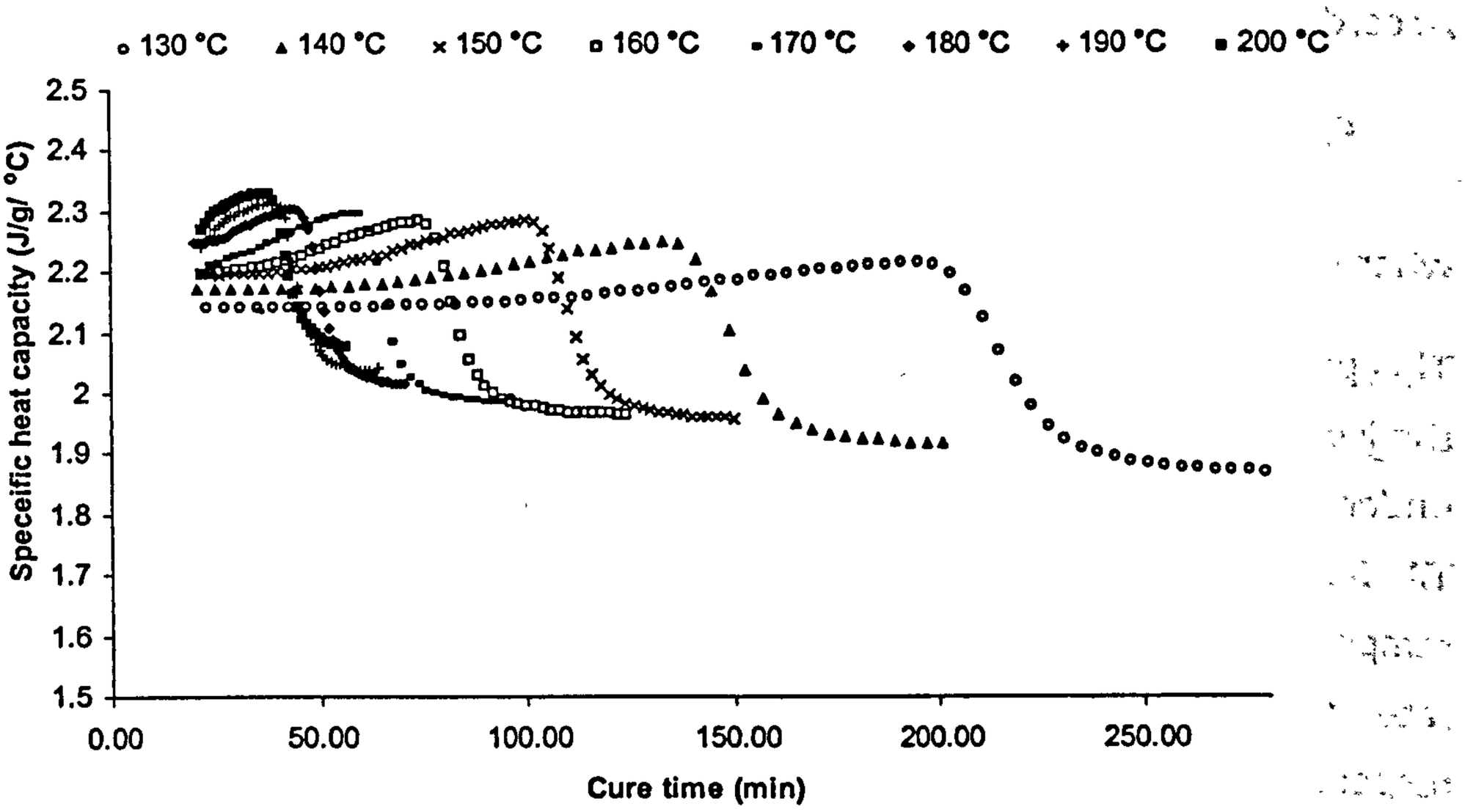

Fig.6.4 *Specific heat capacity versus cure time during isothermal cures of RTM6*

The specific heat capacity of the reinforcements used in this study (E-glass and T300 carbon) has been measured using MDSC. Two dynamic cure experiments were performed at 2 °C/min for each reinforcement. The period and amplitude of modulation were the same as in the case of isothermal resin cure experiments. The heat capacity versus temperature curves, as calculated from the results of these experiments using Eq. 6.15, are given in Fig. 6.5.

The dependence of the heat capacity on temperature can be expressed for modelling implementation purposes as a linear function. Linear regression applied to the data of Fig. 6.5 results in the following expressions for the specific heat capacity of E-glass fibre:

$$c_{pG} = 0.0014T + 0.841 \qquad \text{(Eq. 6.19)}$$

and

$$c_{pC} = 0.0023T + 0.765 \qquad \text{(Eq. 6.20)}$$

for the case of T300 carbon fibre. In both cases the regression constant was very high (0.996 and 0.997 respectively).

In Eqs. 6.19 and 6.20 temperature is expressed in °C and the specific heat capacity in J/g/ °C. These relations can be used for the incorporation of the heat capacity of the reinforcements and its dependence on temperature into the models.

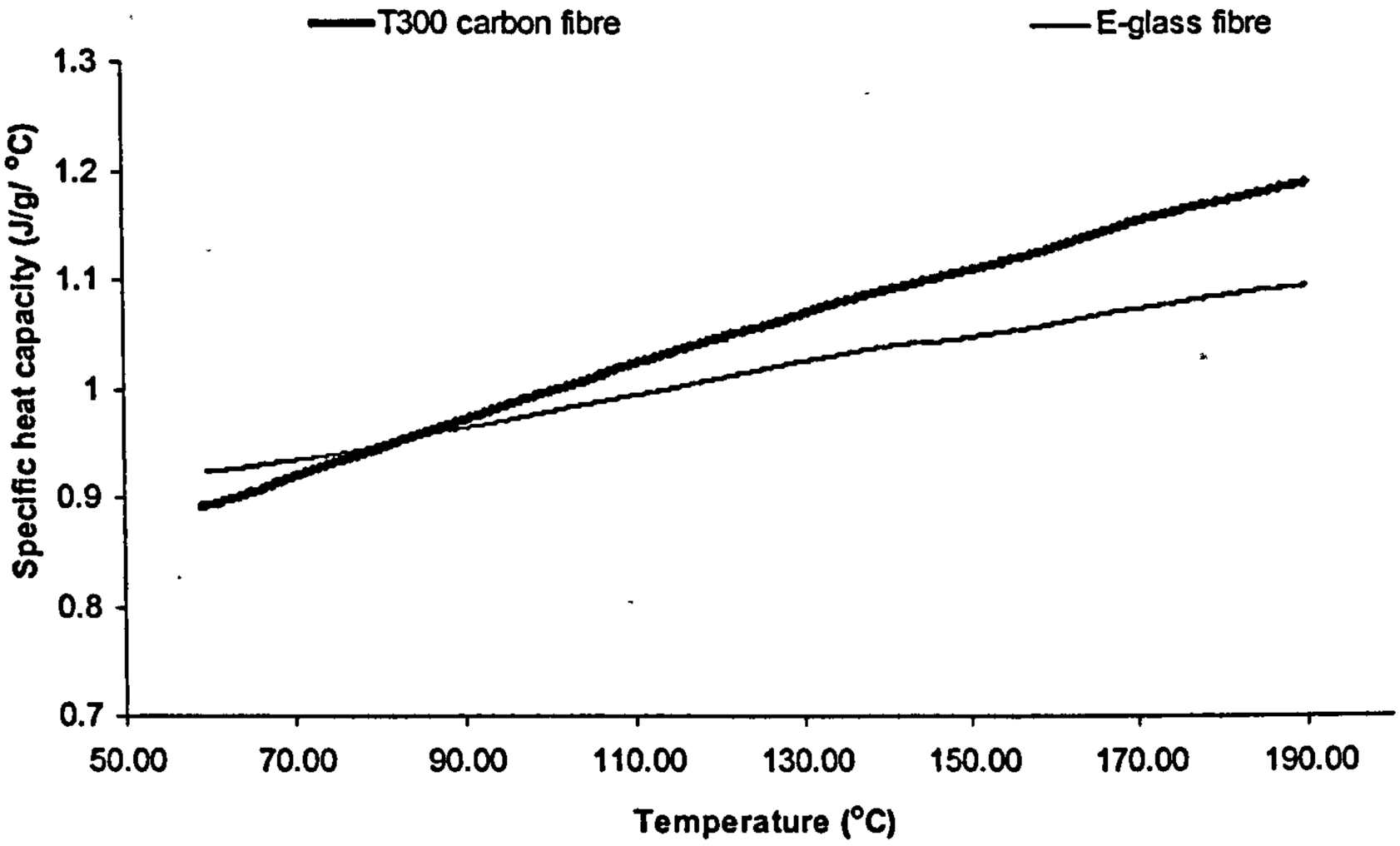

Fig.6.5 *Specific heat capacity versus temperature for E-glass fibre and T300 fibre*

6.3.2 Submodel algorithm

The heat capacity of the composite can be found using the specific heat capacity of the constituents and an appropriate form of the rule of mixtures (Eq. 2.25). The heat capacity of the reinforcement is incorporated by using Eq. 6.19 or Eq. 6.20, according to its type. In order to calculate the specific heat capacity of the matrix, a model similar to the cure kinetics model presented in chapter 5 is employed. The heat capacity of the resin is considered as a unique function of the degree of cure and the temperature, i.e. a surface in the heat capacity, temperature and degree of cure phase space. Two-dimensional interpolation is applied directly to the experimental data in order to obtain a heat capacity value at specific temperature and conversion.

An algorithm, which operates in three stages, has been developed and implemented in order to perform this task. Initially the experimental data curves of Fig.6.4 and the point of temperature-conversion space for which the specific heat capacity is required are inserted. Then the heat capacity at the specific conversion for all curves is calculated using linear interpolation and an isoconversional curve of the capacity as a function of the temperature is built. The isoconversional curves of RTM6 for various fractional conversions are illustrated in Fig. 6.6. Finally, the isoconversional curve is interpolated,

by a second degree polynomial, in the vicinity of the required output temperature and the specific heat capacity is calculated. Subsequently, the appropriate model for the heat capacity of the reinforcement is used to calculate the fibre heat capacity and the rule of mixtures is employed to obtain the value corresponding to the composite.

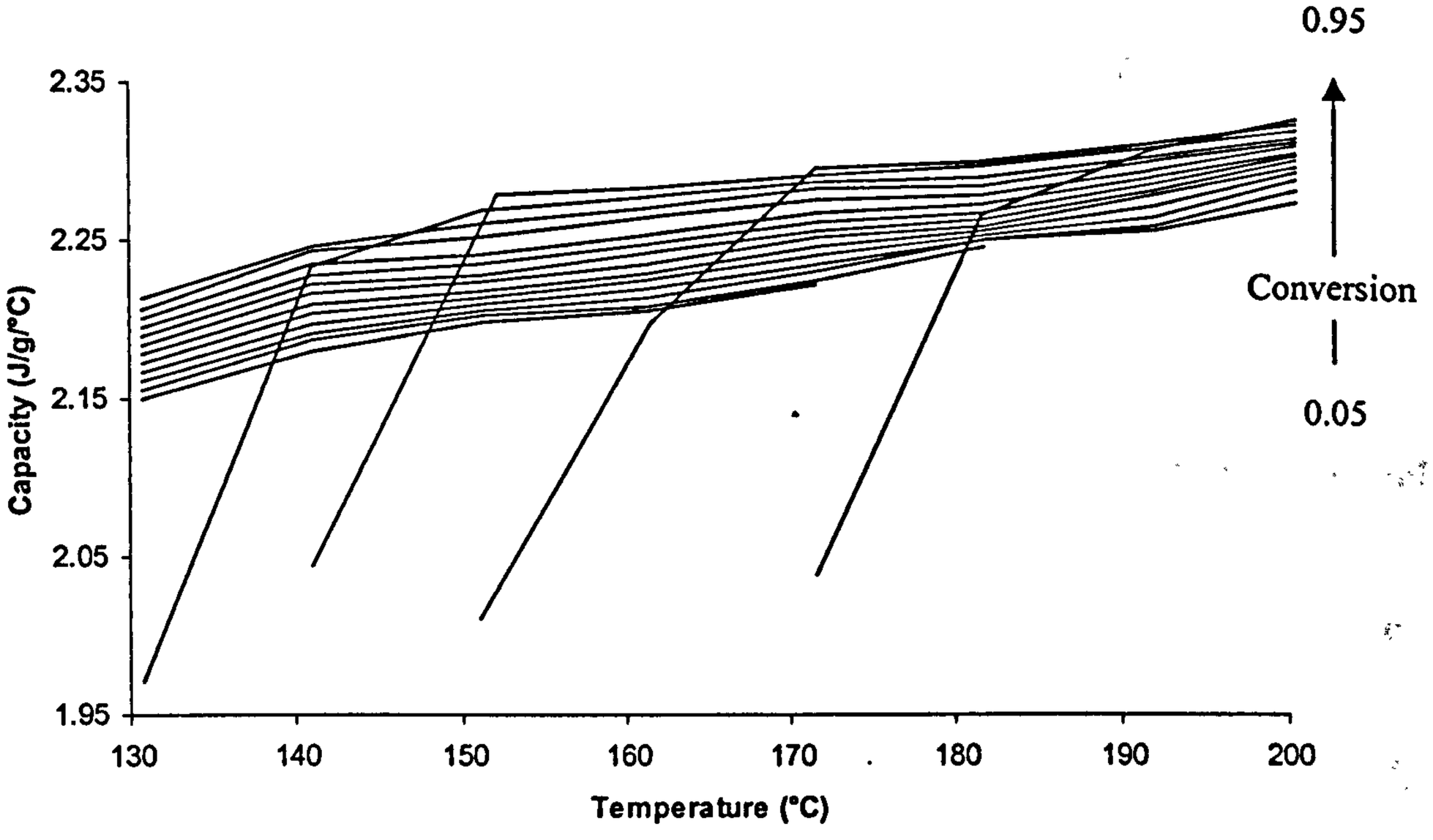

Fig.6.6 *Specific heat capacity versus temperature isoconversional curves of RTM6 epoxy resin*

A schematic representation of the algorithm is given in Fig. 6.7. The results of the submodel in the case of 50 % weight fraction glass fibre/RTM6 and 50% carbon fibre/RTM6 for a characteristic thermal programme of RTM curing are illustrated in Fig. 6.8. It can be observed that changes in the heat capacity of the resin during the cure dominate the variation of the composite heat capacity.

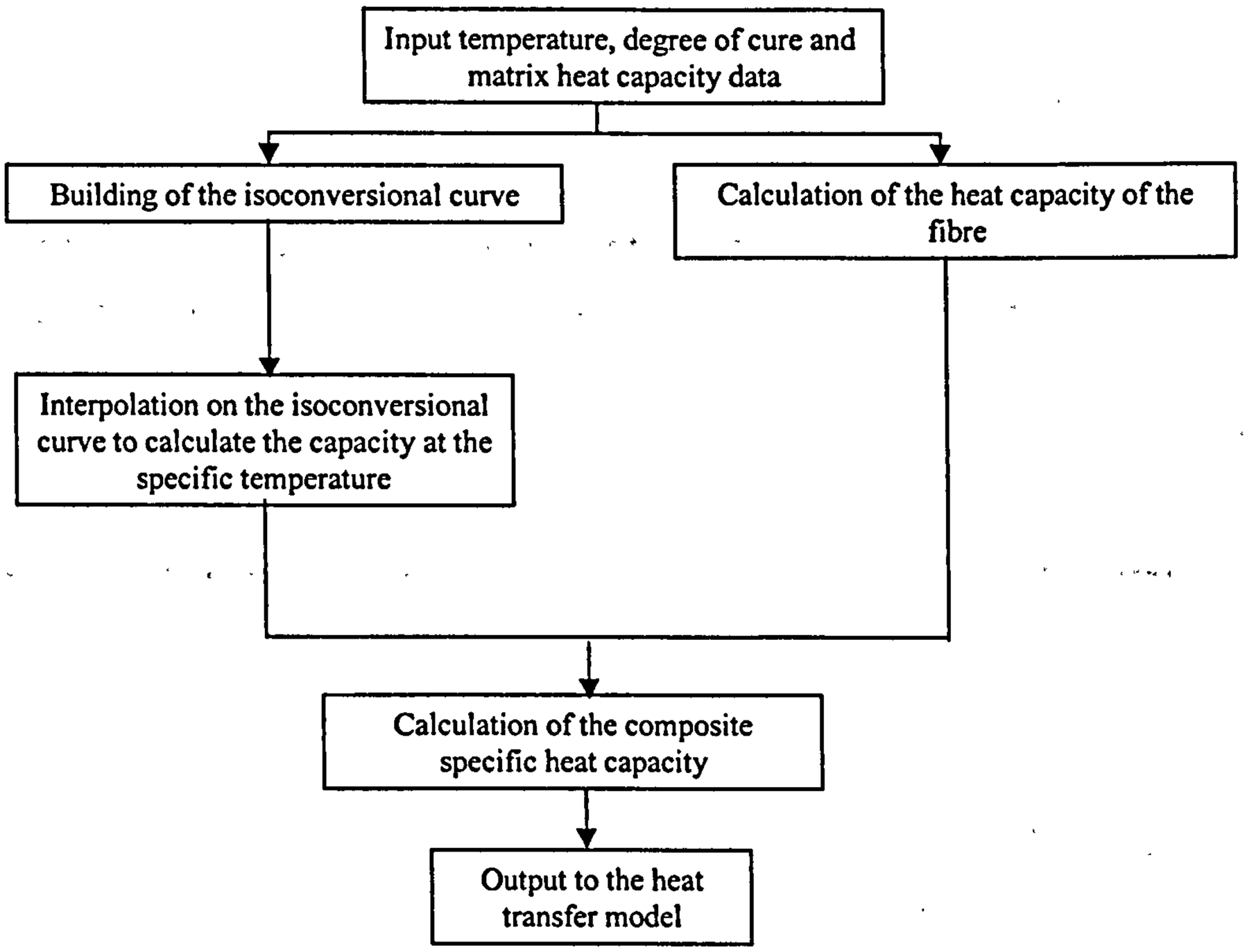

Fig.6.7 *Schematic representation of the specific heat capacity submodel algorithm*

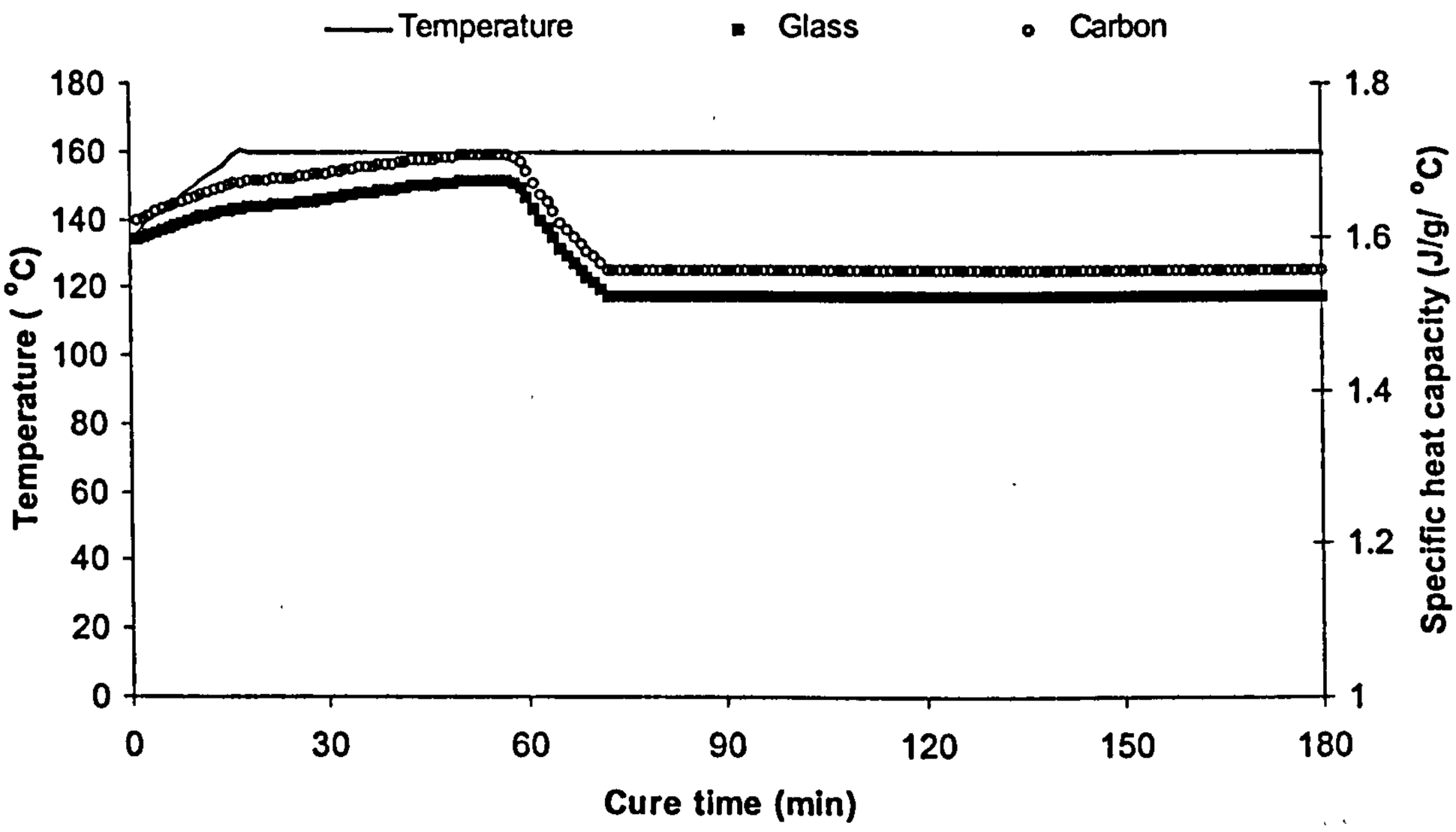

Fig.6.8 *Results of the specific heat capacity submodel for 50 wt% carbon/RTM6 and 50 wt% glass/RTM6 composites*

6.4 Thermal conductivity submodel

An analytical model for the calculation of the thermal conductivity tensor has been developed. The thermal conductivity of the resin has been measured using a new experimental method while published data were used for the incorporation of the conductivity of the reinforcements.

6.4.1 Apparatus for the measurement of matrix thermal conductivity during the cure

The specially designed and built measurement cell is illustrated in Fig. 6.9 . It comprises a cylindrical copper block with a cylindrical opening in its centre and cooling fins on its outside, two insulating disks on the top and the bottom of the copper block, a disposable copper tube which is inserted into the block opening and a linear heating element which is wound onto the copper block in the spaces between fins. The top insulating disk has two holes for the insertion of the measurement and the control thermocouples. The control thermocouple is inserted in the copper block, near the disposable tube and the measurement thermocouple is inserted in the centre of the tube containing the resin. The inner diameter of the disposable tube is 8 mm and its wall thickness 1mm. The height of the copper block is 40 mm.

The geometry presented in Fig.6.9 has been selected instead of the conventional hot wire and hot plate transient thermal conductivity techniques, due to the nature of the material tested which undergoes a liquid to solid transition accompanied by shrinkage during the measurement. Since the resin system used is appropriate for resin transfer moulding, it reaches very low viscosity when unreacted. Thus any arrangement involving plates, is more likely to allow resin leakage than a closed cylinder. Dimensional changes impede the use of hot wire methods, where a linear heating source and a thermocouple at a specific distance are used. Resin shrinkage would change the relative position of the two and consequently would cause a systematic error in the thermal conductivity determination.

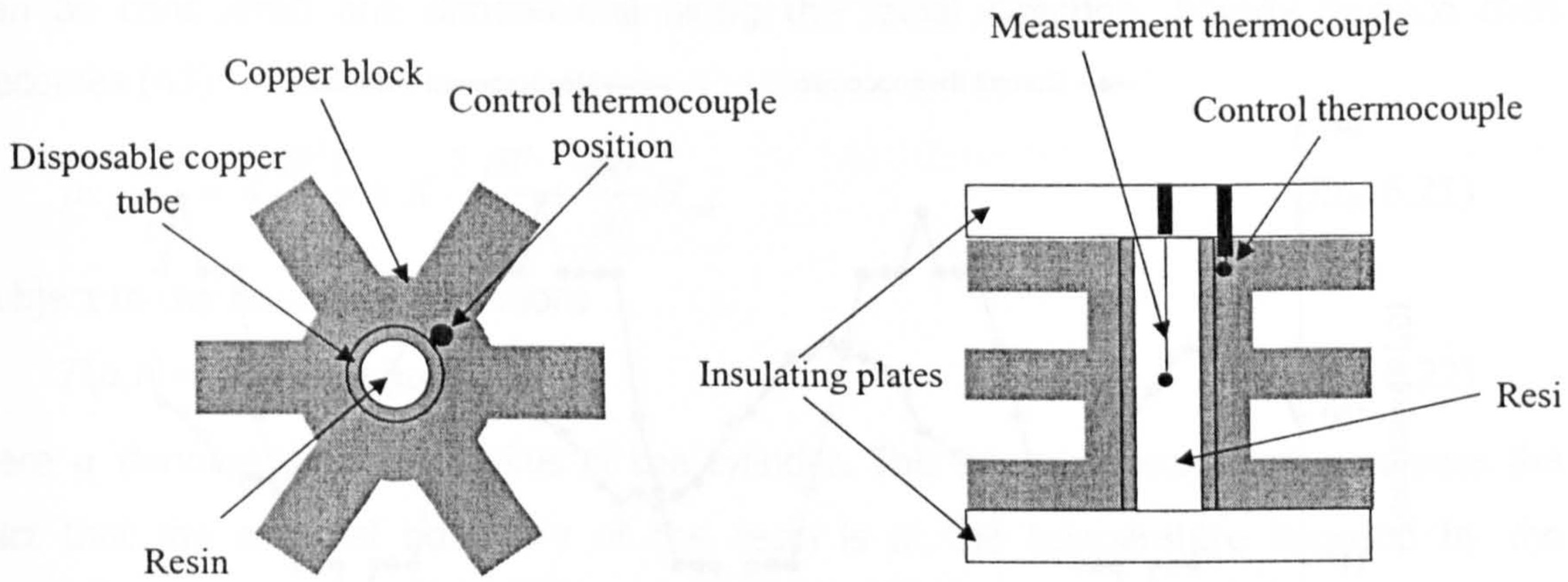

(a) Top view of the copper block (b) Cross section of the whole measurement assembly

Fig.6.9 *Schematic of the experimental configuration used for the measurement of the resin thermal conductivity during cure*

The control thermocouple and a power circuit, which controls the heating element, are connected to a Eurotherm temperature controller which is connected to the serial port of a personal computer. The measurement thermocouple is interfaced with the computer via a Keithley DAS/TC board. A Visual Basic computer code able to communicate with both the Eurotherm controller and the DAS/TC board was developed. This computer code can set the temperature profile measured by the control thermocouple and acquire data from both the Eurotherm controller and from the DAS/TC board.

Prior to the measurement the disposable copper tube was filled with liquid resin and then the measurement thermocouple was placed in the centre of the resin. Then a temperature programme, which was a superposition of an isothermal profile and a modulation, was imposed on the cell. All thermocouples were calibrated prior to the measurement using the control thermocouple as the reference. Isothermal cure experiments of RTM6 epoxy resin were performed at 130, 150 and 170 °C using a modulation with a period of 2 min and an amplitude of 3 °C.

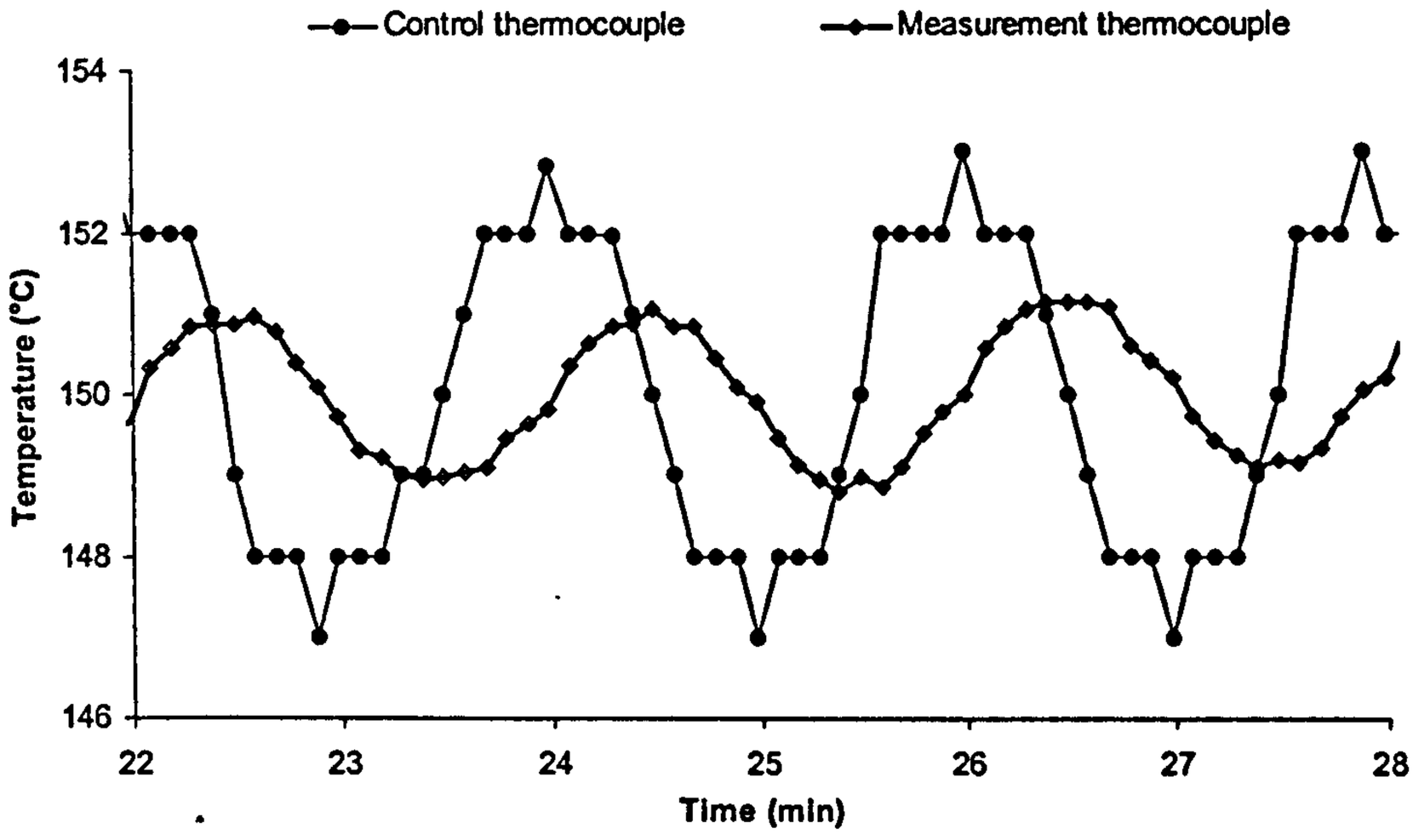

Fig.6.10 *General form of the temperature signals acquired during the cure of RTM6 resin*

The general form of signals acquired during the experiments is shown in Fig.6.10 for the cure of RTM6 resin at 150 °C. It can be observed that the temperature in the middle of the resin lags behind the temperature of the surrounding copper. This thermal lag is the basis for the determination of the thermal conductivity of the curing material as will be analysed in the following paragraph. (Note that the control thermocouple measurement presented in Fig. 6.10 can only give integer values due to the accuracy of the specific controller used in this study. The actual temperature followed by the copper tube has the form of a smooth sinusoidal curve.)

6.4.2 Analysis of the thermal response

The thermal conductivity of copper is sufficiently high to allow the assumption of uniform temperature of the disposable copper cylinder at a short distance away from its ends. The small value of the cylinder radius in comparison to the cylinder length (ratio 1:10) allows us to assume uniformity of the temperature within the resin along the axial direction, i.e. heat transfer can be considered as two dimensional along the radial and the angular directions. The cylindrical symmetry of the measurement assembly results in uniformity of temperature along the angular direction also. Consequently, heat transfer

can be considered one dimensional along the radial direction. Energy balance then becomes (43):

$$\rho c_p \frac{\partial T}{\partial t} = K \frac{\partial^2 T}{\partial r^2} + K \frac{1}{r} \frac{\partial T}{\partial r} + \frac{d\alpha}{dt} H_{tot} \qquad \text{(Eq. 6.21)}$$

subject to the boundary condition:

$$T(a,t) = T_o + A \sin(\omega t) \qquad \text{(Eq. 6.22)}$$

here a denotes the inner radius of the cylinder. This boundary condition expresses the fact that the external boundary of the resin is at the temperature imposed by the controller and measured by the control thermocouple.

The temperature within the resin can be considered as the superposition of an underlying temperature $\overline{T}$ and a cyclic component $\tilde{T}$, as follows:

$$T(r,t) = \overline{T}(r,t) + \tilde{T}(r,t) \qquad \text{(Eq. 6.23)}$$

Substitution of Eq.6.23 in Eq.6.22 results in:

$$\rho c_p \frac{\partial \overline{T}}{\partial t} + \rho c_p \frac{\partial \tilde{T}}{\partial t} = K \frac{\partial^2 \overline{T}}{\partial r^2} + K \frac{\partial^2 \tilde{T}}{\partial r^2} + K \frac{1}{r} \frac{\partial \overline{T}}{\partial r} + K \frac{1}{r} \frac{\partial \tilde{T}}{\partial r} + \frac{d\alpha}{dt} H_{tot} \qquad \text{(Eq. 6.24)}$$

and

$$\overline{T}(a,t) = T_o \qquad \text{(Eq. 6.25)}$$

$$\tilde{T}(a,t) = A \sin(\omega t) \qquad \text{(Eq. 6.26)}$$

This relation expresses the superposition of the two temperature fields, which in the absence of the exothermic heat of reaction term would result in the separation of the heat balance into two equations:

$$\rho c_p \frac{\partial \overline{T}}{\partial t} = K \frac{\partial^2 \overline{T}}{\partial r^2} + K \frac{1}{r} \frac{\partial \overline{T}}{\partial r} \qquad \text{(Eq. 6.27)}$$

$$\rho c_p \frac{\tilde{T}}{t} = K \frac{^2 \tilde{T}}{r^2} + K \frac{1}{r} \frac{\tilde{T}}{r} \qquad \text{(Eq. 6.28)}$$

The heat generation term cannot be separated similarly into two components, since the reaction rate is not a linear function of the temperature. However, the relative effect of the temperature modulation on the exothermic heat of reaction can be investigated. In Fig.6.11 the exothermic heat of reaction, as calculated using the kinetic model presented in chapter 5 for the isothermal cure at 130, 150 and 170 °C, is compared with the results

of the kinetic model for the cure at the same temperatures where a modulation of 2 °C amplitude and 2 min period has been superimposed.

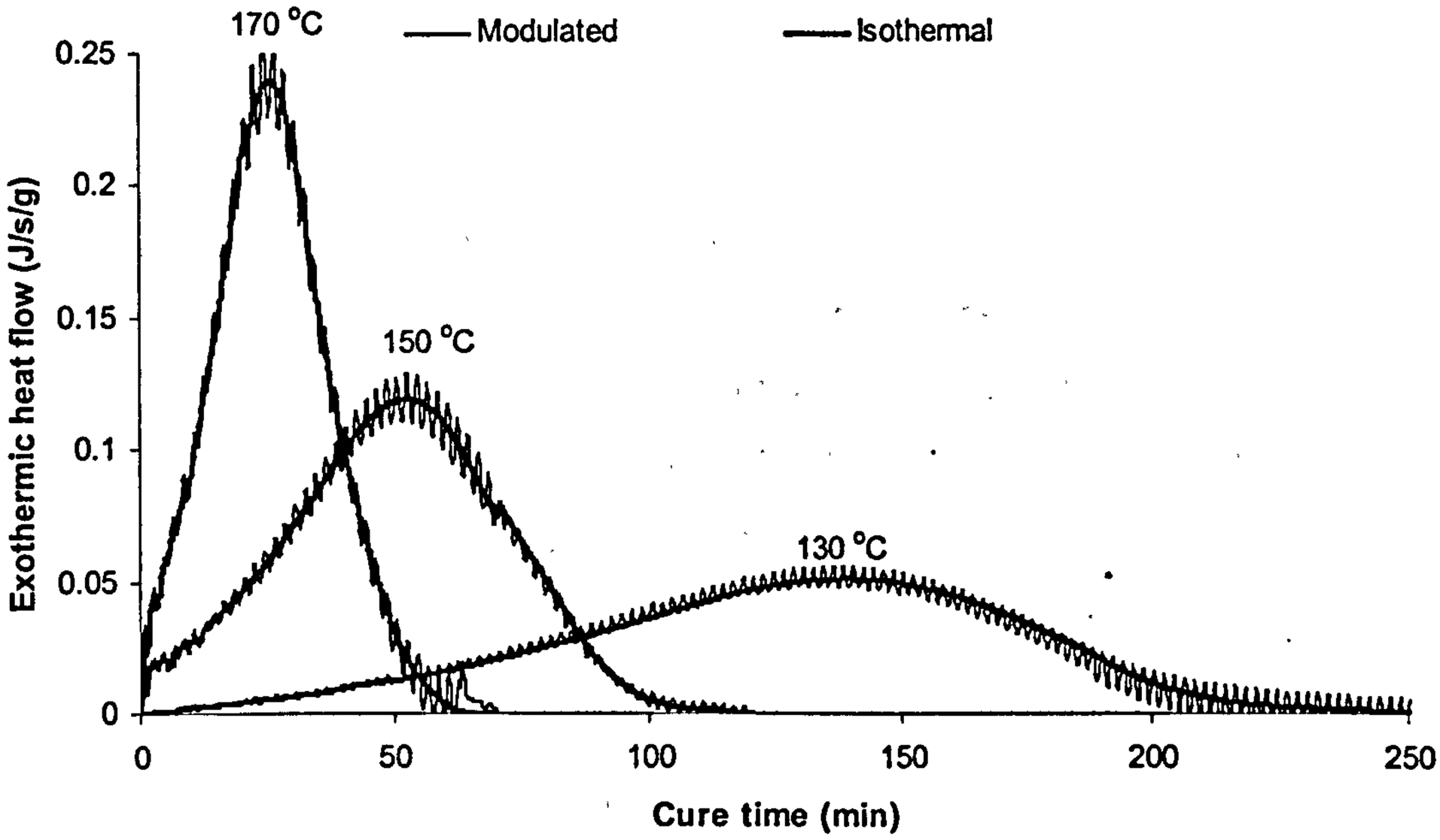

Fig.6.11 *Comparison of the heat generated from the exothermic cure reaction under isothermal and modulated thermal programmes*

It can be observed that the exothermic heat flow of the modulated cases is very close to that of the isothermal thermal programmes. The maximum absolute difference between the exothermic heat flows of the modulated and isothermal cases and their average absolute difference for the three cure temperatures are given in Table 6.1.

	Maximum absolute difference (J/g/s)	Average absolute difference (J/g/s)
130 °C	9.2×10^{-3}	2.2×10^{-3}
150 °C	11.1×10^{-3}	3.1×10^{-3}
170 °C	17.7×10^{-3}	5.8×10^{-3}

Table 6.1 *Differences of the exothermic heat under isothermal and modulated thermal programmes*

According to these results, if the exothermic heat is attributed exclusively to the underlying component of temperature $\overline{T}$, the heat balance of Eq. 6.24 is separated as follows:

$$\rho c_p \frac{\partial \overline{T}}{\partial t} = K \frac{\partial^2 \overline{T}}{\partial r^2} + K \frac{1}{r} \frac{\partial \overline{T}}{\partial r} + \rho H_{tot} \frac{d\alpha}{dt} \qquad \text{(Eq. 6.29)}$$

$$\rho c_p \frac{\tilde{T}}{t} = K \frac{^2\tilde{T}}{r^2} + K \frac{1}{r} \frac{\tilde{T}}{r} \qquad \text{(Eq. 6.30)}$$

An error of the magnitude indicated in Table 6.1 is introduced in Eq.6.30. This error is a part of the energy absorbed or emitted by the material and it should be compared with the term $c_p \frac{\partial \tilde{T}}{\partial t}$ in Eq.6.30. The cyclic temperature time derivative is of the order of 0.1 °C/s, an approximate value of the resin heat capacity is 2 J/g/ °C. Thus the heat flow component due to the heat capacity of the material is approximately 0.2 J/g/s, a value at least one order of magnitude higher than the exothermic heat of reaction corresponding to the cyclic component. Consequently, the behaviour of the cyclic component of the temperature can be approximated by Eq.6.30, subject to the boundary condition expressed by Eq.6.26.

This boundary value problem accepts the following steady periodic solution (209):

$$T(r,t) = AReal\left\{\frac{I_0\left(r\sqrt{i\omega\rho c_p/K}\right)}{iI_0\left(a\sqrt{i\omega\rho c_p/K}\right)} e^{i(\omega t)}\right\} \qquad \text{(Eq. 6.31)}$$

where $I_0(x)$ denotes the modified Bessel function. The modified Bessel function of an argument of the form $z\sqrt{i}$ can be analysed as follows (210):

$$I_0\left(z\sqrt{i}\right) = ber(z) + i\,bei(z) \qquad \text{(Eq. 6.32)}$$

where the real and imaginary parts are:

$$ber(z) = \sum_{n=0}^{\infty} \frac{(-1)^n \left(\frac{1}{4} z^2\right)^{2n}}{(2n)!^2} \qquad \text{(Eq. 6.33)}$$

$$bei(z) = \sum_{n=0}^{\infty} \frac{(-1)^n \left(\frac{1}{4} z^2\right)^{2n+1}}{(2n+1)!^2} \qquad \text{(Eq. 6.34)}$$

Accordingly the solution at the centre of the cylinder becomes:

$$T(0,t) = ARe\,al\left\{\frac{1}{iber\left(a\sqrt{\omega\rho c_p/K}\right) - bei\left(a\sqrt{\omega\rho c_p/K}\right)} e^{i(\omega t)}\right\} \qquad \text{(Eq. 6.35)}$$

or

$$T(0,t) = M\sin(\omega t - \phi) \qquad \text{(Eq. 6.36)}$$

where

$$M = \frac{A}{\sqrt{\left[ber\left(a\sqrt{\omega\rho c_p/K}\right)\right]^2 + \left[bei\left(a\sqrt{\omega\rho c_p/K}\right)\right]^2}} \qquad \text{(Eq. 6.37)}$$

and

$$\phi = \tan^{-1}\left(\frac{bei\left(a\sqrt{\omega\rho c_p/K}\right)}{ber\left(a\sqrt{\omega\rho c_p/K}\right)}\right) \qquad \text{(Eq. 6.38)}$$

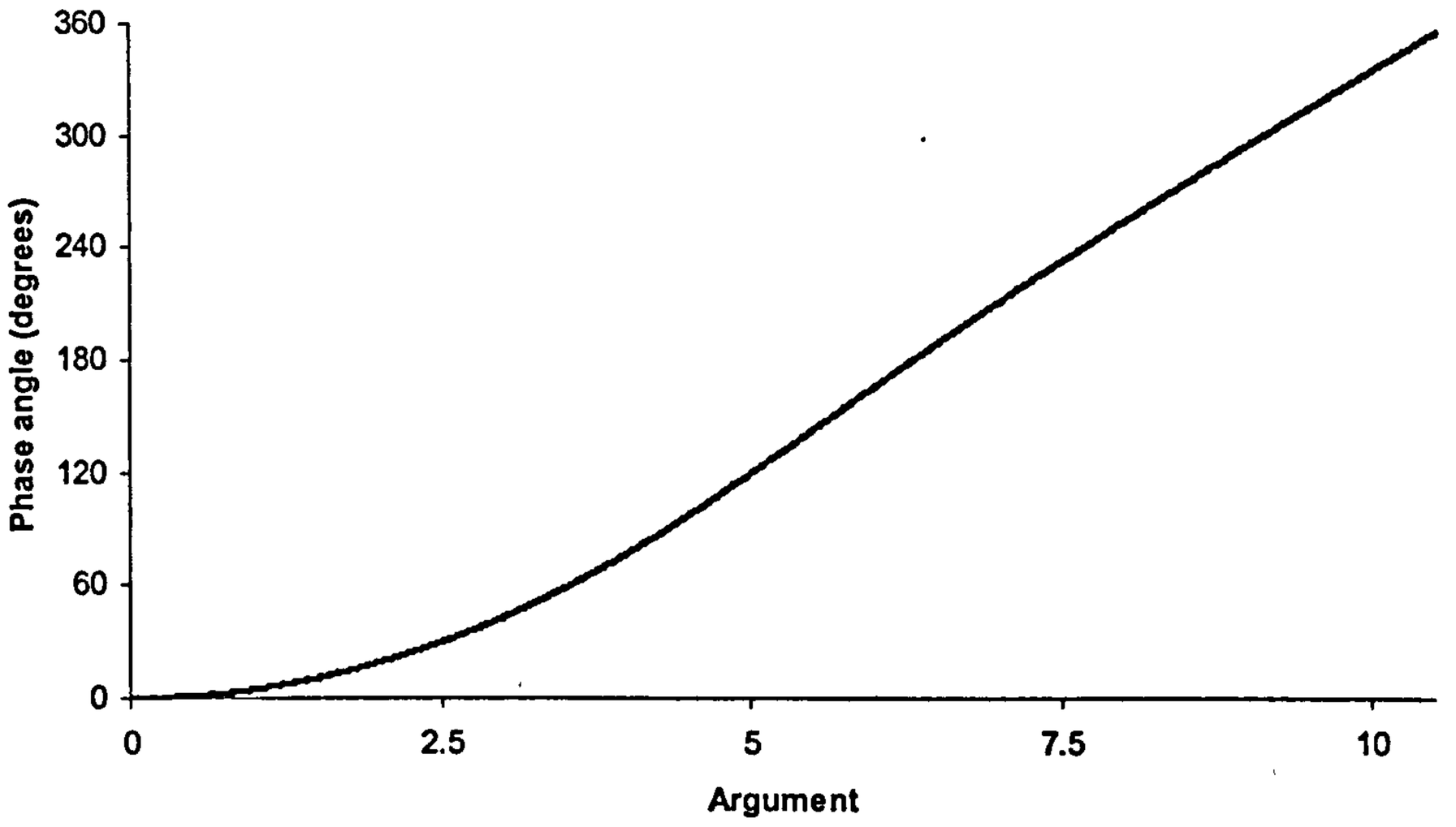

Fig.6.12 *Dependence of the phase angle on the term containing the thermal conductivity*

By calculating the phase difference between the temperature at the centre and the temperature at the copper cylinder wall from the raw data, an estimation of the term $\left(a\sqrt{\omega\rho c_p/K}\right)$ can be carried out. The dependence of the angle ϕ defined in the interval

$[0,2\pi]$on the argument of the functions ber and bei has been performed using the first forty terms of Eqs.6.33 and 6.34 and is illustrated in Fig. 6.12.

6.4.3 Experimental results

A computer code, which executes the tasks below, has been applied to the raw data of the isothermal cure experiments at 130, 150 and 170 °C:

- Estimation of the time difference between the maxima of the temperature at the centre and the wall of the cylinder;
- Calculation of the corresponding phase angle difference using the value of the time difference and the period of the modulation;
- Inversion of Eq.6.38 using the data of Fig. 6.12 in tabulated form in order to calculate the term $Me = \left(a\sqrt{\omega\rho c_p / K}\right)$ from the phase difference;
- Calculation of the density and the heat capacity using the submodels presented in 6.2 and 6.3 for the case of unreinforced material and the kinetic model of chapter 5;
- Estimation of the thermal conductivity using the relation:

$$K = \frac{1}{Me^2} a^2 \omega \rho c_p \qquad \text{(Eq. 6.39)}$$

The thermal conductivity evolution during the cure, as estimated using this procedure, is illustrated in Fig.6.13. It can be observed that the thermal conductivity rises as the reaction progresses, due to the increase in the mean molecular chain size which facilitates the propagation of vibrations caused by thermal motion. The thermal conductivity undergoes a step change at vitrification. This is attributed to the densification of the material occurring at the glass transition. Comparison of the different isothermal curves shows that the thermal conductivity of the liquid and rubbery materials decreases with increasing temperature at a given conversion.

In general the data have significant scatter which can be attributed to the inability to determine with a high accuracy the maxima of the modulated temperature profiles as those shown in Fig.6.13. Thus, for modelling purposes the data in the region below the glass transition are replaced by the lines illustrated in Fig.6.13. These lines result from a linear regression in the corresponding area.

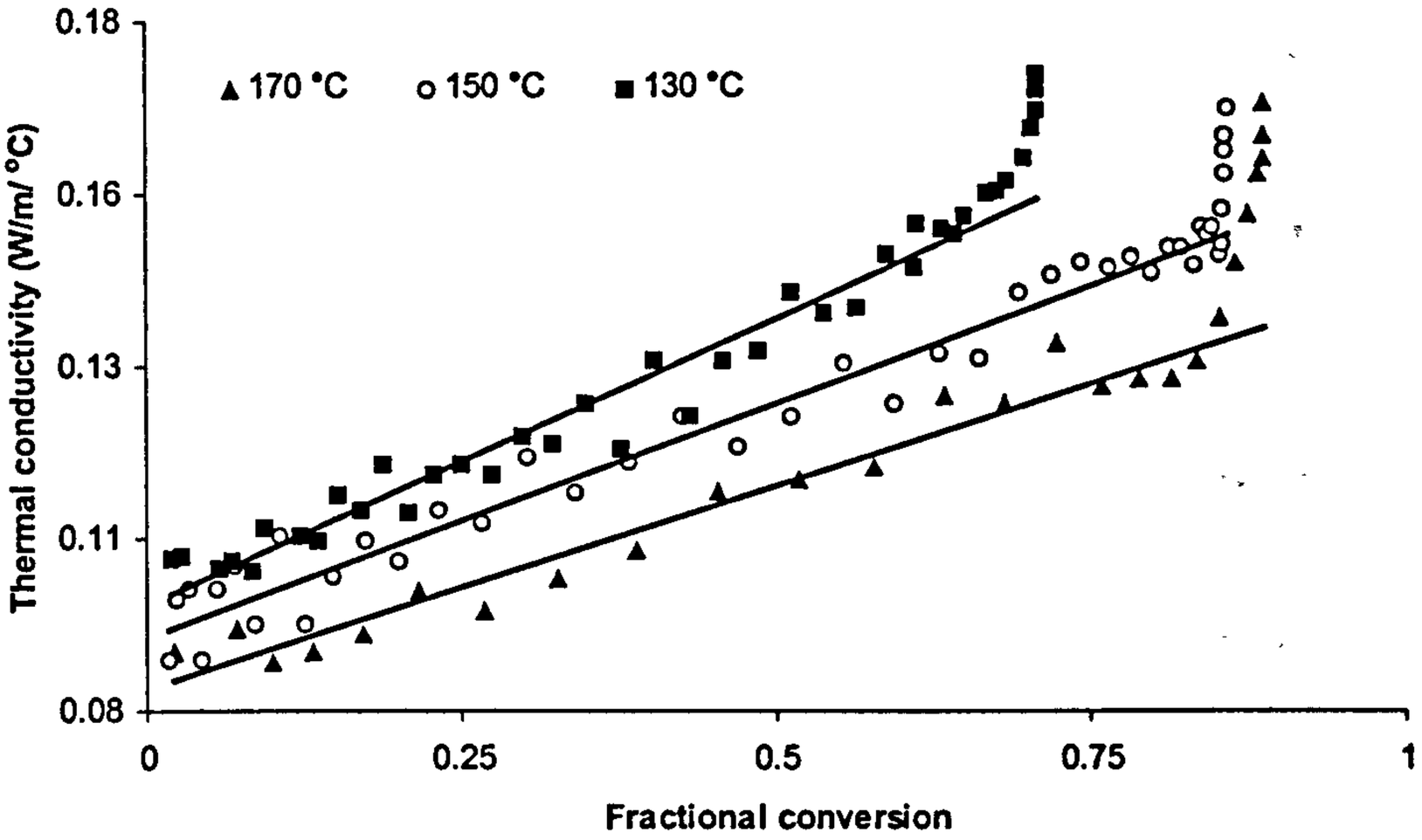

Fig.6.13 *Thermal conductivity of RTM6 epoxy resin as a function of conversion during the cure*

6.4.4 Analytical model for the calculation of the thermal conductivity of the composite

Multivariable regression has been performed on the set of data illustrated in Fig.6.13 and the following model has been obtained for the thermal conductivity of RTM6 epoxy resin:

$$K = 0.0008\,T\alpha^2 - 0.0011T\alpha - 0.0002T - 0.0937\alpha^2 + 0.22\,\alpha + 0.12 \quad \text{(Eq. 6.40)}$$

where temperature is given in °C and thermal conductivity in W/m/°C. The average absolute error of the fit within the range in which the measurements have been performed is 2.1%.

The thermal conductivity of E-glass is 1.03 W/m/°C at ambient temperature (211), while the variation of conductivity of glass with temperature up to 300 °C is negligible (212). The longitudinal thermal conductivity of T300 carbon fibre can be expressed as follows (213):

$$K = 4.8 + 0.0074\,T \quad \text{(Eq. 6.41)}$$

where temperature is given in °C and thermal conductivity in W/m/°C.

The radial thermal conductivity of T300 carbon fibre is 0.84 W/m/°C (211). In this case also the sensitivity of thermal conductivity to temperature changes is expected to be very low; for other types of carbon fibre it has been measured to be 0.06 % per °C (214).

To calculate the thermal conductivity of the composite during the cure a model which expresses it as a function of the thermal conductivities of the constituents is employed.

All the fabrics used in this study comprised unidirectional layers. The thermal conductivity tensor of a single layer has the form (215):

$$\overline{K} = \begin{bmatrix} K_{xx} & K_{xy} & 0 \\ K_{xy} & K_{yy} & 0 \\ 0 & 0 & K_{zz} \end{bmatrix} \qquad \text{(Eq. 6.42)}$$

where xy is the fibre bed plane.

The components of the tensor are connected with the principal conductivities according to the relations:

$$K_{xx} = K_l \cos^2(lx) + K_t \cos^2(tx) \qquad \text{(Eq. 6.43)}$$

$$K_{yy} = K_l \cos^2(ly) + K_t \cos^2(ty) \qquad \text{(Eq. 6.44)}$$

$$K_{xy} = K_l \cos(ly)\cos(lx) + K_t \cos(ty)\cos(tx) \qquad \text{(Eq. 6.45)}$$

$$K_{zz} = K_t \qquad \text{(Eq. 6.46)}$$

Here K_l and K_t denote the thermal conductivity in the direction parallel (longitudinal conductivity) and normal (transverse conductivity) to the fibre respectively, and $\cos(ij)$ is the directional cosine of the angle between the principal axis i and the cartesian system of coordinates axis j.

A variety of models based on considerations of the geometrical arrangement of the constituents have been proposed for the estimation of the principal thermal conductivities of composite materials (216, 217). Among the various models the following expressions, which have been validated experimentally in the case of continuous fibre thermosetting composites by Farmer and Covert (214), have been used in this study:

$$K_l = v_f K_{fl} + (1 - v_f) K_r \qquad \text{(Eq. 6.47)}$$

$$\frac{K_t}{K_r} = v_f\left(\frac{K_{fr}}{K_r} - 1\right) + \left(\frac{1}{2} - \frac{K_{fr}}{2K_r}\right) + \left(\frac{K_{fr}}{K_r} - 1\right)\sqrt{v_f^2 - v_f + \frac{\left(\frac{K_{fr}}{K_r} + 1\right)^2}{\left(\frac{2K_{fr}}{K_r} - 2\right)^2}} \quad \text{(Eq. 6.48)}$$

Combination of Eqs. 6.43-6.48 with the expression of the constituent thermal conductivities presented previously can lead to a calculation of the components of the thermal conductivity tensor. The results of the model in the case of 50 % weight fraction unidirectional glass and carbon fibre for a characteristic thermal programme of RTM curing are illustrated in Figs. 6.14 and 6.15. It can be observed that anisotropy is higher in the case of carbon reinforcements than in the case of glass, while the effect of the variation of the resin thermal conductivity is higher in the transverse direction.

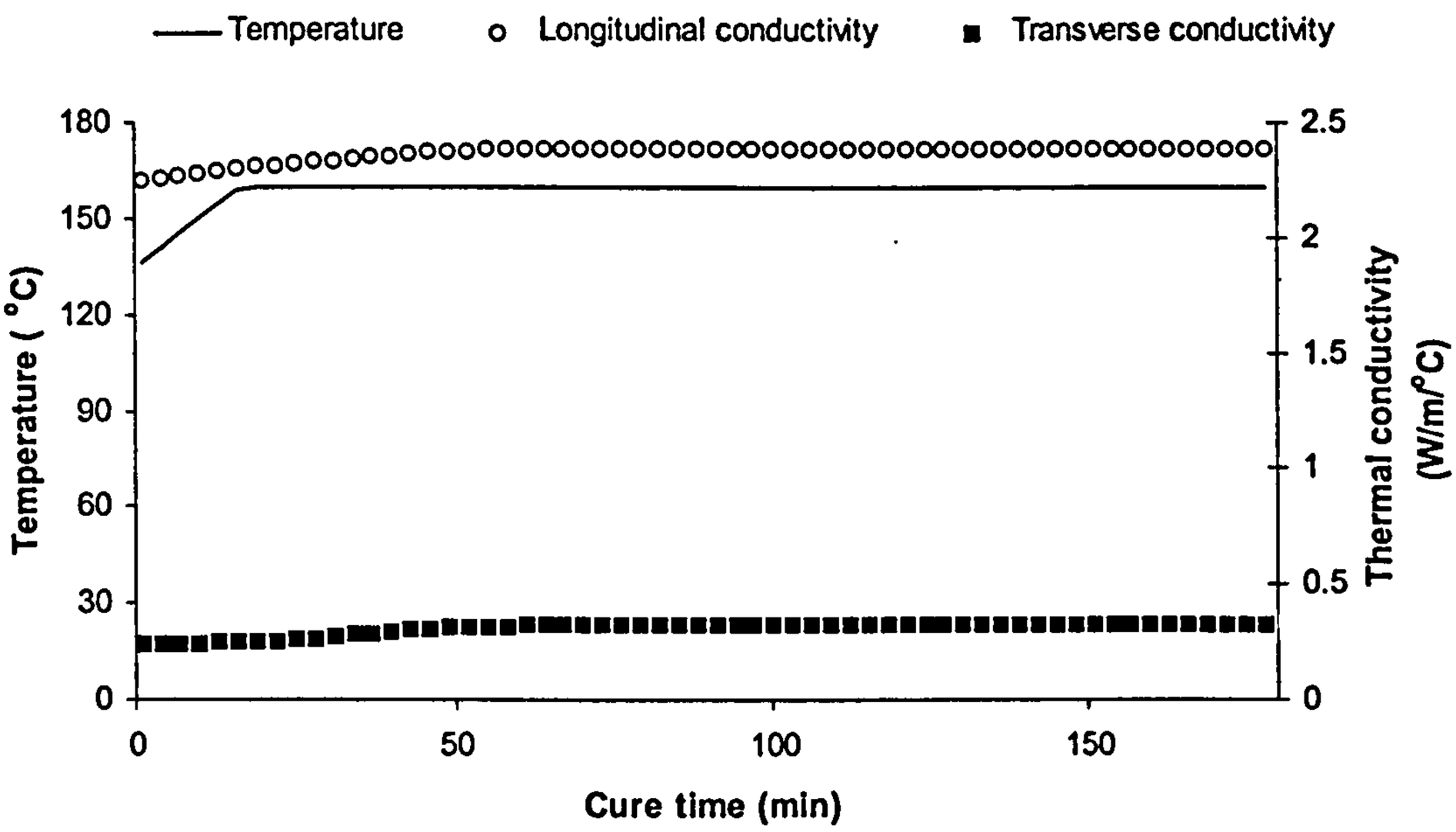

Fig.6.14 *Results of the thermal conductivity submodel in the case of the cure of a 50 wt% (37 v%) T300 carbon/RTM6 resin composite*

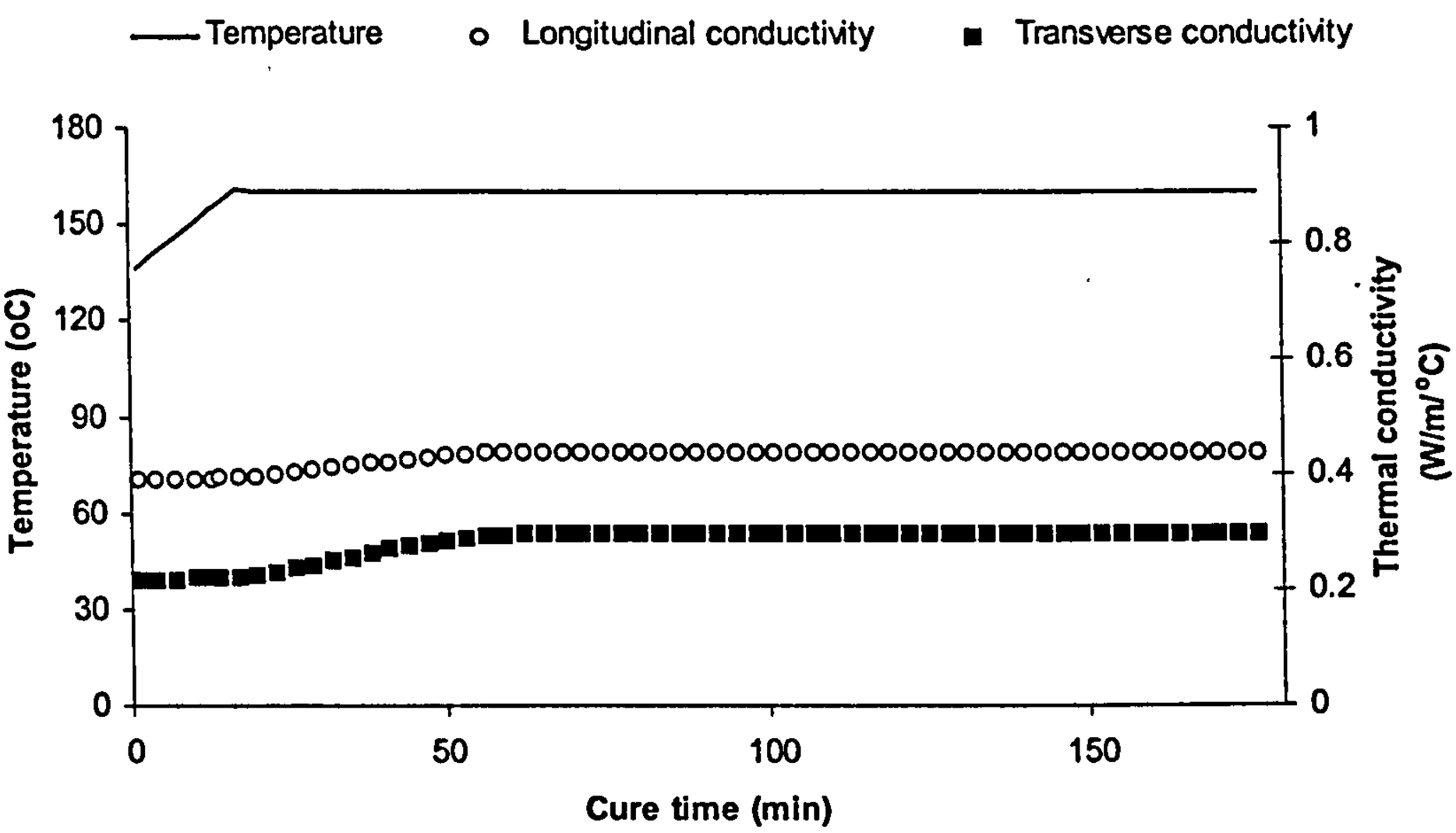

Fig.6.15 *Results of the thermal conductivity submodel in the case of the cure of a 50 wt% (30 v%) E-glass/RTM6 resin composite*

6.5 Overview

Three submodels which incorporate the thermal properties of the composite in the heat transfer model have been developed and described here. The density submodel operates incrementally and takes into account the chemical shrinkage of the resin and the thermal expansion or contraction of the resin and of the fibre. The heat capacity submodel employs direct two-dimensional interpolation applied to experimental data, obtained using MDSC and a calculation procedure which removes the effect of the reaction, for the estimation of the epoxy resin specific heat capacity. The result is combined with the heat capacity of the reinforcement using the rule of mixtures. The thermal conductivity submodel has an analytical form. An experimental method has been developed for the estimation of the resin thermal conductivity as it cures and literature data were used for the thermal conductivity of the reinforcements. The two are combined using an appropriate model based on geometrical considerations.

Chapter Seven

7 Heat transfer modelling of RTM curing

7.1 Introduction

In this chapter the heat transfer model described in chapters 4-6 is applied to composite curing in a resin transfer mould. The convergence of the numerical procedure is tested in the case of RTM curing of a carbon/RTM6 epoxy resin composite. The results of the three dimensional and the one dimensional versions of the simulation are set against experimentally obtained thermal profiles in order to validate the model performance. A series of simulation runs is carried out in order to study the temperature and degree of cure distributions during the cure of carbon or glass/RTM6 epoxy resin composites.

7.2 Convergence of the simulation

An investigation of the dependence of the simulation results upon the time step and the element size has been carried out. The aim of this investigation is to ensure that the algorithm converges and that the values of these parameters in subsequent model runs are within the convergence area. The case of carbon (T300)/RTM6 epoxy resin composite has been selected for the convergence studies as this particular composite is one of the two materials used in subsequent simulations and experiments.

Four layers of carbon fabric (CTLX 816, BTI Europe) have been considered, in a 3 mm thick rectangular mould cavity. The top tooling was considered to be glass with a thickness of 25 mm. The thermal properties of the top tooling are given in Table 7.1.

$c_p\left(J/g/^\circ C\right)$	$K\left(W/m/^\circ C\right)$	$\rho\left(g/cm^3\right)$	$h\left(W/m^2\right)$
0.84	0.78	2.7	8.5

Table 7.1 *Thermal properties of the glass top tooling*

The surface density of the specific fabric is 816 g/m^2 thus, since the density of the fibre is 1.8 g/cm^3 and the initial density of the resin is 1.117 g/cm^3, the fibre weight fraction is 69 %. The initial temperature gradient has been considered linear (1 °C/mm). The boundary conditions were natural air convection on the glass top boundary (T_∞=25 °C), and a predefined thermal profile (heating at 1.5 °C/min from 130 °C to 160 °C and then isothermal) on the lower side of the composite. When the model domain includes some of the in-plane dimensions, an additional boundary condition accounting for perfect insulation (q=0 J/s/m^2) at the corresponding boundaries of the composite is incorporated, while the sides of the top tooling plate are considered to be under natural air convection. The perfect insulation boundary condition on the sides of the composite accounts for the existence of a rubber seal that surrounds the composite in the validation experiments performed in this study.

All these properties and conditions are identical to those used in the validation experiments and the simulation runs for the carbon reinforcement case. Here only the absolute average temperature differences between runs are presented. The detailed evolutions of the temperature and degree of cure distributions are presented in subsequent sections (7.3.2, 7.3.5).

7.2.1 Time discretisation convergence

The one dimensional model using 21 nodes (10 elements with a thickness of 0.3 mm within the curing composite and 10 elements with a thickness of 2.5 mm within the glass top tooling) was solved in 60, 120, 240, 480, 960 and 1920 time steps. The total

duration of the curing was 12000 sec (200 min). The average and maximum percentage differences between the temperature calculated in each case and the temperature calculated in 1920 time steps are illustrated in Fig. 7.1. The average difference was calculated over all the nodes of the model, at all times which are common in the two time discretisations.

The convergence of the model is evident. For discretisations finer than 240 time steps, i.e. for time step duration lower than 50 sec the average temperature error is lower than 0.008 % and the maximum temperature error lower than 0.3 %. Thus, a time step duration of 45 sec is selected for all subsequent simulation runs.

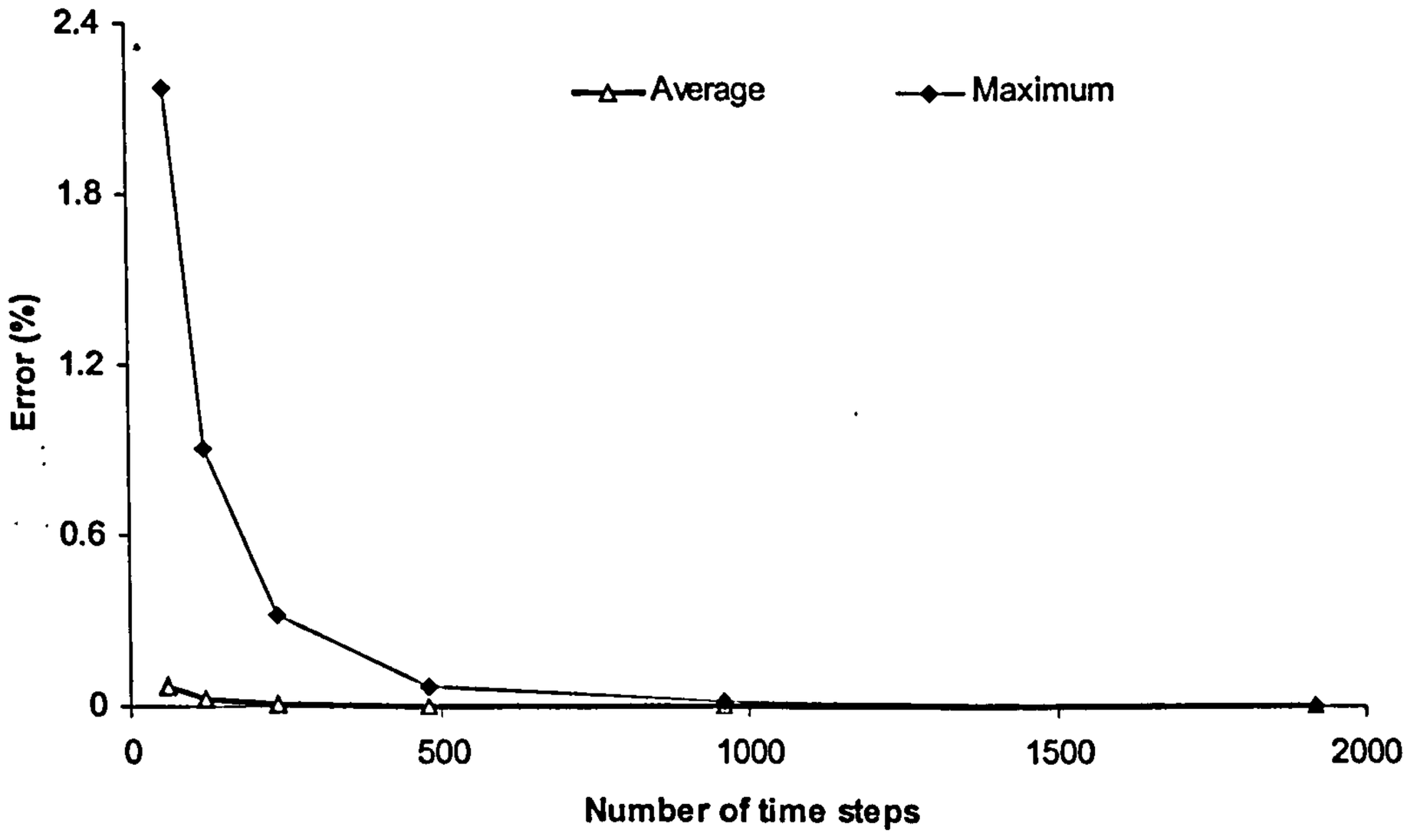

Fig.7.1 *Average and maximum temperature error of the simulation results using the 1920 time steps case as a reference*

7.2.2 Transverse discretisation convergence

The one dimensional model described previously was executed using a number of different spatial discretisations (5, 9, 17, 33 and 65 nodes). The time step duration was fixed at 45 sec. In all cases half of the elements represented the composite region and

the other half the glass top tooling. The average and maximum percentage differences between the temperature in each case and the temperature calculated using the 65 node model are illustrated in Fig. 7.2.

The finite element model converges towards the solution when more than 9 nodes are used. In this area the average and maximum error in temperature estimation are lower than 0.01 % and 0.5 % respectively. Consequently 13 nodes will be used to represent the thickness of the modelling domain in subsequent models. This number of nodes corresponds to 12 elements, 6 with a thickness of 0.05 mm within the composite and 6 with a thickness of 4.167 mm within the top tooling plate.

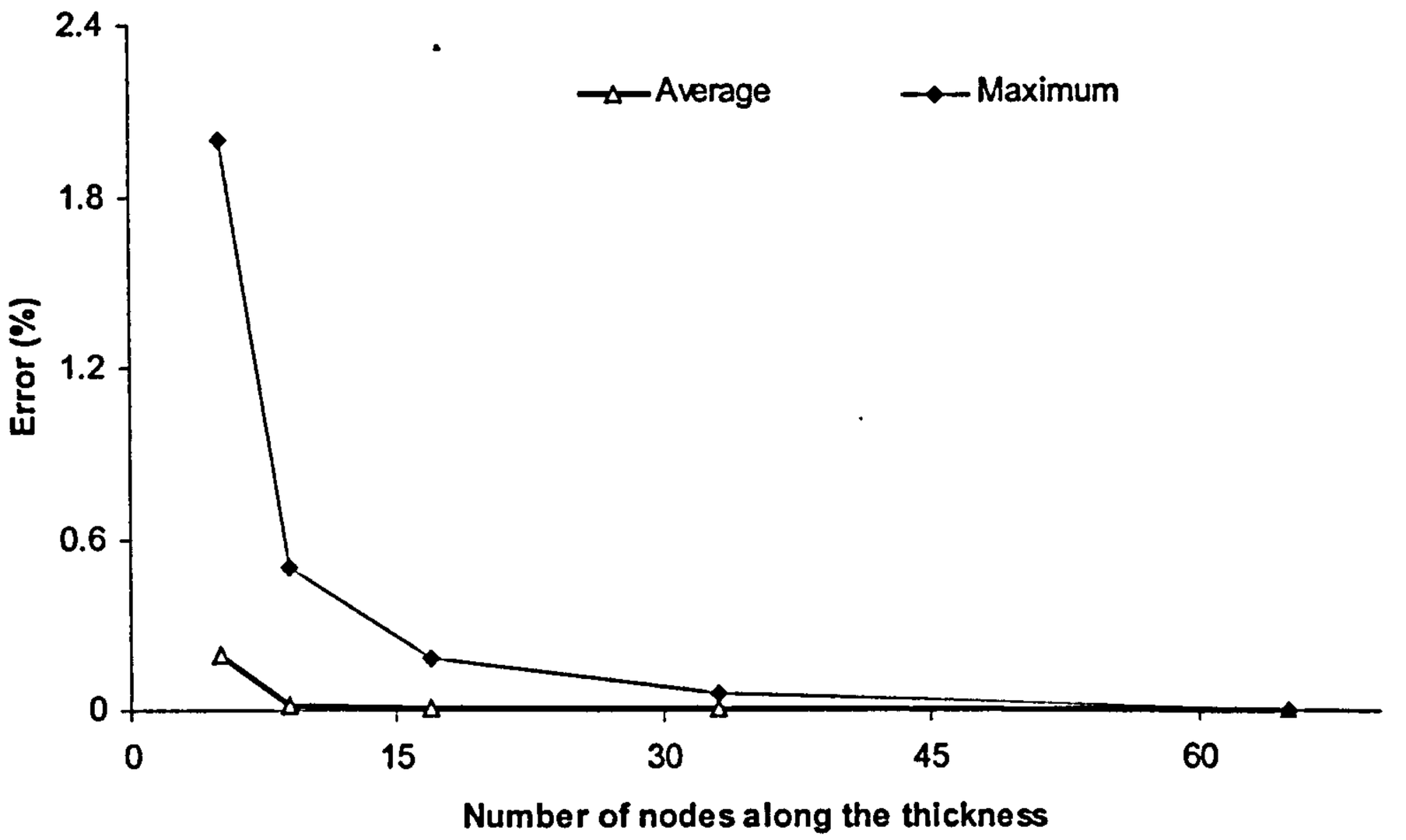

Fig.7.2 *Average and maximum temperature error of the simulation results using the 65 nodes case as a reference*

7.2.3 In-plane discretisation convergence

The two dimensional version of the solver was used in order to calculate the temperature and degree of cure distributions during the cure of the previously described component, considering an in-plane width of 340 mm. The number of nodes in the thickness direction was 13 and the duration of each time step 45 sec. A number of

different discretisations in the in-plane direction (6, 11, 21, 41) were tested in order to investigate the model convergence. The average and maximum differences between the temperature calculated in each case and the temperature calculated using the model comprising 41 nodes in the in-plane direction are illustrated in Fig. 7.3.

The convergence of the model is evident. When more than 17 nodes are used the average absolute temperature difference is lower than 0.05 % and the maximum absolute difference lower than 0.3 %. This discretisation corresponds to elements with a size of 20 mm, which will be the minimum element size in the in-plane directions utilised in subsequent model runs.

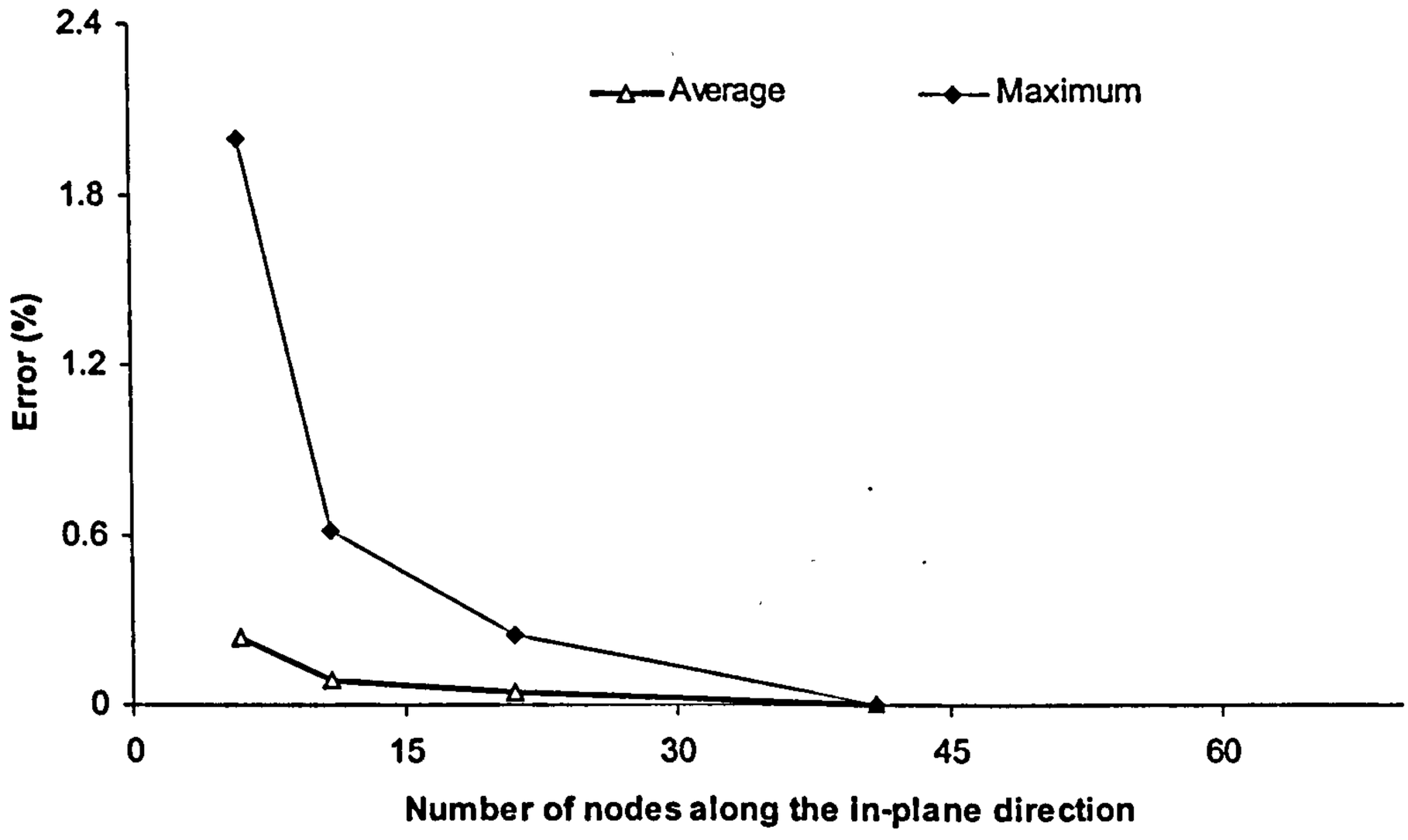

Fig.7.3 *Average and maximum degree of cure error of the simulation results using the 41 nodes case as a reference*

7.3 Model validation and application

7.3.1 RTM curing experiments

An Isojet RTM facility, which is shown in Fig. 7.4, has been utilised for the validation of the heat transfer model. The equipment comprises the resin tank, the control cabinet and the mould tool. The tool is shown schematically in Fig. 7.5. It is manufactured from

an Alcoa aluminium cast machined plate. Clamping pressure is introduced to the top plate, which can be either glass or aluminium, through a clamping plate in which windows have been machined, in order to visualise the resin flow. A silicon rubber seal which surrounds the mould cavity is present between the top and the bottom plates.

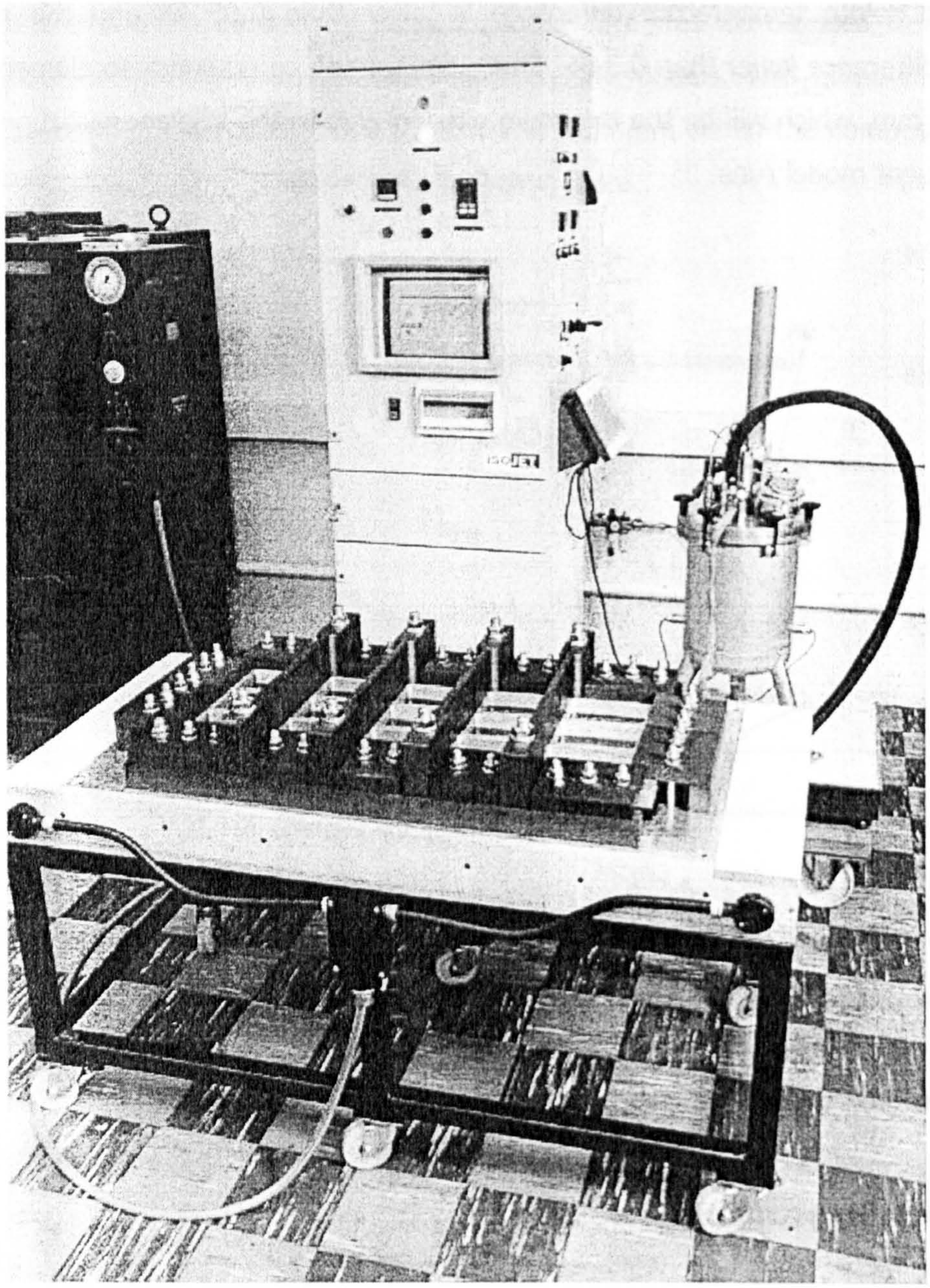

Fig.7.4 *The resin transfer moulding facility utilised for the validation of the heat transfer model*

The temperature profile of the mould cavity surface is mapped with K-type thermocouples. Each thermocouple can be positioned at different heights so that temperature in the thickness direction can also be measured. Temperature data can be downloaded into a PC through a DAS-TC thermocouple input board.

Mould heating is provided by electrical resistance heating elements positioned at the bottom of the tool and can achieve a maximum operating temperature of 200 °C. The temperature is set via a Eurotherm 808 controller connected to one of the central thermocouples of the mould. The controller can be programmed and data are downloaded into a PC via a RS-422 interface.

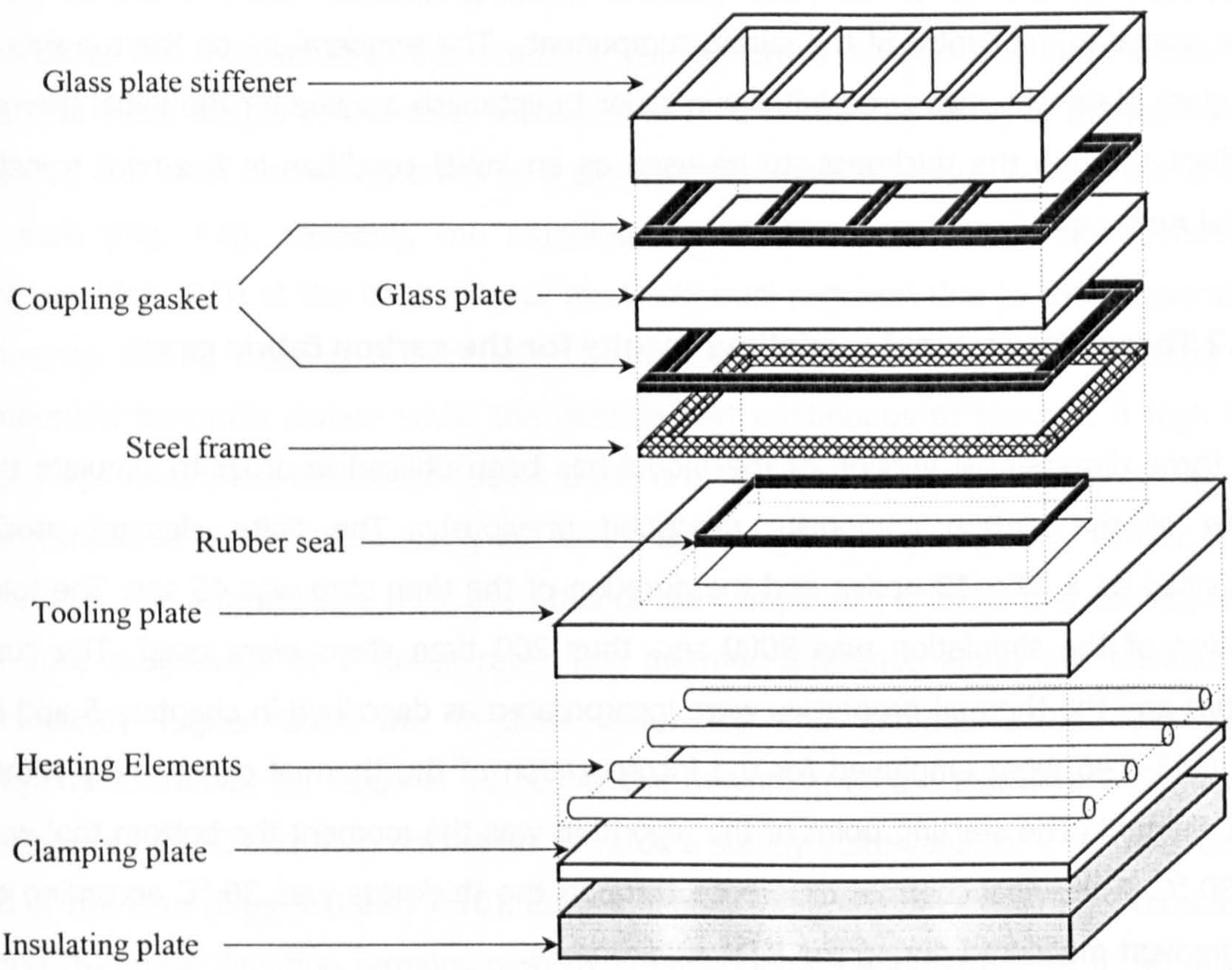

Fig.7.5 *Schematic representation of the tool of the RTM facility*

Two RTM curing experiments were performed using two different types of triaxial reinforcement, T300 carbon and E-glass. The specific fabrics used were CTLX 816 (BTI Europe) and E-BX1769 (BTI Europe). The carbon fabric has a surface density of 816

g/m^2 and comprises three plies (+45/-45/0). Four layers of this material were used in the cavity which has a thickness of 3 mm in order to achieve a fibre weight fraction of 0.69. The total sequence of unidirectional tow plies was +45/-45/0/0/-45/+45/+45/-45/0/0/-45/45. In the case of E-glass the surface density of the fabric is 1769 g/m^2 and the sequence +45/-45/0. Two layers of this material (total sequence +45/-45/0/0/-45/+45) were utilised in order to achieve a fibre weight fraction of 65 %.

The dimensions of the cavity were 800 mm x 340 mm x 3 mm. The filling was carried out at 120 °C. After filling completion, heating up at 1.5 °C/min was performed up to 160 °C, and then the temperature was kept constant. Two additional thermocouples which measure the temperature at the top of the composite and at the mid-thickness were placed in the centre of the curing component. The temperature on the top side of the glass plate was measured initially in order to establish a value for the initial thermal gradient through the thickness, to be used as an initial condition in the heat transfer model runs.

7.3.2 Three dimensional modelling results for the carbon fabric case

The three dimensional version of the model has been utilised in order to simulate the curing of the carbon composite described previously. The finite element model comprised 41 x 17 x 13 nodes and the duration of the time step was 45 sec. The total duration of the simulation was 9000 sec, thus 200 time steps were used. The cure kinetics and the thermal properties were incorporated as described in chapters 5 and 6. Eqs. 6.43-6.46 were employed for the incorporation of the thermal conductivity within each element. The starting point of the algorithm was the moment the bottom tool was at 130 °C. The initial thermal difference through the thickness was 30 °C according to the gradient measured during the RTM experiments.

The symmetry of the thermal properties and the boundary conditions allows only a quarter of the modelling domain to be considered. Two additional zero heat flux boundary conditions are required at mid-length and mid-width in order to implement this simplification. Thus, the final number of nodes is 21 x 9 x 13.

The three dimensional temperature and degree of cure distributions at different times into the cure are illustrated in Figs. 7.6-7.11. In all contour charts five equal divisions

are used. White shading corresponds to the maximum temperature or degree of cure and black to the minimum. Some slight asymmetries observed in the fractional conversion distributions (Figs. 7.9 and 7.11) at the beginning and end of the curing, when the degree of cure is almost uniform, are attributed to the interpolation algorithm used to produce the contour charts, since the data were symmetrical.

In all cases the temperature and degree of cure distributions are mainly one dimensional. The in-plane uniformity is disturbed near the sides of the mould (Figs. 7.6 and 7.7). This is attributed to the lower temperature at the ends of the top tooling due to the application of the natural air convection boundary condition on its sides. The extent of the in-plane thermal gradient is lower than 10 % of the corresponding dimension. The magnitude of the overall in plane thermal difference is approximately 5 °C at the initial stages of the cure, increases to 8 °C at the beginning of the isothermal segment and then decreases towards a steady state value of about 7 °C at the end of the cure (Fig. 7.6). Similarly, the magnitude of the fractional conversion difference becomes high (0.3) at the beginning of the isothermal segment due to the temperature difference during heating up and then decreases as the curing reaction inside the component becomes slower while the outside part continuous to react at a high rate (Fig. 7.7). A very low difference (about 0.01) is established at the end of the curing.

The transverse distributions along the width and length are qualitatively similar (Figs. 7.8-7.11). The temperature near the sides of the component is lower and consequently the cure progresses at a lower rate. The thermal difference along the thickness is significantly higher than the in-plane difference and extends across the whole component. Initially its value is 10 °C. At the beginning of the isothermal segment it increases to 15 °C and then decreases towards a steady state value of 7 °C towards the end of the cure (Figs. 7.8 and 7.10). Consequently, the gradient of fractional conversion in the thickness direction remains high (0.3) for a longer period (from 40 to 90 min) in comparison with the in-plane gradient (Figs. 7.8 and 7.11). These observations lead to the conclusion that the thermal and degree of cure gradients developed during the cure in the thickness direction are more important than the corresponding in-plane gradients.

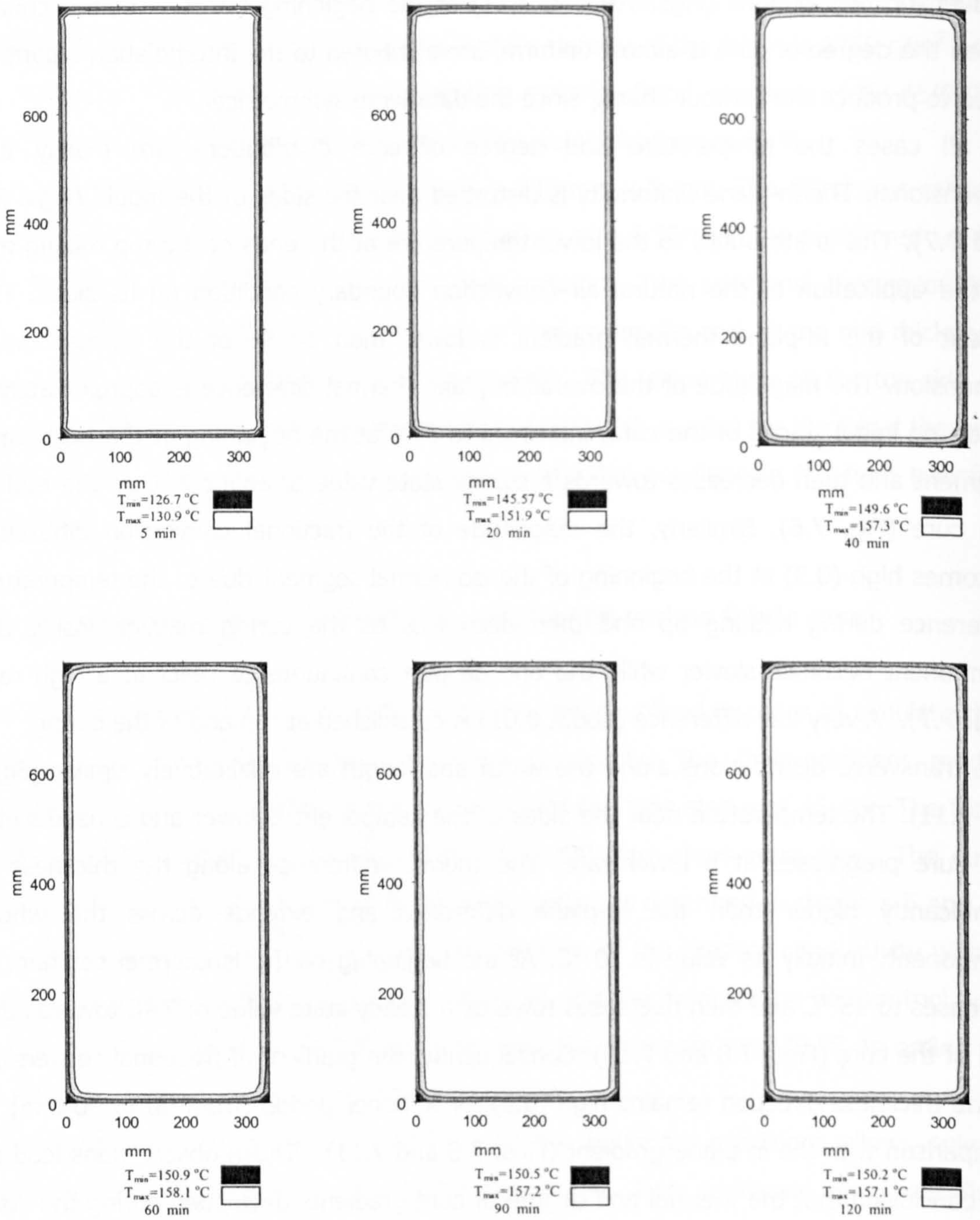

Fig.7.6 *In-plane temperature distribution at mid-thickness during the cure of a carbon/RTM6 composite*

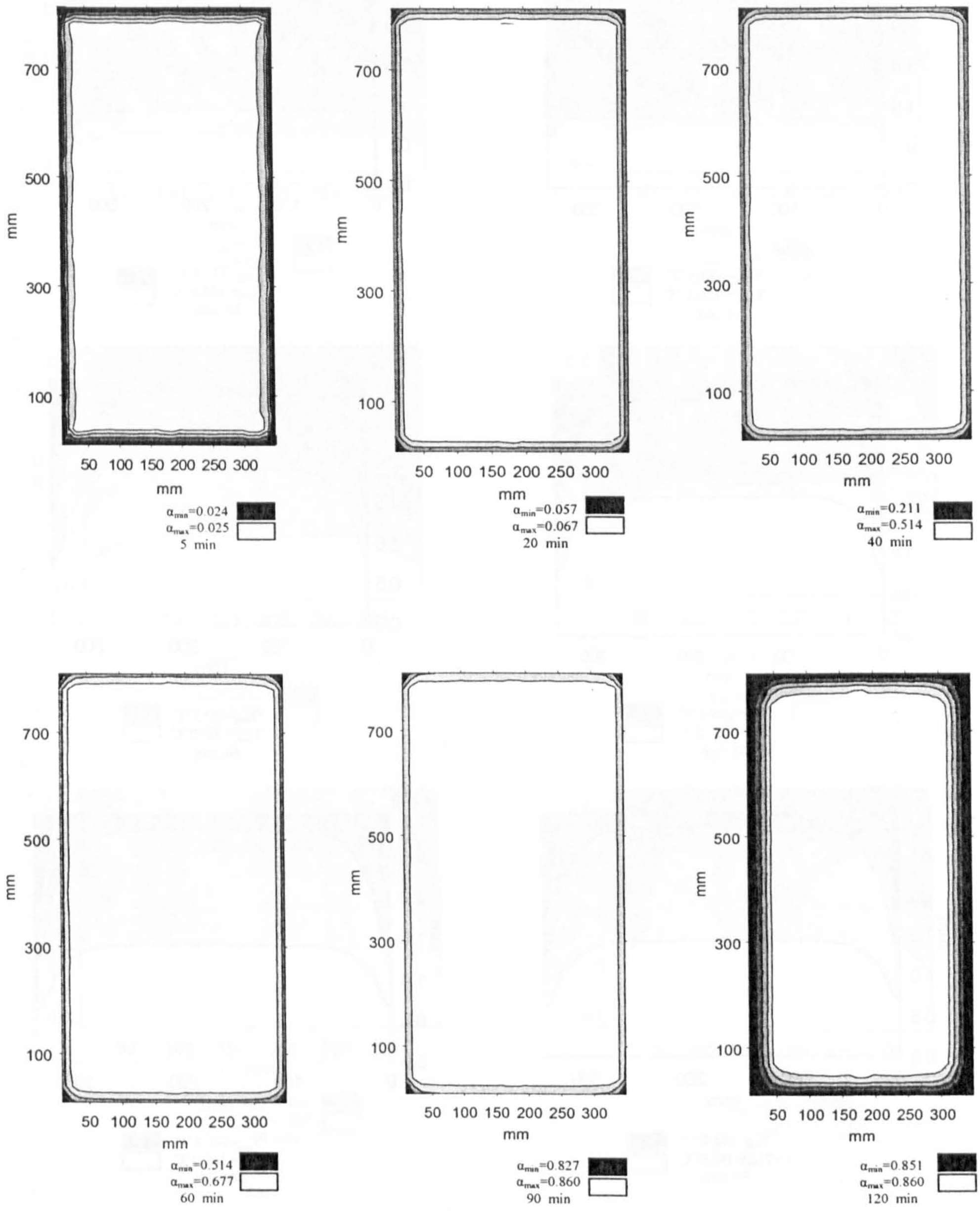

Fig.7.7 *In-plane degree of cure distribution at mid-thickness during the cure of a carbon/RTM6 composite*

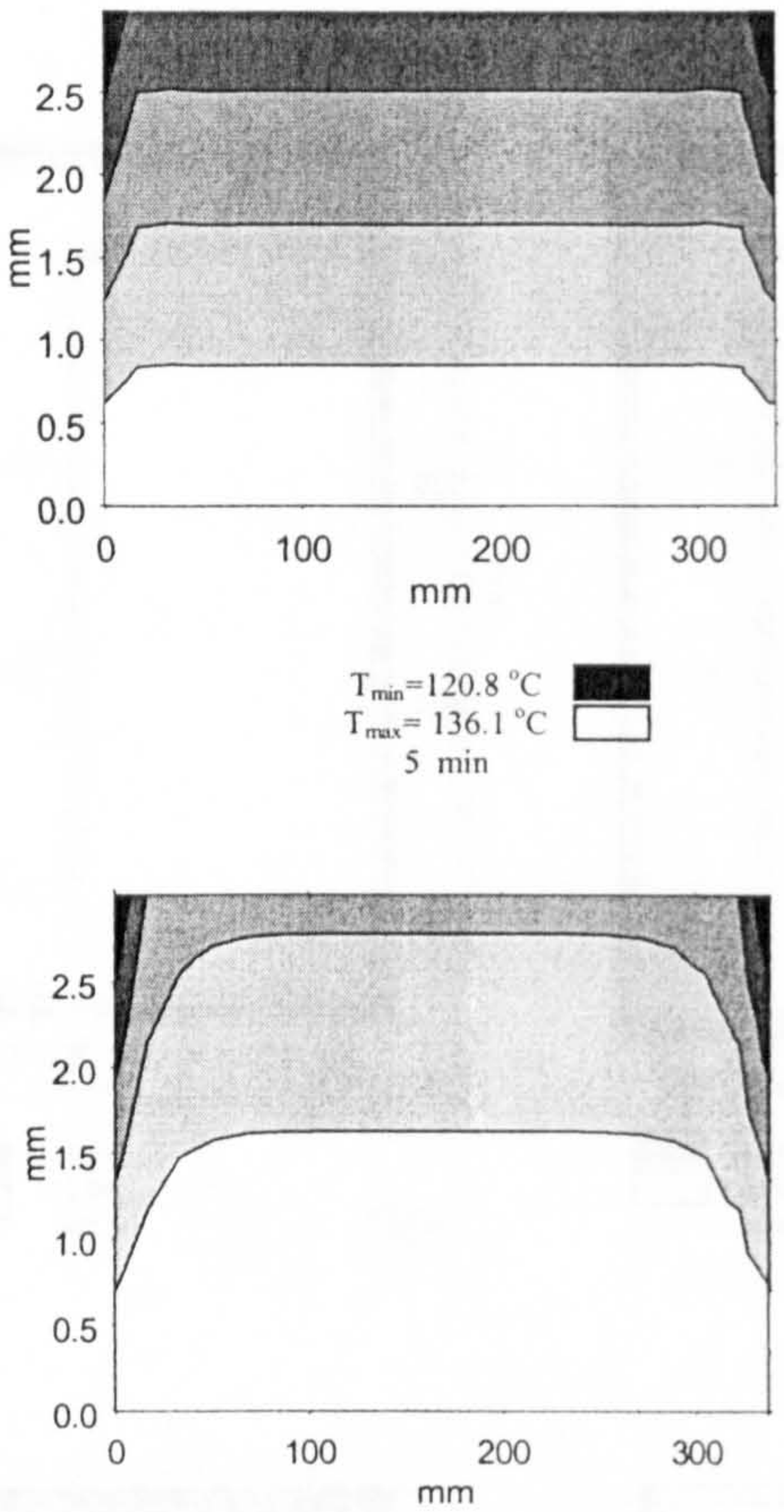

Fig.7.8 *Transverse temperature distribution at mid-length during the cure of a carbon/RTM6 composite*

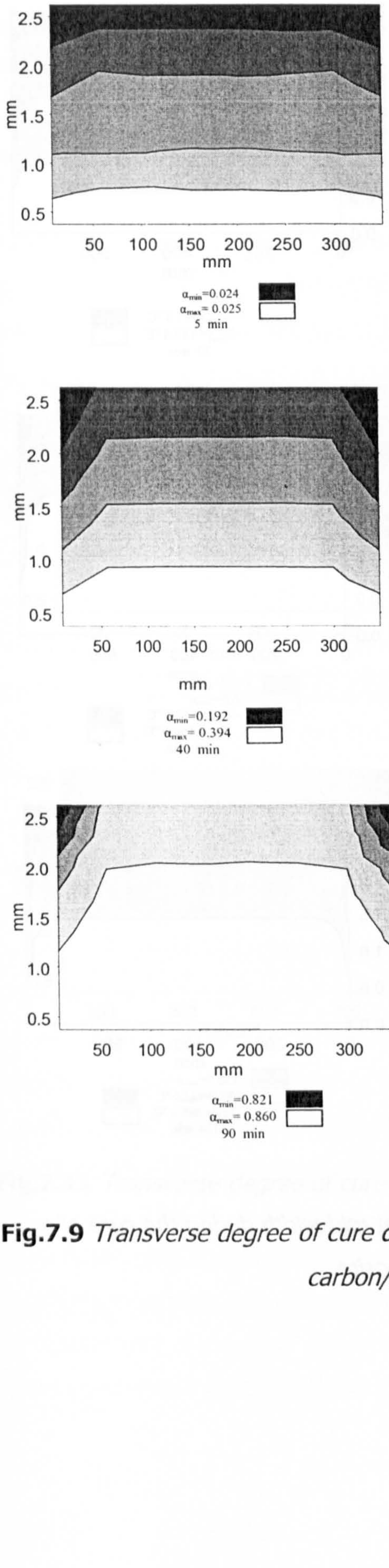

Fig.7.9 *Transverse degree of cure distribution at mid-length during the cure of a carbon/RTM6 composite*

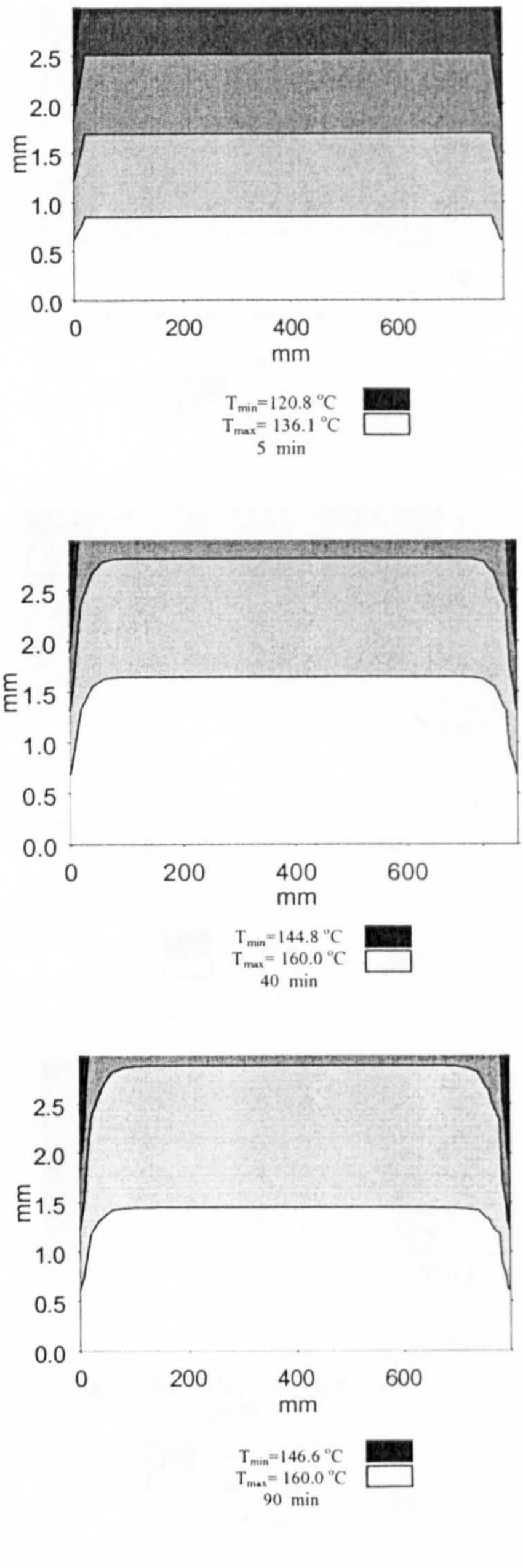

Fig.7.10 *Transverse temperature distribution at mid-width during the cure of a carbon/RTM6 composite*

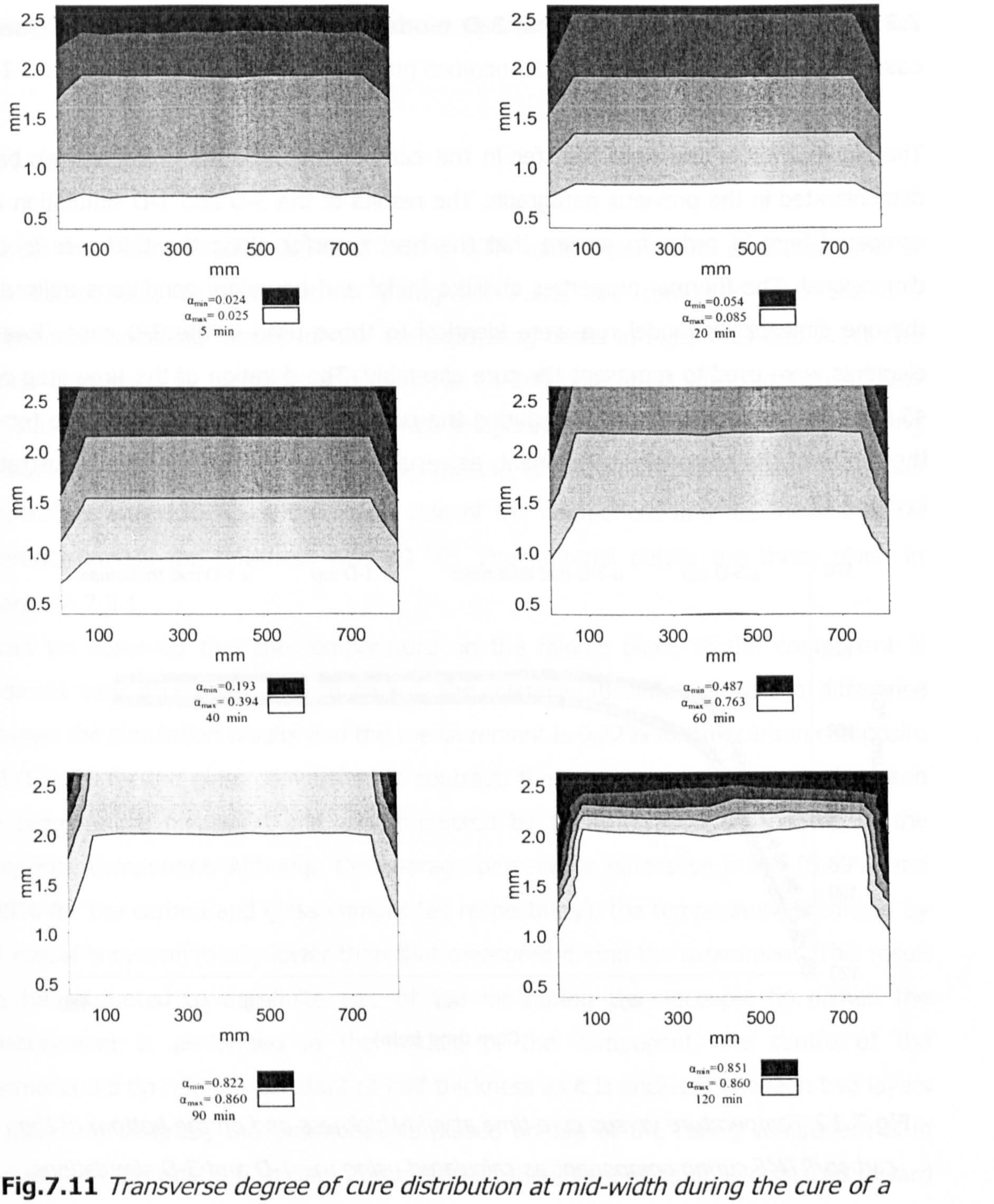

Fig.7.11 *Transverse degree of cure distribution at mid-width during the cure of a carbon/RTM6 composite*

7.3.3 Comparison of the 1-D and 3-D modelling results for the carbon fabric case

The significance of the heat transfer in the component thickness direction has been demonstrated in the previous paragraph. The results of the 3-D and 1-D simulation are compared here in order to ensure that the heat transfer along the thickness is one dimensional. The thermal properties and the initial and boundary conditions utilised in the one dimensional model run were identical to those used in the 3-D case. Twelve elements were used to represent the cure assembly. The duration of the time step was 45 sec. The temperature evolution during the cure at mid-thickness and on the top of the centre of the composite component, as resulting from the two models is illustrated in Fig. 7.12.

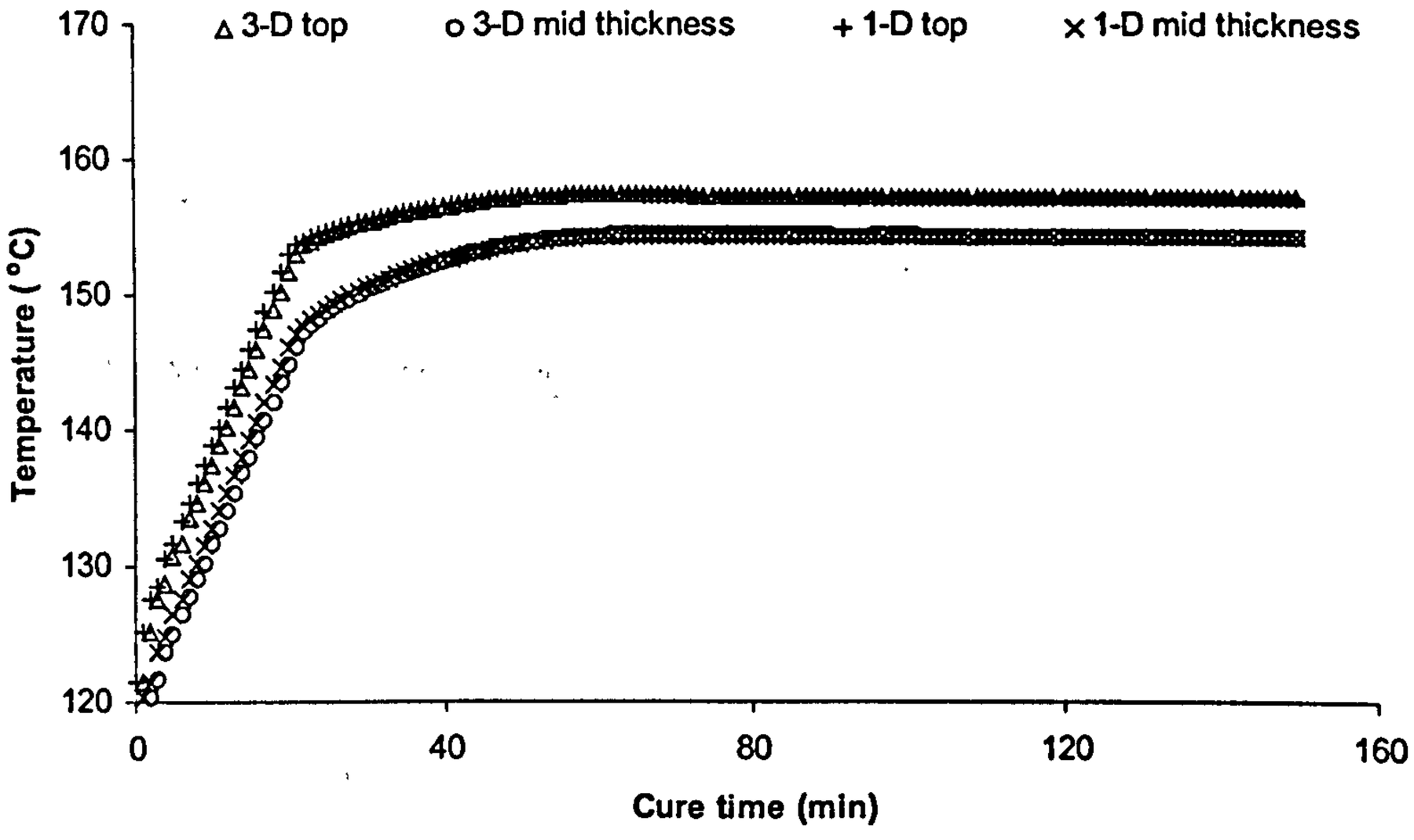

Fig.7.12 *Temperature versus cure time at mid-thickness and on the bottom of the carbon/RTM6 curing component as calculated using the 1-D and 3-D simulations*

It can be observed that the results of the two models are essentially identical. The average percentage difference is 0.05 %. Consequently, one dimensional modelling can be considered representative of the heat transfer in the geometries considered. This conclusion is valid for the glass fibre case also, since the lower axial thermal conductivity

of the glass in comparison with the carbon is expected to limit further the deviation from the 1-D situation in the sides of the curing component.

7.3.4 Validation of the model

Thermal monitoring results gathered during RTM cure experiments of carbon and of glass composites, as described in paragraph 7.3.1, are compared with the one dimensional modelling results for the corresponding cases in Figs. 7.13 and 7.14. The models comprised 12 elements and were run in 200 time steps with duration 45 sec. The boundary conditions were a predefined temperature at the lower side of the curing component and natural air convection on the top of the glass tooling plate. The initial temperature was 130 °C at the lower side of the component and the initial thermal difference across the thickness was 30 °C. The material details are those given in paragraph 7.3.1.

It can be observed that the temperature on the middle plane of the component is predicted very accurately in both cases. The average absolute percentage difference between the simulation results and the measurement is 0.32% for the carbon composite and 0.30 % for the glass composite. In contrast, there is a greater difference between the temperature measured and that predicted by the simulation on the top of the composite component. Although the average percentage difference is low (0.69% and 0.85% for the carbon and glass composites respectively), the temperature predicted by the model is systematically lower than that measured during the experiment. This result can be attributed to the finite size of the measuring thermocouple tip. When the measurement is performed in the middle of the component, the centre of the thermocouple tip remains constant at half thickness as it is enclosed between two layers of fabric. In contrast, the thermocouple placed on top of the curing component is in contact with the rigid top tooling. Consequently, the centre of its tip is displaced toward the lower side of the composite and the temperature it measures is higher than the one corresponding to the composite-tooling interface. Therefore, it can be concluded that the simulation predicts the temperature distribution with a satisfactory accuracy.

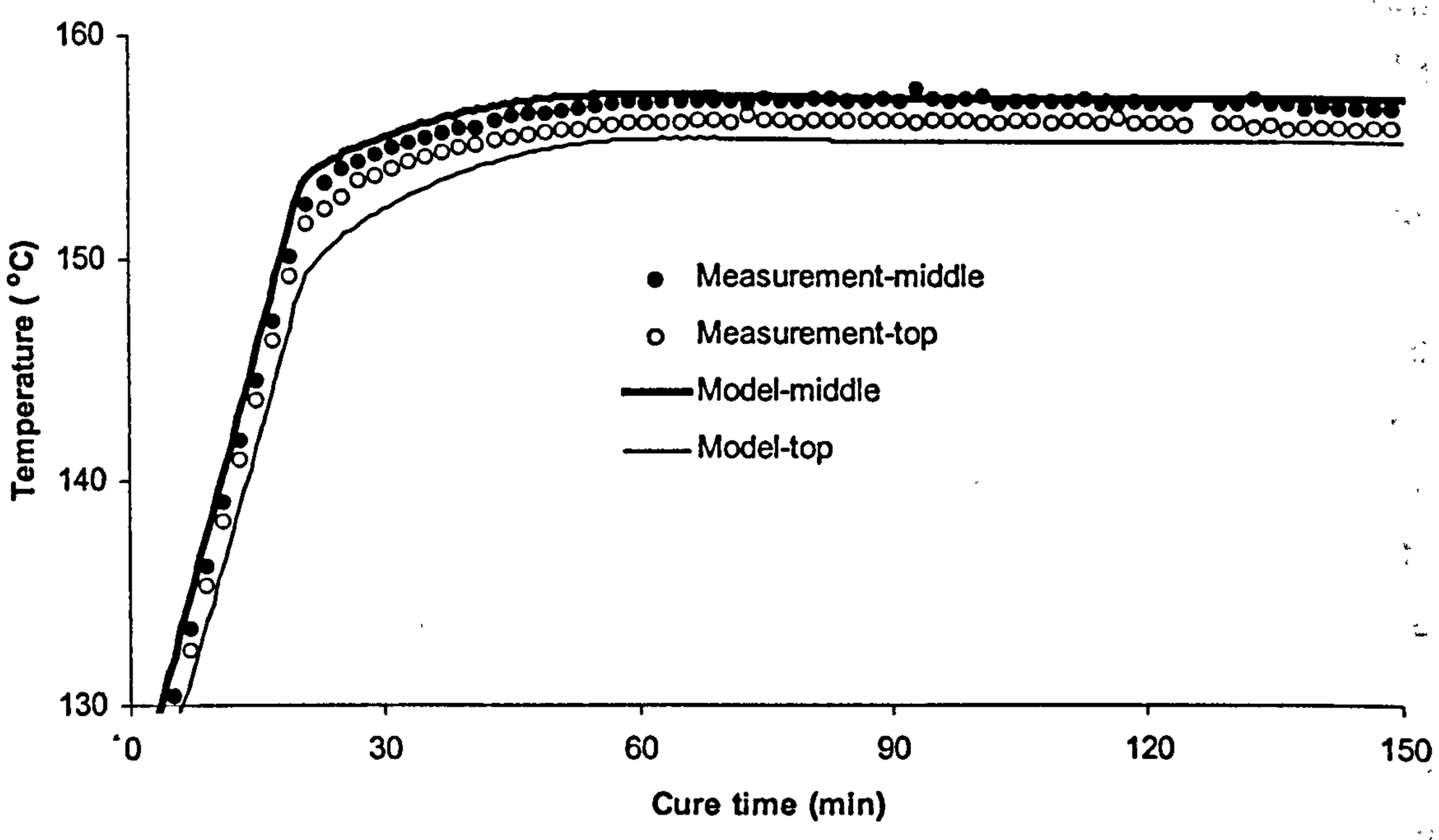

Fig.7.13 *Experimental and simulation temperature versus time curves corresponding to the cure of the carbon/RTM6 composite*

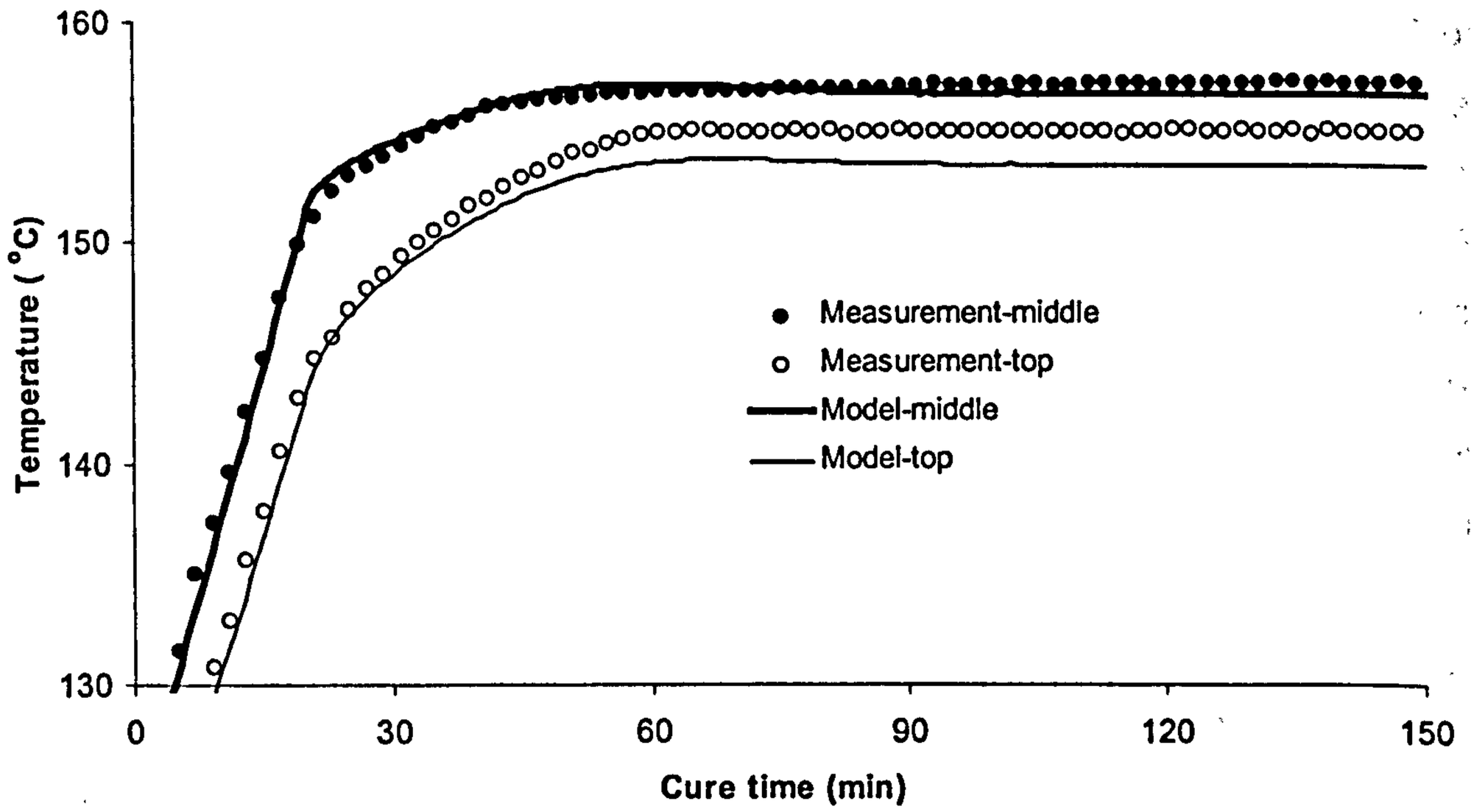

Fig.7.14 *Experimental and simulation temperature versus time curves corresponding to the cure of the glass/RTM6 composite*

7.3.5 One dimensional application of the model

The behaviour of a glass and of a carbon reinforced composite component during the cure using two types of top tooling (glass and aluminium) has been investigated. The details of the 1-D models were identical to those presented in section 7.3.4. The properties of the glass top tooling are given in Table 7.1, while the properties of the aluminium are presented in Table 7.2.

$c_p\left(J/g/^\circ C\right)$	$K\left(W/m/^\circ C\right)$	$\rho\left(g/cm^3\right)$	$h\left(W/m^2\right)$
0.90	160	2.7	2.5

Table 7.2 *Thermal properties of the aluminium top tooling*

The temperature at the nodes and the degree of cure in the elements as functions of cure time are given in Figs. 7.15 and 7.16 respectively, for the glass tooling moulding of the carbon composite. The corresponding curves for the aluminium top tooling case are illustrated in Figs 7.17 and 7.18.

It can be observed that there is a significant thermal gradient in both cases throughout the cure (Figs. 7.15 and 7.17). The temperature in the component decreases as the distance from the bottom tool increases. When the bottom of the composite reaches the temperature of the isothermal segment, the rest of the component continues to heat up until a steady state is established. The time at which the steady state is reached increases with increasing distance from the bottom. The temperature distribution appears wider in the case of the glass top tool. This fact is attributed to the lower heat transfer coefficient corresponding to a metallic surface in comparison with a glass surface. As more heat is released to the environment when the glass top is used, the difference of the temperature on the top and of the temperature on the bottom is higher.

Similarly, the degree of cure shows a significant variation along the thickness during the cure (Figs. 7.16 and 7.18). Initially the fractional conversion gradient increases with time as a result of the cumulative effect of the temperature difference. After a point the reaction deceleration at locations where a high conversion has been achieved causes a

decrease in the conversion gradient, since areas of the component which have a lower conversion continue to react at a high rate. Towards the end of the cure a very low overall gradient in conversion is established (about 1%).

Features of the heat transfer behaviour, which have some special interest in practical terms, are the thermal gradients and the spatial distribution of vitrification times; the former because it is connected to the development of residual stresses in the component and the latter because it controls the duration of the curing stage. The thermal gradient at different location in the component as a function of time is illustrated in Figs. 7.19 and 7.20 for the glass and aluminium top tooling cases respectively. In the glass tool case the thermal gradient increases during heating up due to the temperature lag of the higher areas of the component, whereas its distribution along the thickness is uniform. In the isothermal segment the thermal gradient decreases towards a steady state value. Lower areas of the component have lower thermal gradient as a result of the exothermic character of the cure. As the reaction is faster near the bottom heating surface, the lower levels of the component tend to reach the isothermal temperature and the subsequent minimal gradient faster than the higher levels of the component. With completion of the reaction a steady state uniform value of about 2 °C/mm is established. The thermal gradient distribution in the aluminium top case shows similar behaviour; in this case the lower heat transfer coefficient causes a decrease in thermal gradient from the beginning of the cure. The thermal gradient established at the end of the curing is significantly lower (about 1 °C/mm)

The distributions of vitrification times in the component as estimated by the step in heat capacity, calculated by the appropriate submodel, for the glass and aluminium tooling cases are illustrated in Fig. 7.21. It can be observed that vitrification occurs 20 min later on the top side of the component in the case of glass tooling. The vitrification lag is lower (about 10 min) when the aluminium plate is used due to the existence of smaller thermal gradients.

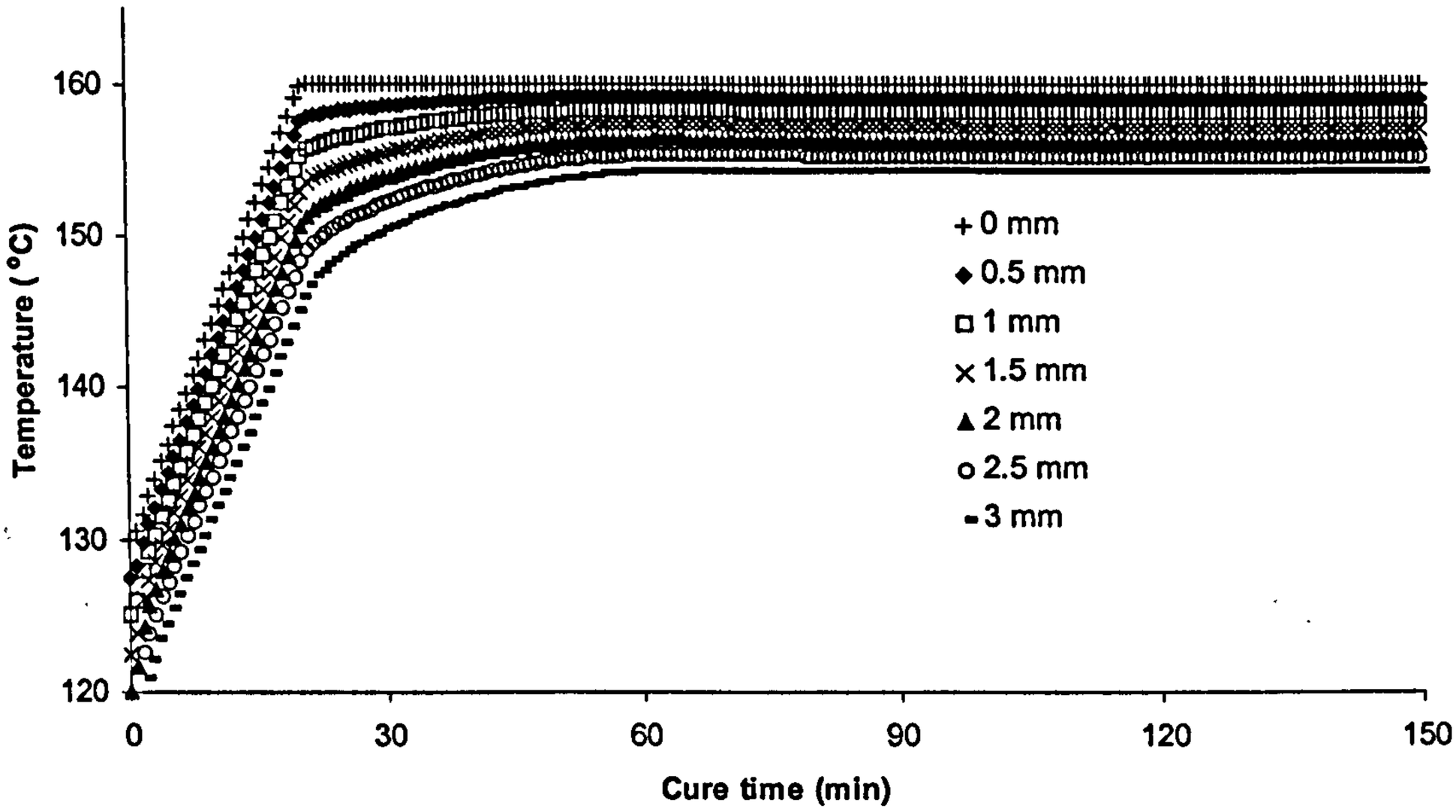

Fig.7.15 *Temperature as a function of cure time at different levels in the carbon/RTM6 composite in the case of glass top tooling*

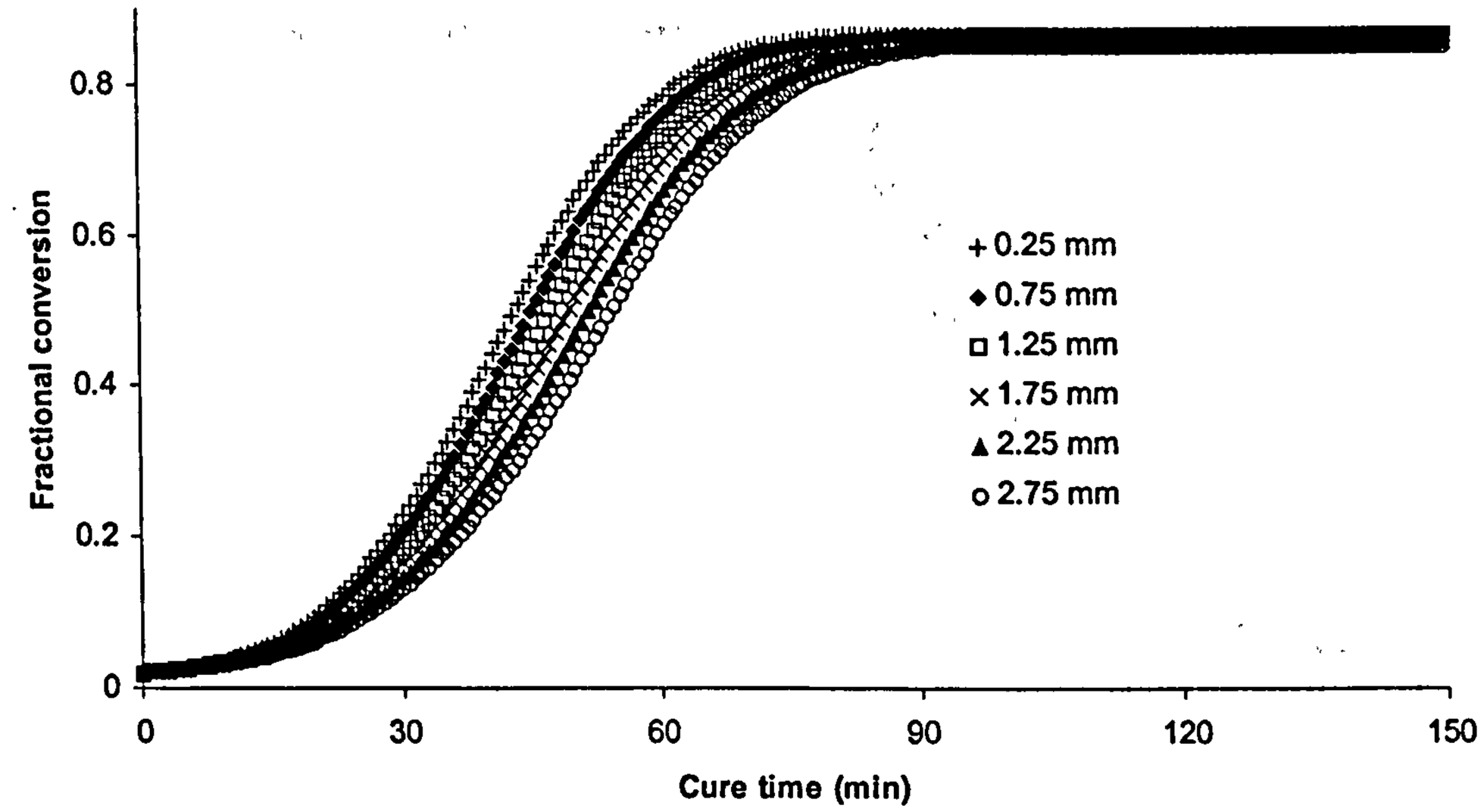

Fig.7.16 *Degree of cure as a function of cure time at different levels in the carbon/RTM6 composite in the case of glass top tooling*

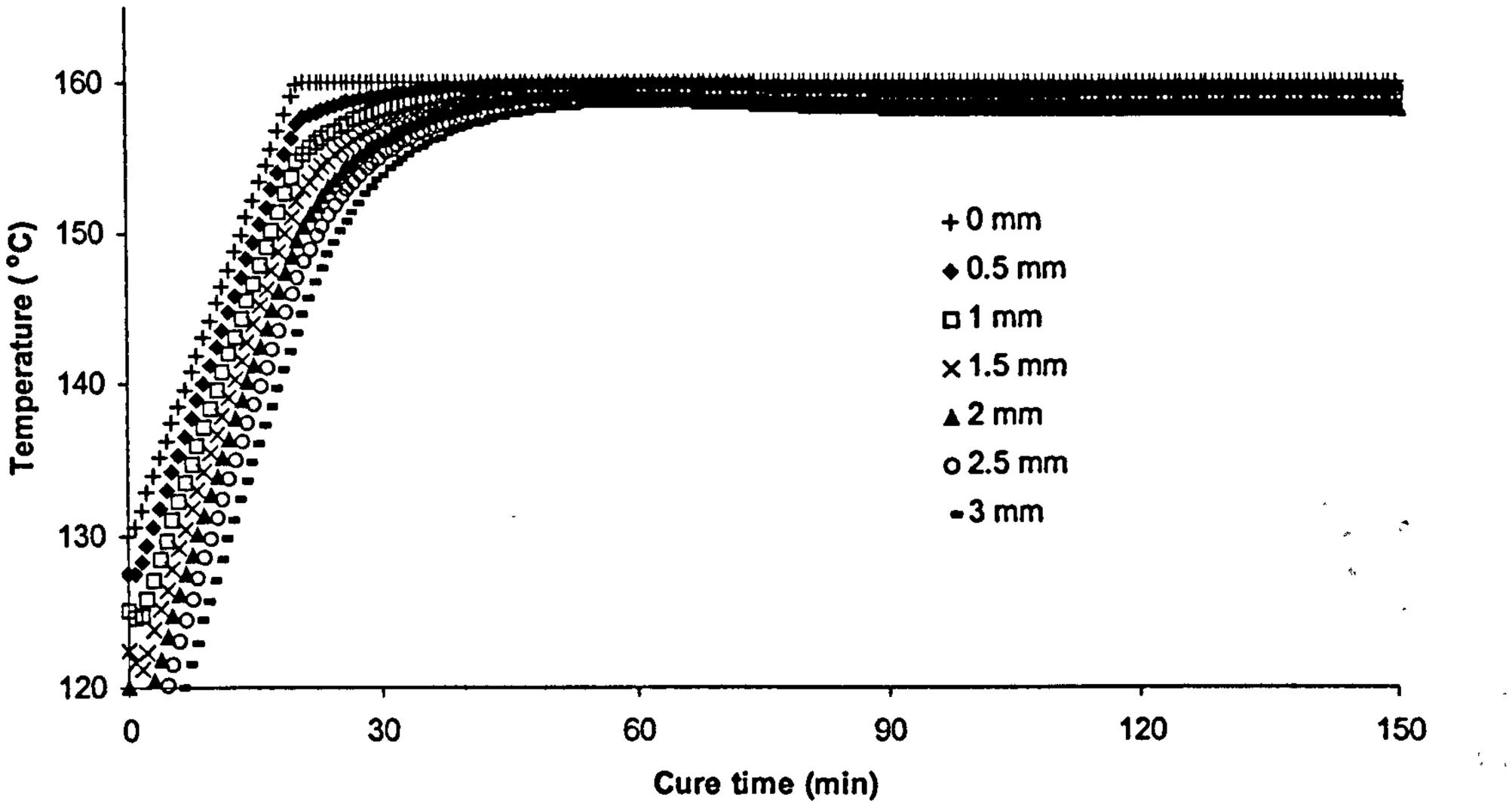

Fig.7.17 *Temperature as a function of cure time at different levels in the carbon/RTM6 composite in the case of aluminium top tooling*

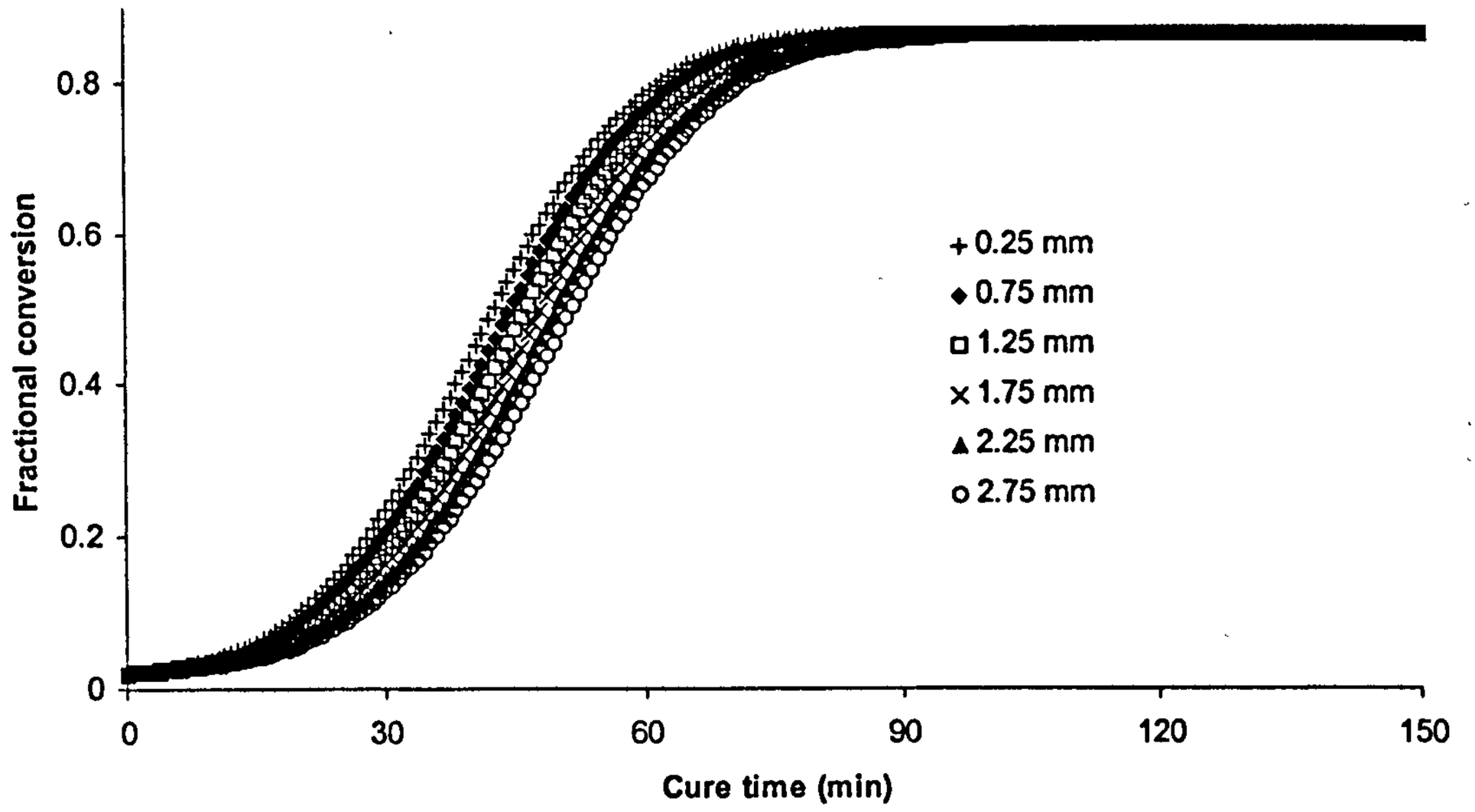

Fig.7.18 *Degree of cure as a function of cure time at different levels in the carbon/RTM6 composite in the case of aluminium top tooling*

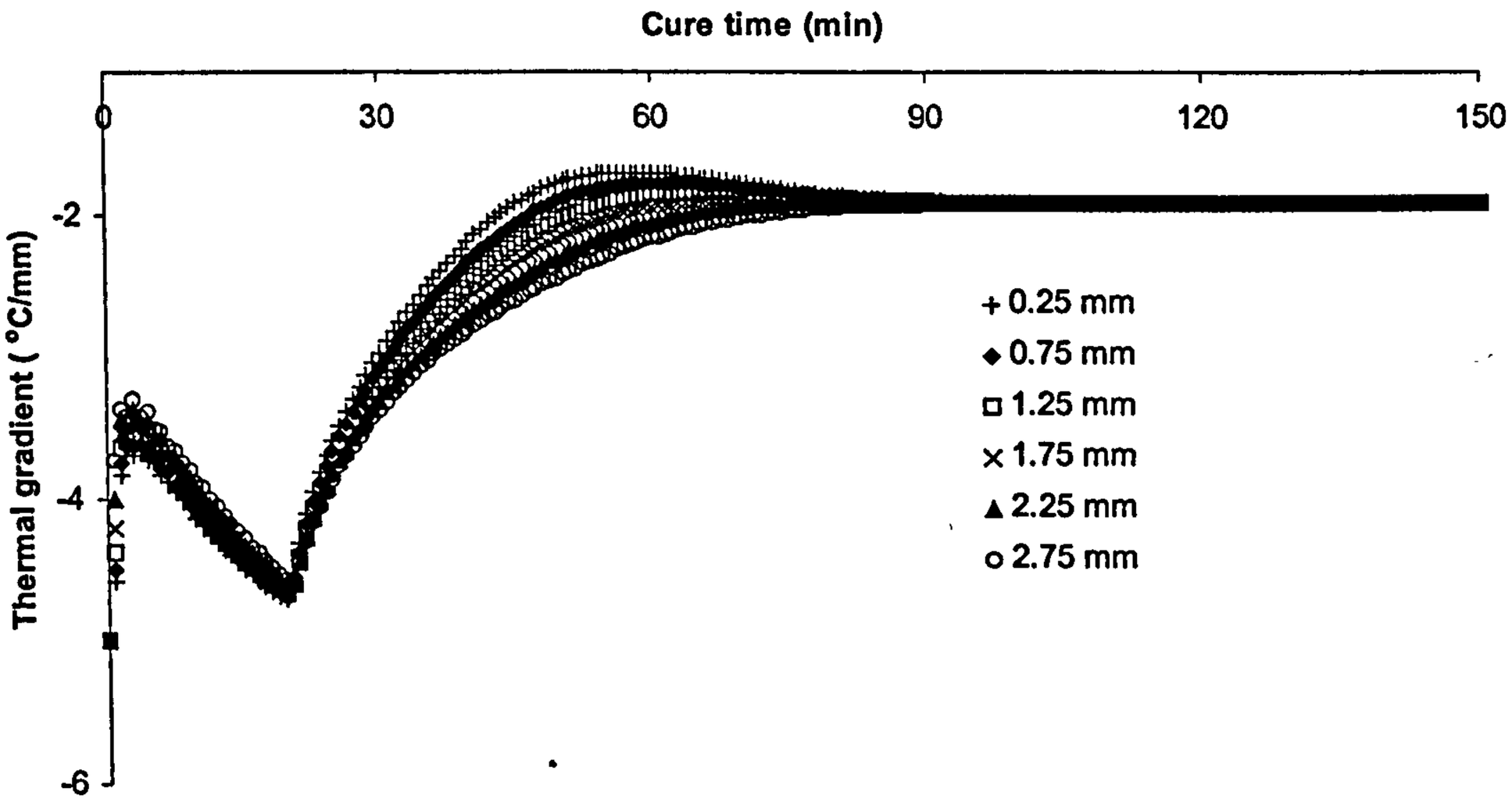

Fig.7.19 *Thermal gradient as a function of cure time at different levels in the carbon/RTM6 composite in the case of glass top tooling*

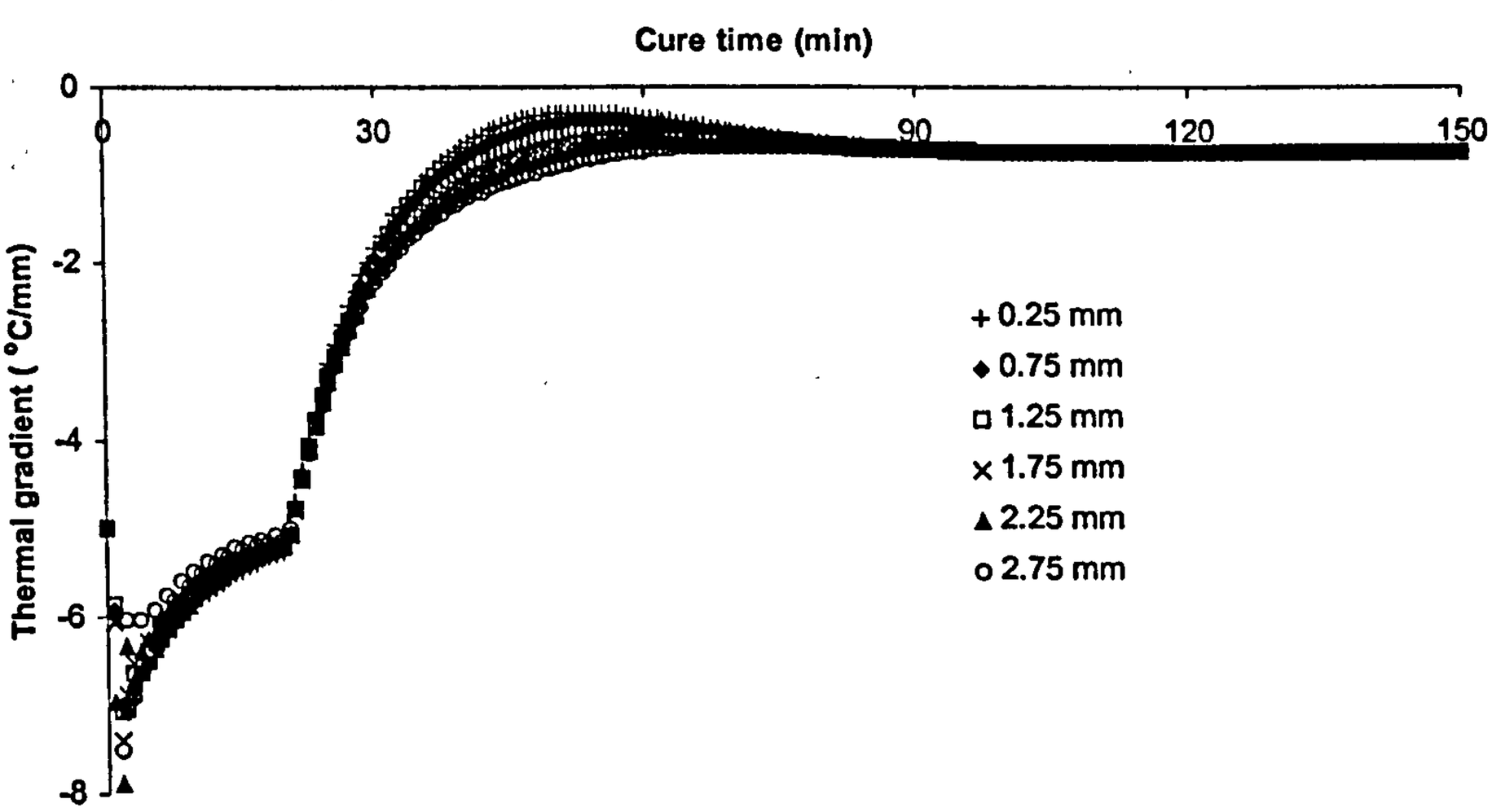

Fig.7.20 *Thermal gradient as a function of cure time at different levels in the carbon composite/RTM6 in the case of aluminium top tooling*

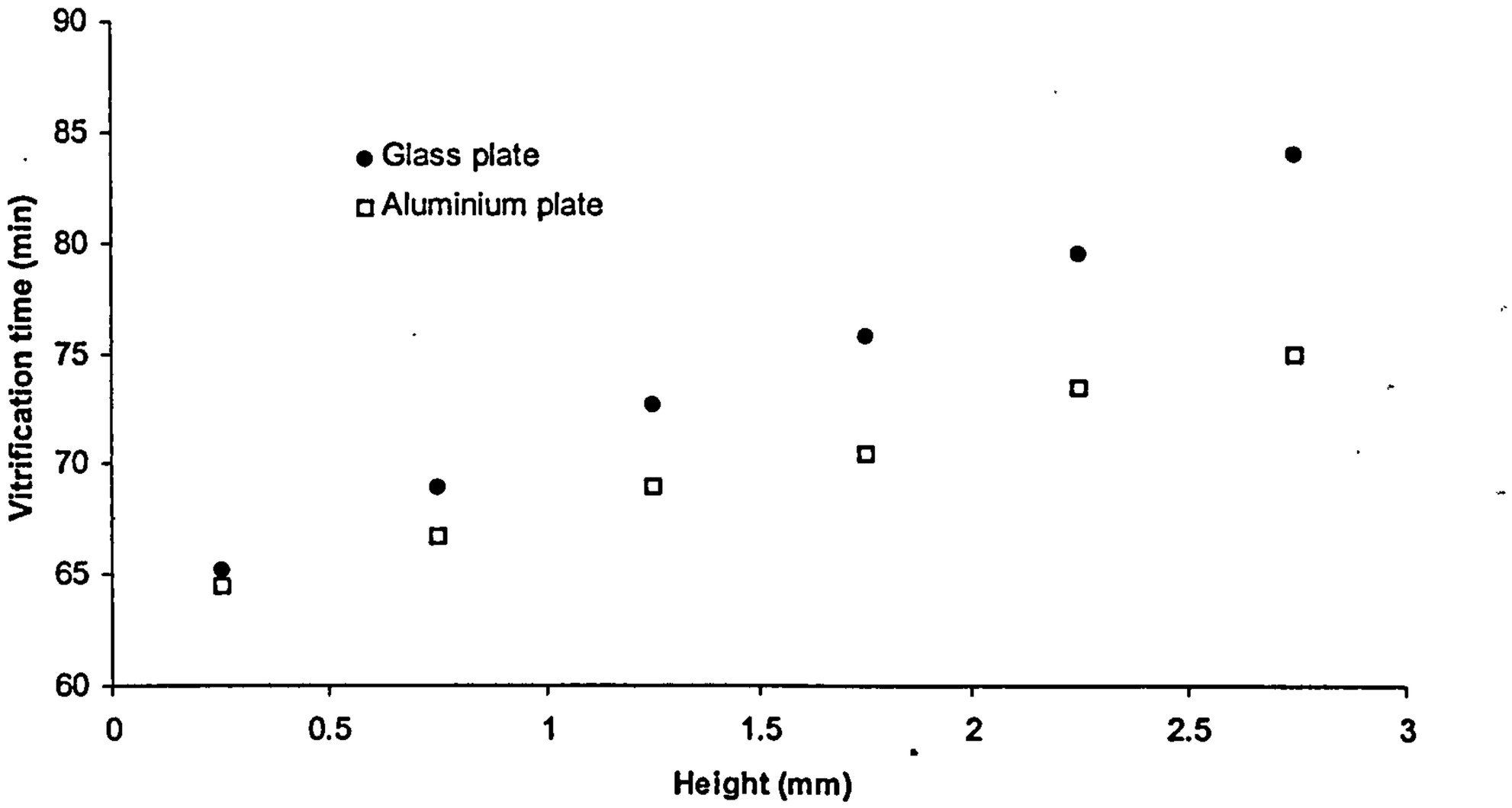

Fig.7.21 *Onset of the step in heat capacity at different levels in the carbon/RTM6 composite*

The behaviour of the glass reinforced composites is presented in Figs. 7.22-7.28. The characteristics are qualitatively identical to those of the carbon-fabric case. Significant thermal (Figs. 7.22 and 7.24) and degree of cure (Figs. 7.23 and 7.25) gradients are developed in both tooling cases (glass and aluminium). The magnitude of gradients is higher in the glass composite (Figs. 7.26 and 7.27) in comparison with the carbon composite due to its lower fibre volume fraction (0.45 in contrast to 0.59), although the radial thermal conductivity of the glass fibre is higher. As a result of the greater thermal gradients the distribution of vitrification times is slightly wider as can be seen in Fig. 7.28 (22 and 12 minutes for the glass and aluminium tool cases respectively).

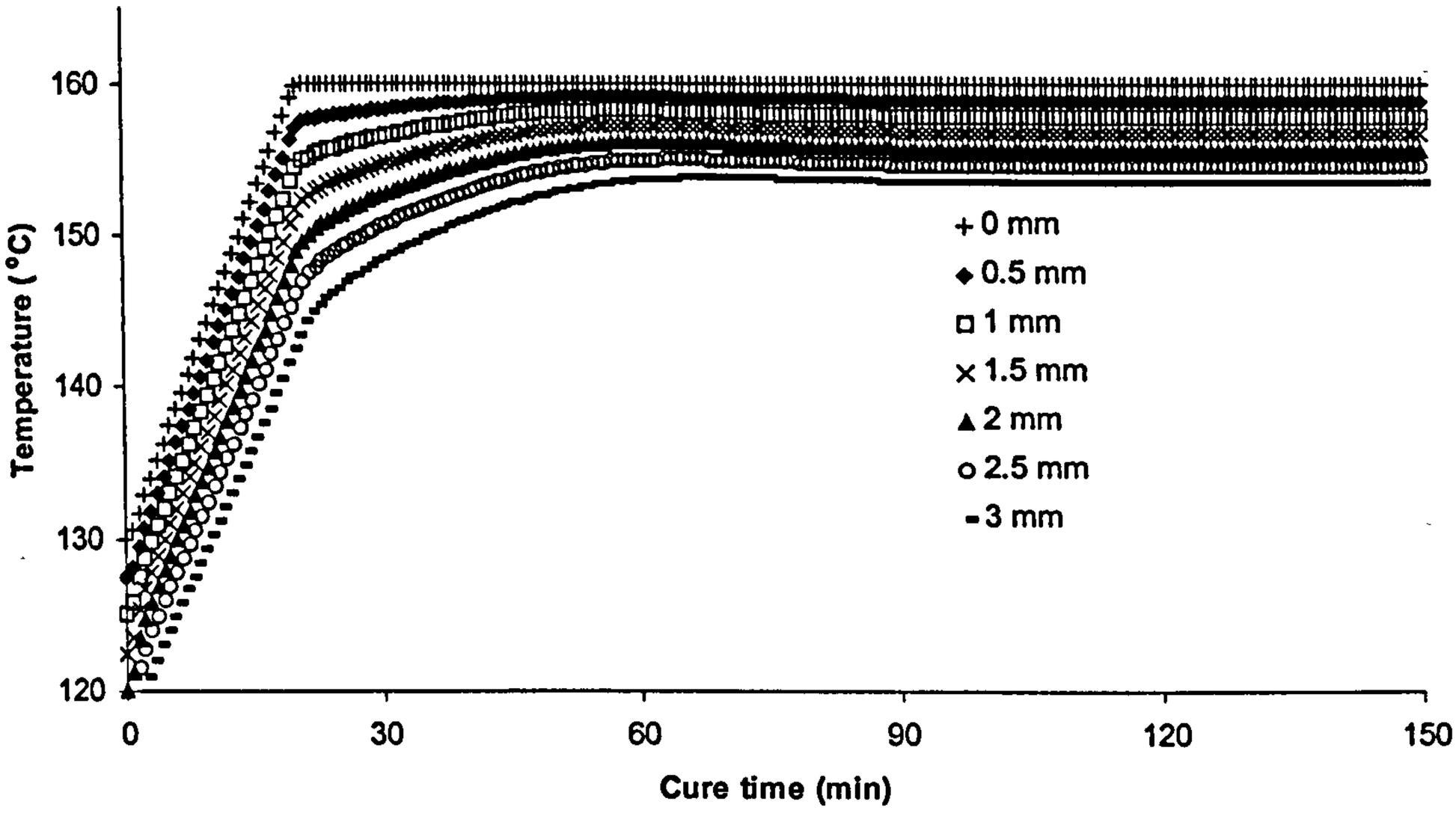

Fig.7.22 *Temperature as a function of cure time at different levels in the glass/RTM6 composite in the case of glass top tooling*

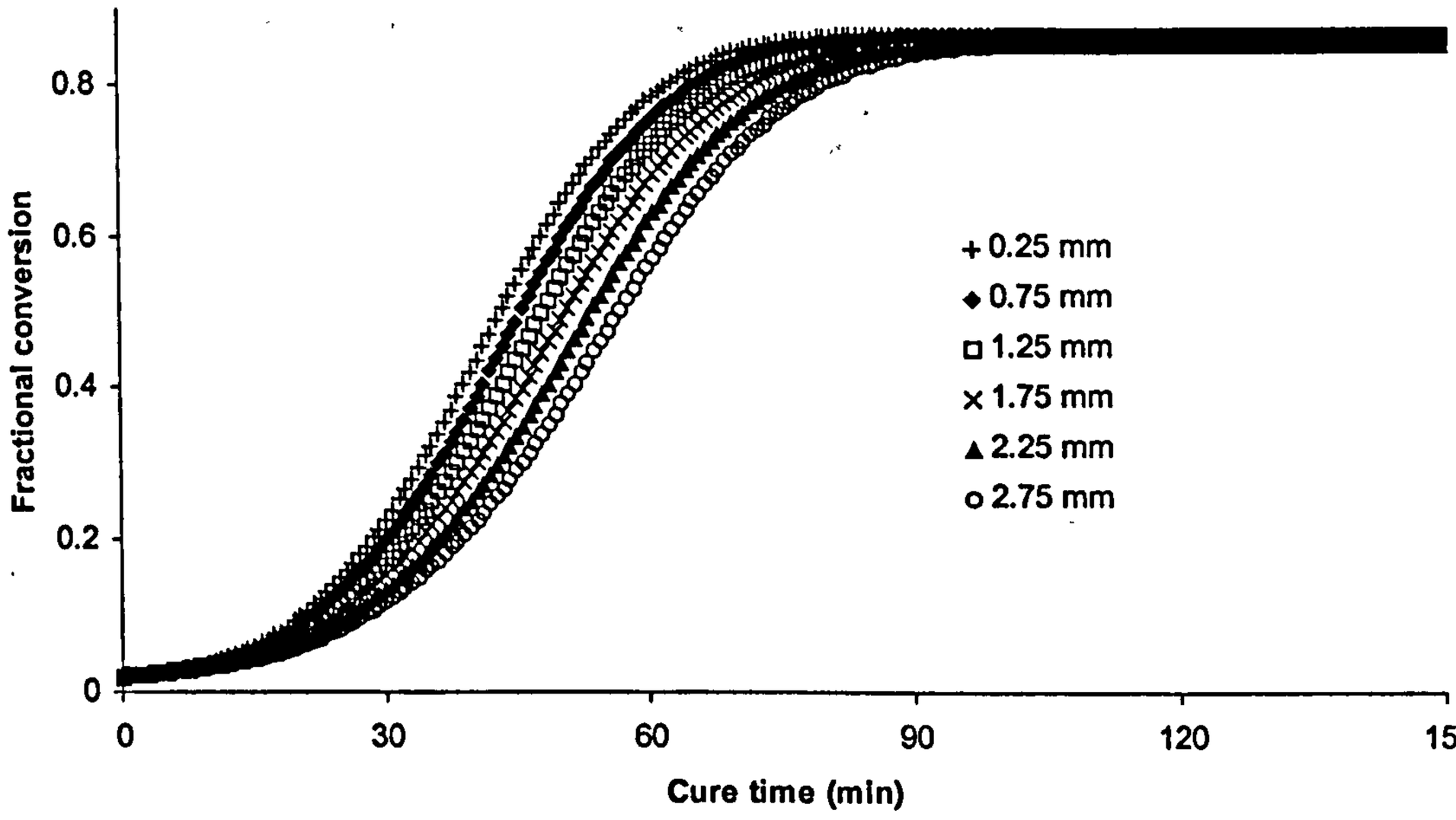

Fig.7.23 *Degree of cure as a function of cure time at different levels in the glass/RTM6 composite in the case of glass top tooling*

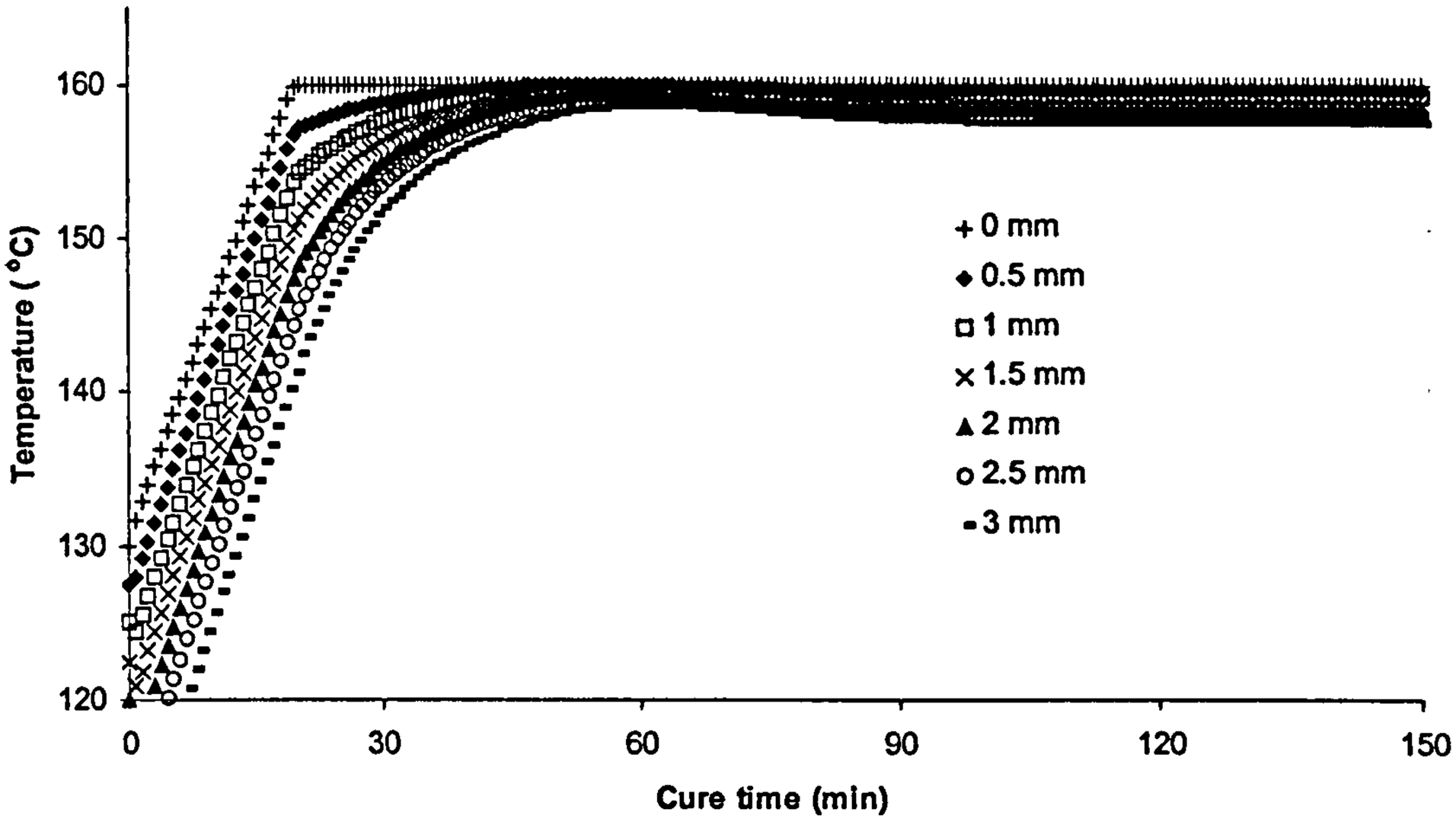

Fig.7.24 *Temperature as a function of cure time at different levels in the glass/RTM6 composite in the case of aluminium top tooling*

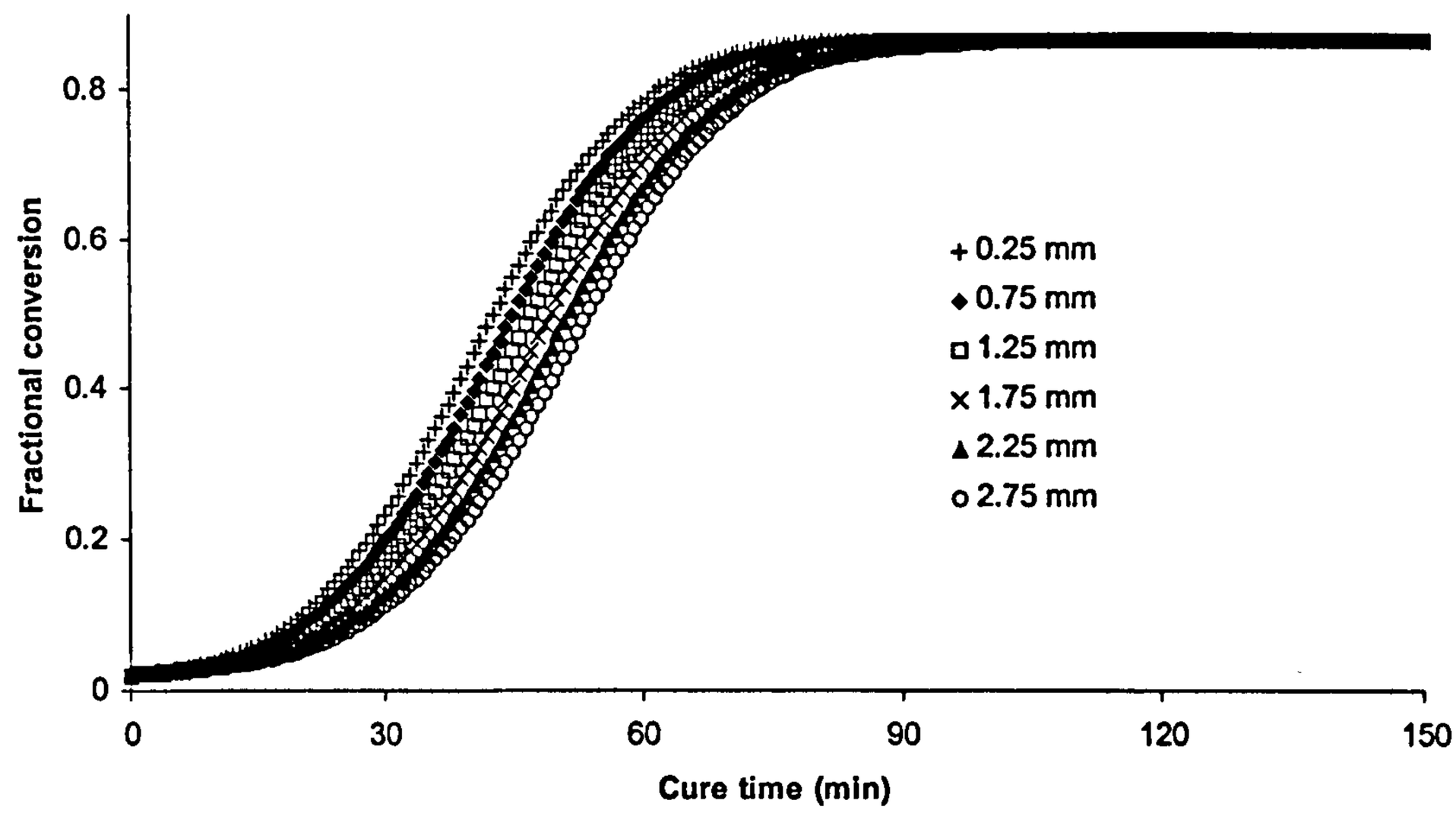

Fig.7.25 *Degree of cure as a function of cure time at different levels in the glass/RTM6 composite in the case of aluminium top tooling*

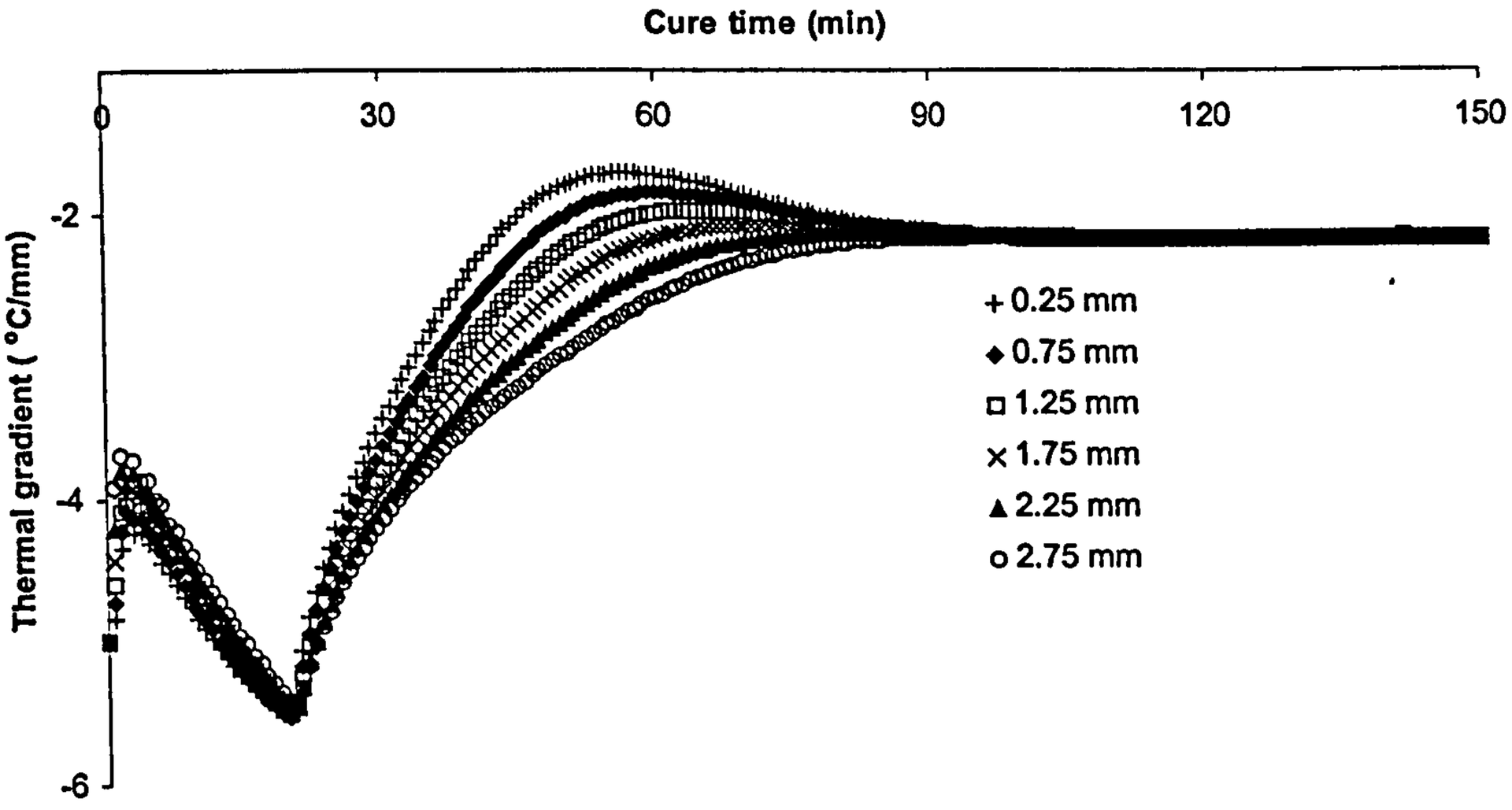

Fig.7.26 *Thermal gradient as a function of cure time at different levels in the glass/RTM6 composite in the case of glass top tooling*

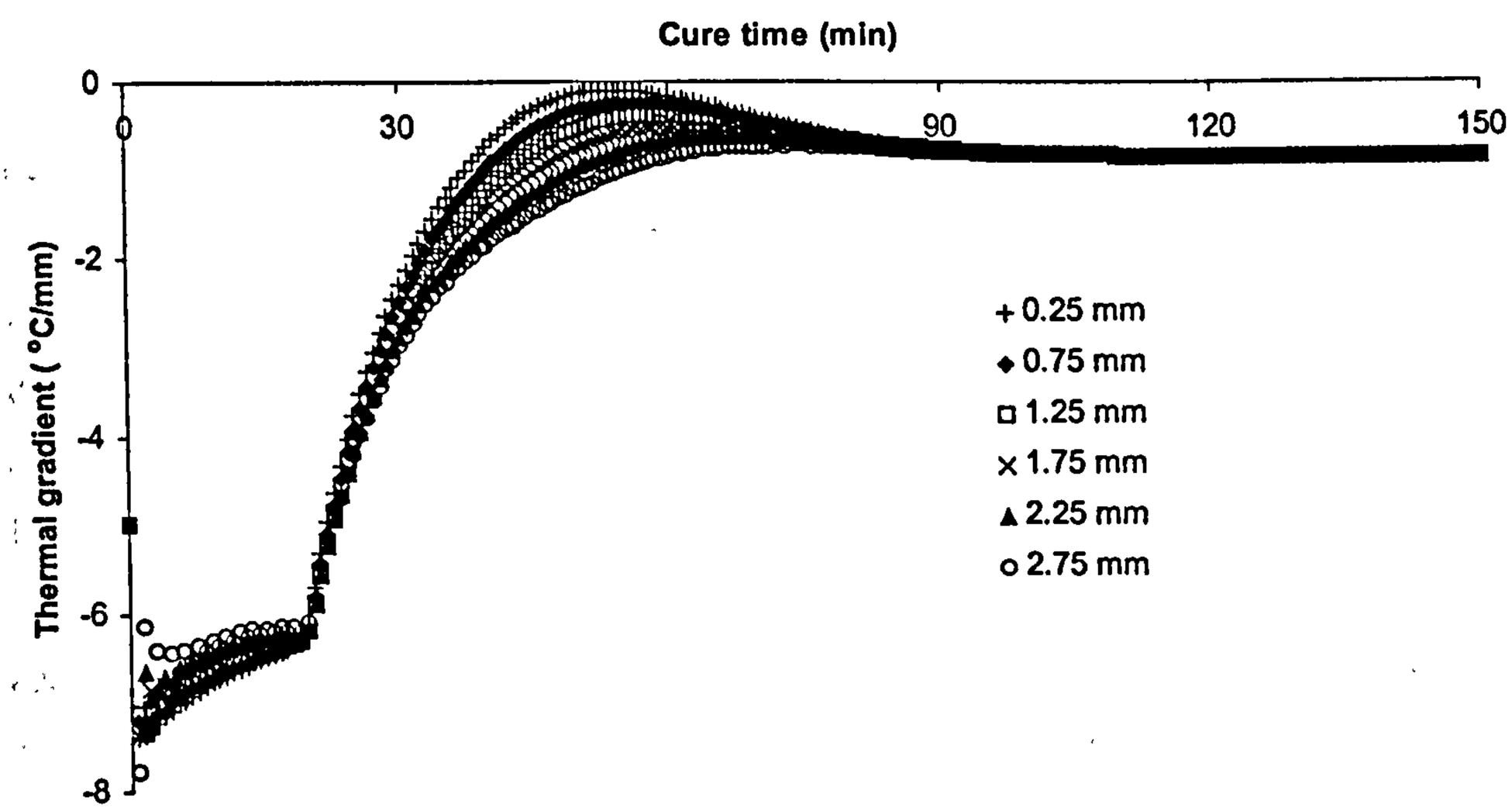

Fig.7.27 *Thermal gradient as a function of cure time at different levels in the glass/RTM6 composite in the case of aluminium top tooling*

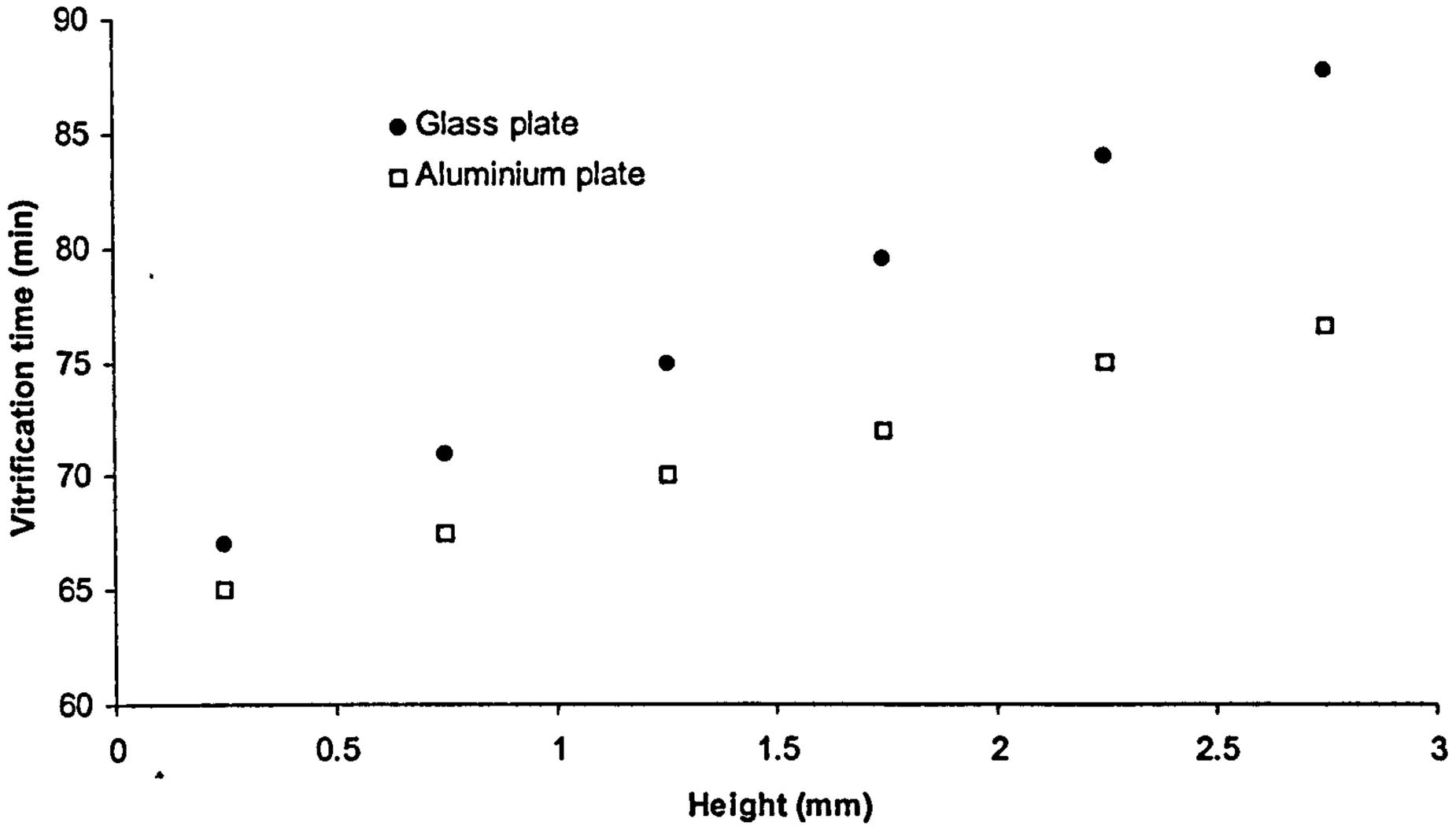

Fig.7.28 *Onset of the step in heat capacity at different levels in the glass/RTM6 composite*

7.4 Overview

The heat transfer model was validated and applied to the case of RTM curing of carbon and glass fibre reinforced/RTM6 composites. The numerical convergence of the simulation was tested and an appropriate range of parameters (time step duration, transverse elements size and in-plane elements size), where convergence is ensured, was found. RTM carbon and glass reinforced composites cure experiments were performed. The comparison of monitoring results with simulation results showed that the model operates with a satisfactory accuracy.

Three dimensional and one dimensional simulations were performed. In the geometries considered, heat transfer phenomena can be represented by the one dimensional model as the in-plane temperature and degree-of-cure distributions were found to be approximately uniform.

As a case study the one dimensional version of the model was used in order to investigate the temperature and degree-of-cure through the thickness distributions during the cure of carbon and glass reinforced composites using different tooling. Significant gradients in both temperature and conversion were observed. These

gradients were higher in the glass composite case in comparison to the carbon and lower in the aluminium top tool plate in comparison to glass. Further application of the model will be reported in chapter 10 where the inverse solution of the heat transfer problem will be described.

Chapter Eight

8 Impedance cure monitoring

8.1 Introduction

In this chapter results from the application of impedance cure monitoring are reported. The technique has been used to monitor both isothermal and dynamic cure of RTM6 epoxy resin. The aim of cure monitoring is to give an accurate estimate of the progress of reaction preferably in-situ and in real time. Since both temperature and degree of cure affect the dielectric and impedance signals, a way to separate their effect is required for industrial composites production monitoring. A method that enables this separation to be made is presented here. The manifestation of structural phenomena like vitrification in the impedance signal is also investigated.

8.2 Experimental details

Impedance measurements were performed using a Solartron SI 1260 frequency response analyser. The instrument communicated with a computer via an IEEE interface. A purpose built software code developed in 1997 by Dr P. I. Karkanas has been utilised to drive the frequency response analyser and collect the raw data.

Commercial sensors (GIA) comprising an assembly of interdigitated electrodes printed on a polymeric film were used in this study. For an illustration of this type of sensors see

Fig. 3.9. After soldering on the cables that connect the analyser to the sensor, the sensor was immersed in a glass tube containing liquid resin. Then the glass tube was placed in a hollow copper cylinder surrounded by heating elements, which were controlled by a Eurotherm temperature controller. A control thermocouple was placed in a hole on the wall of the hollow cylinder. A second thermocouple was placed in the glass tube in order to record the actual thermal profile of the resin.

In all measurements shielded cables were used. Where for flexibility purposes or due to size limitations the use of unshielded wires was necessary, shielding was provided by enclosing the wires in aluminium foil, which was subsequently connected to the earth of the analyser. In all cases the capacitance of the system before connecting the sensor was 50-100 fF, which is negligible in comparison with the air capacitance measured by the sensor (usually in the order of 10 pF). It should be noted that using unshielded cables even with a length in the order of 10 cm results in an open circuit capacitance of some pFs. This capacitance is sensitive to the relative position of the cables and adds a significant and non reproducible error to the measurement.

All experiments were duplicated in order to avoid accidental errors. The measurements were performed in the frequency range between 1 Hz and 1 MHz. Twenty-five frequencies were swept on a logarithmic scale.

8.3 Experimental results

8.3.1 Isothermal experiments

Isothermal cure experiments on RTM6 epoxy resin were performed at 130, 140, 150 and 160 °C. The evolution of real and imaginary impedance spectra during the cure at 150 and 130 °C is illustrated in Figs. 8.1 and 8.2 respectively. The results of isothermal experiments at 140 and 160 °C show equivalent behaviour.

It can be observed that the real impedance spectrum comprises a plateau at low frequencies and a region where the impedance decreases as the frequency increases. The latter region starts as a linear decrease, which becomes less intense towards very high frequencies, indicating the existence of another plateau at frequencies beyond 1 MHz. The imaginary impedance spectrum comprises three linear regions separated by a

minimum and a maximum. At very low frequencies imaginary impedance decreases with frequency, reaches a minimum value and then increases up to a maximum. Further increase of the frequency results in a linear decrease of the imaginary impedance logarithm.

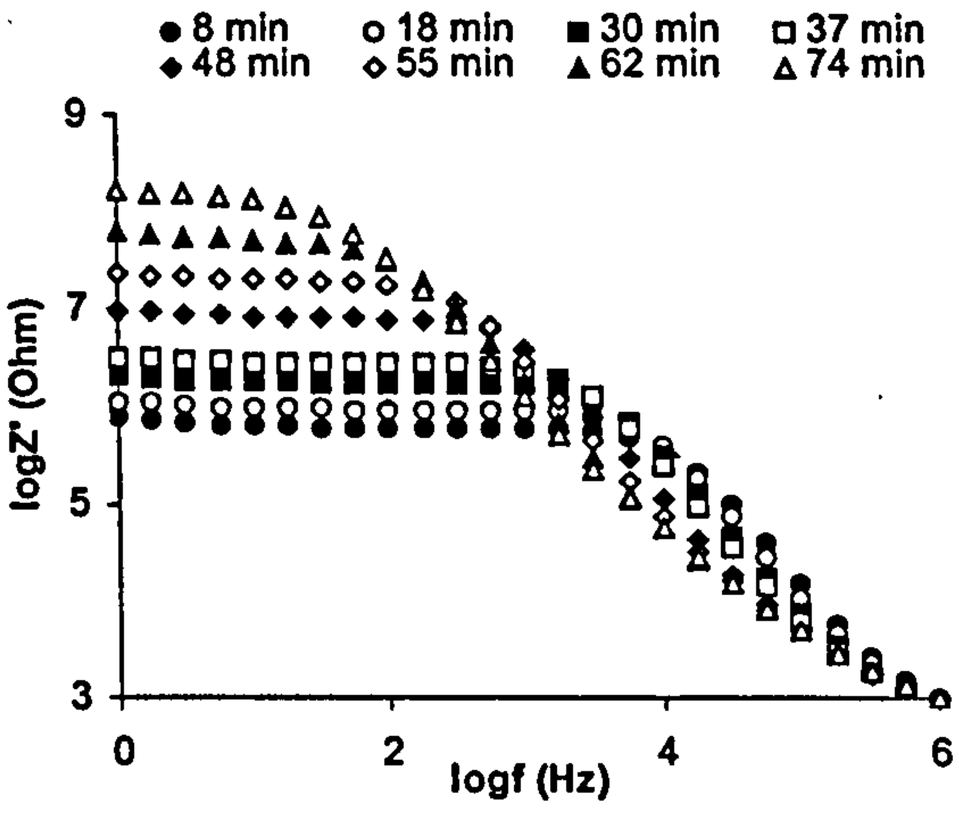

(a) Real impedance

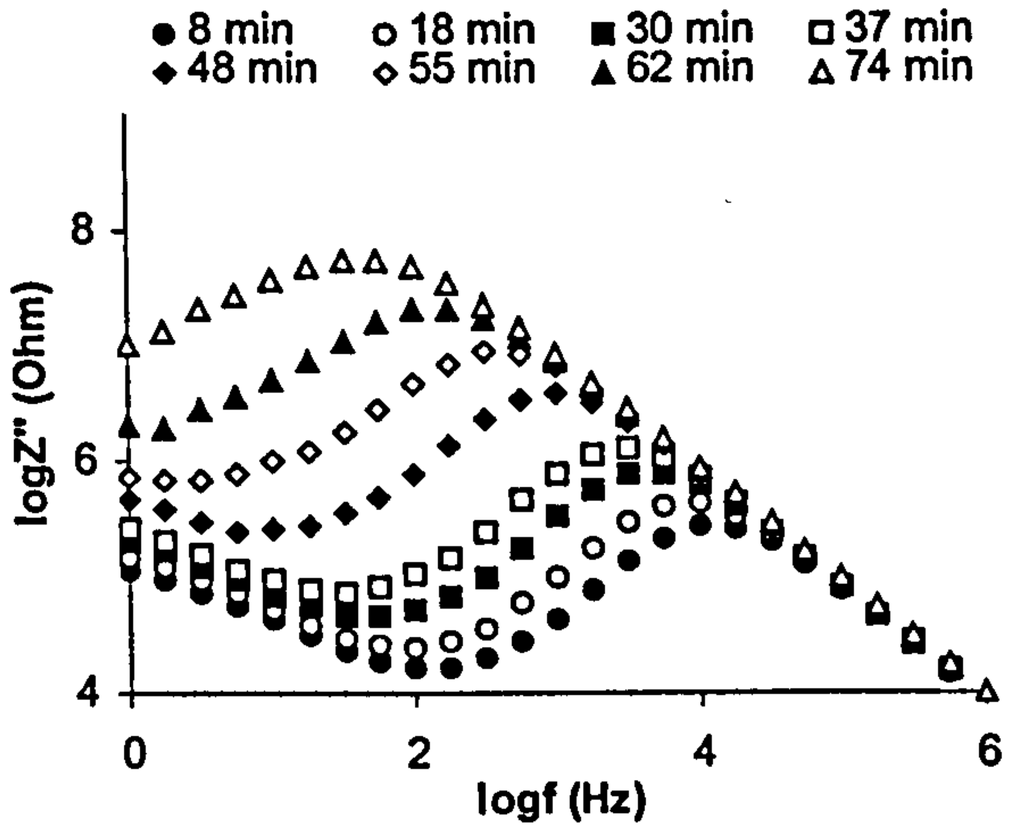

(b) Imaginary impedance

Fig.8.1 *Impedance spectra evolution during isothermal cure at 150°C*

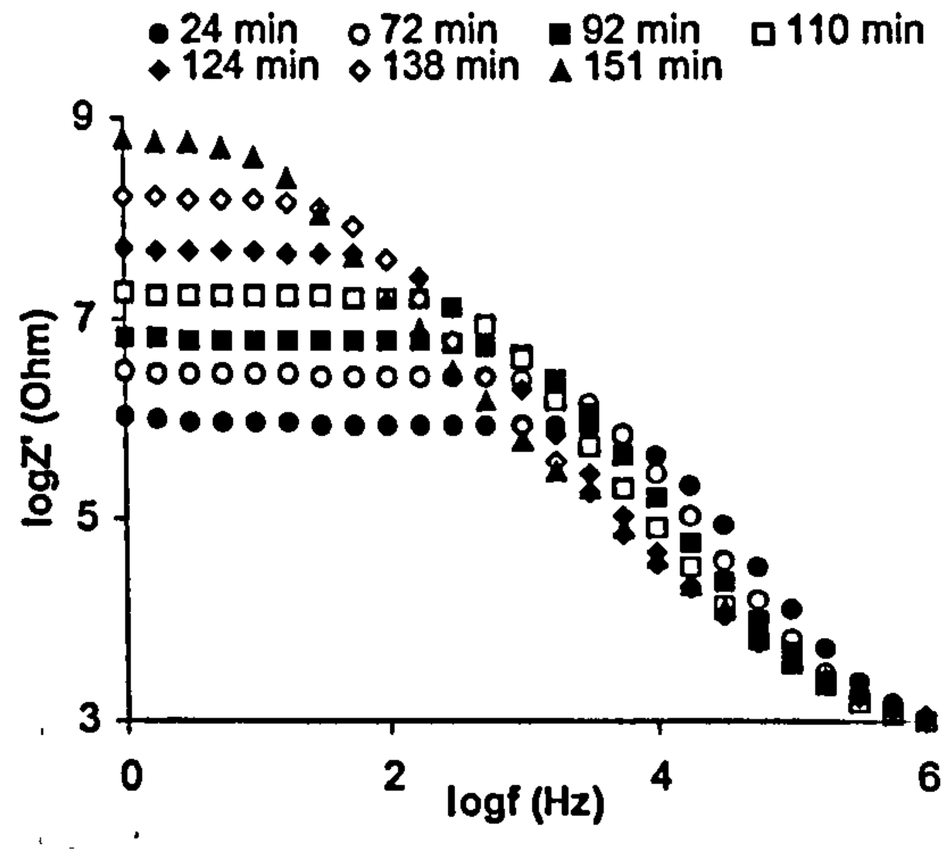

(a) Real impedance

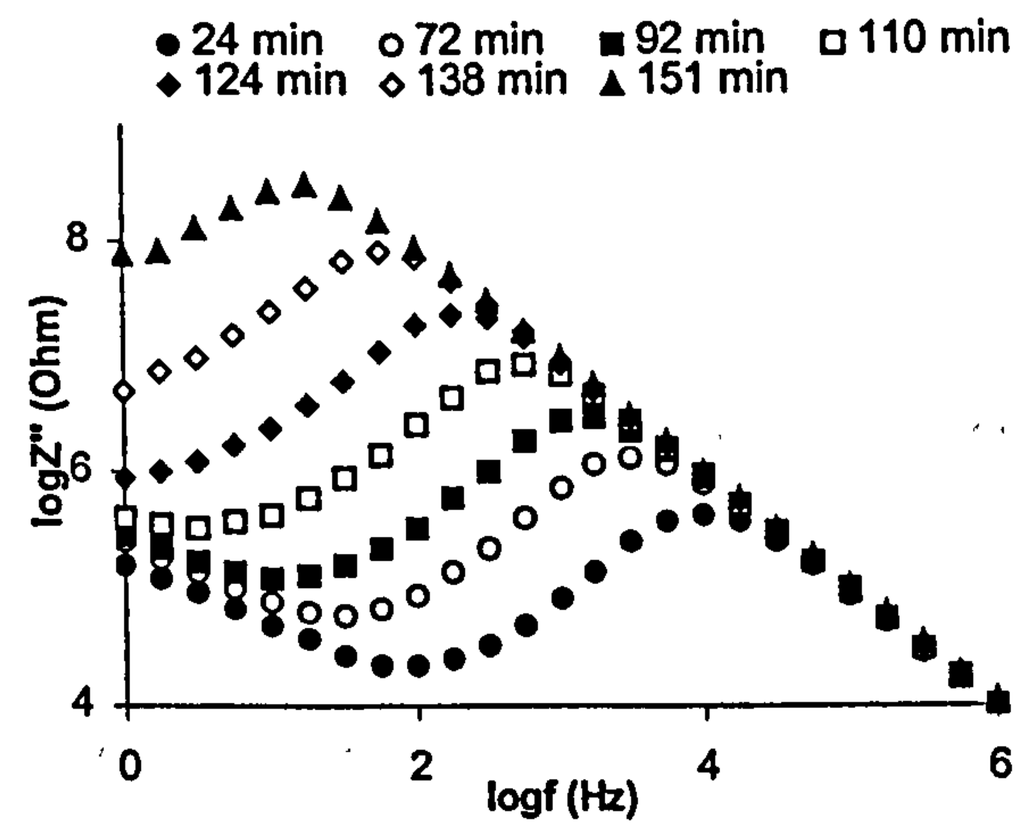

(b) Imaginary impedance

Fig.8.2 *Impedance spectra evolution during isothermal cure at 130°C*

Both spectra show a strong dependence upon material state as it changes during the cure. The real impedance plateau value increases as the curing progresses, whereas the frequency where the plateau ends decreases. Both the minimum and maximum of imaginary impedance increase as curing progresses. The whole imaginary impedance spectrum is shifted to lower frequencies as the reaction progresses but, unlike in the case of the real impedance the final linear part remains constant.

The behaviour of the spectra can be used in order to explain the impedance at a fixed frequency versus time curves illustrated in Fig. 8.3. Here only the results of the cure at 150 °C are presented; the other isothermal experiments yield equivalent results.

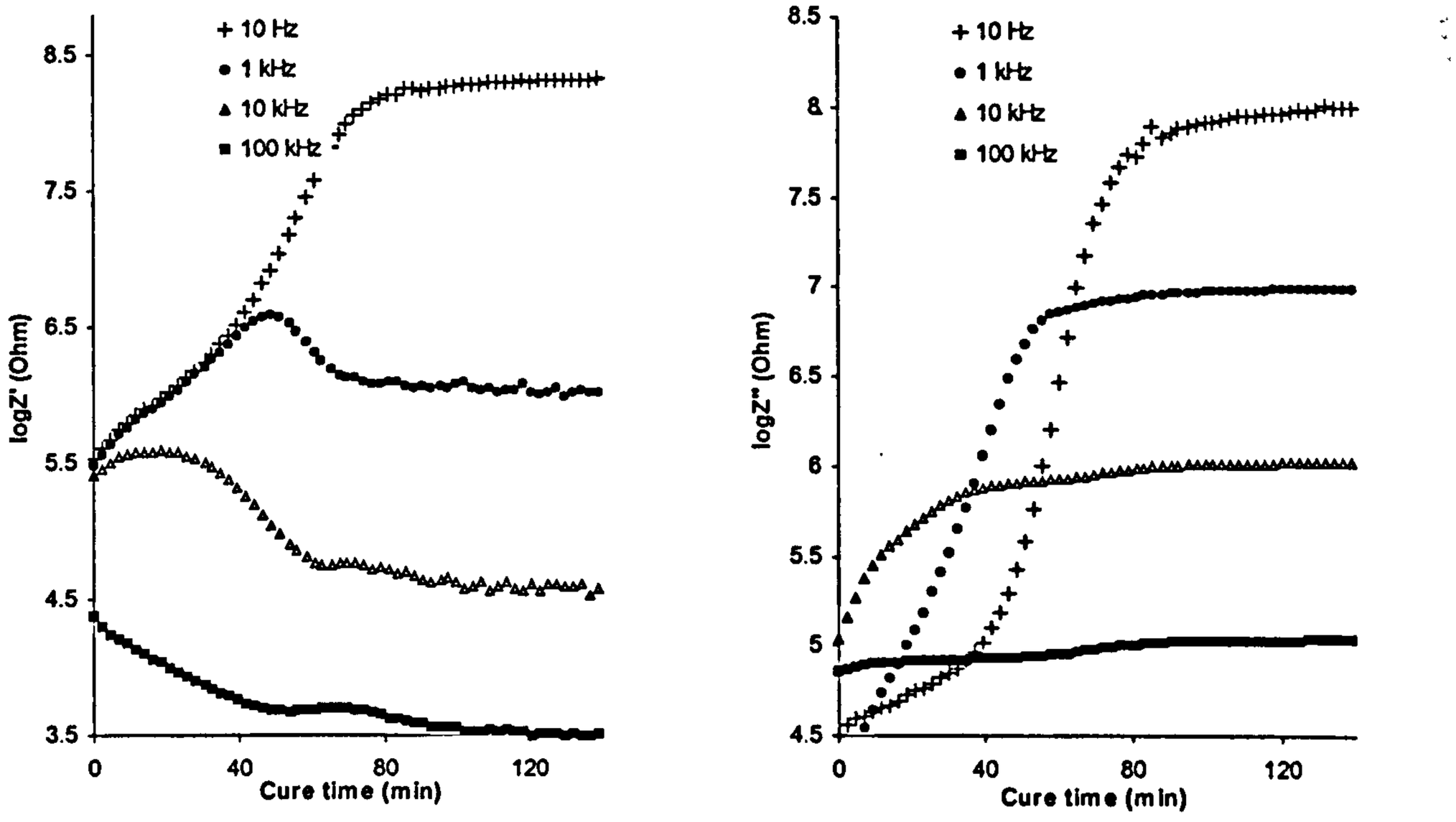

(a) Real impedance (b) Imaginary impedance

Fig.8.3 *Evolution of impedance at fixed frequencies during isothermal cure at 150 °C*

As far as the real impedance is concerned four types of behaviour can be distinguished:

(i) At very low frequencies, which are within the plateau region of the spectrum throughout the cure, real impedance increases monotonously and stabilises towards the end of the cure. The curve corresponding to 10 Hz demonstrates this type of behaviour in Fig. 8.3.a.

(ii) At intermediate to low frequencies (1 kHz in Fig. 8.3.a) as the reaction progresses the real impedance increases up to the point where the transition from the plateau to the linear region is shifted to a frequency lower than the measurement frequency. Then the real impedance decreases, as a result of the shift of the decreasing part of the spectrum towards lower frequencies. Consequently a peak appears in the real impedance versus cure time curve.

(iii) At intermediate to high frequencies (10 kHz in Fig. 8.3.a) the real impedance increases slightly for a short time interval at the beginning of the cure due to the increasing behaviour of the plateau value. Subsequently, the shift of the transition point to lower frequencies causes a real impedance decrease. Towards the end of the cure (at about 70 min) a slight peak occurs. This peak is attributed to the existence of a point in the decreasing part of the spectrum at which the order of the spectra at different times reverses. For example the 74 min cure time spectrum represented by the open triangles in Fig. 8.1.a has the lowest values between 100 Hz and 1 kHz, whereas it has higher values than the 62 min curve at 10 kHz.

(iv) At very high frequencies the value of the real impedance decreases from the beginning of the cure as a result of the fact that very high frequencies are outside the plateau region. The peak towards the end of the cure is more pronounced (see the 100 kHz curve in Fig. 8.3.a). A clear justification of the existence of this peak is illustrated in Fig. 8.4.a, where a detail of the spectra at the end of the isothermal cure at 130 °C is shown. There it can be observed that different spectra intersect and reverse their relative order at a specific frequency. This frequency increases as the cure time of the spectrum corresponding to the lower impedance values at lower frequencies increases. Thus, at 100 kHz an intermediate spectrum, that corresponds to 151 min cure time, has the highest real impedance value. This is demonstrated as the peak observed in the real impedance versus time curves at very high frequencies of Fig. 8.3.a.

The imaginary impedance has monotonous behaviour throughout the cure due the shifting behaviour of the spectrum. However, different types of curves can be distinguished as follows:

(i) At very low frequencies (10 Hz in Fig. 8.3.b) imaginary impedance increases slowly in the early stages of the reaction. Then a steep increase is observed towards a plateau value at the end of cure. This behaviour can be explained by the fact that initially very low frequencies are within the first decreasing segment of the imaginary impedance spectrum (Fig. 8.1.b) which shows a slow change in level. When the minimum of the spectrum approaches the frequency of the measurement the impedance increases rapidly. This is expressed as a step change, which ends when the maximum of the spectrum reaches the measurement frequency.

(ii) At low to intermediate frequencies (1 kHz in Fig. 8.3.b) imaginary impedance shows a fast increase from the beginning of the cure and stabilises towards the end of the reaction. This behaviour occurs as from the beginning of the cure intermediate frequencies are outside the linear decrease region of the spectrum (Fig. 8.1.b).

(iii) At intermediate to high frequencies (10 kHz in Fig. 8.3.b) there is an initial rapid rise of the imaginary impedance value which can be attributed to the initial position of the high frequencies outside the linear decrease regime of the spectrum. Then imaginary impedance stabilises and a second slight step appears (knee). Eventually the imaginary impedance stabilises at the fully cured material value.

(iv) The same behaviour without the initial increase is observed at very high frequencies (100 kHz in Fig. 8.3.b). The knee towards the end of the cure is more pronounced. As observed in Fig. 8.1.b the frequency-time window in which this knee occurs is within the final decrease region of the spectrum. In order to gain an insight in its existence, a detailed examination of this part of the spectrum is required. Fig. 8.4.b shows the imaginary impedance spectra at every 10 minutes towards the end of the cure at 130 °C at frequencies between 10 kHz and 100 kHz. It can be observed that the whole linear part of the spectrum increases as the cure progresses. The rate at which the value of imaginary impedance increases is low between 120 and 140 min, high between 140 and 170 min and low again between 170 and 190 min. Analogous behaviour is observed in the rest of the isothermal experiments. In terms of imaginary

impedance at a fixed frequency this behaviour is translated to the knee observed in Fig. 8.3.b.

In Fig. 8.5 the cure time where the knee of the imaginary impedance and the second peak of the real part of the impedance, as represented by the time of the inflection point and the maximum respectively, occur are plotted versus the frequency at all isothermal cure temperatures (130, 140, 150 and 160 °C). It can be observed that within the accuracy of the measurement the two coincide. In addition, the cure time at which these events take place shows no dependence on frequency of measurement in the range from 10 kHz to 1 MHz.

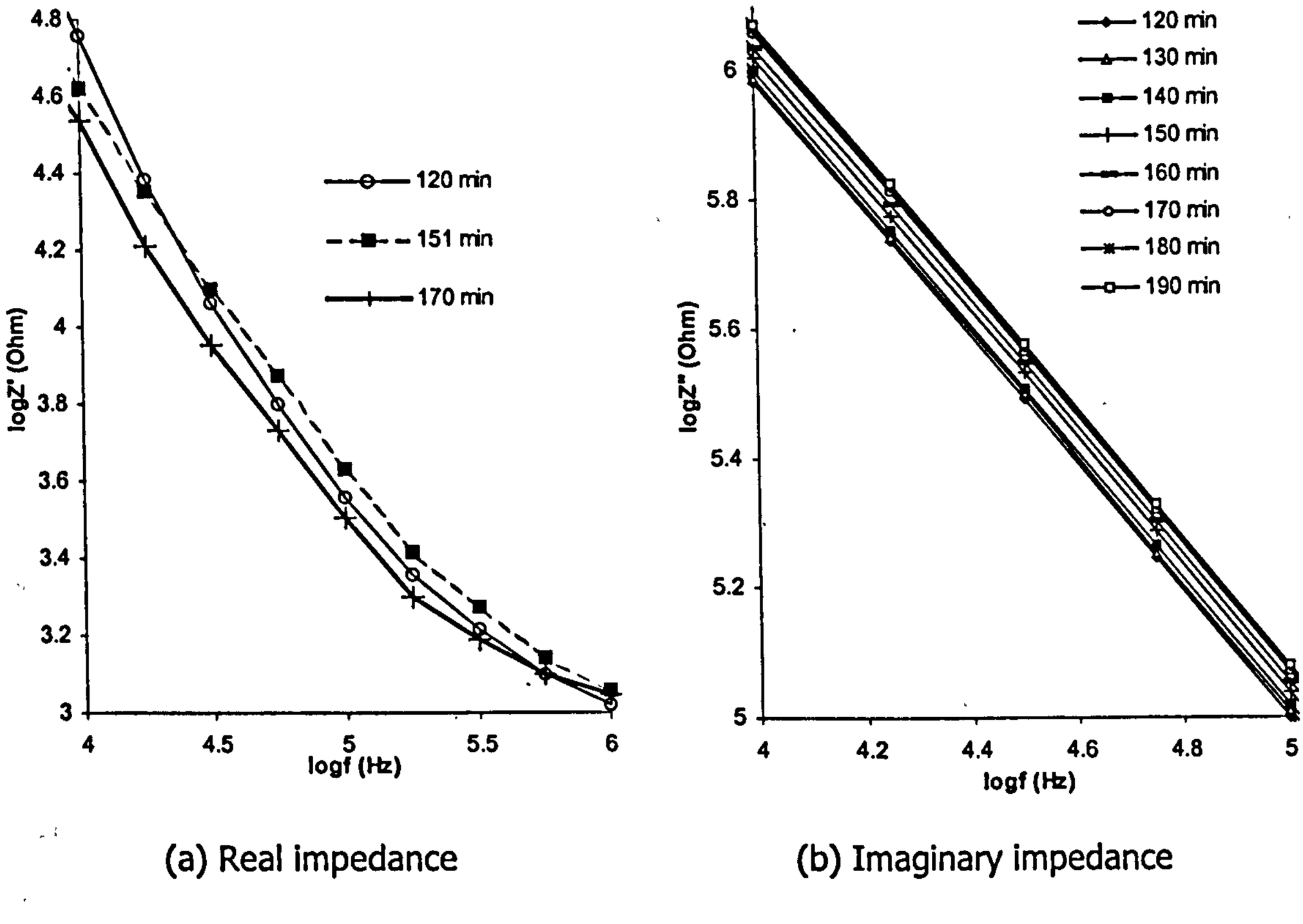

(a) Real impedance

(b) Imaginary impedance

Fig.8.4 *Detail of impedance spectra at high frequencies towards the end of isothermal cure at 130 °C*

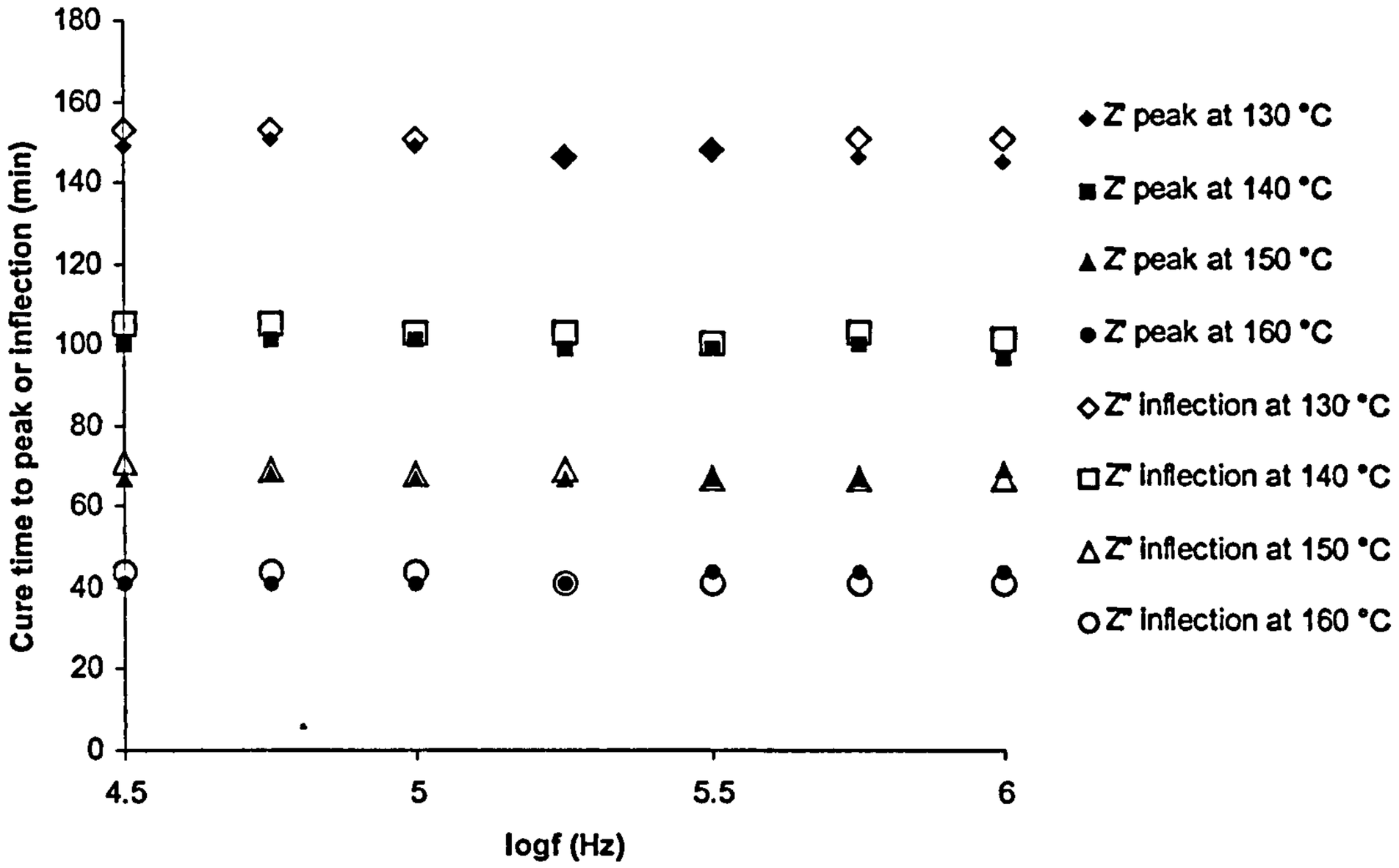

Fig.8.5 *Time into the cure at which the second peak of real impedance and the knee of imaginary impedance appear*

8.3.2 Dynamic experiments

Dynamic cure experiments of RTM6 resin were carried out at 0.25, 0.5, 0.75, 1, 1.25, 1.5, 1.75 and 2 °C/min. The evolution of the real and imaginary impedance spectra for the experiment at 0.25 °C/min is illustrated in Figs. 8.6 and 8.7 respectively.

The behaviour illustrated in Figs. 8.6 and 8.7 is characteristic of all dynamic cure experiments of RTM6 epoxy resin. The form of both spectra is identical to the isothermal case, i.e. the real impedance spectrum comprises a plateau and a linear decrease region, and the imaginary impedance spectrum comprises a minimum, a maximum and three linear regions. However, the evolution of the spectra is more complicated in the dynamic case due to the combined influences of temperature and of state-of-material changes.

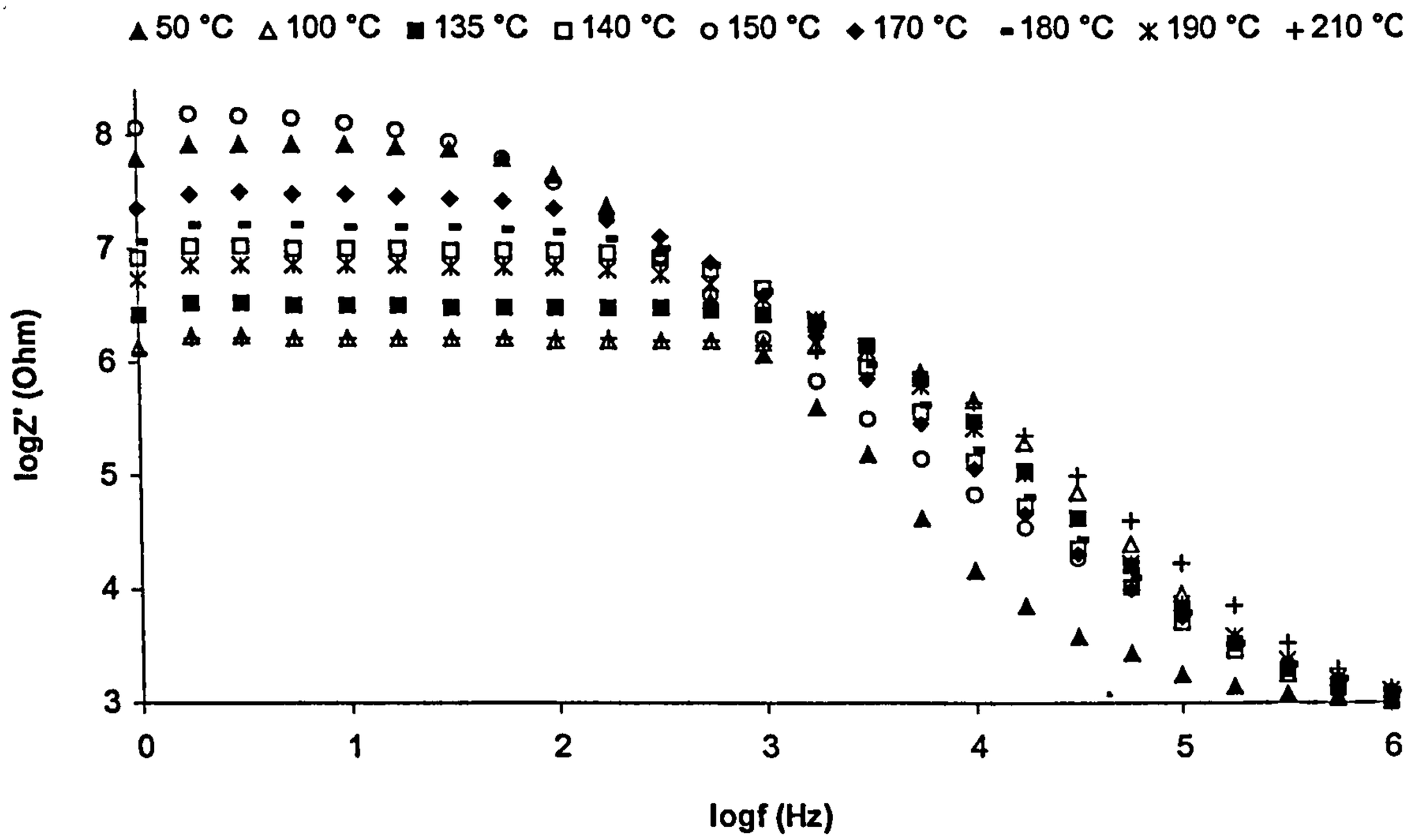

Fig.8.6 *Real impedance spectrum evolution during dynamic cure at 0.25°C/min*

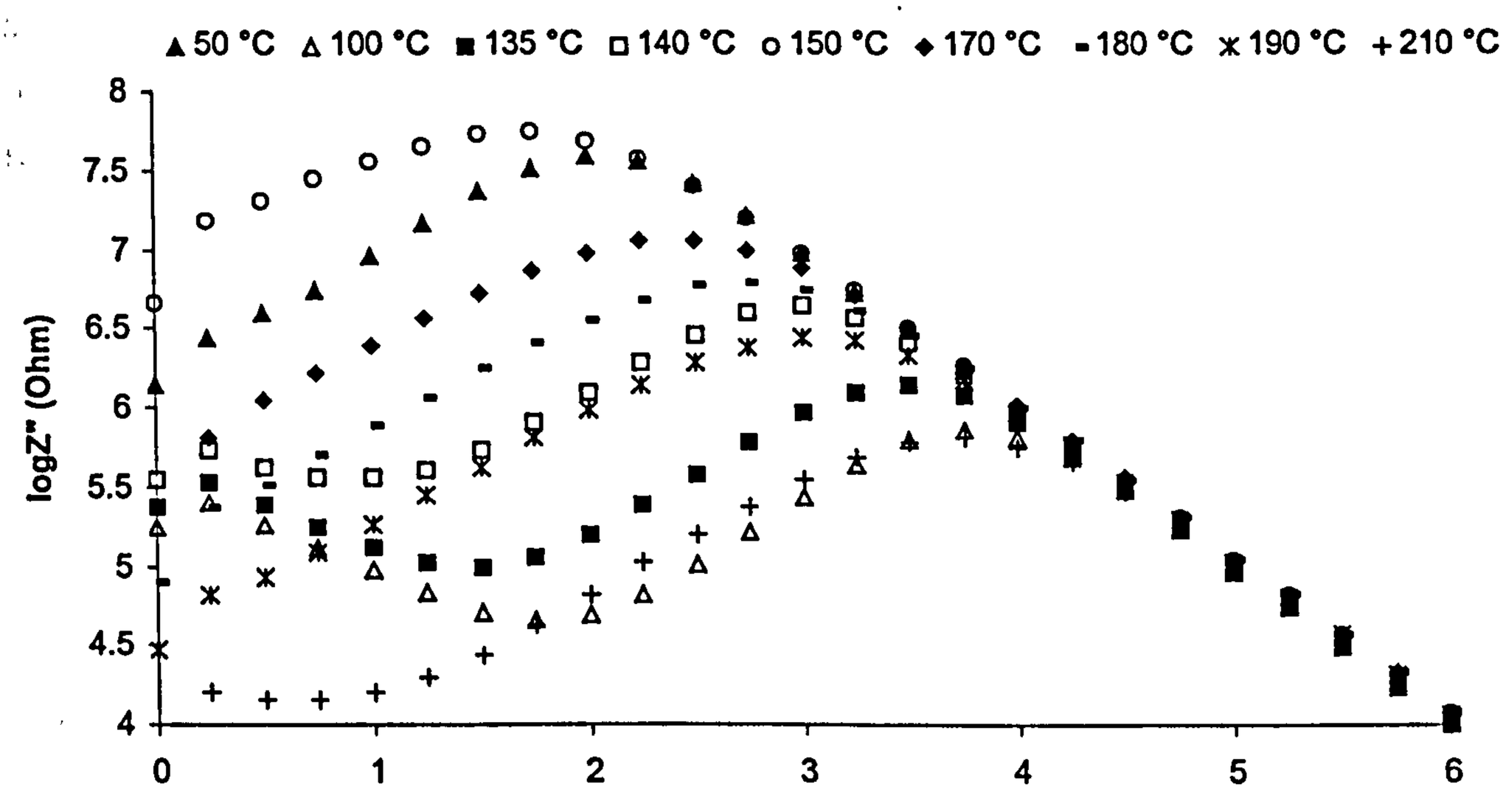

Fig.8.7 *Imaginary impedance spectrum evolution during dynamic cure at 0.25°C/min*

In the initial stages of the dynamic cure the real impedance plateau value decreases and the frequency where the plateau ends increases (curves at 50 and 100 °C in Fig. 8.6) as a result of the rise in temperature. At higher temperatures (curves at 135, 140 and 150 °C in Fig. 8.6) the spectrum shows the behaviour observed in isothermal cure, i. e. the plateau value increases and the plateau end frequency decreases. This can be attributed to the domination of material state connected phenomena to the signal. When temperature increases further the situation reverses (curves at 170, 180, 190 and 210 °C in Fig. 8.6) and due to temperature changes domination in the signal, the plateau value decreases and the plateau end frequency increases. Analogous phenomena are observed in the evolution of the imaginary impedance spectrum. At low temperatures the spectrum is shifted to higher frequencies and the maximum and minimum values decrease (curves at 50 and 100 °C in Fig. 8.7). At intermediate temperatures (curves at 135, 140 and 150 °C in Fig. 8.7) the behaviour observed in isothermal cure is reproduced, i.e. the spectrum is shifted to lower frequencies and the maximum and minimum values increase, implying material state changes domination. Further increase in temperature (curves at 170, 180, 190 and 210 °C in Fig. 8.7) leads to temperature changes domination, i.e. the whole spectrum is shifted to higher frequencies and the maximum and minimum values decrease. The way this complicated behaviour translates to impedance evolution at fixed frequencies is illustrated in Figs. 8.8, 8.9 and 8.10.

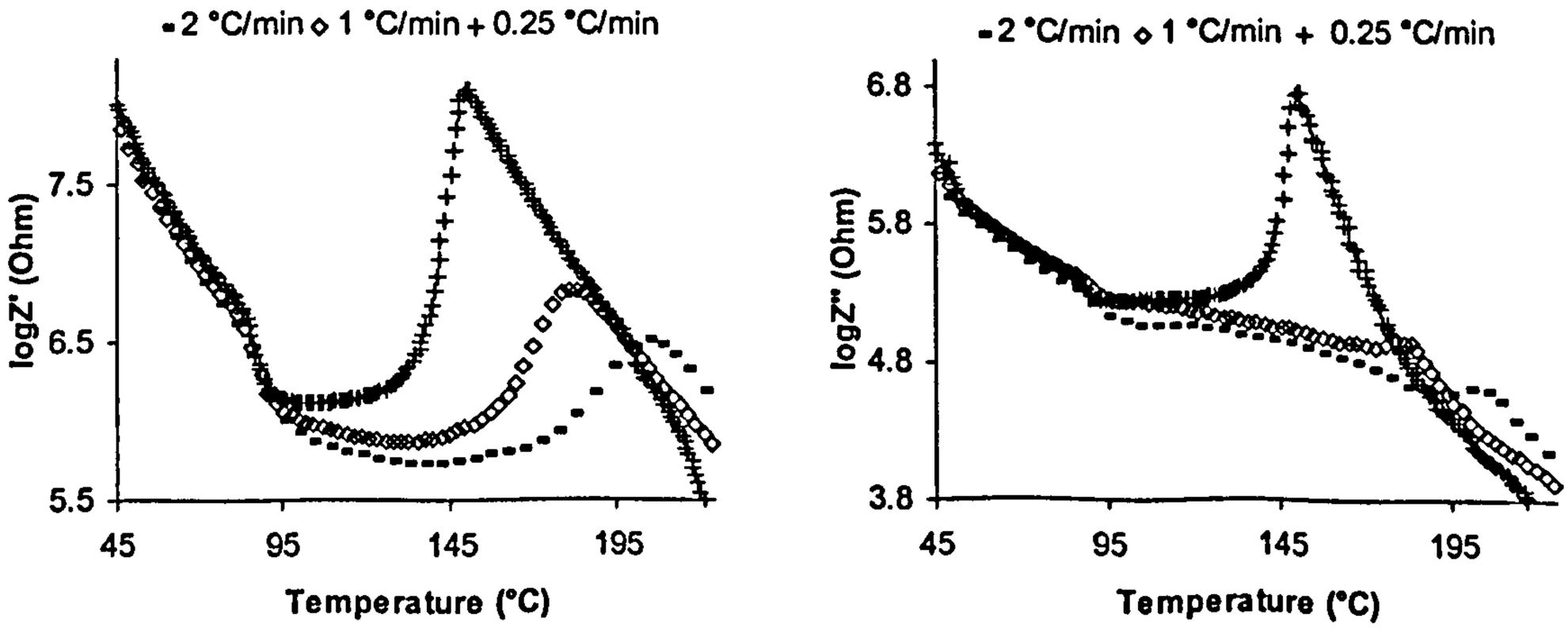

(a) Real impedance (b) Imaginary impedance

Fig.8.8 *Evolution of impedance at 1 Hz during dynamic cure at 0.25, 1 and 2 °C/min*

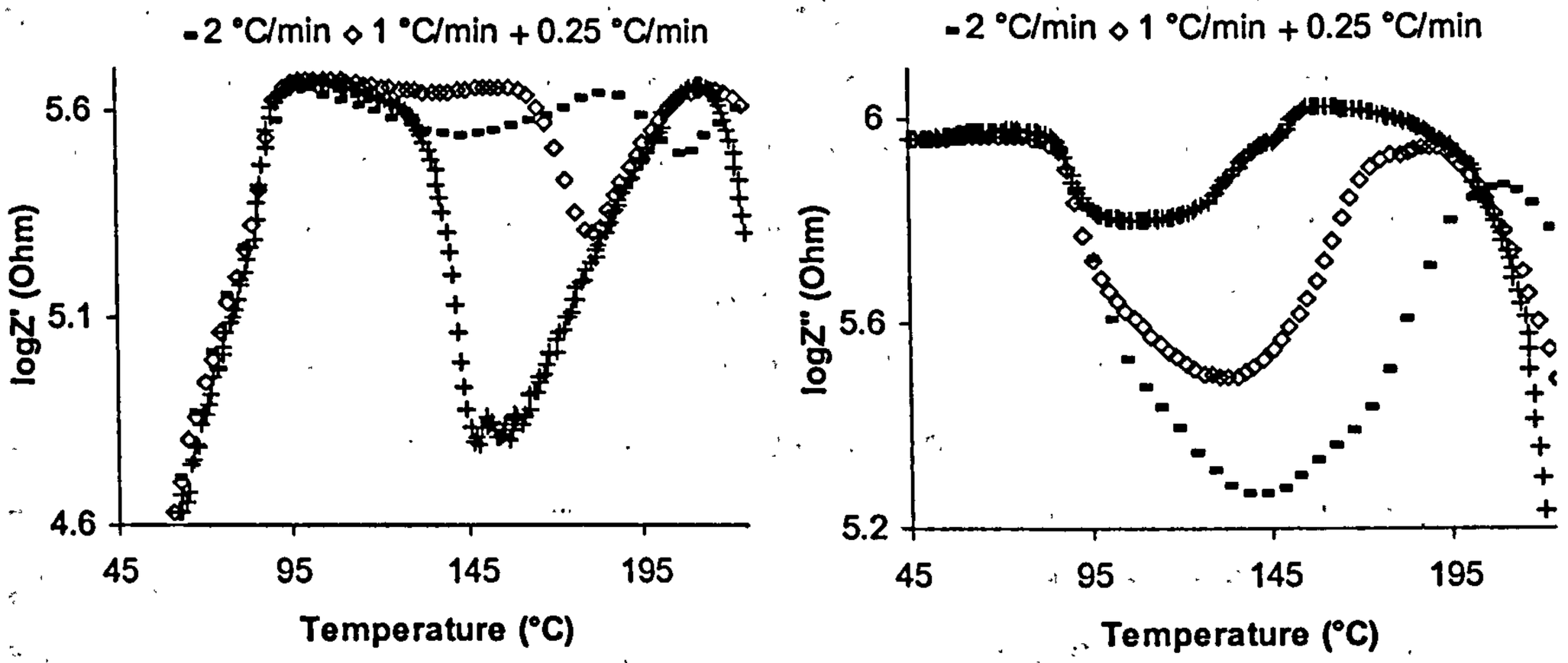

(a) Real impedance (b) Imaginary impedance

Fig.8.9 *Evolution of impedance at 10 kHz during dynamic cure at 0.25, 1 and 2 °C/min*

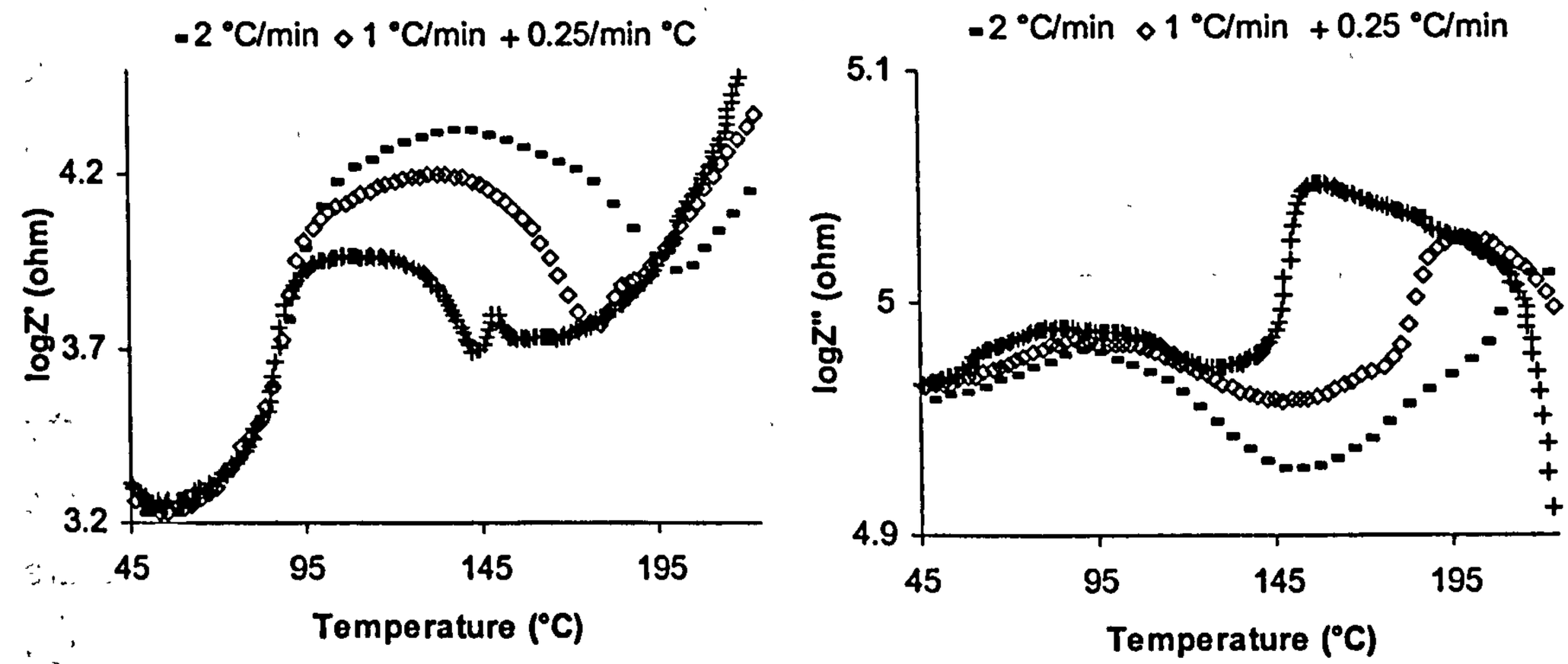

(a) Real impedance (b) Imaginary impedance

Fig.8.10 *Evolution of impedance at 100 kHz during dynamic cure at 0.25, 1 and 2 °C/min*

Three types of behaviour can be distinguished in the real impedance at fixed frequency versus time curves:

(i) At very low frequencies (Fig. 8.8.a) the real impedance curve reflects the changes of the plateau value of the spectrum (Fig. 8.6). Initially the plateau value decreases as a result of heating up while the material state is stable. Further into the cure the plateau value stabilises, indicating the competing and mutually cancelling influence of temperature rise and reaction advancement. At higher temperatures (100 and 150 °C for the 0.25 °C /min curve) the reaction advancement dominates the changes in the plateau value. This phenomenon is combined with the approach of the plateau end region of the spectrum resulting in a steep increase of the real impedance value. When the spectrum reaches its highest level (at 150 °C for the 0.25 °C/min curve), the situation is reversed and the spectrum starts shifting to higher frequencies while the plateau value decreases. This behaviour implies temperature change domination and results in the decrease of the real impedance value. For the slowest heating rate curve at very high temperatures (approximately 220 °C) the negative slope of the real impedance value increases further.

(ii) At intermediate frequencies (Fig. 8.9.a) the evolution of real impedance exhibits different behaviour. It increases initially, then decreases towards a minimum and eventually increases. This behaviour can be explained by the fact that the frequency corresponding to the curves illustrated in Fig. 8.9.a is within the linear decrease regime of the spectrum from the beginning of the cure. Consequently the shift of the spectrum towards higher frequencies during the initial heating up stage results in the rise of the real impedance value. When the reaction dominates, it shifts the spectrum to lower frequencies. This results in the decrease of the real impedance value at a fixed frequency. Towards the completion of the reaction the situation reverses again to the temperature dependence observed during the initial stages of the cure. At very high temperatures the real impedance value decreases as a result of a general translation of the spectrum to lower values. An interesting feature of this frequency range is the slight second peak in the real impedance observed after the decreasing part in the curve of the cure at 0.25 °C/min. This phenomenon is

illustrated in detail in Fig. 8.11. In Fig. 8.11.a it can be observed that this peak occurs at the same time for all intermediate to high frequencies. The reason of its occurrence is the same as that for the real impedance peak observed towards the end of isothermal cure, i.e. the intersection of the spectra at different temperature at a specific frequency which reverses their order (as shown in Fig. 8.11.b).

(iii) At very high frequencies (Fig. 8.10.a) the behaviour is similar to that at intermediate frequencies apart from the initial part of the real impedance versus time curve which shows a constant behaviour. This is attributed to the presence of a second plateau at very high frequencies in the spectrum of the unreacted material, as illustrated in Fig. 8.6. Thus the shift of the spectrum to the right has initially no influence since the spectrum moves along this plateau.

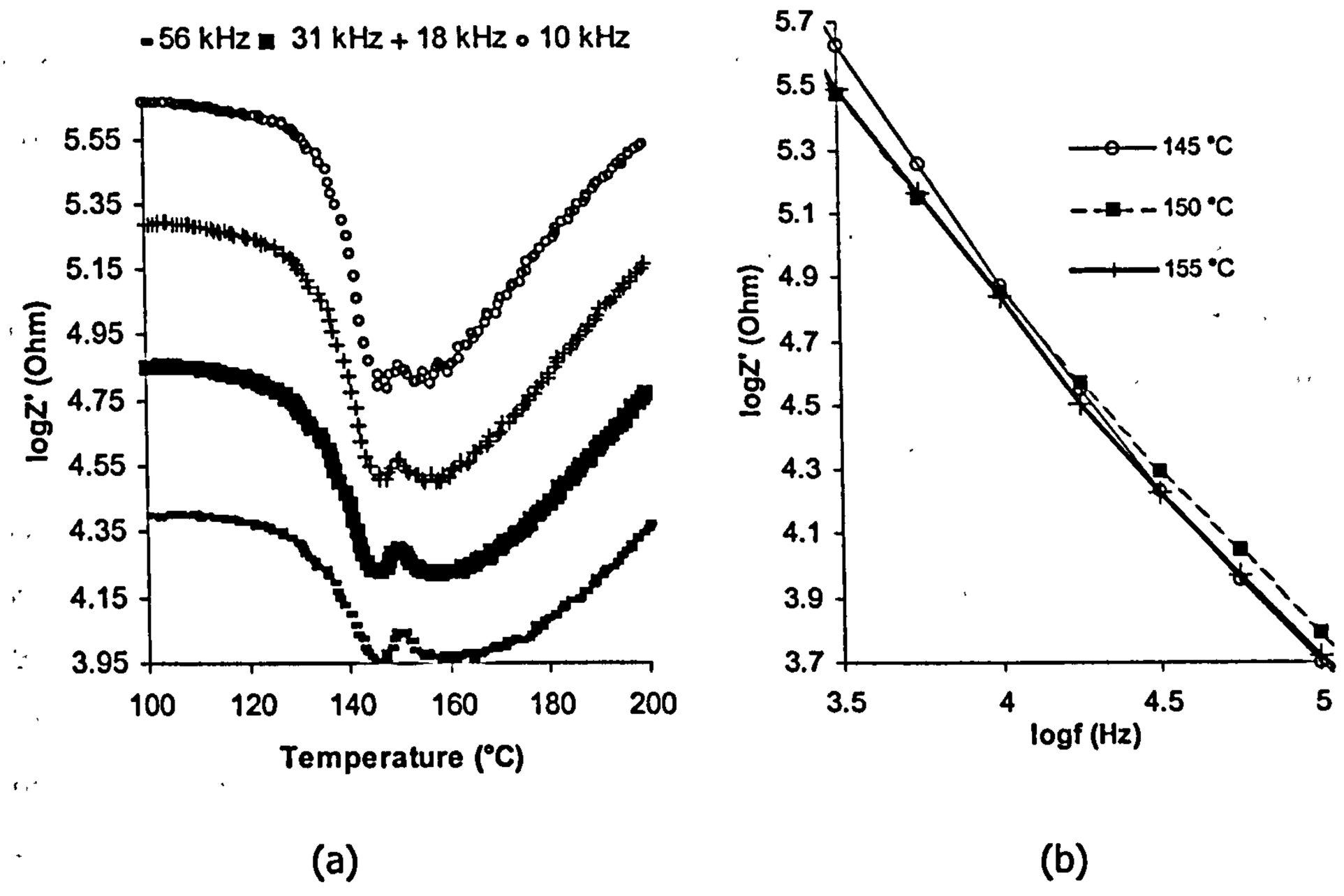

Fig.8.11 *Detail of real impedance spectra at intermediate to high frequencies in the peak region for the curing at 0.25°C/min. (a) Real impedance versus time. (b) Real impedance versus frequency.*

The imaginary impedance curves have the following types of behaviour according to the frequency region the measurement is performed:

(i) At low frequencies (Fig. 8.8.b) imaginary impedance decreases initially, then stabilises, increases and eventually decreases towards the end of the cure. The initial decrease is attributed to the fact that at low temperatures, and when the material is unreacted, frequencies in the order of 1 Hz are very close to the minimum which decreases as a result of the temperature rise (Fig. 8.7). At higher temperatures the frequency is within the first linear part and similarly to the isothermal case, imaginary impedance shows constant behaviour as a result of the shift of the spectrum along this line. When the reaction dominates the signal, the spectrum is shifted to lower frequencies and the maximum and minimum values increase, resulting in the rise of the imaginary impedance value. The final decrease is explained by the decrease of the maximum and minimum value and the shift of the spectrum towards higher frequencies when temperature changes dominate the behaviour of the material near the completion of the reaction.

(ii) At intermediate to high frequencies (Fig. 8.9.b) the imaginary impedance remains constant during the heating up of the unreacted resin. This is a result of the initial position of this frequency range in the final linear part along which the spectrum shifts. When the shift of the spectrum to higher frequencies causes the approach of the spectrum maximum (Fig. 8.7) to the measurement frequency, further shift lowers the value of imaginary impedance. Subsequently the general increase of the spectrum due to the domination of the reaction increases the imaginary impedance. Towards the end of the reaction, when temperature changes dominate again, the behaviour is reversed and the imaginary impedance decreases. The existence of a knee can be observed in the increasing part of the imaginary impedance versus time curve corresponding to 0.25 °C/min of Fig. 8.9.b. This knee is shown for different frequencies in the range of 3-20 kHz in Fig. 8.12.a. The corresponding spectrum window illustrated in Fig. 8.12.b shows that the explanation of the knee existence is identical to the isothermal case, i.e. the uniform shift of the final linear part of the spectrum in a step fashion.

(iii) At very high frequencies (Fig.8.10.b) imaginary impedance reflects the changes in the final linear part of the spectrum. Since phenomena occurring in the rest of the spectrum do not influence this frequency range, the knee at the end of the cure is more pronounced.

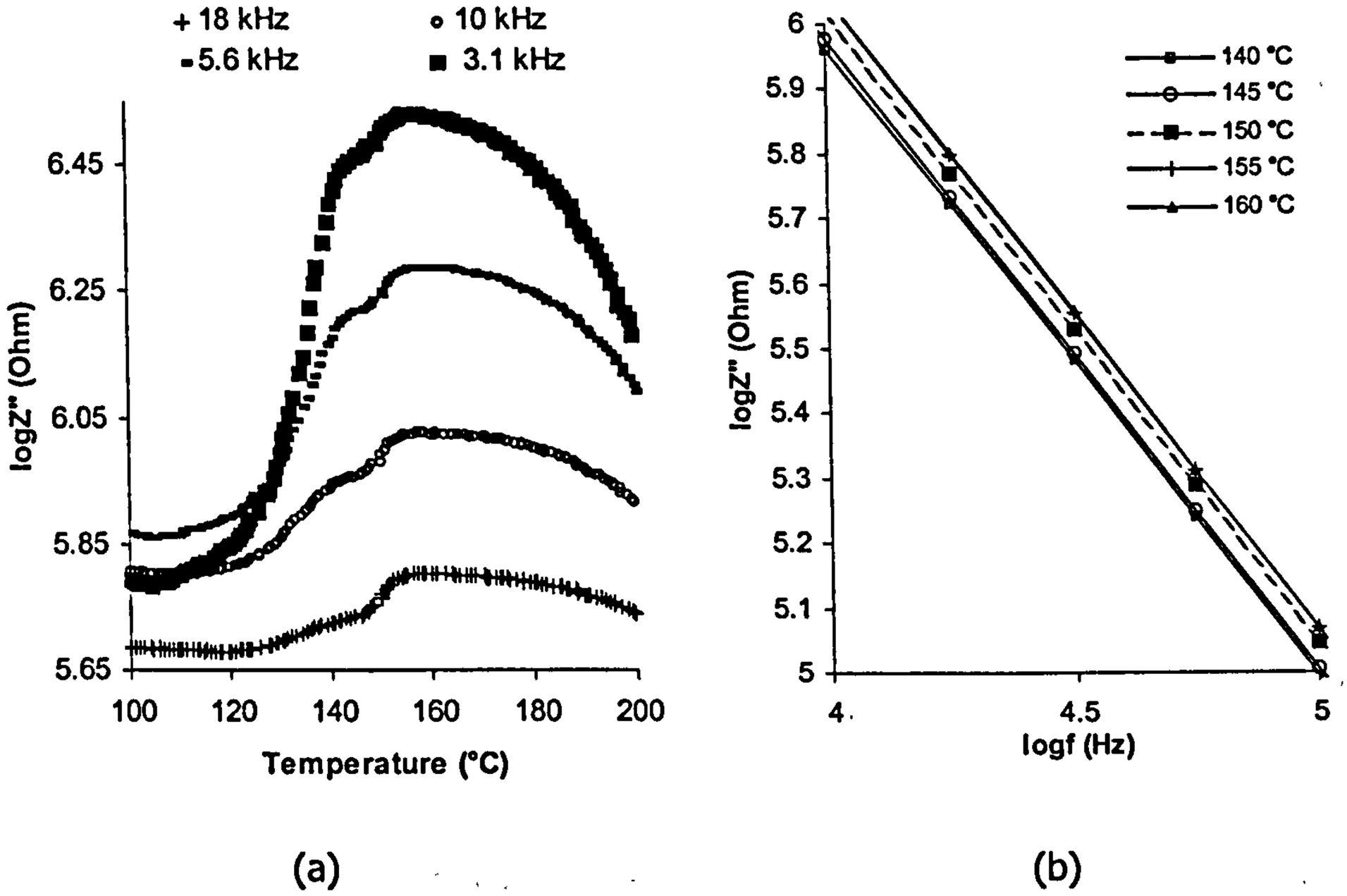

Fig.8.12 *Detail of imaginary impedance spectra at intermediate to high frequencies in the peak region for the curing at 0.25°C/min. (a) Imaginary impedance versus time. (b) Imaginary impedance versus frequency.*

The cure temperature at which the knee of the imaginary impedance and the second peak of the real impedance occur, as represented by the corresponding inflection point and maximum, are illustrated in Fig. 8.13. It can be observed that, similarly to the isothermal case, the temperatures of the inflection point of the imaginary part of impedance and of the maximum of the real part coincide and show no dependence on the frequency of the measurement. The peak of the real impedance at intermediate frequencies begins to be hindered by the rest of the material response as the heating

rate of the experiment increases. When the heating rate increases beyond 1.25 °C/min the two characteristic points disappear from the impedance response.

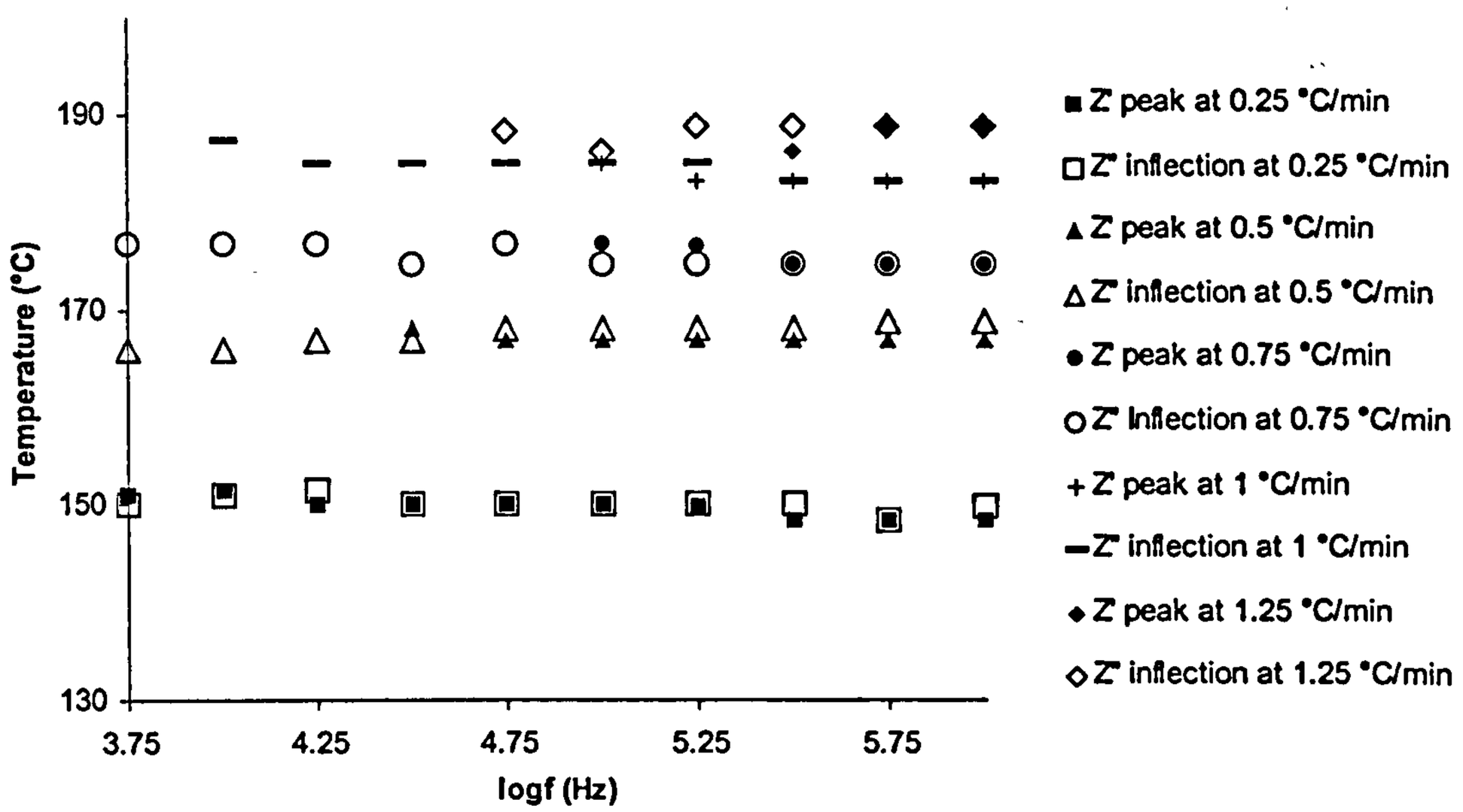

Fig.8.13 *Temperature at which the second peak of real impedance and the knee of imaginary impedance appear*

8.4 Equivalent circuit representation of the material response

In order to obtain an equivalent electrical circuit representation of the material response, the general form of real and imaginary impedance spectra as illustrated in Figs. 8.2, 8.6 and 8.7 has to be compared with the response given by circuits that imitate the physical phenomena occurring in the material. As mentioned in paragraph 3.4.4, the general equivalent circuit of thermosetting systems comprises two capacitors, representing electrode polarisation, connected in series with a subcircuit of a resistor, which represents migrating charges, and a relaxation circuit connected in parallel. The relaxation circuit comprises a resistor and a capacitor corresponding to permanent dipoles in parallel with another capacitor corresponding to induced dipoles. This circuit and its impedance response are shown in Figs. 3.6 and 3.7 respectively. The real impedance spectrum comprises a plateau at low frequencies, a step drop towards a second plateau at intermediate frequencies and a linear decrease region at high

frequencies. The imaginary impedance spectrum comprises a linear decrease segment at low frequencies, a minimum which is followed by a linear increase at intermediate frequencies, a maximum which is followed by a linear decrease and a shoulder which is followed by a linear decrease. According to Eqs. 3.16 and 3.17 the impedance of this circuit is:

$$Z = \frac{R_i\left[\omega^2 {C_{sd}}^2 R_{sd}(R_{sd}+R_i)+1\right]}{\omega^2\left(C_{sd}R_i + C_{sd}R_{sd} + C_{id}R_i\right)^2 + \left(\omega^2 C_{sd}R_{sd}R_i C_{id} - 1\right)^2} - j\left[\frac{R_i\left[\omega^3 {C_{sd}}^2 {R_{sd}}^2 R_i C_{id} + \omega R_i(C_{id}+C_{sd})\right]}{\omega^2\left(C_{sd}R_i + C_{sd}R_{sd} + C_{id}R_i\right)^2 + \left(\omega^2 C_{sd}R_{sd}R_i C_{id} - 1\right)^2} + \frac{2}{C_e\omega}\right] \quad \text{(Eq. 8.1)}$$

Accordingly the behaviour of such a circuit at very high and very low frequencies becomes:

$$\left.\frac{d\log Z'}{d\log\omega}\right|_{\omega\to 0} = 0 \quad \text{(Eq. 8.2)}$$

$$\left.\frac{d\log Z'}{d\log\omega}\right|_{\omega\to\infty} = -2 \quad \text{(Eq. 8.3)}$$

$$\left.\frac{d\log Z''}{d\log\omega}\right|_{\omega\to 0} = -1 \quad \text{(Eq. 8.4)}$$

$$\left.\frac{d\log Z''}{d\log\omega}\right|_{\omega\to\infty} = -1 \quad \text{(Eq. 8.5)}$$

The experimental spectra slopes at very high and very low frequencies are given in Table 8.1. For each experiment the values of the slopes when the corresponding linear segment is well formed in the spectrum were averaged for the calculation.

	$\left.\frac{d\log Z'}{d\log\omega}\right\|_{\omega\to 0}$		$\left.\frac{d\log Z'}{d\log\omega}\right\|_{\omega\to\infty}$		$\left.\frac{d\log Z''}{d\log\omega}\right\|_{\omega\to 0}$		$\left.\frac{d\log Z''}{d\log\omega}\right\|_{\omega\to\infty}$	
	Average	St. dev.	Average	St. dev.	Average	St. dev.	Average	St. dev.
130 °C	-0.05	0.01	-0.88	0.05	-0.43	0.02	-0.99	0.01
140 °C	-0.05	0.01	-1.00	0.11	-0.47	0.01	-0.99	0.01
150 °C	-0.06	0.01	-1.27	0.21	-0.46	0.01	-0.99	0.01
160 °C	-0.03	0.01	-0.97	0.11	-0.51	0.01	-1.00	0.01
0.25 °C/min	-0.02	0.02	-1.16	0.08	-0.55	0.03	-0.99	0.01
0.5 °C/min	-0.01	0.01	-1.20	0.07	-0.56	0.02	-0.99	0.01
0.75 °C/min	-0.01	0.02	-1.20	0.08	-0.49	0.03	-0.98	0.01
1 °C/min	-0.01	0.03	-1.25	0.08	-0.50	0.04	-0.98	0.01
1.25 °C/min	-0.01	0.03	-1.28	0.08	-0.51	0.05	-0.98	0.01
1.5 °C/min	-0.01	0.03	-1.22	0.15	-0.52	0.04	-0.98	0.02
1.75 °C/min	-0.01	0.02	-1.24	0.12	-0.49	0.04	-0.98	0.01
2 °C/min	-0.01	0.03	-1.27	0.13	-0.53	0.04	-0.99	0.02

Table 8.1 *Slopes of the real and imaginary impedance spectra of RTM6 at high and low frequencies*

It can be observed that the experimental slope of imaginary impedance at very high frequencies and of real impedance at low frequencies follow the prediction of the equivalent circuit model. In contrast the slope of imaginary impedance at low frequencies is -0.50±0.03, a value which is half of the value predicted by the model, and the slope of real impedance at high frequencies ranges from -1.28 to -0.88 instead of –2 which is the model value. Another general observation is that the real impedance spectrum does not have the double step form corresponding to the equivalent circuit model, and the imaginary impedance does not present the relaxation shoulder at high frequencies. Consequently discrepancies appear between the model and experimental spectra at very high and very low frequencies.

By a careful examination of the real impedance spectra in Figs. 8.1.a, 8.2.a and 8.6 it can be observed that at high conversion and low temperature the beginning of a second plateau is apparent. By taking into account the fact that relaxation is shifted to lower frequencies as the curing reaction progresses or the temperature decreases, the

manifestation of relaxation is expected to occur towards the end of the frequency range of the measurement. In addition, there is the possibility that relaxation is hindered by phenomena connected to the migration of charges. In order to subtract the extrinsic and intrinsic conductivity effects, which appear as a linear drop of imaginary impedance after the peak, the spectrum of the following quantity has to be studied:

$$\log Z'', = \log Z'' + \log \omega \qquad \text{(Eq. 8.6)}$$

The transformation expressed by Eq. 8.6 corresponds to a rotation of the spectrum by 45° and produces a horizontal line in the region where the original spectrum is a line with slope −1. In Fig. 8.14 the spectrum of this quantity at high frequencies is illustrated at various instances for a dynamic cure at 0.25 °C /min and an isothermal cure at 150 °C.

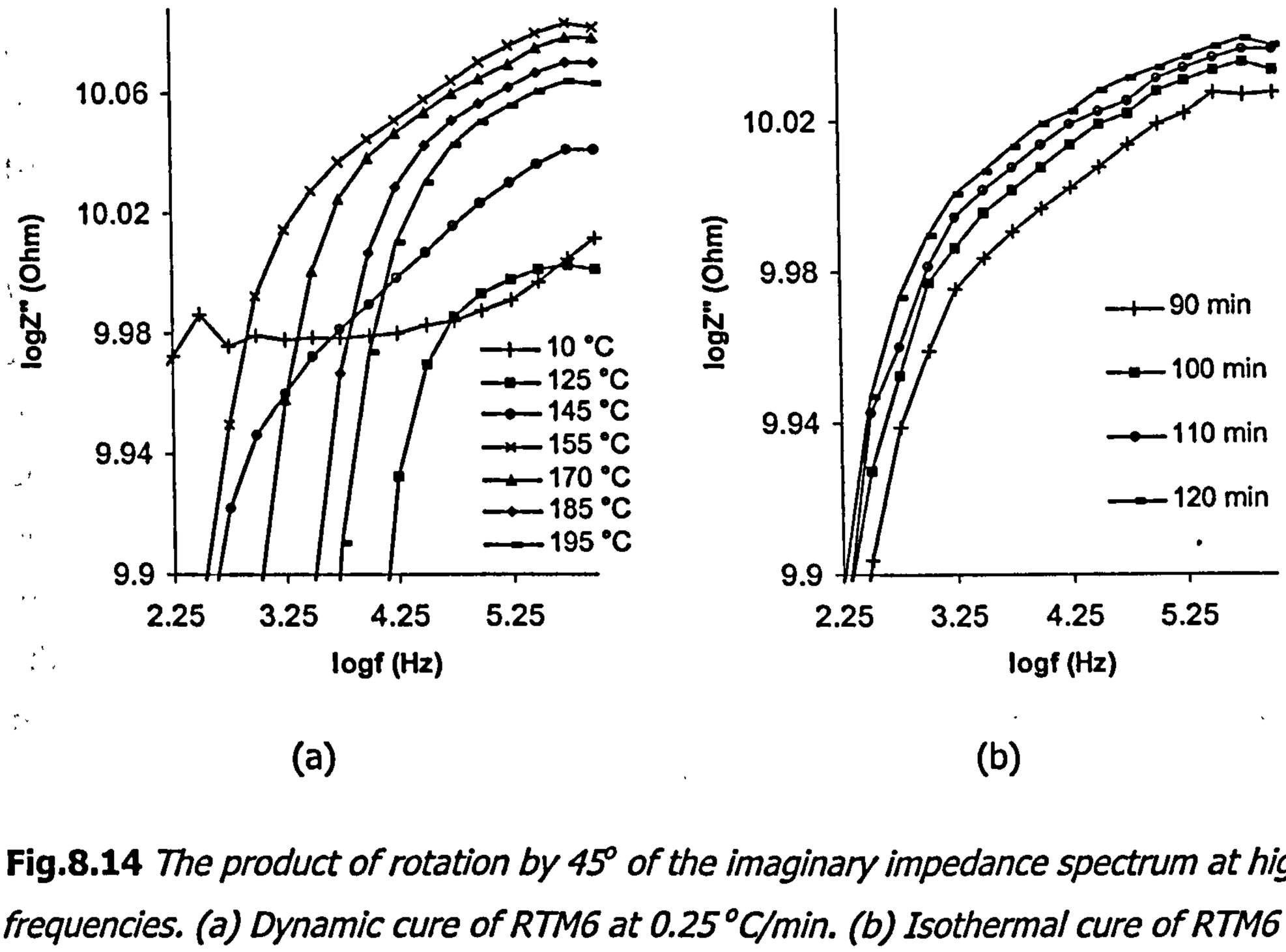

Fig.8.14 *The product of rotation by 45° of the imaginary impedance spectrum at high frequencies. (a) Dynamic cure of RTM6 at 0.25 °C/min. (b) Isothermal cure of RTM6 at 150 °C.*

Relaxation is apparent at the beginning of the dynamic cure as the beginning of a step over 10 kHz. In later stages of the cure and at higher temperatures the transformed quantity increases with frequency as a consequence of the existence of the migrating

charges peak. Although this increase is very small in terms of the original spectrum it shows that migrating charges influence the impedance signal up to the end of the spectrum. It can be observed that a region exists where the spectrum has lower curvature. This effect is more evident in the curves of Fig.8.14.a corresponding to 145 °C and 155 °C and in all curves of Fig.8.14.b. The existence of this linear part is attributed to the superposition of the shoulder caused by dipolar relaxation on the migrating charges governed curve. The frequency range this interference occurs (500 Hz to 100 kHz) as well as its evolution as the reaction progresses or the temperature changes (it shifts to lower frequencies as the reaction progresses and to higher frequencies as the temperature increases) are identical to those usually observed in thermosetting systems (218). Thus, the discrepancy in the final slope of the real impedance spectrum is attributed to the fact that relaxation is partially manifested within the frequency range of the measurement. When relaxation is manifested, it is hindered by the migrating charges contribution to the signal, since it causes changes of the order of magnitude 0.01 in the logarithm of imaginary impedance, whereas the global signal undergoes changes of around 1.

The behaviour of the material at very low frequencies, where the second discrepancy occurs, is governed by electrode polarisation phenomena. The standard equivalent circuit described in paragraph 3.4.4 uses a single capacitor to represent electrode polarisation. It has been found that this representation does not suffice for the modelling of the electrode-electrolyte interface. This fact has been ignored in the thermosetting cure monitoring literature, largely as a result of the consideration of electrode polarisation as an undesirable phenomenon, which does not participate in the real material response. For a more realistic representation of the phenomena taking place in the interface, a constant phase element (CPE) with the following impedance:

$$Z_{CPE} = \frac{1}{(A\omega)^n} \qquad \text{(Eq. 8.7)}$$

where

$$0 \le n \le 1 \qquad \text{(Eq. 8.8)}$$

should be used (219, 220).This behaviour arises from the non-uniform character of diffusion within the interface due to the roughness of a real electrode (219). Using this model for the electrode polarisation, Eq. 8.1 becomes:

$$Z = \frac{R_i\left[\omega^2 {C_{sd}}^2 R_{sd}\left(R_{sd}+R_i\right)+1\right]}{\omega^2\left(C_{sd}R_i + C_{sd}R_{sd} + C_{id}R_i\right)^2 + \left(\omega^2 C_{sd}R_{sd}R_iC_{id} - 1\right)^2} - \frac{2\cos\left(\frac{n\pi}{2}\right)}{\left(A_e\omega\right)^n}$$

$$- j\left[\frac{R_i\left[\omega^3 {C_{sd}}^2 {R_{sd}}^2 R_iC_{id} + \omega R_i\left(C_{id}+C_{sd}\right)\right]}{\omega^2\left(C_{sd}R_i + C_{sd}R_{sd} + C_{id}R_i\right)^2 + \left(\omega^2 C_{sd}R_{sd}R_iC_{id} - 1\right)^2} + \frac{2\sin\left(\frac{n\pi}{2}\right)}{\left(A_e\omega\right)^n}\right] \quad \text{(Eq. 8.9)}$$

where A_e corresponds to the electrode polarisation CPE. Thus, the behaviour of the model circuit at extreme frequencies becomes:

$$\left.\frac{d\log Z'}{d\log\omega}\right|_{\omega\to 0} = -n \quad \text{(Eq. 8.10)}$$

$$\left.\frac{d\log Z'}{d\log\omega}\right|_{\omega\to \infty} = -n \quad \text{(Eq. 8.11)}$$

$$\left.\frac{d\log Z''}{d\log\omega}\right|_{\omega\to 0} = -n \quad \text{(Eq. 8.12)}$$

$$\left.\frac{d\log Z''}{d\log\omega}\right|_{\omega\to \infty} = -n \quad \text{(Eq. 8.13)}$$

For the case of RTM6 epoxy resin the slope of imaginary impedance spectrum at very low frequencies has been found to be 0.5. Consequently,

$$n = \frac{1}{2} \quad \text{(Eq. 8.14)}$$

and

$$Z = \frac{R_i\left[\omega^2 {C_{sd}}^2 R_{sd}\left(R_{sd}+R_i\right)+1\right]}{\omega^2\left(C_{sd}R_i + C_{sd}R_{sd} + C_{id}R_i\right)^2 + \left(\omega^2 C_{sd}R_{sd}R_iC_{id} - 1\right)^2} - \frac{2}{\sqrt{A_e\omega}} -$$

$$j\left[\frac{R_i\left[\omega^3 {C_{sd}}^2 {R_{sd}}^2 R_iC_{id} + \omega R_i\left(C_{id}+C_{sd}\right)\right]}{\omega^2\left(C_{sd}R_i + C_{sd}R_{sd} + C_{id}R_i\right)^2 + \left(\omega^2 C_{sd}R_{sd}R_iC_{id} - 1\right)^2} + \frac{2}{\sqrt{A_e\omega}}\right] \quad \text{(Eq. 8.15)}$$

In order to evaluate the consistency of the model expressed by Eq. 8.15, the spectrum it generates when the constants of the circuit approximate the values corresponding to RTM6 has been calculated and is illustrated in Fig. 8.15. The value of the CPE constant A_e has been evaluated using the intersection of the imaginary impedance spectrum with the $log\,\omega = 0$ line, which occurs at about $10^{5.5}$ ohms (see for example Fig.8.7.), for spectra in which electrode polarisation is dominant at low frequencies. The value of R_i is equal to half of the imaginary impedance maximum (ranges between $10^{5.5}$ and $10^{7.5}$) in the region of the charge migration domination. The value of C_{id} has been calculated from the final line of the imaginary impedance spectrum, which should intersect with the $log\,Z'' = 0$ line at a angular frequency ($2\pi 10$ in Fig.8.7) equal to $1/C_{id}$. The values of C_{sd} and R_{sd}, although relaxation is not apparent in the global spectrum and they could have been omitted, have been chosen to be consistent with RTM6 resin permittivity values ($\varepsilon_r - \varepsilon_\infty / \varepsilon_\infty = 2.5$) reported elsewhere (17) and with the relaxation time corresponding to the frequency range relaxation as manifested in Fig.8.14. Accordingly the approximate values used are those given in Table 8.2.

A_e (Mohm/s$^{0.5}$)	R_i (Mohm)	C_{id} (pF)	C_{sd} (pF)	R_{sd} (Mohm)
3.1	1.0	15.0	22.5	0.7

Table 8.2 *Approximate values for the elements of the equivalent circuit of RTM6*

At very high and very low frequencies the CPE containing model presents linear regions with a slope of –0.5, corresponding to electrode polarisation in both imaginary and real impedance spectra. A comparison of the position of the spectra as calculated using the approximate values of Table 8.2, within the frequency range in which the experiments were performed, shows that this equivalent circuit model is in good accordance with the experimental results. The real impedance spectrum as obtained experimentally does not show the first initial decrease due to the manifestation of electrode polarisation at lower frequencies in its spectrum. That explains the difference between the value given in Table 8.1 for the initial slope of the real impedance spectrum (0.01) and the value given

in Eq. 8.10. The manifestation of electrode polarisation in the imaginary impedance spectrum occurs at a higher frequency, thus is within the experimental window. Consequently, the experimental spectrum has a slope of 0.5 at low frequencies, identical to the value given in Eq. 8.12. Similarly to the model presented in paragraph 3.4.4, charge migration is manifested by the first peak in the imaginary impedance spectrum and the first step in the real impedance, and relaxation is manifested by a shoulder and the second step in the corresponding spectra. Relaxation is located at the high end of the spectrum and is less pronounced, especially in the imaginary impedance spectrum. This explains the difficulties in distinguishing relaxations in the experimental spectra. The experimental slope at high frequencies is different to that predicted by Eqs. 8.11 and 8.13. This occurs because the high end of the experimental window is well below the manifestation of electrode polarisation at high frequencies. Thus charge migration, which governs imaginary impedance at about 1 MHz, results in the observed experimental slope of –1. Similarly, the slope of the real impedance spectrum in this frequency is located at the beginning of relaxation. Thus, the behaviour of the specific resin system can be described satisfactorily by the equivalent circuit model illustrated in Fig. 8.16.

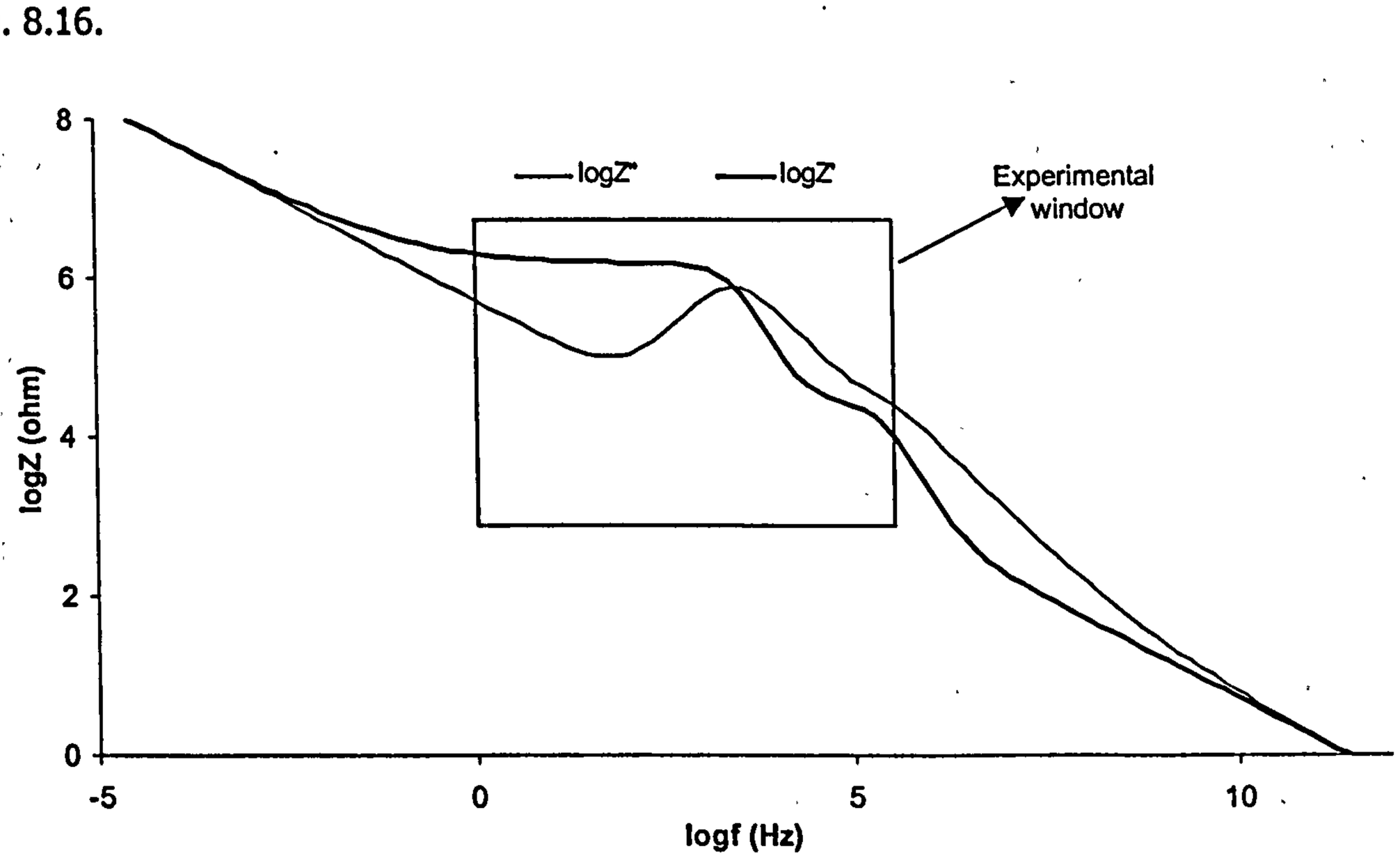

Fig.8.15 *Real and imaginary impedance spectra of the equivalent circuit which represents polarisation as a constant phase element based on the approximate elements values for RTM6*

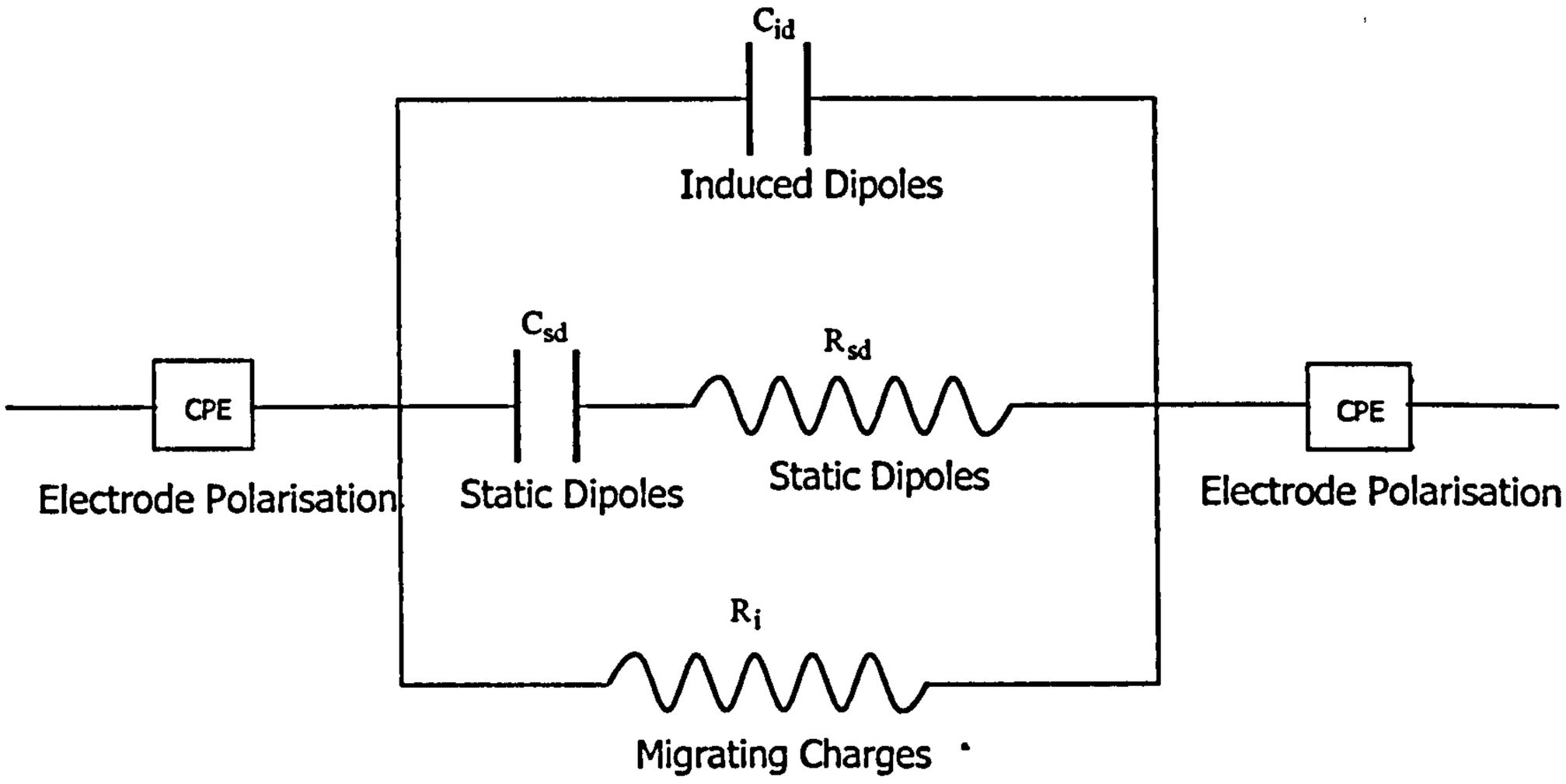

Fig.8.16 *Equivalent circuit representing polarisation as a constant phase element*

8.5 Identification of vitrification

As mentioned in paragraph 3.4.4, vitrification has previously been found to coincide with a knee in the imaginary impedance versus time curve and a peak in the real impedance versus time curve (150, 155), but the underlying molecular mechanisms causing this correlation have never been elucidated. The results presented in paragraphs 8.3.1 and 8.3.2 showed that a peak appears in the real impedance curve and a knee in the imaginary impedance curve at the instances illustrated in Figs. 8.5 and 8.13. In order to check whether these features are a manifestation of vitrification, these results are compared with calorimetric vitrification as measured by the step in heat capacity occuring in MDSC experiments. The heat capacity (as determined by MDSC) versus conversion (as calculated by the kinetic model described in chapter 5) for the isothermal experiments at 130, 140, 150 and 160 °C, and for the dynamic experiments at 0.25, 0.5 and 1 °C /min are illustrated in Fig. 8.17. This type of curves has been selected for the comparison of impedance and calorimetric data, rather than the heat capacity versus time or temperature curves, because a temperature overshoot of about 2-3 °C occurred in the dielectric experiments. This temperature difference does not allow a direct

comparison to be made of the cure times or temperatures at which the material undergoes a glass transition.

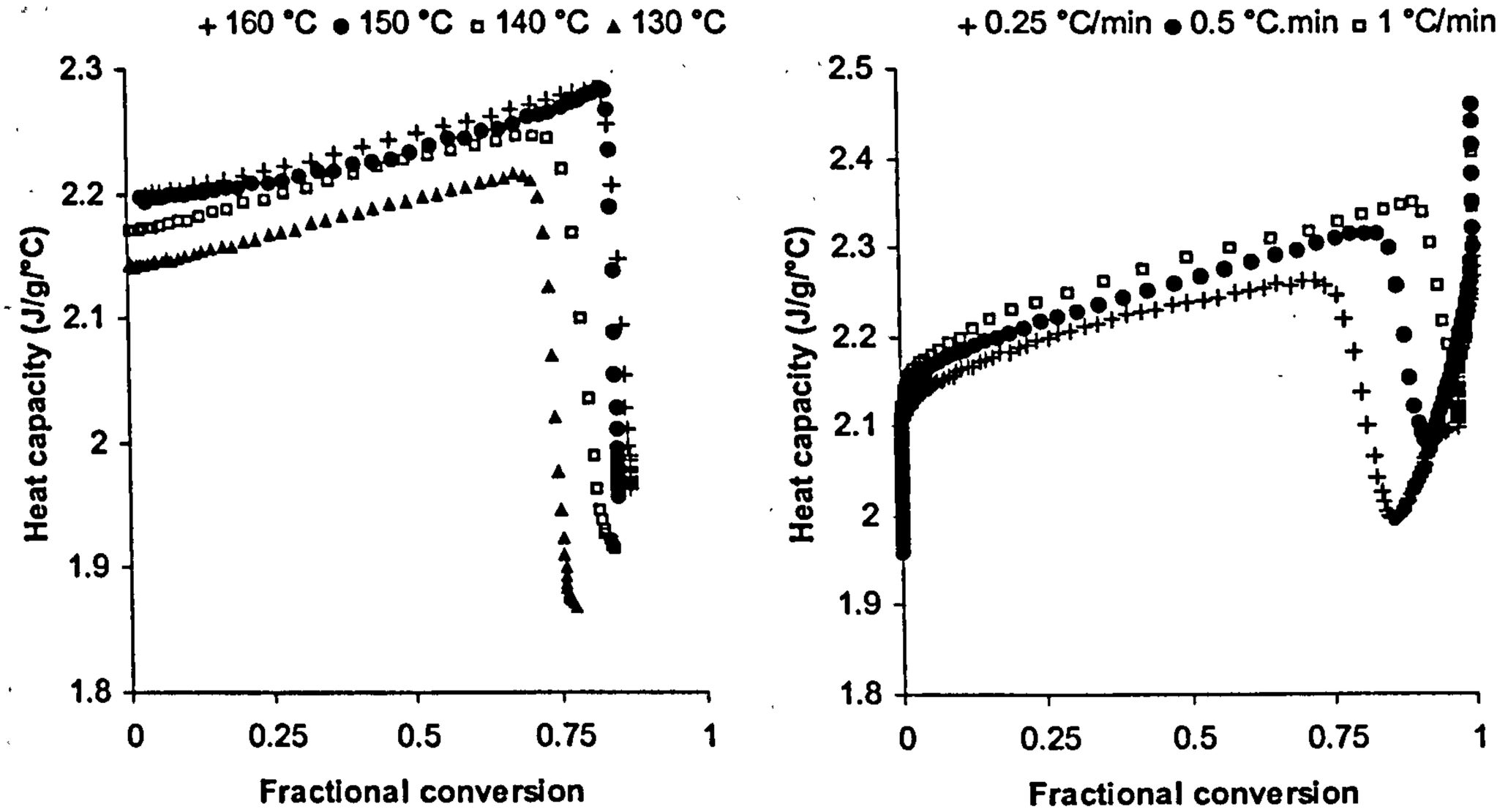

(a) (b)

Fig.8.17 *Heat capacity versus conversion curves. (a) Isothermal MDSC measurements. (b) Dynamic MDSC measurements.*

The conversion at which vitrification occurs (as determined by the conversion where the step drop of heat capacity occurs is given in Table 8.3, together with the average conversion where the knee and peak of the imaginary and real impedance appear in the dielectric experiments. The conversion profiles of the dielectric experiments were calculated using the kinetic model presented in chapter 5.

It can be observed that the two sets of data have a high correlation (0.98). The dielectric vitrification appears to be occuring at slightly lower conversions than that determined by calorimetry. This is attributed to the different frequency range of the measurements. MDSC experiments correspond to an angular frequency of the order of 0.01 Hz while the peak and knee of real and imaginary impedance occur at frequencies in the order of 10 kHz. As the glass transition is a time scale dependent phenomenon, vitrifications defined and measured at different frequencies are expected to differ. Since vitrification occurs when molecular relaxation times become significantly higher than the

experimental time scale (221), an increase in the time scale, i.e. lower frequency, causes a rise in the apparent network density, or a decrease in the temperature at which vitrification is observed. Consequently, calorimetric vitrification is expected to be detected at conversions higher than those of dielectric vitrification.

	Calorimetric vitrification fractional conversion	**Dielectric vitrification fractional conversion**
130 °C	0.69	0.63
140 °C	0.73	0.71
150 °C	0.81	0.79
160 °C	0.83	0.80
0.25 °C/min	0.74	0.72
0.5 °C/min	0.83	0.80
1 °C/min	0.89	0.85

Table 8.3 *Calorimetric and dielectric vitrification conversions in isothermal and dynamic cure of RTM6 resin*

The molecular mechanisms leading to the manifestation of glass transition in the impedance versus time curves can be uncovered by a careful examination of the spectra evolution during cure. In paragraphs 8.3.1 and 8.3.2 the occurrence of the peak in the real impedance and the knee in the imaginary versus time curves has been attributed to the behaviour of the spectra in the kHz to MHz frequency range. There, the real impedance spectra at different times intersect at some frequency resulting in the manifestation of the peak (Figs. 8.4.a and 8.11.b) and the imaginary impedance spectra are shifted in a step fashion resulting in the manifestation of the knee (Figs. 8.4.b and 8.12.b).

The frequency range in which these phenomena take place is the same as the frequency range where the hindered dipolar relaxation occurs. There, the real impedance spectrum is a decreasing function of frequency and is shifted to lower frequencies and higher values as curing progresses or temperature decreases (Figs. 8.1.a, 8.2.a and 8.6). The imaginary impedance spectrum has the form of a linear drop which is shifted towards lower frequencies and higher values. The combination of the two shifts is such that the

spectrum remains along the same line, as illustrated in Figs. 8.1.b, 8.2.b and 8.7. An imitation of this behaviour by the equivalent circuit model spectra presented in Fig. 8.15 has been produced in the frequency range of relaxation and is illustrated in Fig. 8.18. There it can be observed that at a fixed frequency (line AA') the real impedance increases initially with increasing cure time and after a certain point decreases. Similarly the imaginary impedance at a fixed frequency (line AA') is constant when the relaxation occurs at higher frequencies, increases rapidly as the relaxation part of the spectrum passes through the fixed frequency and then stabilises again when the relaxation is moved to lower frequencies. Consequently, the experimental observation of the correlation of the peak of real impedance and the knee of imaginary impedance with the vitrification point is attributed to the dipolar relaxation and its gradual shift through the frequency range of the measurement. This means that impedance monitoring yields equivalent results, as far as the vitrification is concerned, with conventional dielectric analysis, where the dielectric loss peak and the permittivity step indicating vitrification are attributed to the same mechanism of the shift of relaxation as the cure progresses.

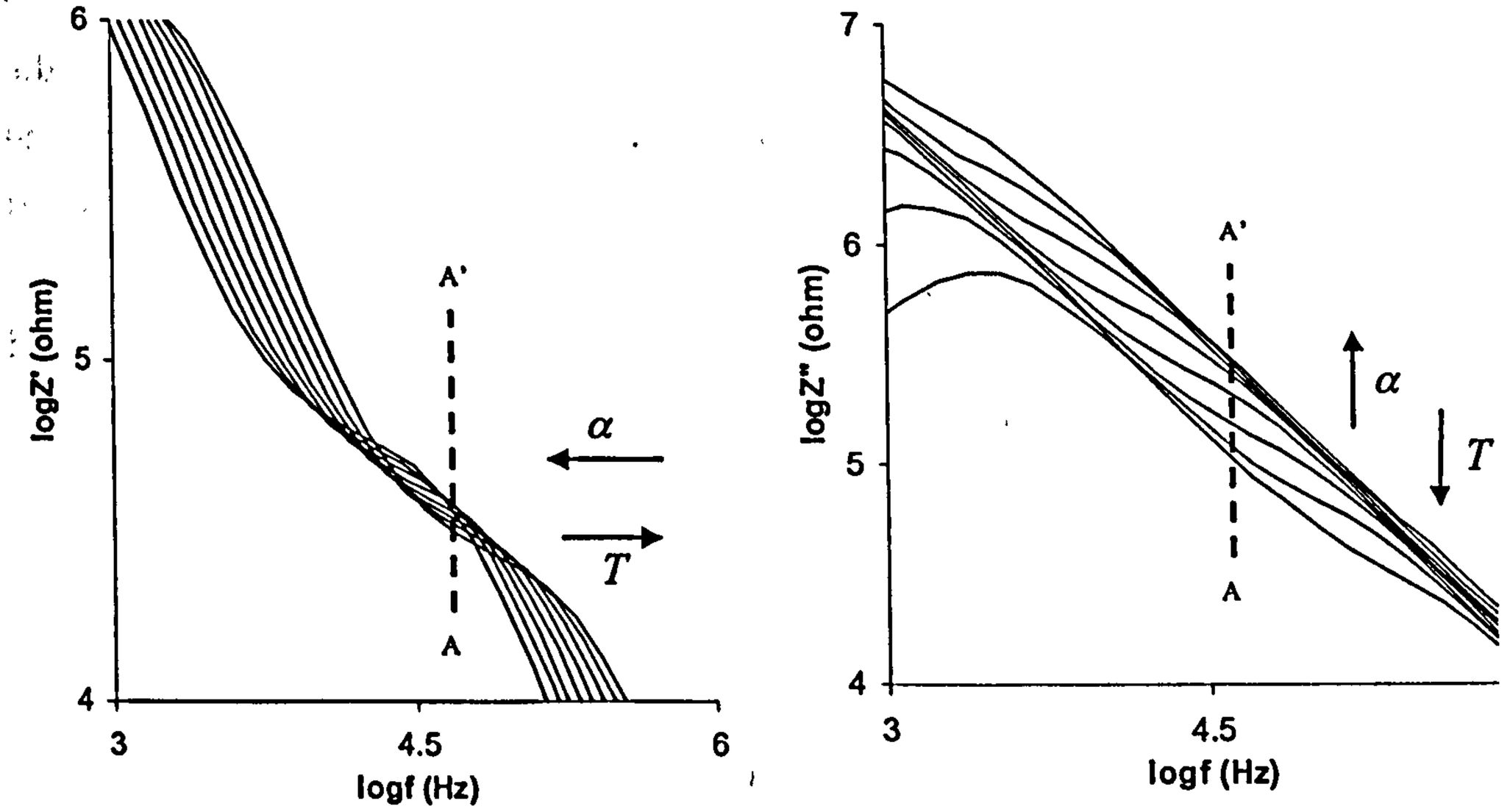

(a) Real impedance (b) Imaginary impedance

Fig.8.18 *Evolution of the relaxation region of impedance spectra*

8.6 Estimation of the progress of reaction

It has been shown that following the changes of the imaginary impedance spectrum maximum can give an accurate estimation of the fractional conversion under isothermal conditions (17, 138, 149, 150). In Figs. 8.19, 8.20 and 8.21 the evolution of the imaginary impedance maximum together with the degree of cure evolution (as calculated using the kinetic model described in chapter 5) for the isothermal experiments at 130, 140, 150 and 160 °C and the dynamic experiments at 0.25, 0.5, 0.75, 1, 1.25, 1.5, 1.75 and 1 °C/min are given. Lines indicating the cure time of maximum reaction rate in each experiment are superimposed on the curves, in order to facilitate the comparison between impedance and progress of reaction data. In Fig. 8.19 it can be observed that the imaginary impedance maximum imitates the conversion curves very closely. The start, end and maximum rate points are very similar in the two curves. Thus, normalisation of the impedance data can lead to a direct estimation of the reaction progress in isothermal experiments. In contrast, under dynamic conditions, as illustrated in Figs 8.20 and 8.21, the combined influence of temperature and reaction complicates the imaginary impedance maximum behaviour. At the beginning of the curing temperature governs the maximum value, which drops as the viscosity of the resin decreases. When reaction becomes fast it starts to dominate the signal and the imaginary impedance maximum increases, as the formation of the network impedes migration of the extrinsic charges. The situation is reversed back to temperature domination towards the end of the reaction. The reaction onset, maximum rate and end points do not coincide with the corresponding points of the impedance versus cure time curves. Consequently following the evolution of maximum impedance cannot provide the means for reaction monitoring under dynamic heating conditions.

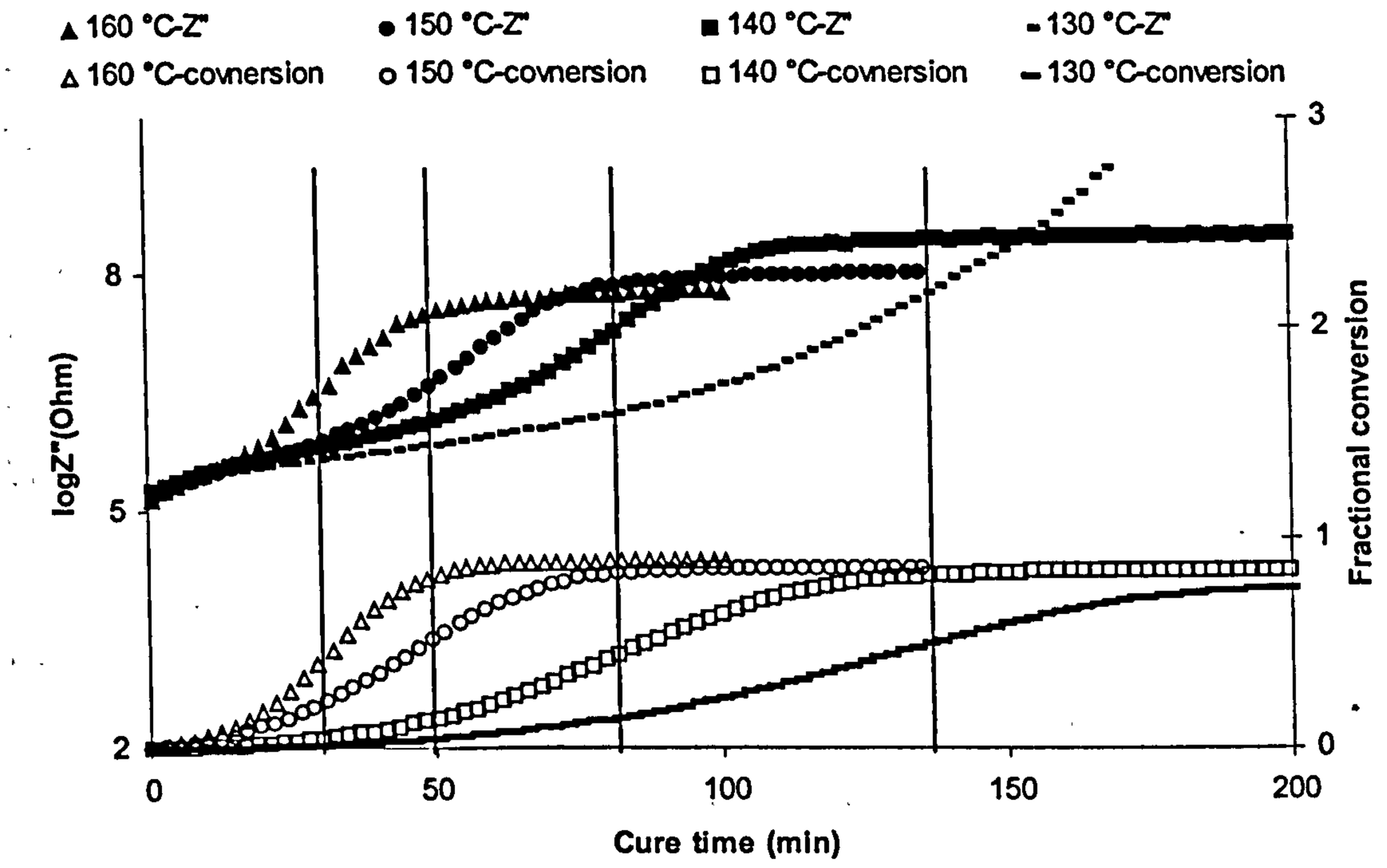

Fig.8.19 *Imaginary impedance maximum and conversion versus time in isothermal cure of RTM6 resin*

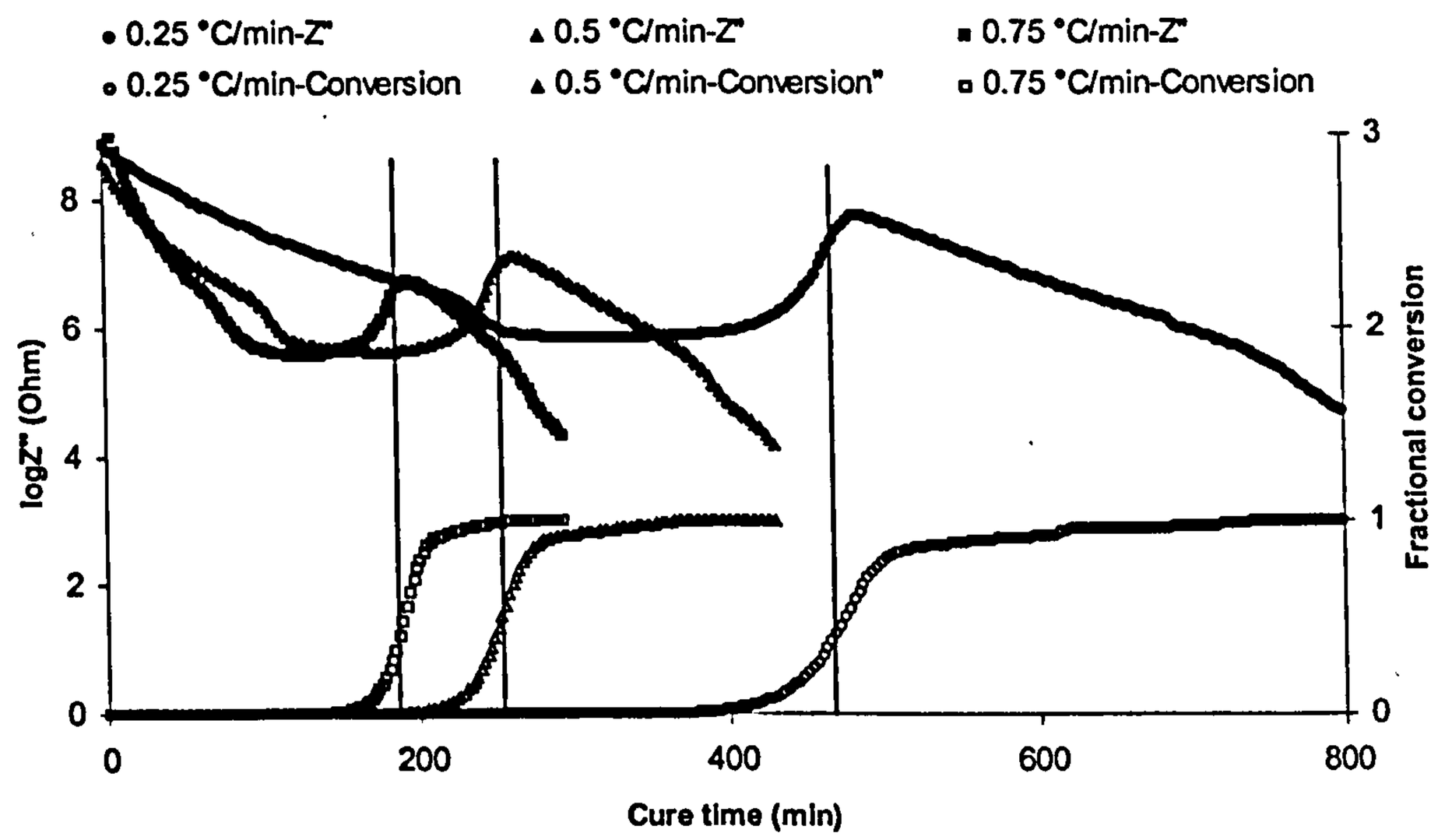

Fig.8.20 *Imaginary impedance maximum and conversion versus time in dynamic cure of RTM6 resin at low heating rates*

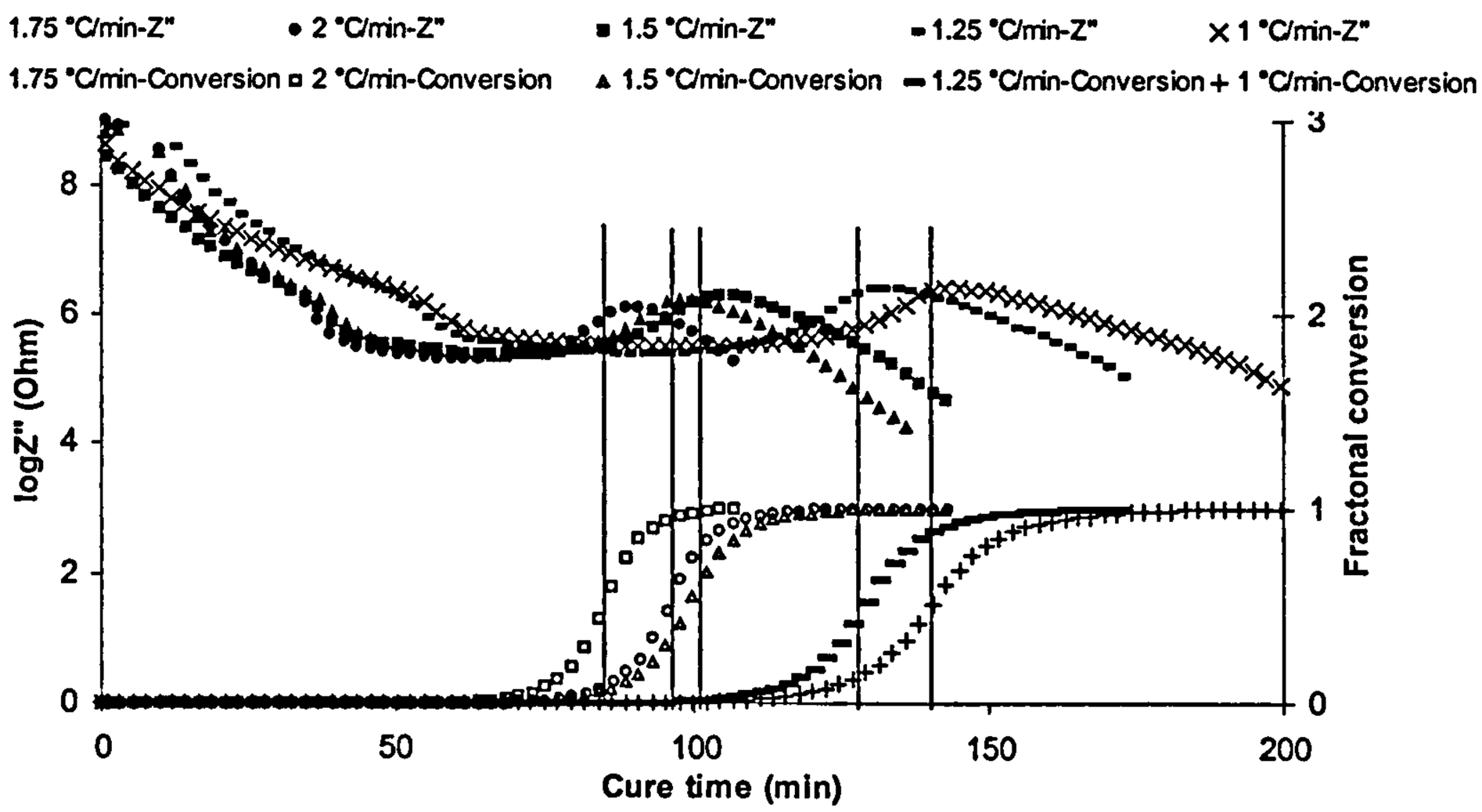

Fig.8.21 *Imaginary impedance maximum and conversion versus time in dynamic cure of RTM6 resin at high heating rates*

Here a different procedure is proposed for the exploitation of impedance data for reaction monitoring. As presented in paragraphs 8.3.1 and 8.3.2 the imaginary impedance spectrum has two extremes; a maximum corresponding to charge migration and a minimum at the point where electrode polarisation stops to control the impedance and charge migration becomes the dominant mechanism. Both extremes are shifted during the cure, to lower frequencies as the reaction progresses and to higher frequencies as temperature increases. This behaviour is illustrated in Figs. 8.22, 8.23 and 8.24 for the isothermal and dynamic experiments performed in this study. The minimum of imaginary impedance is shifted outside the experimental spectrum at intermediate to high conversion combined with low and intermediate temperature, thus the available experimental data are limited in isothermal experiments. An observation significant for the monitoring of the reaction is that the two extremes show similar shifts when temperature changes, whereas the drop of the frequency of the minimum is more sensitive to the reaction progress. This behaviour is manifested clearly in the higher heating rate dynamic curves illustrated in Fig. 8.24. For example in the 2 °C/min

experiment the maximum shifts by 1.7 decades from 18 to 43 min, while the minimum shifts by 1.8 under the influence of the temperature increase, which is not accompanied by progress of the reaction. In contrast between 79 and 93 min, where the progress of reaction dominates the signal, the maximum shifts by 0.6 and the minimum by 1.4. At high heating rates (1.5, 1.75 and 2 °C/min) where both the minimum and maximum remain within the measurement frequency range throughout the cure another observation can be made. The minima of the frequencies of the two extremes appearing towards the end of the reaction occur at different times. This is illustrated by the lines which coincide with the minimum of the lower curves (frequency of minimum) in Fig. 8.24, whereas they intersect with the upper curves (frequency of maximum) at a time later than their minimum.

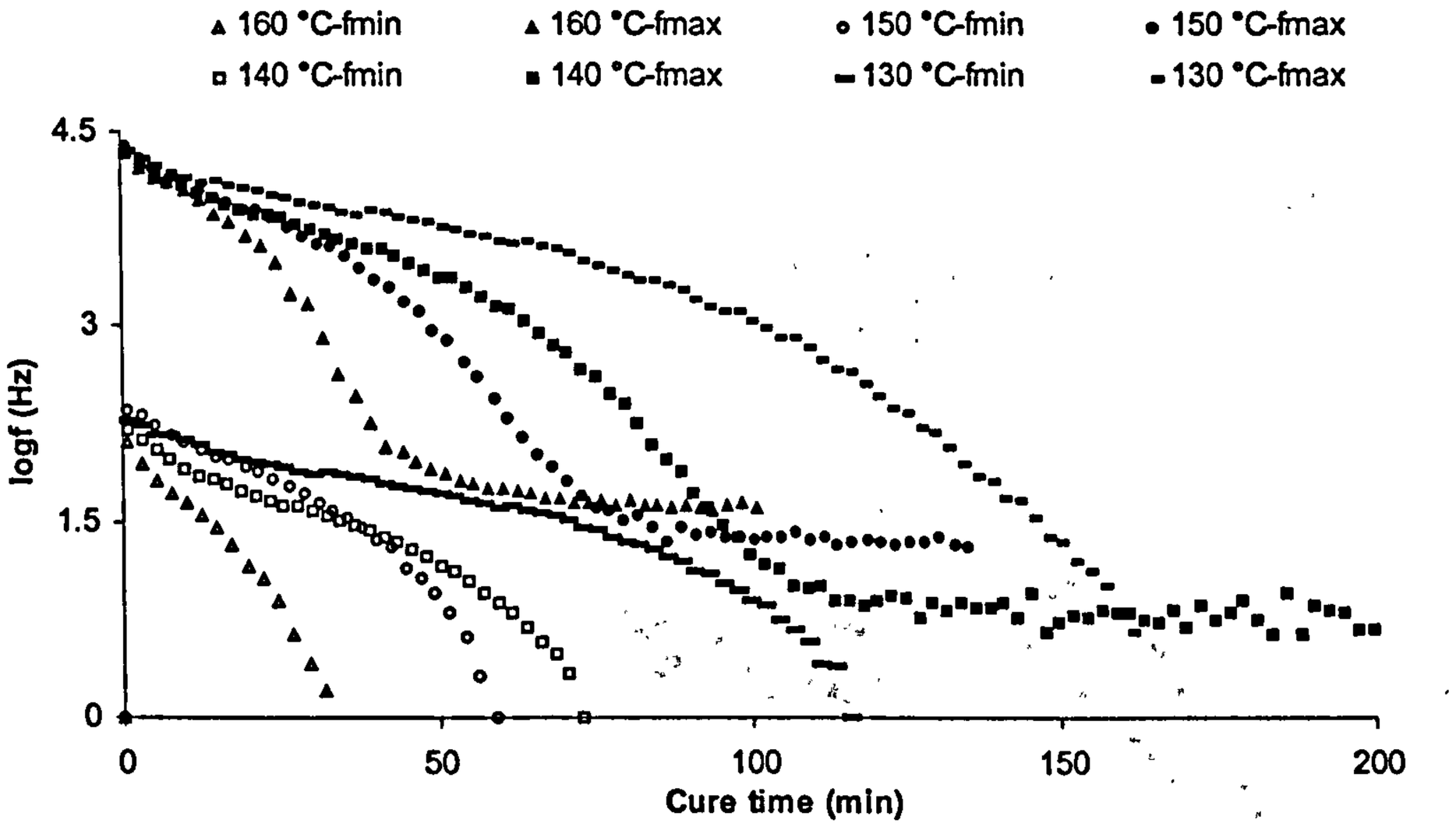

Fig.8.22 *Frequencies of the impedance spectrum maximum and minimum in isothermal cure of RTM6 resin*

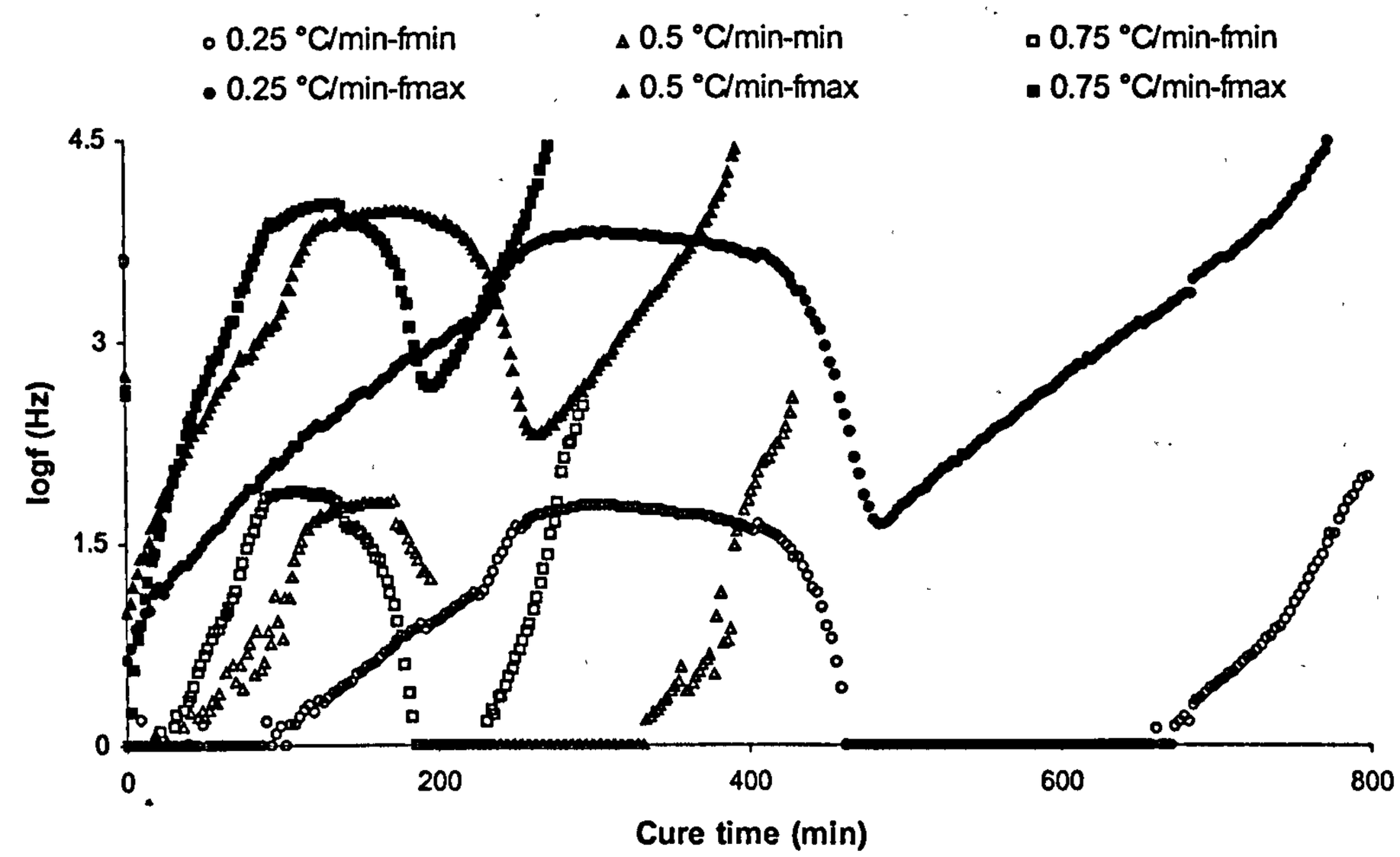

Fig.8.23 *Frequencies of the impedance spectrum maximum and minimum in dynamic cure of RTM6 resin at low heating rates*

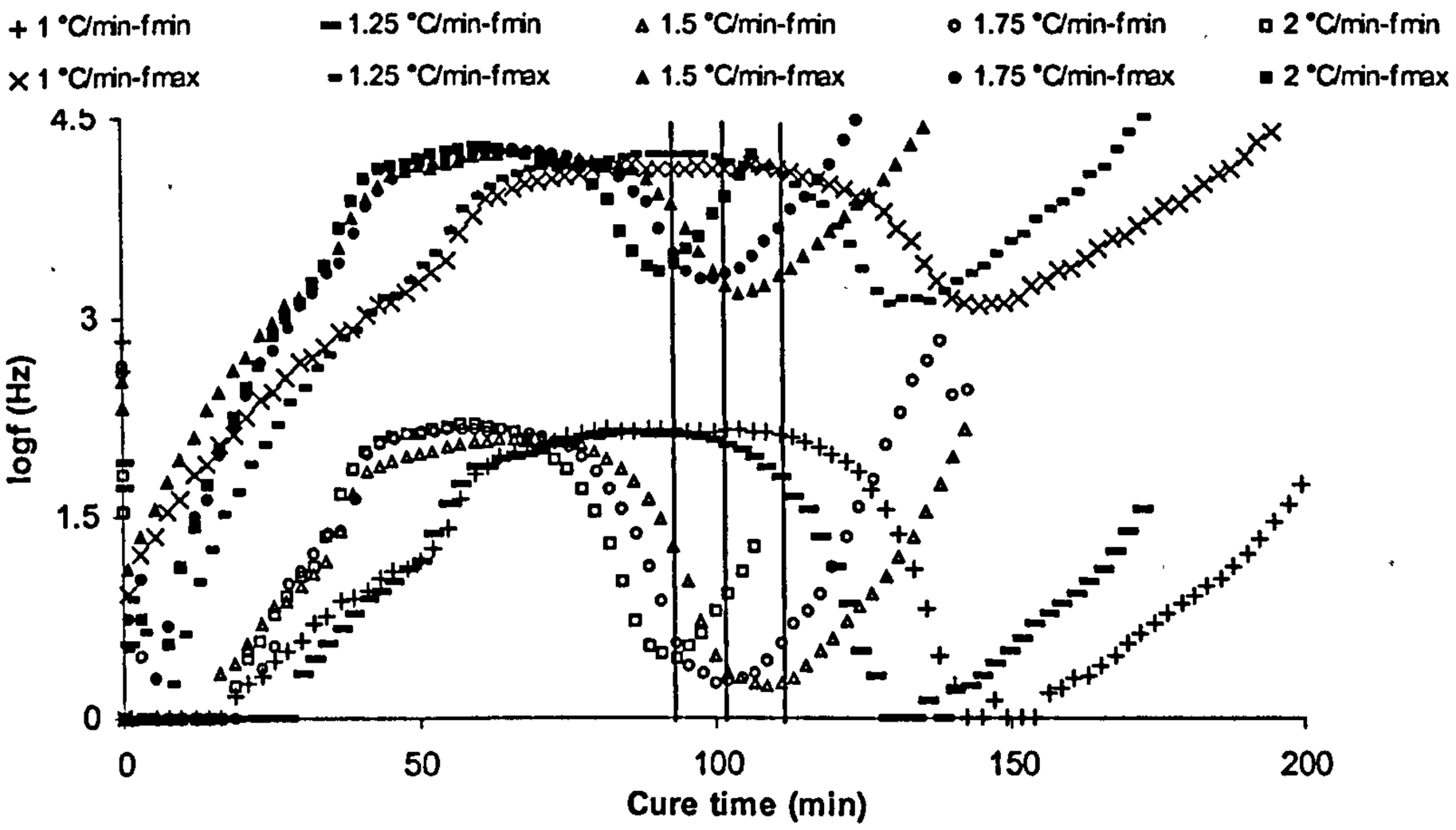

Fig.8.24 *Frequencies of the impedance spectrum maximum and minimum in dynamic cure of RTM6 resin at high heating rates*

The different sensitivities of the extremes shift to the progress of the reaction can be used in order to eliminate the problems arising from the combined influence of temperature and degree of cure on the monitoring signals. In Fig. 8.25 the difference between the frequency of maximum and the frequency of minimum of the imaginary impedance spectrum is compared with the progress of reaction, for the high heating rate dynamic experiments. The frequency difference undergoes a step change. The times of onset, maximum rate and end of the step coincide with the corresponding times of the kinetics curves. When the material does not react the frequency difference remains constant. Thus, the frequency difference shows a strong dependence on the degree of cure, whereas its sensitivity to temperature variation appears low.

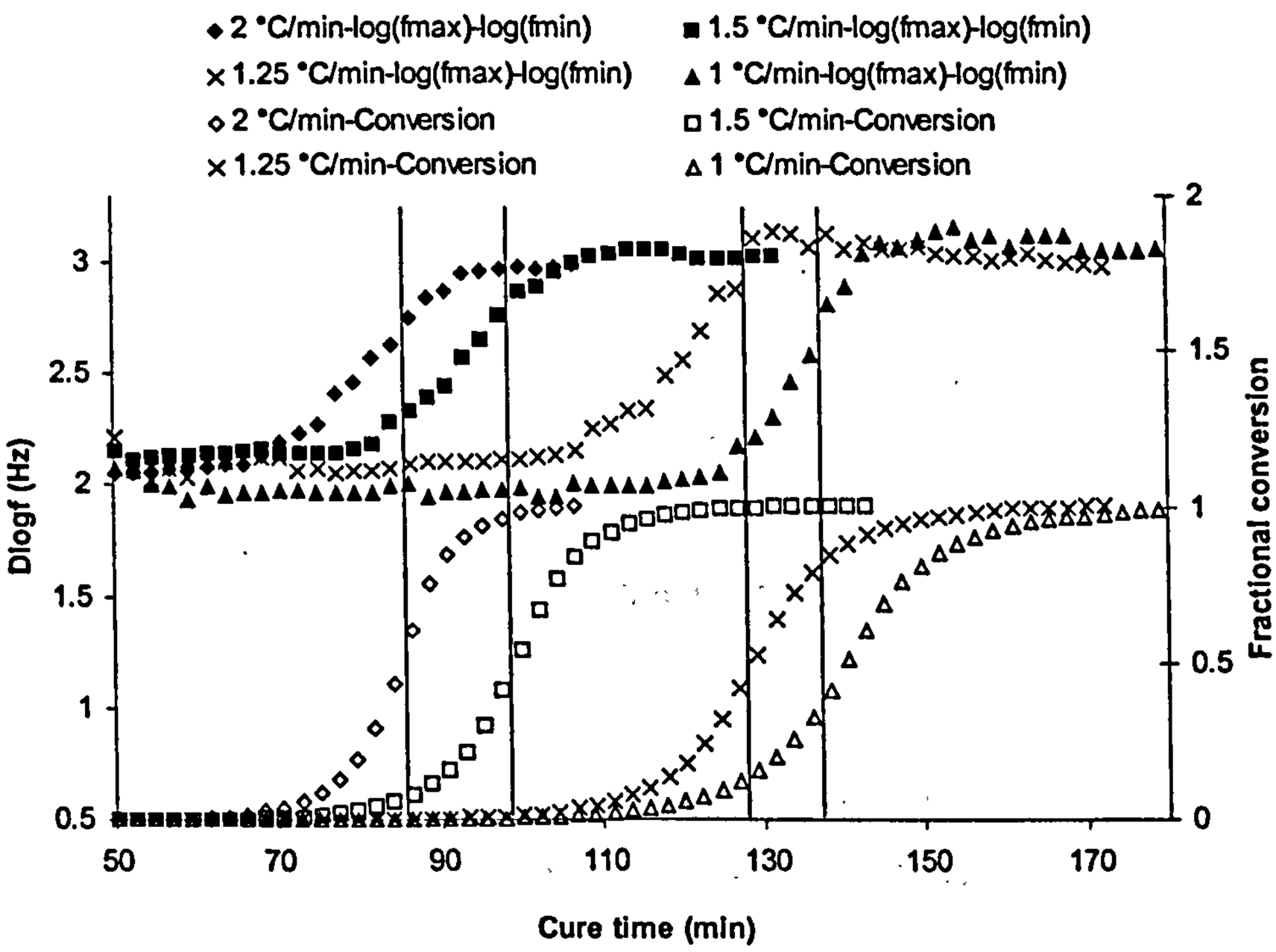

Fig.8.25 *Impedance spectra maximum and minimum frequencies difference and degree of cure versus cure time in dynamic cure of RTM6*

In Fig. 8.26 the dependence of the maximum-minimum frequencies difference on the conversion is illustrated. There, data corresponding to spectra with both extremes from

dynamic and isothermal experiments are shown. In order to quantify the correlation a third degree polynomial was fitted to the data. The equation of the fit is:

$$\alpha = 0.15 D\log f^3 - 0.38 D\log f^2 - 0.23 D\log f + 0.81 \qquad \text{(Eq. 8.16)}$$

and the regression constant is 0.94. This relation is purely empirical, but it provides the means for a direct estimation of the degree of cure at any temperature from the instantaneous imaginary impedance spectrum. Its validity is currently limited to the specific resin system and the type of sensor used in this study.

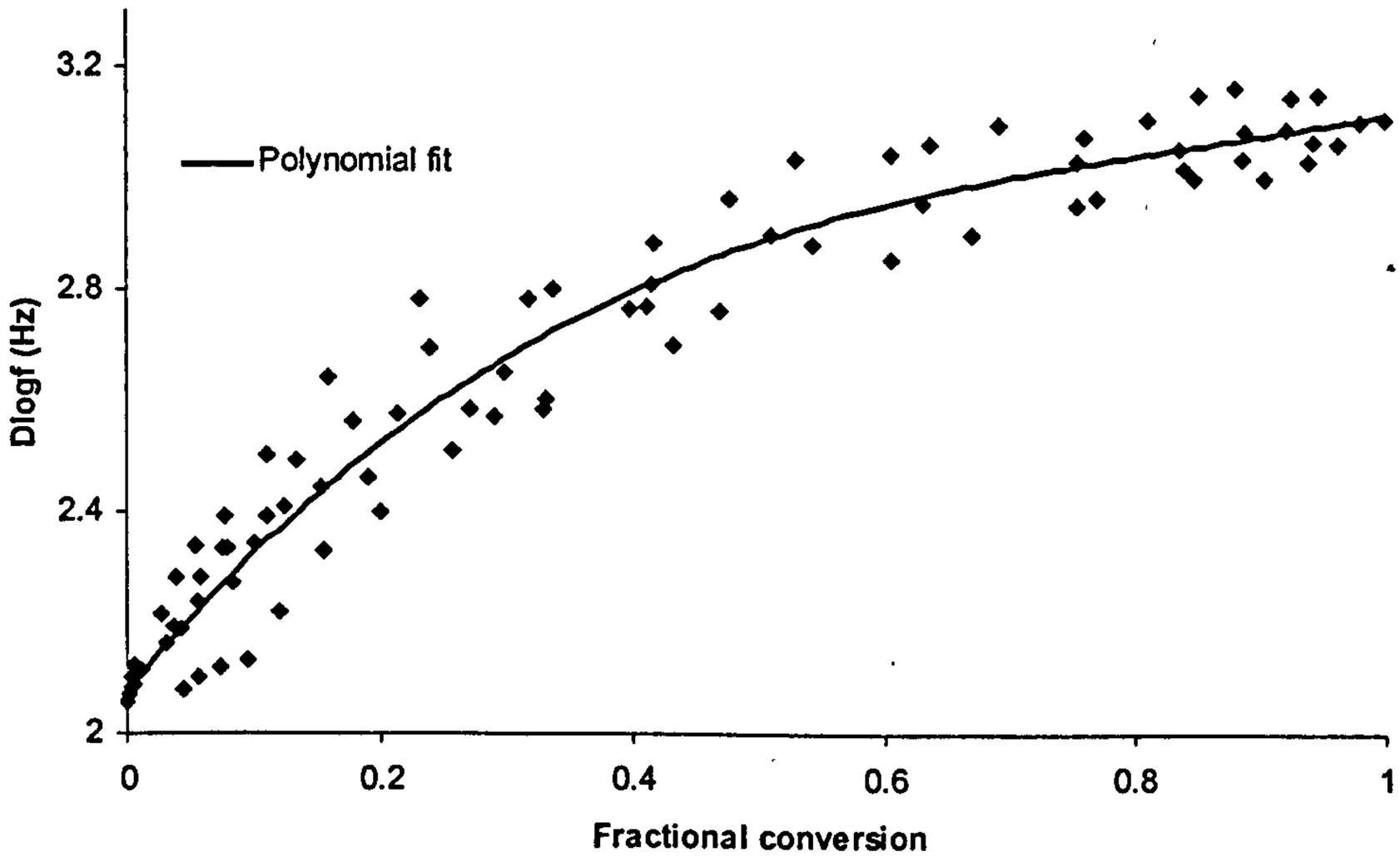

Fig.8.26 *Impedance spectra maximum and minimum frequencies difference versus degree of cure for a number of different isothermal and dynamic cure experiments*

For a possible explanation of this phenomenon an analysis based on the equivalent circuit of the material impedance response can be carried out. The minimum of the imaginary impedance spectrum occurs at frequencies where electrode polarisation and charges migration dominate the signal. Thus the imaginary impedance becomes:

$$Z = \frac{\omega R_i^2 C_d}{1+\omega^2 C_d^2 R_i^2 C} + \frac{2\cos\left(\frac{n\pi}{2}\right)}{(A_e\omega)^n} \qquad \text{(Eq. 8.17)}$$

Here C_d denotes all dipolar contributions. By including all constants involved in the electrode polarisation in one coefficient A and considering that the part of the response due to charges is in their low frequency range, Eq. 8.9 can be approximated as follows:

$$Z = \omega R_i^2 C_d + \frac{1}{A\omega^n} \qquad \text{(Eq. 8.18)}$$

Eq. 8.18 has a minimum at

$$\omega = \frac{n^{\frac{1}{n+1}}}{A^{\frac{1}{n+1}} C^{\frac{1}{n+1}} R^{\frac{2}{n+1}}} \qquad \text{(Eq. 8.19)}$$

Similarly the maximum occurs in the charge dominated part of the spectrum. There imaginary impedance can be approximated as follows:

$$Z = \frac{\omega R_i^2 C_d}{1 + \omega^2 C_d^2 R_i^2 C} \qquad \text{(Eq. 8.20)}$$

which has a maximum at

$$\omega = \frac{1}{CR} \qquad \text{(Eq. 8.21)}$$

Consequently the frequency difference becomes:

$$log\, f_{max} - log\, f_{min} = log\left(\frac{\omega_{max}}{\omega_{min}}\right) = log\left(\frac{A^{\frac{1}{n+1}} R^{\frac{1-n}{n+1}}}{C^{\frac{n}{n+1}} n^{\frac{1}{n+1}}}\right) \qquad \text{(Eq. 8.22)}$$

In order to investigate the temperature dependence of the quantities involved in Eq. 8.22 a dynamic experiment at 1.25 °C/min has been performed in fully cured RTM6 resin at the same rate. The evolution of the imaginary impedance spectrum during heating is illustrated in Fig. 8.27. The value of R decreases with increasing temperature, as shown by the behaviour of the impedance peak. C is represented by the intersection of the imaginary impedance spectrum with the $log\, Z'' = 0$ line. The spectrum at high frequencies presents slight changes during the cure. Consequently its extrapolation to the ω axis will remain constant relative to the other features of the spectrum. A is represented by the intersection of the part of the spectrum corresponding to electrode polarisation with the $log\, f = 0$ line. This is expressed by the relation:

$$log\, A = -n\, log\, 2\pi - log\, Z''_{log\, f=0} \qquad \text{(Eq. 8.23)}$$

which shows that A is a decreasing function of the impedance at 1 Hz. It can be observed that the imaginary impedance value at 1 Hz drops with increasing temperature, consequently A is expected to increase. Thus, the ratio on the right side of Eq. 8.23 contains a term which decreases with temperature and a term which increases with temperature. A possible explanation of the low sensitivity of the frequency difference to the temperature lies in the mutually cancelling effect of these terms.

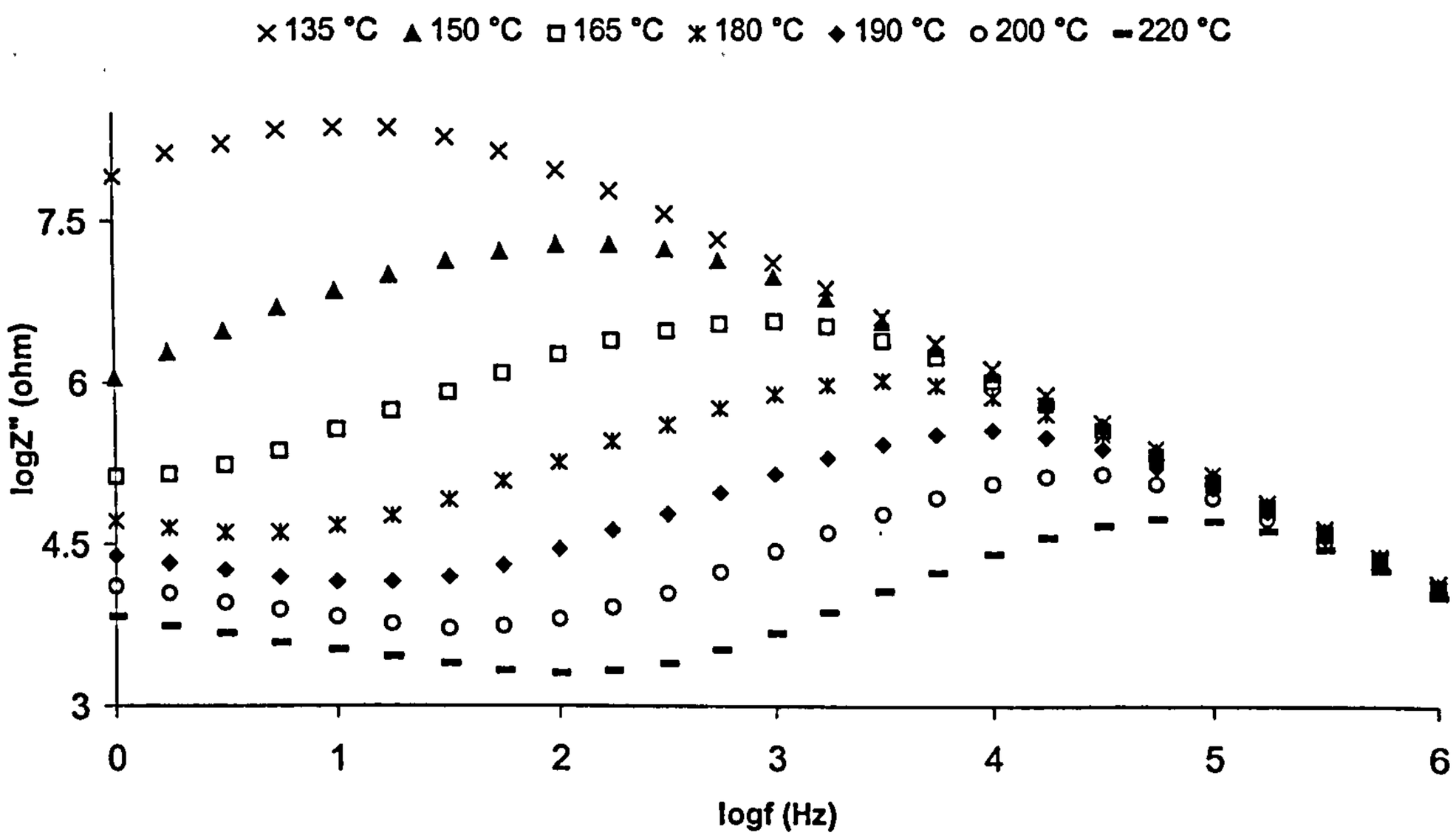

Fig.8.27 *Impedance spectrum evolution during heating up at 1.25°C/min of fully cured RTM6 resin*

The above procedure for estimating the degree of cure from impedance data, although empirical and material specific, has the advantage of using the electrode polarisation contribution to the signal. Electrode polarisation has been overlooked up to now in the literature because it arises as an artefact of the measurement, however especially in microelectrodes, it cannot be ignored. The fact that it is sensor dependent can be used in order to manipulate the useful frequency range, thus providing flexibility in designing an appropriate measurement practice.

8.7 Overview

Results from the application of impedance spectroscopy to the monitoring of isothermal and dynamic cure of RTM6 epoxy resin have been presented. The evolution of the real and imaginary impedance at fixed frequencies has been explained in terms of the general behaviour of the spectra. The equivalent circuit model of thermosetting systems currently used in the literature has been proved inadequate to describe the behaviour of the specific resin system and a new model, which represents electrode polarisation using a constant phase element, has been developed.

The manifestation of vitrification as a peak in the real impedance versus time curves and as a knee in the real impedance versus time curves has been confirmed and tested against MDSC data. This phenomenon has been attributed to the gradual shifting of the dipolar relaxations to lower frequencies as the curing reaction progresses. The possibility of using impedance spectroscopy for the estimation of the degree of cure in both isothermal and dynamic conditions has been investigated. A purely experimental method based on the different sensitivity of the extremes of the imaginary impedance spectrum to temperature and conversion has been developed and validated for the specific resin system. A potential explanation of this method in terms of the equivalent circuit model has been given.

Chapter Nine

9 Flow monitoring

9.1 Introduction

The filling has been identified as the critical stage of liquid moulding composites production methods and has constituted the focus of relevant modelling studies. In contrast, flow monitoring has not received analogous attention and an industrially realisable technique to perform this task has yet to be established. In this chapter, the possibility of using dielectrics as the means for flow monitoring is investigated. The practicalities involved in the measurement vary according to the electrical behaviour of the reinforcement. Thus, different methods are devised for flow monitoring when glass and carbon reinforcements are used.

9.2 Flow monitoring in non-conductive reinforcements filling

9.2.1 Sensor description and principle of operation

The geometry of the dielectric sensor appropriate for flow sensing in glass composites production is illustrated in Fig. 9.1. It comprises two parallel flat copper electrodes embedded between two layers of a polymeric film. A very thin layer of adhesive exists between the electrodes and the polymeric film and between the two layers of the

polymeric film. Some air is trapped in the area between the two electrodes. One side of the sensor is covered by metal foil in order to provide screening of the field. Thus, with application of voltage a semicylindrical field is formed that penetrates a portion of the space where the filling of the fabric by liquid resin takes place.

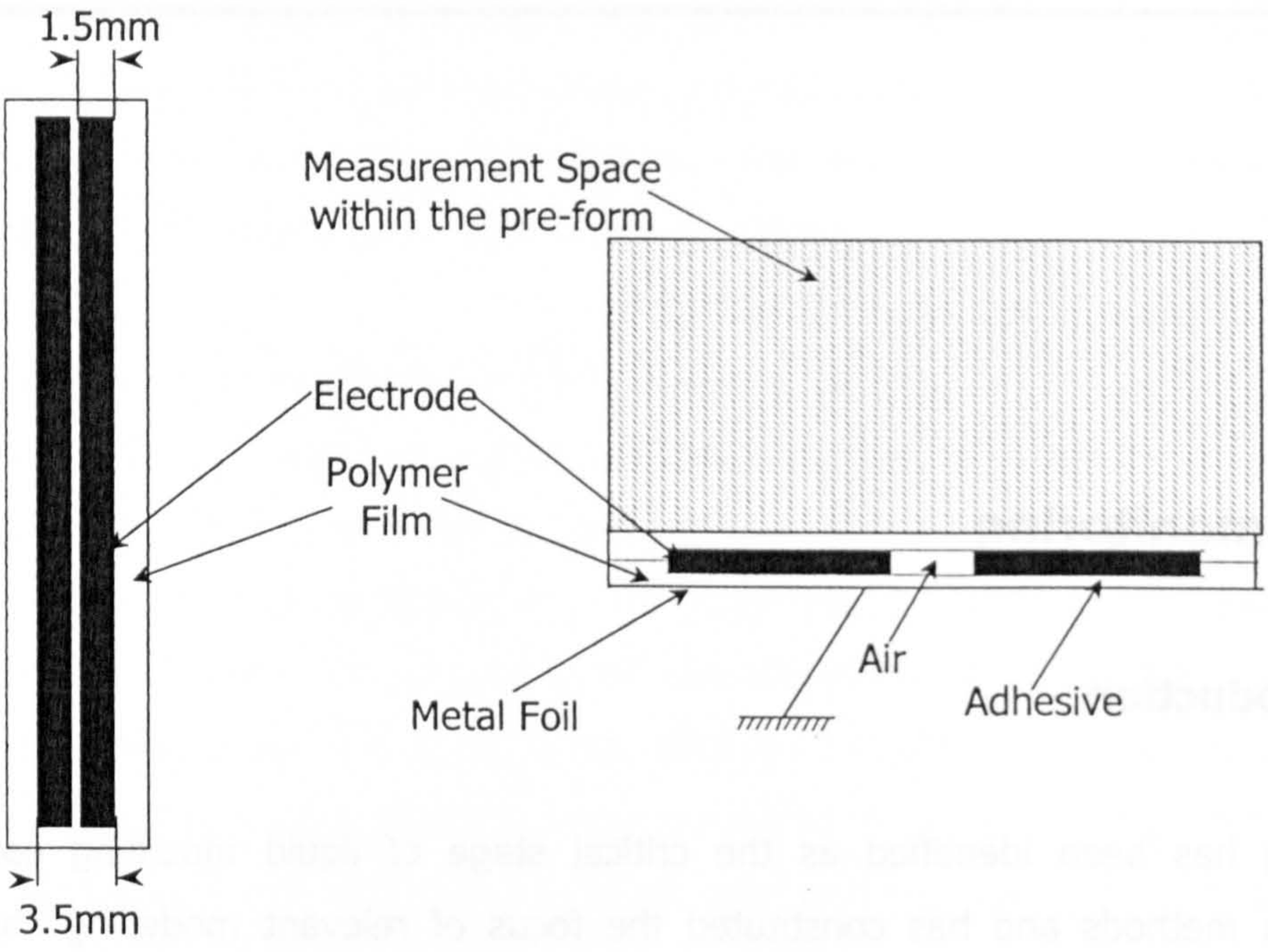

Fig.9.1 *Geometry of the sensor setup for non-conductive reinforcements*

During operation the sensor is aligned parallel to the expected direction of the resin flow front as illustrated in Fig. 9.2. The sensing area is divided into two parts, the impregnated by resin 'wetted' area and the 'dry' part. As the impregnation progresses the 'wetted' area percentage increases and the 'dry' area percentage decreases.

This process is illustrated by the photographs shown in Fig. 9.3. In Fig. 9.3.a the sensor, placed on the bottom of the mould, is completely hidden by the dry glass fabric. As resin impregnation progresses (Fig. 9.3.b) it becomes possible to see the sensor through the wetted part of the fabric. Fig. 9.3.c shows a completely impregnated pre-form, with the sensor visible across the entire length of the mould. Since the electrical properties of the liquid resin differ significantly from those of the air, monitoring the evolution of the sensor dielectric response can provide quantitative information about the mould filling process.

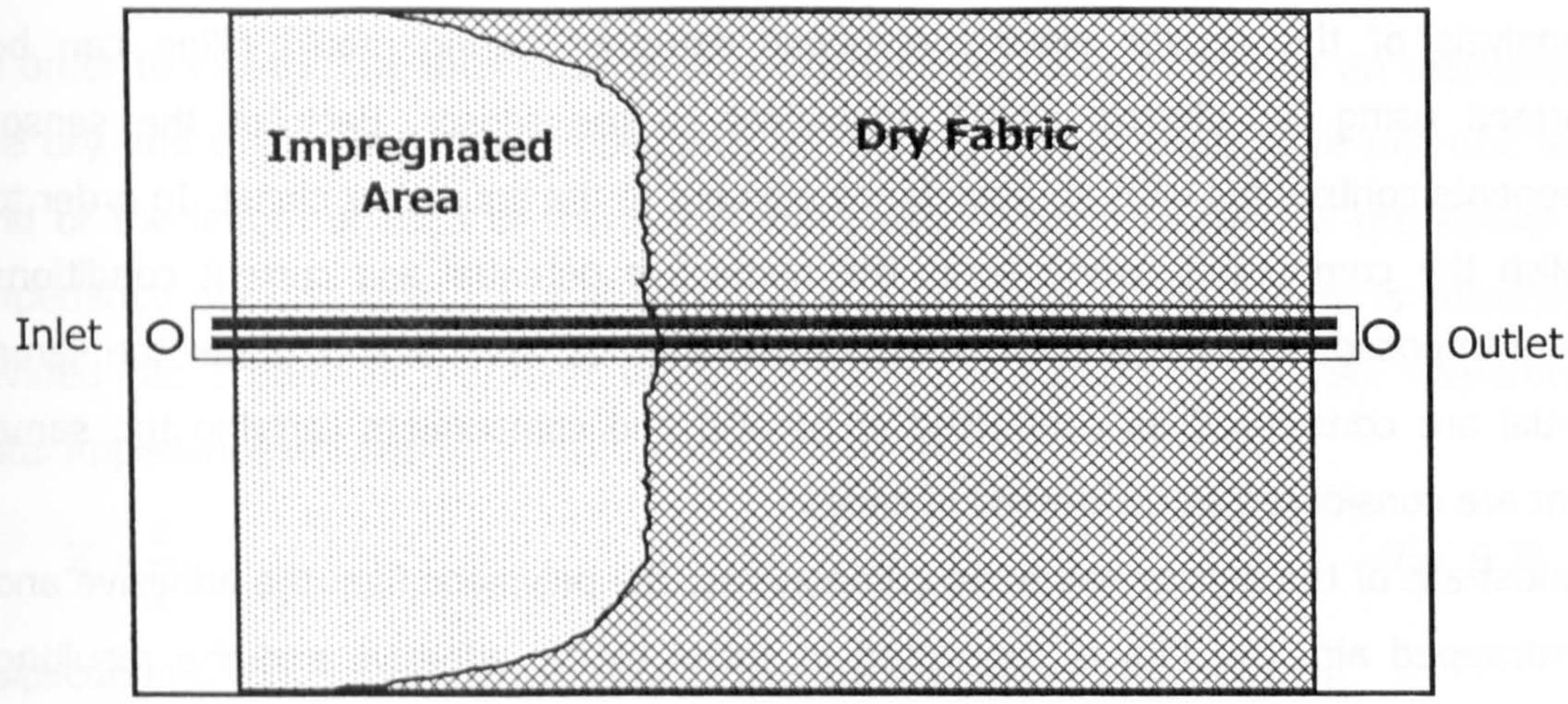

Fig.9.2 *Schematic representation of the operation principle of the sensor*

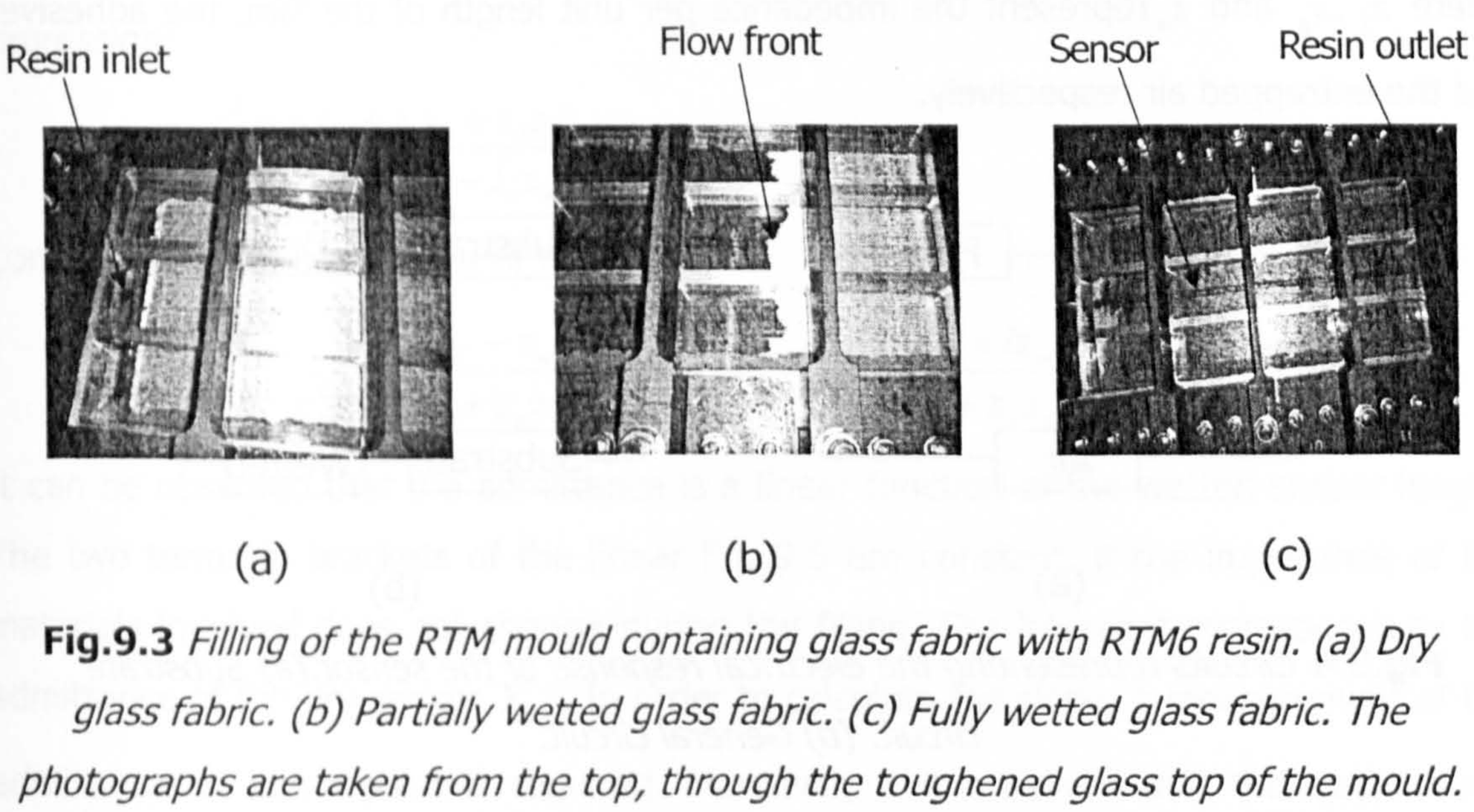

Fig.9.3 *Filling of the RTM mould containing glass fabric with RTM6 resin. (a) Dry glass fabric. (b) Partially wetted glass fabric. (c) Fully wetted glass fabric. The photographs are taken from the top, through the toughened glass top of the mould.*

An analysis of the sensor electric response expected during mould filling can be performed using an electric circuit equivalent to the sensor. Each of the sensor components contributes with an impedance element to the equivalent circuit. In order to establish the component connections, the respective potential and current conditions that are imposed on them are taken into account. Thus, components under the same potential are considered as connected in parallel and components carrying the same current are considered as connected in series.

The substrate of the sensor has three components: the polymeric film, the adhesive and the entrapped air. The film is connected in series to the adhesive and the resulting subcircuit is connected in parallel to the air entrapped between the electrodes, as shown in Fig. 9.4.a. Consequently, the total impedance of the substrate per unit length is given by the relation:

$$z_s = \frac{1}{\frac{1}{z_f + z_g} + \frac{1}{z_a}} \qquad \text{(Eq. 9.1)}$$

where z_f, z_g and z_a represent the impedance per unit length of the film, the adhesive and the entrapped air respectively.

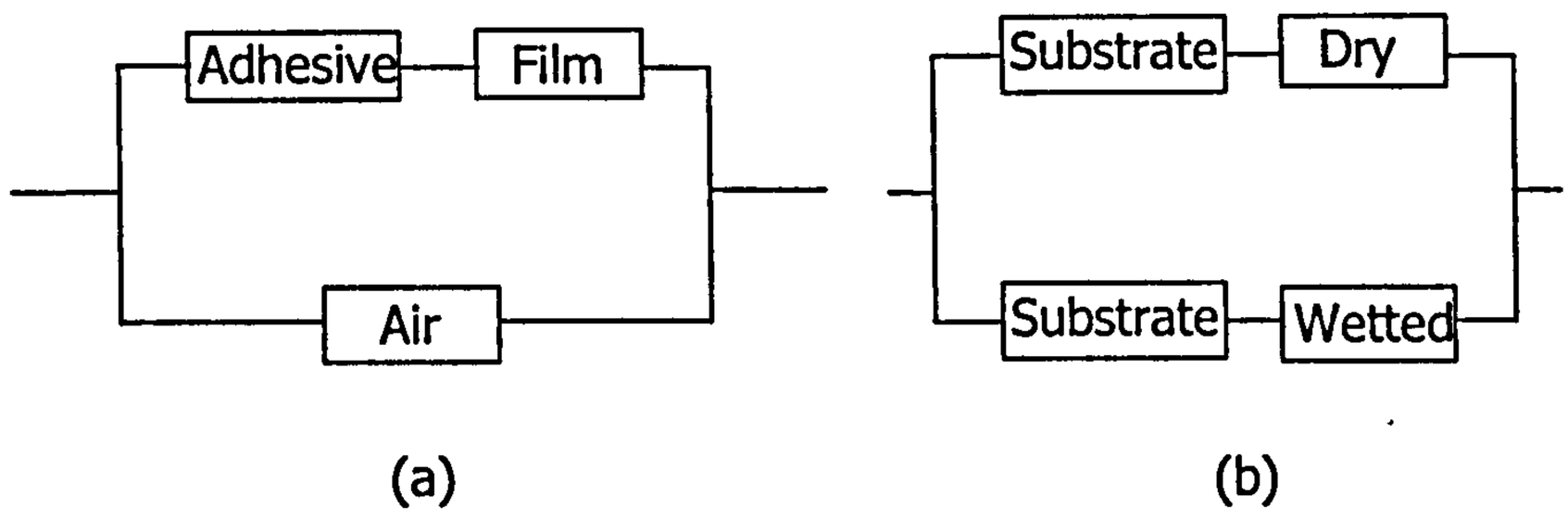

Fig.9.4 *Circuits representing the electrical response of the sensor.(a) Substrate circuit. (b) General circuit.*

The sensor can be considered as a parallel circuit of the wetted and the dry regions. Each of these two regions can be analysed further into a serial circuit of the substrate and the corresponding measurement area. According to these, the circuit representing the electrical behaviour is the one shown in Figure 9.4.b.

In order to express the total impedance explicitly, it is required to find an expression of the dry and the wetted areas impedance as function of the impedance per unit length and of the length of each of them. For this reason a uniform part of the sensor with impedance per unit length z and length l is considered. If the sensor is conceptually divided into l parts each of them will be connected in parallel to the rest. Therefore the total impedance will be:

$$Z = \frac{z}{l} \qquad \text{(Eq. 9.7)}$$

Application of Eq. 9.1 to the circuit of Figure 9.4.b results in the relation:

$$Z_{sensor} = \frac{1}{\frac{l_w}{z_s + z_w} + \frac{l - l_w}{z_s + z_d}} \qquad \text{(Eq. 9.3)}$$

where l denotes the total length of the sensor, l_w the length of the covered by resin (i.e. wetted) part, z_w the impedance per unit length of the wetted part and z_d the impedance per unit length of the dry part. Algebraic manipulation of Eq. 9.3 leads to the expression:

$$Z_{sensor} = \frac{z_s^2 + z_s z_w + z_s z_d + z_d z_w}{l z_s + l_w z_d + l z_w - l_w z_w} \qquad \text{(Eq. 9.4)}$$

Consequently the admittance of the sensor is:

$$Y_{sensor} = l_w \left(\frac{z_d - z_w}{z_s^2 + z_s z_d + z_s z_w + z_w z_d} \right) + \left(\frac{l z_s + l z_w}{z_s^2 + z_s z_d + z_s z_w + z_w z_d} \right) \qquad \text{(Eq. 9.5)}$$

It can be observed that the admittance is a linear function of the wetted sensor length. The two terms in brackets of the linear Eq. 9.5 are constant, if the impedance of the materials involved does not change during the filling. The intercept corresponds to the admittance of the dry sensor Y_{dry}. In order to calculate the slope, a measurement of the admittance at some point is required. Moreover, it is observed that the slope is not dependent on the total length of the sensor, so its value is constant for sensors of different lengths in the same moulding. Thus Eq. 9.5 becomes:

$$l_w = \frac{Y_{sensor} - Y_{dry}}{Y_{cov} - Y_{dry}} l_t \qquad \text{(Eq. 9.6)}$$

where Y_{cov} is the measured admittance when length l_t of the sensor is covered by the resin at time t of the filling stage.

9.2.2 Verification of the performance of the sensor

Individual sensors were fabricated by embedding two flat copper wires between two layers of a polymeric film. A single electrode width was 1.5 mm and the interelectrode distance was 0.5 mm. The sensor performance was validated during the filling of a glass cavity with silicone oil (Dow Corning 2000) and during the filling and curing of an RTM6/glass reinforced composite in a partially transparent RTM tool.

In the first case the total sensor length was 27.8 cm and the cavity thickness was 8 mm. The filling was performed at ambient temperature. In the second case the sensor length was 73 cm and the mould thickness 3 mm. The filling temperature was 100 °C. Admittance data were gathered over a range of frequencies using a Solartron 1260 impedance analyser. Visual determination of the flow front position was recorded against time in both cases. After completion of the filling step the mould temperature was increased to 160 °C to cure the resin.

Eq. 9.6 has been used to calculate the flow front position from the admittance data. The admittance measured when the sensor is fully covered by resin has been used as Y_{cov}.

That means that knowledge of the final measurement was necessary in order to perform the covered length calculation. In a real application where on-line estimation of the flow front position is required, another characteristic length should be used. One possibility is a measurement from an additional short length sensor, which would be fully covered by resin before the wetting of the actual sensor commences. Alternatively measurement from the actual sensor can be used, with the field interrupted by electrode screening over a short length at a specific point.

It can be observed from Eq. 9.6 that the calculated length is a ratio of two complex numbers. In the ideal case the numerator and denominator of the ratio would be in phase and consequently, the resulting length would be a real number. However, measurement inaccuracies and occurrence of phenomena which alter the impedance of the materials involved (e.g. local temperature variations), can cause some phase difference resulting in the existence of an imaginary component of the calculated length.

The real and the imaginary parts of the wetted length, combined with the visual flow front position measurements, for the filling of the cavity with silicone oil and the filling of the RTM mould with epoxy resin are illustrated in Figs. 9.5 and 9.6 respectively. The corresponding measurement statistics are given in Table 9.1. It can be observed that in both cases the calculated flow front location closely follows the visual observation. The statistical analysis shows that there is a correlation between the measured imaginary length and the error in the flow front location. Thus, high values of the imaginary length imply a significant error in the flow front location. In all measurements the imaginary part never exceeded 0.6 cm which is low in comparison with the sensor length; therefore the final accuracy can be considered to be satisfactory.

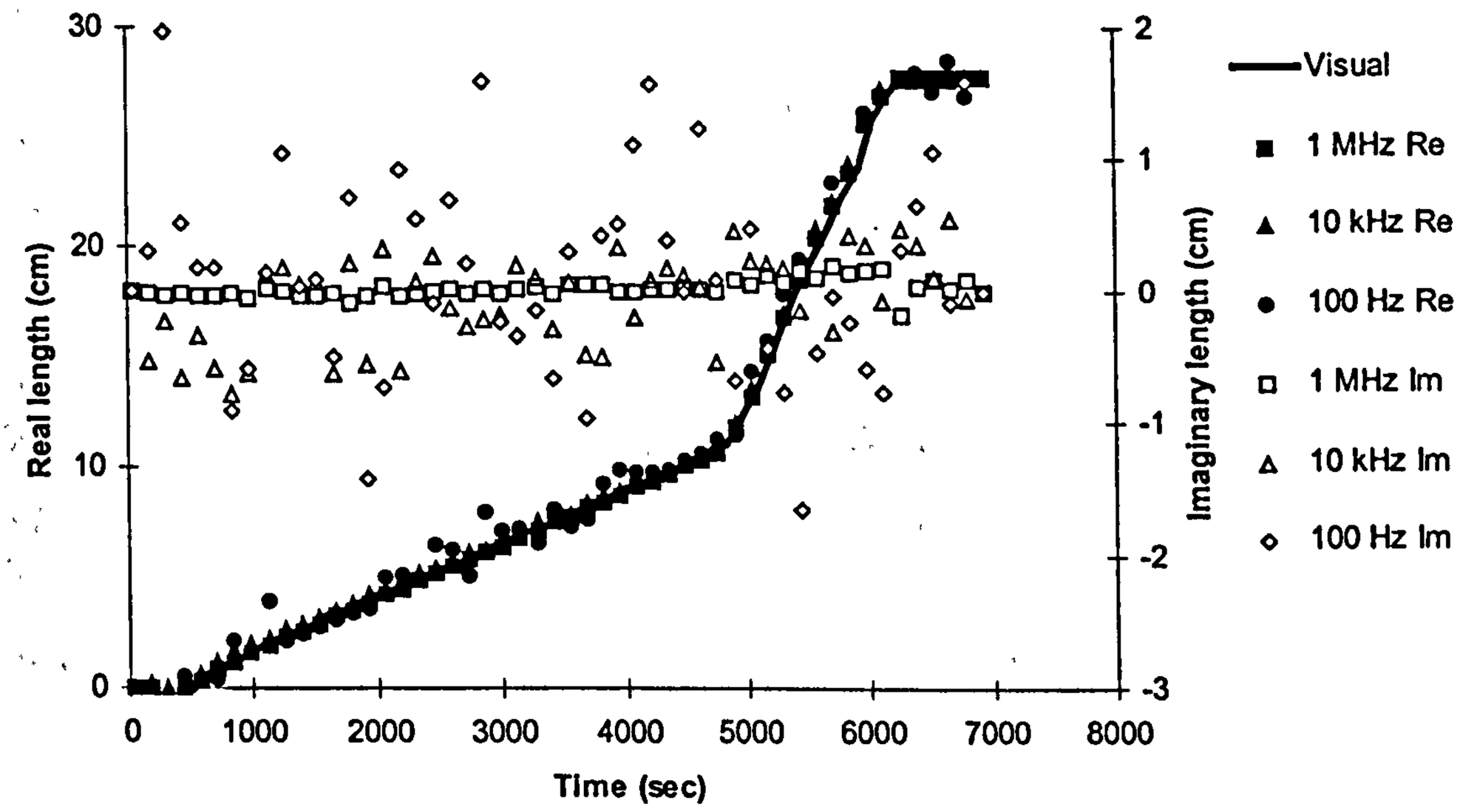

Fig.9.5 *Comparison of visual measurement with dielectric flow measurement for silicone oil filling*

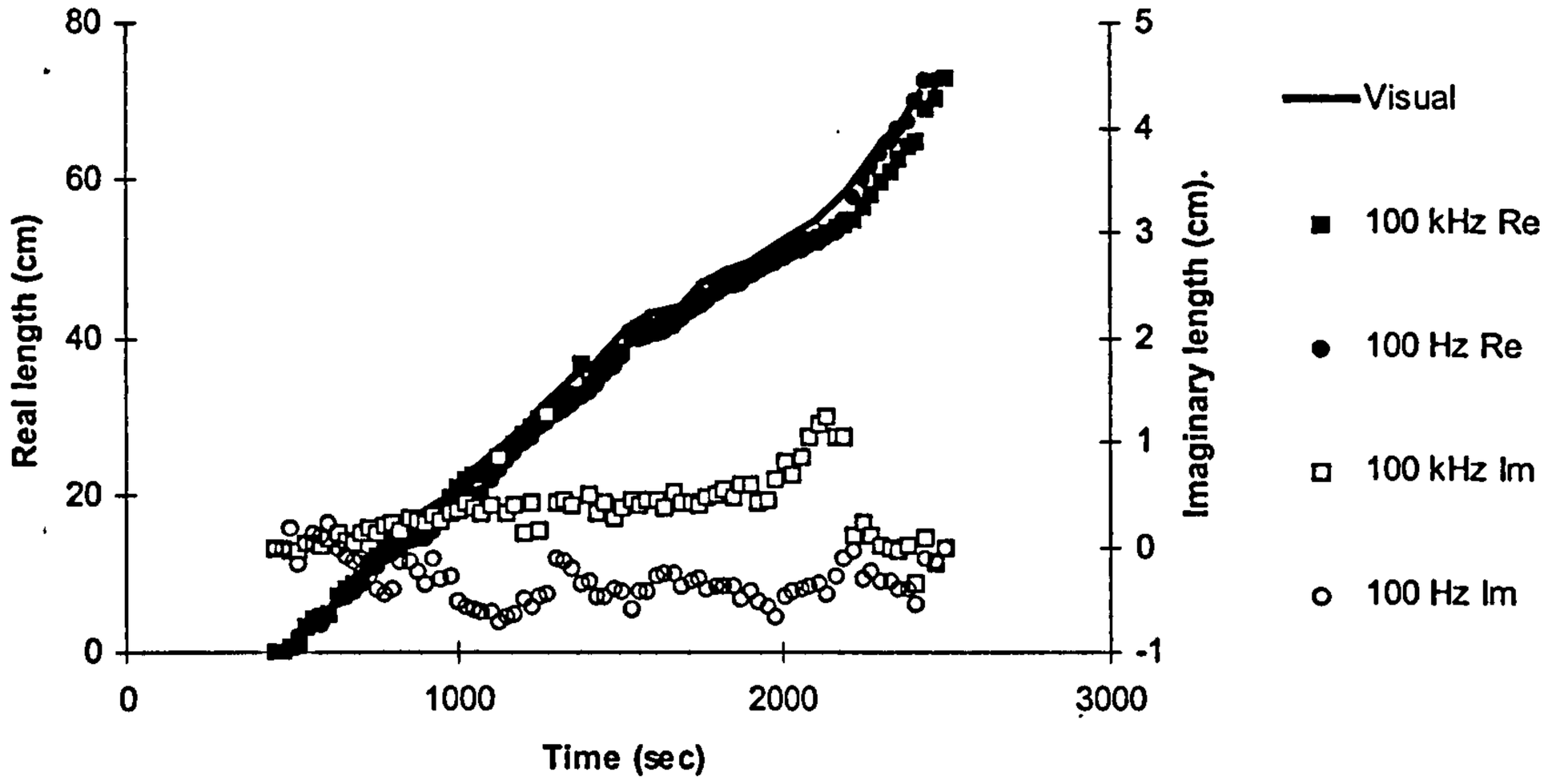

Fig.9.6 *Comparison of visual measurement with dielectric flow measurement for filling during resin transfer moulding of an RTM6/glass composite*

	Silicone oil filling			RTM filling	
	100 Hz	10 kHz	1 MHz	100 Hz	100 kHz
Average absolute imaginary length (cm)	0.60	0.29	0.05	0.38	0.30
Average error in flow front location (cm)	0.47	0.24	0.17	0.69	0.99

Table 9.1 *Average error in flow front determination and average imaginary length at different frequencies*

9.2.3 Cure monitoring performance of the flow sensor

The performance of the flow sensor developed for monitoring in non-conductive reinforcement as a cure monitoring sensor has been investigated. Data of the imaginary impedance evolution after the filling gathered by the flow sensor are given in Fig. 9.7. Results of an impedance experiment using GIA microelectrodes (chapter 8) for a thermal program similar to the one performed in RTM curing are illustrated in Fig. 9.8.

In order to facilitate comparison the imaginary impedance data have been normalised against their minimum and maximum values during the cure as follows:

$$Normalised\ log\ Z'' = \frac{log_{10} Z'' - log_{10} Z''_{min}}{log_{10} Z''_{max} - log_{10} Z''_{min}} \qquad \text{(Eq. 9.7)}$$

where Z''_{min}, Z''_{max} are the minimum and maximum values of the imaginary impedance during the cure.

The information derived from the two different experiments is similar. The time ranges where the first step appears at different frequencies are within 300 seconds of each other. The vitrification is indicated in both cases by the knee in imaginary impedance (see sections 3.4.5 and 8.5) approximately 4000 seconds after the beginning of the thermal program. In the microdielectrometry experiment the vitrification occurs slightly earlier, therefore the knee is obscured by the reaction step at low frequencies. During the cure of the component, significant temperature gradients can be expected to exist within the sensing region of the global sensor. The microdielectrometry experiment was performed at the temperature representing the bottom layer of the curing component, which is higher than the average temperature in the RTM mould. Therefore vitrification in the microdielectrometry experiment occurs earlier than in the RTM experiment. Consequently cure monitoring results obtained using the flow sensor are in fair agreement with impedance data obtained using the comb microelectrodes. Thus the sensor developed for flow monitoring in non-conductive reinforcements can be used for cure monitoring after filling completion.

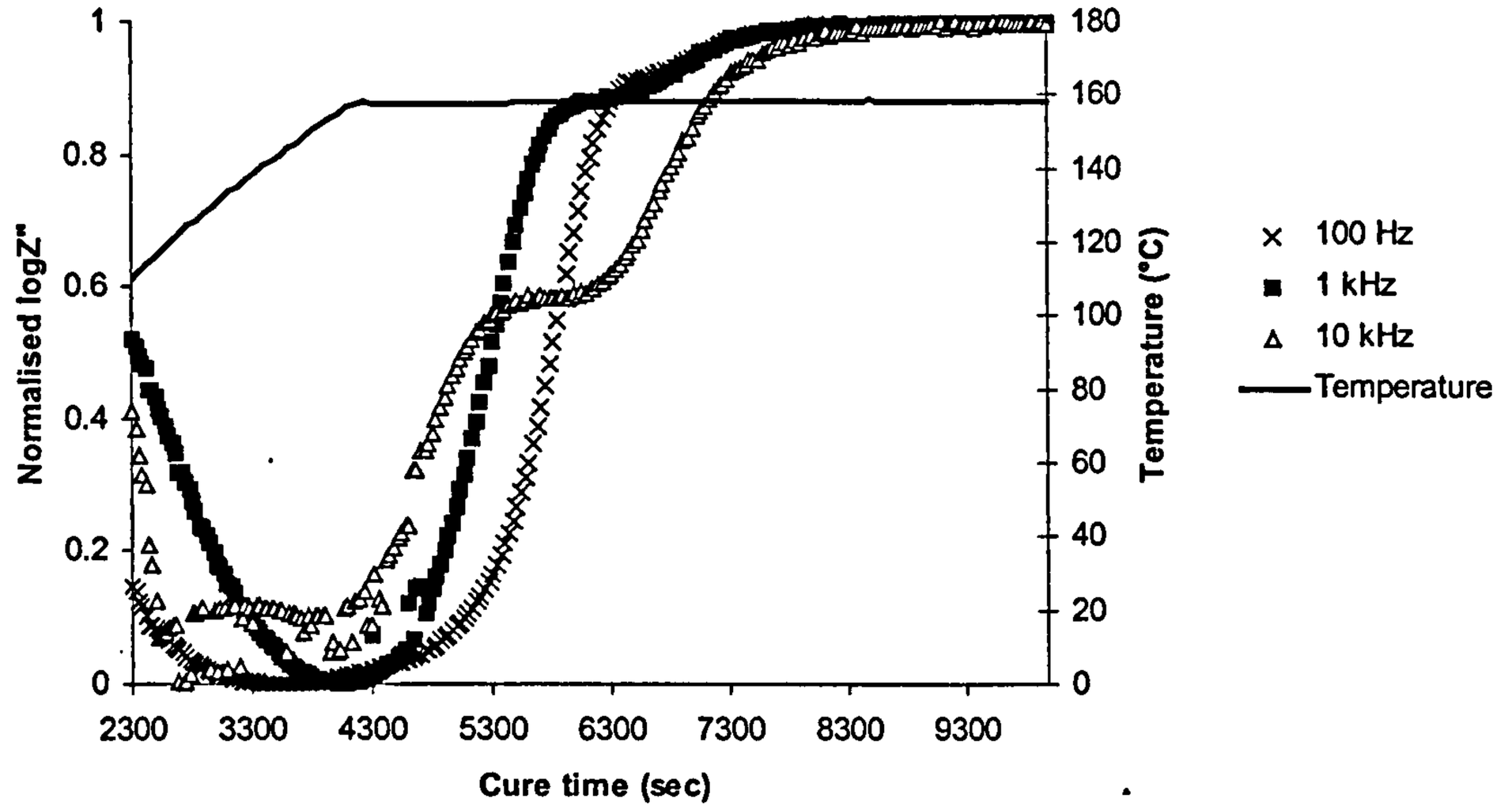

Fig.9.7 *Temperature and normalised impedance at different frequencies versus time using the flow monitoring setup in an RTM mould*

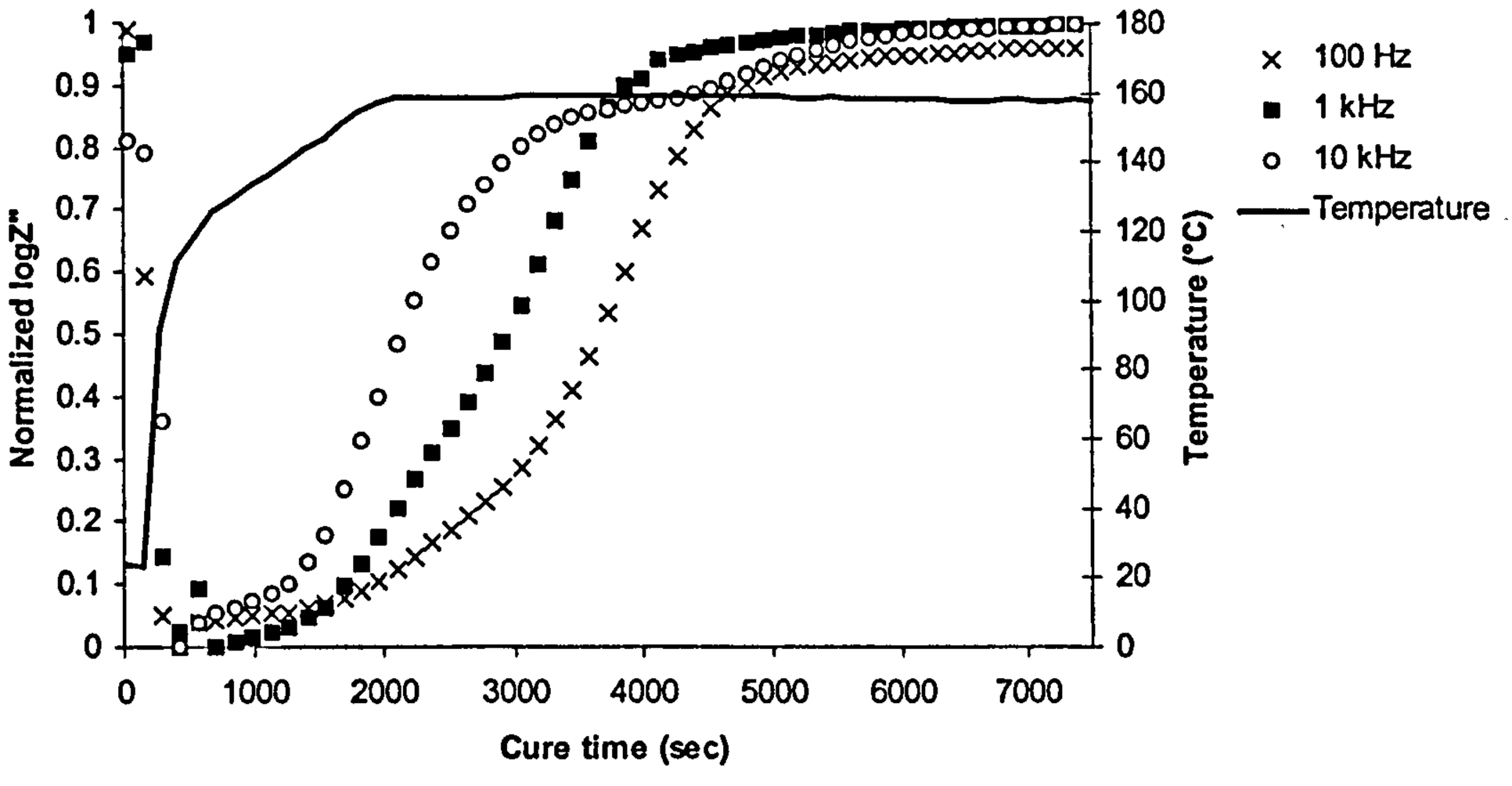

Fig.9.8 *Temperature and normalised impedance at different frequency versus time using microdielectrometry for a thermal profile similar to that followed during RTM curing*

9.3 Flow monitoring in conductive reinforcements filling

9.3.1 Sensor setup and principle of operation

When carbon reinforcements are used, the conductive nature of the fibre produces some complications in the application of dielectric monitoring for flow or cure. The presence of a conductor between the electrodes interrupts the electric field and, if in contact with the electrodes, short-circuits the measuring device. In the case of microelectrodes the use of porous PTFE film between the sensor and the composite offers a solution (158), since it isolates the electrodes from the conductive reinforcement and allows the resin to permeate and occupy some of the electric field space. Obvious disadvantages of this approach are the addition of an extra layer in the sensing setup and the dependence of the resin permeation to viscosity, which varies during the cure. Such a solution cannot be adopted in the case of a macro-sensor, where an impregnated by resin porous film with a thickness which would not disturb the composite component geometry, would not produce a detectable signal. Thus, a totally different sensing setup appropriate for conductive reinforcements is proposed here.

The setup comprises an array of thin insulated wires which are in contact with the carbon preform and are connected to the impedance analyser. The reinforcement is connected to the analyser and the measurement is performed between the array of wires and the fibres of the pre-form. A schematic of the arrangement of fibre tows and wires is given in Fig. 9.9. In the case illustrated, the wires are in contact with the tool. As the fibre tows conform around the hard wire some pores are formed. With the application of a voltage an electric field is formed between the conductive core of the wire and the fibre. The field occupies the insulating coating of the wire and the pore regions. When the reinforcement is dry the pores are filled with air. As the impregnation process progresses more and more of the pores are filled with the resin. Similarly to the glass reinforcement case, it is expected that the difference in electrical properties of air and of the liquid resin will result in gradual change in the electrical response as the filling progresses.

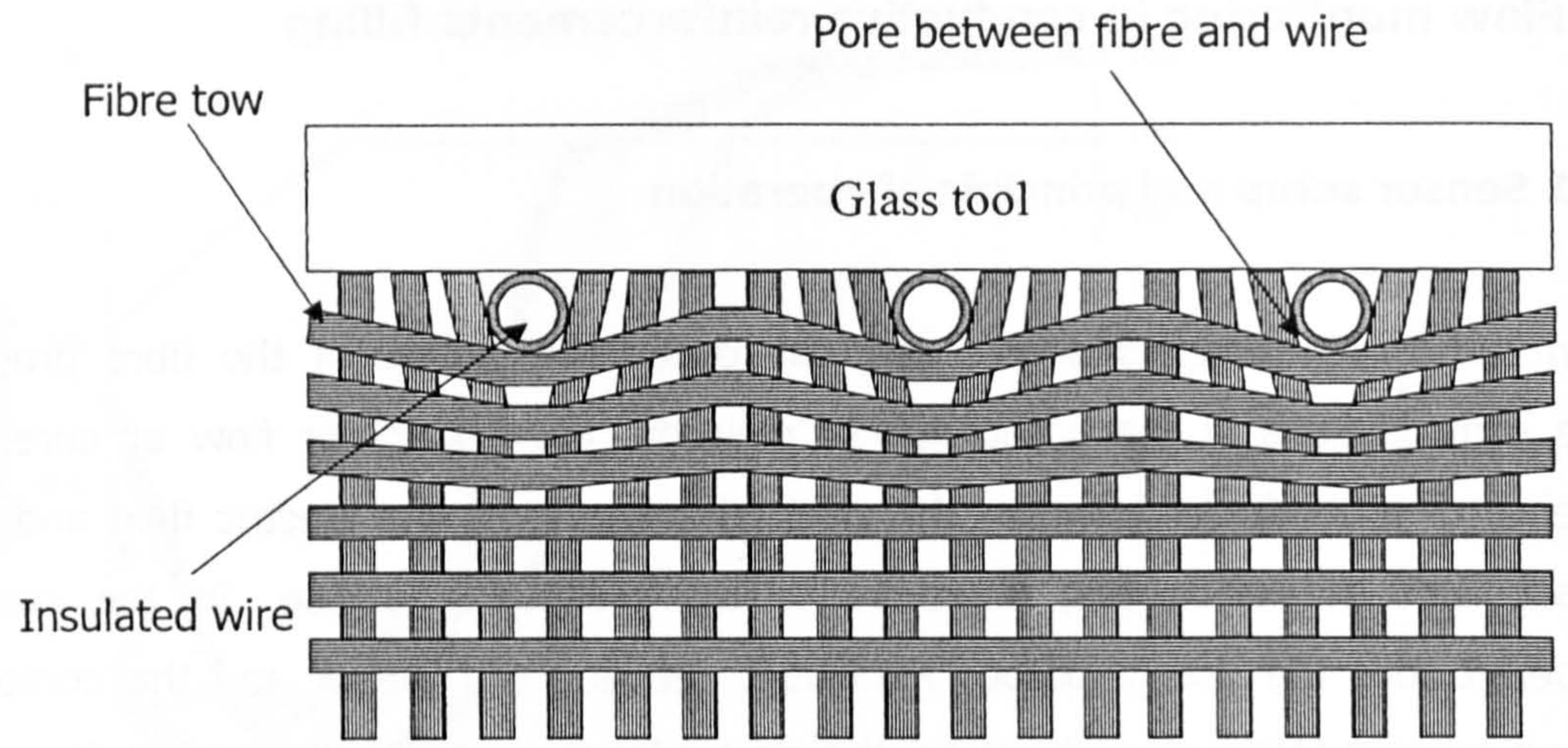

Fig.9.9 *Sensing configuration for flow monitoring in carbon reinforcements*

The sensing configuration can be considered as the sum of a number of wire and fabric segments with length unity. Assuming that the carbon reinforcement is under uniform potential, all the segments corresponding to one wire are connected in parallel. Each of these segments contains two elements connected in series, one corresponding to the insulating coating and one to the pores. If the unit length is large compared with the size of the pores, the impedance of the element corresponding to pores will be equal to z_{dry} for all the n segments in the dry region of the mould, and equal to z_{wetted} for all the m segments in the wetted region. This situation can be represented by the circuit of Fig. 9.10.a, which reduces to the circuit represented in Fig. 9.10.b.

The circuit of Fig.9.10 is equal to the circuit of Fig.9.4.b which represents the behaviour of the sensor designed for the non-conductive reinforcement case. Consequently, Eq. 9.5 is expected to hold as follows:

$$Y_{sensor} = m\left(\frac{z_d - z_w}{z_c^2 + z_c z_d + z_c z_w + z_w z_d}\right) + \left(\frac{(m+n)z_c + (m+n)z_w}{z_c^2 + z_c z_d + z_c z_w + z_w z_d}\right) \qquad \text{(Eq. 9.8)}$$

where z_c denotes the impedance per unit length of the insulating layer of the sensing wire. Similarly to the case of the glass reinforcement, a linear expression of the sensor admittance as a function of the length of the wire in contact with liquid resin (Eq. 9.6) can be derived.

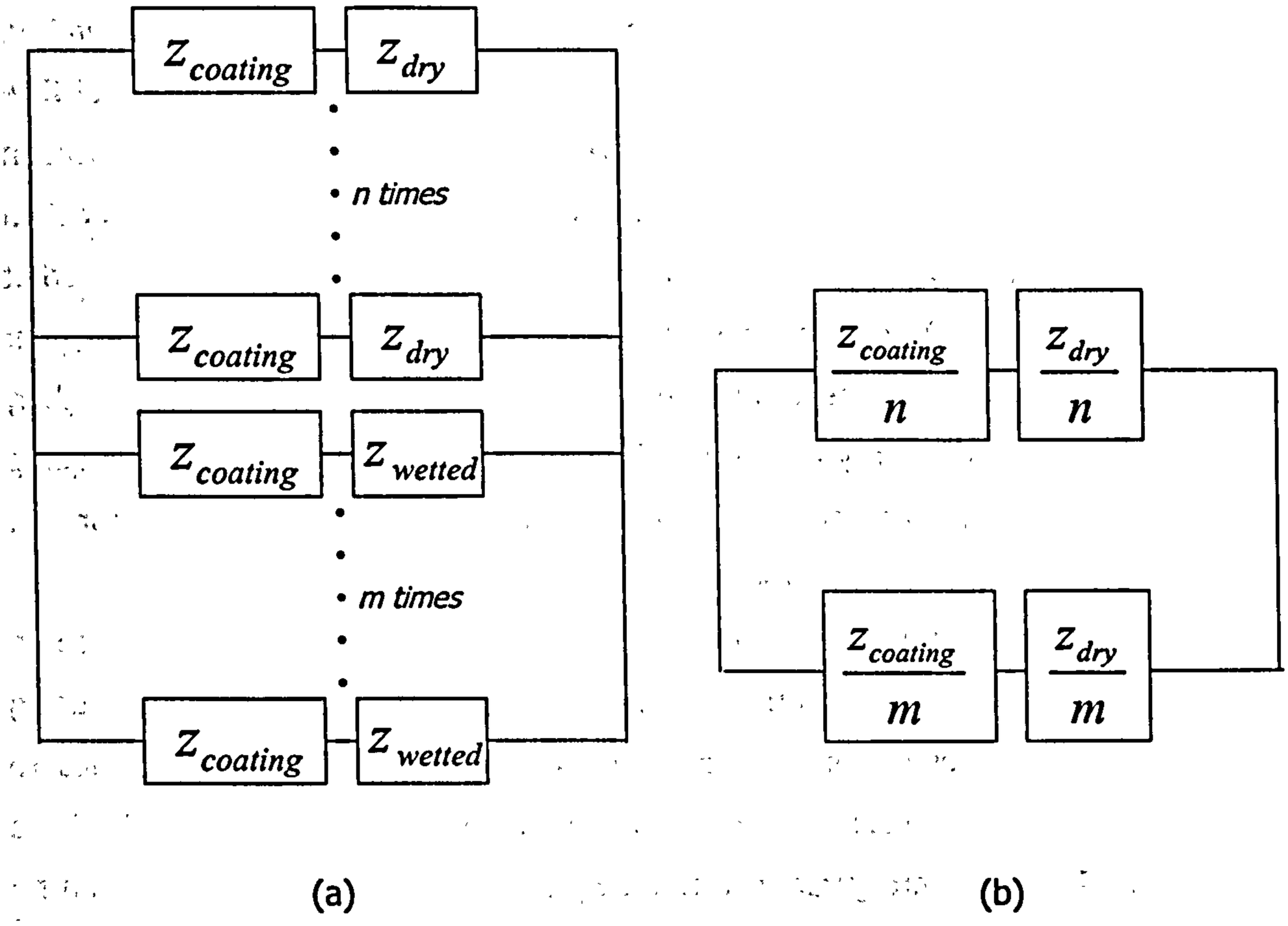

Fig.9.10 *Equivalent circuit representing the response of the sensing setup for conductive reinforcements*

9.3.2 Flow and cure monitoring performance of the sensor

The sensor performance was validated during the filling and curing of an continuous carbon fibre/RTM6 composite in a partially transparent RTM tool. The sensor comprised an array of three insulated (polyurethane coated) copper wires, with a diameter of 0.25 mm, placed in the centre of the mould in contact with the glass top tooling. The distance between the wires was 2 mm. The sensor length was 28 cm and the mould thickness 3 mm. The filling was performed at 120 °C. Admittance data were gathered using a Solartron 1260 impedance analyser. Visual determination of the flow front position was recorded against time. After completion of the filling stage the mould temperature was increased to 160 °C to cure the composite.

Eq. 9.6 was used to calculate the flow front position from the admittance data. The admittance measured when the sensor is fully covered by resin has been used as Y_{cov}.

Similarly to the glass reinforcement case, the calculated length is a complex number. The real and imaginary part of the length are illustrated together with the visual flow front position measurement in Fig. 9.11. The average of the error in flow front location and the average imaginary length are given in Table 9.2. It can be observed that data gathered at 1 MHz are very close to the visual flow front measurement. Data obtained at a lower frequency (10 kHz) present some deviation. The imaginary length shows higher value at the frequency where the error in the flow front location estimation is higher, indicating deviation from linearity as described by Eq. 9.6. Thus, as in the sensing setup for non-conductive reinforcements, the imaginary length offers the means for self estimation of the measurement accuracy.

Cure monitoring results obtained using the sensing configuration are illustrated in Fig.9.12. There, the evolution of normalised impedance at 10 kHz as calculated using Eq. 9.7 is shown. The results of an experiment using GIA comb microelectrodes to monitor the cure of RTM6 resin subject to a thermal programme similar to the one applied during RTM curing are given in Fig.9.8. By comparison of the results, it can be observed that the sensing setup has a response equivalent to that of the microelectrodes. Normalised impedance undergoes a step change during the cure and vitrification is manifested as a knee towards the end of the curing. In comparison with measurements carried during the cure of unreinforced RTM6 resin, vitrification is observed at a later cure time in the mould, since the sensing setup performs the measurement on the top side of the curing component which experiences a lower temperature than the side of the component adjacent to the bottom side of the mould.

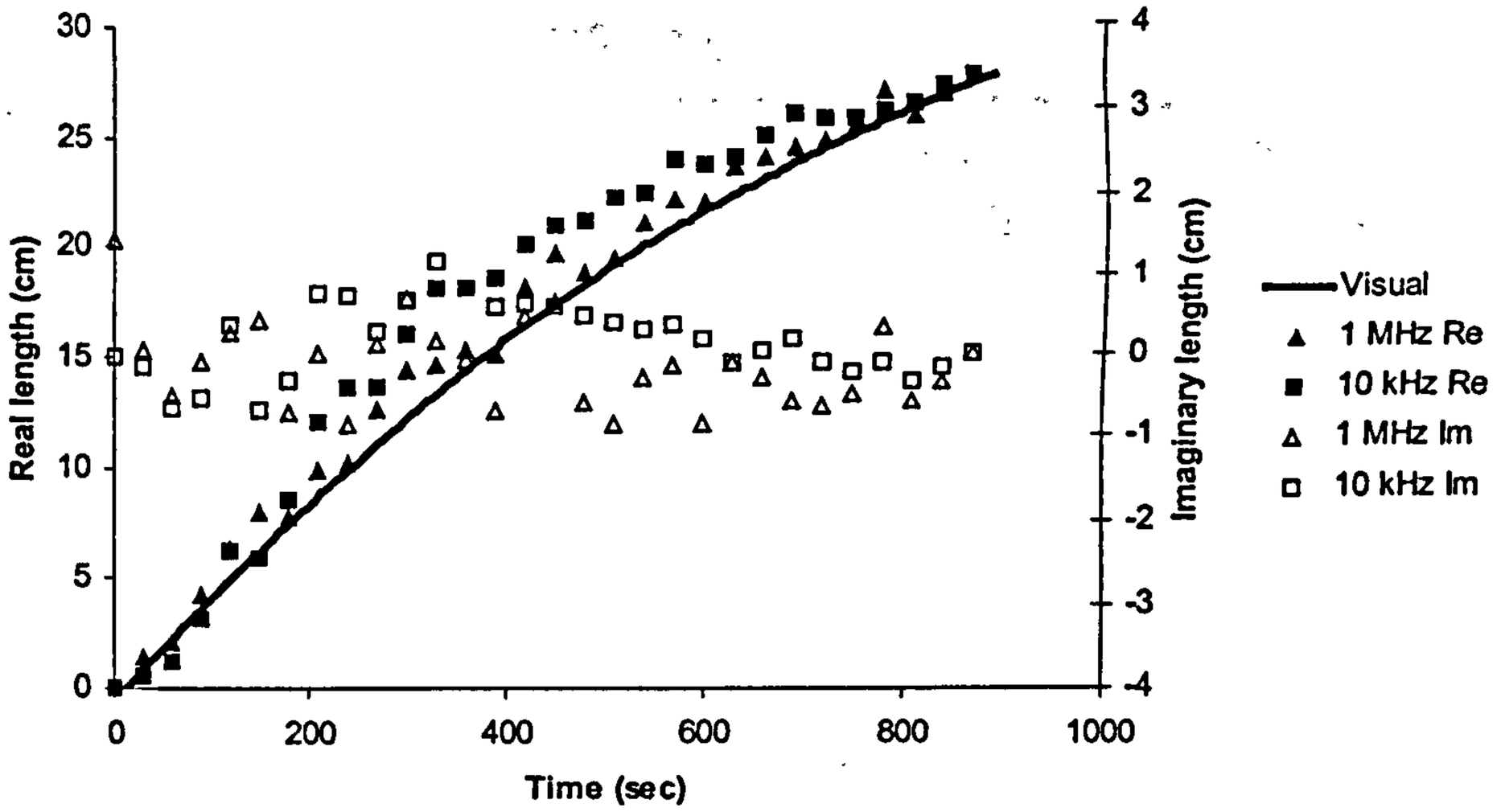

Fig.9.11 *Comparison of visual measurement with dielectric flow measurement for filling during resin transfer moulding of an RTM6/carbon composite*

	10 kHz	1 MHz
Average absolute imaginary length (cm)	0.38	0.20
Average error in flow front location (cm)	1.98	0.84

Table 9.2 *Average error in flow front determination and average imaginary length in carbon reinforcement*

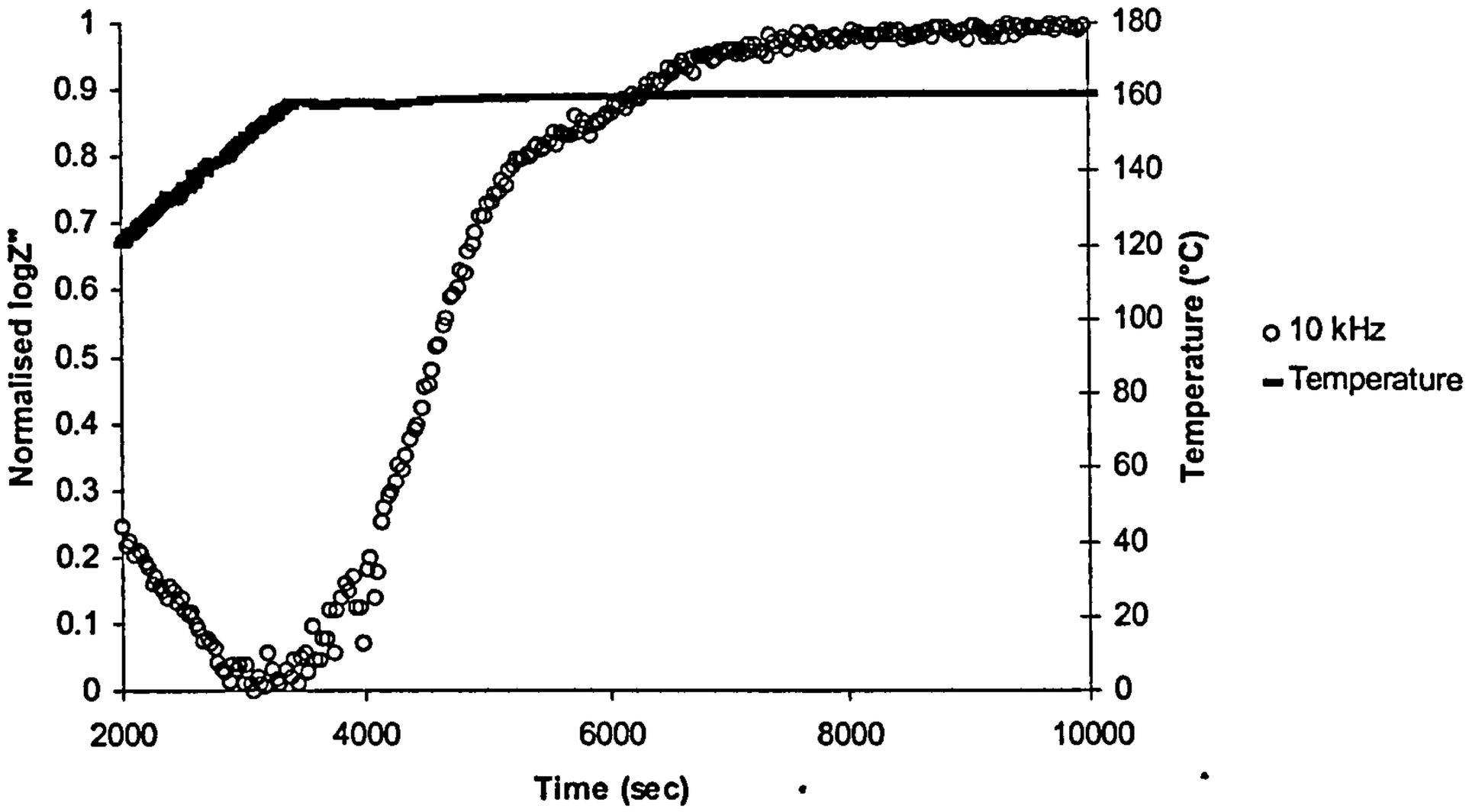

Fig.9.12 *Temperature and normalised impedance during cure versus time using the flow monitoring setup in an RTM6/carbon composite moulding*

9.4 Overview

Sensing configurations appropriate for flow monitoring during RTM filling of conductive and non-conductive reinforcements were proposed. Equivalent circuit analysis demonstrated the linear dependence of the admittance, measured by the presented sensors, upon the flow front position. Experiments confirmed that the flow front position can be located continuously with a satisfactory accuracy. In addition, the existence of an imaginary component of the measured flow front position can be utilized as self-assessment tool of the measurement performance. The sensors also presented the ability to monitor the cure of the resin after the end of the filling stage.

Chapter Ten

10 Inverse heat transfer modelling of RTM curing

10.1 Introduction

In this chapter the development and the application of a heat transfer inversion procedure based on genetic algorithms is presented. The inversion procedure is then used to optimise cure process parameters and to integrate modelling and monitoring under a new scheme, which has the ability to extend the monitoring results spatially, using the heat transfer simulation.

10.2 Genetic algorithm for parameters estimation

The term genetic algorithms describes a family of evolutionary optimisation methods which involve a population of points in the search space of solutions (generation) and employ a performance sensitive selection procedure and crossover and mutation operations in order to reproduce a new population. The members of the population (individuals) are usually encoded in bit strings and the algorithm is iterated until some convergence criteria are met.

A conventional genetic algorithm comprises the following steps (222):

1. Production of a random population of individuals representing specific points of the solution space.

2. Calculation of the performance (fitness) of each individual using the direct model.
3. Selection of a pair of individuals. The method of selection should ensure that the probability to select an individual increases with increasing fitness.
4. Application of crossover and mutation to the two selected individuals in order to create two new individuals.
5. Iteration of steps 3 and 4 until a new generation has been created.
6. Iteration of steps 2-5 until the fitness of the best individual is higher than a predefined limit.

Such a procedure has been utilised to perform an inverse solution of the heat transfer model. An algorithm which performs these basic steps and uses as a direct model the one dimensional heat transfer simulation presented in chapters 4-7 has been implemented using Visual Basic 5. A schematic representation of the code is given in Fig. 10.1.

The initial N values of each parameter corresponding to the first generation are created using a random number generator, which outputs a random number between 0 and 1 each time it is called. The inverse of a normalisation transformation is used to translate this random number into a random parameter value within its predefined range. Then the 1-D simulation is executed N times and the results corresponding to each individual are stored in a file. The fitness of the individuals is calculated subsequently by comparing the output of the direct model with a target, which drives the inversion. The form of the fitness function and the inversion target are specific to the application of the inversion procedure; details will be given separately in the following paragraphs.

The next step of the algorithm is the encoding of the individuals. In this stage, each individual which comprises one or more parameters is translated into a unique binary string. The length of the string defines the accuracy of the algorithm. Subsequently, the individuals are sorted according to their fitness. A limited number of individuals (m) with the best fitness are passed directly into the new generation. The rest of the individuals of the new generation are produced with a combination of selection, crossover and mutation. The selection is performed using a standard procedure called "roulette wheel". In this procedure each individual is assigned a slice of a circular wheel, the size of the slice being proportional to the fitness of the individual. Then two random numbers between 0 and 360 are generated and the individuals corresponding to them are

selected. The application of a crossover operation to the two selected individuals follows. Generally in genetic algorithms a variety of crossover operations is used; here the uniform crossover procedure is utilised as it is believed to offer greater versatility in comparison with single or multiple point crossovers (222). In this operation a predefined probability (exchange probability) is compared with a random number between 0 and 1 at each bit of the binary string. If the number is greater than the exchange probability the two selected individuals exchange their bit values, otherwise the values are preserved. At the end of this operation two new individuals have been produced, each of them containing parts of the old individuals. Subsequently, a mutation operation is applied to the two new individuals. In this stage a very low probability (mutation probability) is compared with a random number for each bit of the two new strings. If the mutation probability is greater than the random number, the bit of the string switches from 1 to 0 or from 0 to 1, otherwise it remains unchanged. When N-m individuals have been produced, the selection-reproduction procedure stops. These N-m individuals together with the m best individuals of the previous generation form the new generation and the individuals are decoded back to decimal parameters. At that point the convergence of the algorithm is tested according to a criterion specific to the application which is applied to the best individual. If convergence has been reached, the algorithm outputs the appropriate data and exits. Otherwise the execution of the direct heat transfer model for the new individuals is performed and the whole procedure of fitness calculation, sorting, encoding, selection, reproduction and decoding is iterated until convergence is achieved.

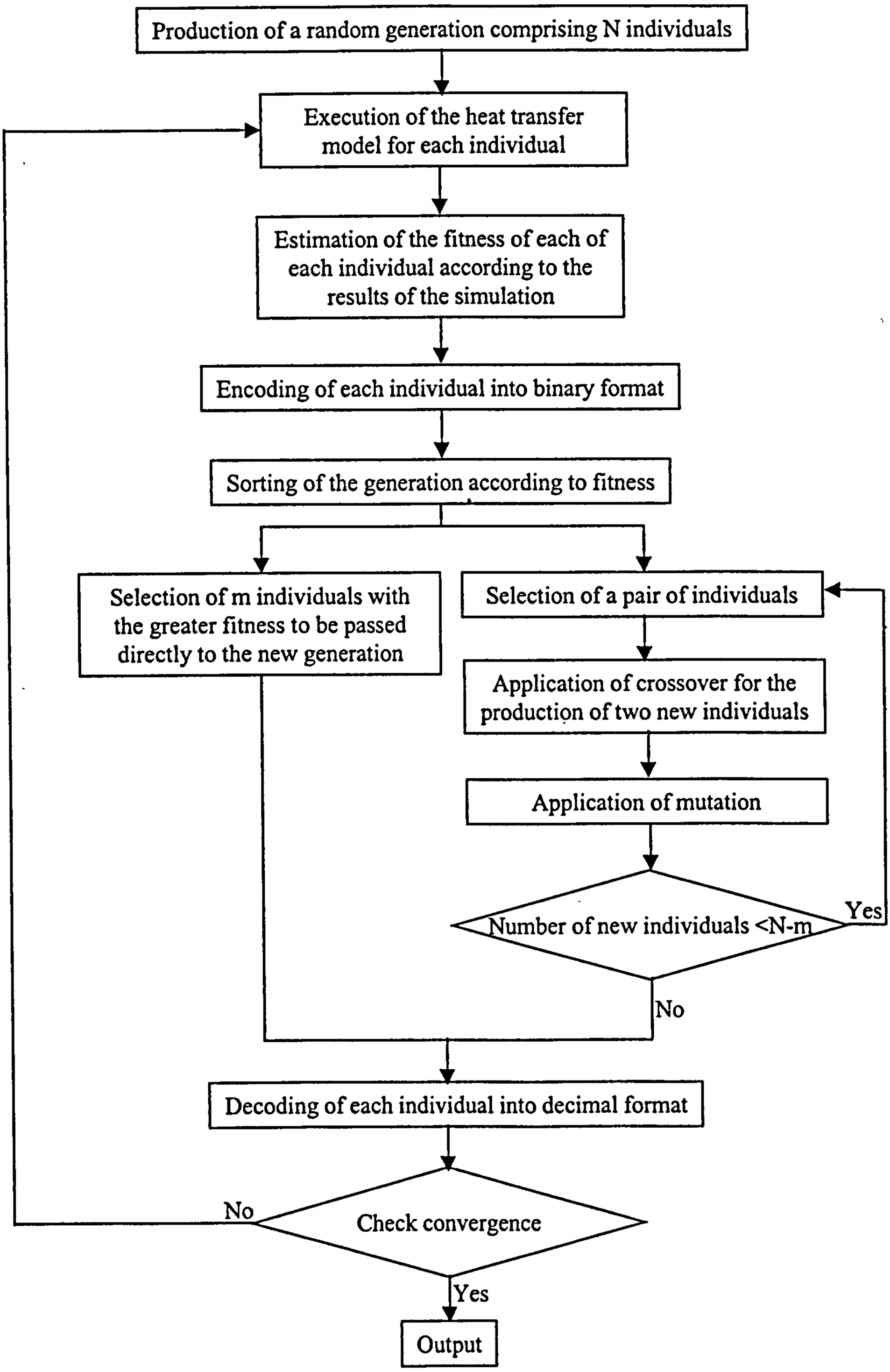

Fig.10.1 *Genetic algorithm utilised for the inversion of the heat transfer model*

10.3 Process parameters optimisation

A major application of heat transfer modelling is the testing and optimisation of cure process parameters during process design. The inversion procedure proposed here can be utilised in this context as an automatic optimisation tool. Two case studies will be presented here, one concerns the selection of an appropriate cure schedule so that the duration of the curing stage is minimised subject to constraints related to the thermal gradient and the other the selection of a proper top tool material so that the thermal gradients within the curing component are minimised for a fixed cure schedule.

10.3.1 Thermal profile optimisation

The thermal profile optimisation is performed for the case of the carbon/RTM6 composite investigated in chapter 7. Glass was selected as the top tooling material. The thermal properties, moulding parameters and finite element runs features are identical to those presented in paragraph 7.3.5. The thermal profile comprises a linear heating up and an isothermal segment, thus can be characterised by two parameters:- (i) the ramp up rate and (ii) the isothermal temperature. These two parameters are the subject of the optimisation. The fitness function was selected so that it rewards the parameter values which reduce the duration of the curing stage, i.e. it increases as the time t_c to reach a fractional conversion of 0.84 in all elements of the component decreases. This is implemented by the function:

$$Fitness = 1/t_c \qquad \text{(Eq. 10.1)}$$

which is subject to the constraint

$$\left|\frac{dT}{dz}\right|_{max} < 2.5\ ^{\circ}C/mm,\ for\ \alpha > 0.6 \qquad \text{(Eq. 10.2)}$$

The meaning of the constraint is that for fractional conversions at which the material has reached the rubber state (17) and residual strain can build up, the maximum thermal gradient must be kept lower than the thermal gradients achieved during the conventional cure schedules described in chapter 7. The implementation of the constraint is performed by excluding from the selection and reproduction procedures all individuals which violate it.

The values of the optimisation parameters are selected within practically meaningful ranges, i.e. a heat up rate from 0 to 4 °C/min and an isothermal temperature from 150 to 190 °C. The algorithm is considered to have converged when the individuals of a generation have limited variation, i.e. the average percentage difference between the members of the population and the average is lower than 0.5 %. The parameters of the genetic algorithm run are given in Table 10.1.

Total number of individuals	Number of individuals passed directly to the next generation	Length of the bit string	Exchange probability	Mutation probability
13	3	100	0.4	0.02

Table 10.1 *Parameters of the genetic algorithm run in the thermal programme optimisation case*

The convergence of the optimisation is illustrated in Fig. 10.2. The problem involves only two parameters, thus convergence occurs very fast within six generations. The optimal values found are a heating rate of 3 °C/min and an isothermal temperature of 169 °C. Global optimality cannot be ensured, the effectiveness of the optimisation can be evaluated by comparing the resulting cure completion time of 64.5 min with the cure completion time of the conventional thermal programme described in chapter 7 which was 87.5 min. A reduction in cure cycle time 26% is achieved, which could have a very significant impact on the total cost of production.

The temperature and degree of cure distributions and their evolutions with cure time obtained using the optimal values, are illustrated in Figs. 10.3 and 10.4. In comparison with Figs. 7.15 and 7.16,which correspond to the conventional cure schedule, higher thermal and fractional conversion gradients occur (overall thermal gradients 16 °C and 12 °C respectively) in the initial stages of the isothermal segment, when residual strain cannot build up. In later stages when high conversions have been achieved, the gradients are quite close (overall thermal difference 6.5 °C and 6 °C respectively), thus the relevant constraint is satisfied.

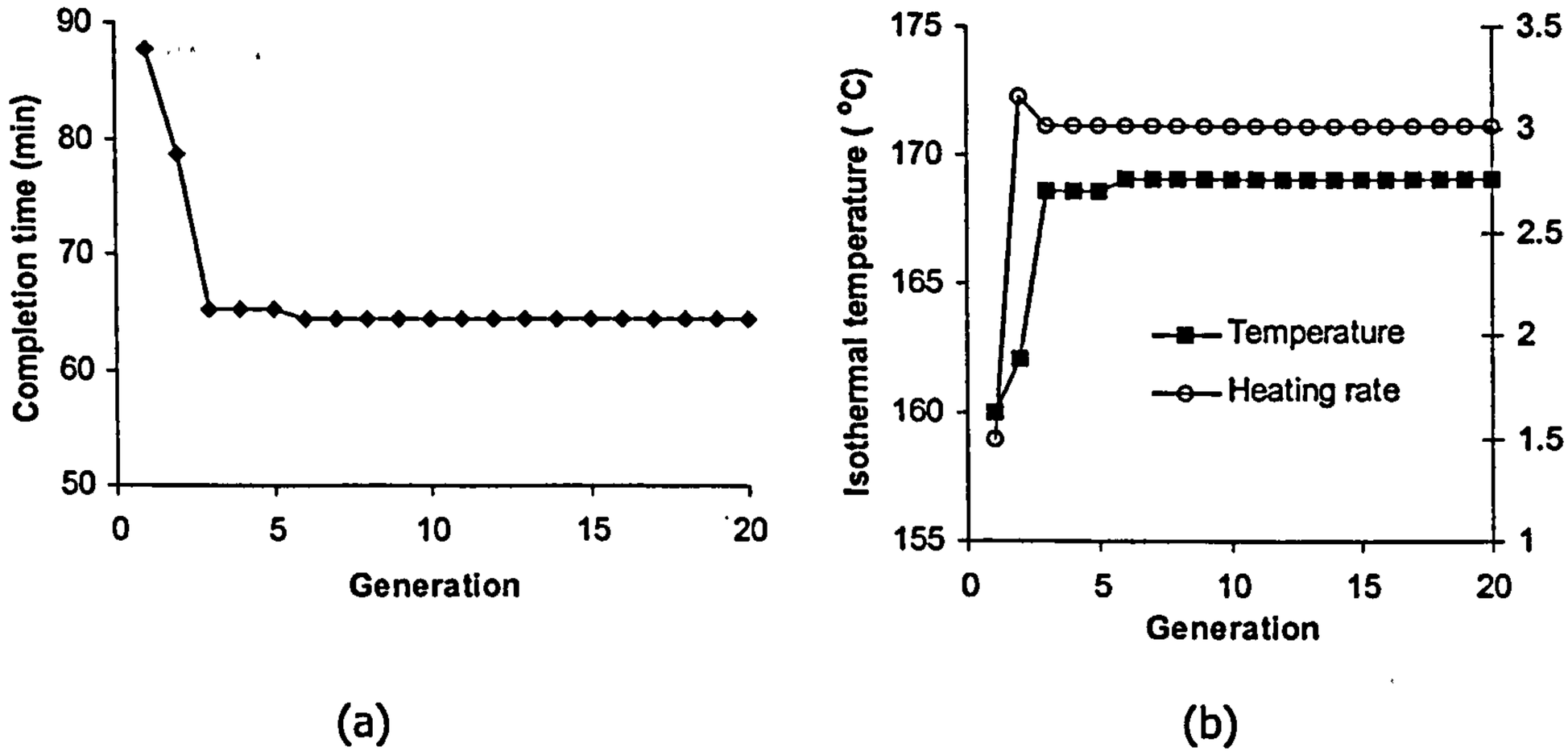

(a) (b)

Fig.10.2 *Convergence of the genetic algorithm in the case of thermal programme optimisation. (a) Cure completion time versus generation number. (b) Isothermal temperature and heating rate versus generation number.*

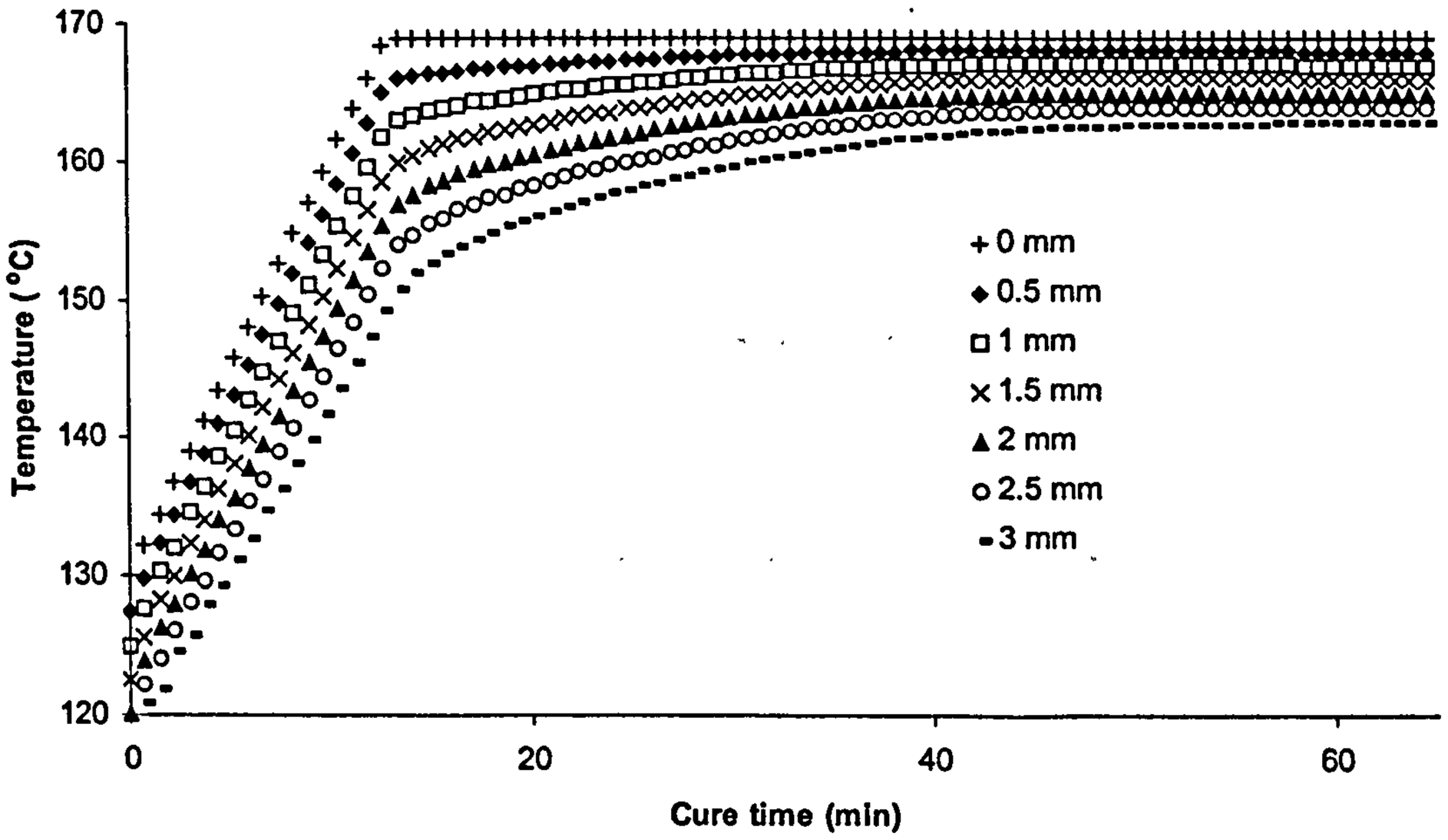

Fig.10.3 *Temperature as a function of cure time at different levels in the composite in the case of the optimum cure schedule*

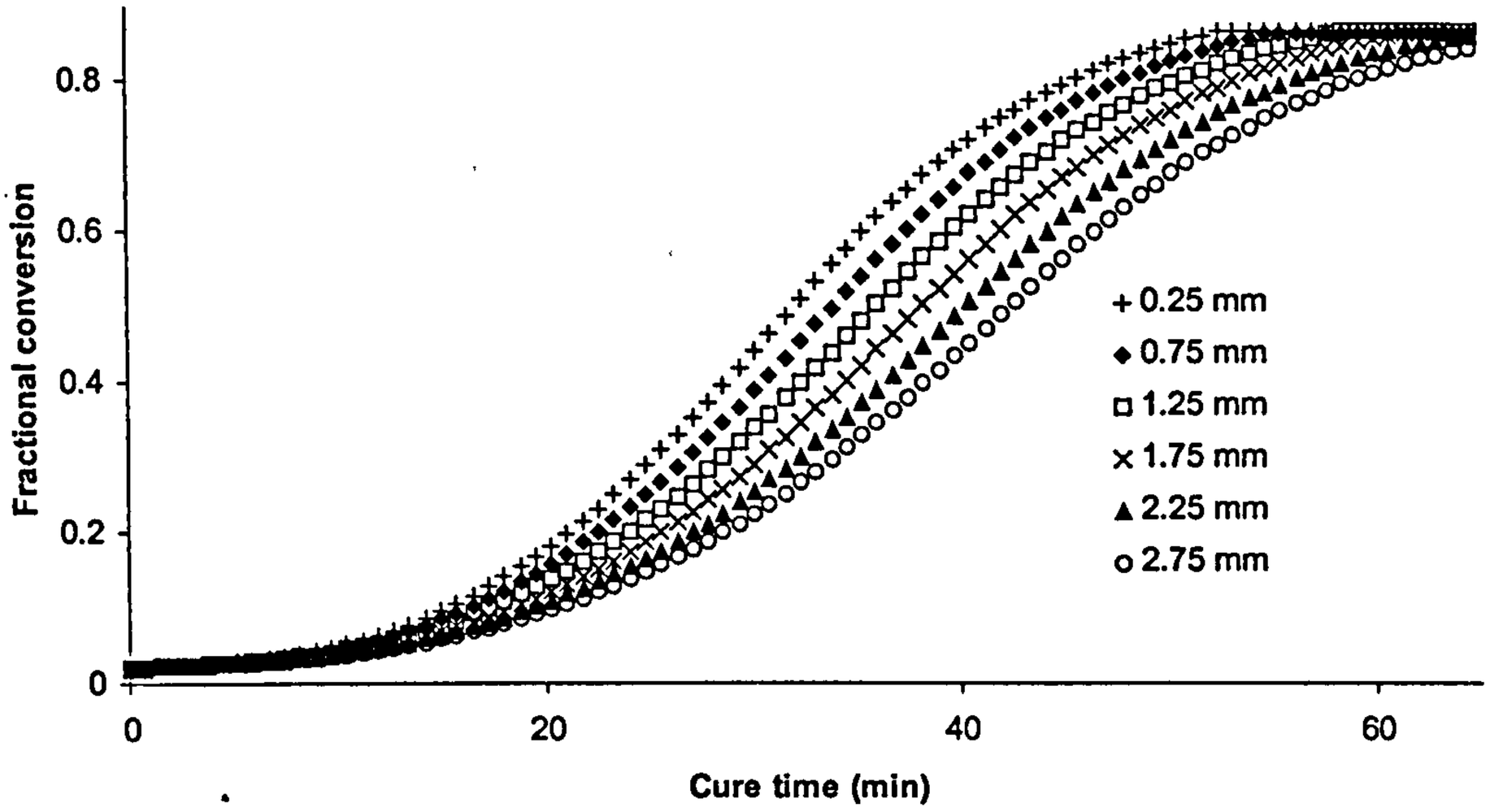

Fig.10.4 *Degree of cure as a function of cure time at different levels in the composite in the case of the optimum cure schedule*

10.3.2 Tooling material optimisation

A tooling optimisation was performed also for the carbon/RTM6 composite. The curing schedule was identical to the conventional schedule described in paragraph 7.3.5. The optimisation parameters were the top tool thermal conductivity, ranging from 0.1 to 100 W/m/°C and the tool surface heat transfer coefficient, ranging from 2 to 14 W/m^2. The optimisation criterion was the minimisation of the maximum thermal gradient above gelation, implemented using the following fitness function:

$$Fitness = 1/\left|\frac{dT}{dz}\right|_{max}, \ for\ \alpha > 0.6 \qquad \text{(Eq. 10.3)}$$

In that case the duration t_c of the curing, i.e. the time to reach a minimum conversion of 0.84 within the whole curing component, serves as a constraint as follows:

$$t_c < 90\ min \qquad \text{(Eq. 10.4)}$$

implemented similarly to the constraint of the optimisation presented in paragraph 10.3.1. The convergence of the algorithm is illustrated in Fig. 10.5.

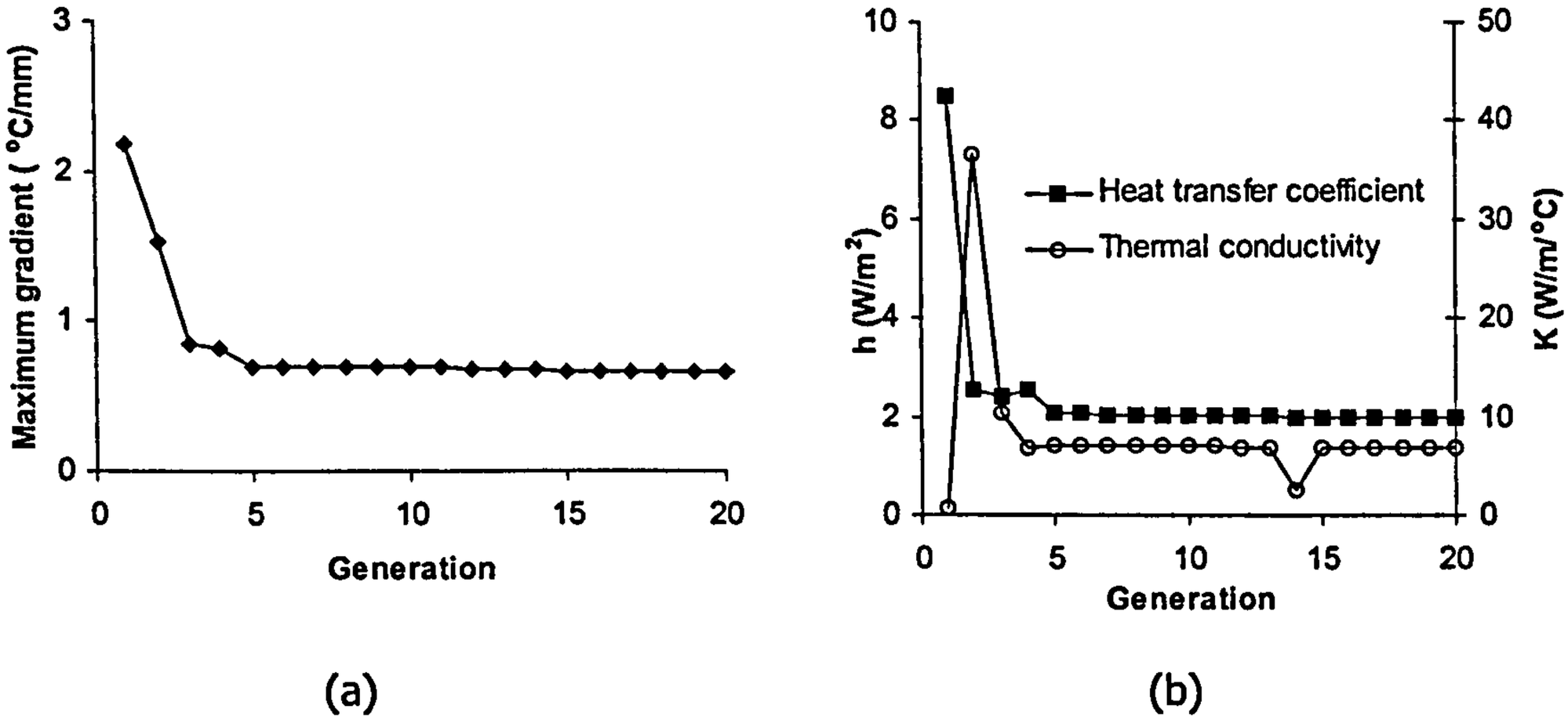

(a) (b)

Fig.10.5 *Convergence of the genetic algorithm in the case of top tooling optimisation. (a) Maximum thermal gradient versus generation number. (b) Heat transfer coefficient and thermal conductivity versus generation number.*

The algorithm converges after 15 generations, to a heat transfer coefficient of 2 W/m^2 and a thermal conductivity of 6.7 W/m/°C. The maximum thermal gradient above gelation for this set of parameters is 0.67 °C/mm. Thus the maximum thermal gradient decreases in comparison to the glass top tool case by 70%. The heat transfer coefficient has the minimum value, since the less heat is released on the top of the cure assembly the lower the thermal gradient is. The thermal conductivity has an intermediate value since for high values the maximum possible thermal gradient is established, whereas for very low values the transient state is extended to the later stages of the cure resulting in higher thermal gradients. Materials that could offer the optimal properties are metal matrix particulate composites comprising steel and ceramic or some very high Ni content steels. In the case of metal matrix composites the surface should be treated so that it has a very low emissivity.

The temperature and degree of cure distributions corresponding to the optimal values are illustrated in Figs. 10.6 and 10.7. The curing is completed in about 80 min. The thermal gradient at the beginning of the isothermal segment is similar to the glass top tooling curing case (Fig. 7.15) and decreases as the curing progresses.

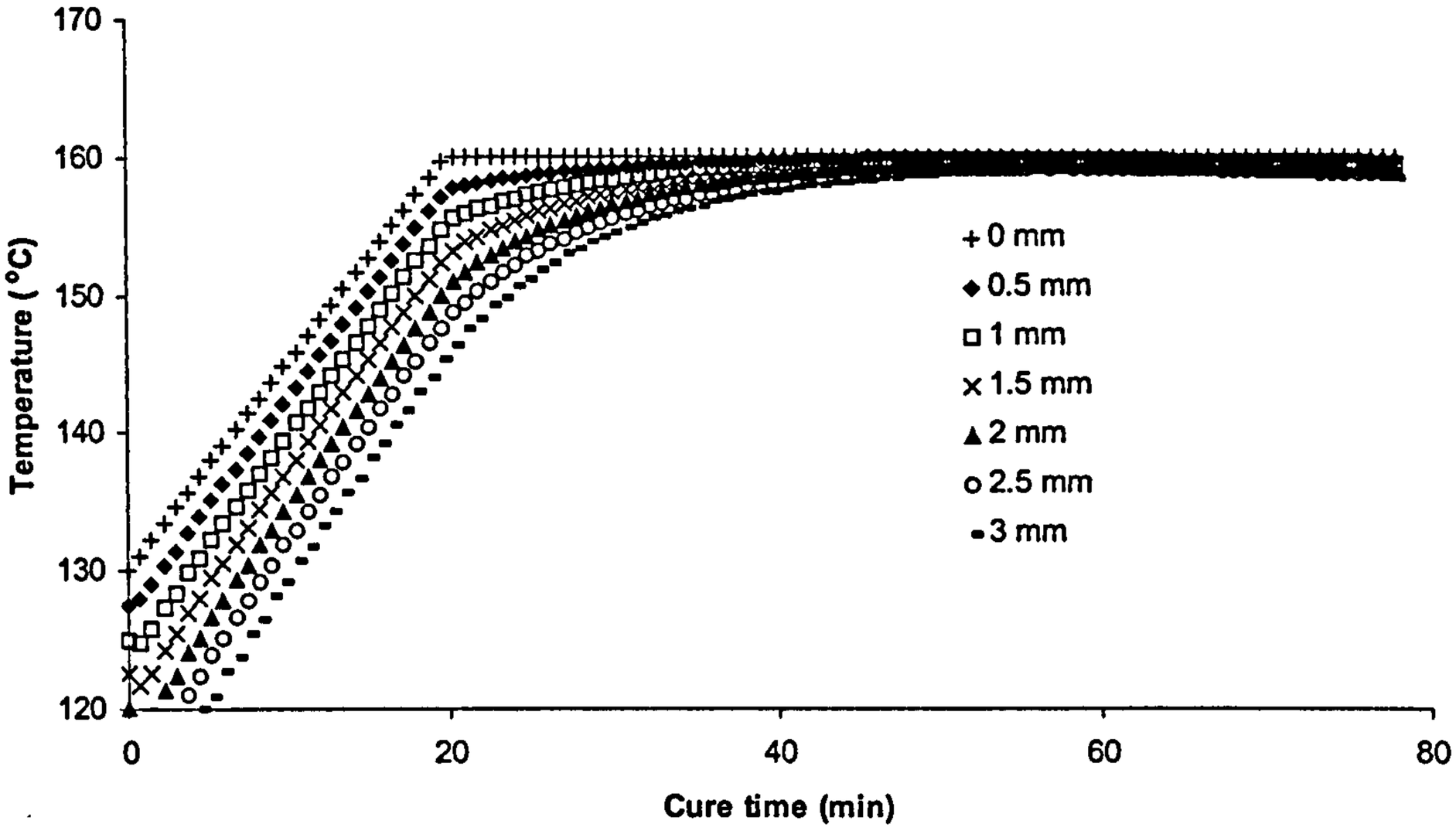

Fig.10.6 *Temperature as a function of cure time at different levels in the composite in the case of the optimum top tooling material properties*

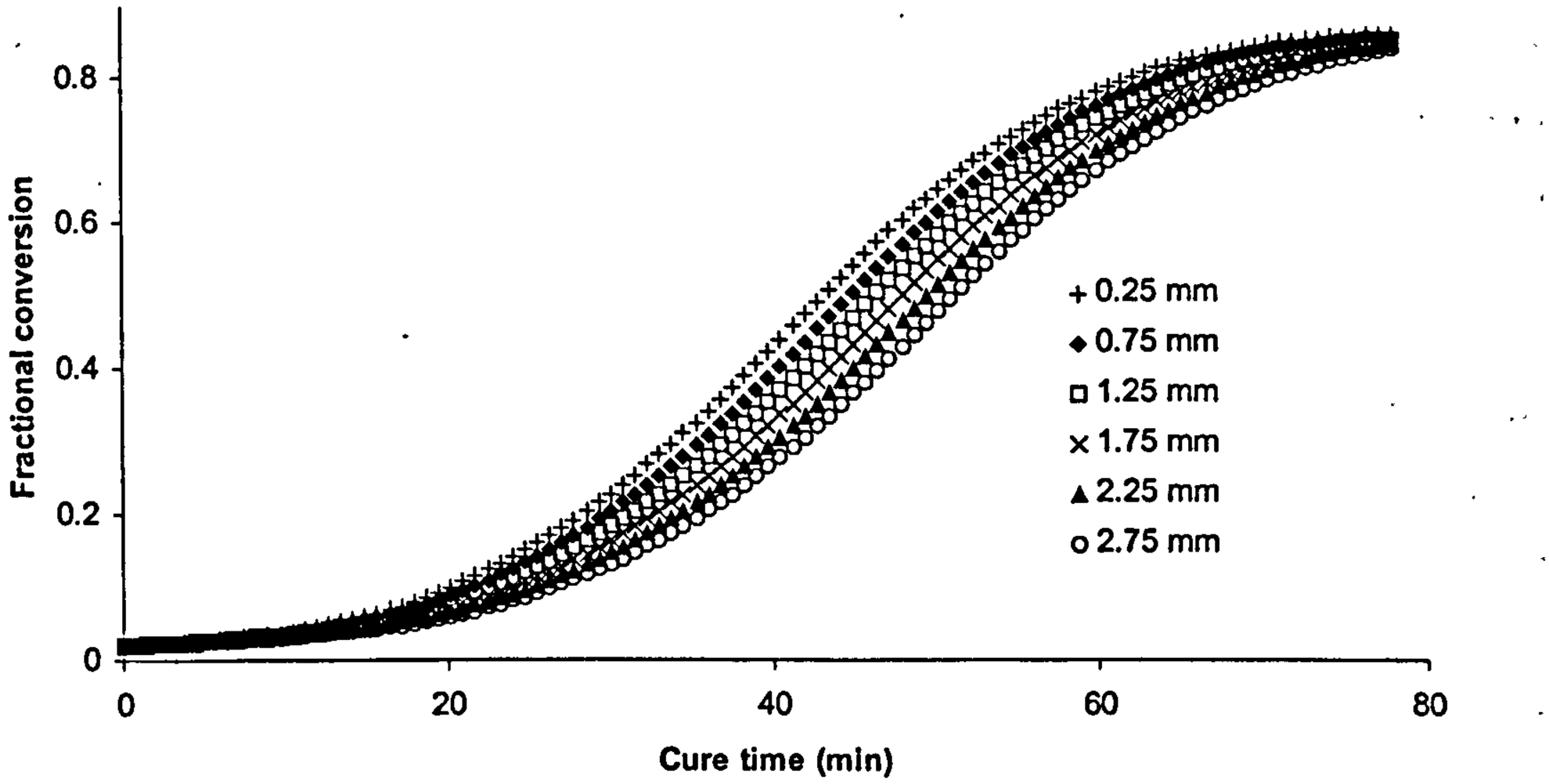

Fig.10.7 *Degree of cure as a function of cure time at different levels in the composite in the case of the optimum top tooling material properties*

10.4 Monitoring-modelling integration

Heat transfer modelling combined with the inversion procedure and thermal or cure monitoring can be used to provide information on the distributions of temperature and degree of cure. Monitoring alone provides local information, usually at locations of the component which are not structurally critical, whereas modelling is subject to the validity of the thermal properties and of the cure kinetics submodels. In this study heat transfer simulation results were of satisfactory accuracy as a result of the experimental and computational effort spent on the development and implementation of submodels. In industrial situations with material variability, the development of such submodels may not be cost-efficient. Thus, a methodology that could allow for some uncertainty in the thermal properties and/or in the cure kinetics may find extensive use. In this context the inversion procedure developed here is utilised in order to alter the thermal conductivity in the heat transfer model so that monitoring results coincide with simulation predictions. When this step is completed, the simulation can provide global information about the distributions of temperature and degree of cure. Thermal conductivity has been selected as the variable thermal property as it is the most difficult property of a curing composite to determine.

In paragraphs 10.4.1 and 10.4.2 the results from the application of this procedure to two cases are presented. In the first case temperature measurement results are used in order to determine the dependence of the composite thermal conductivity on the fractional conversion and temperature and, subsequently, to calculate the global temperature and degree of cure distributions. In the second case the same task is performed using artificial data from a hypothetical cure monitoring measurement that could give results identical to the results of heat transfer modelling. The artificial data were used, since, although a methodology to estimate conversion from impedance measurements independent of temperature, has been established (see paragraph 8.6), it is impossible to perform the measurement over the entire frequency range required to follow the cure throughout.

10.4.1 Integration using thermal monitoring signals

Temperature measurements performed at the mid-depth of a curing carbon/RTM6 composite (paragraph 7.3.1) are used as the target of the genetic algorithm. The details of the finite element model are identical to those of paragraphs 10.3.1 and 10.3.2. The variable parameters are the coefficients of a polynomial, which expresses the dependence of the composite thermal conductivity on fractional conversion and temperature as follows:

$$K = (\alpha^2 Par1 + \alpha Par2 + Par3)(TPar4 + Par5) \qquad \text{(Eq. 10.5)}$$

The fitness of an individual is calculated as follows:

$$Fitness = \Big/^{1}\Big/_{\sum_{i=1}^{120} \left| T_i^4 - T_{Mi} \right|} \qquad \text{(Eq. 10.6)}$$

where T_i^4 is the temperature at node 4, which corresponds to the middle of the composite, calculated by the simulation at the i-th time step and T_{Mi} is the temperature measurement at time $0.75i$ min. The range of the five parameters was from –1 to 1.

The parameters of the genetic algorithm run are given in Table 10.2 and the convergence behaviour is illustrated in Fig. 10.8.

Total number of individuals	Number of individuals passed directly to the next generation	Length of the bit string	Exchange probability	Mutation probability
26	5	100	0.4	0.02

Table 10.2 *Parameters of the genetic algorithm in the modelling-monitoring integration runs*

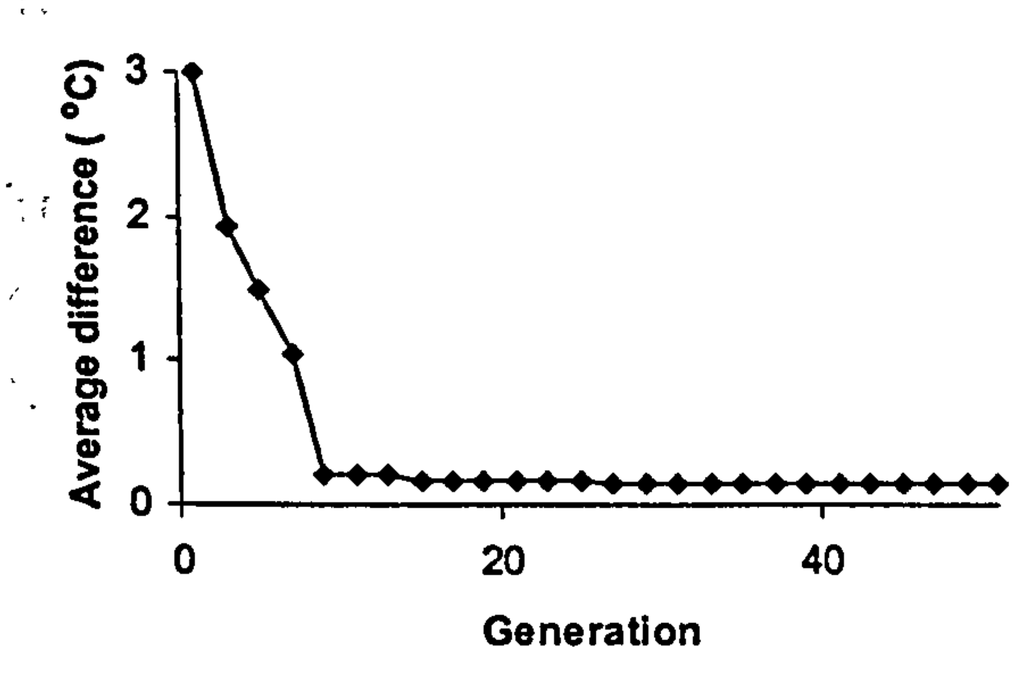

(a)

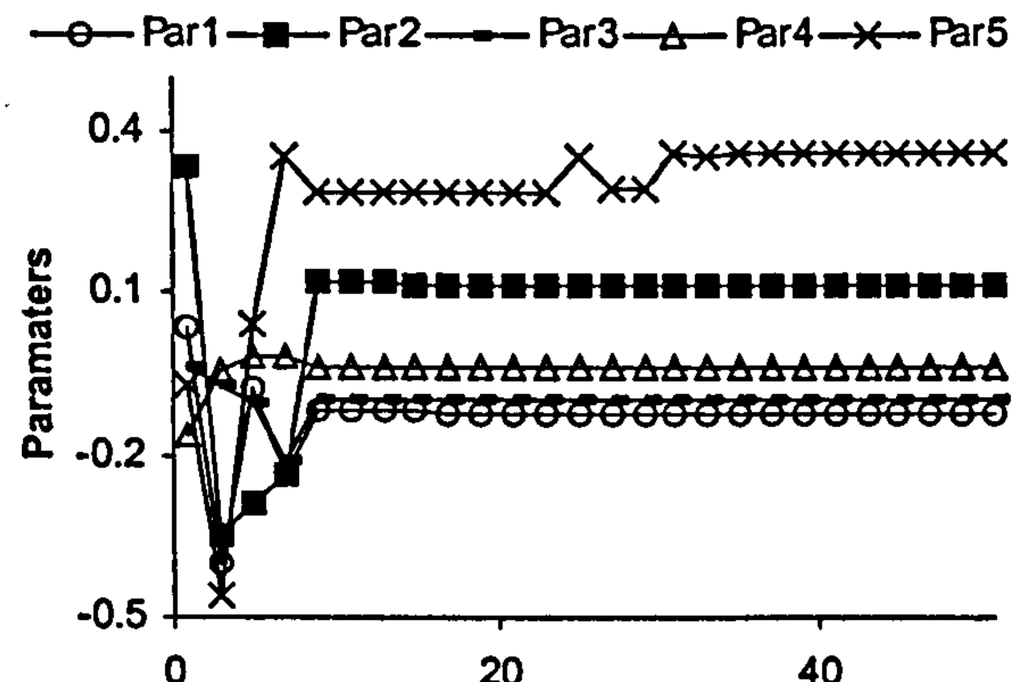

(b)

Fig.10.8 *Convergence of the genetic algorithm in thermal monitoring-modelling integration. (a) Average temperature difference between the measurement and the inverse modelling results versus generation number (b) Parameters of the thermal conductivity polynomial versus generation number.*

The algorithm converges after about 30 generations. Note that the problem in that case involved five parameters and about 900 iterations of the direct model were required for their estimation. A search method equivalent in terms of computational time would have resulted in a accuracy of about 0.5 in the parameter estimation. The solution of the inverse problem can be expressed as:

$$K = (-0.125\alpha^2 + 0.117\alpha - 0.094)(-0.034\,T + 0.358) \qquad \text{(Eq. 10.7)}$$

Using this model for the calculation of thermal conductivity, the distributions of temperature and degree of cure can be calculated. Their comparison with the results of the simulation presented in chapter 7, which was shown to be in agreement with the thermal monitoring results utilised here for the inversion, is illustrated in Figs. 10.9 and 10.10. It can be observed that the monitoring-modelling scheme predicts the global distribution of temperature and degree of cure with satisfactory accuracy. The average error in temperature estimation is 0.29 °C and in fractional conversion determination 0.0019. The error in temperature is lower than the accuracy of the direct model (see paragraph 7.3.4), whereas the error in fractional conversion estimation is very low due to the fact that the higher differences in temperature between the inversion results and the direct model occur at low conversions when the reaction rate is very low.

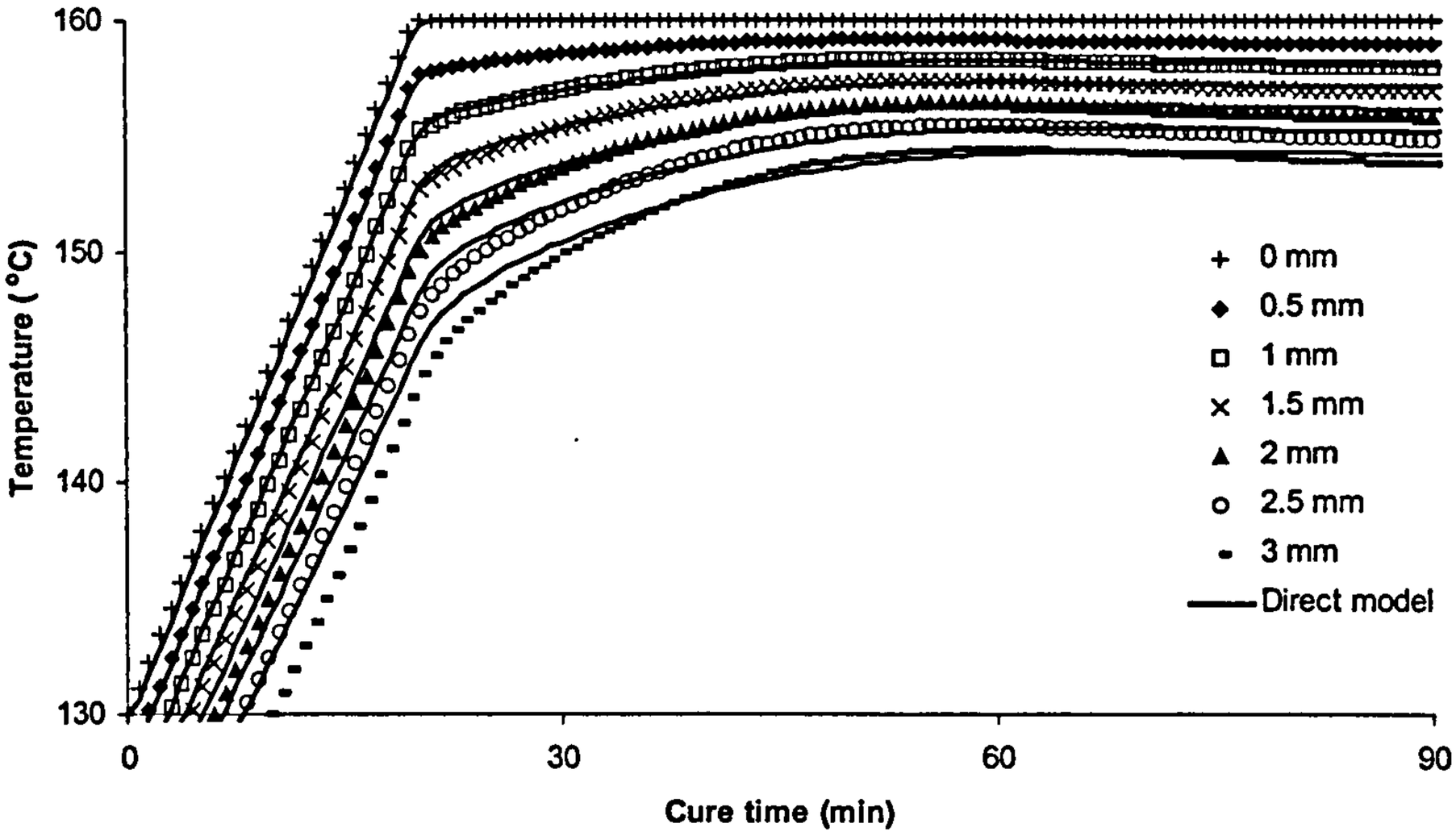

Fig.10.9 *Temperature as a function of cure time at different levels in the composite as resulting from the inversion procedure (points) and the from direct model (solid line)*

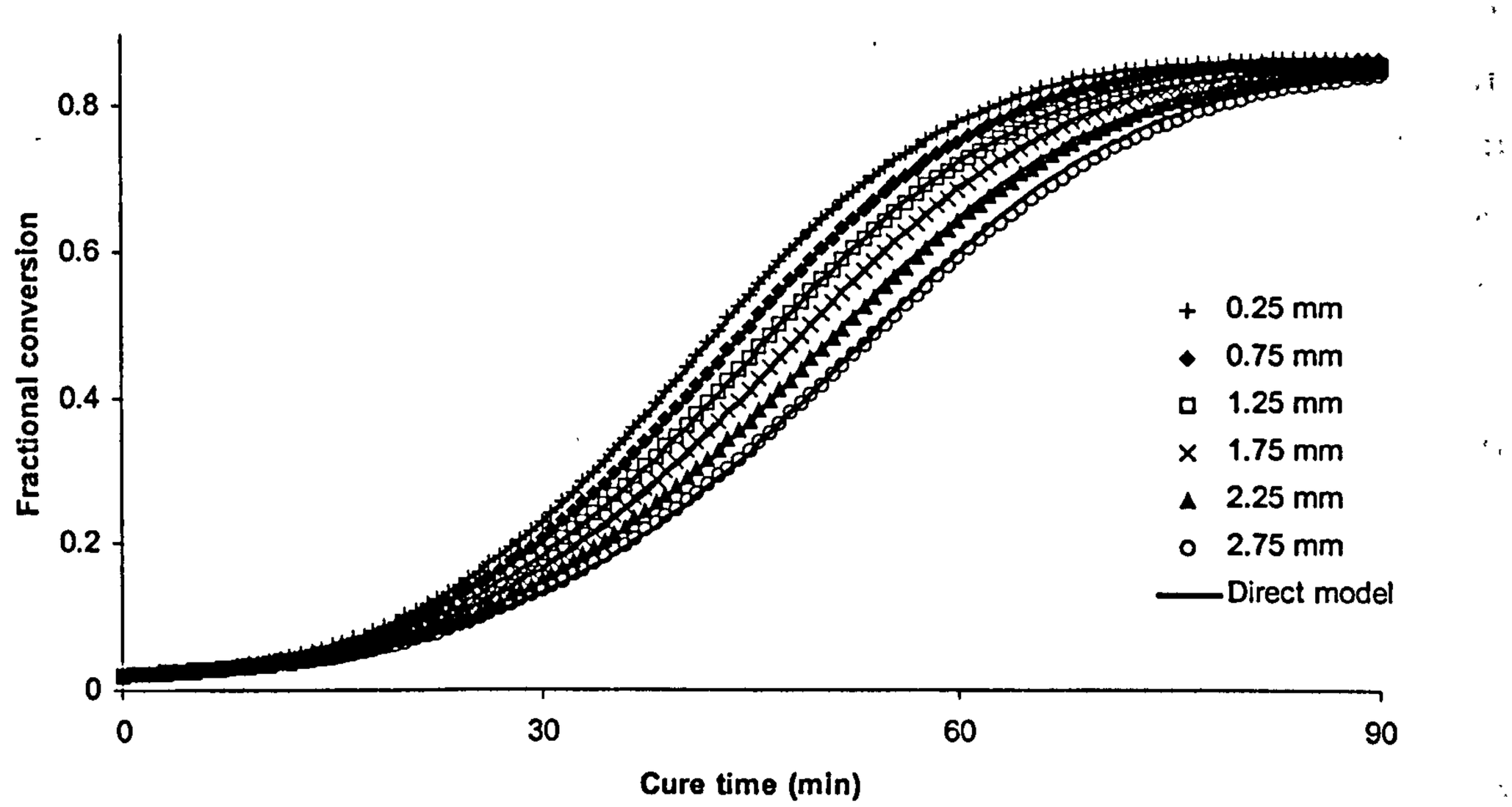

Fig.10.10 *Degree of cure as a function of cure time at different levels in the composite as resulting from the inversion procedure (points) and from the direct model (solid line)*

10.4.2 Integration using cure monitoring signals

The procedure described in the previous paragraph has been executed using artificial cure monitoring data as the target of the inversion. The fitness was calculated according to the relation:

$$Fitness = \Big/ \sum_{i=1}^{120} \left| \alpha_i^4 - \alpha_{Mi} \right| \qquad \text{(Eq. 10.8)}$$

where α_i^4 is the conversion at node 4, i.e. the average of conversion in the two adjacent elements 3 and 4 and α_{Mi} the artificial measurement which was considered equal to the results of the 1-D simulation for the carbon fabric case presented in chapter 7. The parameters of the algorithm are those given in Table 10.2. The convergence of the algorithm is illustrated in Fig. 10.11. The use of artificial data which are produced by the model facilitates the algorithm which converges within 18 generations. The thermal conductivity is estimated to have the following functional form:

$$K = (-0.163\alpha^2 + 0.106\alpha - 0.140)(-0.021\,T + 0.326) \qquad \text{(Eq. 10.9)}$$

which results in the temperature and degree of cure distributions illustrated in Figs. 10.12 and 10.13. Both the temperature and the fractional conversion are very close to the original values of the direct model. The average errors are 0.23 °C and 0.0006 respectively. Errors in the temperature are observed towards the end of the cure, due to the very low sensitivity of the reaction to the temperature once vitrification has occurred. The inversion and direct model fractional curves are essentially identical.

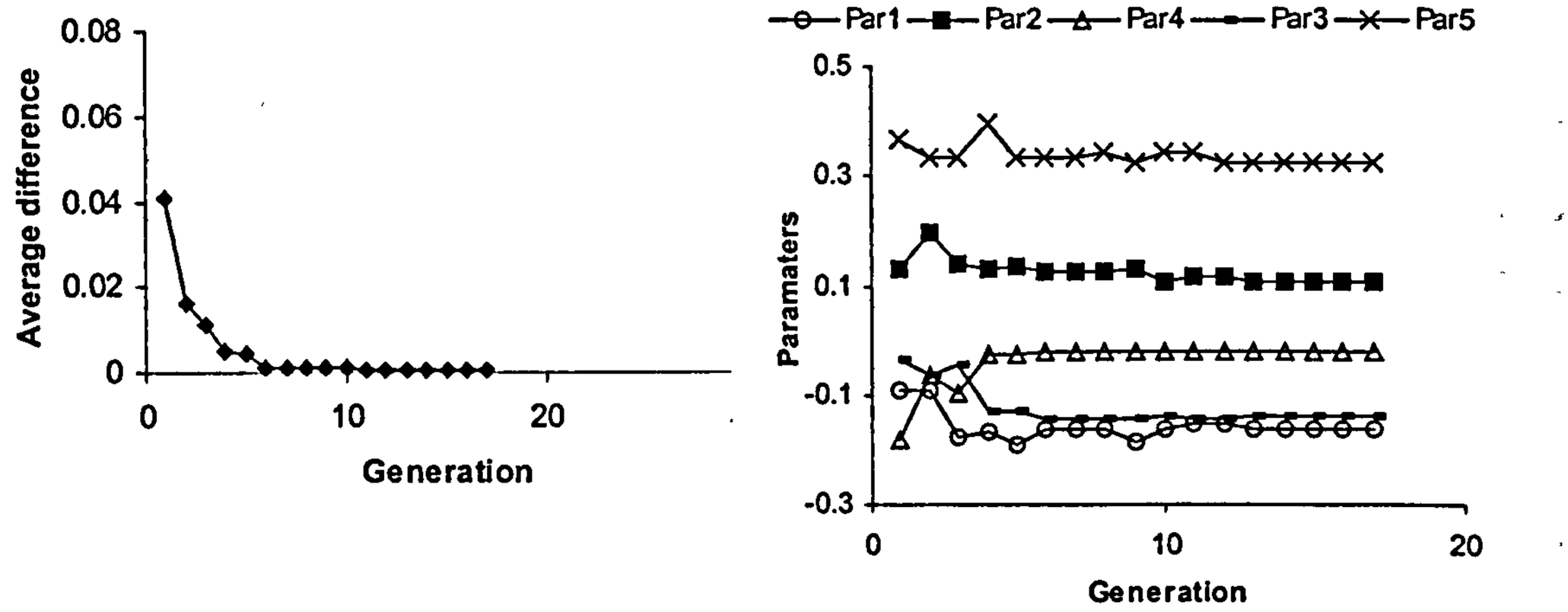

(a) (b)

Fig.10.11 *Convergence of the genetic algorithm in cure monitoring-modelling integration. (a) Average fractional conversion difference between the measurement and the inverse modelling results versus generation number (b) Parameters of the thermal conductivity polynomial versus generation number.*

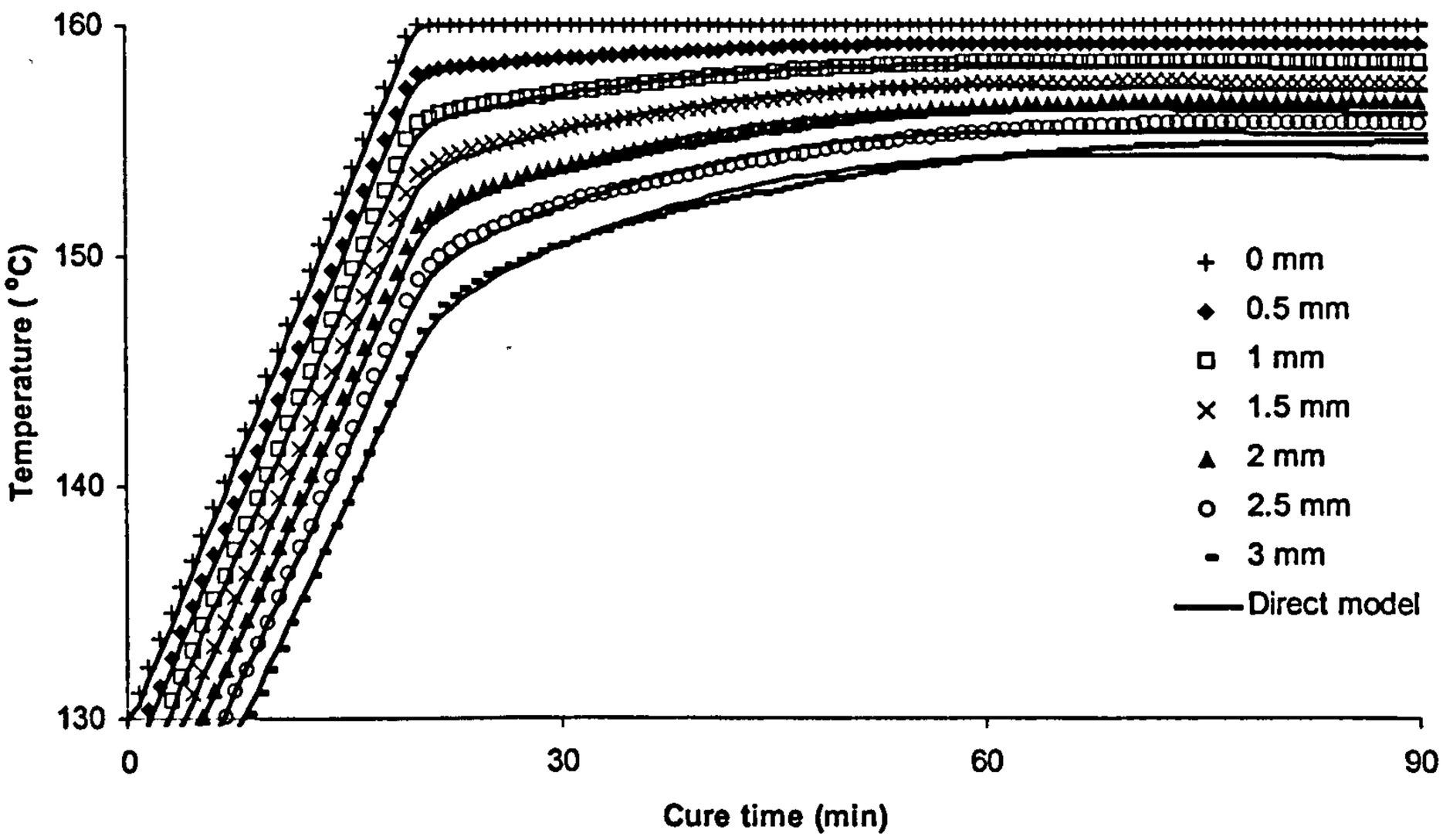

Fig.10.12 *Temperature as a function of cure time at different levels in the composite as resulting from the inversion procedure (points) and from the direct model (solid line)*

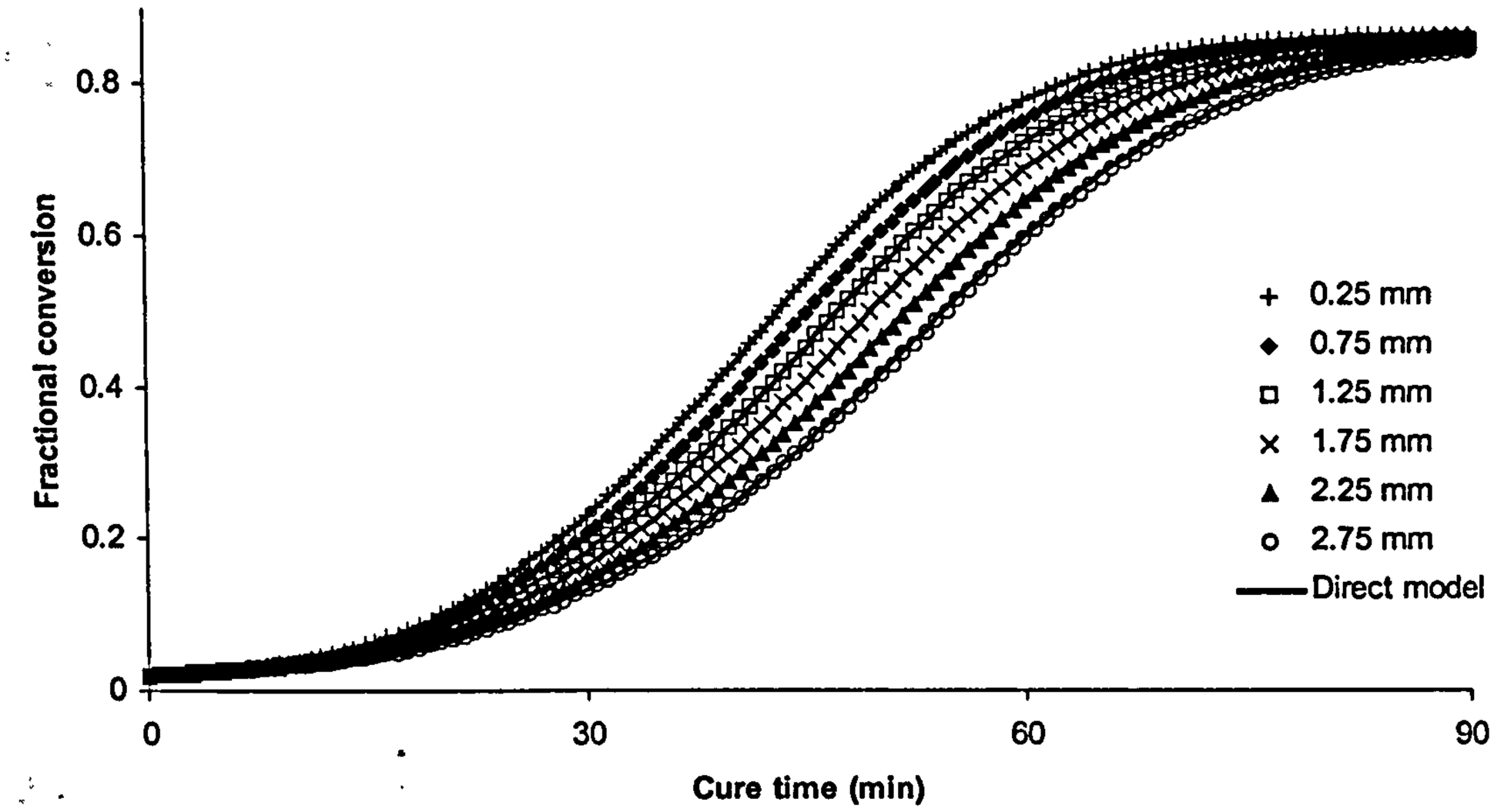

Fig.10.13 *Degree of cure as a function of cure time at different levels in the composite as resulting from the inversion procedure (points) and from the direct model (solid line)*

10.5 Overview

An inversion procedure based on genetic algorithms was applied to the heat transfer simulation for optimisation and monitoring-modelling integration. Optimal cure schedules with respect to total curing process duration and theoretically optimal top tooling materials with respect to thermal gradients occurring during the cure were found for a specific carbon/RTM6 composite component. The monitoring-modelling combined scheme, which offers the possibility to infer temperature and degree of cure distributions from limited local thermal or cure monitoring signals, was tested and verified. Local monitoring results combined with the inversion procedure result in a very accurate estimation of the temperature and degree of cure evolutions during the cure.

Chapter Eleven

11 Overall discussion

This investigation concerned the development and implementation of models and monitoring techniques appropriate for the resin transfer moulding manufacturing process. Modelling studies were focused on the curing stage of the process, whereas monitoring was applied to both the filling and the curing stages of RTM.

Up to now modelling efforts on RTM have focused on the filling stage of the process. Simplified models of the heat transfer phenomena occurring during the cure stage, which involve gross assumptions as far as the cure kinetics and the thermal properties are concerned, have been developed. In this study, a heat transfer simulation of RTM curing which accepts and uses accurate submodels for the cure kinetics and for the various thermal properties (specific heat capacity, thermal conductivity and density) was developed. The simulation is based on finite elements solution of the heat conduction equation. Other modes of heat transfer are not significant in the conditions of composites manufacturing.

The cure kinetics were modelled using a non-parametric procedure. This technique uses interpolation, which is applied directly to experimental data, and does not involve any closed form expression. Isothermal and dynamic DSC data are incorporated directly into the computer subroutine. Such a technique is appropriate for systems with reaction mechanisms independent of the temperature history. This assumption, which is ignored in most cure kinetics models that express the reaction rate explicitly as a function of

temperature and fractional conversion, was experimentally verified for the specific epoxy system utilised in this study (RTM6). The cure kinetics submodel gives accurate results and successfully simulates the chemical phenomena as well as structural phenomena such as vitrification and devitrification. Conventional modelling cannot yield similar results, especially as far as the structural phenomena are concerned. The use of conventional models requires a modification of the cure kinetics model so that it can account for diffusion limitations effects. Thus, an additional model, which allows the estimation of the glass transition temperature, is required. In contrast, the algorithm developed here can simulate the cure in one step using the same range of experimental data required for the development of a conventional model. Thus, it becomes much more attractive especially if it aims to serve as a submodel of a heat transfer simulation, where it can be implemented directly as a subroutine. Prior to the application of the kinetics model, the effect of the specific reinforcements used in this study was investigated using DSC. Neither the carbon nor the glass reinforcement had any influence on the cure kinetics of RTM6 resin.

The heat capacity submodel operates similarly to the kinetics submodel, with direct interpolation applied to data acquired during isothermal MDSC experiments. The rule of mixtures is used in order to calculate the composite material specific heat capacity from the constituent values. This method reproduces successfully the effect of the resin vitrification on the heat capacity. The calculation of density is performed using the rule of mixtures and an incremental formulation, which then allows the sequential computation of the resin and fibre densities from the thermal expansion coefficient and the chemical shrinkage. The calculation of the composite material thermal conductivity is performed by an explicit model, which incorporates expressions for the constituent thermal conductivities in a model appropriate to fibrous composites. An apparatus of cylindrical symmetry and an appropriate analysis procedure were developed in order to measure the thermal conductivity of the unreinforced resin during the cure.

As a result of the high accuracy of the submodels the heat transfer simulation gives an accurate prediction of the thermal profiles during RTM curing of both carbon/RTM6 and glass/RTM6 composites. The heat transfer was demonstrated to be one-dimensional in the geometries considered. Significant thermal gradients were shown to be developed during the cure, resulting in significant vitrification time differences between different

points of the curing component (of about 10 to 30 minutes depending on the tooling material). The existence of degree of cure gradients was identified also, however, their existence is temporary as they are minimised towards the end of the cure process.

The predictive capabilities of the heat transfer simulation can be used for the optimisation of the curing process during the design stage. A genetic algorithm was utilised to achieve the inversion of the heat transfer model required for the optimisation. Different criteria were tested and it was possible to find optimal cure schedules or tooling materials, which result in minimum process duration or minimum thermal gradients respectively. Significant cost reductions and quality improvements may be achieved using such a procedure.

Although the heat transfer simulation can give very useful information as a predictive tool, its validity is subject to the use of appropriate material submodels. The development of accurate submodels requires the allocation of significant resources, which may not be available in an industrial environment. Furthermore, batch to batch material variability can affect the validity of submodels. A scheme, which allows the adaptation of models according to in-situ monitoring results, was developed here, in order to overcome such problems. Its implementation requires an inversion of the heat transfer simulation, which is performed similarly to the optimisation studies using a genetic algorithm. The combined scheme was applied to RTM curing of carbon/RTM6 composites. Thermal monitoring results were utilised to drive the inversion and it was possible to reproduce temperature and degree of cure distributions successfully by altering the thermal conductivity submodel. The same procedure could be applied using multiple thermal monitoring results and multiple target submodels; the choice of thermal conductivity was made here since this was the most difficult thermal property to determine. Under this scheme, it is possible to integrate modelling and monitoring and to produce global estimations from local measurements, on which feedback loop control can be based. At the moment the algorithm cannot be implemented in real time as the inversion requires a long time (in the order of tens of minutes) to be executed. However, improvements of the computer hardware and the algorithm implementation can lead to a real-time application.

In cases where the inversion target is related to the cure kinetics model, it is expected that the thermal monitoring results will not have high sensitivity to the cure kinetics

parameters. This statement can be justified by the absence of significant temperature overshoots in the curing experiments and in simulations performed in this study. Thus, in cases where an uncertainty of the simulation is caused by the cure kinetics, the inversion should be driven by cure monitoring results. In this respect, dielectric cure monitoring was investigated. Earlier works have established methods for correlating impedance cure monitoring signals with the progress of the reaction under isothermal conditions. In this study the evolution of the real and imaginary impedance spectra during the cure of RTM6 was investigated under both isothermal and dynamic heating conditions in order to establish a temperature independent correlation between the monitoring signals and the degree-of-cure. Such a correlation is necessary for process control based on the cure reaction progress.

The basic mechanisms of electrode polarisation, charge migration and dipolar relaxation were identified and a new form of electrical equivalent circuit, which represents electrode polarisation using a constant phase element, was established. In addition, the manifestation of vitrification as a peak in the real impedance versus time curves, and as a knee in the imaginary impedance versus time curves, was observed and explained in terms of the part on the spectra which is affected by dipolar relaxation. The principal features of the imaginary impedance spectra were found to correlate with the progress of the reaction. More specifically, the difference between the frequencies of the minimum and maximum of the imaginary impedance was found to have a low sensitivity to temperature and a high sensitivity to fractional conversion. This correlation could not be utilised in the RTM curing experiments, as the minimum of the imaginary impedance spectrum moves to frequencies outside the measurement range as the curing progresses at the curing temperature used. Thus, the inversion procedure was applied using artificial data, which were results of the heat transfer model. The ability to extend the monitoring signals to the whole component was demonstrated in that case also. The implementation of this scheme to composite production would enable cure sensing performed at a structurally non-critical region of the curing component to give an estimation of the material state in other regions in which the placing of a sensing device would not be acceptable.

An aspect of liquid moulding processes, which has not received adequate attention up to the moment, is the monitoring of the filling stage. Although flow models have been

developed and problems connected with permeability, which is the core parameter of these models, have been identified, no systematic efforts have been made in this direction. In this study dielectric sensors appropriate for flow monitoring during the impregnation of conductive and non-conductive reinforcements were designed and tested. In non-conductive reinforcements, lineal sensors producing a fringing field which permeates part of the filling composite gave an accurate estimation of the flow front position. In conductive reinforcement insulated wires form a field with the conductive fibres, enabling the location of the flow front to be performed. In both cases the measurements are continuous and are performed in real time. As such, they can be easily incorporated in a control system. In addition, the inversion procedure implemented here to integrate the heat transfer simulation with thermal and cure monitoring signals, could be used to integrate flow models with the dielectric flow monitoring results to obtain the flow front distribution by altering the value of permeability used in the flow model, in real time.

Chapter Twelve

12 Conclusions

The main points resulting from this study are summarised in the following.

<u>Cure kinetics:</u>

- The kinetics of RTM6 and of any resin system with reaction mechanisms independent of temperature history can be modelled by non-parametric modelling.
- Non-parametric modelling can simulate chemical and structural phenomena in a single procedure.
- The reinforcements used in this study do not alter the cure kinetics of RTM6.

<u>Thermal properties:</u>

- The heat capacity of a thermosetting system can be modelled using an interpolation routine.
- The thermal conductivity of a thermosetting system has been measured during cure.

<u>Heat transfer modelling:</u>

- Conduction is the only significant mode of heat transfer in RTM.
- In the geometries considered the heat transfer was mainly one-dimensional.

- Significant thermal gradients are developed during RTM curing. The thermal gradients decrease with decreasing surface heat transfer coefficient of the top tooling material.
- The degree-of-cure gradients developed during RTM curing are temporary and vanish towards the end of the process.
- Significant differences between times at which vitrification occurs at different locations are observed during RTM curing.

Impedance cure monitoring:

- The impedance spectrum of RTM6 is governed by three phenomena, electrode polarisation, charge migration and dipolar relaxation. The dipolar relaxation contribution is hindered by charge migration.
- An equivalent electrical circuit in which a constant phase element accounts for electrode polarisation represents accurately the behaviour of RTM6.
- Vitrification is manifested as a peak in the real impedance and as a knee in the imaginary impedance. This behaviour is explained by the shift of the spectra in the frequency range in which dipolar relaxation occurs.
- The imaginary impedance maximum value can provide the means for reaction monitoring in isothermal conditions. In contrast, in dynamic conditions the influence of temperature changes does not allow such a correlation to be made.
- The difference between the frequencies at which the imaginary impedance maximum and minimum occur correlates with the progress of reaction under both isothermal and dynamic conditions. This correlation is practically feasible only in the conversion-temperature window in which electrode polarisation is clearly manifested in the imaginary impedance spectrum.

Flow monitoring:

- Lineal dielectric sensors provide the means for flow and macroscopic cure monitoring in non-conductive reinforcements.
- Configurations comprising insulating wires can be used for dielectric flow and cure monitoring in conductive reinforcements.

- The imaginary part of the flow progress measurement using dielectric sensing provides the means for self-evaluation of the quality of the measurement.

Process optimisation :

- The inverse solution of the heat transfer simulation can be performed by a genetic algorithm.
- Optimisation targets which could result in process cost-efficiency and/or increased process quality can be achieved using the inverse solution.

Modelling-monitoring scheme:

- Modelling can be combined with monitoring results in an inverse algorithm which alters the heat transfer submodels in order to produce modelling solutions which are compatible with the monitoring results.
- The combined scheme can reproduce successfully the distributions of temperature and of degree of cure.

Chapter Thirteen

13 Suggestions for further investigation

The non-parametric cure kinetics algorithm developed here is suitable for those thermosetting systems which do not show any dependence of their kinetics on the temperature history. Most of the commercial thermosetting systems fall into this category, at least within the accuracy required for practical use. However, an algorithm which could operate in a non-parametric way and account for temperature history effects would be a generic and free of assumptions solution to the problem of kinetics, which could be extended outside the context of cure kinetics. The development of such a methodology should be based on data from a technique which can distinguish between different reactions, e.g. infrared spectroscopy, but the final objective should be to implement a procedure that could operate using data from an experimental technique that cannot distinguish between different reactions, e.g. calorimetry.

The method for the measurement of thermal conductivity developed here provides a cost-effective solution to the problem of the measurement of this property in reacting thermosets. The thermal conductivity data available in the international literature are very limited as the alternative laser pulse method is very expensive to use. Consequently, most of the cure simulations operate under major assumptions as far as the value of this property is concerned. An optimised apparatus based on the principles set out here can enable the measurement of the thermal conductivity to be performed for a series of commercial thermosetting systems in order to develop an appropriate

database. Furthermore, as thermal conductivity is related to phonon transfer, its accurate measurement during the cure could offer an additional insight into the cross-linking network development.

The heat transfer simulation developed here can be integrated with a residual stress/strain development model in order to extend the predictive capabilities of a model for the manufacture of composites and to relate its results to some of the critical properties of the final product. Although this extension is not very demanding in terms of numerical implementation, experimental methodologies capable of providing the values of the material properties involved in such a simulation (mechanical moduli, resin shrinkage) need to be developed, in order to achieve the required level of model accuracy. This is a very challenging task as currently there do not exist any experimental techniques capable to perform such measurements in a general way. Once an integrated heat transfer/residual stress model is available the process optimisation methodology applied here can be extended to use as criteria or constraints measures of the stress/strain development. Similarly, the monitoring-modelling combined scheme could incorporate the general model and in-situ strain monitoring techniques. Thus, a complete curing simulation could operate in combination with thermal, curing and strain monitoring and provide the manufacturer with a global picture of the process progress on which control actions can be based.

Real time operation of the inversion algorithm is a prerequisite for application to the control problem. Currently the inversion is performed within time periods in the order of ten minutes. That duration should decrease to about one minute or less before any real time application is possible. This can be achieved with improvements in the model and inversion algorithm and the use of a faster programming language, e.g. C or C++. Furthermore, genetic algorithms lend themselves to very effective parallel processing. Taking into account that multiprocessing systems are becoming cheaper, parallel processing could be a solution to the real time application problem.

The inversion procedure can be applied to the filling stage of liquid composite moulding. An appropriate flow model based on Darcy's law can be combined with the flow monitoring signals provided by the devices developed in this study. An on line estimation of permeability can be performed and the flow problem can be solved using these realistic values. Similarly to the curing stage, control based on the global picture of the

filling progress can be performed. Such a procedure would be very attractive taking into account the practical difficulties in estimating fibre pre-form permeability a priori.

The methodologies developed here for the interpretation of the cure monitoring signals should be investigated further as the conclusions drawn here are based on experimental results from one resin system. The new equivalent circuit and the procedure to estimate the degree of cure under dynamic cure conditions from the imaginary impedance spectrum should be tested in different resin systems in order to verify whether their validity is universal. Another aspect that should be investigated further is the relative magnitude of the temperature and degree of cure changes in the dielectric/impedance signals. This can be performed by imposing modulated thermal programs in a fashion similar to that used in modulated differential scanning calorimetry. Thus, reversible phenomena, i.e. viscosity and mobility changes due to temperature variation can be separated by non-reversible phenomena, i.e. viscosity and mobility changes due to network formation and dipole moments changes due to chemical changes.

The flow monitoring sensing setup for conductive reinforcements can be extended to new sensor designs which will be capable of overcoming the most significant practical limitation of dielectric/impedance flow monitoring which is the need to embed a sensing element in the composite.

The insulated wire can be replaced by an hybrid fibre tow which comprises a carbon fibre core surrounded by glass fibres. The conductive core of such a tow can be used as the electrode of impedance sensing while the glass fibres can provide the required insulation. A range of possible setups can be used according to the monitoring objectives, e.g. a pair of tows of this type running along the mould can provide the means for flow sensing and macroscopic cure monitoring, or a comb configuration can provide the means for local cure monitoring.

REFERENCES

1. Y. R. Chachad, J. A. Roux and J. G. Vaughan, "Manufacturing model for three-dimensional irregular pultruded graphite/epoxy composites", Composites Part A, **27A**, 201, (1996)
2. J. A. Roux, J. G. Vaughan, R. Shanku, E. S. Arafat, J. L Bruce and V. R. Johnson, "Comparison of measurements and modeling for pultrusion of a fiberglass/epoxy I-beam", Journal of Reinforced Plastics and Composites, **17**, 1557, (1998)
3. R. Gorthala, J. A. Roux and J. G. Vaughan, "Resin flow, cure and heat transfer analysis for pultrusion process", Journal of Composite Materials, **28**, 486, (1994)
4. B. S. Suratno, L. Ye and Y. W. Mai, "Simulation of temperature and curing profiles in pultruded composite rods", Composites Science and Technology, **58**, 191, (1998)
5. k. Azaar, A. El Brouzi, R. Granger and J. M. Vergnaud, "Modelling the cure of thermosetting polymers. Effect of the coefficient of surface heat transfer", Plastics Rubber and Composites Processing and Applications, **18**, 95, (1992)
6. J. M. Salla and X. Ramis, "Comparative study of the cure kinetics of an unsaturated polyester resin using different procedures", Polymer Engineering and Science, **36**, 835, (1996)
7. J. H. Lee and J. W. Lee,"Kinetic parameters estimation for cure reaction of epoxy based vinyl ester resin", Polymer Engineering and Science, **34**, 742, (1994)
8. A. Yousefi, P. G. Lafleur and R. Gauvin,"Kinetic studies of thermoset cure reactions: A review", Polymer Composites, **18**, 157, (1997)
9. J. M. Kenny, " Determination of autocatalytic kinetic model parameters describing thermoset cure ", Journal of Applied Polymer Science, **51**, 761, (1994)
10. M. R. Dusi, W. I. Lee, P. R. Ciriscioli and G. S. Springer,"Cure kinetics and viscosity of Fiberite 976 resin", Journal of Composite Materials, **21**, 243, (1987)
11. R. J. Williams, M. A. Benavente, R. A. Ruseckaite, M. S. Churio and H. G. Hack, "Criteria for selecting cure cycles in autoclave processing of graphite/epoxy composites", Polymer Engineering and Science, **30**, 1140, (1990)

12. D. J. Michaud, A. N. Beris and P. S. Dhurjati, "Curing behaviour of thick-sectioned RTM composites", Journal of Composite Materials, **32**, 1273, (1998)
13. P. I. Karkanas, I. K. Partridge and D. Attwood, "Modelling the cure of a commercial epoxy resin for applications in resin transfer moulding ", Polymer International, **41**, 183, (1996)
14. P. I. Karkanas and I. K. Partridge," Cure modelling and monitoring of epoxy/amine resin systems. Part I: Cure kinetics modelling ", Journal of Applied Polymer Science, **77**, 1419, (2000)
15. C. W. Wise, W. D. Cook and A. A. Goodwin," Chemico-diffusion kinetics of model epoxy-amine resins ", Polymer, **38**, 3251, (1997)
16. K. C. Cole," A new approach to modeling the cure kinetics of epoxy amine thermosetting resins. 1. Mathematical development ", Macromolecules, **24**, 3093, (1991)
17. P. I. Karkanas," Cure modelling and monitoring of epoxy/amine resin systems ", PhD thesis, Cranfield University, UK, (1998)
18. L. Chiao L. and R. E. Lyon," A fundamental approach to resin cure kinetics ", Journal of Composite Materials, **24**, 739, (1990)
19. M. Hojjati and S. V. Hoa," Curing simulation of thick thermosetting composites ", Composites Manufacturing, **5**, 159, (1994)
20. W. I. Lee, A. C. Loos and G. S. Springer," Heat of reaction, degree of cure and viscosity of hercules 3501-6 resin ", Journal of Composite Materials, **16**, 510, (1982)
21. V. M. Gonzalez-Romero and N. Cassilas," Isothermal and temperature programmed kinetic studies of thermosets ", Polymer Engineering and Science, **29**, 295, (1989)
22. J. Mijovic," Cure kinetics of neat versus reinforced epoxies ", Journal of Applied Polymer Science, **31**, 1177, (1986)
23. S. Wang and A. Garton," The effect of carbon surface functionality on tetrafunctional epoxy rein-diaminodiphenylsulfone cure reactions ", Journal of Applied Polymer Science, **40**, 99, (1990)
24. M.-F. Grenier-Loustalot and P. Grenier," The mechanism of epoxy-resin curing in the presence of glass and carbon fibres ", Polymer, **33**, 1187, (1992)

25. J. Bear, "Dynamics of fluids in porous media", American Elsevier Publishing Company Inc., New York, (1972)
26. J. H. Spurk, "Fluid Mechanics", Springer, Germany, (1997)
27. R. S. Maier, T. F. Rohaly, S. G. Advani and K. D. Fickie, "A fast numerical method for isothermal resin transfer mold filling", International Journal for Numerical methods in Engineering, **39**, 1405, (1996)
28. R. Gauvin, F. Trochu, Y. Lemmen and L. Diallo, "Permeability measurement and flow simulation through fiber reinforcement", Polymer Composites, **18**, 460, (1997)
29. F. R. Phelan, "Simulation of the injection process in resin transfer molding", Polymer Composites, **17**, 34, (1996)
30. A. C. Long, P. J. Blancard, C. D. Rudd and P. Smith, "The development of an integrated process model for liquid composite moulding", Composites Part A, **29A**, 847, (1998)
31. B. Friedrichs and S. I. Guseri, "A hybrid numerical technique to model 3- flow fields in resin transfer moulding", Polymer Engineering and Science, **35**, 1834, (1995)
32. W. B. Young "Three-dimensional non-isothermal mold filling simulations in resin transfer moulding", Polymer Composites, **15**, 118, (1994)
33. A. W. Chan and S. T. Hwang "Modeling resin transfer molding of axisymmetric composite parts", Journal of Materials Processing and Manufacturing Science, **1**, 105, (1992)
34. L. J. Lee, W. B. Young and R. J. Liu "Mold filling and cure modelling of RTM and SRIM processes", Composite Structures, **27**, 109, (1994)
35. K. Velten "Quantitative analysis of the resin transfer molding process", Journal of composite Materials, **32**, 1865, (1998)
36. J. Ni, Y. Zhao. L. J. Lee and S. Nakamura "Analysis of two-regional flow in liquid composite molding", Polymer Composites, **18**, 254, (1997)
37. W. B. Young and C. L. Lai "Analysis of the edge effect in resin transfer molding", Composites Part A, **28A**, 817, (1997)
38 C. J. Wu, L. W. Hourng and J. C. Liao "Numerical and experimental study on the edge effect of resin transfer moulding", Journal of Reinforced Plastics and Composites , **14**, 694, (1995)

39. R. S. Parnas, A. J. Salem, T. A. K. Sadiq, H.-S. Wang and S. G. Advani, "The interaction between micro- and macro-scopic flow in RTM preforms", Composite Structures, **27**, 93, (1994)
40. A. W. Chan and R. J. Morgan, "Tow impregnation during resin transfer molding of bi-directional nonwoven fabrics", Polymer Composites, **14**, 335, (1993)
41. C. Y. Chang, L. W. Hourng and C. J. Wu, "Numerical study on the capillary effect of resin transfer moulding", Journal of Reinforced Plastics and Composites, **16**, 566, (1997)
42. K. M. Pillai and S. G. Advani, "A model for unsaturated flow in woven fiber preforms during mold filling in resin transfer molding", Journal of Composite Materials, **32**, 1735, (1998)
43. J. Taine and J. P. Petit, "Heat Transfer", Prentice Hall, UK, (1993)
44. D. M. Gao, F. Trochu and R. Gauvin, "Heat transfer analysis of non-isothermal resin transfer molding by the finite element method", Materials and Manufacturing Processes, **10**, 57, (1995)
45. R. B. Dessenberger and C. L. Tucker III, "Thermal dispersion in resin transfer moulding", Polymer Composites, **19**, 495, (1995)
46. C. L. Tucker III, "Heat transfer and reaction issues in liquid composite molding", Polymer Composites, **17**, 60, (1996)
47. O. Mal, A. Couniot and F. Dupret, "Non-isothermal simulation of the resin transfer moulding process", Composites Part A, **29A**, 189, (1998)
48. A. Apicella, M. A. Del Nobile, G. Mensitieri, M. Montanino and P. R. Stupak, "Thermal, mechanical and rheological evolution during the processing of multilayer thermosetting composite structures", Composite Structures, **27**, 121, (1994)
49. D. Frank-Susich, D. H. Laananen and Ruffner, "Cure cycle simulation for thermoset composites", Composites Manufacturing, **4**, 139, (1993)
50. A. C. Loos and G. S. Springer, "Curing of epoxy matrix composites", Journal of Composite Materials, **17**, 135, (1983)
51. C. E. Morrison and M. G. Bader, "Computer modelling of resin flow during laminate cure", Composites, **20**, 9, (1989)
52. T. G. Gutowski, T. Morigagi and Z. Cai, "The consolidation of laminate composites", Journal of Composite Materials, **21**, 172, (1987)

53. T. G. Gutowski, Z. Cai, S. Bauer, D. Boucher, J. Kingery and S. Wineman, "Consolidation experimetns for laminate composites", Journal of Composite Materials, **21**, 650, (1987)
54. R. Dave, "A unified approach to modeling resin flow during composite processing", Journal of Composite Materials, **24**, 22, (1990)
55. W. B. Young, "Consolidation and cure simulations for laminated composites", Polymer Composites, **17**, 142, (1996)
56. L. Tredoux and J. Van der Westhuizen, "Development of a numerical code that simulates combined heat transfer, resin flow and compaction during composites processing", Composites Manufacturing, **6**, 85, (1995)
57. D. C. Blest, B. R. Duffy, S. McKee and A. K. Zulkifle, "Curing simulation of thermoset composites", Composites Part A, **30**, 1289, (1999)
58. J. M. Kenny, A. Apicella and L. Nicolais, "A model for the thermal and chemorheological behavior of thermosets. I: Processing of epoxy-based composites", Polymer Engineering and Science, **29**, 973, (1989)
59. V. Plesu, K. Azaar and J. M. Vergnaud, "Effect of the operational conditions on the process of cure of thermoset resins", European Polymer Journal, **29**, 1059, (1993)
60. T. E. Twardowrski, S. E. Lin and P. H. Geil, "Curing in thick composite laminates: Experiments and simulation", Journal of Composite Materials, **27**, 216, (1993)
61. N. Rai and R. Pitchumani, "Optimal cure cycle for the fabrication of Thermosetting-matrix composites", Polymer Composites, **18**, 566, (1997)
62. T. A. Bogetti and J. W. Gillespie, "Two-dimensional cure simulation of thick thermosetting composites", Journal of Composite Materials, **25**, 239, (1991)
63. M. K. Telikichela, M. C. Altan and F. C. Lai, "Autoclave curing of thermosetting composites: Process modeling for the cure assembly", International Communications in Heat and Mass Transfer, **21**, 785, (1994)
64. M. Hojjati and S. V. Hoa, "Model laws for curing of thermosetting composites", Journal of Composite Materials, **29**, 1741, (1995)
65. S. M. Moschiar, M. M. Reboredo, H. Larrondo and A. Vasquez, "Pultrusion of epoxy matrix composites: pulling force model and thermal stress analysis", Polymer Composites, **17**, 850, (1996)

66. R. Gorthala, J. A Roux and J. G. Vaughan, "A model to predict resin pressure/back flow in the tapered inlet of a pultrusion die", Journal of Reinforced Plastics and Composites, **13**, 484, (1994)
67. D. Sharma, T. A. McCarthy, J. A. Roux and J. G. Vaughan, "Investigation of dynamic pressure behavior in a pultrusion die", Journal of Composite Materials, **32**, 929, (1998)
68. K. S. Raper, J. A. Roux, J. G. Vaughan and E. Lackey, "Permeability impact on the pressure rise in a pultrusion die", Journal of Thermophysics and Heat Transfer, **13**, 91, (1999)
69. D. H. Kim, P. G. Han, G. H. Jin and W. I. Lee, "A model for thermosetting pultrusion process", Journal of Composite Materials, **31**, 2105, (1997)
70. M. Giordano and L. Nicolais, "Resin flow in a pultrusion process", Polymer Composites, **18**, 681, (1997)
71. D. Sharma, T. A. McCarthy, J. A. Roux and J. G. Vaughan, "Pultrusion die pressure response to changes in die inlet geometry", Polymer Composites, **19**, 180, (1998)
72. D. Sharma, T. A. McCarthy, J. A. Roux and J. G. Vaughan, "Fluid mechanics analysis of a two-dimensional pultrusion die inlet", Polymer Engineering and Science, **38**, 1611, (1998)
73. S. Voorakaranam, B. Joseph and J. L. Kardos, "Modelling and control of an injection pultrusion process", Journal of Composite Materials, **33**, 1173, (1999)
74. S. M. Moschiar, M. M. Reboredo, J. M. Kenny and A. Vasquez, "Analysis of pultrusion processing of unsaturated polyester resins with glass fibers", Polymer Composites, **17**, 479, (1996)
75. A. G. Gibson, C. Y. Lo, D. W. Lamb and J. A. Quinn, "Understanding the factors controlling the pultrusion process", Plastics and Rubber Processing and Applications, **12**, 191, (1989)
76. S. R. deGroot and P. Mazur, "Non-equilibrium thermodynamics", Dover Publications, New York, (1984)
77. D. Han, D. S. Lee and H. B. Chin, "Development of a model for the pultrusion process", Polymer Engineering and Science, **26**, 393, (1986)

78. D. Han and H. B. Chin, "Development of a mathematical model for the pultrusion of unsaturated polyester resins", Polymer Engineering and Science, **28**, 321, (1988)
79. S. Kommu, B. Khomami and J. L. Kardos, "Modeling of injected pultrusion processes: A numerical approach", Polymer Composites, **19**, 335, (1998)
80. R. M. Hackett and S. Z. Zhu, "Two-dimensional finite element model of the pultrusion process ", Journal of Reinforced Plastics and Composites, **11**, 1322, (1992)
81. S.-Y. Lee and G. S. Springer, "Filament winding cylinders: I. Process model", Journal of Composite Materials, **24**, 1275, (1990)
82. S. C. Mantell and G. S. Springer, "Filament winding process models", Composite Structures, **27**, 141, (1994)
83. Z. Cai and T. Gutowski, "Winding and consolidation analysis for cylindrical composite structures", Journal of Composite Materials, **26**, 1374, (1992)
84. A. Banerjee, L. Sun, S. C. Mantell and D. Cohen, "Model and experimental study of fiber motion in wet filament winding", Composites Part A, **29A**, 251, (1998)
85. S. P. Timoshenko, J. N. Goodier, "Theory of elasticity", MacGraw-Hill, New York, (1970)
86. Z. Cai and T. Gutowski, "The 3-D deformation behavior of a lubricated fiber bundle", Journal of Composite Materials, **26**, 1207, (1992)
87. E. A. Kempner and H. T. Hahn, "Effect of radial stress relaxation on the fibre stress in filament winding of thick composites", Composites Manufacturing, **6**, 67, (1995)
88. H. T. Hahn, E. A. Kempner and S. S. Lee, "The stress development during filament winding of thick cylinders", Composites Manufacturing, **4**, 147, (1993)
89. J. T. Tzeng and A. C. Loos, "A cure analysis for axisymmetric composites", Composites Manufacturing, **4**, 157, (1993)
90. V. N. Korotkov, Y. A. Chekanov and B. A. Rozenberg, "The simultaneous process of filament winding and curing for polymer composites", Composites Science and Technology, **47**, 383, (1993)
91. S. R. White and Z. Zhang, "The effect of mandrel material on the processing-induced residual stresses in thick filament wound composite cylinders", Journal of Reinforced Plastics and Composites, **12**, 698, (1993)

92. J. T. Burwasser and G. S. Springer, "Electrothermal curing of filament wound composite cylinders", Journal of Composite Materials, **22**, 81, (1988)

93. B. C. Chern, T. J. Moon and J. R. Howell, "Thermal analysis of in-situ curing of thermoset, hoop wound structures using infrared heating: Part I-Predictions assuming independent scattering", Journal of Heat Transfer-Transactions of the ASME, **117**, 674, (1995)

94. R. G. C. Arridge and J. H. Speake, "Mechanical relaxation studies of the cure of epoxy resins: 1. Measurement of cure", Polymer, **13**, 443, (1972)

95. J. H. Speake, R. G. C. Arridge and G. J. Curtis, "Measurement of the cure of resins by ultrasonic techniques", Journal of Physics D: Applied Plysics, **7**, 412, (1974)

96. E. P. Papadakis, "Monitoring the moduli of polymers with ultrasound", Journal of Applied Physics, **45**, 1218, (1974)

97. D. D. Shepard and K. R. Shepard, "A new ultrasonic measurement system for the cure monitoring of thermosetting resins and composites", Journal of Thermal Analysis, **49**, 95, (1997)

98. A. Maffezzoli, E. Quarta, V. A. M. Luprano, G. Montagna and L. Nicolais, "Cure monitoring of epoxy matrices for composites by ultrasonic wave propagation", Journal of Applied Polymer Science, **73**, 1969, (1999)

99. A. W. Chow and J. L. Bellin, "Simultaneous acoustic wave propagation and dynamic mechanical analysis of curing of thermoset resins", Polymer Engineering and Science, **32**, 182, (1992)

100. R. T. Harrold and Z. N. Sanjana, "Acoustic waveguide monitoring of the cure and structural integrity of composite materials", Polymer Engineering and Science, **26**, 367, (1986)

101. B. Mitra and D. J. Booth, "Remote cure monitoring of epoxy materials using optical techniques", Ultrasonics, **53**, 569, (1998)

102. R. J. Freemantle and R. E. Challis, "Combined compression and shear wave ultrasonic measurements on curing adhesive" Measurement Science and Technology, **9**, 1291, (1998)

103. M. Younes, S. Watrewing, D. Lellinger, B. Strehmel and V. Strehmel, "The curing of epoxy resins as studied by various methods", Polymer, **35**, 5269, (1994)

104.S. I. Rokhlin and E. Segal, "Study of the cure kinetics of structural adhesives by ultrasonic interface waves", Journal of Materials Science, **20**, 3300, (1985)

105.T. M. Whitney and R. E. Green Jr, "Cure monitoring of carbon epoxy composites: An application of resonant ultrasound spectroscopy", Ultrasonics, **34**, 347, (1996)

106.Y. M. Liu, G. Ganesh, J. P. H. Steele and J. E. Jones "Fiber optic sensor development for real time in-situ epoxy cure monitoring", Journal of Composite Materials, **31**, 87, (1997)

107.G. A. George, P. Cole-Clarke, N. St John and G. Friend "Real-time monitoring of the cure reaction of a TGDDM/DDS epoxy resin using fiber optic FT-IR", Journal of Applied Polymer Science, **42**, 643, (1991)

108.J. Mijovic and S. Andjelic "Monitoring of reactive processing by remote mid infra-red spectroscopy", Polymer, **37**, 1295, (1996)

109.J. Mijovic and S. Andjelic "In situ real-time monitoring of reactive systems by remote fibre-optic near-infra-red spectroscopy", Polymer, **36**, 3783, (1995)

110.S. Cossins, M. Connel, B. Cross, R. Winter and J. Kellar "In-situ near-IR cure monitoring of a model epoxy matrix composite", Applied Spectroscopy, **50**, 900, (1996)

111.J. Mijovic and S. Andjelic "A study of reaction kinetics by near-infrared spectroscopy. 1. Comprehensive analysis of a model epoxy/amine system", Macromolecules, **28**, 2787, (1995)

112.G. F. Fernando, T. Liu, P. Crosby, C. Doyle, A. Martin, D. Brooks, B. Ralph and R. Badcock "A multi-purpose optical fibre sensor design for fibre reinforced composite materials", Measurement Science and Technology, **8**, 1065, (1997)

113.L. Xu and J. R. Schlup "Application of near-infrared attenuated total reflectance spectroscopy for monitoring epoxy resin/amine cure reactions", Applied Spectroscopy, **50**, 109, (1996)

114.J. R. Dunkers, K. M. Flynn and R. S. Parnas "A mid-infrared attenuated total internal reflection cure sensor for control of resin transfer moulding of a pre-ceramic polymer", Composites, **28A**, 163, (1997)

115.J. R. Dunkers, K. M. Flynn, M. T. Huang and W. McDonough "Fourier transform near-infrared monitoring of reacting resins using an evanescent wave high-index fiber-optic sensor", Applied Spectroscopy, **52**, 552, (1998)

116.G. A. George, G. A. Cash and L. Rintoul "Cure monitoring of aerospace epoxy resins and prepregs by Fourier transform infrared emission spectroscopy", Polymer International, **41**, 169, (1996)

117.B. G. Min, Z. H. Stachurski, J. H. Hodgkin and G. R. Heath "Quantitative analysis of the cure reaction of DGEBA/DDS epoxy resins without and with thermoplastic polysulfone modifier using near-infrared spectroscopy", Polymer, **34**, 3620, (1993)

118.W. Brugel, "An introduction to infrared spectroscopy", Methuen and Co Ltd, London, (1962)

119.A. M. Skith "Materials interaction in optical fiber sensors", in *Optical fiber sensors: Principles and components, by J. Dakin and B. Culshaw,* Vol. 1, Chapter 6, Artech House Inc., London, (1988)

120.J. D. Graybeal, "Molecular spectroscopy", MacGraw-Hill, New York, (1988)

121.B. Sandner, S. Kammer and S. Wartewig "Crosslinking copolymerization of epoxy methacrylates as studied by Fourier transform Raman spectroscopy", **37**, 4705, (1996)

122.R. E. Lyon, K. E. Chike and S. M. Angel "In situ cure monitoring of epoxy resins using fiber –optic Raman spectroscopy", Journal of Applied Polymer Science, **53**, 1805, (1994)

123.F. W. Wang, R. E. Lowry and B. M. Fanconi "Novel fluorescence method for cure monitoring of epoxy resins", Polymer, **27**, 1529, (1986)

124.A. Stroeks, M. Shmorhum, A. M. Jamieson and R. Simha "Cure monitoring of epoxy resins by excimer fluorescence", Polymer, **29**, 467, (1988)

125.R. L. Levy and S. D. Schwab "Monitoring the composite curing process with a fluorescence-based fiber-optic sensor", Polymer Composites, **12**, 96, (1991)

126.F. W. Wang and E. Wu "Cure monitoring of epoxy resins by fluorescence recovery after photobleaching", Polymer Communications, **28**, 73, (1987)

127.W. Dang and N. H. Sung "In-situ cure monitoring of diamine cured epoxy by fiber-optic fluorimetry using extrinsic reactive fluorophore", Polymer Engineering and Science, **34**, 707, (1994)

128.D. L. Woederman, K. M. Flynn, J. P. Dunkers and R. S. Parnas "The use of evanescent wave fluorescence spectroscopy for control of the liquid molding process", Journal of Reinforced Plastics and Composites, **15**, 922, (1996)

129.D. L. Woederman, J. K. Spoerre, K. M. Flynn and R. S. Parnas "Cure monitoring of the liquid composite molding process using fiber optic sensors", Polymer Composites, **18**, 133, (1997)

130.R. A. Neff, D. L. Woederman, and R. S. Parnas "Use of charged coupled device (CCD) camera for evanescent wave optical fiber cure monitoring of liquid composite molding resins", Polymer Composites, **18**, 518, (1997)

131.H. Frohlich, "Theory of dielectrics. Dielectric constant and dielectric loss", Clarendon Press, Oxford, (1949)

132.S. Havriliak Jr. and S. J. Havriliak, "Dielectric and mechanical relaxation in materials. Analysis, interpretation and application to polymers", Hanser Publishers, Munich, (1997)

133.I. D. Raistrik, J. R. Macdonald and D. R. Franceschetti, "The electrical analogs of physical and chemical processes ", in *Impedance spectroscopy: Emphasizing solid materials and systems* by J. R. Macdonald, Chapter 2.1, John Wiley & Sons Inc., USA, (1987)

134.P. Hedvig, "Dielectric spectroscopy of polymers", Adama Hilger Ltd, Bristol, (1977)

135.S. D. Senturia and N. F. Sheppard Jr, "Dielectric analysis of thermoset cure", Advances in Polymer Science, **80**, 1, (1986)

136.J. M. Kenny, A. Trivisano and L. A. Berglund, "Chemorheological and dielectric behavior of the epoxy matrix in a carbon fiber prepreg", SAMPE Journal, **27**, 39, (1991)

137.M. B. M. Mangion and G. P. Johari, "Relaxations in thermosets. IX Ionic conductivity and gelation of DGEBA-based thermosets cured with pure and mixed amines", Journal of Polymer Science: Part B: Polymer Physics, **29**, 1177, (1991)

138.J. Mijovic and F. C. W. Yee, "Use of complex impedance to monitor the progress of reactions in epoxy/amine model systems", Macromolecules, **27**, 7287, (1994)

139.D. Kranbuehl, S. Delos, E. Yi, J. Mayer and T. Jarvie, "Dynamic dielectric analysis: Nondestructive material evaluation and cure cycle monitoring", Polymer Engineering and Science, **26**, 338, (1986)

140.F. Bellucci, M. Valentino, T. Monneta, L. Nicodemo, J. Kenny, L. Nicolais and J. Mijovic, "Impedance Spectroscopy of Reactive Polymers. 2. Multifunctional epoxy/amine formulations", Journal of Polymer Science: Part B: Polymer Physics, **33**, 433, (1995)

141.J. Mijovic, J. M. Kenny, A. Maffezzoli, A. Trivisano, F. Bellucci and L. Nicolais, "The principles of dielectric measurements for in situ monitoring of composite processing", Composites Science and Technology, **49**, 277, (1993)

142.P. R. Ciriscioli and G. S. Springer, "Dielectric cure monitoring - A critical Review", SAMPE Journal, **25**, 35, (1989)

143.V. Adamec, "Electrical properties of an epoxy resin during and after cure", Journal of Polymer Science, **10A**, 1277, (1972)

144.D. R. Day, T. J. Lewis, H. L. Lee and S. S. Senturia, "The role of boundary layer capacitance at blocking electrodes in the interpretation of dielectric cure data in adhesives", Journal of Adhesion, **18**, 73, (1985)

145.V. Adamec and J. H. Calderwood, "Electrode Polarization in polymer dielectrics", IEEE Transactions on Electrical Insulation, **24**, 205, (1989)

146.F. Bellucci, M. Valentino, T. Monneta, L. Nicodemo, J. Kenny, L. Nicolais and J. Mijovic, "Impedance Spectroscopy of Reactive Polymers. 1", Journal of Polymer Science: Part B: Polymer Physics, **32**, 2519, (1994)

147.J. O. Simpson and S. A. Bistrup, "Rheological and dielectric changes during isothermal epoxy-amine cure", Journal of Polymer Science: Part B: Polymer Physics, **33**, 55, (1995)

148.K. A. Nass and J. C. Seferis, "Analysis of the dielectric response of thermosets during isothermal and nonisothermal cure", Polymer Engineering and Science, **29**, 315, (1989)

149.D. R. Day, "Dielectric determination of cure state during non-isothermal cure", Polymer Engineering and Science, **29**, 334, (1989)

150.J. Mijovic, S. Andjelic, B. Fitz, W. Zurawsky, I. Mondragon, F. Bellucci and L. Nicolais, "Impedance spectroscopy of reactive polymers. 3. Correlations between dielectric, spectroscopic and rheological properties curing cure of a trifunctional epoxy resin", Journal of Polymer Science: Part B: Polymer Physics, **34**, 379, (1996)

151.A. Maffezzoli, A. Trivisano, M. Opalicki, J. Mijovic and J. M. Kenny, "Correlation between dielectric and chemorheological properties during cure of epoxy-based composites", Journal of Materials Science, **29**, 800, (1994)

152.G. Levita, A. Livi, P. A. Rolla and C. Culicchi, "Dielectric monitoring of epoxy cure", Journal of Polymer Science: Part B: Polymer Physics, **34**, 2731, (1996)

153.D. Lairez, J. R. Emery, D. Durrand, D. Hayward and R. A. Pethrick, "Real time dielectric measurements of network formation in a crosslinked epoxy resin system", Plastics, Rubber and Composites Processing and Applications, **16**, 231, (1991)

154.G. Boiteux, P. Dublineau, M. Feve, C. Mathieu, G. Seytre and J. Ulanski, "Dielectric and viscoelastic studies of curing epoxy-amine model systems", Polymer Bulletin, **30**, 441, (1993)

155.S. Andjelic, J. Mijovic and F. Bellucci, "Impedance spectroscopy of reactive polymers. 5. Impedance as a measure of chemical and physical changes in glass formers", Journal of Polymer Science: Part B: Polymer Physics, **36**, 641, (1998)

156.D. E. Kranbuehl, P. Kingsley, S. Hart, G. Hasko, B. Dexter and A. C. Loos, "In situ sensor monitoring and intelligent control of the resin transfer molding process", Polymer Composites, **15**, 299, (1994)

157.G. M. Maistros and I. K. Partridge, "Dielectric monitoring of cure in a commercial carbon-fibre composite", Composites Science and Technology, **53**, 355, (1995)

158.G. M. Maistros and I. K. Partridge, "Monitoring autoclave cure in commercial carbon fibre/epoxy composites", Composites, **29B**, 245, (1998)

159.J.-S. Kim and D. G. Lee, "On-line cure monitoring and viscosity measurement of carbon fiber epoxy composite materials", Journal of Materials Processing Technology, **37**, 405, (1993)

160.D. Abraham and R. McIlhager, "Glass fibre epoxy composite cure monitoring using parallel plate dielectric analysis in comparison with thermal and mechanical testing techniques", Composites, **29A**, 811, (1998)

161.D. J. Melotik, M. Czaplicki, T. J. Whalen and D. R. Day, "Analysis of the resin transfer molding process using in-mold dielectric sensors", Thermochimica Acta, **217**, 251, (1993)

162.J. M. Methven and Y. Katramados, "In-line quality monitoring of pultruded profiles using dielectric measurements", Polymers and Polymer Composites, **5**, 15, (1997)

163.F. Stephan, X. Duteurtre and A. Fit, "In-process control of epoxy composite by microdielectrometric analysis. Part II: On-line real-time dielectric measurements during a compression molding process", Polymer Engineering and Science, **38**, 1566, (1998)

164.G. Lebrun, R. Gauvin and K. N. Kendall, "Experimental investigation of resin temperature and pressure during filling and curing in a flat steel RTM mould", Composites, **27A**, 347, (1996)

165.P. R. Ciriscioli, Q. Wang and G. S. Springer, "Autoclave curing-comparisons of model and test results", Journal of Composite Materials, **26**, 90, (1992)

166.C. Kim, H. Teng, C. L. Tucker III and S. R. White, "The continuous curing process for thermoset polymer composites. Part 1: Modeling and demonstration", Journal of Composite Materials, **29**, 1222, (1995)

167.P. R. Ciriscioli and G. S. Springer, "An expert system for autoclave curing of composite", Journal of Composite Materials, **25**, 1542, (1991)

168.J. H. Choi and D. G. Lee, " Expert cure system for the carbon fiber epoxy composite materials", Journal of Composite Materials, **29**, 1181, (1995)

169.V. Pillai, A. N. Beris and P. Dhurjati, "Intelligent curing of thick composites using a knowledge-based system", Journal of Composite Materials, **31**, 22, (1997)

170.M. J. Perry, L. J. Lee and C. W. Lee, "On-line cure monitoring of epoxy/graphite composites using scaling analysis and a dual heat flux sensor", Journal of Composite Materials, **26**, 274, (1992)

171.L. Lai, G. Garman, S. Chiou, P. Kukuchek and D. Echternach, "Processing monitoring of carbon/phenolic composites using smart sensors", Smart Materials and Structures, **4**, 118, (1995)

172.P. Ferland, D. Guittard and F. Trochu, "Concurrent methods for permeability measurement in resin transfer molding", Polymer Composites, **17**, 149, (1996)

173.J. Mogavero and S. G. Advani, "Experimental investigation of flow through multi-layered preforms", Polymer Composites, **18**, 649, (1997)

174.A. W. Chan, D. E. Larive and R. J. Morgan, "Anisotropic permeability of fiber preform: Constant flow measurement", Journal of Composite Materials, **27**, 996, (1993)

175.B. R. Gebart and P. Lidström, "Measurement of in-plane permeability of anisotropic fiber reinforcements", Polymer Composites, **17**, 43, (1996)

176.A. Hammami, F. Trochu, R. Gauvin and S. Wirth, "Directional permeability measurement of deformed reinforcement", Journal of Reinforced Plastics and Composites, **15**, 552, (1996)

177.C. D. Rudd, A. C. Long, P. McGeehin and P. Smith, "In-plane permeability determination for simulation of liquid composite molding of complex shapes", Polymer Composites, **17**, 52, (1996)

178.D. R. Calchoun, S. Yalvac, D. G. Wetters and C. Å. Raeck, "Critical issues in model verification for the resin transfer molding process", Polymer Composites, **17**, 11, (1996)

179.T. S. Lundstrom, R. Stenberg, R. Bergstrom, H. Partanen and P.-A. Birkeland, "In-plane permeability measurements: a nordic round-robin study ", Composites, **31A**, 29, (2000)

180.S. D. Schwab, R. L. Levy and G. G. Glover, "Sensor system for monitoring impregnation and cure during resin transfer molding", Polymer Composites, **17**, 312, (1996)

181.D. D. Shepard, "Resin flow front monitoring saves money and improves quality", SAMPE Journal, **34**, 31, (1998)

182.M. L. Diallo, R. Gauvin and F. Trochu, "Experimental analysis and simulation of flow through multi-layer fiber reinforcements in liquid composite moulding", Polymer Composites, **19**, 246, (1998)

183.J. R. Weitzenbock, R. A. Shenoi and P. A. Wilson, "Measurement of three-dimensional permeability", Composites, **29A**, 159, (1998)

184.P. Barooah, B. Berker and J. Q. Sun, "Lineal sensors for liquid injection molding of advanced composite materials", Journal of Materials Processing and Manufacturing Science, **6**, 169, (1998)

185.R. Mathur, S. G. Advani, R. S. Parnas and B. K. Fink, "Evanescent wave fluorescence fiber optic flow sensor for resin transfer molding", *Proceedings of the 29th SAMPE Technical Conference,* (Orlando, USA), (1997)

186.R. W. Lewis, K. Morgan, H. R. Thomas and K. N. Seetharamu, "The finite element method in heat transfer analysis", John Wiley & Sons Ltd, England, (1996)

187.A. J. Nowak, "Inverse thermal problems", Adama Hilger Ltd, Bristol, (1996)

188.D. Angirasa and G. P. Peterson, "Upper and lower Rayleigh number bounds for two-dimensional natural convection over a finite horizontal surface situated in a fluid-saturated porous medium", Numerical Heat Transfer Part A, **33**, 477, (1998)

189.J. A. Holmberg, "Influence of post cure and chemical shrinkage on springback of RTM U-beams", SICOMP Technical Report 97-004, (1997)

190.O. C. Zienkiewicz, "The finite element method", McGraw-Hill Ltd., UK, (1977)

191.O. C. Zienkiwicz and C. J. Parekh, "Transient field problems: Two-dimensional and three-dimensional analysis by isoparametric finite elements", International Journal for Numerical methods in Engineering, **2**, 61, (1970)

192.W. L. Wood, "Practical time-stepping schemes", Clarendon Press, Oxford, (1990)

193.J. C. Bruch and G. Zyvoloski, "Transient two dimensional heat conduction problems solved by the finite element method", International Journal for Numerical methods in Engineering, **8**, 481, (1974)

194.J. Ronda, O. Mahrenholtz and R. Hamman, "Quality of the TF-3D. A new FEM solver of nonlinear heat transfer problem", Numerical Heat Transfer Part B, **22**, 25, (1992)

195.J. M. Barton, "The application of differential scanning calorimetry (DSC) to the study of epoxy resin curing reactions", Advances in Polymer Science, **72**, 112, (1985)

196.I. Hamerton, "Recent developments in epoxy resins", RAPRA Review Reports, **8**, 7, (1996)

197.U. Bandara, "A systematic solution to the problem of sample background correction in DSC curves", Journal of Thermal Analysis, **31**, 1063, (1986)

198.G. Van Assche, A. Van Hemelrijck, H. Rahier and B. Van Mele, "Modulated differential scanning calorimetry: Non-isothermal cure, vitrification and devitrification of thermosetting systems", Thermochimica Acta, **286**, 209, (1996)

199.R. Serra, J. Sempere and R. Nomen, "A new method for the kinetic study of thermoanalytical data: The non-parametric kinetics method", Thermochimica Acta, **316**, 37, (1998)

200.M. Schimbo, M. Ochi and Y. Shigeta, "Shrinkage and internal stress during curing of epoxy resins", Journal of Applied Polymer Science, **26**, 2265, (1981)

201.T. A. Bogetti and J. W. Gillespie "Process induced stress and deformation in thick section thermoset composite laminates", Journal of Composite Materials, **26**, 626, (1992)

202.D. E. Bowles and O. H. Griffin "Micromechanics analysis of space simulated thermal stresses in composites. Part II: Multidirectional laminates and failure predictions", Journal of Composite Materials, **26**, 626, (1992)

203.P. S. Gill, S. R. Sauerbrunn and M. Reading, "Modulated differential scanning calorimetry", Journal of Thermal Analysis, **40**, 931, (1993)

204.M. Reading, D. Elliot and V. L. Hill, "A new approach to the calorimetric investigation of physical and chemical transitions", Journal of Thermal Analysis, **40**, 949, (1993)

205.A. A. Lacey, C. Nikolopoulos and M. Reading, "A mathematical model for modulated differential scaning calorimetry", Journal of Thermal Analysis, **50**, 279, (1997)

206.A. Boller, Y. Jin and B. Wunderlich, "Heat capacity measurement by modulated DSC at constant temperature", Journal of Thermal Analysis, **42**, 307, (1994)

207.M. Reading, A. Luget and R. Wilson, "Modulated differential scanning calorimetry", Thermochimica Acta, **238**, 295, (1994)

208.M. Varma-Nair, Y. Jin and B. Wunderlich "Non isothermal heat capacities and chemical reaction using a modulated DSC", Journal of Thermal Analysis, **46**, 879, (1996)

209.H. S. Carslaw and J. C. Jaeger, "Conduction of heat in solids", Oxford University Press, UK, (1959)

210.I. N. Sneddon, "Special functions of mathematical physics and chemistry", Oliver and Boyd Ltd., Holland, (1956)

211.Q. C. Ning and T. W. Chou, "A closed-form solution of the transverse effective thermal conductivity of woven fabric composites", Journal of Composite Materials, **29**, 2280, (1995)

212.J. P. Van Den Brink and M. H. M. Rongen, "Thermal conductivity of glasses at high temperatures", in *Thermal Conductivity 22* by T. W. Tong, p 70, Technomic Publishing, USA, (1994)

213.T. Yamane, S. Katayama, M. Todoki and I. Hatta, "The measurements of thermal conductivity of carbon fibers", in *Thermal Conductivity 22 by T. W. Tong*, p 313, Technomic Publishing, USA, (1994)

214.J. D. Farmer and E. E. Covert, "Thermal conductivity of a thermosetting advanced composite during its cure", Journal of Thermophysics and Heat Transfer, **10**, 467, (1996)

215.J. L. White and B. A. Knutsson, "Theory of thermal conductivity, heat conduction and convective heat transfer in fiber filled polymer composites", Polymer Engineering Reviews, **2**, 71, (1982)

216.R. C. Progelhof, J. L. Throne and R. R. Ruetsch, "Methods for predicting the thermal conductivity of composite systems: A review", Polymer Engineering and Science, **16**, 615, (1972)

217.G. P. Peterson and L. S. Fletcher, "A review of thermal conductivity in composite materials", AIAA Reports, **1586**, (1987)

218.G. Williams, I. K. Smith, P. A. Halmes and S. Varma, "Real-time dielectric studies of polymerizing systems", Journal of Physics: Condensed Matter, **11**, 57, (1999)

219.J. B. Bates and Y. T. Chu, "Electrode-electrolyte interface impedance: Experiments and model", Annals of Biomedical Engineering, **20**, 349, (1992)

220.J. C. Wang, "Model for impedance of a solid ionic conductor sandwiched between blocking electrodes", Electrochimica Acta, **38**, 2111, (1993)

221.R. Zallen, "The physics of amorphous solids", John Wiley & Sons Inc., USA, (1983)

222.M. Mitchell, "An introduction to genetic algorithms", MIT Press, USA, (1998)